

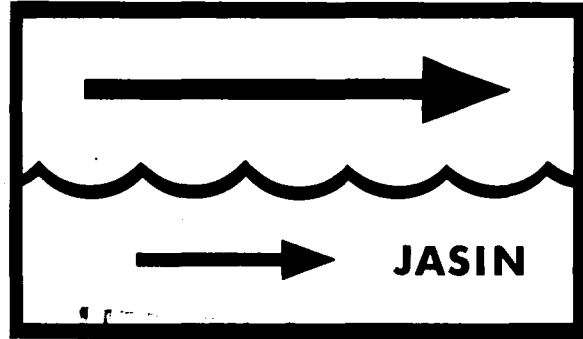
NASA-CR-164,360

JPL PUBLICATION 80-62, VOLUME I

NASA-CR-164360
19810016147

Seasat-JASIN Workshop Report

Volume I: Findings and Conclusions



LIBRARY COPY

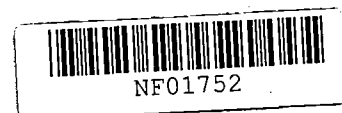
JUN 11 1985

LANGLEY RESEARCH CENTER
LIBRARY, NASA
HAMPTON, VIRGINIA

December 1980

National Aeronautics and
Space Administration

Jet Propulsion Laboratory
California Institute of Technology
Pasadena, California



JPL PUBLICATION 80-62, VOLUME I

Seasat-JASIN Workshop Report

Volume I: Findings and Conclusions

December 1980

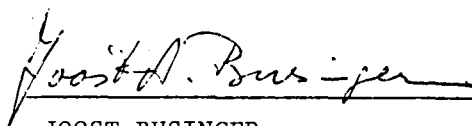
National Aeronautics and
Space Administration

Jet Propulsion Laboratory
California Institute of Technology
Pasadena, California

N81-24682[#]

The research described in this publication was carried out by the Jet Propulsion Laboratory, California Institute of Technology, under contract with the National Aeronautics and Space Administration.

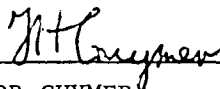
Officers of the Seasat-JASIN Workshop



JOOST BUSINGER
Workshop Co-chairman
University of Washington



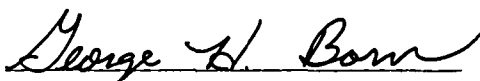
ROBERT H. STEWART
Workshop Co-chairman
Scripps Institution of
Oceanography and Jet
Propulsion Laboratory



TREVOR GUYMER
JASIN Data Manager
Institute of Oceanographic
Sciences



DAVID B. LAME
Workshop Manager
Jet Propulsion Laboratory



GEORGE H. BORN
Evaluation Manager
Jet Propulsion Laboratory

This Page Intentionally Left Blank

FOREWORD

This report documents the results of a Seasat-JASIN workshop which was held in Pasadena, California, during 18-26 March 1980. This workshop was the third major Seasat evaluation workshop.

The Joint Air-Sea Interaction (JASIN) Experiment was a UK-led multinational experiment that took place off the coast of Scotland in the summer of 1978. This experiment involved over 10 years of planning with ships, aircraft, buoys, radio-sondes, tethered balloons, satellites, etc., from nine nations collecting and exchanging data. The analysis of the data from this successful undertaking will be an ongoing effort for many years.

The Seasat Project was a US effort with the goal of proving the concept of a dedicated ocean surveillance satellite with a multiplicity of sensors operating in the microwave regime. The satellite was launched in June 1978 and suffered a catastrophic failure in the power system in October 1978. Fortunately, most of the original proof-of-concept goals can still be met with the data collected in the limited satellite lifetime.

Preliminary planning of the Seasat-JASIN workshop began in the early spring of 1979 with the selection of the key workshop participants. Detail planning then began in June 1979 with a meeting of the principals at the University of Washington. Two additional major sessions were convened at the Institute of Oceanographic Sciences in October 1979 and January 1980. The University of Washington, the Institute of Oceanographic Sciences, and JPL were the principals in the processing of the JASIN data. The Seasat data was provided primarily by the Seasat Evaluation Task Groups and the Algorithm Development Task Group at JPL.

The first volume of this seven-volume report contains the results and conclusions derived from the workshop. The succeeding volumes (II through VII) contain most of the data used in the workshop. The supplementary data volumes are available upon request in microfiche format.

ACKNOWLEDGMENTS

From the UK, the support and encouragement of Henry Charnock and Raymond Pollard for this joint Seasat-JASIN workshop were crucial to its success. Likewise, for the US, Stanley Wilson and Patrick Rygh provided the necessary guidance and backing for the workshop.

The team formed to prepare the JASIN data for comparison with Seasat data performed magnificently. They accomplished years of work in a few months. This team was guided by Joost Businger and was led by Trevor Guymer. Peter Taylor was responsible for the radiosonde processing; Timothy Liu for the sea-surface temperatures; Robert Brown and Arnie Hansen for the large-scale wind fields; Mark Albright for the small-scale wind fields; Trevor Guymer, Alan Macklin, Mark Albright, Arnie Hansen, and Jim Anderson for the initial reformatting, intercomparing, and organizing the data set; Chuck Klose, Debbie Hagar, Gregg Cowdery, and Jim Brown for the data base development, merging, and comparison processing.

The Seasat data was prepared under the guidance of Richard Lipes, Linwood Jones, Byron Tapley, and Robert Stewart for the SMMR, SASS, ALT, and SAR, respectively. Once again, Dale Boggs and Emedio Bracalente provided an outstanding set of SASS products on an extremely short schedule. Barbara Wind was instrumental in generating the SMMR data. Jack Lorell organized the ALT data production. Walter Brown supervised the JPL SAR data effort.

Most all of the data was processed, merged, compared, and displayed by the ADF Operations Team under the supervision of John Swift and Dawn Sexton. They devoted 25 hours a day, 8 days a week for almost two months to this effort.

The interactive display capability so heavily used at the workshop was the result of intensive development efforts by Russ Coons, Suzi Ben-Chorin, and David Coons.

The organization of the support facilities at the workshop that so enhanced the technical accomplishments was in the capable hands of Inge Jefferies. The excellent documentation support of the workshop was led by Harold Yamamoto.

WORKSHOP PANEL MEMBERS

SASS

W. L. Jones, Leader
D. H. Boggs
E. M. Bracalente
J. W. Brown
R. A. Brown
G. Dome
I. M. Halberstam
B. Hinton
M. M. Holl
J. L. Mitchell
S. Peteherych
W. J. Pierson
J. S. Satran
G. Schacher
D. Schelton
L. C. Schroeder
J. L. Sweet
F. J. Wentz
J. C. Wilkerson
P. M. Woiceshyn
M. G. Wurtele

SMMR

R. G. Lipes, Leader
R. A. Brown
V. J. Cardone
T. J. Chester
E. J. Christensen
C. Gautier
T. Guymer
K. B. Katsaros
T. Liu
A. Milman
E. G. Njoku
A. L. Riley
P. W. Rosenkranz
P. K. Taylor
F. J. Wentz
T. T. Wilheit
B. B. Wind

ALT

B. D. Tapley, Leader
G. H. Born
J. Lorell
M. E. Parke
M. A. Richards

SAR

R. H. Stewart, Leader
B. M. Holt
R. Shuchman
T. W. Thompson
J. F. Vesecky

JASIN

T. Guymer, Leader
M. D. Albright
J. J. Anderson
J. W. Brown
R. A. Brown
G. V. Cowdery
D. A. Hagar
A. M. Hansen
J. C. Klose
T. W. Liu
S. A. Macklin
P. K. Taylor

This Page Intentionally Left Blank

CONTENTS

VOLUME I: FINDINGS AND CONCLUSIONS

I.	INTRODUCTION	1-1
II.	JASIN DATA PROCESSING	2-1
A.	INTRODUCTION	2-1
B.	JASIN OVERVIEW	2-1
	1. Oceanography	2-1
	2. Aircraft	2-9
	3. Ships and Buoys	2-9
	4. Meteorological Conditions	2-18
C.	ANALYSIS OF SURFACE DATA	2-18
	1. Availability of Data	2-18
	2. Initial Procedures	2-26
	3. Intercomparison Analysis	2-26
	4. Absolute Calibration of W2	2-41
	5. Summary of Surface Data Analysis	2-44
D.	ANALYSIS OF RADIOSONDE DATA	2-44
	1. Available Data	2-44
	2. Characteristics of Each Data Set	2-45
	3. Estimate of Radiosonde Errors	2-46
E.	ANALYSIS OF WAVE DATA	2-61
	1. Introduction	2-61
	2. Methods	2-61
	3. Summary of the Intercomparisons	2-64
	4. The JASIN Wave Field	2-68

F.	JPL PROCESSING OF JASIN OBSERVATIONS	2-68
1.	Surface	2-68
2.	Radiosonde	2-72
	REFERENCES	2-73
III.	SEASAT DATA PROCESSING	3-1
A.	INTRODUCTION	3-1
B.	SCATTEROMETER	3-1
C.	SCANNING MULTICHANNEL MICROWAVE RADIOMETER	3-1
D.	ALTIMETER	3-4
E.	SYNTHETIC APERTURE RADAR	3-5
IV.	SASS PANEL REPORT	4-1
A.	INTRODUCTION	4-1
B.	SASS CELL MATCHING	4-6
1.	SASS Cell Pairing	4-6
2.	SASS Cell Binning	4-9
C.	SASS ATMOSPHERIC ATTENUATION	4-9
1.	Comparison of Kansas and Wentz Attenuation	4-9
2.	Dependence of Atmospheric Attenuation Calculation on Sea-Surface Temperature and Wind Speed	4-10
D.	MODEL FUNCTION SUBPANEL	4-11
1.	Introduction	4-11
2.	The Boulder Workshop	4-12
3.	Pre-JASIN Workshop	4-12
4.	JASIN Workshop	4-20
E.	SASS/SURFACE TRUTH WIND VECTOR COMPARISONS SUBPANEL	4-38
1.	SASS/Surface Observation Data Quality Assessment	4-38
2.	SASS/60-Min Autologgers Comparisons	4-40

3.	Comparison of Wind Direction Errors for Different Polarization Pair Combinations	4-44
4.	Comparison of SASS Estimates and Surface Observations of the Wind Vector	4-47
5.	Comparison of SASS Estimates and Analysis of Surface Wind Fields	4-53
F.	SASS WIND DIRECTION AMBIGUITY REMOVAL SUBPANEL	4-61
1.	Introduction	4-61
2.	Data Set	4-61
3.	Procedure	4-61
4.	Results of Evaluation	4-63
5.	Summary, Conclusions, and Recommendations	4-71
G.	SASS ANOMALIES SUBPANEL	4-73
1.	SASS Anomaly Study	4-73
2.	Analysis of Surface and Upper Air Data for Revs 556 and 557	4-75
3.	SASS σ^0 Analysis	4-75
4.	Post-Workshop Analysis	4-79
H.	CONCLUSIONS	4-83
	REFERENCES	4-85
	BIBLIOGRAPHY	4-86
V.	SMMR PANEL REPORT	5-1
A.	INTRODUCTION AND OVERVIEW	5-1
B.	DEVELOPMENTS IN SMMR ALGORITHMS	5-4
1.	Sensor File Algorithm Development	5-4
2.	Geophysical File Development	5-8

C.	ATMOSPHERIC WATER EVALUATIONS	5-26
1.	JASIN Area Evaluations of Integrated Water Vapor . . .	5-26
2.	JASIN Area Evaluation of Liquid Water and Precipitation Predictions	5-32
3.	Tropical Area Evaluation of Integrated Water Vapor . .	5-38
4.	Tropical Area Liquid Water and Precipitation Algorithm Intercomparison	5-38
D.	SURFACE WIND SPEED EVALUATIONS	5-47
E.	SEA-SURFACE TEMPERATURE EVALUATIONS	5-52
1.	JASIN Area Evaluations	5-52
2.	Northwest Pacific Area Evaluations	5-65
3.	Tropical Area Evaluations	5-73
F.	SMMR AND SASS INTERCOMPARISON	5-73
1.	Case Study of Thunderstorms in JASIN	5-73
2.	Relative Bias Between SMMR and SASS Wind Determinations	5-79
G.	CONCLUSIONS AND SUMMARY	5-81
1.	Atmospheric Water Determinations	5-81
2.	Wind Determinations	5-81
3.	SST Determinations	5-81
4.	Sensor File Algorithm Development	5-82
5.	Assessment of SMMR Algorithm Status	5-82
H.	RECOMMENDED DIRECTIONS FOR SMMR EVALUATION ACTIVITIES . . .	5-83
1.	General Remarks	5-83
2.	The Problem of Large T_B Biases	5-83
3.	Possible Approaches to Eliminating Large T_B Biases . .	5-85
VI.	ALTIMETER WIND EVALUATION	6-1

VII. SAR PANEL REPORT	7-1
A. INTRODUCTION	7-1
B. ABILITY OF SAR TO OBSERVE OCEAN WAVES	7-2
C. LARGE FEATURES IN THE IMAGES	7-3
D. SHIPS	7-4
E. MEASUREMENTS OF WIND SPEED USING SAR	7-4
F. DOCUMENTATION OF THE SAR SYSTEM	7-5

APPENDICES

A. DETAILS OF WMO COMPARISONS	A-1
B. THERMAL EFFECTS IN THE SMMR	B-1
C. DESCRIPTION OF WORK ON CALIBRATION ALGORITHMS	C-1
D. A COMPARISON OF SATELLITE AND SEA SURFACE MEASUREMENTS OF SIGNIFICANT WAVE HEIGHT	D-1
E. A COMPARISON OF SEASAT-1 MEASUREMENTS OF WAVE HEIGHT WITH MEASUREMENTS MADE BY A PITCH-ROLL BUOY - PRELIMINARY REPORT	E-1
F. REMOTE SENSING OF THE OCEAN WAVEHEIGHT SPECTRUM USING SYNTHETIC-APERTURE-RADAR IMAGES	F-1
G. SEASAT-JASIN WORKSHOP SURFACE TRUTH USER'S GUIDE	G-1

Figures

2-1. The JASIN Area in Relation to the British Isles	2-2
2-2. Ship and Aircraft Timetable	2-3
2-3. The Five Regions in the JASIN Experimental Area	2-5
2-4. Areas of Ship Operation	2-6
2-5. Moorings in the Large Scale Area	2-7
2-6. Moorings in the Fixed Intensive Array	2-8
2-7. Meteorological Instrumentation on Ships	2-10
2-8. Meteorological Instrumentation on Buoys	2-12
2-9. Surface Meteorological Measurements	2-14

2-10.	Radiosonde Launches	2-15
2-11.	Daily Weather Maps	2-19
2-12.	Fifteen-min Averages of Vector Wind Speed, Direction, and Air Temperature at 3.5 m Above the Mean Water Line, Sea Temperature at 60-cm Depth, Insolation and Air Pressure From the Vector Averaging Wind Recorder Deployed on W2 for the Period 20:00 GMT 30 July to 18:30 GMT 6 September 1978	2-24
2-13.	Data Processing for WMO Observations	2-27
2-14.	Data Processing for Autologged Data	2-28
2-15.	Ship Positions During Formal Meteorological Ship Intercomparison Periods	2-32
2-16.	Overlaid Plots of W2 and W2M Wind Speeds	2-32
2-17.	Difference Between WMO Wind Speed Measurements After Systematic Biases Have Been Removed	2-34
2-18.	As Figure 2-17, but for Wind Direction	2-35
2-19.	As Figure 2-17, but for Atmospheric Pressure	2-35
2-20.	As Figure 2-17, but for Dry-Bulb Temperature	2-36
2-21.	As Figure 2-17, but for Sea-Surface Temperture	2-36
2-22.	Inter-platform Differences in the FIA as a Function of Time	2-38
2-23.	Wind Speed Correction for Discovery vs W2 as a Function of Relative Wind Direction	2-40
2-24.	Differences With Respect to W2	2-42
2-25.	Comparisons Relative to B1	2-43
2-26.	Endurer Time Cross Section of RH, 26-30 July	2-48
2-27.	Endurer Time Cross Section of RH, 31 July-4 August	2-49
2-28.	Endurer Time Cross Section of RH, 4-8 August	2-50
2-29.	Endurer Time Cross Section of RH, 22-26 August	2-51
2-30.	Hecla Time Cross Section of RH, 22-26 August	2-52
2-31.	John Murray Time Cross Section of RH, 22-26 August	2-53

2-32.	Endurer Time Cross Section of RH, 27-31 August	2-54
2-33.	Hecla Time Cross Section of RH, 27-31 August	2-55
2-34.	Endurer Time Cross Section of RH, 31 August-4 September	2-56
2-35.	Hecla Time Cross Section of RH, 31 August-4 September	2-57
2-36.	Endurer Time Cross Section of q, 22-26 August	2-58
2-37.	Endurer Time Cross Section of q, 27-31 August	2-59
2-38.	Endurer Time Cross Section of q, 31 August-4 September	2-60
2-39.	Integrated Water Vapor Content--Phase 1	2-62
2-40.	Integrated Water Vapor Content--Phase 2	2-62
2-41.	Comparison of Endurer, Hecla, and John Murray Determinations of Water Vapor Content on 24 and 25 August 1978	2-63
2-42.	Daily Average of All Significant Wave Heights Recorded by Instruments Within 50 km of the Fixed Intensive Array, Mostly by Meteor Using Waverider Buoys	2-69
2-43.	Same as Figure 2-42, Except that Frequency of Waves at the Peak in the Frequency Spectrum Is Shown	2-70
2-44.	Direction From Which Waves Come	2-70
3-1.	SAR Coverage in JASIN	3-7
4-1.	SASS Swath Geometry	4-2
4-2.	SASS Cell Centers and Wind Solution Points	4-7
4-3.	Cell Pairing Separation Distance Distributions	4-8
4-4.	Power Law for the Wentz and CUNY Model Functions Used for the Boulder Workshop for Vertical Polarization	4-13
4-5.	Example of How the W-5, CUNY, and University of Kansas Model Functions Were Merged to Produce CWK	4-14
4-6.	Power Law for the Wentz-7 and CWK Model Functions for Vertical Polarization	4-16
4-7.	Power Law for Horizontal Polarization	4-17
4-8.	σ° Comparisons for Model Functions W-5, W-6, W-7, and CWK for V-Pol Upwind	4-18

4-9.	σ° Comparisons for Model Functions W-5, W-6, W-7, and CWK for V-Pol Downwind	4-19
4-10.	σ° Comparisons for Model Functions W-5, W-6, W-7, and CWK for V-Pol Crosswind	4-20
4-11.	SASS σ° vs $\log_{10} U$ for $\theta = 52^\circ$, V-Pol, Downwind Aspect	4-21
4-12.	SASS σ° vs $\log_{10} U$ for $\theta = 22^\circ$, H-Pol, Crosswind Aspect	4-22
4-13.	σ° vs Wind Speed for Constant Incidence Angle for CWK and W-7 Model Functions, Upwind and H-Pol	4-26
4-14.	σ° vs Wind Speed for Incidence Angles 20 to 28 deg for CWK and W-7 Model Functions, Upwind and H-Pol	4-26
4-15.	σ° vs Wind Speed for Incidence Angles 50 to 58 deg for CWK and W-7 Model Functions, Upwind and H-Pol	4-27
4-16.	σ° vs Wind Speed for Incidence Angles 20 to 28 deg for CWK and W-7 Model Functions, Downwind and V-Pol	4-27
4-17.	Differences Between the Wind Speeds Predicted by W-7 and CWK for Wind Speeds Near 5 m/s	4-28
4-18.	Differences Between the Wind Speeds Predicted by W-7 and CWK for Wind Speeds Near 10 m/s	4-29
4-19.	SASS Minus Autologger Buoy W2 Winds Versus Separation Distance for W-7 Model Function	4-41
4-20.	SASS Minus Autologger Buoy W2 Winds Versus W2 Wind Speed for W-7 Model Function	4-42
4-21.	SASS Minus Autologger Buoy W2 Winds Median Value Versus W2 Wind Speed for W-7 Model Function	4-43
4-22.	SASS Minus Autologger Buoy W2 Winds Versus W2 Wind Speed for CWK Model Function	4-45
4-23.	Median Value of SASS Minus Autologger Buoy W2 Winds Versus W2 Wind Speed for CWK Model Function	4-46
4-24.	Mean Wind Speed Difference Between SASS and Small-Scale Surface Fields, V-Polarization, W-7 Model Function	4-59
4-25.	Mean Wind Speed Difference Between SASS and Small-Scale Surface Fields, V-Polarization, CWK Model Function	4-59
4-26.	Mean Wind Speed Difference Between SASS and Small-Scale Surface Fields, H-Polarization, W-7 Model Function	4-60

4-27.	Mean Wind Speed Difference Between SASS and Small-Scale Surface Fields, H-Polarization, CWK Model Function	4-60
4-28.	SASS Wind Direction Ambiguity Removal Subpanel Procedure	4-64
4-29.	A Pattern of Singular-Point Patterns From Rev 801, 00:24, 8/22/78, Cyclone-Col-Cyclone	4-65
4-30.	UW-Brown Sea Level Pressure Analysis and Derived Wind Vectors Superimposed Over the AES/JPL Team's SASS-Only Direction Analysis for Rev 949	4-67
4-31.	UW-Brown Sea Level Pressure Analysis and Derived Wind Vectors Superimposed Over the UCLA Team's SASS-Only Direction Analysis for Rev 949	4-68
4-32.	WMO Surface Analysis for 1 September 1978, 0600Z	4-69
4-33.	SASS Wind Vectors for Rev 557	4-74
4-34.	SASS Wind Vectors for Rev 556	4-76
4-35.	Surface Chart for Approximately 2130Z	4-77
4-36.	SASS σ_{HH}° Contours for Rev 556	4-78
4-37.	Synthetic Aperture Radar Image - Rev 556	4-80
4-38.	SASS σ_{VV}° Contours for Rev 557	4-81
4-39.	SASS σ_{HH}° Contours for Rev 557	4-82
5-1.	Distribution of Cloud Content for GOASEX Passes	5-9
5-2.	SMMR Wind Speed Emissivity vs SASS Friction Velocity for 10.7-GHz H-Pol	5-11
5-3.	SMMR Wind Speed Emissivity vs SASS Friction Velocity for 37-GHz H-Pol	5-12
5-4.	T_B Sensitivity to Wind vs Frequency	5-13
5-5.	JASIN Wind Speed Comparisons - Rosenkranz Algorithm	5-16
5-6.	Water Vapor Comparisons - Rosenkranz Algorithm	5-17
5-7.	SMMR-SASS Geophysical Retrievals for Rev 1135	5-19
5-8.	SMMR-SASS Geophysical Retrievals for Rev 331	5-21

5-9.	SMMR-SASS Geophysical Retrievals for Rev 791	5-23
5-10.	SMMR-SASS Geophysical Retrievals for Rev 599	5-24
5-11.	Difference Between SMMR-SASS and SMMR SST vs Difference Between SMMR-SASS and SMMR Wind	5-25
5-12.	Mean Water Vapor Content for Each Atmospheric Layer Calculated From Each Data Set	5-27
5-13.	Water Vapor Comparisons - Wentz Algorithm	5-29
5-14.	Contour Plot of Water Vapor - Rev 958 - Wentz Algorithm	5-31
5-15.	Contour Plot of Contribution of Sidelobe Corrections to Water Vapor - Wentz Algorithm	5-33
5-16.	Correlation of SST "Error" With Sidelobe Correction . . .	5-34
5-17.	Wentz vs Wilheit Liquid Water - JASIN	5-39
5-18.	Wentz vs Wilheit Rain - JASIN	5-40
5-19.	Wentz Water Vapor Near Guam - Rev 384	5-44
5-20.	Wentz Water Vapor Near Guam - Rev 628	5-45
5-21.	Wentz vs Wilheit Liquid Water - Tropics	5-46
5-22.	Wentz vs Wilheit Rain - Tropics	5-48
5-23.	Wentz Wind Speed Comparisons - JASIN High Priority Set	5-49
5-24.	Wentz Wind Speed Comparisons - Meteor Hits	5-50
5-25.	Wentz Wind Speed Comparisons - GOASEX Revs 1298 and 1094, Wind Fields	5-51
5-26.	Wentz Wind Speed Comparisons - GOASEX Revolutions, Spot Reports	5-53
5-27.	Histograms of SST for Six Different Regions of JASIN Separately for Ascending and Descending Revolutions . . .	5-55
5-28.	Wentz SST Plots - "Open Ocean" Cross Section, Ascending Revolutions	5-59
5-29.	Wentz SST Plots - "Land to Land" Cross Section, Ascending Revolutions	5-60

5-30.	Wentz SST Plots - "Open Ocean" Cross Section, Descending Revolutions	5-61
5-31.	Wentz SST Plots - "Land to Land" Cross Section, Descending Revolutions	5-62
5-32.	Wentz SST Comparisons, Extended JASIN Revs 599 and 800 .	5-64
5-33.	SST Correlation With Liquid Water, Rosenkranz Algorithm .	5-67
5-34.	SMMR Coverage of the Northwest Pacific Area	5-68
5-35.	National Marine Fisheries Service September 1978 Monthly Mean SST Contour Map	5-69
5-36.	Wentz SST Comparisons - NW Pacific, Descending Revolu- tions, Unfiltered	5-71
5-37.	Wentz SST Comparisons - NW Pacific, Ascending Revolutions, Unfiltered	5-72
5-38.	Wentz SST Comparisons - NW Pacific, Descending Revolutions, Filtered	5-74
5-39.	Wentz SST Comparisons - NW Pacific, Ascending Revolutions, Filtered	5-75
5-40.	Wentz Water Vapor Distribution, Rev 556	5-77
5-41.	Wentz Liquid Water Distribution, Rev 556	5-78
5-42.	SMMR 18-GHz T_B Contours, Rev 556	5-80
5-43.	Brightness Temperature Biases vs Frequency for Vertical and Horizontal Polarizations	5-84
6-1.	Orbit Passes Used for JASIN Area Study	6-2

Tables

2-1.	Julian Day and Date	2-4
2-2.	Details of Radiosonde Sensors	2-18
2-3.	Available Data	2-25
2-4.	Comments on Sensor Performance	2-29
2-5.	Formal Meteorological Intercomparison Periods	2-33
2-6.	FIA Intercomparisons	2-34

2-7.	Corrections Applied to Reduce Data to W2 Standards . . .	2-39
2-8.	Uncertainties in Biases	2-40
2-9.	Sets of Wave Measurements Used for Intercomparisons . . .	2-64
2-10.	Summary of Comparisons	2-65
2-11.	Comparisons Among Waverider Observations of Wave Height	2-66
2-12.	Z/L State Table	2-72
3-1.	SMMR and SASS JASIN Revolution Sets	3-2
3-2.	SMMR Revolution Sets	3-3
3-3.	Altimeter JASIN Revolutions	3-4
3-4.	Summary of JASIN SAR Data	3-6
4-1.	Summary of Workshop Activities	4-5
4-2.	Model Function Power Laws for Vertical Polarization From the Boulder Workshop	4-12
4-3.	W-7 and CWK Model Function Power Laws for Models Tested in the JASIN Workshop, V-Pol	4-15
4-4.	Wind Speed and Direction Statistics for SASS Minus Surface Truth Fields Analyses	4-23
4-5.	Difference in Model Calculated Wind, $U_7 - U_c$, for Nominal Winds at 5 and 10 m/s	4-25
4-6.	Statistics for σ° vs Log U Using W-7 Algorithm to Interpolate to Desired Incidence Angles	4-31
4-7.	Statistics for σ° vs Log U Using the CWK Algorithm to Interpolate to Desired Incidence Angles	4-32
4-8.	Statistics for Comparison of Observed σ° With Model - Derived σ_{TH}° , Using the W-7 Algorithm	4-33
4-9.	Statistics for Comparison of Observed σ° With Model - Derived σ_{TH}° , Using the CWK Algorithm	4-34
4-10.	Statistics for σ° vs Log U Using the CWK and W-7 Model Functions for H-Polarization	4-36
4-11.	Statistics for σ° vs Log U Using the CWK and W-7 Model Functions for V-Polarization	4-37

4-12.	SASS-Surface Observation Wind Direction Statistics as a Function of Polarization Pairs	4-47
4-13.	SASS Minus Spot Observations, Statistics by Revolution, W-7 Model Function, V- and H-Polarizations Combined, Autologger 60-Min Averages	4-49
4-14.	SASS Minus Spot Observations, Statistics by Revolution, W-7 Model Function, V- and H-Polarizations Combined, WMO Standard Observations	4-50
4-15.	SASS Minus Spot Observations, Statistics by Revolution, CWK Model Function, V- and H-Polarizations Combined, Autologger 60-Min Averages	4-51
4-16.	SASS Minus Spot Observations, Statistics by Revolution, CWK Model Function, V- and H-Polarizations Combined, WMO Standard Observations	4-52
4-17.	SASS Minus Small-Scale Fields Statistics for Wind Speeds and Directions, W-7 Model Function and V-Polarization	4-55
4-18.	SASS Minus Small-Scale Fields Statistics for Wind Speeds and Directions, CWK Model Function and V-Polarization	4-56
4-19.	SASS Minus Small-Scale Fields Statistics for Wind Speeds and Directions, W-7 Model Function and H-Polarization	4-57
4-20.	SASS Minus Small-Scale Fields Statistics for Wind Speeds and Directions, CWK Model Function and H-Polarization	4-58
4-21.	SASS Revolutions Used for Wind Direction Ambiguity Removal	4-62
4-22.	Statistics for Direction Differences From Comparisons Made Against In Situ Ship Observations in the JASIN Meteorological Triangle Area	4-70
4-23.	Statistics for Direction Differences From Comparisons Made Against UW-Brown Wind Fields Derived From Surface Pressure Measurements in the JASIN Meteorological Triangle Area	4-70
5-1.	SMMR Passes in the JASIN Area	5-3
5-2.	SMMR Passes in the Northwest Pacific	5-5
5-3.	Radiosonde Stations in the South Pacific Ocean	5-6

5-4.	SMMR Passes in the Tropics	5-7
5-5.	SMMR Passes to Test Algorithm Revisions	5-7
5-6.	Biases Added to APC T_B 's in Wentz Algorithm	5-10
5-7.	Surface Truth and Spacecraft Determinations of Total Water Vapor Content	5-28
5-8.	Difference in Water Vapor Content	5-30
5-9.	Comparison of the Different Algorithms for Total Water Vapor	5-30
5-10.	Precipitation in the JASIN Area During Seasat Revolutions	5-35
5-11.	Rain and Liquid Water Algorithms for Wilheit and Wentz at Ship Locations Reporting Precipitation	5-41
5-12.	Precipitable Water Vapor at Tropical Stations	5-43
5-13.	SST Statistics for the Eight Priority Revolutions	5-56
5-14.	Wind Speed Statistics for the Eight Priority Revolu- tions	5-56
5-15.	SST Means and Standard Deviations for Each Region of JASIN	5-57
5-16.	Correlation of S/C SST With Other S/C-Derived Variables	5-66
5-17.	Comparison Statistics for Unfiltered SMMR and XBT SSTs	5-70
5-18.	Comparison Statistics for Filtered SMMR and XBT SSTs	5-70
5-19.	SMMR Sea-Surface Temperature in the Tropical Pacific Compared to "Ships of Opportunity" Measurements	5-76
6-1.	Wind Data Comparison: Windspeed	6-3
6-2.	Wind Data Comparison Statistics	6-5
7-1.	Classes of JASIN Data	7-6
7-2.	Accuracy of the Location of Features in SAR Images	7-7

VOLUME II: SASS, SMMR, AND ALT DATA PLOTS (Microfiche)

1. Description of Data Sets
2. SASS Plots
3. SMMR Plots
4. ALT Plots

VOLUME III: SMALL SCALE WIND FIELDS AND EDITED JASIN
DATA LISTINGS (Microfiche)

- 1.0 Interplatform Comparisons of JASIN WMO Observations
- 2.0 Small Scale Wind Magnitude Fields
- 3.0 Small Scale Wind Direction Fields
- 4.0 Surface Data Listings

4.1	John Murray	WMO Reports
4.2	Hecla	WMO Reports
4.3	Meteor	WMO Reports
4.4	Gardline Endurer	WMO Reports
4.5	John Murray	Avg. Winds, Auto Log
4.6	Tydeman	Avg. Winds, Auto Log
4.7	Discovery	Avg. Winds, Auto Log
4.8	W2M	Avg. Winds, Auto Log
4.9	W2	Avg. Winds, Auto Log
4.10	H2	Avg. Winds, Auto Log
4.11	J1	Avg. Winds, Auto Log
4.12	S1-3	Avg. Winds, Auto Log
4.13	B4	15 min Avg.
4.14	B4	60 min Avg.
4.15	All Platforms - Edited	

VOLUME IV: UNEDITED JASIN DATA SET (Microfiche)

- | | | |
|-----|------------------|----------|
| 1. | Hecla | WMO |
| 2. | Gardline Endurer | WMO |
| 3. | John Murray | WMO |
| 4. | Meteor | WMO |
| 5. | Discovery | Auto Log |
| 6. | S1-3 | Auto Log |
| 7. | WM2 | Auto Log |
| 8. | W2 | Auto Log |
| 9. | H2 | Auto Log |
| 10. | Tydemman | Auto Log |
| 11. | J1 | Auto Log |
| 12. | John Murray | Auto Log |
| 13. | B4 | 15 min |
| 14. | B4 | 60 min |

VOLUME V: JASIN TIME SERIES PLOTS (Microfiche)

1. Wind Speed
2. Wind Direction
3. Sea Surface Temperature
4. Wet Bulb
5. Dry Bulb
6. Pressure
7. SASS Pass Overlay

VOLUME VI: RAW SMMR IMAGES (Microfiche)

VOLUME VII: RAW VIRR IMAGES (Microfiche)

SECTION I

INTRODUCTION

When the JASIN (Joint Air-Sea Interaction) experiment was in the planning stages, the possibility that Seasat would substantially contribute to JASIN was considered remote. On the other hand, the JASIN experiment was soon recognized by the Seasat community as a major source of ground truth for the scatterometer and the microwave radiometer. It is, therefore, no surprise that the initiative to organize a Seasat-JASIN workshop came from the Seasat Project Office at JPL.

The algorithms for the Seasat sensors had gone through many iterations and were ready to be tested on an independent data set by the time the JASIN data would become available. It was decided, therefore, to use the JASIN data set as a high quality withheld data set, which would be made available shortly before the workshop. A careful selection was made of the Seasat overpasses that covered the JASIN area, and then the geophysical data derived from the Seasat sensors was calculated for these selected passes with the best algorithms available at that time. This information was also made available shortly before the workshop. Care was taken that the two data sets (JASIN and Seasat) were separate and could be considered fully independent.

The deadline for the workshop required accelerated data reduction of the JASIN observations. This was accomplished by hiring experienced meteorologists and oceanographers who, under the supervision of Trevor Guymer and Peter Taylor from the Institute of Oceanographic Sciences, carried out the work. We were fortunate to find the necessary dedicated workers at the time that we needed them. In Section II, the results of this effort are described in detail.

The Seasat data set was prepared by the individual panels for each instrument. The algorithms developed for previous workshops were improved and used on the JASIN overpasses. The improvements included two modified model functions for the SASS, a much improved SASS attenuation algorithm, a revised SMMR T_A algorithm, multiple SMMR geophysical algorithms, and a new SMMR-SASS algorithm. Also, for the first time, a serious attempt was made to remove the SASS alias. This effort is discussed in Section IV. Furthermore, a SASS-SAR comparison has been initiated.

The actual confrontation of the two data sets took place at the workshop, which was held from 18 to 26 March 1980 in the Huntington Sheraton Hotel in Pasadena. The relaxed atmosphere of this beautiful hotel provided an ideal environment for an undisturbed concentrated scientific effort.

Although the workshop merely dealt with the comparison of two data sets and an evaluation of how well Seasat performed, a fair amount of scientific excitement was generated when it became apparent how well Seasat performed. It was possible to identify mesoscale systems with the SASS as well as fronts; the SMMR provided accurate water vapor content of the atmosphere; the SAR showed evidence of helical rolls in the marine boundary layer; a SASS anomaly could be traced back to thunderstorm activity, etc.

What was originally thought to be a one-way street of contributions from JASIN to Seasat has now become clearly a two-lane highway. JASIN has not only profited from the extra effort in data analysis, but now stands to gain a great deal more in the detailed, accurate and varied information that Seasat can provide.

Volumes II through VII of this report contain most of the data that were used in the workshop and have been published separately as microfiche packages (available upon request). Appendix G to this volume provides the reference information necessary to interpret the data sets contained in the supporting volumes.

SECTION II

JASIN DATA PROCESSING

A. INTRODUCTION

Since August 1979 a program has been under way at the Institute of Oceanographic Sciences (IOS) to collate, analyze, and intercalibrate as much of the JASIN meteorological data as possible to produce a unified, high quality data set covering sufficient time and space scales for comparison with Seasat measurements. Particular emphasis has been placed upon the measurements of wind speed and direction, sea-surface temperature (SST), and integrated water vapor. A brief overview of the JASIN experiment is first given followed by a description of the analysis undertaken, discussion of the accuracy of the data and implications for the workshop. The final section describes the subsequent processing of the data sets at JPL and their integration with the satellite data.

B. JASIN OVERVIEW

JASIN was not conducted as a validation experiment for Seasat but as the fruit of 10 years planning, originally initiated as the British contribution to GARP (Royal Society, 1979). It involved 50 teams of investigators from 9 countries using 14 ships, 3 aircraft, and 35 mooring systems and took place in deep water 200 km off NW Scotland (Figure 2-1) during July to September 1978. Figure 2-2 shows the timetable of ships and aircraft with two main observational phases and several intercomparison periods (see Table 2-1 for date to Julian Day conversion). In Figure 2-3 are displayed five nested regions, each being identified with a particular sub-program. Figure 2-4 shows the deployment of ships within these areas for the two main phases.

1. Oceanography

In the Large Scale Area the aim was to study the response of the ocean to atmospheric forcing on the scale of the North Rockall Trough. Vertical soundings were made from ships, and current and temperature measurements were recorded on moorings (see Figure 2-5). Of particular importance were the repeated surveys by Tydeman and Challenger, which indicate the variability in the ocean and where fronts may be situated. Small-scale structure of the upper ocean and thermocline was studied in the Oceanographic Intensive Area, (OIA) and Fixed Intensive Array (FIA), including surface-generated internal waves, mixed layer structure (cm to km scale), surface fluxes, and surface waves (using waveriders, pitch/roll buoys, ship-borne wave recorders, visual observations from ships and aircraft photographs). Particularly dense coverage was obtained in the FIA (Figure 2-6).

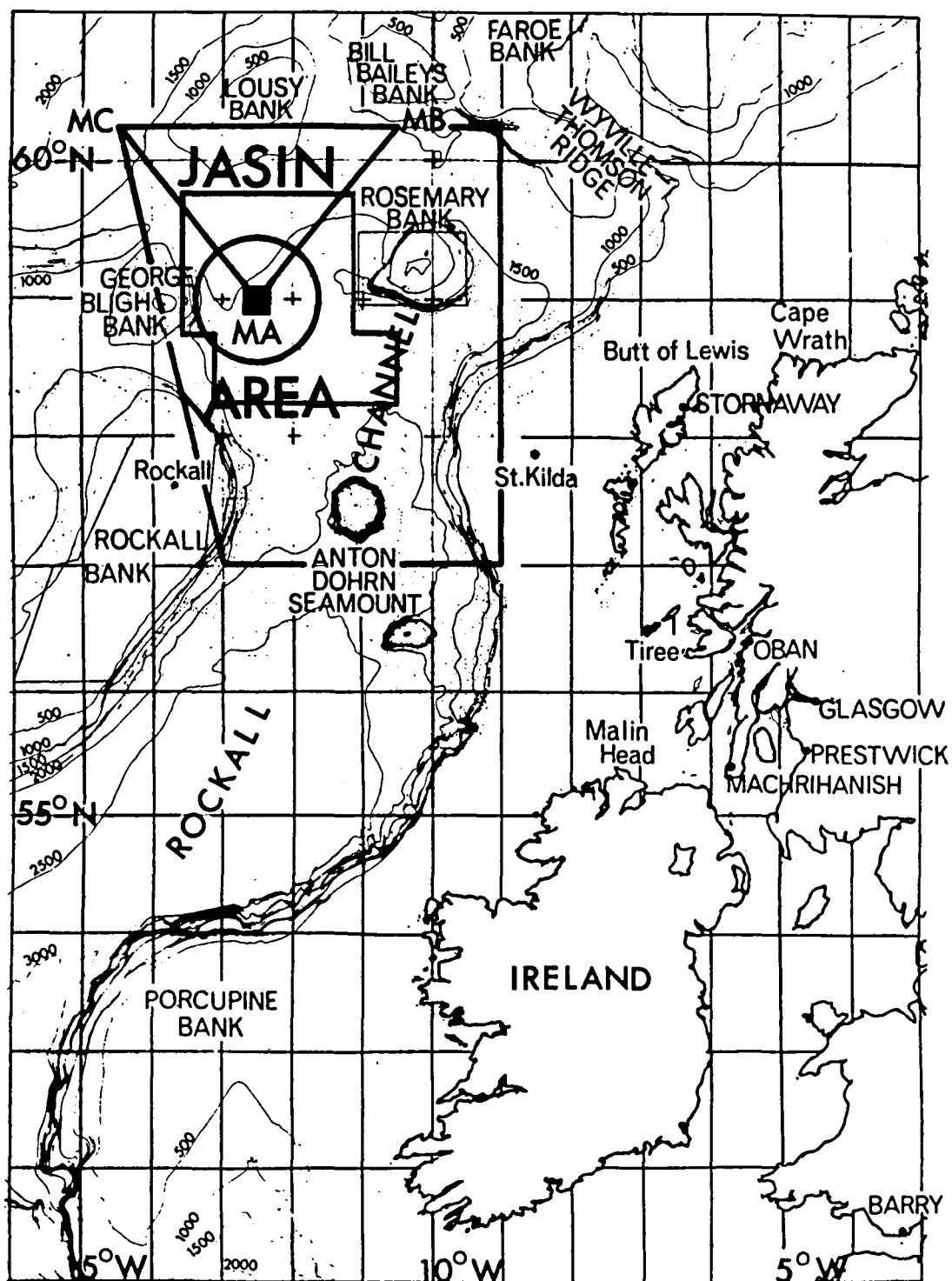


Figure 2-1. The JASIN Area in Relation to the British Isles (Bases for ships (Glasgow) and aircraft (RAF Machrihanish) are also shown)

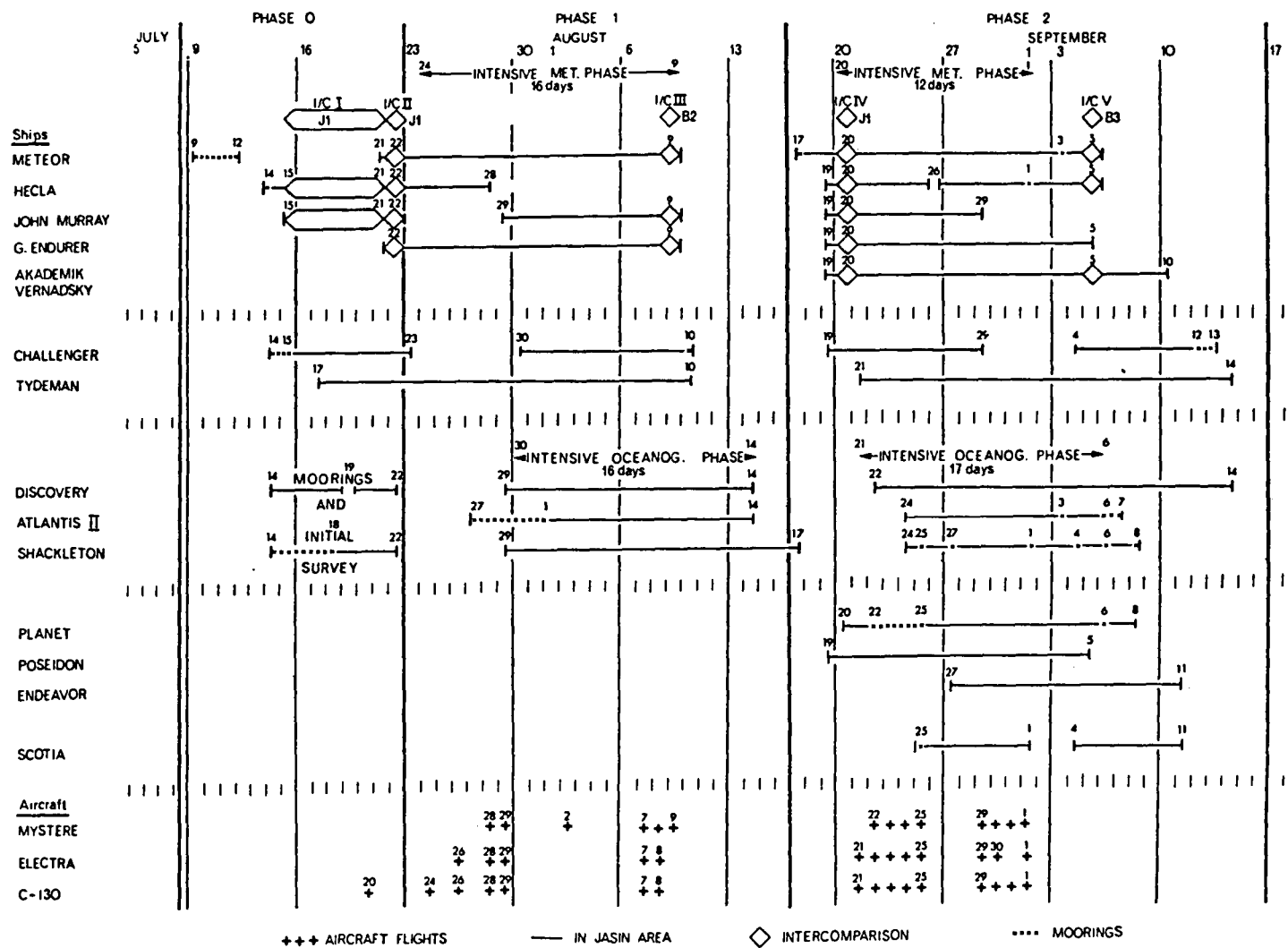


Figure 2-2. Ship and Aircraft Timetable

Table 2-1. Julian (Year) Day and Date

Date	Day	Date	Day	Date	Day
July 12	193	Aug. 1	213	Sept. 1	244
13	194	2	214	2	245
14	195	3	215	3	246
15	196	4	216	4	247
16	197	5	217	5	248
17	198	6	218	6	249
18	199	7	219	7	250
19	200	8	220	8	251
20	201	9	221	9	252
21	202	10	222	10	253
22	203	11	223	11	254
23	204	12	224	12	255
24	205	13	225	13	256
25	206	14	226	14	257
26	207	15	227	15	258
27	208	16	228	16	259
28	209	17	229	17	260
29	210	18	230		
30	211	19	231		
31	212	20	232		
		21	233		
		22	234		
		23	235		
		24	236		
		25	237		
		26	238		
		27	239		
		28	240		
		29	241		
		30	242		
		31	243		

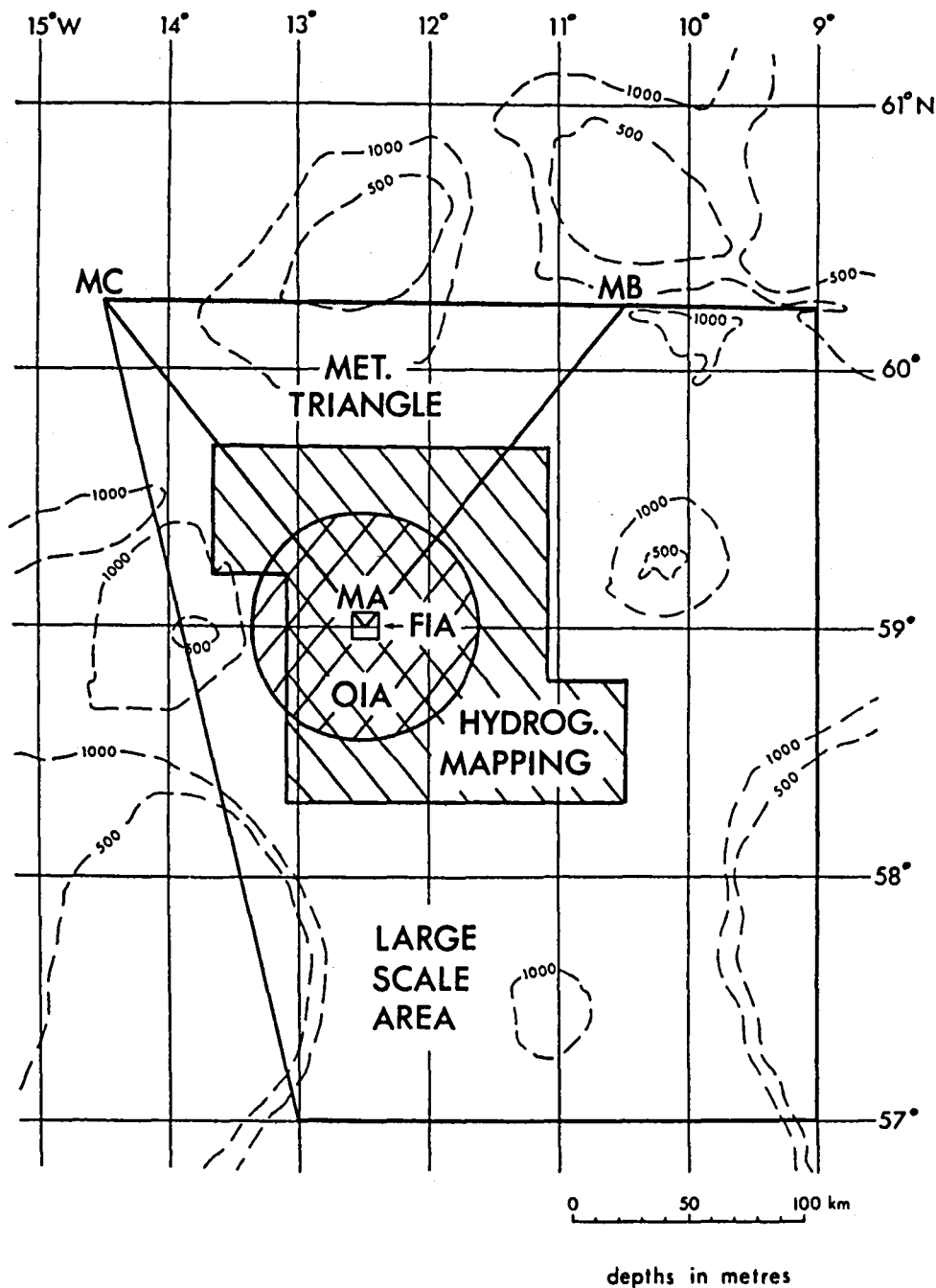


Figure 2-3. The Five Regions in the JASIN Experimental Area: Large Scale Area, 150-km Square (z-shaped area); Meteorological Triangle, 180 x 180 x 220 km (triangle MA, MB, MC); Oceanographic Intensive Area (OIA), 100-km Diameter Circle; and the Fixed Intensive Array, 6-km Square in Center of OIA (59°N, 12°30'W) (Bathymetry is shown with depth in meters)

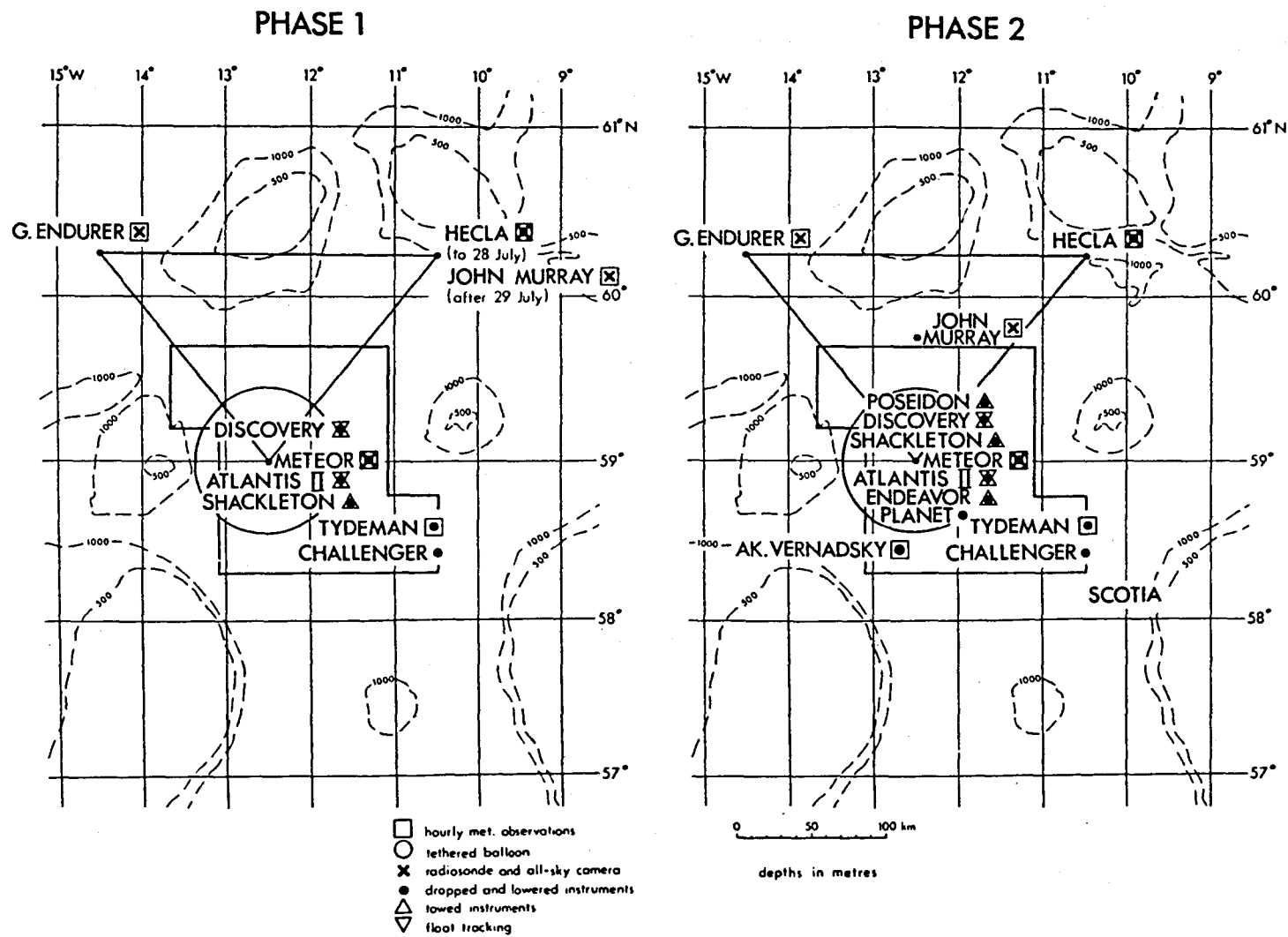


Figure 2-4. Areas of Ship Operation

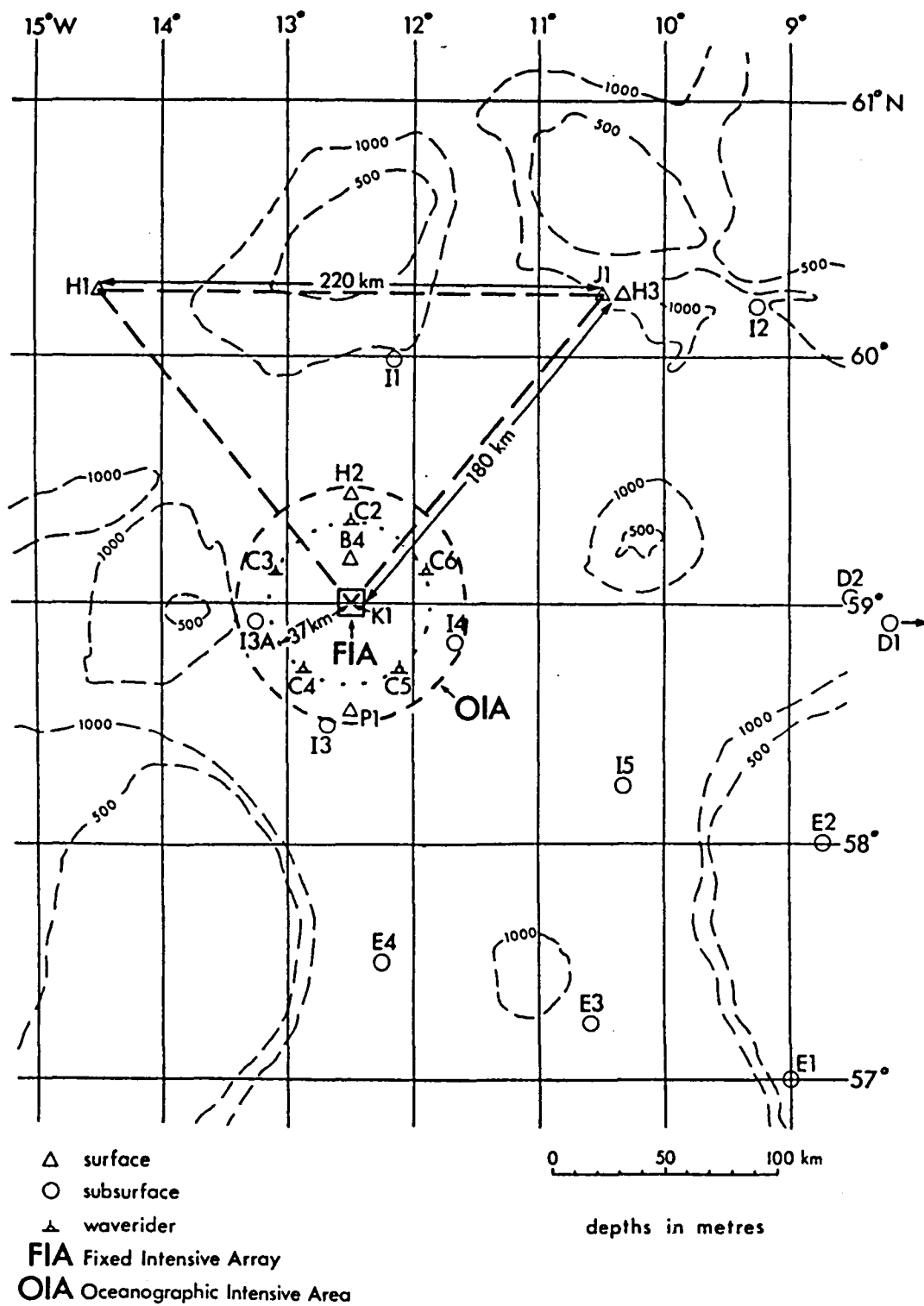
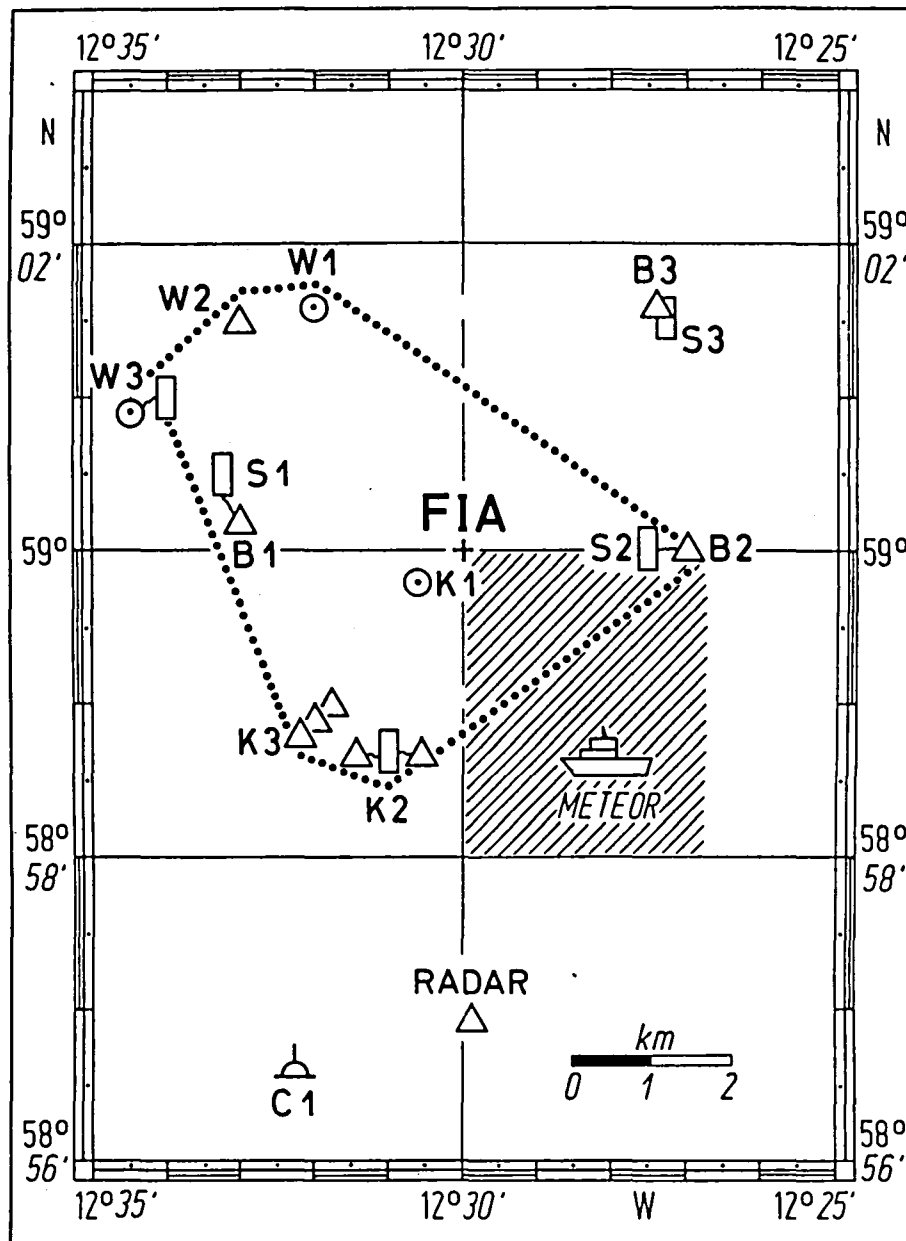


Figure 2-5. Moorings in the Large Scale Area



- ⊙ SUBSURFACE BUOY
- ▭ SPAR BUOY
- △ SURFACE BUOY
- NO-PASS ZONE
- ⌒ WAVE RIDER

Figure 2-6. Moorings in the Fixed Intensive Array

2. Aircraft

Up to 3 aircraft flew on 18 days in coordinated patterns to measure mean winds and temperatures (plus their turbulent fluctuations for obtaining direct estimates of the boundary layer fluxes). They were also equipped with radiation instruments, including those for sensing SST.

3. Ships and Buoys

A large effort was expended in the shipboard meteorological program, the measurements of which are needed by most JASIN investigators. Four "meteorological" ships (Meteor, Hecla, John Murray, Gardline Endurer) logged surface variables and launched radiosondes at the corners and (during Phase 2) center of a 200-km-sided triangle. Two of the ships, Meteor and Hecla, also flew tethered balloons.

The meteorological ships had two independent sets of instruments for surface measurements - WMO (hourly, manual, and including subjective observations and comments) and automatically recorded data (1-min sampling). Other ships also made WMO observations but at a lower sampling rate. Tydeman and Discovery had autolog systems, and the former is particularly useful because the ship roves over a large area enhancing the spatial coverage. The location of the instruments on the various ships is shown in Figure 2-7. Several buoys carried meteorological sensors (see Figure 2-8) and a number of these were situated within a few kilometers of one another at the FIA. Disappointingly, several buoy instruments failed completely, including one system in H2, all surface instruments on H1, H3, and almost certainly on P1. This throws greater weight on ship measurements to sample the larger scale. Figure 2-9 is a time table of all the surface measurements made.

The radiosonde ascents were concentrated into the two main phases with approximate dates 22 July to 9 August (days 203-221) and 20 August to 5 September (days 232-248). During these periods each of the corner ships launched radiosondes at 00:00, 06:00, 12:00, 18:00 GMT, which were tracked to the tropopause (3 hourly at Meteor). The 00:00 GMT flights from Meteor were analyzed to synoptic standards and transmitted over the WMO Global Telecommunications System. On a number of Intensive Radiosonde Days, selected for meteorological interest, all of the ships launched additional flights to 500 mbars (~5 km) to give 60- to 90-min resolution during the period 06:00 to 21:00 GMT. Figure 2-10 summarizes the radiosonde measurements.

The Endurer, Hecla, and Meteor all used LO-CATE system W3 ground stations (Beukers Laboratories, New York) to track VIZ Model 1223 radiosondes equipped with premium sensors. The John Murray used a LO-CATE WL2 ground station to track VIZ Model 1220 radiosondes equipped with a low-level baroswitch and premium sensors. The premium thermistor and hygristor used were similar to those used in NWS radiosondes but were factory selected to give closer response tolerances. Details of the sensors are given in Table 2-2.

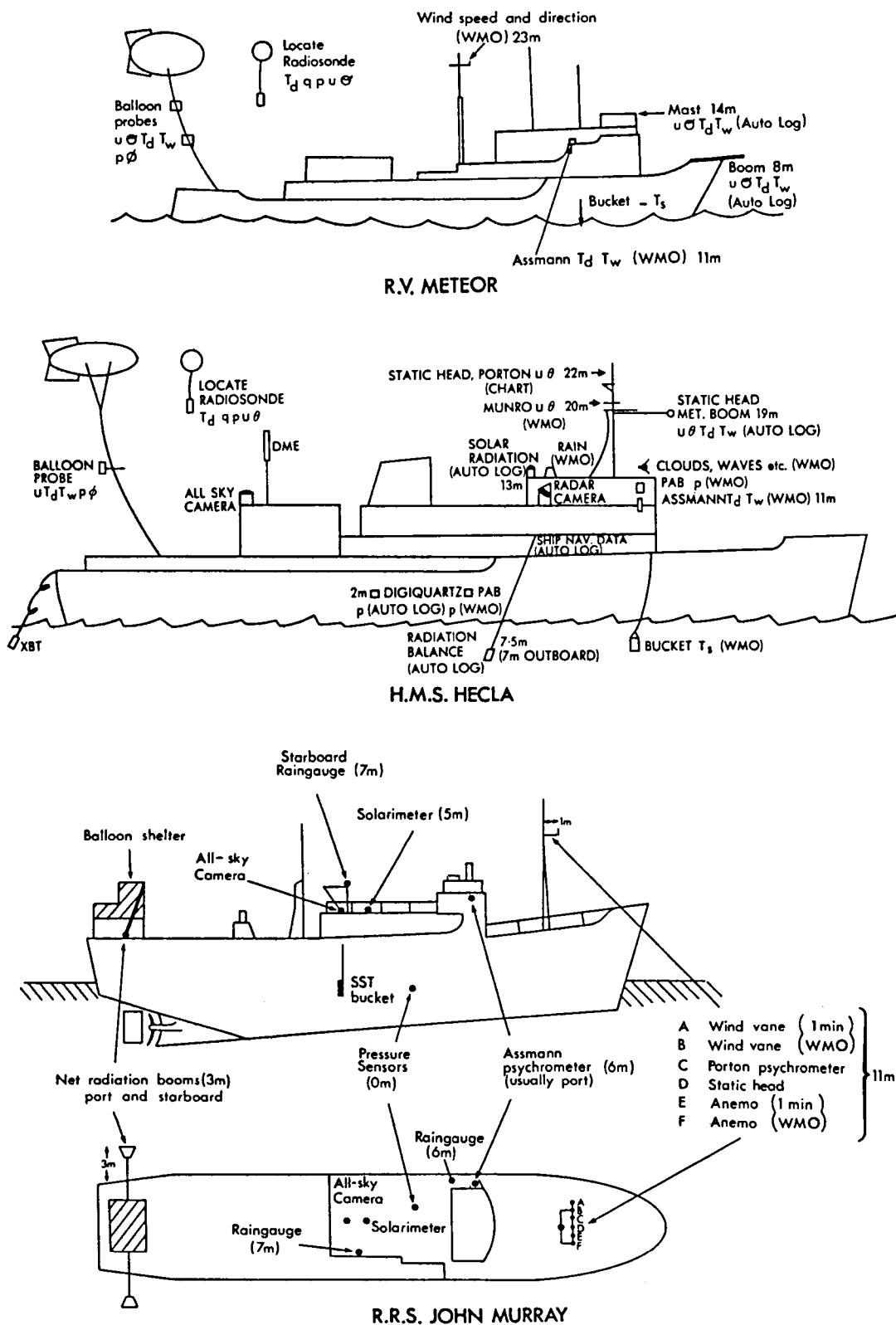


Figure 2-7. Meteorological Instrumentation on Ships

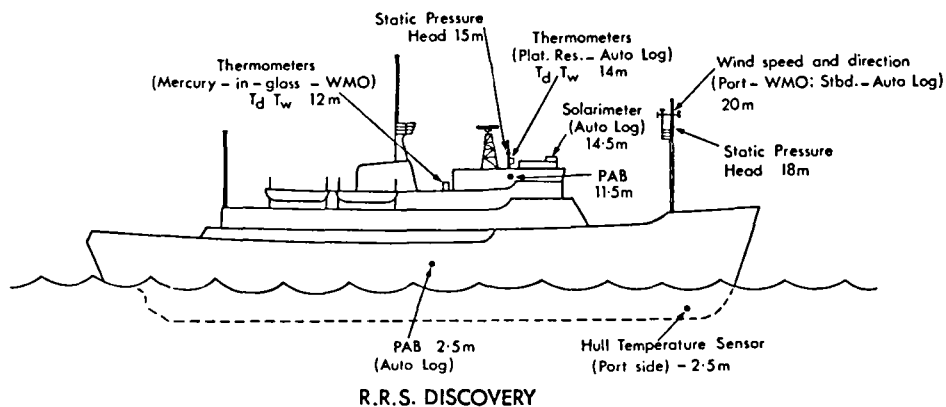
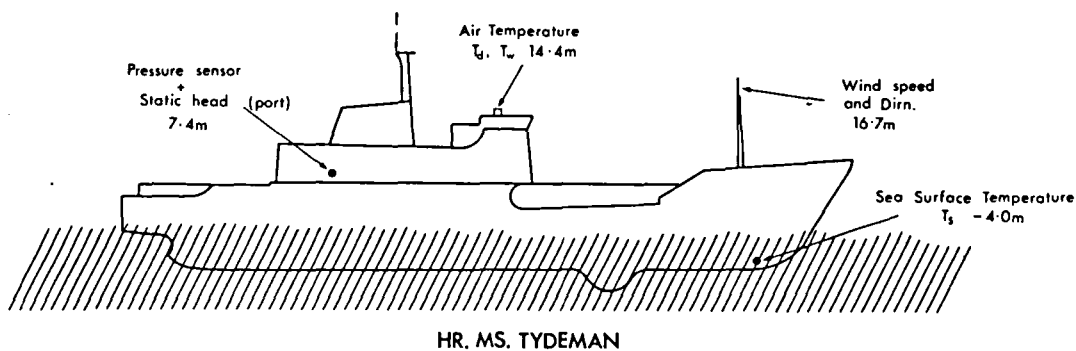
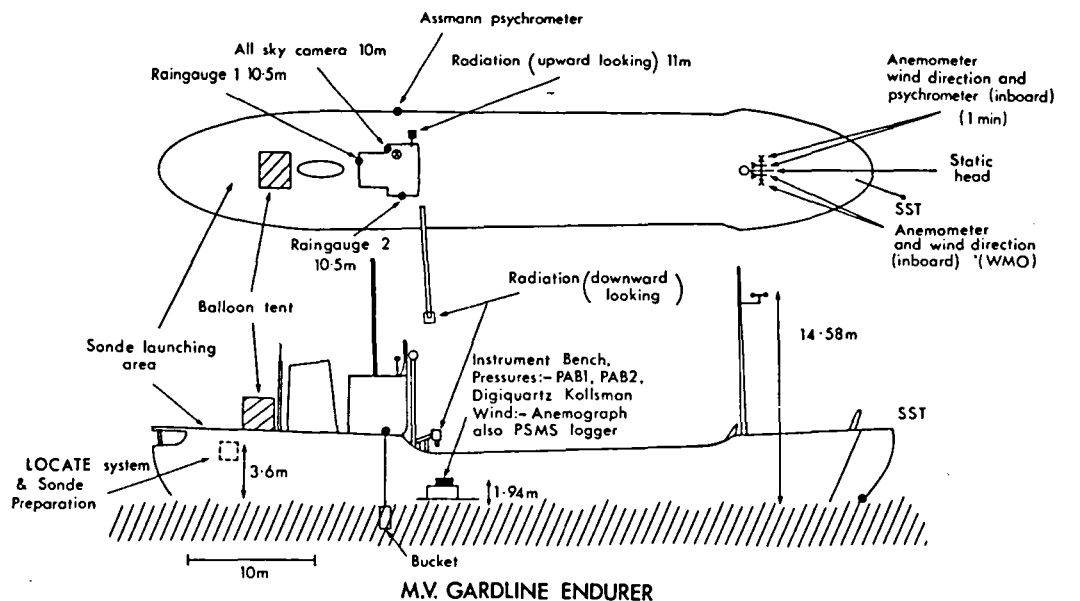


Figure 2-7 (contd)

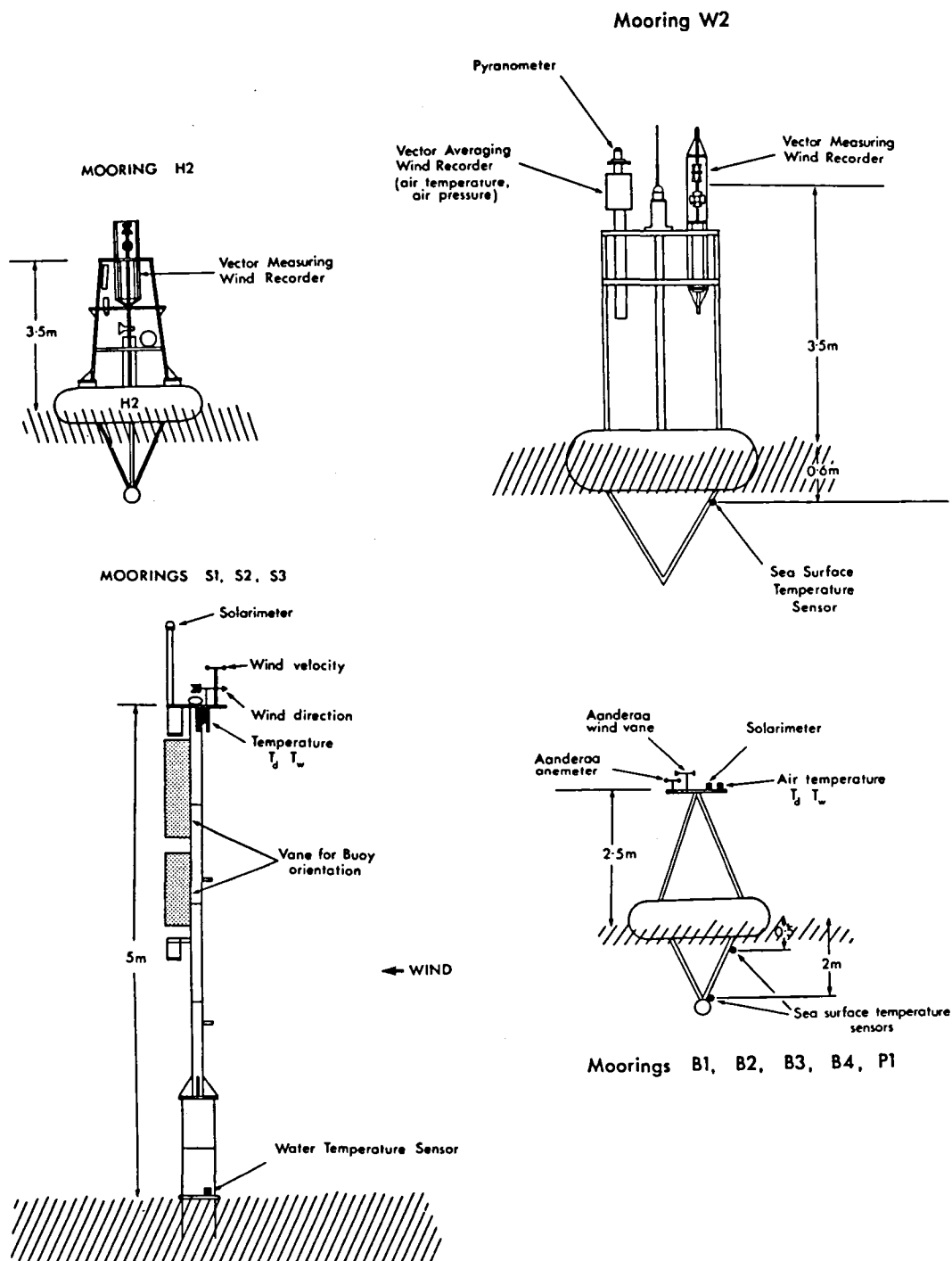
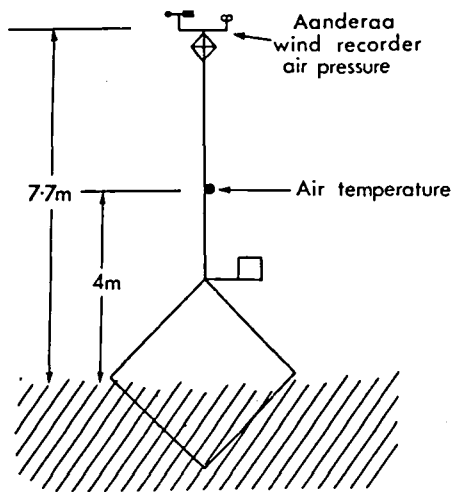
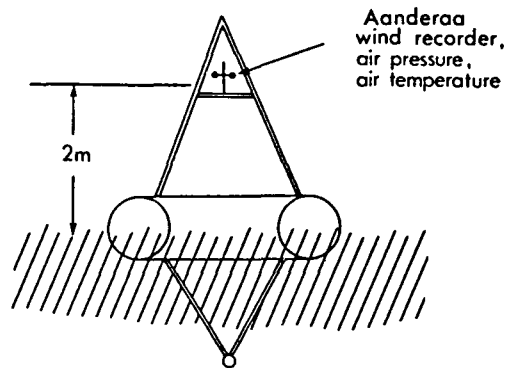


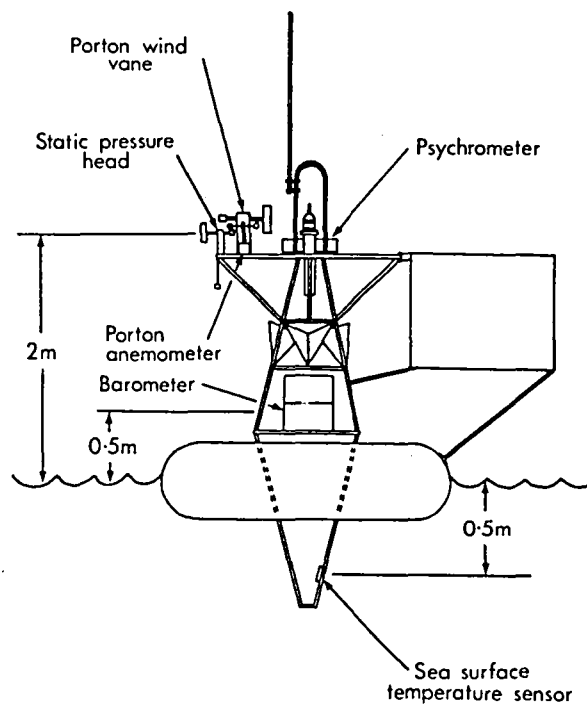
Figure 2-8. Meteorological Instrumentation on Buoys



Mooring K2



Mooring K3



Mooring J1

Figure 2-8 (contd)

DATE DAY			9 July 190	11 192		16 197	21 202	26 207	31 212	1 August 217	5 217	10 222	15 227	20 232	25 237	30 242	1 Sept. 247	4 247	9 252	14 257
WMO OBSERVATIONS	VARIABLES *	SAMP. INT.																		
METEOR		1 hr	3 hr																	
HECLA	• Rainfall	1 hr																		
JOHN MURRAY	• Rainfall	1 hr																		
G. ENDURER	• Rainfall	1 hr																		
CHALLENGER		6 hr																		
TYDEMAN		1 hr																		
DISCOVERY		6 hr																		
ATLANTIS II	Y	1 hr																		
SHACKLETON	Others • Rainfall	3 or 4 hr																		
PLANET		6 hr																		
		3 hr daytime																		
AUTOMATIC LOGGING ON SHIPS																				
METEOR																				
HECLA	Y, P, T _d , T _w , T _s , R _n	1 min																		
JOHN MURRAY	Y, P, T _d , T _w , T _s , R _n	1 min																		
G. ENDURER	Y, P, T _d , T _w , T _s , R _n	1 min																		
CHALLENGER	Y, T _d , T _{dew}	40 sec																		
TYDEMAN	Y, P, T _d , T _w , T _s , R _n	1 min																		
DISCOVERY	Y, P, T _d , T _w , T _s , R _n	1 hour																		
PLANET	Y, P	2 min																		
A. VERNADSKY		analogue																		
MEASUREMENTS ON BUOYS																				
H2	Y	2 min																		
W2	Y(VAWR), P, T _d , T _w , R _n	15 min																		
B1	Y(VAWR)	2 min																		
B2																				
B3	Y, T _d , T _w , R _n	35 min																		
B4	T _s	10 min																		
S1, S2, S3	Y, T _d , T _w , T _s , R _n	15 sec																		
K2	Y, P, T _d	10 min																		
K3	Y, P, T _d	10 min																		
P1																				
J1	Y, P, T _d , T _w , T _s	1 min																		

* WMO variables were as follows unless otherwise stated: Y, P, T_d, T_w, T_s, clouds, waves, weather, visibility

Key: R_n = radiation

Figure 2-9. Surface Meteorological Measurements

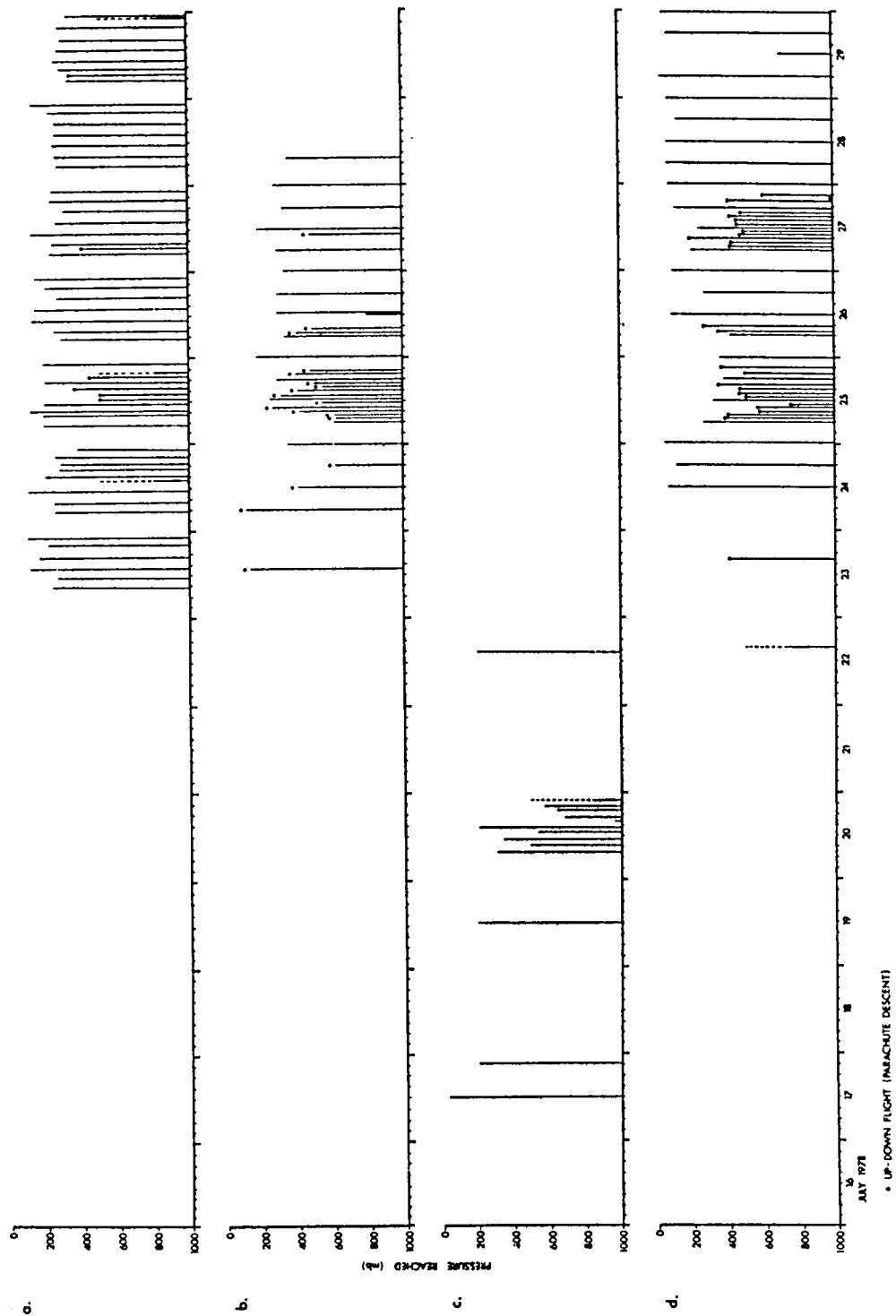


Figure 2-10. Radiosonde Launches: (a) Meteor, (b) Hecla, (c) John Murray, (d) G. Endurer

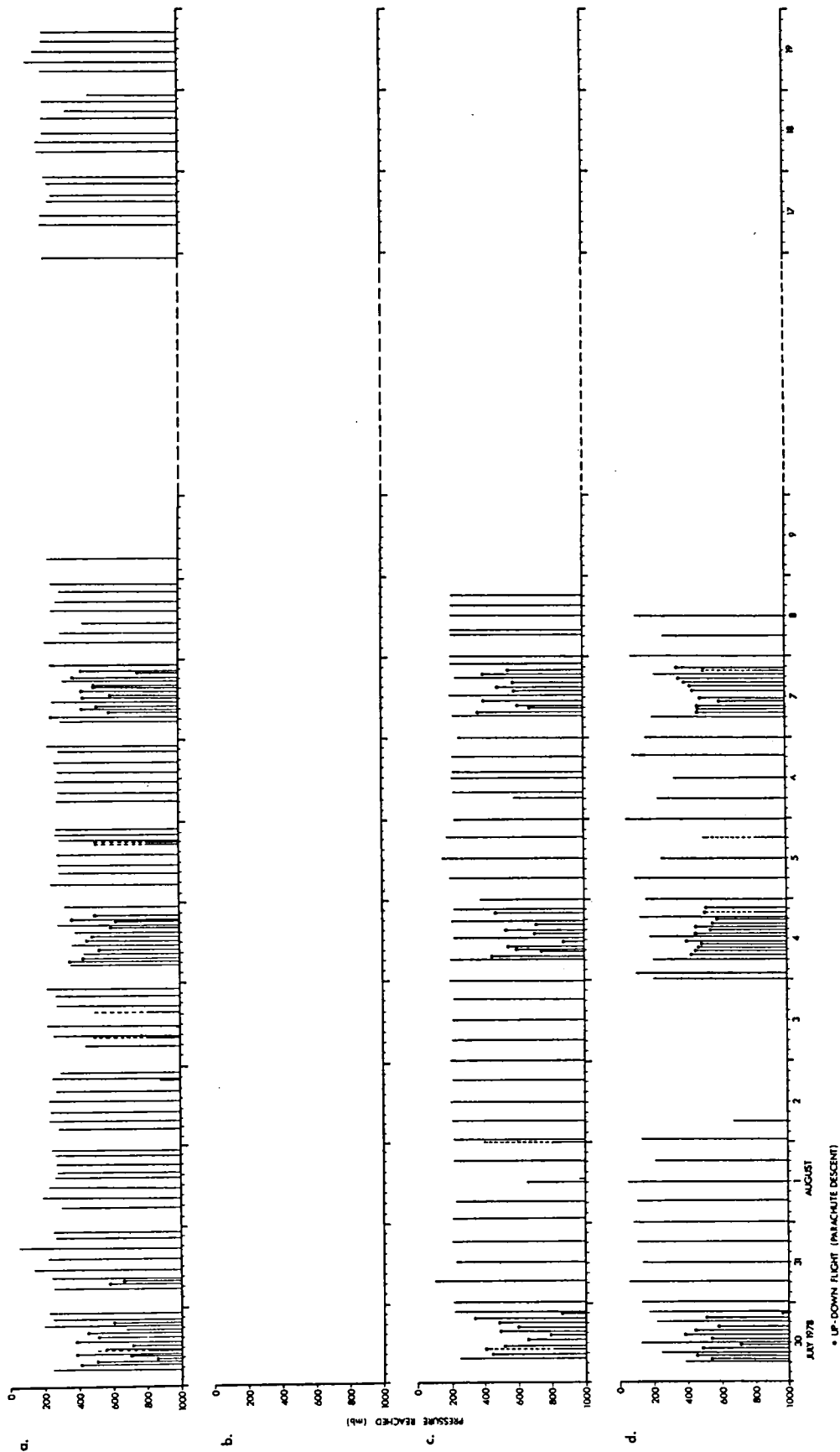


Figure 2-10 (contd)

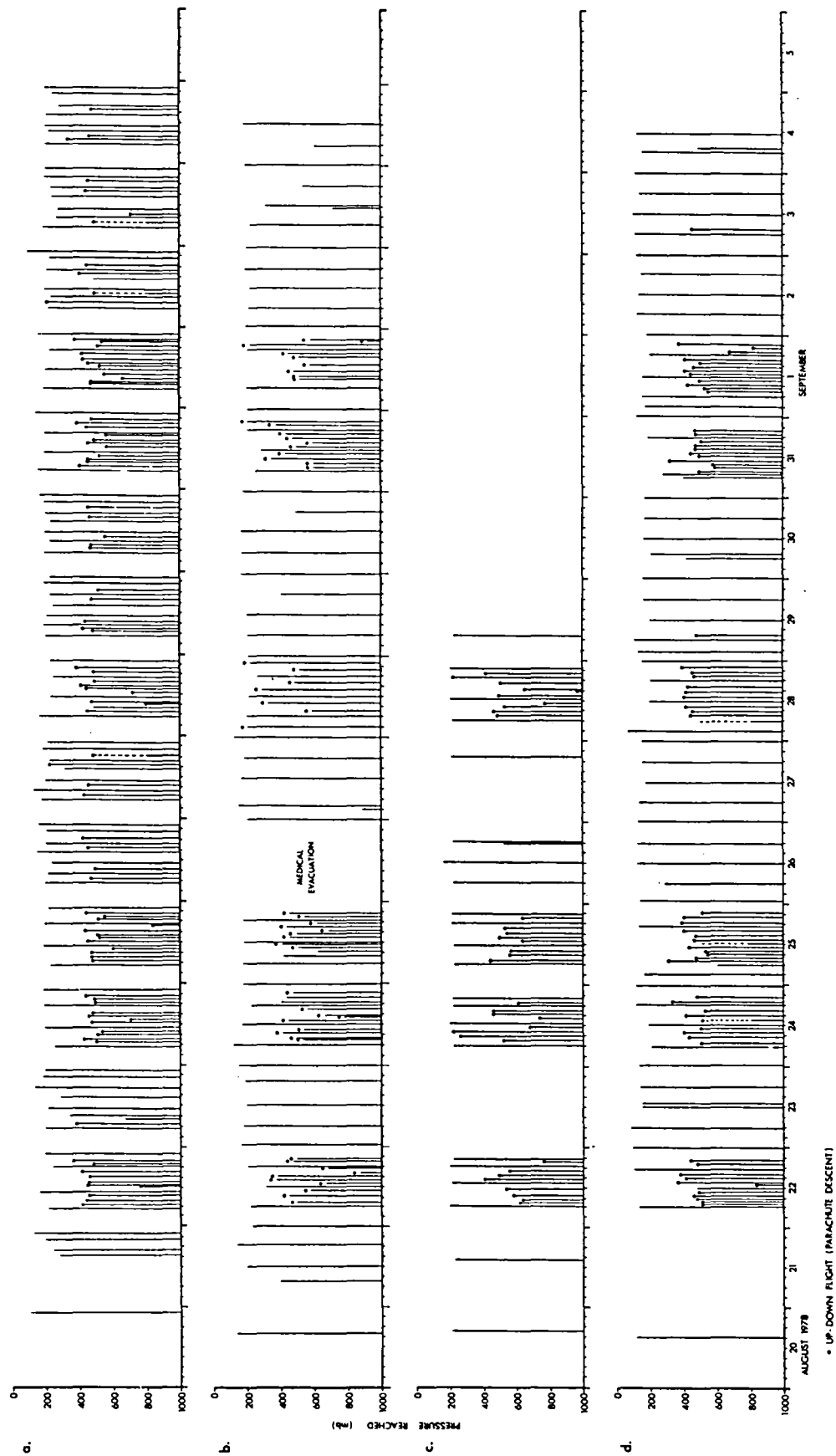


Figure 2-10 (contd)

Table 2-2. Details of Radiosonde Sensors

<p><u>Thermistor</u>: Model VIZ 1366-211</p> <p>Rod-type resistor of NWS pattern, nominal resistance 14000 ohms at 30°C.</p> <p><u>Factory specification</u>: accuracy of $\pm 0.1^{\circ}\text{C}$ (rms) for 40°C to -70°C. (for comparison standard sensor is within 0.3°C)</p>
<p><u>Hygristor</u>: Model VIZ 1386-060</p> <p>Fast response carbon film hygristor of NWS pattern, nominal resistance 10000 ohms at 33% r.h. and 25°C</p> <p><u>Factory specification</u>: accuracy of ± 2 percent RH in range 10 percent to 100 percent (for comparison standard sensor is within 5 percent)</p>
<p><u>Baroswitch</u>: Endurer, Hecla, and Meteor: Model VIZ 1292-213 John Murray: Model VIZ 1160-113 (low level)</p> <p>Precision 180-contact baroswitch actuated by a Ni-Span-C aneroid capsule.</p> <p><u>Factory specification</u>: Within 1 mbar for 1050 to 5 mbars (Standard instrument is within 5 mbars).</p>

4. Meteorological Conditions

Figure 2-11 is a sequence of daily 12:00 GMT surface synoptic charts adapted from "Weather" by courtesy of the Royal Meteorological Society. Particular features to notice are the blocked conditions of 30 July-10 August, and the passage of fronts on 13,17/18,20,30 August and 2 September. Surface conditions at one point in the JASIN area (buoy W2) are displayed as time series in Figure 2-12. Wind speeds varied from 0 to 17 m/s at a height of 3.5 m.

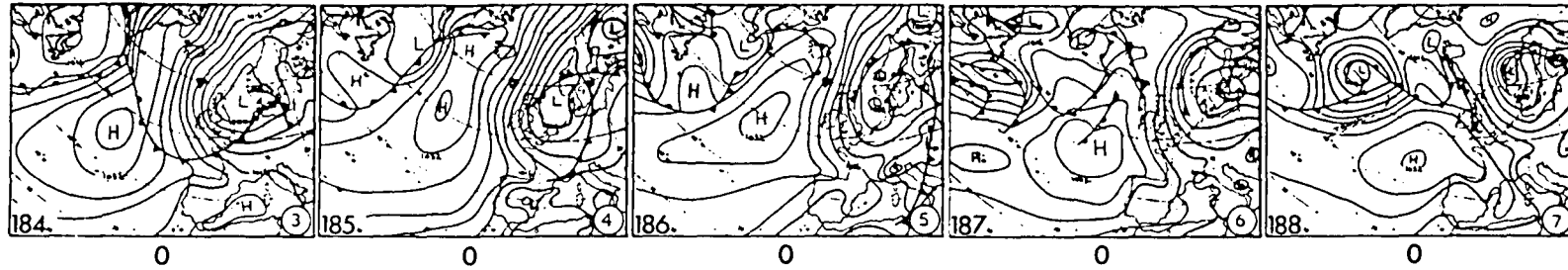
C. ANALYSIS OF SURFACE DATA

1. Availability of Data

Table 2-3 shows the data available at the time of the workshop. Within the FIA there is some redundancy because the separation of the platforms is very much less than a SASS footprint. Therefore, a subset was selected for the workshop based on estimates of data reliability and temporal coverage. However, the other platforms were included in the intercomparison analysis to provide checks and because they are needed to pursue scientific aims within the JASIN context. Principal investigators were asked to provide data after carrying out initial reduction to meteorological quantities. Some data sets could not be processed

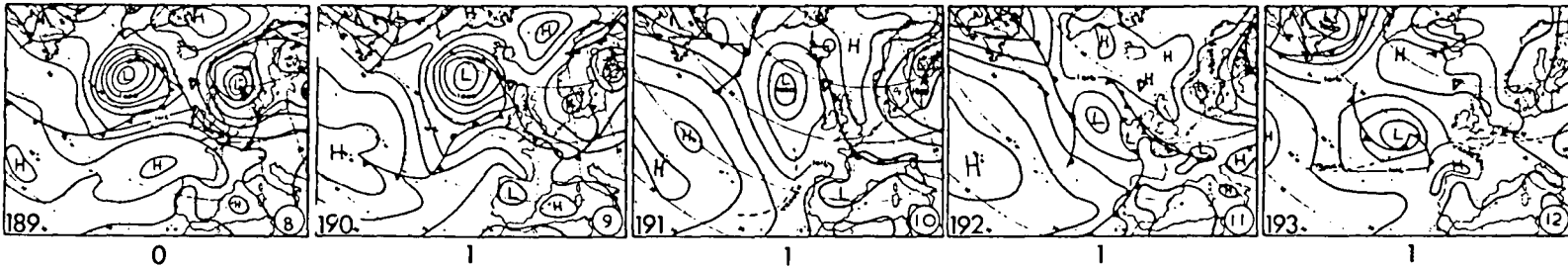
(12GMT) 3 - 17 JULY 1978

JULY

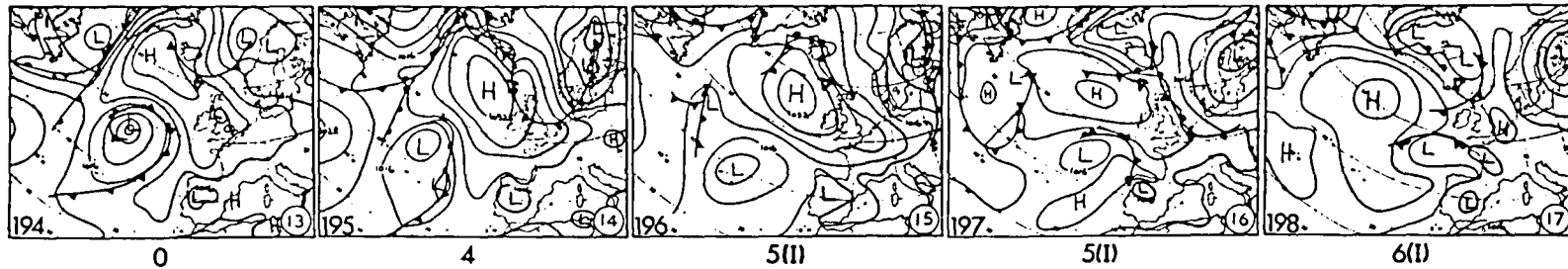


JULY

PHASE 0



JULY - PHASE 0 (contd.)

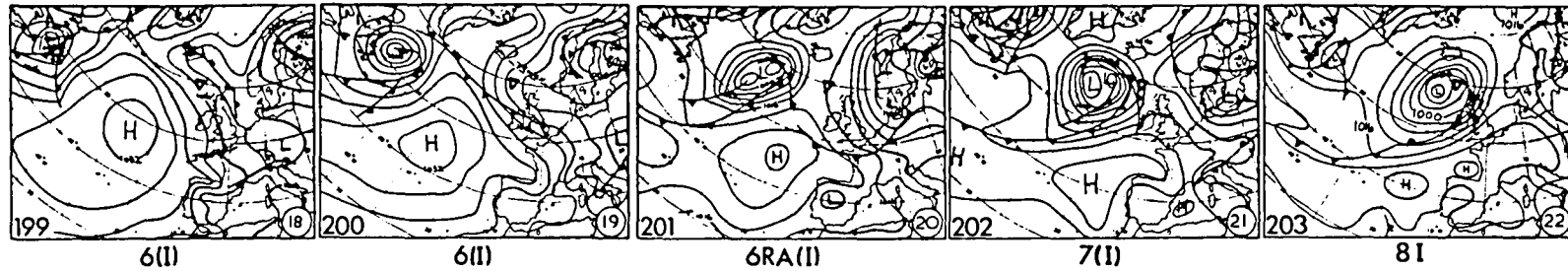


n = no. of ships on station , (I) = partial intercomparison

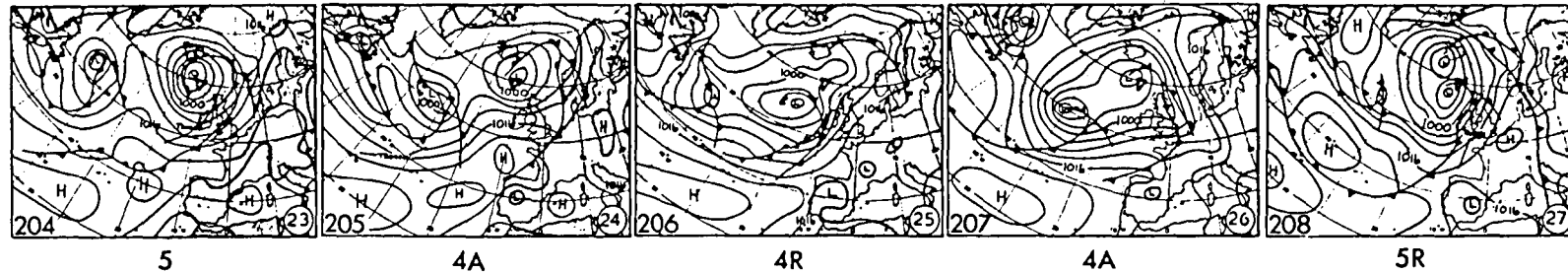
Figure 2-11. Daily Weather Maps

(12 GMT) 18 JULY - 1 AUGUST 1978

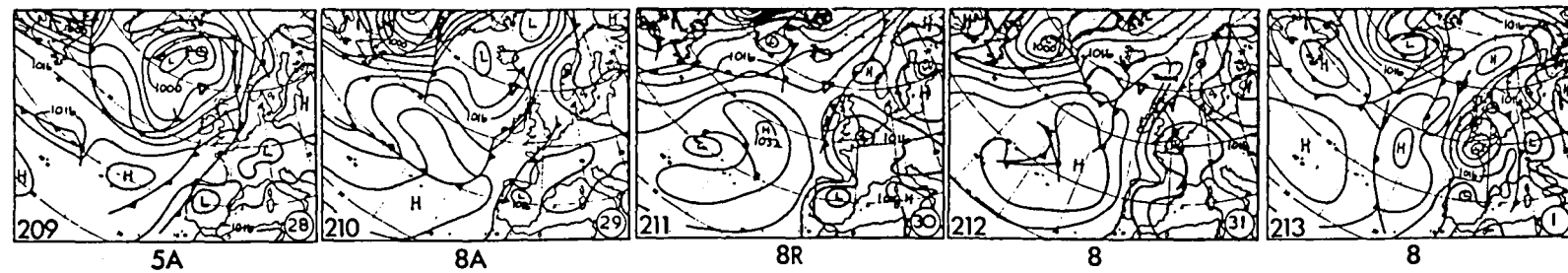
JULY - PHASE 0 (contd.)



JULY - PHASE 1



JULY - PHASE 1 (contd.)



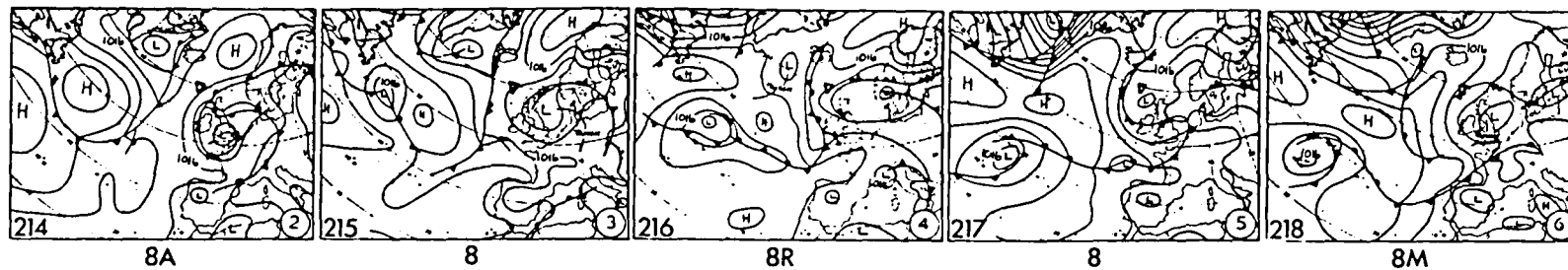
AUGUST

n = no. of ships on station , R = intensive radiosondes , A = aircraft operating , I = full intercomparison
(I) = partial intercomparison

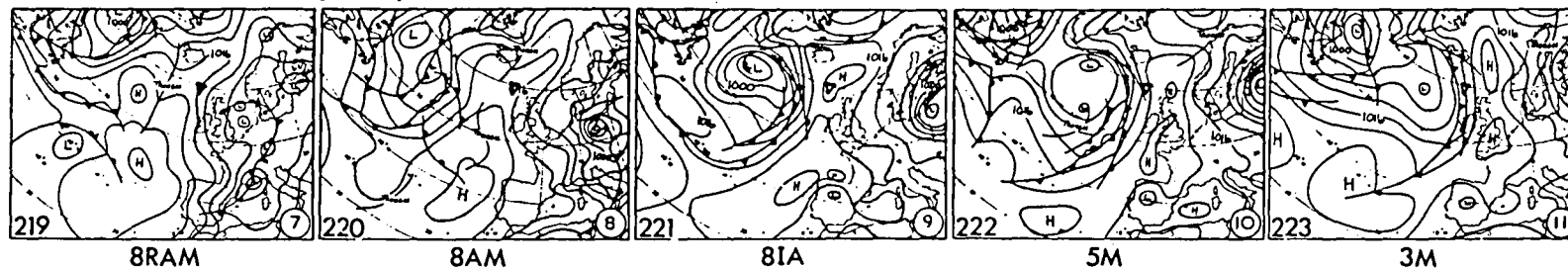
Figure 2-11 (contd)

(12GMT) 2 - 16 AUGUST 1978

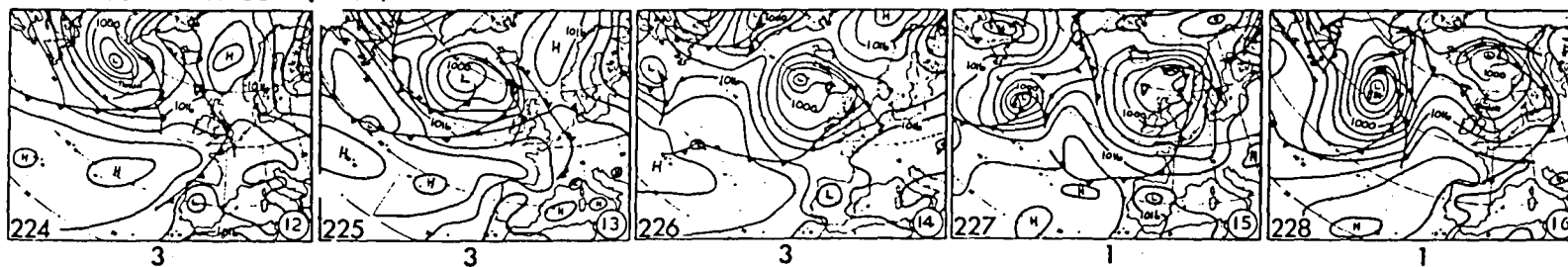
AUGUST - PHASE 1 (contd.)



AUGUST - PHASE 1 (contd.)



AUGUST - PHASE 1 (contd.)

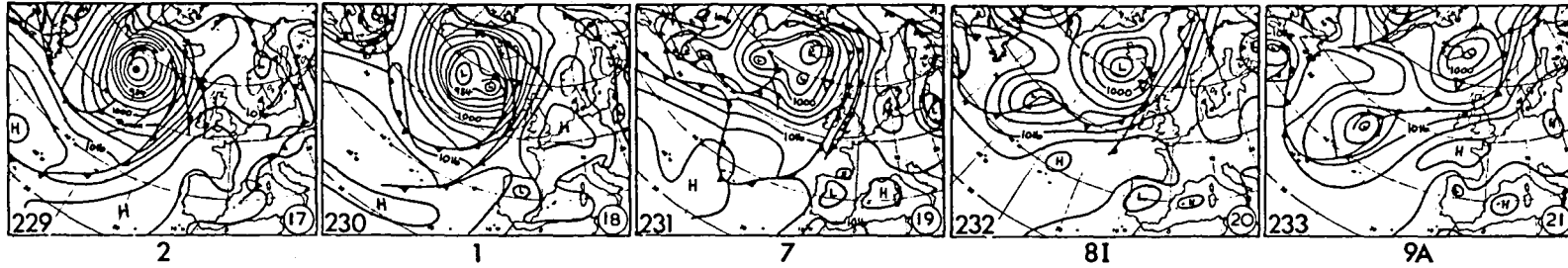


n = no. of ships on station , R = intensive radiosondes , A = aircraft operating , I = full intercomparison ,
M = oceanographic multiship experiment

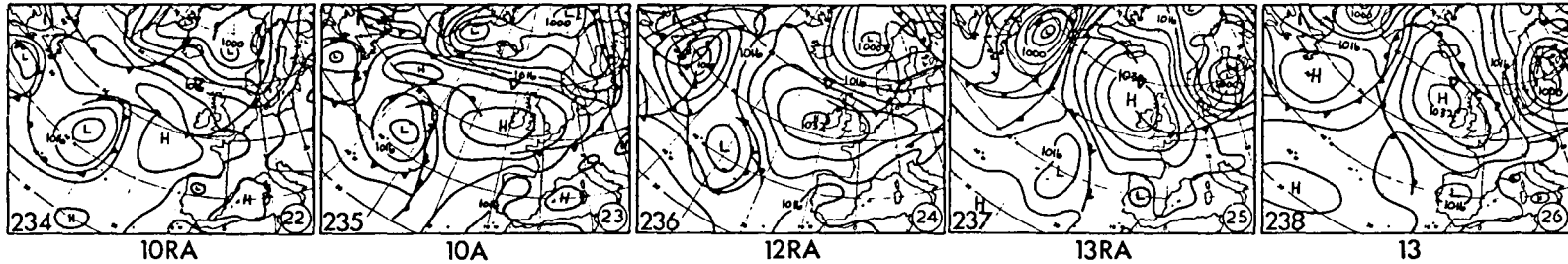
Figure 2-11 (contd)

(12 GMT) 17 - 31 AUGUST 1978

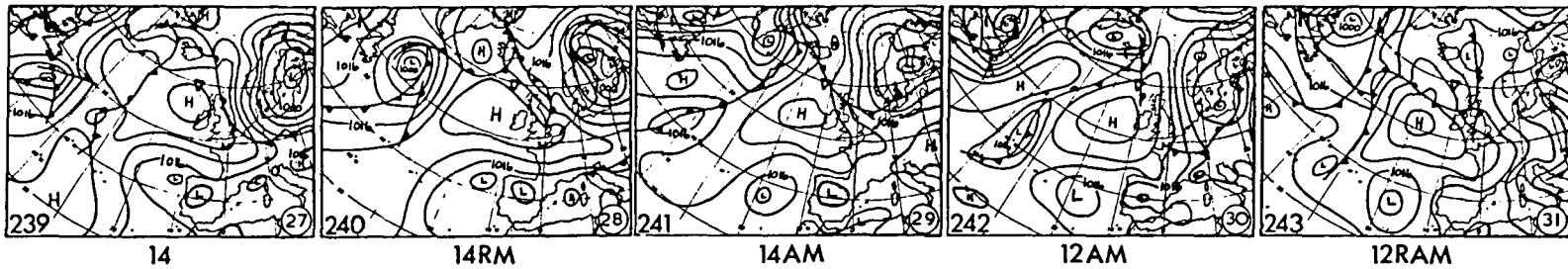
AUGUST - PHASE 2



AUGUST - PHASE 2 (contd.)



AUGUST - PHASE 2 (contd.)

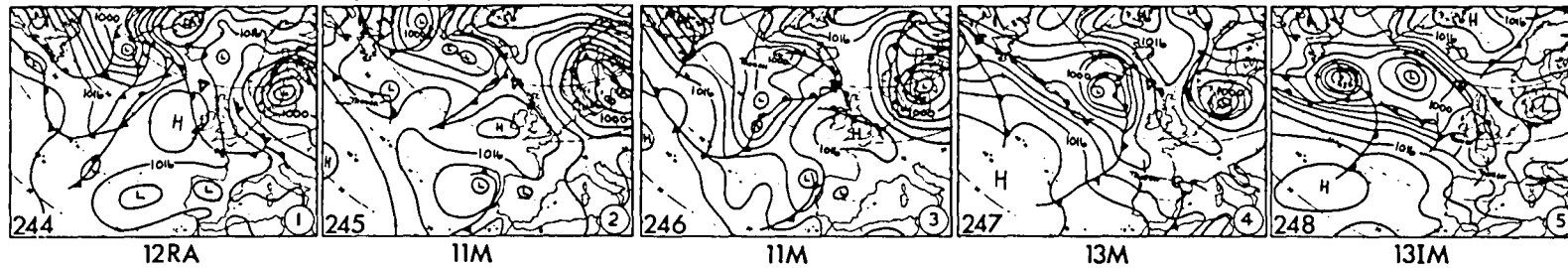


n = no. of ships on station , R = intensive radiosondes , A = aircraft operating , I = full intercomparison
M = oceanographic multiship experiment

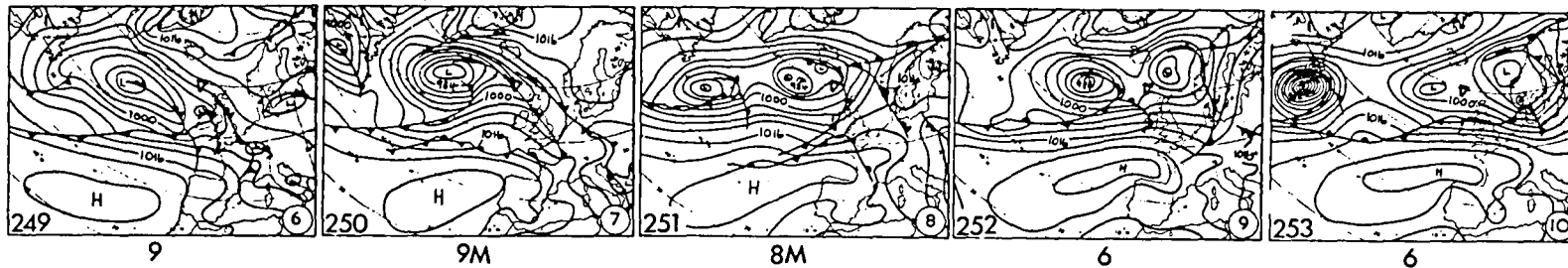
Figure 2-11 (contd)

(12GMT) 1 - 15 SEPTEMBER 1978

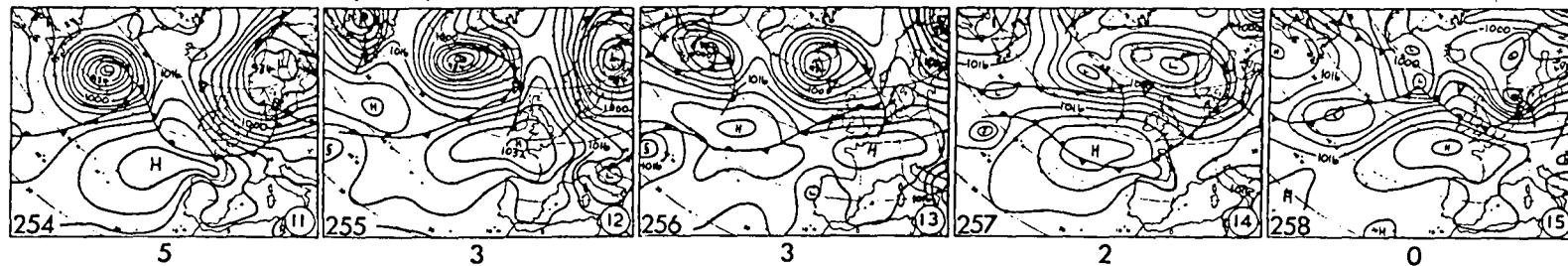
SEPTEMBER - PHASE 2 (contd.)



SEPTEMBER - PHASE 2 (contd.)



SEPTEMBER - PHASE 2 (contd.)



n = no. of ships on station , R = intensive radiosondes , A = aircraft operating , I = full intercomparison
M = oceanographic multiship experiment

Figure 2-11 (contd)

W2 METEOROLOGY

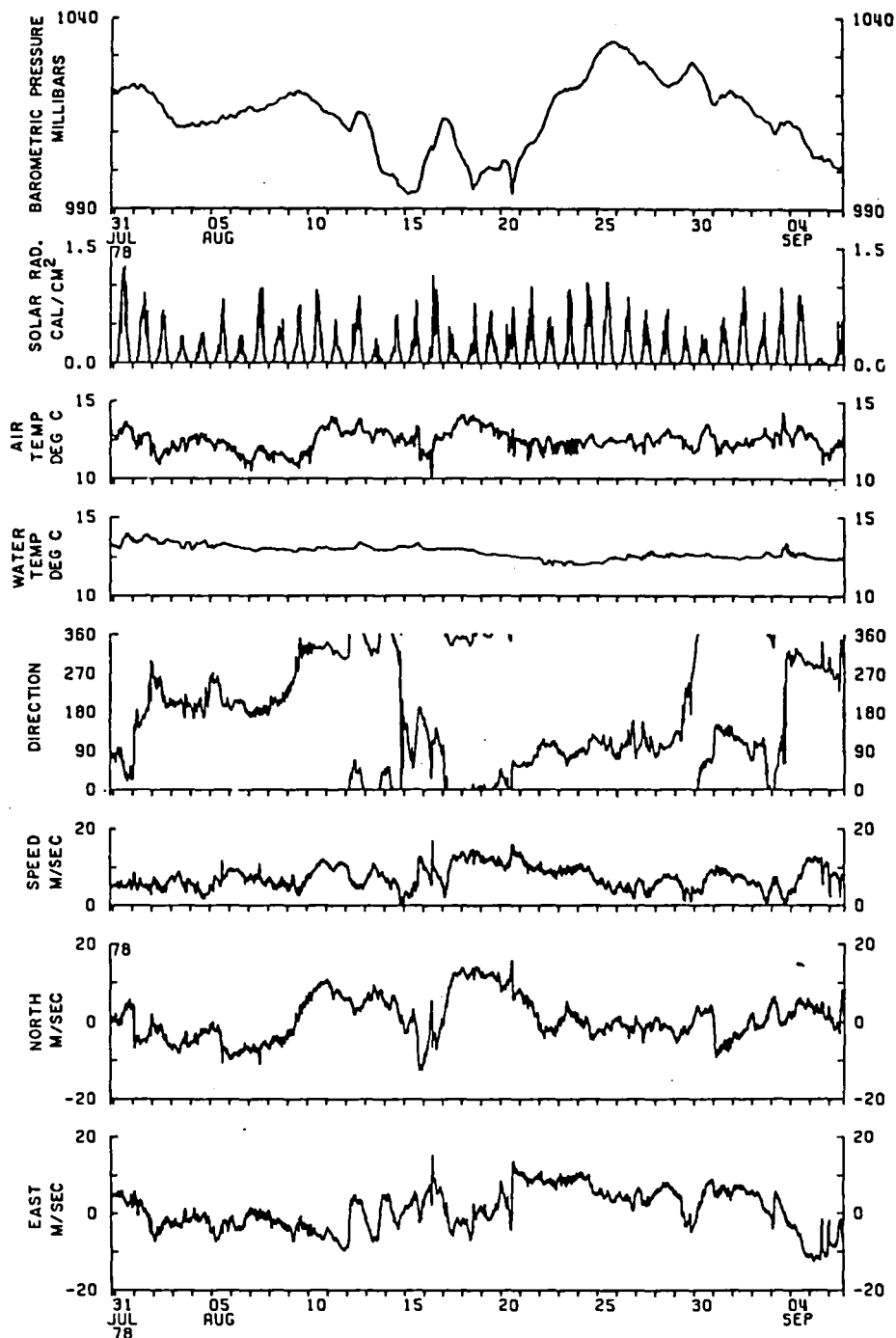


Figure 2-12. Fifteen-min Averages of Vector Wind Speed, Direction, and Air Temperature at 3.5 m Above the Mean Water Line, Sea Temperature at 60-cm Depth, Insolation and Air Pressure From the Vector Averaging Wind Recorder Deployed on W2 for the Period 20:00 GMT 30 July to 18:30 GMT 6 September 1978 (Wind is shown both as components and as speed and direction to which the wind is blowing)

Table 2-3. Available Data

Platform	Type ^a	Sampling	Variables
Meteor	WMO	1 h	Speed, direction, p, T, T _W , T _S + clouds
Hecla	WMO	1 h	Speed, direction, p, T, T _W , T _S + clouds
J. Murray	WMO	1 h	Speed, direction, p, T, T _W , T _S + clouds
Endurer	WMO	1 h	Speed, direction, p, T, T _W , T _S + clouds
Meteor	AUT	Not available for several months	
Hecla	AUT	Arrived just before workshop	
J. Murray	AUT	1 min	Speed, direction, p, T, T _W
Endurer	AUT	As Hecla Aut	
Tydemann	AUT	1 min	Speed, direction, p, T, T _W , T _S
Discovery	AUT	6 min	Speed, direction, p, T, T _W
W2	AUT	15 min	Speed, direction, p, T, T _S
W2M	AUT	2 min	Speed, direction
S13	AUT	1 h	Speed, direction, T, T _W , T _S
H2	AUT	2 min	Speed, direction
B4	AUT	15 min	Speed, direction, T, T _S
J1	AUT	2 min	Speed, direction, p, T, T _W , T _S
^a WMO = Manually logged according to World Meteorological Organization Standards AUT = Automatic recording system			

in time for the workshop. Although priority has been given to selected Seasat passes (Section III), the tapes provided to JPL covered most of the recording period of each platform and, therefore, represent a large proportion of the JASIN surface meteorological data set.

2. Initial Procedures

Figures 2-13 and 2-14 outline the steps involved. After converting to a standard format and ensuring that all required variables were present, e.g., obtaining true winds from apparent wind and ship's velocity, conversion of components to speed/direction, the data were plotted to standard scales and inspected for inconsistencies. These plots have proved very valuable and are included elsewhere in the workshop documentation. In the case of autologged data from ships, it was sometimes necessary to calibrate data against WMO values because of drift problems and incorrect pre-JASIN calibrations. These and other aspects of the data are detailed in Table 2-4.

3. Intercomparison Analysis

Data obtained during intercomparison periods were used to identify instrument bias. These periods can be divided into 3 types:

- (1) Formal meteorological ship intercomparisons (see Figure 2-15 and Table 2-5 for details).
- (2) FIA intercomparisons (Table 2-6).
- (3) Ad hoc intercomparisons (ship-ship and ship-buoy).

Useful information has also been obtained by overlaying plots. An example of a systematic bias between wind sensors on the same platform is shown in Figure 2-16. During the first three days the difference is anomalously large compared with the rest of the 6-wk period (not shown).

In (1), above, the meteorological ships rendezvoused for prearranged periods ranging from 3 to 12 h. The frequency of WMO observations was increased to half-hourly. In (2) platforms are close enough together for the entire measurement period to be considered as an intercomparison. Sub-periods have been selected, and consistency between the differences from one period to the next has been investigated. For (3) occasions of small separation were selected from cruise reports and other documentation. Routines were run on the data to produce merged files sorted by variable, and statistics of inter-platform differences were computed. For WMO observations these differences were first of all calculated adopting Meteor as the standard (see Appendix A for details). Systematic biases were noted, some of which were due to known calibration defects. These are detailed in Table 2-4. When comparing wind speeds, the expected differences due to variations in sensor height have been allowed for by applying a stability-dependent model of the wind in a constant flux layer. The remaining, unexplained differences are plotted in Figures 2-17--2-21 for wind speed, direction, pressure, dry bulb, and sea-surface temperatures.

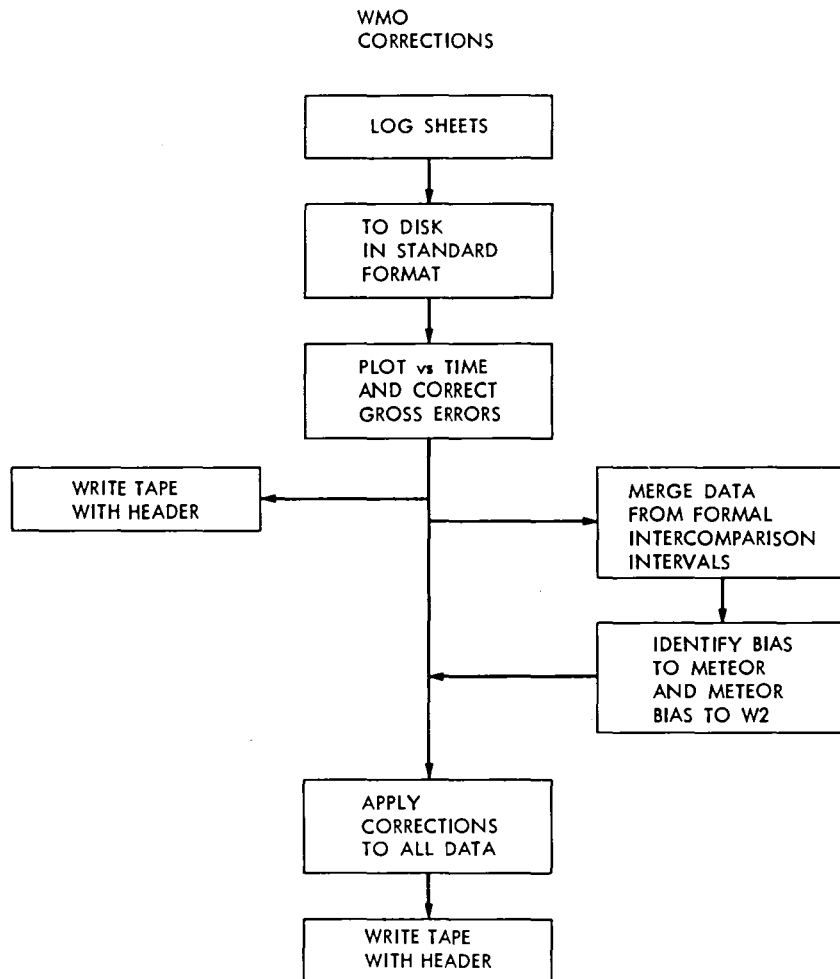


Figure 2-13. Data Processing for WMO Observations

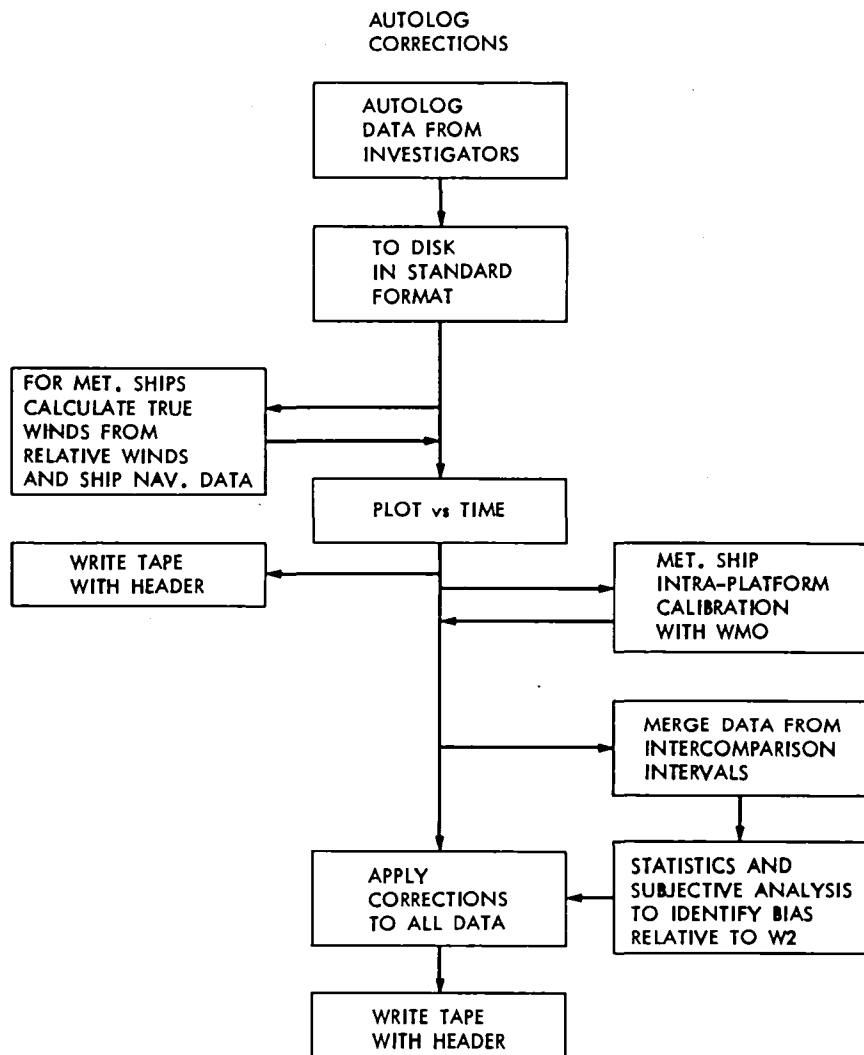


Figure 2-14. Data Processing for Autologged Data

Table 2-4. Comments on Sensor Performance (as at 20 March 1980)
(These will be updated as further information becomes available)

Platform	Effects Corrected for in JPL Data Set	Effects Which Remain in JPL Data Set
Meteor WMO	<p>Bucket temps showed sudden changes in calibration</p> <p>WMO I/Cs suggested change in direction offset with time not supported by FIA I/C. Constant value of 10° used</p>	<p>Some variation of wind speed differences from W2, days 234-248.</p>
Hecla WMO	<p>Anemometer oversped. Linear relation with Meteor ($r = 0.97$). Consistent with heavy design</p> <p>Pressure sensor replaced on 28 July, read 0.3 mbar higher</p>	<p>Diurnal effect on air temps</p>
J. Murray WMO	<p>Suffered measured shift in direction measurements of 15°. Believed to have occurred on approximately 23 July, supported by I/C analysis. Initial vane alignment also 5° too low</p> <p>Pressures not subjected to manufacturer's calibration - results are underestimate. Linear regression on Meteor ($r = 0.99$) carried out</p>	<p>Diurnal effects on air temps</p>
Gardline Endurer	<p>Wind vane broken from 07:00 GMT 24 Aug - 23:00 GMT 27 Aug. Visual observations of vane orientation used after 12:00 GMT 24 Aug.</p> <p>Pressures from above platforms corrected to sea level</p>	<p>Directions suspect 07:00-12:00 GMT 24 Aug</p> <p>Diurnal effects on air temps</p>

Table 2-4 (contd)

Platform	Effects Corrected for in JPL Data Set	Effects Which Remain in JPL Data Set
J. Murray (Autologged)	<p>Supplied direction calibration. New calibration derived from intra-platform comparison with WMO, only partially successful. Errors in direction also affect speed in stats files because of averaging method</p> <p>Drifts found in wet bulb. Good values retrieved by calibrating against WMO.</p> <p>SST sensor failed. Any values in stats should be ignored</p>	<p>Bad orbits where direction still in error are:</p> <p>547, 590, 815</p> <p>Speeds will also be affected</p> <p>Data contains many spikes which may be contaminating statistics</p>
Tydemann	<p>Directions 14° too high, pressures 0.5 mbar too large</p>	<p>In calm, sunny weather very marked diurnal effect on air temps. Nighttime values used in estimating biases</p> <p>Ship continually steaming on variety of headings. Effect of airflow being distorted by ship likely to be significant</p>
Discovery	<p>Speed biased 1.5 m/s low but also variation of difference with relative wind direction</p>	
W2	<p>Used as JASIN standard. No wet-bulb measurements so Meteor values used - made consistent with dry bulbs</p>	<p>Speeds are high by approx 0.4 m/s compared with mean of JASIN platforms</p> <p>On day 211-213 speeds appear anomalously high (by approx 2 m/s)</p>
W2M	<p>0.7 m/s lower than W2. Small direction difference. Winds only recorded</p>	

Table 2-4 (contd)

Platform	Effects Corrected for in JPL Data Set	Effects Which Remain in JPL Data Set
S13	Composite of S1, S2, S3 (spatial separation approx 4 km), data originally recorded at 15-s intervals. Averaged over 1 h. Only good data segments included in composite	
	Directions 14° too low (? neglect of magnetic variation), otherwise excellent agreement with W2	
K3	Used in assessing data but not sent to JPL because of poor quality and redundancy. Pressure and directions very noisy	
H2	Biases derived w.r.t. W2 assumed no N-S gradient of mean wind over 2 weeks. Only winds measured. Meteor values used for stability.	Possible overestimate of winds by 0.4 m/s
B4	Directions 40° too low, otherwise excellent agreement with W2 even though 16 km (10 mi) north of FIA	Error in JPL routines on direction. Therefore stats incorrect for direction and, because of averaging method, for speed also
J1	Direction - problems with calibration up to 29 July, retrieved by calibration against Hecla WMO	Speed sensor O.K. up to 07:00 29 Aug; then failed. Direction U/S for Phase II. Many spikes Buoy, removed from water at 19:00 1 Sept and placed on Hecla's foredeck. Continued to record and data included

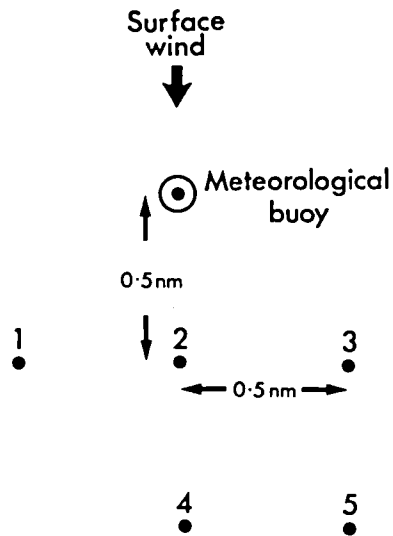


Figure 2-15. Ship Positions During Formal Meteorological Ship Intercomparison Periods (Numbers cross-referenced to Table 2-5)

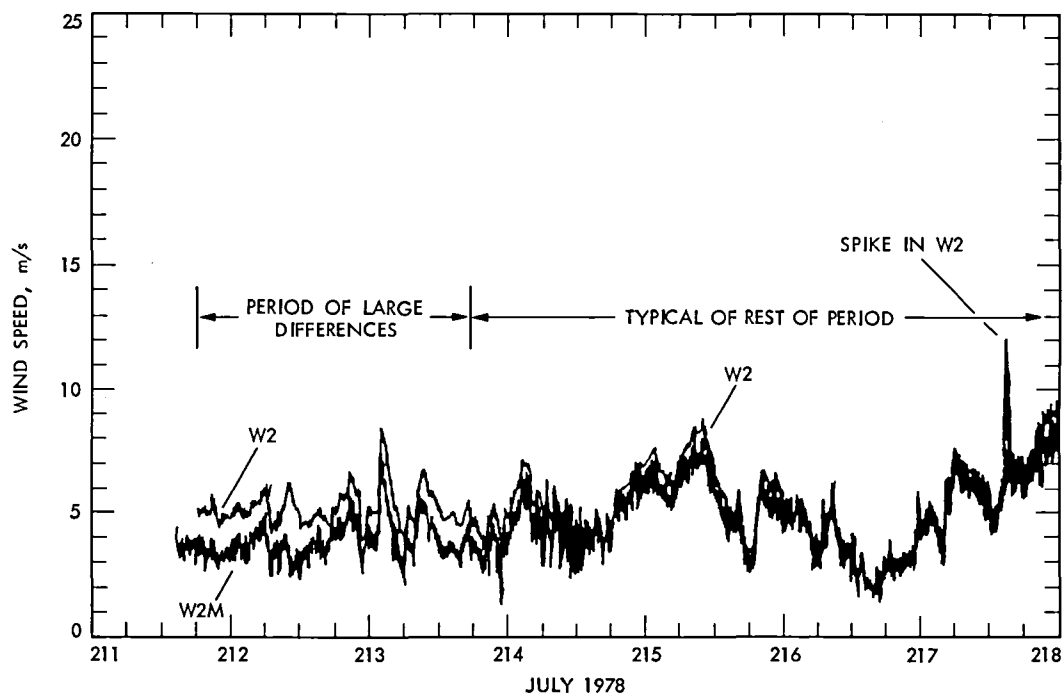


Figure 2-16. Overlaid Plots of W2 and W2M Wind Speeds (two independent systems on same platform)

Table 2-5. Formal Meteorological Intercomparison Periods

I/C No.	Date	Duration	Location	Ships Involved and Position Code (See Fig. 2-15)	1-min. Obs.	WMO ($\frac{1}{2}$ -hourly)	Pressure	Radio- sonde Launches	Tethered Balloons	Precip. Radar	Weather	Comments
I	15-21 Jul		J1	Hecla	x	Hourly	x		x		Generally convective Winds 0-15 m/s between W and N	Two ships generally within 2 nm
				John Murray	x	Hourly	x	x		x		
II	22 Jul	0900-2000	J1	Meteor (4)	x	x	x	x	x	x	Wind 8 m/s /150° Stable, mainly St	Hecla's balloon lost in strong winds of previous night
				Hecla (2)	x	x	x					
				J. Murray (1)	x	x	x	x				
				G. Endurer (3)	x	x	x					
III	9 Aug	0900-1200	B2	Meteor (2)	x	x	x	x			Wind 4 m/s /100° Unstable. Precipita- tion with sight. Cb and Sc	
				J. Murray (1)	x	x	x					
				G. Endurer (3)	x	x	x	x				
IV	20 Aug	0900-1900	J1	Meteor (4)	x	x	x	x			Wind increasing to 18 m/s /170°. Stable precipitation Frontal passage 17:00 GMT	Rough conditions prevented tethered balloons being flown. Vernadsky arrived 14:00 GMT
				Hecla (2)	x	x	x	x				
				J. Murray (1)	x	x	x	x				
				G. Endurer (3)	x	x	x	x				
				A. Vernadsky (5)	x	x	x					
V	5 Sep	0530-0805	B3	Meteor (2)	x	x	x	x	x		Wind 15 m/s /110° Status, rain to- wards end. Near neutral. Frontal passage 10:30 GMT	Endurer not in position due to rough weather but tracked radiosonde
				Hecla (3)	x	x	x		x			
				G. Endurer			Not on station					
				A. Vernadsky (1)	x	x	x					

Notes: A radiosonde intercomparison consisted of a launch from one ship being tracked by all ships (except Vernadsky).

Table 2-6. FIA Intercomparisons

Start	End	Platforms	Variables	\bar{V} , m/s	$\bar{d}d$, °T	\bar{P} , mbars	\bar{T} , °C	\bar{T}_S , °C
0000Z/234	2300Z/236	<div style="text-align: center;"> \uparrow W2, Meteor, S13, K3 \downarrow </div>	Speed	9.1	275	1021	12.3	12.1
0000Z/237	2300Z/239		Direction	4.6	285	1031	12.4	12.5
0000Z/240	2300Z/242		p(not S13)	5.8	225	1024	12.6	12.6
0000Z/243	2300Z/246		T	6.5	285	1018	12.4	12.5
0000Z/247	2300Z/249		T_S (not K3)	5.1	170	1012	13.0	12.8

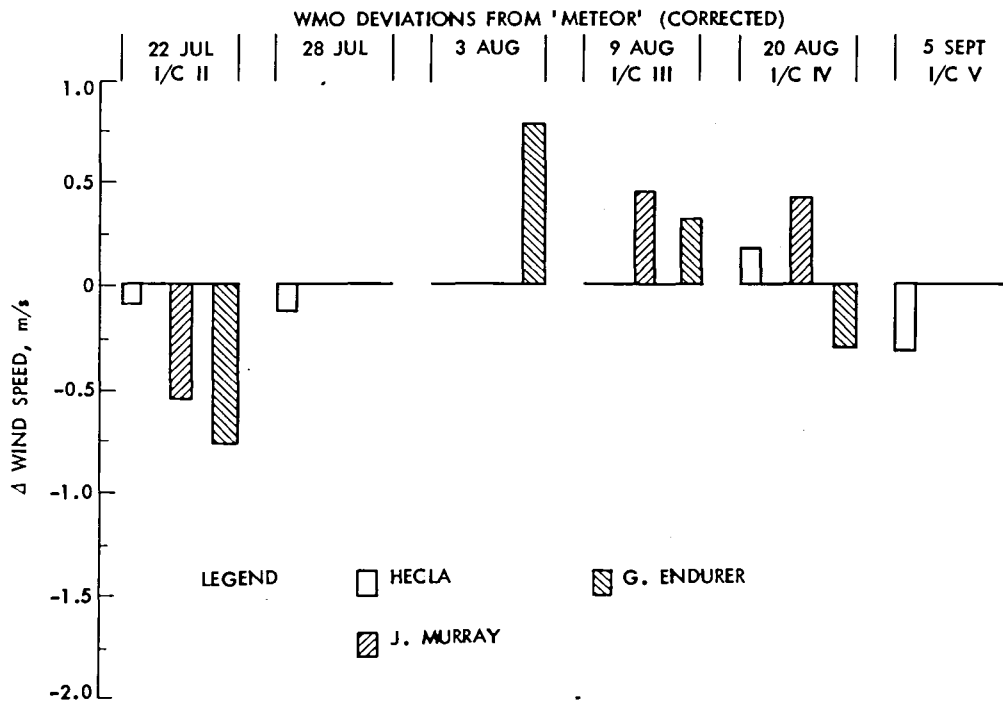


Figure 2-17. Difference Between WMO Wind Speed Measurements (Meteor is standard) After Systematic Biases (e.g., due to sensor height) Have Been Removed

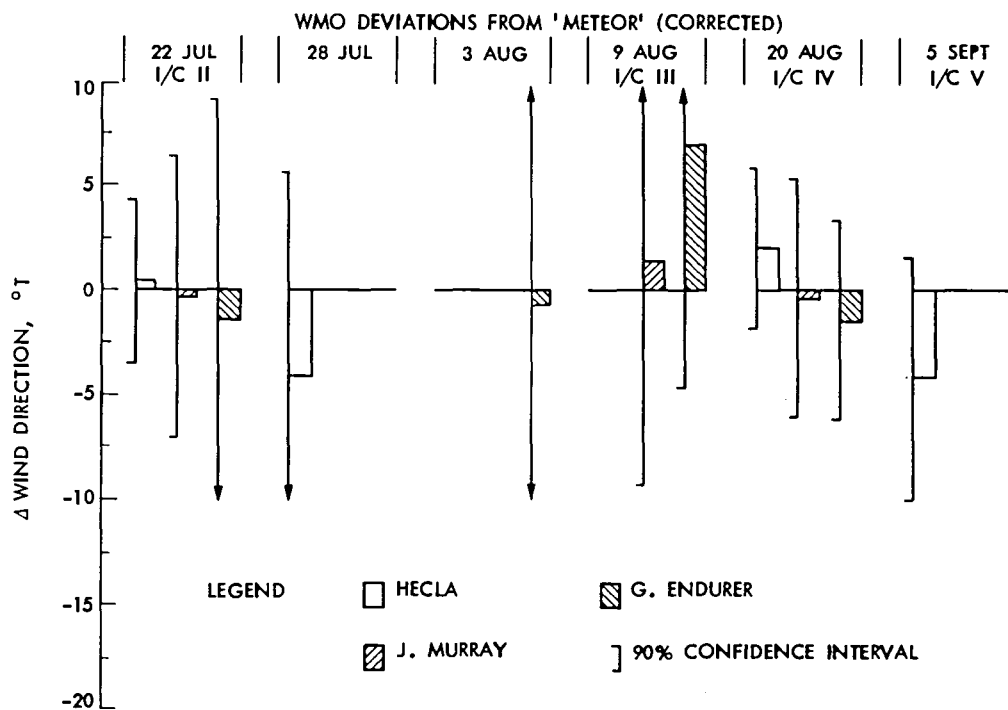


Figure 2-18. As Figure 2-17, but for Wind Direction

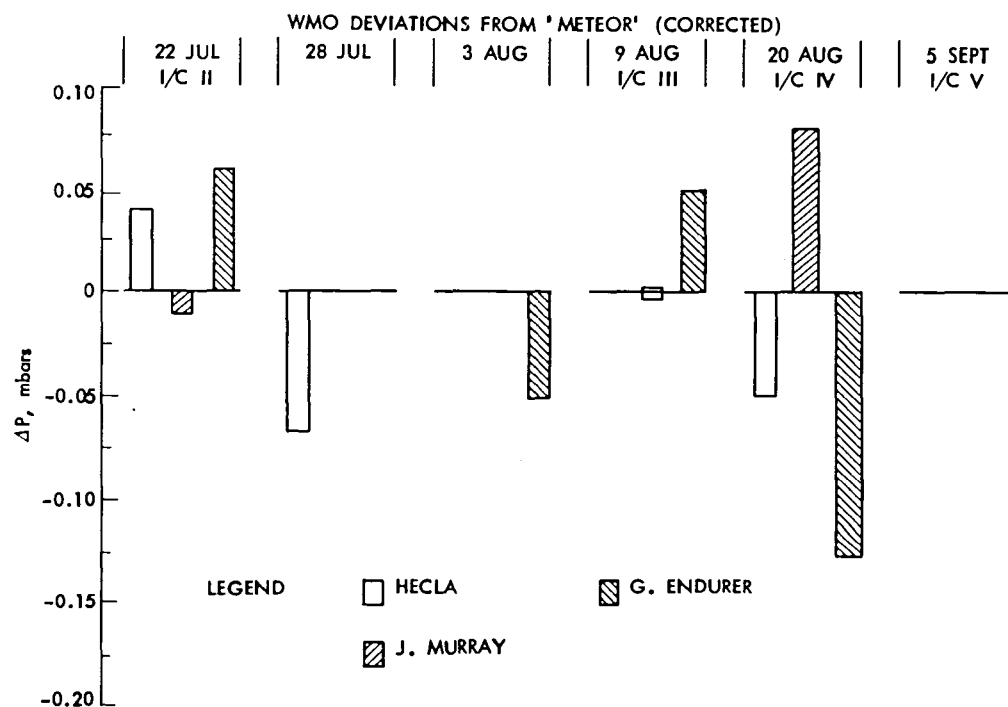


Figure 2-19. As Figure 2-17, but for Atmospheric Pressure (Differences due to sensor height have been taken into account)

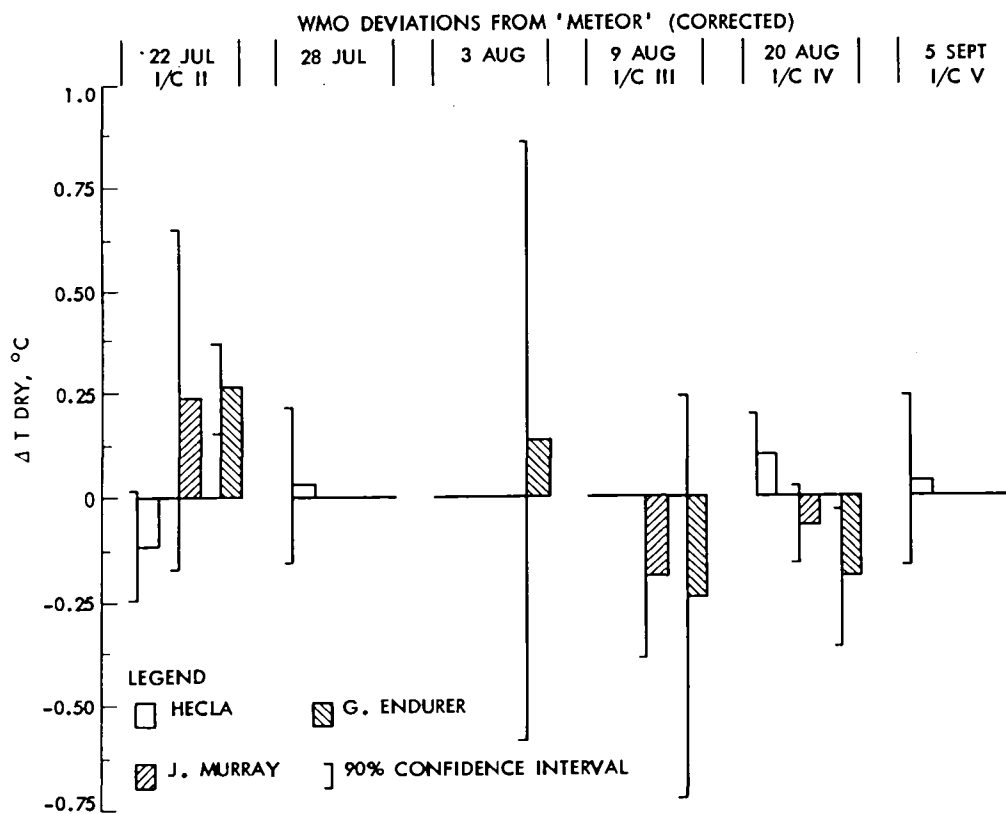


Figure 2-20. As Figure 2-17, but for Dry-Bulb Temperature

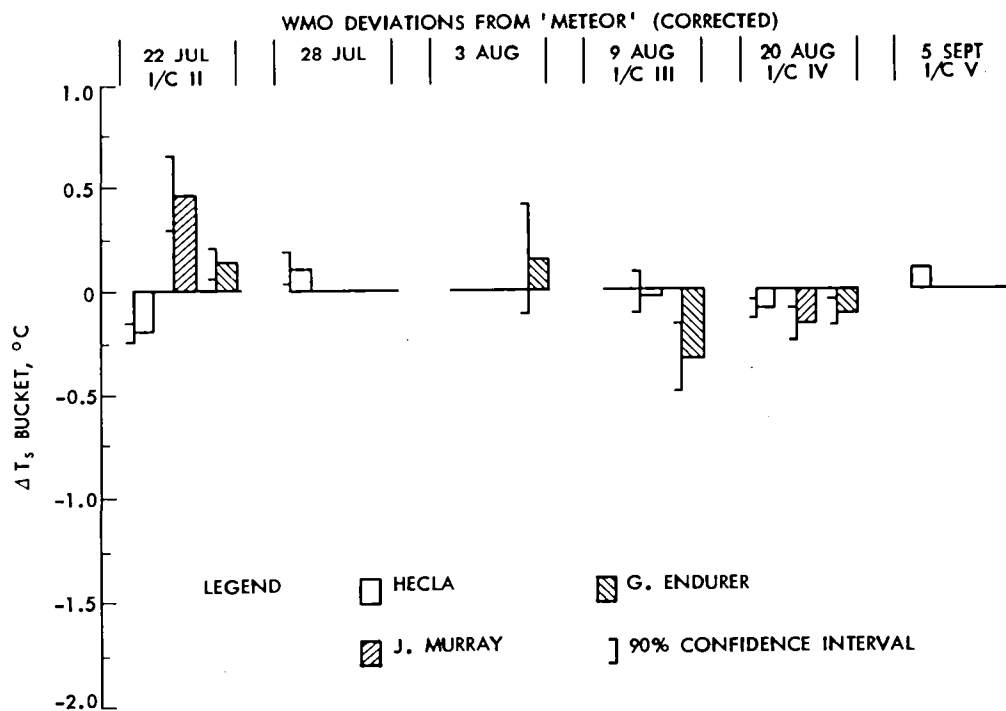


Figure 2-21. As Figure 2-17, but for Sea-Surface Temperature

The next step was to examine differences between FIA platforms, including Meteor since this was her station position. In this way the WMO observations from the four meteorological ships and the buoy data could be indirectly compared. Figure 2-22 presents mean values of the variables for the 3-day periods defined in Table 2-5 expressed relative to W2. We note that K3-W2 wind and pressure differences have large offsets, which in the case of direction and pressure are not constant with time. The standard deviation of individual differences about the 3-day means is also large, and this was one reason for not submitting K3 data to the workshop. None of the data are corrected for height so, as expected, S13 speeds exceed those of W2. One also expects Meteor W2 to be positive, and the small negative values in days 237-243 possibly indicate a wind speed-dependent error. It is particularly encouraging that W2-S13 differences vary little with time and that standard deviations are small.

After careful inspection of the data and recognizing that W2 was the longest continuous record available from a buoy (exposure superior to that of a ship), W2 was selected as the JASIN standard to which all other measurements were referred. (The choice of a single platform as a standard is preferred to using the overall mean because it facilitates subsequent modification as new information comes to light.) The extent to which W2 represents an absolute measure of each of the variables is discussed below, including some post-workshop analysis.

Finally, autologged data from outside the FIA were included in the analysis. For this, it was assumed that horizontal gradients over 40 km averaged to zero over periods of a few days so that B4 and H2 could be compared directly with W2. Since Hecla maintained station close to J1, her WMO observations have been used to derive biases for J1. Additionally, occasions when Tydeman, Discovery, and John Murray were close to W2 have been examined.

On the basis of these intercomparisons, corrections have been deduced and applied to the data (Table 2-7). Generally, these are simple offsets because the range of conditions sampled is rarely large enough to yield meaningful statistics, e.g., dependence of wind speed bias on ambient wind speed. Only the long time series from the FIA data set is suited to this purpose.

Data sets (with and without corrections) and appropriate headers were written to tape and sent to JPL for merging with the satellite data (see Subsection F). Some platforms did not measure one or more of the following: pressure, dry bulb, wet bulb, and SST. In such cases the closest Meteor WMO value (suitably corrected to W2) was inserted except when Meteor was off station. Some care has been taken to ensure that corrections to dry- and wet-bulb temperatures do not result in humidities greater than 100 percent.

Inter-platform differences, which are not systematic or cannot be related to other variables, remain as uncertainties in the system. These values are stated in Table 2-8 and represent the accuracy to which we can produce an internally consistent data set. Any improvement in the accuracy of the surface data set will require extensive analysis of sensor location and platform characteristics. Figure 2-23 shows preliminary results of the effect of apparent wind direction on Discovery's indicated wind speed.

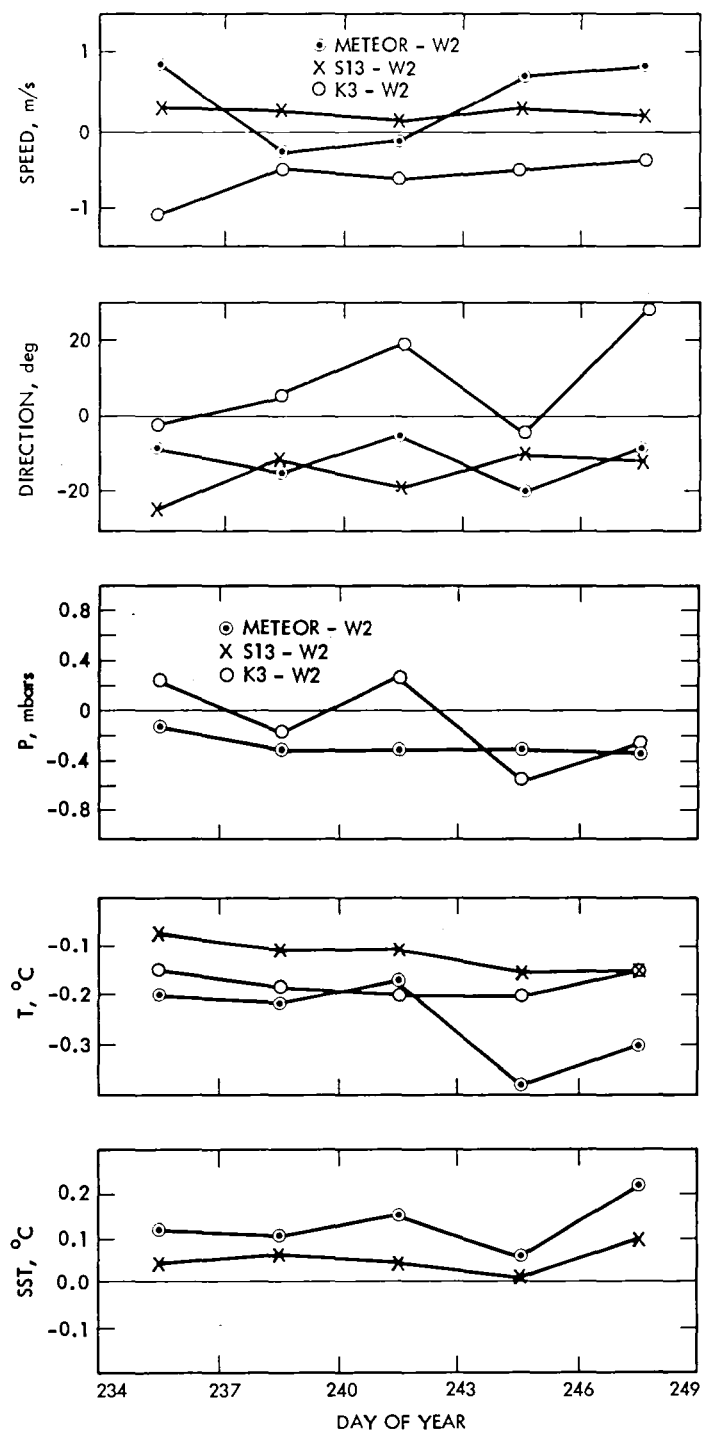


Figure 2-22. Inter-platform Differences in the FIA as a Function of Time (W2 taken as standard; not corrected for height; each point is mean for 72-h period)

Table 2-7. Corrections Applied to Reduce Data to W2 Standards

Platform	Speed, m/s	Direction, deg	P, mbars	T, °C	T _W , °C	T _S , °C
Meteor WMO	0 ± 0.5	+10 ± 5	+0.2 ± 0.1	+0.25 ± 0.1	+0.2 ± 0.1	
Hecla WMO	S = 0.89S' + 0.3 (± 0.3)	-0 ± 5	+0.3 ± 0.1 +0.6 after 28 July	-0.05 ± 0.2	-0.1 ± 0.2	
J. Murray WMO	0 ± 0.5	+5 ± 5 + 20 after 28 July	P = 1.0064 P' -6.0 (± 0.1)	-0.25 ± 0.5	-0.3 ± 0.3	
Endurer WMO	0 ± 0.7	0 ± 5	+0.6 ± 0.2	-0.25 ± 0.6	-0.3 ± 0.2	
J. Murray (1-min)	0 ± 0.2	?	+0.5 ± 0.2	0 ± 0.2	0 ± 0.2	
Tydemann	+0.2 ± 0.5	-14 ± 5	-0.5 ± 0.2	-0.1 ± 0.4	0 ± 0.4	
Discovery	+1.4 ± 0.3	+3 ± 5	-0.23 ± 0.2	+0.15 ± 0.2	+0.15 ± 0.1	-0.11 ± 0.1
W2M	+0.7 ± 0.3	+5 ± 5	-	-	-	
S13	-0.1 ± 0.2	+15 ± 6	-	+0.11 ± 0.1	+0.10 ± 0.1	-0.04 ± 0.1
K3	+0.6 ± 0.2	-8 ± 14	+0.1 ± 0.4	+0.18 ± 0.1	-	Not used in workshop
H2	+0.7 ± 0.3	-5 ± 5	-	-	-	-
J1	0	?	+0.1 ± 0.2	+0.20 ± 0.2	+0.15 ± 0.2	
B4	S = 1.04S' ± 0.2	+40 ± 3	-	0 ± 0.1	-	

Table 2-8. Uncertainties in Biases

Wind speed	± 0.5 m/s	(± 0.3 m/s for buoys only)
Wind direction	$\pm 5^\circ$	
P	± 0.2 mbar	
T	$\pm 0.5^\circ\text{C}$	
T _W	$\pm 0.2^\circ\text{C}$	
SST	$\pm 0.1^\circ\text{C}$	(cannot be derived from I/Cs because of real spatial variability over short distances)

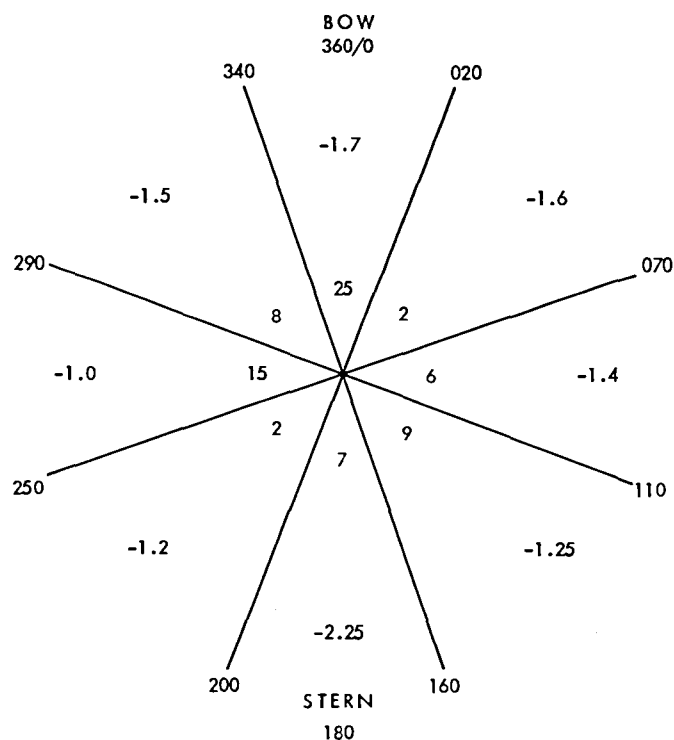


Figure 2-23. Wind Speed Correction for Discovery vs W2 (ship wind minus buoy wind) as a Function of Relative Wind Direction; Bow is 0/360. Note: Corrections take into account the difference in anemometer height of the two platforms. The number nearest the center is the number of 15-min samples in each sector. The wind speeds were between 2 and 6 m/s; the period was days 237--238

4. Absolute Calibration of W2 (Post-Workshop Analysis)

For all variables except wind speed, the derived biases are distributed equally about zero; in the case of speed, most of the biases are negative, indicating a possible overestimate by W2. Since the workshop, R. Weller and R. Payne at Woods Hole Oceanographic Institution, who were responsible for both instrument packages on W2 and a third on H2, have investigated discrepancies between winds from W2 and W2M. They conclude that W2 speeds should be multiplied by 0.87, which for the mean wind speed during JASIN of 8 m/s would imply an average overestimate of 0.7 m/s, precisely the bias attributed to W2M in the previous section. In light of this, FIA wind speeds were carefully re-examined with particular emphasis on determining any wind speed dependence and making use of data from B1, B2, B3, and B4 that were not available at the workshop.

First, differences between W2 and each of the other platforms were plotted as a function of W2 wind speed (Figure 2-24). Values have been corrected to 10 m except for W2-W2M, where both were measured at the same height of 3.5 m. W2 data up to 06:00 GMT 2 August have been removed from the comparisons because of the anomalous behavior already noted; three spikes were also removed. Although curves are displaced by differing amounts, the broadly similar trends of all traces suggest that there is a nonlinear calibration problem with W2 such that it underestimates at 0-3 m/s and >12 m/s but overestimates for speeds between 3 and 12 m/s. It is also apparent that W2-W2M shows a roughly linear increase with speed giving the following relationship:

$$W2M = 0.91W2 + 0.14 \quad (r = 0.92)$$

This is similar to Weller and Payne's result, the difference in slope perhaps being due to the omission of the first three days and the minor de-spiking. Thus, one interpretation is that W2 over-reads by 5-10 percent. However, we notice that W2M is not typical of other platforms; B1, B2, B3 and S13 all show closer agreement for $V > 3$ m/s, and, although K3 lies closer to W2M, the larger scatter in speed and direction imply that K3 should be treated with caution. Indeed, it is surprising that W2M and K3 should differ from other FIA data by more than B4, situated some 10 km to the north, over which distance real gradients may exist.

Because of the apparent wind speed dependence of W2's calibration, comparisons have also been made relative to B1 (Figure 2-25). For $V > 3$ m/s most curves show little dependence on ambient wind speed, which suggests that the calibration of B1 itself is good and, considering that the time series is almost as long as W2's, that it might prove a better alternative as a standard. (The behavior at < 3 m/s is unimportant in the Seasat context because it is below the threshold used in comparisons with the JASIN data set.) The clearest effect of wind speed is on B4 ($B4 = 0.95B1 + 0.04$; $r = 0.99$), but there is also a suggestion that W2M differences increase with wind speed, as well as having the largest offset.

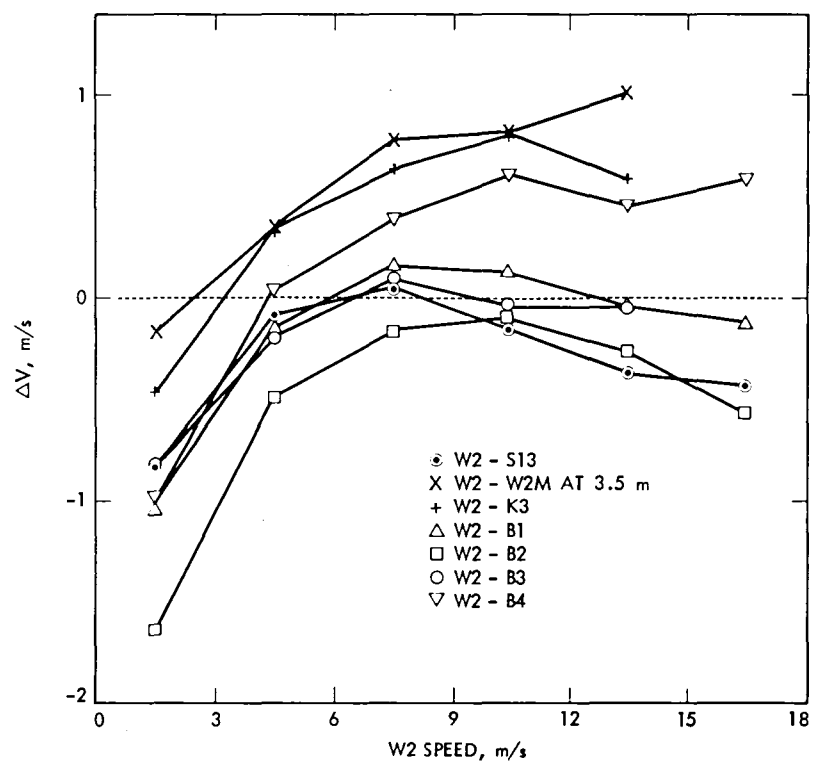


Figure 2-24. Differences With Respect to W2 (direct comparisons; corrected to 10 m)

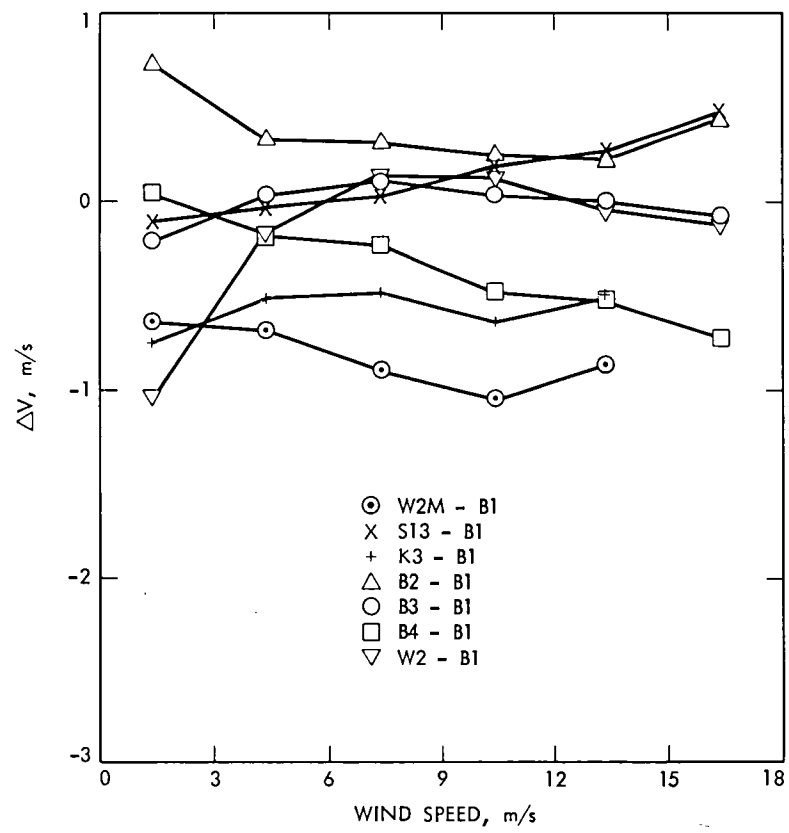


Figure 2-25. Comparisons Relative to B1

If we took B1 as the JASIN standard, then the following corrections to W2 would be implied:

0-3 m/s	+1.05 m/s
3-6	+0.15
6-9	-0.15
9-12	-0.15
12-15	+0.05
15-18	+0.10

Thus, over the range 3-18 m/s, the results above imply that the differences involved in using W2 as the standard rather than B1 are less than 4 percent and, therefore, negligible.

Finally, there is some independent evidence from flux measurements (which are more sensitive to wind speed errors) that W2 speeds are not seriously in error. Weller and Payne's suggestion that W2 overestimates by 13 percent implies that the momentum flux using bulk aerodynamic methods will be 26 percent too large. W. Large (University of British Columbia) made independent measurements of the flux on Meteor in the FIA, and these agree with those calculated from W2 winds to within 5 percent over a period of several weeks.

Thus, our conclusion is that W2 winds are in error by no more than 4 percent for $3 < V < 18$ m/s. No consideration has been given to the different types of sensor used, but it should be stated that propeller wind recorders, as on W2M and H2, have only recently come into use and their characteristics in field operations are largely unknown.

5. Summary of Surface Data Analysis

The JASIN surface data set appears to be consistent in the mean to 0.5 m/s in speed, 5 deg in direction, 0.2 mbar in pressure, 0.5 K dry bulb, 0.2 K wet bulb, and 0.1 K SST. The hope is that SASS can measure wind to ± 2 m/s and ± 20 deg, and SMMR SSTs will be good to ± 1.5 K. Indications are that JASIN data are capable of showing how far this specification is met. Further analysis of the effect of airflow over the ships may yield improved wind and pressure data.

D. ANALYSIS OF RADIOSONDE DATA

1. Available Data

The data available for the workshop represents that data from the ships Endurer and Hecla for which JASIN stage 1 processing has been completed, chosen John Murray flights specially processed for Seasat, and Meteor synoptic reports for 00:00 GMT transmitted on the GTS. Data is also available for Meteor flights on 24 July (day 205).

The data sets will be numbered as follows:

- (1) Endurer data from 27 July to 8 August (days 208 to 220), and from 22 August to 4 September (days 234 to 247).
- (2) Hecla data from 20 August to 5 September (days 232 to 248).
- (3) Chosen John Murray flights.
- (4) Meteor synoptic reports.
- (5) Meteor flights on 24 July (day 205).

2. Characteristics of Each Data Set

Details of the estimated accuracy of each data set are given in Sub-section 3, below. The general characteristics of each data type are as follows:

Data sets (1), (2), and (5) are derived from data transmitted by the radiosondes at 0.8-s intervals and recorded on board ship on magnetic tape. These data have been subjected to sophisticated data processing programs, including de-spiking, filtering, sensor calibration, and sensor lag correction routines before construction of 5-mbar layer mean values. These means have then been integrated to give atmospheric water vapor content values. In both accuracy and temporal coverage, data sets (1) and (2) represent the highest quality JASIN radiosonde data.

Data set (3) has been prepared by digitizing the paper chart records of selected flights from the John Murray. The flights were chosen to ensure that for at least some passes radiosonde data was available from at least three positions in the JASIN radiosonde array. Also, a number of flights were chosen for one day to give a statistically significant estimate of the spatial variation of water vapor content on that day.

These data have been reduced with a simpler processing system which uses the sensor response curves which are normally used in processing standard synoptic radiosonde ascents. However, the vertical resolution of the data points, about every 3 mbars, is much better.

These values have then been integrated using the same program as data sets (1), (2), and (5).

Data set (4) consists of the standard synoptic reports transmitted by Meteor. The significant level data has been used, these being defined as those values of pressure, temperature, and dew point depression required to define the temperature and relative humidity profiles to within 1°C and 10 percent, respectively. The standard level data is normally obtained by interpolation between

the significant levels. Tests have shown that including the standard level data altered the water vapor total by a negligible amount (less than 0.02 kg/m^2); therefore, it has not been used.

Data set (5) consists of the Meteor data for 24 July, which has been processed in a similar manner to sets (1) and (2).

3. Estimate of Radiosonde Errors

In this section we will estimate the errors due to the limits of precision of the sensors, the recording and processing techniques used, and uncertainties in the sensor calibrations. It will be assumed throughout that the errors are random and independent. Factory precision specifications will be used, these having usually proved to be reasonable (e.g., Taylor, 1973). Radiational heating, an important source of humidity error in the past, will be assumed to be negligible. This is to be justified by the use of a new hygistor duct design (Friedman, 1972), the smaller radiational heating at a mid-latitude site, and the predominance of Seasat passes at dawn, dusk, and night.

a. Radiosonde Errors - John Murray (Data Set 3)

(1) Temperature

Estimated errors (rms) are :

Precision of instrument	+0.1°C
Digitization of chart	+0.2°C
Processing program	+0.1°C
Calibration error	+0.2°C

Combining these gives an overall error of +0.3°C.

(2) Relative Humidity

Estimating errors in the measurement of humidity is difficult; an overall accuracy of 4 percent will be assumed for the John Murray data.

(3) Specific Humidity

$$q = 0.622e/(p-0.378e)$$

where the vapor pressure e and pressure p are in millibars. The saturation vapor pressure s is given by

$$s = 6.1078 \exp (17.2694 T)/(T + 237.3)$$

where T = temperature in degrees Celsius, and s is related to the specific humidity by

$$e = Us$$

where U is the relative humidity, which is measured by the radiosonde. Hence, at 0°C the error in e due to +0.3°C uncertainty in temperature is 0.12 mbar. The error in q is then +0.45 g/kg, errors due to the error in the pressure measurement, +1 mbar, being negligible. With increasing height the same error in T and RH results in smaller errors in q and leads to the following uncertainties in integrated water vapor Q:

Surface to 200 mbars +2.0 kg/m²
 Surface to 500 mbars +2.0 kg/m²
 Surface to 700 mbars +1.5 kg/m²

b. Radiosonde Errors - Endurer, Hecla, Meteor (Data Sets 1,2, and 5)

(1) Temperature

Precision of instrument	+0.1°C
Recording and processing	+0.05°C
Calibration error	+0.2°C

giving an overall error of +0.23°C.

(2) Relative Humidity

An error of +3 percent will be assumed.

(3) Specific Humidity

The resulting error in saturation vapor pressure s is +0.09 mbar, leading to an error in specific humidity q of +0.34 g/kg. The resulting errors in the integrated water vapor content Q would be:

Surface to 200 mbars +1.5 kg/m²
 Surface to 500 mbars +1.5 kg/m²
 Surface to 700 mbars +1.2 kg/m²

(4) Variability of Moisture Structure

Apart from errors in the radiosonde measurements, the other factor that affects comparisons between radiosondes or between sondes and satellite measurements is the representativeness of the data. This is particularly true of frontal situations where relative humidity can change rapidly in time and space. The time-height sections in Figures 2-26 through 2-38 show how the structure varies in Phases 1 and 2. On one occasion (day 208, Figure 2-26) a marked decrease in RH was shown by one flight leading to a decrease in the integrated water vapor, Q, up to 500 mbars from 22.2 to 14.2 kg/m² followed by an increase to 21.9 kg/m² on successive flight. Inspection of the data shows that

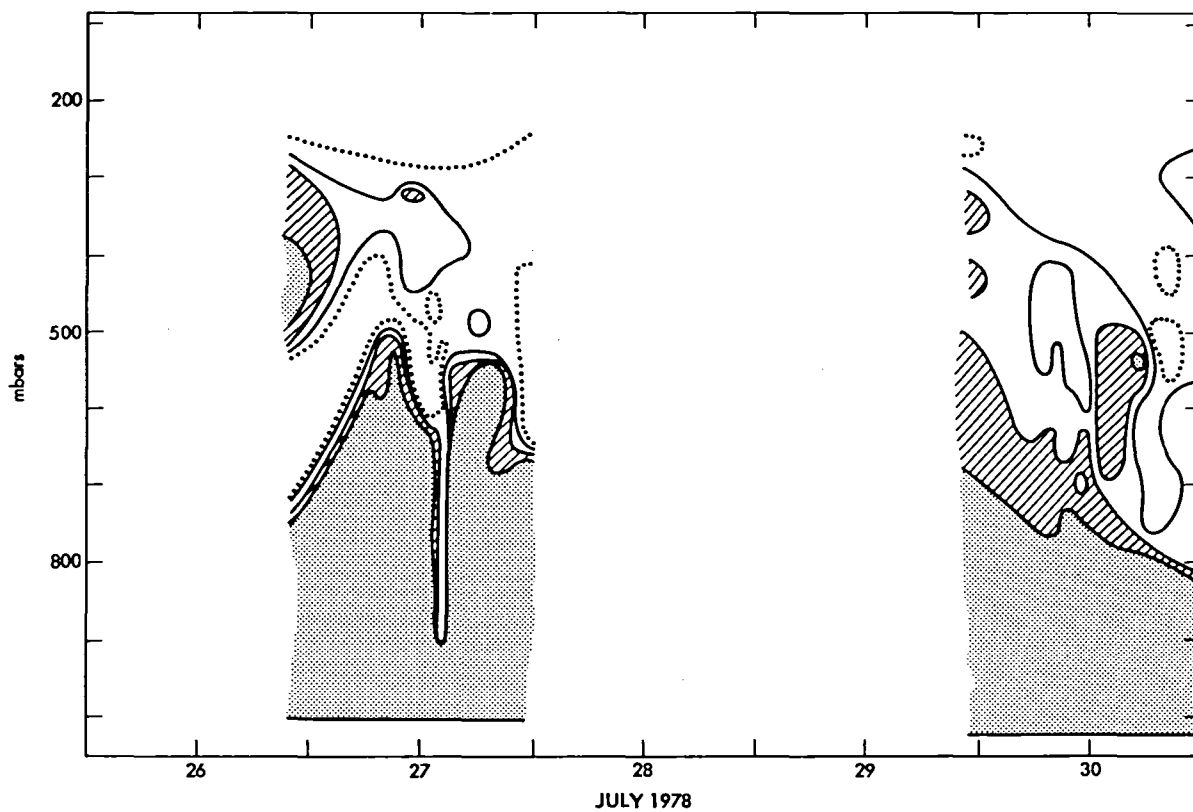


Figure 2-26. Endurer Time Cross Section of RH, 26-30 July (shaded >80 percent, striped >60 percent, continuous line 40 percent, dotted 20 percent)

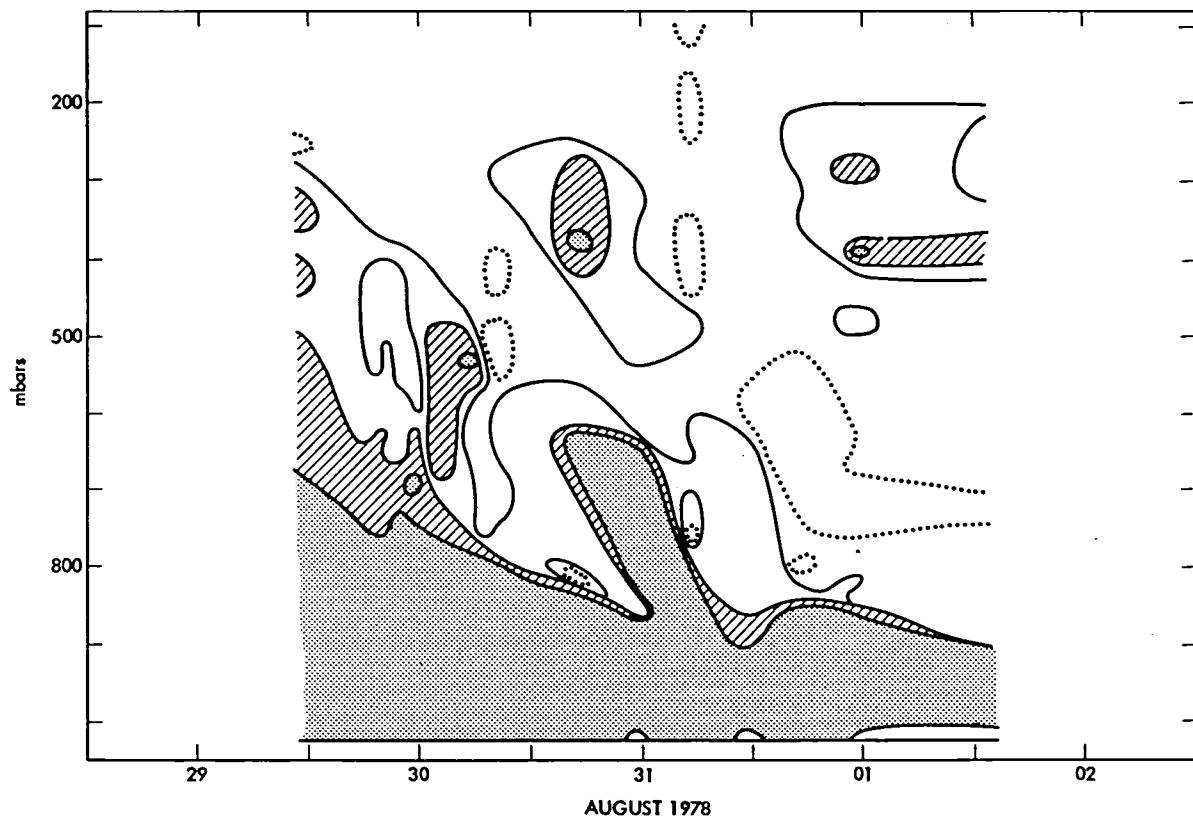


Figure 2-27. Endurer Time Cross Section of RH, 31 July-4 August (shaded >80 percent, striped >60 percent, continuous line 40 percent, dotted 20 percent)

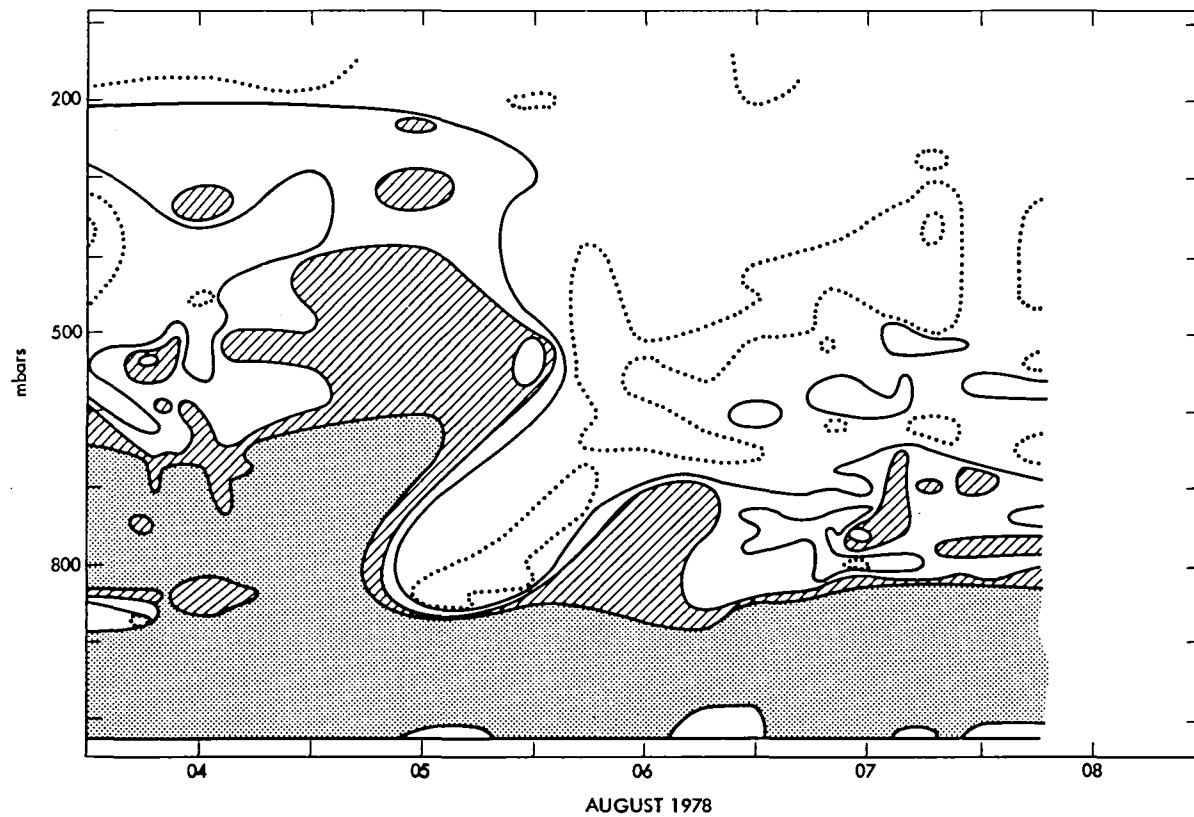


Figure 2-28. Endurer Time Cross Section of RH, 4-8 August (shaded >80 percent, striped >60 percent, continuous line 40 percent, dotted 20 percent)

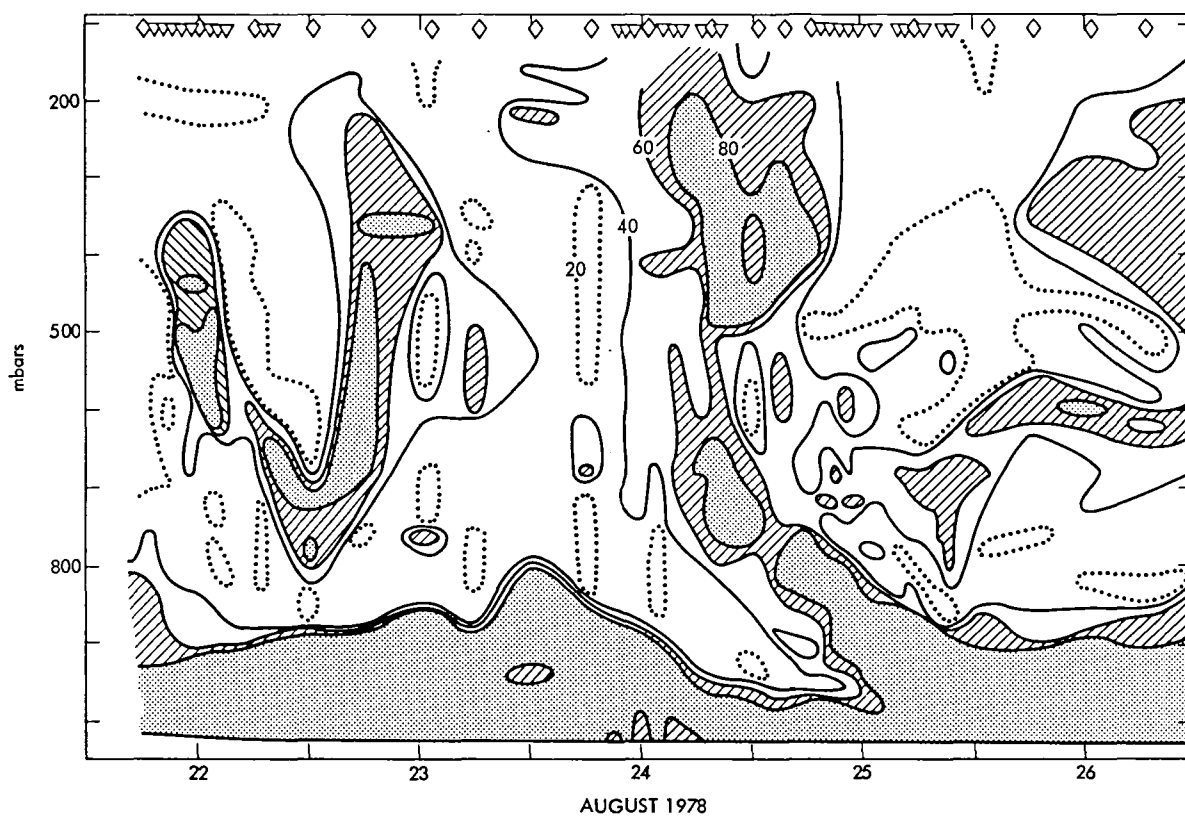


Figure 2-29. Endurer Time Cross Section of RH, 22-26 August (shaded >80 percent, striped >60 percent, continuous line 40 percent, dotted 20 percent)

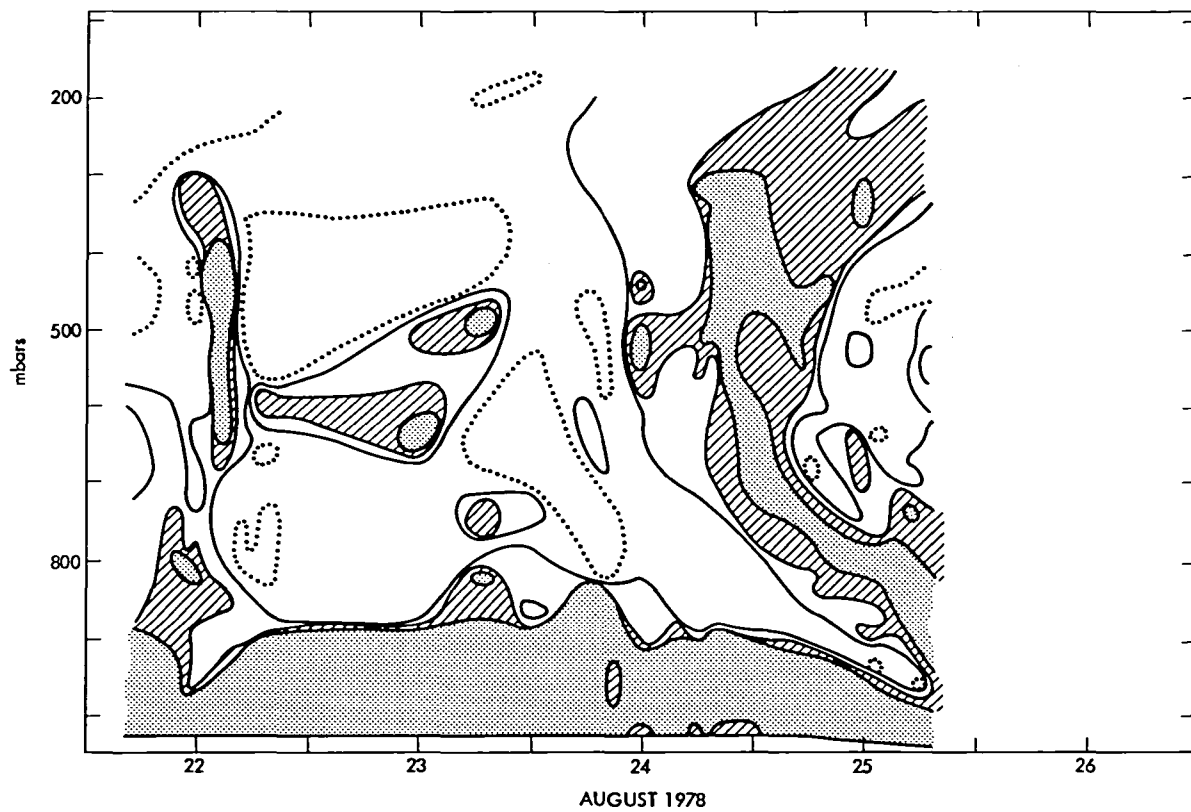


Figure 2-30. Hecla Time Cross Section of RH, 22-26 August (shaded >80 percent, striped >60 percent, continuous line 40 percent, dotted 20 percent)

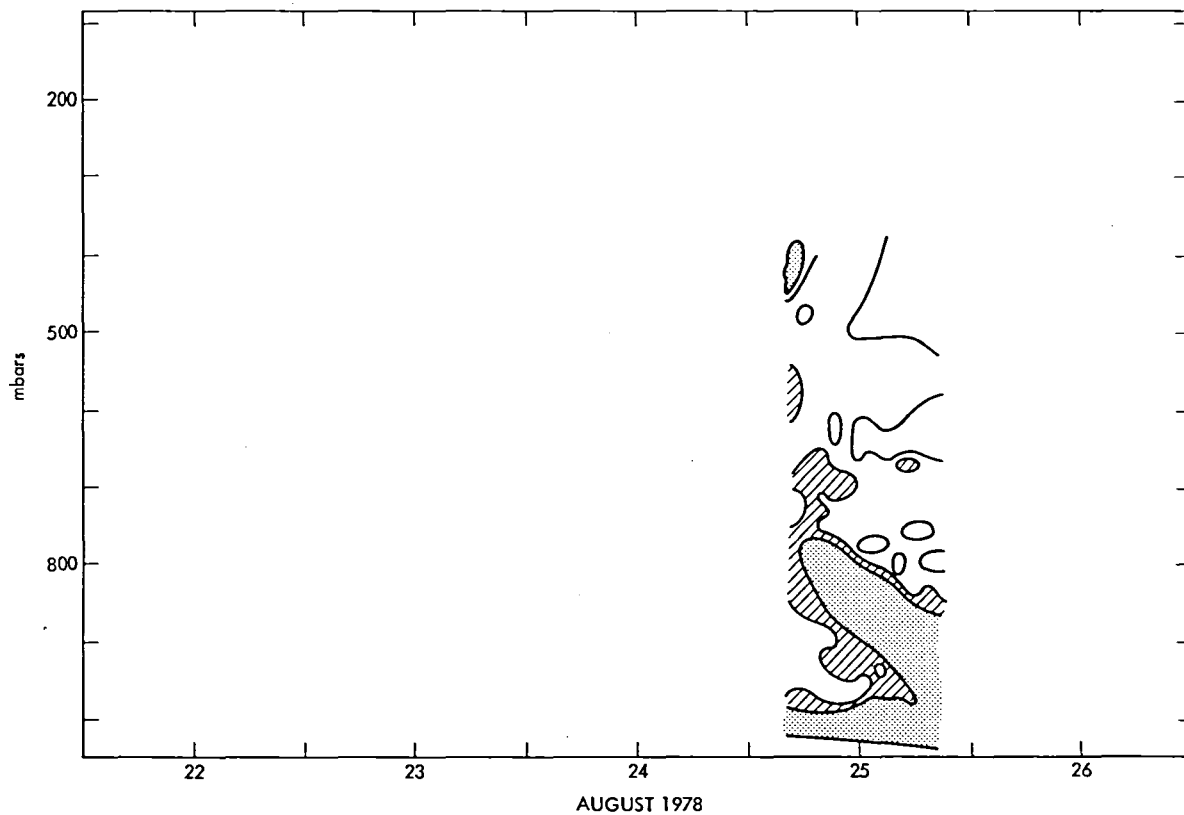


Figure 2-31. John Murray Time Cross Section of RH, 22-26 August
(shaded >80 percent, striped >60 percent, continuous
line 40 percent, dotted 20 percent)

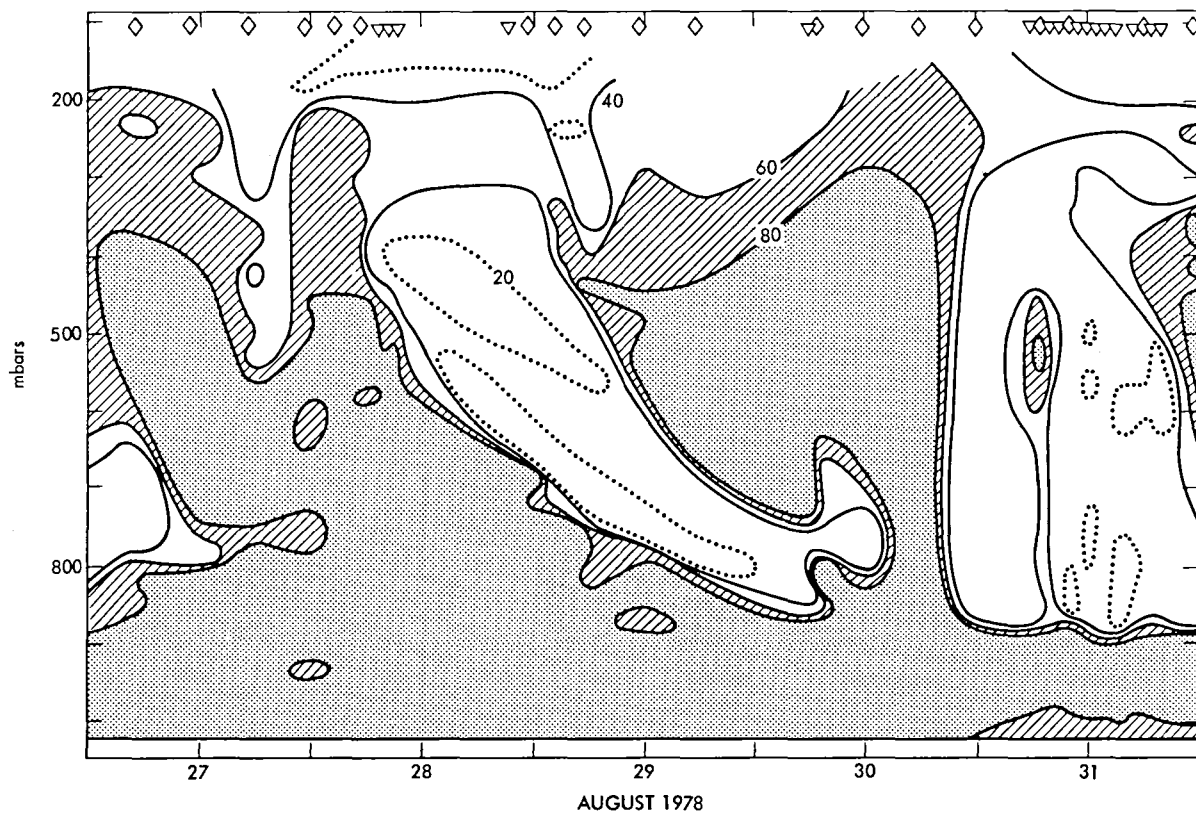


Figure 2-32. Endurer Time Cross Section of RH, 27-31 August (shaded >80 percent, striped >60 percent, continuous line 40 percent, dotted 20 percent)

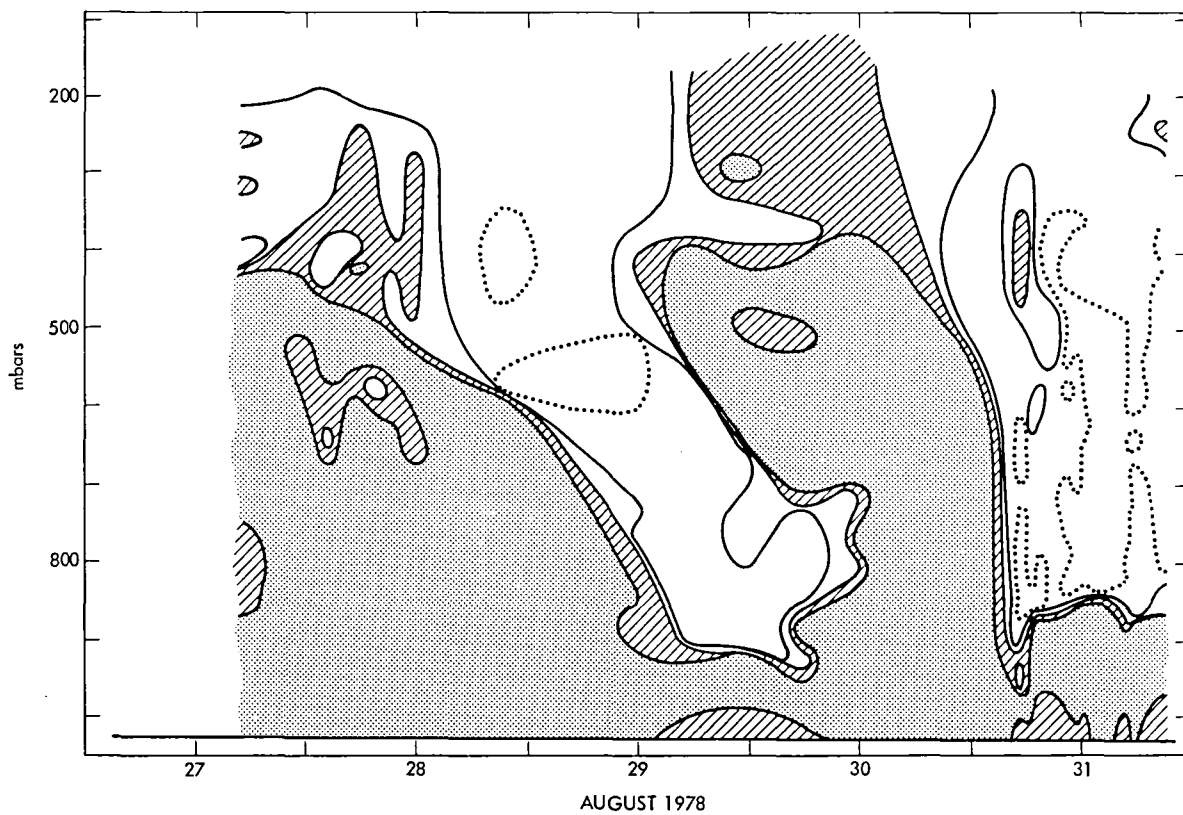


Figure 2-33. Hecla Time Cross Section of RH, 27-31 August (shaded >80 percent, striped >60 percent, continuous Line 40 percent, dotted 20 percent)

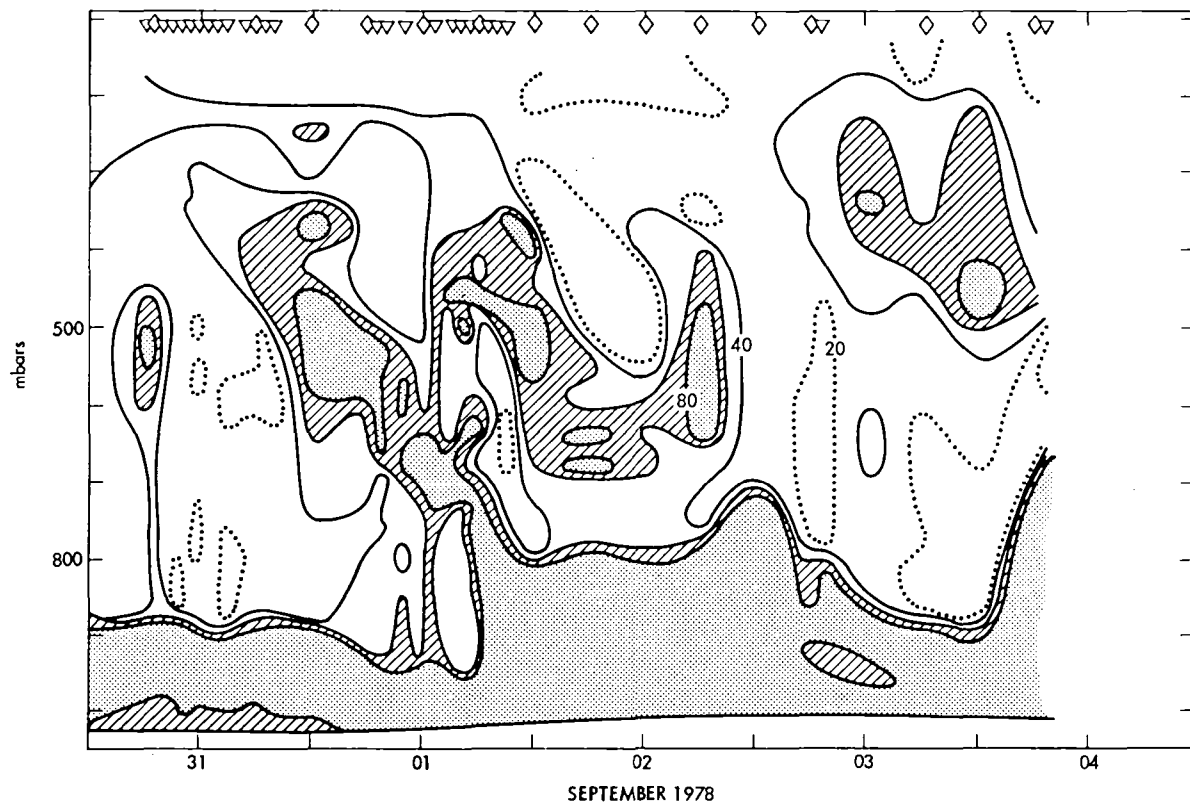


Figure 2-34. Endurer Time Cross Section of RH, 31 August-4 September (shaded >80 percent, striped >60 percent, continuous line 40 percent, dotted 20 percent)

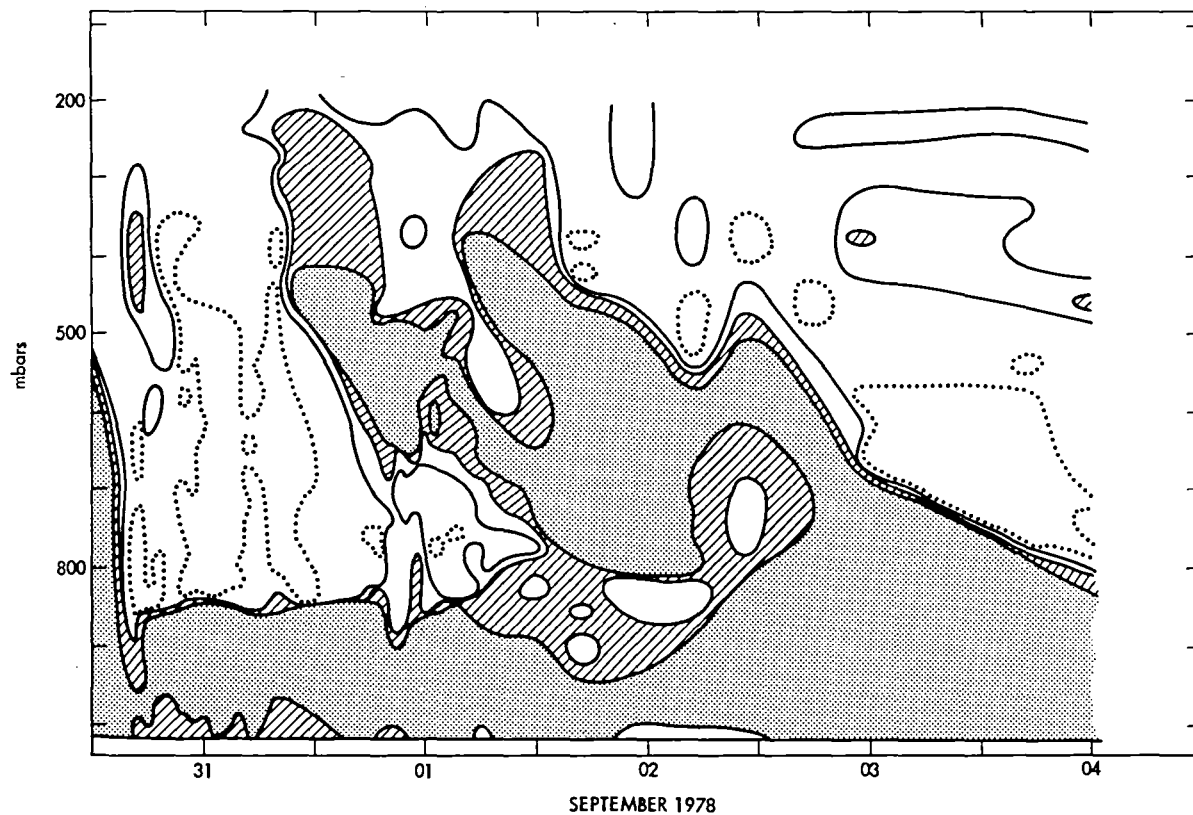


Figure 2-35. Hecla Time Cross Section of RH, 31 August-4 September
(shaded >80 percent, striped >60 percent, continuous line 40
percent, dotted 20 percent)

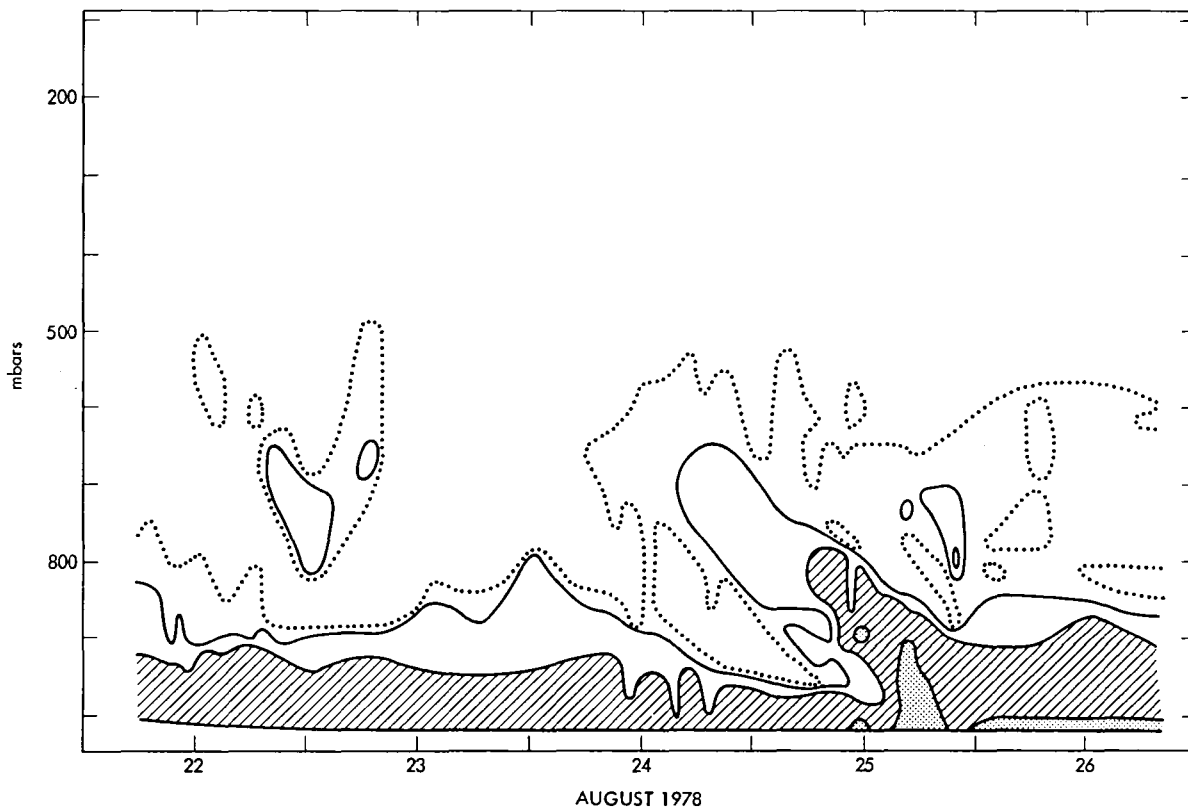


Figure 2-36. Endurer Time Cross Section of q (g/kg), 22-26 August (shaded >8 , striped >6 , continuous line 4, dotted 2)

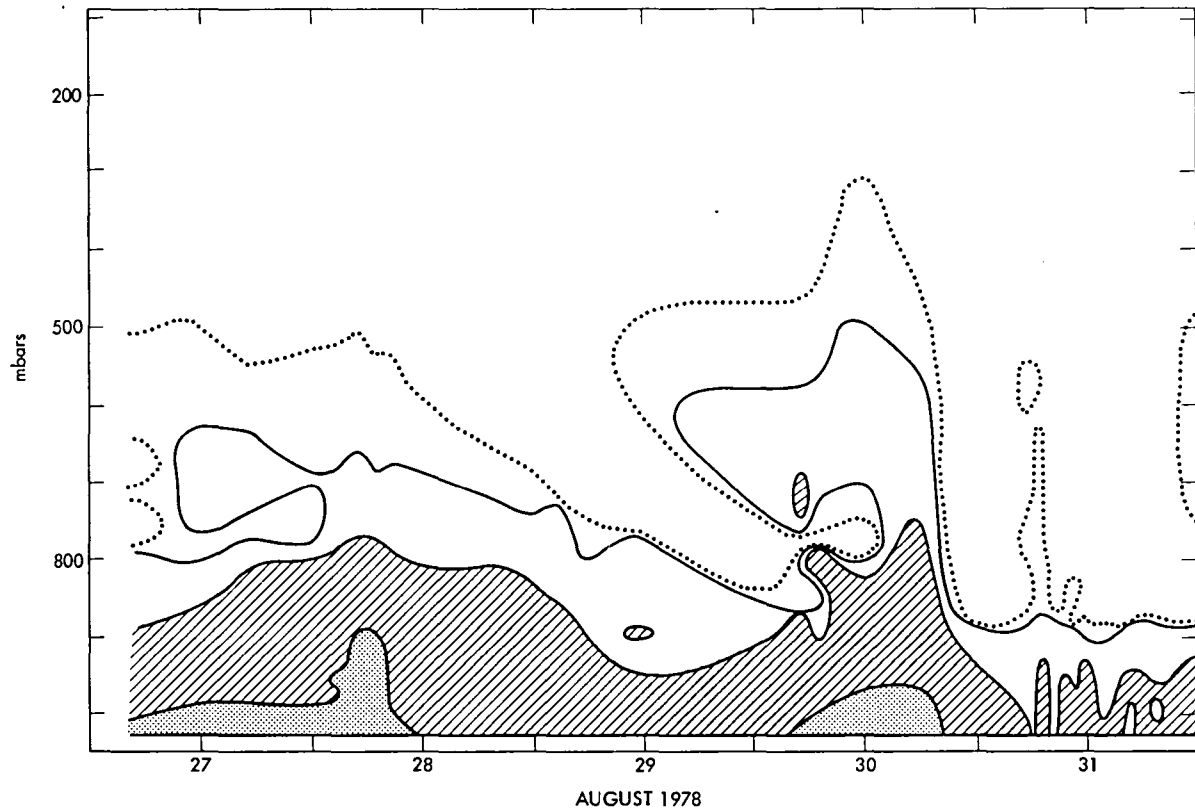


Figure 2-37. Endurer Time Cross Section of q (g/kg), 27-31 August (shaded >8 , striped >6 , continuous line 4, dotted 2)

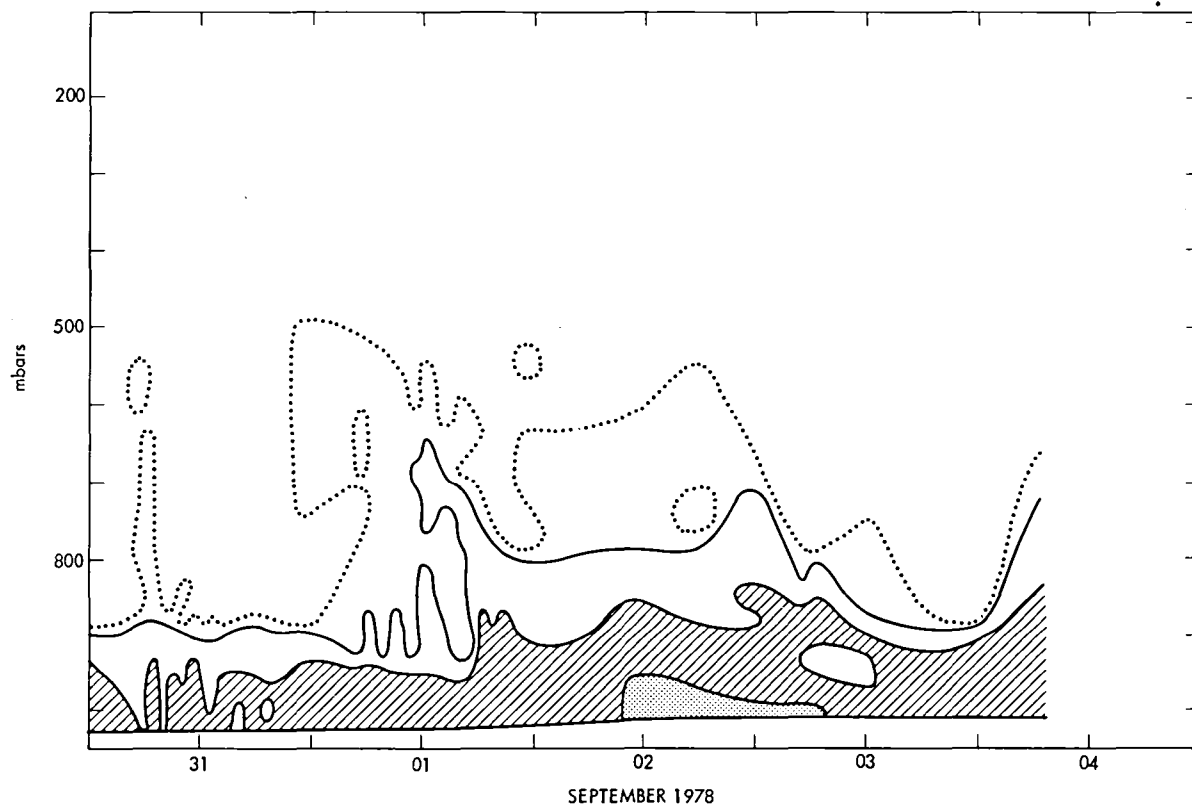


Figure 2-38. Endurer Time Cross Section of q (g/kg), 31 August-4 September (shaded >8 , striped >6 , continuous line 4, dotted 2)

this variation was real; it was, for example, linked with a marked and permanent change in the wind field, and was probably due to an associated front. Clearly, care has to be taken when making SMMR/radiosonde comparisons that differences due to real changes in the atmosphere are minimized; to achieve this it is necessary to inspect horizontal fields of water vapor on each orbit.

(5) Integrated Water Vapor

Figures 2-39 and 2-40 show the integrated water vapor for the surface to 200-mbar layer during Phases 1 and 2. Values range from 13 to 37 kg/m², and similar trends are observed at all ships. Figure 2-41 shows results in more detail for a 2-day period in Phase 2. The final product, consisting of (for each flight) Q over various layers, latitude/longitude, and time of launch, was made available to JPL to be merged with the relevant SMMR data.

(6) Summary of Water Vapor Estimates

A major component of the JASIN meteorological program was to obtain vertical profiles of temperature, humidity, and wind regularly and on a 200-km scale. The accuracy and scope of these measurements probably provides a better test of SMMR's ability to estimate integrated water vapor than any other source of data during Seasat's life. It is concluded that, at worst, errors in the determination of Q by radiosondes amount to 2 kg/m² (0.2 g/cm²).

E. ANALYSIS OF WAVE DATA

1. Introduction

Because of their fundamental importance to many experiments, ocean waves were measured by many observers using a variety of instruments and methods. An attempt is made here to estimate the accuracy of these observations, first, by intercomparing observations made by calibrated instruments, then, using these as standards, comparing them to visual observations.

2. Methods

Using the sets of data listed in Table 2-9, pairs of observations made close together in time (within a few hours) and close in space (within around 50 km) were extracted. For wave height, the square root of the variance of surface elevation measured by the wave buoys over periods of 0.3-1.0 hours was used. The visual observations of wave height were divided by four to obtain a comparable measure. Wave directions were measured as a function of frequency by the pitch-roll buoys. These observations were averaged over bands of frequencies over which directions appeared to be constant to obtain mean wave directions. The bands were approximately 0.05 Hz wide, and were narrower for swell than for wind waves.

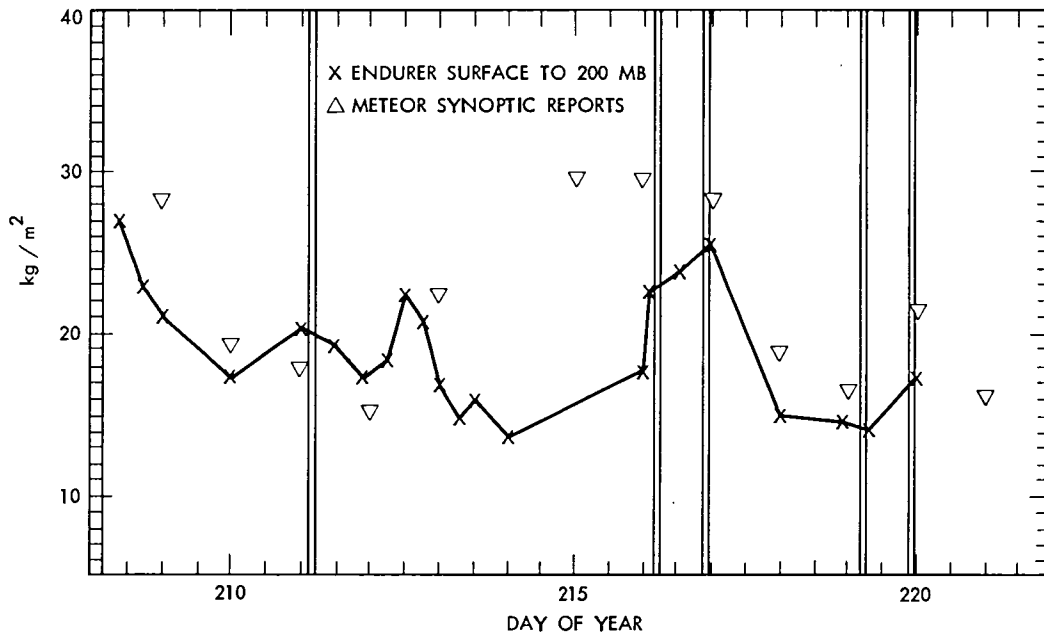


Figure 2-39. Integrated Water Vapor Content (Q) - Phase 1

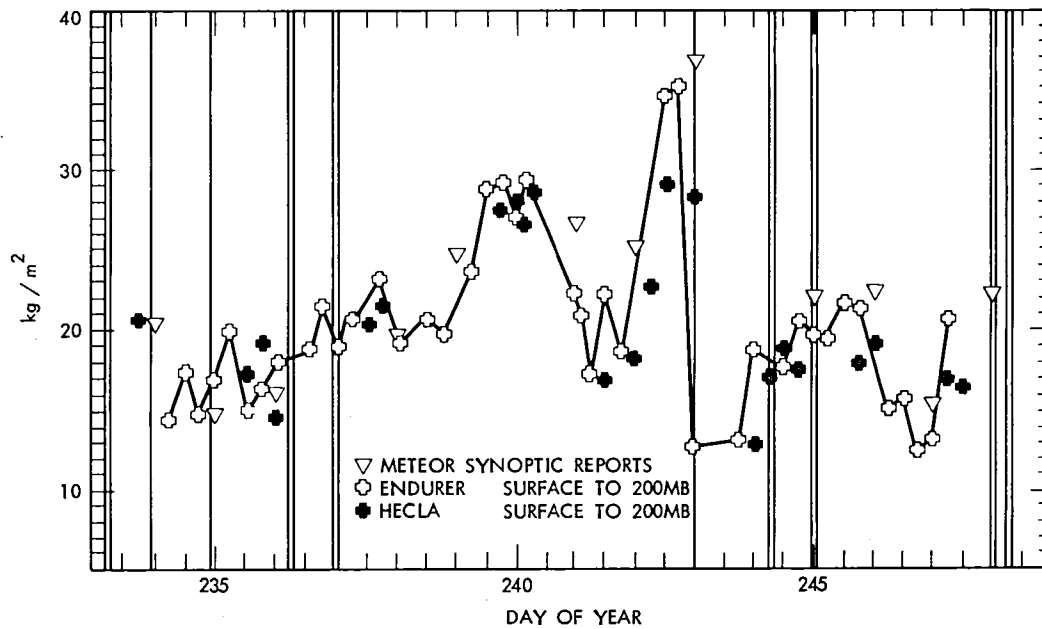


Figure 2-40. Integrated Water Vapor Content (Q) - Phase 2

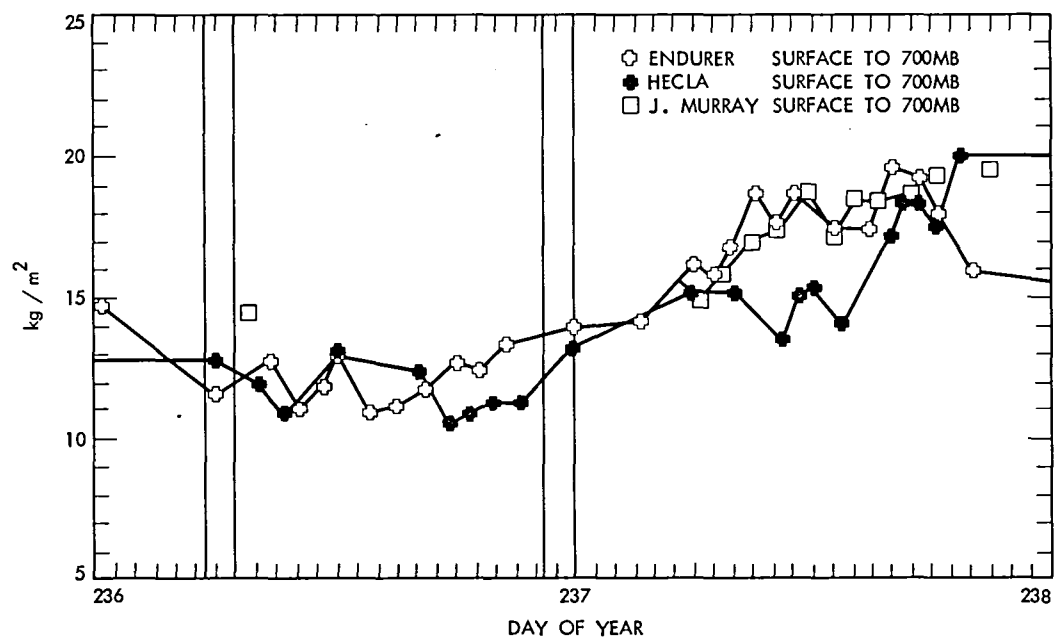


Figure 2-41. Comparison of Endurer, Hecla, and John Murray Determinations of Water Vapor Content on 24 and 25 August 1978

Table 2-9. Sets of Wave Measurements Used for Intercomparisons

Accelerometer Buoys:

- (1) Discovery pitch-roll buoys (2), data provided by David Webb.
- (2) Waverider buoys (6) at moorings C1 and C6, data provided by Herbert Carlson.
- (3) Atlantis II pitch-roll buoy, data provided by Robert Stewart.

Shipboard Wave Recorders:

- (1) Discovery wave recorder, data from Discovery cruise report.
- (2) John Murray wave recorder, data provided by Trevor Guymer.

Visual observations at World Meteorological Organization (WMO) Standard Times, all data provided by Trevor Guymer:

- (1) Meteor
 - (2) John Murray
 - (3) Hecla
 - (4) Endurer
 - (5) Tydeman
-

Next, the sample means of the differences in wave heights and directions among sets of observations plus an estimate of the standard deviation of the mean were calculated. The means, their uncertainty, and the number of pairs of observations are summarized in Table 2-10. The intercomparisons among Waverider observations are summarized in Table 2-11.

3. Summary of the Intercomparisons

- (1) There exist statistically significant differences among the pitch-roll buoy observations, but these are small, less than 8 percent, and are based on a small number of observations. Because the differences are not consistent, and because of the time and distances separating the observations, it was concluded that they are due to differences in the wave field rather than to the response of the buoys.

Table 2-10. Summary of Comparisons

(Mean Difference \pm Standard Deviation of the Mean)

Pitch-roll buoys and Waveriders:

Discovery P-R (D) vs Atlantis II P-R (A): (D-A)/A	(6.6 \pm 3.0)% N = 8
Discovery P-R vs Waveriders (W): (D-W)/W	(-7.5 \pm 2.9)% N = 7
Atlantis II P-R vs Waveriders: (A-W)/W	(0.65 \pm 1.9)% N = 14

Shipboard wave recorders and buoys:

Discovery wave recorder (D) vs Waveriders: (D-W)/W	(16.6 \pm 3.1)% N = 5
Discovery wave recorder vs Discover P-R (B): (D-B)/B	(29 \pm 8)% N = 3
Discovery wave recorder vs Atlantis II P-R: (D-A)/A	(18 \pm 3)% N = 5
Discovery wave recorder vs all buoys:	(20 \pm 3)% N = 13
Discovery wave recorder vs John Murray wave recorder (JM): (JM-D)/D	41% N = 1

Visual observations (WMO) and buoys:

Meteor WMO (M) vs Atlantis II P-R: (M-A)/A	(-6.3 \pm 9.3)% N = 9
Meteor WMO vs Waveriders: (M-W)/W	(-12.0 \pm 11.1)% N = 7
Tydemar WMO (T) vs Waveriders: (T-W)/W	(-3.8 \pm 5.8)% N = 16
John Murray WMO (JM) vs Waveriders: (JM-W)/W	(3 \pm 18)% N = 2
Hecla WMO (H) vs Atlantis II P-R: (H-A)/A	-19% N = 1
Endurer WMO (E) vs Atlantis II P-R: (E-A)/A	(8 \pm 3)% N = 2

Wave directions:

Discovery P-R vs Atlantic II P-R: (D-A)	(3.4 \pm 4.8)° N = 7
Atlantis II P-R vs all visual observations of sea (WMO): (A-WMO)	(12 \pm 6)° N = 11

Table 2-11. Comparisons Among Waverider Observations of Wave Height*

(Mean Difference \pm Standard Deviation of the Mean)

Waverider Mooring	C_j			
	C2	C3	C4	C6
C1	$(-5.6 \pm 1)\%$ n=36 ---		$(0.8 \pm 1.4)\%$ n=41 ---	$(-0.2 \pm 1.3)\%$ n=42 ---
C2		--- $(-1.2 \pm 2.2)\%$ n=21	$(6.9 \pm 2.1)\%$ n=35 $(6.0 \pm 2.0)\%$ n=24	$(7.0 \pm 2.1)\%$ n=34 $(2.6 \pm 3.1)\%$ n=22
C_i C3			--- $(7.7 \pm 1.4)\%$ n=47	--- $(2.8 \pm 1.9)\%$ n=42
C4				$(0.3 \pm 1.6)\%$ n=40 $(3.6 \pm 1.5)\%$ n=50 $(-7.5 \pm 1.0)\%$ n=75 (9 Aug-3 Sept)

*Table of the mean value of $(C_i - C_j)/C_j$, where C_k denotes wave height measured by the buoy at mooring C_k .

The upper set of numbers is data from the period 23-30 July 1978; the lower set of numbers is from the period 31 July-8 August 1978.

- (2) There exist statistically significant differences among the sets of Waverider buoy observations. These, too, are small, less than 8 percent, but tend to be consistent. That is, C2 and C3 observations tend to be approximately 5 percent larger than observations from C1 and C4, while those from C6 appear to be 7 percent larger than those from C4, especially toward the end of the experiment. Because these differences are small, and because real differences should exist in the wave field over the distances between the buoys, it is concluded that the differences are probably due to waves. However, the consistent difference between C4 and C6 may indicate a difference in the response of these two buoys.
- (3) The Discovery wave recorder observations are consistently and significantly larger than the buoy measurements by (20 ± 3) percent based on 13 comparisons.
- (4) The visual observations are not significantly different from the buoy observations.
- (5) The standard deviation of the differences depends on the type of observation. It was 8 percent for the comparisons using pitch-roll buoy data, 10 percent for the intercomparisons between Waveriders observations, and 24 percent between the visual observations and the buoys. The variability is partly due to the statistical variability in each estimate of wave height, partly to the spatial and temporal variability of the wave field, and partly on the inaccuracy of the observations. The first depends on the length of record used to compute wave height and is around 2 percent for the pitch-roll buoys. The second can be reduced using observations close in time and space and is about the same for each class of comparisons. The larger variance in the visual observations implies that each of these observations is uncertain by approximately 23 percent, assuming that on average the first two sources contribute 8 percent to the uncertainty in the inter-comparison.
- (6) The pitch-roll buoys gave consistent estimates of swell and sea directions.
- (7) Shipboard observers can estimate the directions of wind-driven seas with nearly the same accuracy as buoys. Their observations of directions are consistent with those observed by buoys, and the standard deviation of the difference among buoy observations was 13° compared with 20° for the buoys versus visual observations.
- (8) Shipboard observers cannot accurately determine whether or not swell is present or its direction. For ten of eleven cases, swell was noted in the logs, but the observation was seldom correct. On three occasions, swell was observed by the buoy but not by the observers, even when the swell height was 70 percent of the significant wave height. On four occasions, swell was noted by the observers but not by the buoy. This latter discrepancy depends partially on the definition of swell. Swell was defined to be

- either those waves that have a separate and distinct peak in the frequency spectrum or that travel in a distinctly different direction from the wind generated sea. By this definition low-frequency waves persisting after the wind drops are not considered to be swell because there is no easy way for a wave buoy or an observer to distinguish these waves from a wind sea. In this sense the distinction between sea and swell is artificial, but there is no other known practical distinction between the two that can be used to test the accuracy of the visual observations.

4. The JASIN Wave Field

Because the various observations of wave height and direction are consistent and unbiased, the observations can be combined to yield time series of significant wave height and the frequency and direction of waves at the peak in the spectrum (Figures 2-42 through 2-44). In these figures, the dominant source of wave height and frequency was Waverider observations analyzed by Herbert Carlson, supplemented by pitch-roll observations analyzed by David Webb and Robert Stewart. Wave directions were from my buoy observations.

F. JPL PROCESSING OF JASIN OBSERVATIONS

1. Surface

All surface observations used during the Seasat-JASIN workshop were prepared at the Institute of Oceanographic Sciences (IOS), Wormley, England, under the direction of T. H. Guymer. Meteorological observation types included wind speed and direction, sea-surface temperature, wet-bulb temperature, dry-bulb temperature, and sea-level pressure. All observation records were time tagged and located.

IOS-prepared observations were recorded on magnetic tape and shipped to the Jet Propulsion Laboratory (JPL) in Pasadena, California. At JPL the observations were operated on by a sequence of processors whose final product was a merged surface and satellite observation data record. From the merged file a statistics processor selected desired subsets of merged records and generated reports that displayed the difference between the individual surface truth and satellite observations and a statistical summary of all comparisons.

Initial data processing of JASIN surface observations at JPL adjusted wind speeds from their recorded height to a standard height of 19.5 m above the sea surface. A surface layer model developed by W. T. Liu at the University of Washington was used to make this adjustment. In addition to anemometer height, the model requires dry-bulb, wet-bulb, and sea-surface temperatures to accurately model the surface layer. In most cases these three temperatures were available with the surface wind observation, but in those instances where one or more were missing the following assumptions were made: (1) If either wet bulb or dry bulb were missing, a relative humidity of 0.70 was assumed; and (2) if either dry bulb or sea-surface temperature were missing, a neutral atmospheric stability was assumed (accomplished by setting both dry-bulb and sea-surface temperatures to 12.0°C).

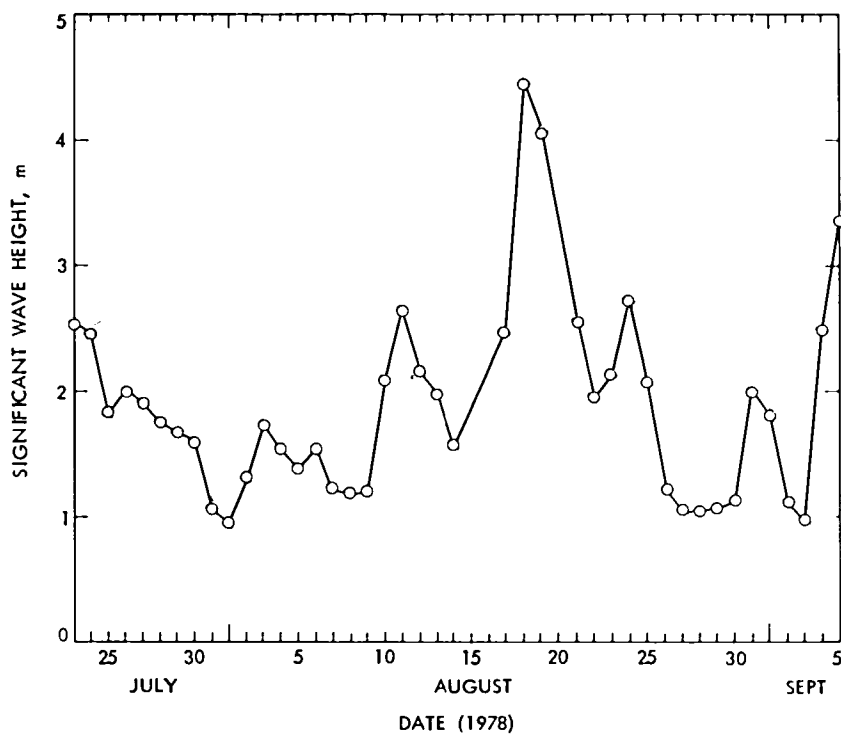


Figure 2-42. Daily Average of All Significant Wave Heights Recorded by Instruments Within 50 km of the Fixed Intensive Array, Mostly by Meteor Using Waverider Buoys (The tick marks are at 00:00 GMT, and wave height is four times the standard deviation of surface elevation)

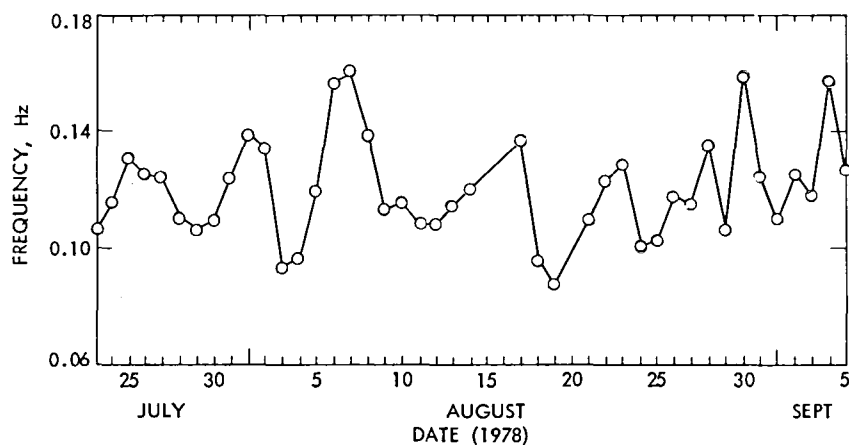


Figure 2-43. Same as Figure 2-42, Except that Frequency of Waves at the Peak in the Frequency Spectrum Is Shown

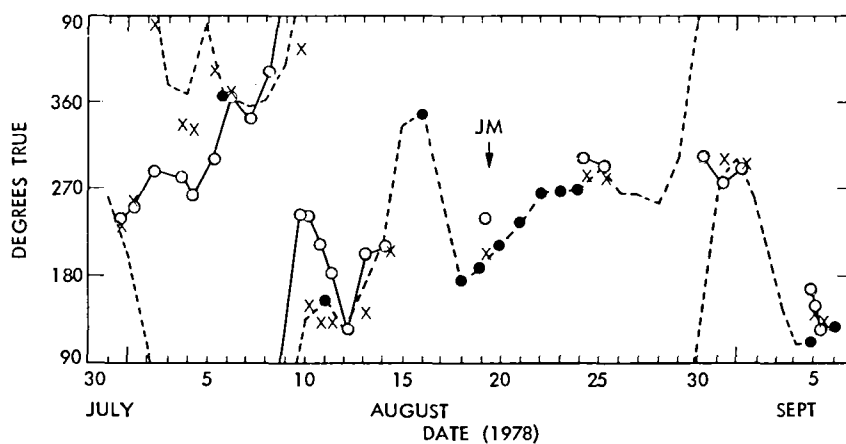


Figure 2-44. Direction From Which Waves Come: Open Circles are for Waves at the Peak in the Spectrum; Crosses Are High-Frequency Waves; Dashed Line Is Wind Direction at 00:00 GMT Recorded at W2; Solid Circles Are Times When Wind Speed Exceeded 8 m/s (Data are from the Atlantis II pitch-roll buoy, except for one visual estimate of wave direction at the John Murray)

The surface layer model also produced a surface layer stability code corresponding to the range of Z/L values listed in Table 2-12. This stability code was carried along with the surface wind observation for later use in stratifying surface and satellite observation comparison statistics.

The surface data record received from IOS represented a complete time history of surface observations by platform. For the workshop only those observations that had a high likelihood of being matched with satellite observations were needed. Two editing schemes were used to select those observations. Selected observations were then entered into the workshop surface truth data base.

Wind observations from MET ships and the morning S13 and sea-surface temperature observations from MET ships and autolog platforms were treated as spot observations. Spot observations were edited by selecting only those observations that bracketed a satellite overpass time. Then linear interpolation was used to compute surface observations at the time of the overpass. Only the interpolated spots were entered into the workshop surface truth data base.

Wind observations from autolog platforms were used to produce average wind observations. Averaging intervals of 15 and 60 min centered about the satellite overpass time were chosen. Only the average wind record was entered onto the workshop surface truth data base; the spot observations used in computing the average wind records were not compared with satellite observations.

Observations from the workshop surface truth data base were merged with satellite observations for each pass being studied in the workshop. Previous editing steps guaranteed that all surface observations were sufficiently close in time to the satellite observation and that only a distance tolerance needed to be checked to determine coincidence. Seventy-five km was chosen as the maximum distance separating coincidence surface and satellite observations. All pairs of surface and satellite observations that met this coincidence criteria were combined to form a merged data record.

A SASS wind observation can have up to four solutions or aliases, each with a different wind speed and direction. When merging SASS winds with surface wind observations, the SASS wind solution that was closest in wind direction to the direction of the surface observation was selected for inclusion into the merged data record. The remaining solutions were not kept and, therefore, not compared with surface observations.

A merged record contains two comparable sets of observations, one set containing surface observations and the other satellite observations. The content of the two sets is satellite instrument-dependent. For SASS-merged records, the observation sets contain wind speed and direction; for SMMR-merged records, the two sets contain sea-surface temperature and wind speed. All merged records contained the time and distance separating surface and satellite observation sets.

Merged files were stratified based on a value or a range of values of one or more parameters in the merged record. Once stratified, merged files were passed through a statistics package. Here, differences between surface and satellite observations for all merged records were computed and displayed.

Table 2-12. Z/L State Table (Z = 19.5 m)

Z/L	Stability Code
<-0.1/-0.1	1
-0.1/-0.01	2
-0.01/-0.001	3
-0.001/0	4
0/0.001	5
0.001/0.01	6
0.01/0.03	7
0.03/0.05	8
0.05/0.10	9
0.10/>0.10	0

Additionally, for each satellite pass, a statistical summary was displayed. This summary included the minimum value, the maximum value, and the mean value for each surface observation type; the minimum value, the maximum value, and the mean value for each satellite observation type; and the mean difference between surface and satellite observations of like type and the standard deviation about the mean differences.

2. Radiosonde

JASIN radiosonde observations were prepared at IOS under the direction of P. Taylor. Processing procedures at IOS used the raw radiosonde data to compute the total water vapor in a column of air bounded by the sea surface at the bottom and the maximum height of the balloon flight at the top. All radiosonde water vapor observations were time-tagged and Earth-located.

IOS-processed radiosonde observations were recorded on punch cards and sent to JPL. Because the number of radiosonde flights was small (≈ 250) when compared to the number of surface meteorological observations ($\approx 100,000$), there was no need to edit the radiosonde observations prior to entry onto the workshop surface truth data base. All radiosonde observations received from IOS were entered on the workshop surface truth data base.

When merging radiosonde observations with satellite observations, both time and distance tolerances had to be checked to determine coincidence. One hour was chosen as the maximum time separation, and 75 km was chosen as the maximum distance separation. All pairs of radiosonde and satellite observations that met both coincidence criteria were combined to form a merged record. The resultant merged file was passed through the statistics package, and the results were used to validate the SMMR water vapor observations.

REFERENCES

- Friedman, M., "A New Radiosonde Case: The Problem and the Solution," Bull. Am. Met. Soc., Vol. 53, No. 9, pp. 884-886, 1972.
- Royal Society, Air-Sea Interaction Project: Field Phase Summary, London, 1979.
- Taylor, P. K., An Observational Study of the Atmospheric Boundary Layer Over the Sea, PhD Thesis, Univ. of Southampton, England, 1973.

SECTION III

SEASAT DATA PROCESSING

A. INTRODUCTION

The SASS and SMMR revolution sets selected for the Seasat-JASIN workshop were determined after lengthy and intensive examination of all possible coverage of the JASIN area by Seasat. These data sets and subsets were selected on the basis of surface conditions, surface data availability, satellite coverage of the Fixed Intensive Array (FIA), satellite data availability, nearly contiguous coverage, and the appropriateness of various geophysical algorithms.

B. SCATTEROMETER (SASS)

The 45 SASS revolutions were divided into several subsets: (1) a set of 23 priority revolutions, (2) a coset of 22 revolutions which taken with the 23 priority revolution set yielded the total 45 revolution set, (3) a set of 9 attenuation revolutions, (4) a set of 12 large scale field revolutions, and (5) a set of 24 alias revolutions. The 23 priority set was chosen for best coverage of the FIA and for best cross section of the wind speeds encountered in JASIN. This set was processed with two model functions (CUNY and Wentz), three polarization options (V, H, VH), and with two cell matching algorithms (pairing and binning). Small scale wind fields were produced by UW for all of the 23 priority revolutions. The nine attenuation revolutions were those revolutions on the 23 priority set for which satisfactory SMMR coverage was available. The 12 large scale field set was chosen to be compared with large scale surface wind fields generated by UW. The 24 alias revolution set was selected for a test of a subjective alias resolution scheme. Table 3-1 identifies the revolutions in each set plus those in the SMMR set. Printouts and plots were generated for all revolution sets for all processing options.

C. SCANNING MULTICHANNEL MICROWAVE RADIOMETER (SMMR)

The SMMR data were divided into five revolution sets. Two were JASIN sets and three were not. These sets are: (1) the basic JASIN 30 revolution set, (2) the 8 priority JASIN set, (3) the 12 Northwest Pacific revolution set, (4) the 12 radiosonde revolution set, and (5) the 4 GOASEX revolution set. The eight priority revolution set was processed through several different geophysical algorithms for algorithm intercomparison. The Northwest Pacific revolution set was processed to compare with a set of XBT data. The radiosonde set was processed to compare with radiosonde data obtained from tropical stations. The GOASEX data was processed to compare with reworked surface field data from the GOASEX experiment. Table 3-1 identifies the 30 basic JASIN revolutions and the 8 priority JASIN revolutions. Table 3-2 identifies the other revolution sets.

Table 3-1. SMMR and SASS JASIN Revolution Sets

Rev	SASS Basic (45)	SMMR Basic (30)	SMMR Priority (8)	SASS Priority (23)	SASS Atten (9)	SASS Field (12)	SASS Test (23)	SASS .Alias (20+4)
355		✓						
431	✓							
432	✓	✓						
474	✓							
475	✓	✓						
546	✓							
547	✓	✓		✓	✓		✓	
556	✓	✓		✓	✓		✓	
557	✓			✓			✓	
589	✓							
590	✓	✓	✓	✓	✓		✓	
599	✓	✓	✓	✓			✓	
632	✓							✓
633	✓	✓	✓	✓	✓		✓	✓
642	✓	✓		✓			✓	✓
643	✓			✓			✓	✓
675	✓							
676	✓	✓						
718	✓							
719	✓	✓						
748		✓						
757	✓	✓	✓	✓	✓		✓	
758	✓			✓			✓	
762		✓						
790	✓			✓		✓	✓	✓
791	✓	✓	✓	✓	✓	✓	✓	✓
800	✓	✓		✓	✓	✓	✓	✓
801	✓			✓		✓	✓	✓
805		✓	✓					
814	✓					✓		✓
815	✓			✓		✓	✓	✓
829		✓	✓					
833	✓							✓
834	✓	✓		✓	✓		✓	✓
843	✓	✓		✓		✓	✓	✓
844	✓			✓		✓	✓	✓
872		✓						
886		✓						
929	✓	✓		✓		✓	✓	✓
930	✓			✓		✓	✓	✓
944		✓						
948	✓			✓		✓	✓	✓
949	✓	✓		✓		✓	✓	✓
958	✓	✓						✓
959	✓							✓
1001	✓	✓	✓	✓	✓		✓	✓
1002	✓							✓

Table 3-1 (contd)

Rev	SASS Basic (45)	SMMR Basic (30)	SMMR Priority (8)	SASS Priority (23)	SASS Atten (9)	SASS Field (12)	SASS Test (23)	SASS Alias (20+4)
1005	✓							✓
1006	✓	✓						✓
1045		✓						
1048	✓							
1049	✓	✓						
1134	✓							
1135	✓							

Table 3-2. SMMR Revolution Sets

Radiosonde	GOASEX	Northwest Pacific
1	1120	1208
2	1135	1214
3	1212	1215
4	1298	1222
5		1223
6		1228
7		1229
8		1230
9		1237
10		1242
11		1243
12		1244

D. ALTIMETER (ALT)

There were 20 ALT revolutions which came reasonably close to the FIA. These revolutions are identified in Table 3-3.

Table 3-3. Altimeter JASIN Revolutions

Item	Revolution
1	274
2	432
3	475
4	499
5	518
6	542
7	547
8	561
9	585
10	590
11	628
12	633
13	719
14	762
15	791
16	805
17	815
18	829
19	834
20	872

E. SYNTHETIC APERTURE RADAR (SAR)

The Synthetic Aperture Radar on Seasat viewed the Northeast Atlantic on 19 occasions (passes) between 1 August and 11 September during the JASIN experiment. Of these, the pass on 1 August is lost, and six other passes viewed regions that were far from the JASIN area. Of the remaining twelve, five viewed the Fixed Intensive Array (FIA) of JASIN, where surface and subsurface observations were made by a variety of instruments, and another seven were close enough that they could be used to assess the radar observations of ocean surface waves.

Data from all SAR passes were processed on the JPL optical correlator, and a few were reprocessed either by the digital correlator at JPL or by the optical correlator at the Environmental Research Institute of Michigan (ERIM).

The optically processed images, in the form of 70-mm photographic negatives, were distributed to Stewart and Vesecky for studies of the ability of SAR to view ocean waves. Each negative showed a swath of ocean 25 km wide with a resolution of approximately 40 m. In addition, the images were also reproduced at a scale of 1:1,000,000 in order to display more clearly the large features seen in some images and to compare images with maps of bottom topography. These images were 100 km wide by 300-500 km long and showed large portions of the JASIN area. Lastly, digitally processed data were recorded on magnetic tape and on photographic negatives for use in the workshop. These images showed a swath of ocean 100 km on a side with a resolution of 25 m.

The SAR data available at the workshop, or soon thereafter, are summarized in Table 3-4, and the location of the images is sketched in Figure 3-1.

Table 3-4. Summary of JASIN SAR Data

Date 1978	Time	Pass No.	JPL Optical Image	JPL Digital Image	Photo Montage	Comments
1 Aug.	21:27	513				Data tape lost
4 Aug.	06:15	547	X		X	
4 Aug.	21:35	556	X		X	
7 Aug.	06:22	590	X		X	
7 Aug.	21:43	599	X		X	
10 Aug.	06:29	633	X		X	
10 Aug.	21:50	642	X		X	
15 Aug.	22:35	714	X		X	
16 Aug.	06:43	719	X		X	
18 Aug.	22:40	757	X		X	
19 Aug.	06:41	762	X		X	
21 Aug.	07:24	791	X	X	X	
24 Aug.	07:29	834	X		X	
1 Sept.	23:54	958	X		X	
5 Sept.	00:06	1001	X		X	
5 Sept.	08:15	1006	X	X	X	
8 Sept.	08:18	1044	X		X	
8 Sept.	08:27	1049	X	X	X	
11 Sept.	00:30	1087	X		X	
11 Sept.	08:39	1092				No signal recorded
14 Sept.	08:50	1135				Poor data recorded

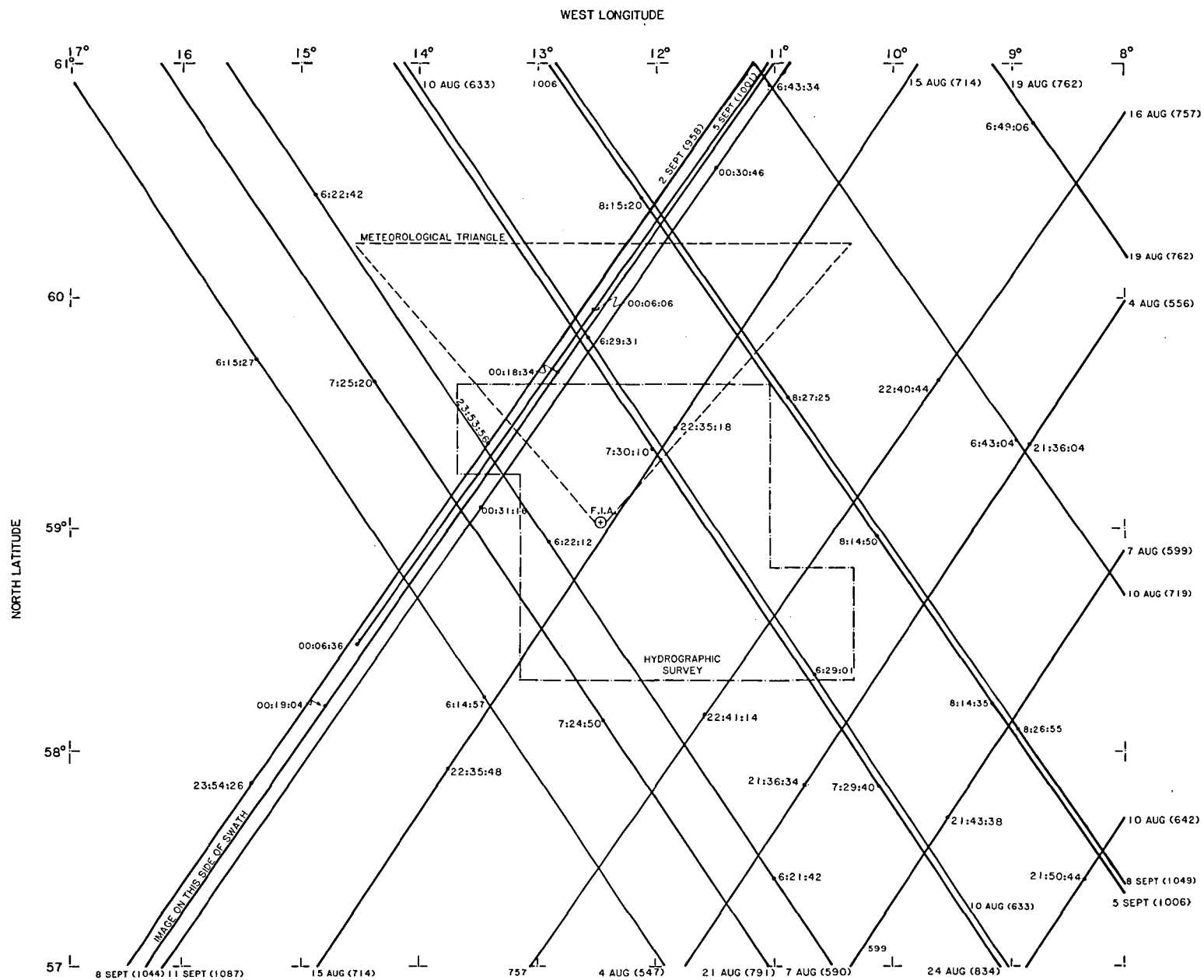


Figure 3-1. SAR Coverage in JASIN

SECTION IV

SASS PANEL REPORT

A. INTRODUCTION

For those outside of the remote sensing community, the use of a satellite radar to measure properties of the ocean's surface may be difficult to comprehend. To promote the acceptance of this new technique, a brief description of the sensor and technique is presented. For a better understanding, the reader is referred to detailed descriptions of the sensor and its data interpolation algorithms [Grantham et al., 1977; Jones, Wentz, and Schroeder, 1978; Johnson et al., 1980; and Bracalente et al., 1980].

The Seasat-A Satellite Scatterometer (SASS) was an active microwave sensor (frequency = 14.6 GHz; $\lambda = 2.1$ cm), which was used to remotely sense wind vector over the oceans. For Seasat, specifications for the SASS were developed from requirements of the "Seasat User Working Group," viz., wind-speed-measurement range of 4 to 26 m/s with an accuracy of ± 2 m/s or 10 percent (whichever is greater), and wind direction 0 to 360 deg with an accuracy of ± 20 deg.

The physical basis for this technique is the Bragg scattering of microwaves from centimeter length capillary ocean waves. The strength of radar backscatter (normalized radar cross section, NRCS, σ^0) is a function of the capillary wave amplitude that is proportional to the wind speed at the sea surface. Further, the radar backscatter is anisotropic; therefore, wind direction can be derived from scatterometer measurements at different azimuths.

The Seasat implementation used four dual-polarized (vertical, V-pol; horizontal, H-pol) antennas, each oriented 45 deg relative to the subsatellite track, to yield the required observations separated in azimuth by 90 deg (Figure 4-1). Twelve Doppler filters were used to subdivide electronically the broad antenna footprint into resolution cells approximately 50 km on a side. In addition, measurements from incidence angles near nadir provided coverage (wind speed only) along the subtrack.

Nine operating modes for the instrument are listed below. The antenna numbering convention is defined in Figure 4-1. Modes 1 and 2 are single polarization measurements over the full swath; modes 3 and 4 are dual polarization measurements over one-half swath, and modes 5-8 are single polarization measurements over one-half swath. The antenna switching cycle in modes 3 and 4 is such that both vertical and horizontal polarization measurements are made before switching antenna positions.

<u>Mode</u>	<u>Polarization Sequence</u>	<u>Antenna Sequence</u>
1	VV, VV, VV, VV	1, 2, 3, 4
2	HH, HH, HH, HH	1, 2, 3, 4

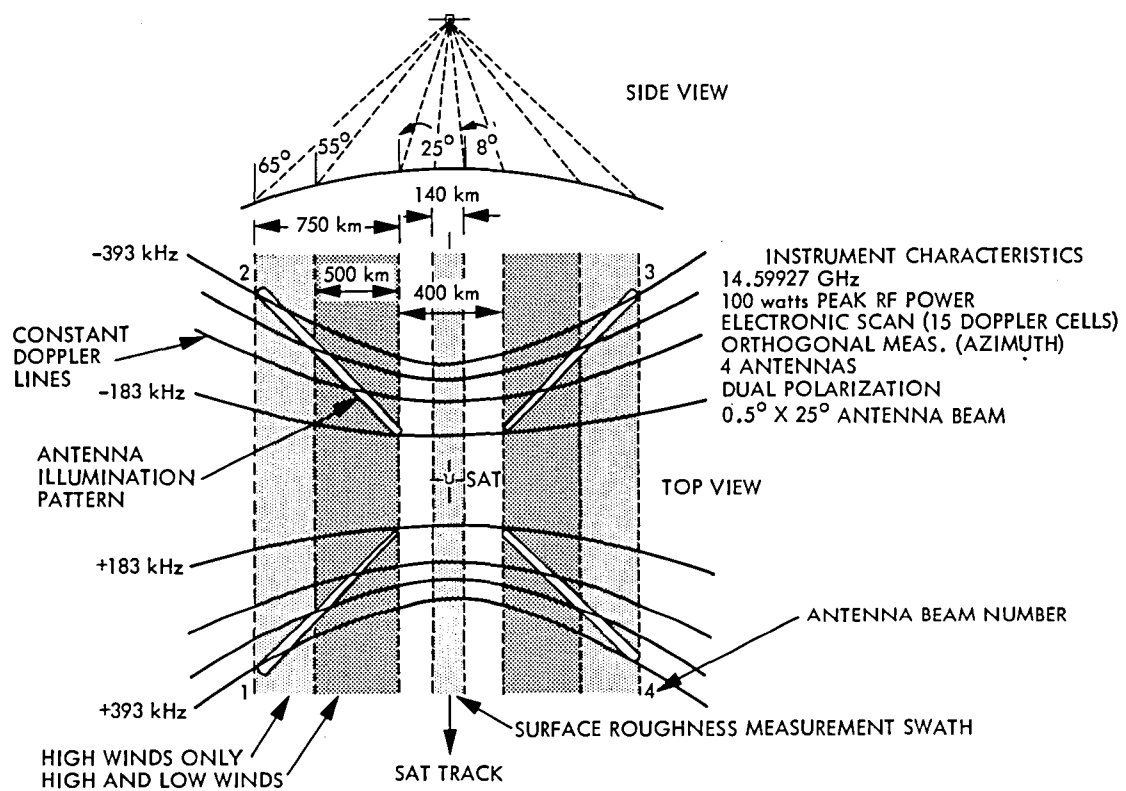


Figure 4-1. SASS Swath Geometry

<u>Mode</u>	<u>Polarization Sequence</u>	<u>Antenna Sequence</u>
3	VV, HH, VV, HH	3, 3, 4, 4
4	VV, HH, VV, HH	1, 1, 2, 2
5	VV, VV, VV, VV	3, 3, 4, 4
6	VV, VV, VV, VV	1, 1, 2, 2
7	HH, HH, HH, HH	3, 3, 4, 4
8	HH, HH, HH, HH	1, 1, 2, 2
9	Calibration Mode - not polarization or antenna related	

The sensor and geophysical algorithms for SASS have been developed by an interdisciplinary panel of scientists and engineers - the SASS Evaluation Task Group (ETG). Prior to the launch of Seasat, three candidate geophysical algorithms for inferring ocean wind vector from radar backscatter measurements were developed. Basic to all was an empirical relationship (model function) between wind vector and σ^0 (as a function of incidence angle, azimuth angle, and polarization). The initial model function was derived using a limited base of airborne radar measurements [Jones, Schroeder and Mitchell, 1977]. Because of the harmonic nature of the σ^0 anisotropy, the geophysical algorithm recovers between one and four (usually two or four) solutions for each grid point. These solutions are nearly equal in speed, but vary widely in direction. This effect is called aliasing.

Since the launch of Seasat, the SASS algorithms have matured through comparisons with independent surface wind measurements during a series of data analysis workshops. Table 4-1 is a summary of this activity.

Prior to this workshop, the surface truth measurements (from GOASEX and Storms workshops) were used to "tune" the model function such that the SASS winds were unbiased with minimum standard deviations. JASIN data, however, constituted a "withheld" set, thereby providing an independent assessment of the sensor's capabilities.

The SASS panel was subdivided into the following subpanels:

(1) Cell Pairing

J. W. Brown - Chairman
D. H. Boggs
E. M. Bracalente

(2) Atmospheric Attenuation Correction

G. Dome - Chairman
F. J. Wentz

(3) Model Function

W. J. Pierson - Chairman
I. M. Halberstam
G. Schacher
L. C. Schroeder
F. J. Wentz

(4) Wind Vector Comparisons

W. L. Jones - Chairman
E. M. Bracalente
D. H. Boggs
R. A. Brown
G. Dome
L. C. Schroeder
D. Schelton

(5) Wind Alias Removal

P. Woiceshyn - Chairman
W. Appleby
M. Albright
D. H. Boggs
M. Borowski
R. A. Brown
G. F. Cunningham
A. M. Hanson
B. Hinton
M. Holl
S. Peteherych
M. G. Wurtele

The report from each follows.

Table 4-1. Summary of Workshop Activities

Workshop	Date	Accomplishment/Caveat
Gulf of Alaska Seasat Experiment (GOASEX)	January 1979	First comparison of SASS and "surface truth" winds <ul style="list-style-type: none"> • No σ° bias correction applied • No atmospheric attenuation correction applied • Three wind vector algorithms • Used prelaunch model function • Wind aliases removed by selecting "closest" direction to ST • (SASS-ST) wind speeds $\bar{X} \approx 3$ m/s, $\sigma \approx 2.5$ m/s • (SASS-ST) wind directions $\bar{X} < 10^\circ$, $\sigma \approx 20^\circ$
SASS ETG Mini-Workshop	March 1979	Creation of SASS-I wind vector algorithm <ul style="list-style-type: none"> • Incorporated desirable features of three candidate algorithms
GOASEX-II	June 1979	GOASEX revisited <ul style="list-style-type: none"> • Improved "surface truth" analysis • SASS-I wind vector algorithm • Modified model functions (adj. to GOASEX) • Preliminary atmosphere attenuation algorithm evaluation • σ° biases determined and corrections applied • (SASS-ST) wind speeds $\bar{X} \approx 2$ m/s, $\sigma \approx 1.5$ m/s • (SASS-ST) wind direction $\bar{X} < 5^\circ$, $\sigma \approx 15^\circ$
Seasat Storms Mini-Workshop	August 1979	First high wind speed (> 20 m/s) comparison <ul style="list-style-type: none"> • Hurricane and extra tropical cyclone • GOASEX-II model function and SASS-I wind vector algorithm • Preliminary atmospheric attenuation correction applied

Table 4-1 (contd)

Workshop	Date	Accomplishment/Caveat
SASS ETG Mini-Workshop	February 1980	<ul style="list-style-type: none"> • SASS wind speeds greater than ST for low winds; less than ST for high winds $\bar{X} \approx +1$ to -3 m/s, $\sigma \approx 1-2$ m/s <p>Model functions adjusted ("tuned") to minimize (SASS-ST) difference</p> <ul style="list-style-type: none"> • σ° bias corrections applied • Used selected GOASEX-11 and Storms "high quality" ST • (SASS-ST) wind speeds $\bar{X} < 1$ m/s, $\sigma \approx 2$ m/s correlation coeff $> 90\%$ • (SASS-ST) wind direction $\bar{X} < 2^\circ$, $\sigma \approx 14^\circ$ correlation coeff $> 90\%$
JASIN	March 1980	<p>Evaluation of SASS winds using "withheld" surface truth data set</p> <ul style="list-style-type: none"> • 23 priority reves • 2 model functions

B. SASS CELL MATCHING

1. SASS Cell Pairing

Two JASIN passes (547 and 556) were examined in detail to assess the performance of the cell pairing algorithm. Plots were generated (e.g., Figure 4-2) showing the location of SASS measurement cell centers for only those cells with σ° between -50 dB and $+20$ dB, and normalized standard deviation, $\Delta\sigma^\circ/\sigma^\circ$, (NSD) less than 1.0, which are the values used for data validation in the wind estimation. Fore beam measurements were distinguished from aft beam measurements on the plots, so that the cells which were paired could be determined easily. Wind solutions generated at pair separation tolerances of 30, 33, and 37 km were overlaid on these plots, and the number of "good" SASS σ° measurements not paired was determined for each case. At JASIN latitudes (55° to 63° N for this exercise), this resulted in about 3 percent of the measurements within the overlap swath not being paired at 30 km, and practically none at 37 km. In general, it appears that those cells not paired at 33-km tolerance are located in the area of calibration frames (from the opposite beam), or areas in which data are sparse for other reasons, such as telemetry dropouts or low winds (poor NSD). Other revolutions (557, 599, 791) were examined in less detail with similar qualitative results.

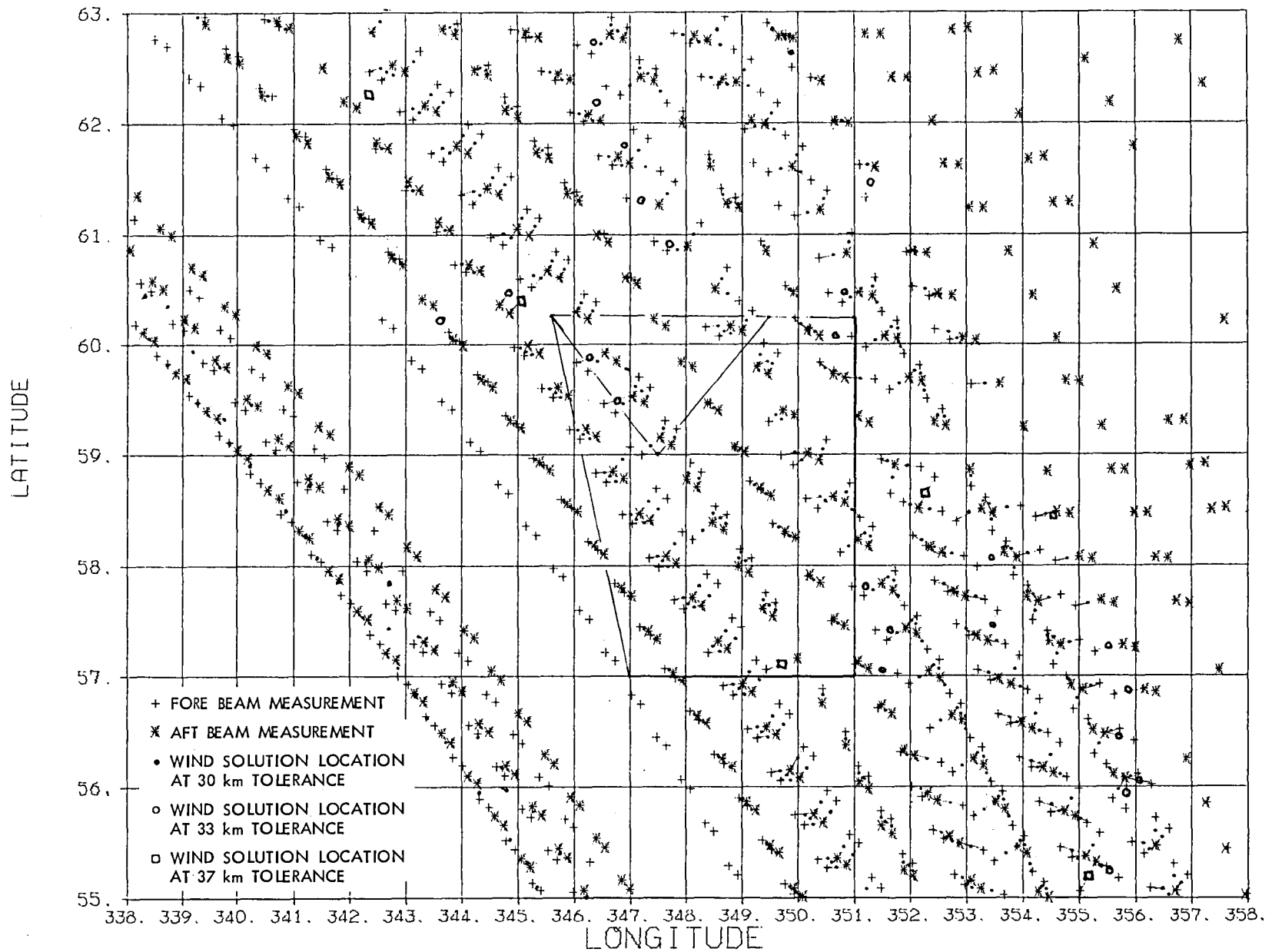


Figure 4-2. SASS Cell Centers and Wind Solution Points (Rev 547)

There is a tradeoff to be made between maximizing the number of solutions obtained (minimizing unpaired cells) on the one hand and optimizing spatial resolution on the other. For JASIN latitudes, in modes 3-8, the optimum tolerance appears to lie between 30 and 33 km. However, for considerations listed below, the recommendation for GDR production is 37 km.

A similar exercise for equatorial latitudes, conducted shortly after the workshop, indicates that the optimum tolerance lies between 36 to 42 km. (See Figure 4-3.) The recommended value is 37 km for modes 3-8 and 50 km for modes 1-2.

There was some question as to whether cells of opposite polarization should be paired. Based on a wind direction error analysis presented in Subsection E, it was determined that VH and HV pairs should be eliminated. Further, it is recommended that the pair separation tolerance be relaxed to 37 km to compensate for the loss of wind vector solutions which would occur where only VH or HV combinations were paired. [Note: Later reprocessing of the data using an improved

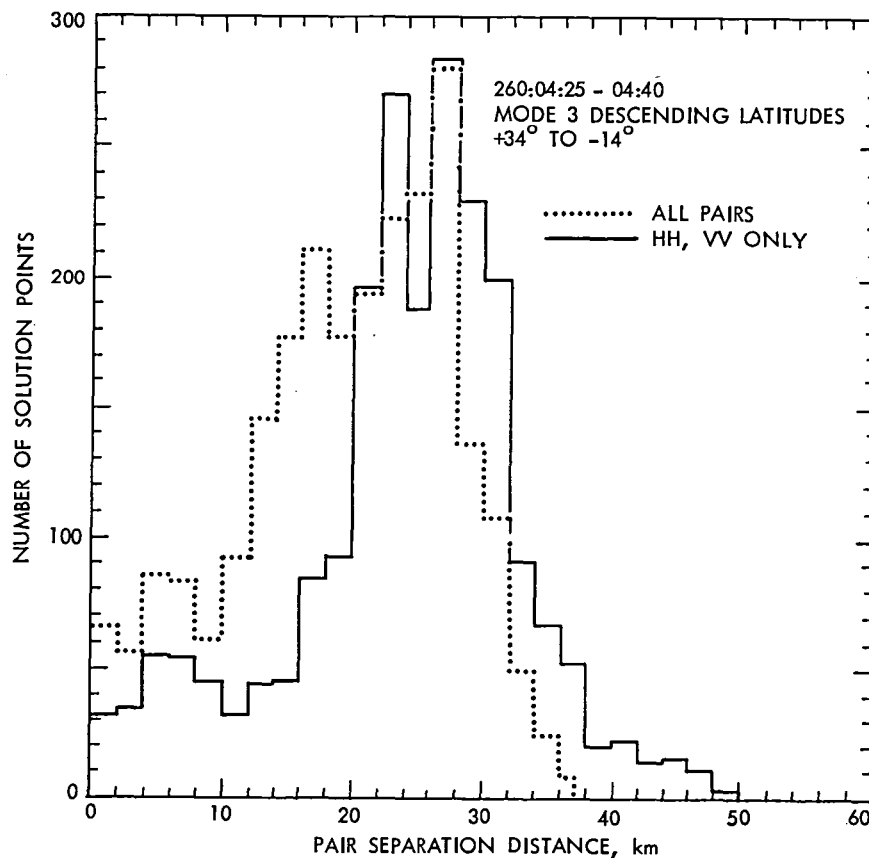


Figure 4-3. Cell Pairing Separation Distance Distributions

model function indicates that the problem has largely been removed. To avoid large data gaps when polarization changes, the GDR will be produced with VH pairs enabled.]

2. SASS Cell Binning

Near-nadir cells (14 and 15) are always processed in a binning or box mode, but a solution can be obtained from a single cell, if desired. Outer swath solutions can be obtained using a box mode option, but require at least one measurement for each of the fore and aft antennas. Thus, while the only trade-off is between noise and spatial resolution for the nadir cells, the outer swath also requires a tradeoff between spatial resolution and loss of data. The fixed 0.5° latitude-longitude boxes used for processing some of the JASIN passes showed substantial loss of data, even in modes 3-8, where the measurements are double the density of modes 1-2. This occurs because one-half degree of longitude represents only around 27 km at 60° latitude. There are many areas where the cell lineup is such that a half-degree box contains only fore or only aft measurements.

Thus, it is recommended that, for the outer swaths, the box option be modified to provide a latitude-dependent longitude interval, so that box sizes are maintained at a constant size in kilometers, the recommended nominal value being 55 km, which is 0.5° at the equator. (Note that this option will only be used for nadir cells for GDR production.)

C. SASS ATMOSPHERIC ATTENUATION

1. Comparison of Kansas and Wentz Attenuation

Prior to the JASIN workshop, interested members of the SASS evaluation team reviewed the attenuation algorithm developed by the University of Kansas. This algorithm uses only vertical polarization measurements at 37.0 GHz (for low attenuations) and 18.0 GHz (for moderate to high attenuation cases). This committee recommended that the algorithm use sea-surface temperatures (SSTs) obtained from climatology data and a surface wind of 10 m/s. These modifications were implemented in the algorithm for evaluation during the JASIN workshop.

To evaluate the algorithm at the workshop, the two-way nadir atmospheric transmittances estimated using the Kansas attenuation algorithm were compared with those values estimated using the SMMR-SASS algorithm developed by F. J. Wentz, Remote Sensing Systems. The Wentz algorithm uses all ten SMMR channels to estimate SST, wind speed, water vapor, and liquid water content. Using the estimated values of water vapor and liquid water, the transmittances of the atmosphere are determined at the SMMR grid-3 points.

For the comparison, the Kansas attenuation algorithm was modified to also provide estimates on the SMMR grid-3. The evaluation was limited to hurricanes Fico (Rev 331) and Ella (Rev 952). Using these data, the attenuation subpanel

was able to conclude:

- (1) The atmospheric transmittances predicted by both algorithms agree at low-to-moderate levels of attenuation (corresponding to clear skies and clouds).
- (2) Considerable disagreement in the estimates occurs for high attenuation cases (corresponding to rain).

To determine the cause for this discrepancy, the SMMR brightness temperatures T_B in regions of high attenuation were studied. Before the T_B 's are used for geophysical processing by either algorithm, biases are added as described by Wentz in the SMMR T_B Panel Report. This procedure introduces a relative H-pol to V-pol separation as well as elevating the V-pol T_B . For reasons explained in the SMMR Section, it appears that the biases should be tapered off to zero as the Earth scene T_B increases and approaches the SMMR warm calibration reference load. Since this adjustment was not performed for the attenuation comparisons, the T_B 's for high attenuation areas were in error. The SMMR/SASS algorithm saw high and artificially polarized T_B 's and gave too low of an attenuation because of the polarization separation. The Kansas algorithm saw only high vertical polarization and gave too high of an attenuation.

Post-workshop activity is planned to redo the attenuation comparisons using the properly biased T_B 's and to verify that the two algorithms will give similar results [Dome et al., 1980a; Black, 1980; and Griffith, 1980].

2. Dependence of Atmospheric Attenuation Calculation on Sea-Surface Temperature and Wind Speed

The SASS atmospheric attenuation algorithm [Dome, et al., 1980b] requires the specification of sea-surface temperature T_S and sea-surface emissivity ξ . The variation in these two parameters must be accounted for in order to calculate accurate attenuations from brightness temperatures measured by the SMMR. The SST dependence arises from using an atmospheric model that has a surface air temperature T_a equal to T_S and has a linear decrease in air temperature with altitude. For highly attenuating atmospheres the brightness temperature observed by the SMMR is approximately proportional to the air temperature at one penetration depth into the absorbing cloud. Hence, since the modeling correlates the air temperature in the cloud with the sea-surface temperature T_S , the brightness temperature strongly depends on T_S when high attenuation occurs. The dependence of the algorithm on sea-surface emissivity comes from the fact that the SMMR-observed brightness temperature increases with increasing surface emission. The emissivity varies because of changing sea-surface temperature and wind speed.

Two options for specifying sea-surface temperature were explored. The first was to use the SMMR-inferred SST. However, this option would have required that complete SMMR geophysical processing be done before the SASS attenuation calculations. This processing design seemed too complicated in view of the estimated 3° to 5°C accuracy required for SST in the attenuation calculation. The second option was to use a climatic table of SST [Wentz, private communication, 1980]. The table increments are 10° in latitude, 30° in longitude, and single month steps for July, August, and September. After a tri-linear interpolation

to the time and place of the SMMR footprint, the climatic SST is probably accurate to within 3°C, except for high SST gradient areas such as in portions of North Atlantic and Pacific. This second option was chosen as satisfactory and implemented into the attenuation algorithm.

The emissivity dependence of the attenuation calculation is small and is easily handled by using a mean emissivity rather than a specular emissivity. The mean emissivity is defined as the emissivity for a wind speed on 10 m/s and a sea-surface temperature of 290 K. The rms variation of the actual emissivity about its specified value is minimized by using the 10-m/s value rather than the 0-m/s specular value.

D. MODEL FUNCTION SUBPANEL

1. Introduction

The SASS model function is the empirical relationship used to describe the dependence of the ocean normalized radar cross section σ° on the 19.5-m neutral stability wind vector. For the wind vector algorithm, it is specified in the form of a G-H table that gives these two coefficients for the equation

$$\log_{10} \sigma^\circ = G(\theta, \chi) + H(\theta, \chi) \log_{10} U \quad (1)$$

where θ is the incidence angle, χ is the relative azimuth angle (angle between wind direction and radar azimuth), and U is the wind speed, m/s. The σ° is a function of the radar parameters: incidence angle, relative azimuth angle, and polarization; therefore, the G and H coefficients are tabulated separately for V and H polarizations every two degrees in incidence and every ten degrees in relative azimuth. These tables thus define the theoretical values of wind speed for any measured backscatter value, given the aspect and incidence angles. The coefficients at upwind, downwind, and crosswinds are the most important because they determine the maxima and minima of the function.

The initial G-H table was developed from a set of σ° data collected pre-launch using an airborne microwave scatterometer. During December 1979, a combined set of SASS/"surface truth" data was created using high quality buoy and ship observations and fields from the GOASEX and STORMS workshops. An initial set of 17,000 σ° values was edited to produce approximately 1000 σ° values with associated wind speeds and directions, and was supplied to three candidate model function developers: City University of New York (CUNY), University of Kansas (UK), and Remote Sensing Systems (RSS) (formerly Wentz Associates). The objective of the exercise was to adjust ("tune") the model function to eliminate biases between SASS and "surface truth" winds and to minimize the standard deviation of the difference.

2. The Boulder Workshop

A model function evaluation was conducted in Boulder, CO (February 1980) using the tuned model functions described above. The model function developed by RSS (G-H table W-5) yielded best results for high winds; however, there were questions raised concerning weak power laws at low incidence angles and very strong power laws at high incidence angles.

The vertical polarization H coefficient for the CUNY and RSS model functions is shown in Figure 4-4. There are substantial differences between the two model functions over the range from 20 to 58 deg although values greater than about 55-deg incidence are irrelevant since the SASS cells cannot be paired at these high angles. The values for 20, 36, and 52 deg are summarized in Table 4-2.

Another model function comparison was made using plots of σ° versus incidence angle and versus relative azimuth angle. For incidence angles between 25 and about 40 deg, the two curves were quite close together and roughly parallel (RSS being lower). For smaller and larger angles, where limited SASS data exist, the two curves diverged.

3. Pre-JASIN Workshop

Because of several deficiencies uncovered during the Boulder meeting, the CUNY and RSS model functions were revised before production of the SASS winds for the JASIN workshop. For CUNY the revised model function for incidence angles greater than 20 deg was a merger of the three G-H tables evaluated at Boulder. The procedure used was to plot three curves (CUNY, UK, RSS) of σ° versus incidence angle for each 10-deg relative azimuth angle at 5- and 20-m/s wind speed (e.g., see Figure 4-5). The values from RSS were used over the middle range of incidence angles, especially for 20 m/s. For 5 m/s, a compromise between all three was selected: at low incidence angles, the CUNY curves were weighted more heavily; and at incidence angles greater than about 45 deg, the concepts introduced by UK were used to constrain the zero intercept and the power laws. Thus, the new

Table 4-2. Model Function Power Laws (H Values) for
Vertical Polarization From the Boulder Workshop

Wind Direction	Incidence Angle					
	20°		36°		52°	
	CUNY	RSS	CUNY	RSS	CUNY	RSS
Upwind	1.02	0.47	1.72	1.55	1.90	2.30
Downwind	1.20	0.65	1.95	1.95	2.23	2.55
Crosswind	1.37	0.35	2.50	2.25	2.92	3.00

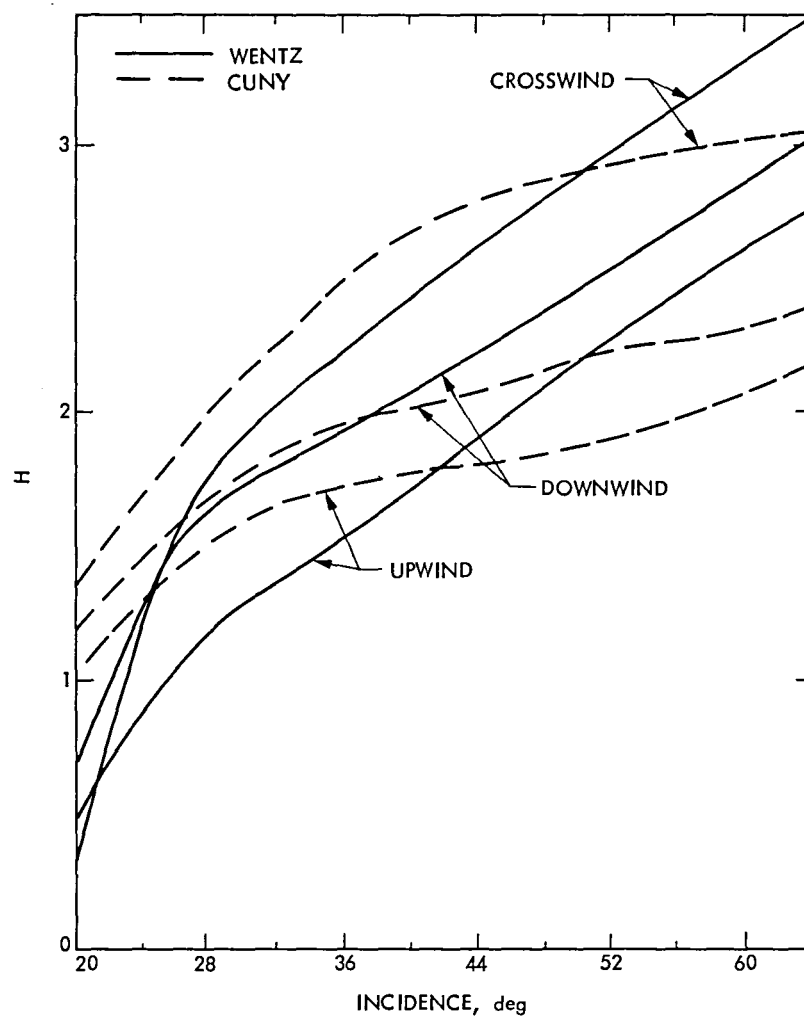


Figure 4-4. Power Law (H Values) for the Wentz and CUNY Model Functions Used for the Boulder Workshop for Vertical Polarization

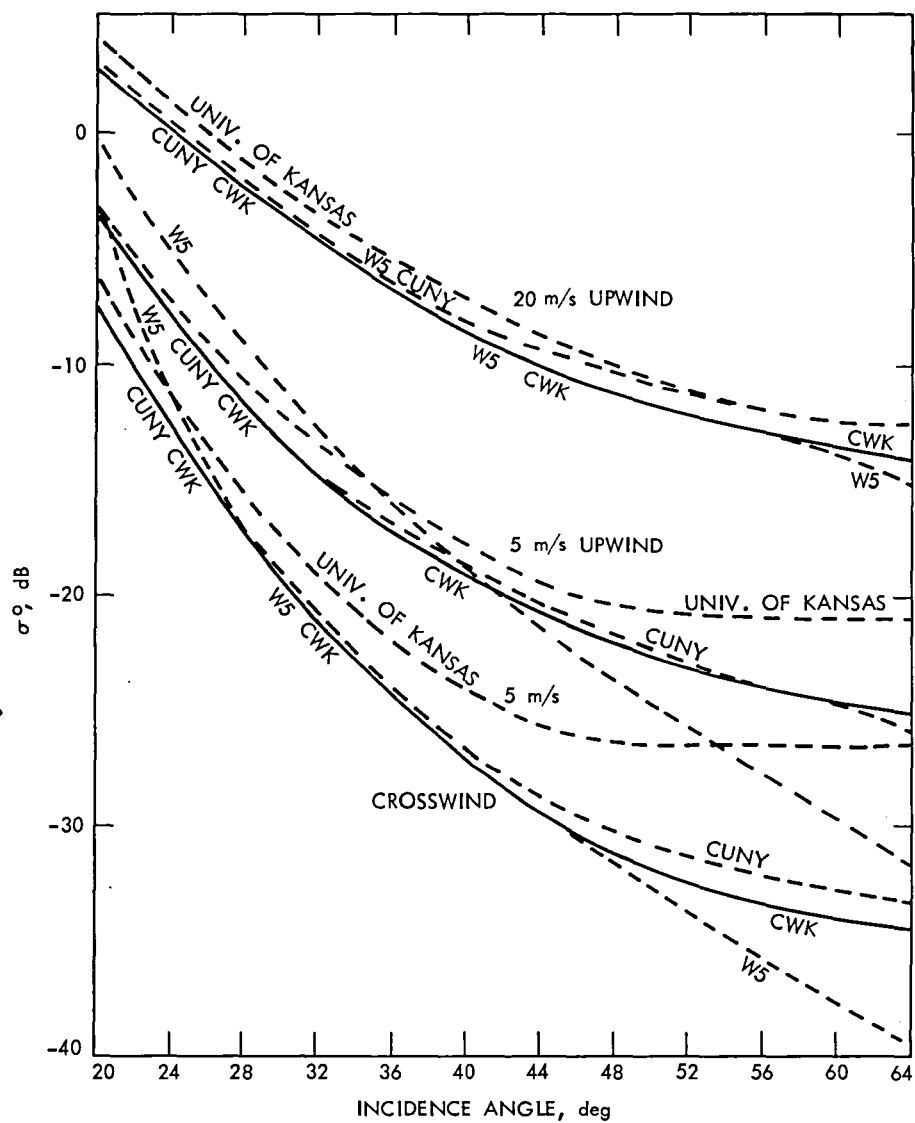


Figure 4-5. Example of How the W-5, CUNY, and University of Kansas Model Functions Were Merged to Produce CWK

combined model function resulted from an effort to use the best features of all three model functions and was named CUWENKAN or CWK for short. This is one of the model functions used to process JASIN data.

Concurrently, the model function W-5 was also altered. Previously, Wentz used the combined aircraft/spacecraft data set to solve for 11 ocean surface parameters in his two-scale scattering model [Jones, Wentz, and Schroeder, 1978]. Next, the model was run parametrically as a function of wind speed, incidence angle and relative azimuth angle to generate the necessary data for the G-H table. The final step was to adjust both the G and H values of the table to minimize the mean square difference between the SASS and surface truth wind speeds and directions. After Boulder, Wentz modified his final procedure to constrain the slopes (H coefficient) to those produced by the two-scale theory and to adjust the G coefficient to minimize the SASS minus surface truth differences. This procedure produced model W-6, which became W-7 after minor revisions were made in the near-nadir table to agree more closely with the altimeter wind speed algorithm.

The resulting V-pol and H-pol slopes are compared in Figures 4-6 and 4-7. The power laws are more alike in this figure than the previous comparison (Figure 4-4); however, there are still some differences, especially at low and high incidence angles. Results are summarized for V-pol in Table 4-3.

The σ° versus incidence angle curves for CWK, W-5, W-6, and W-7 are shown in Figures 4-8 through 4-10 for upwind, downwind, and crosswind for vertical polarization. From these graphs, it is clear that the pre-JASIN activities brought the two model functions into closer agreement.

Prior to the JASIN workshop SASS data production, the W-6 and CWK model functions were further examined at both the σ° and wind vector levels. For the σ° , the slope of the airborne AAFE RADSCAT and SASS σ° versus log U curves for constant incidence angle and relative azimuth angle was compared to the corresponding H coefficients. For the aircraft data, the wind speed power laws were approximately: 1 for $\theta = 20$ deg, 2 for $\theta = 40$ deg, and 1.5 - 3.5 for $\theta = 60$ deg. For the SASS, however, the results are not conclusive at low and high incidence

Table 4-3. W-7 and CWK Model Function Power Laws (H Values) for Models Tested in the JASIN Workshop, V-Pol

Wind Direction	Incidence Angle					
	20°		36°		52°	
	CWK	W-7	CWK	W-7	CWK	W-7
Upwind	0.80	0.70	1.66	1.52	1.20	2.18
Downwind	1.02	0.95	1.90	1.95	2.35	2.45
Crosswind	1.10	0.73	2.08	2.25	2.77	2.86

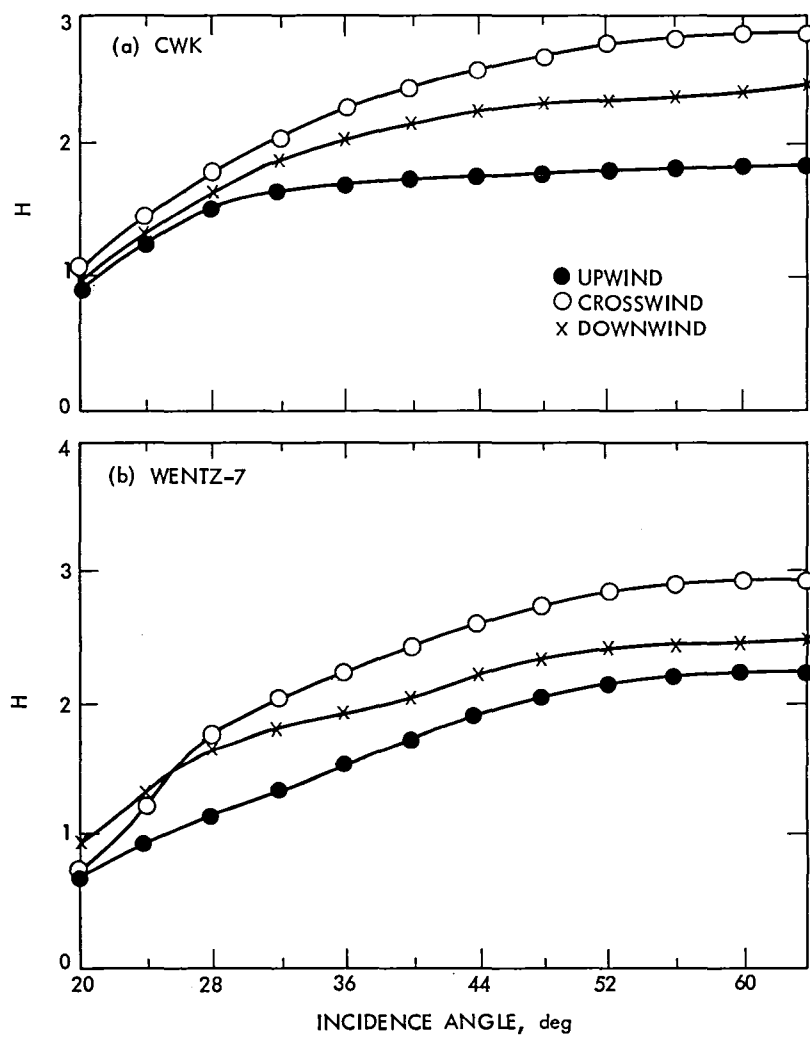


Figure 4-6. Power Law (H Values) for the Wentz-7 and CWK Model Functions for Vertical Polarization

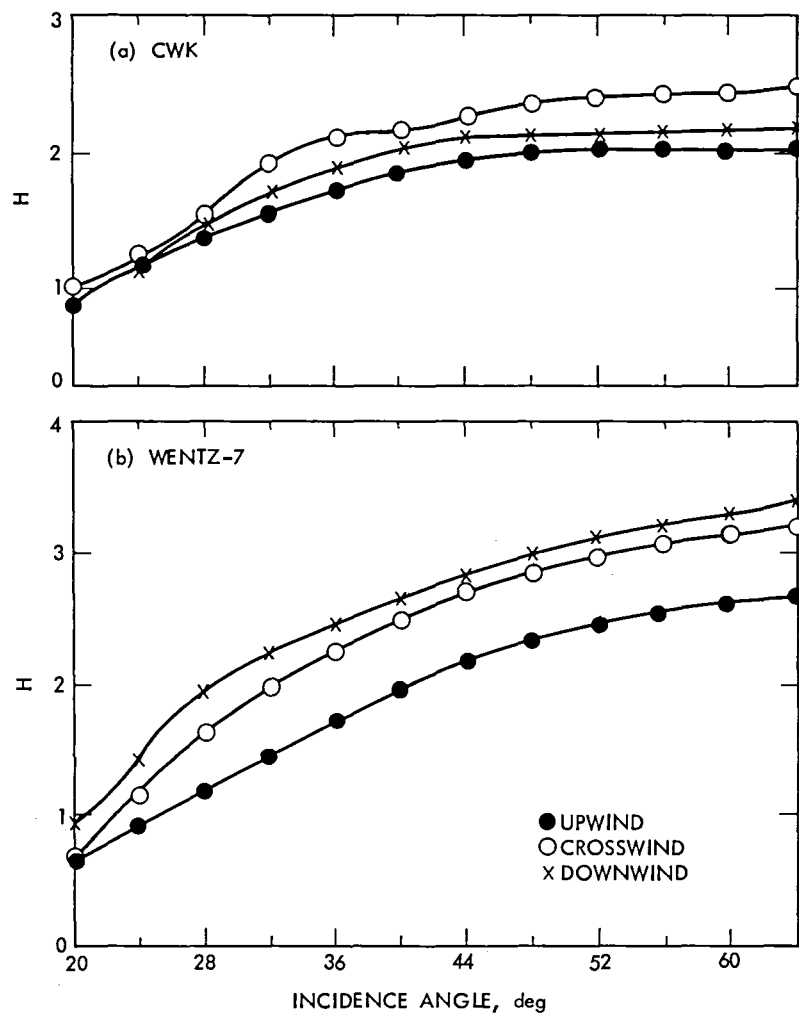


Figure 4-7. Power Law (H Values) for Horizontal Polarization

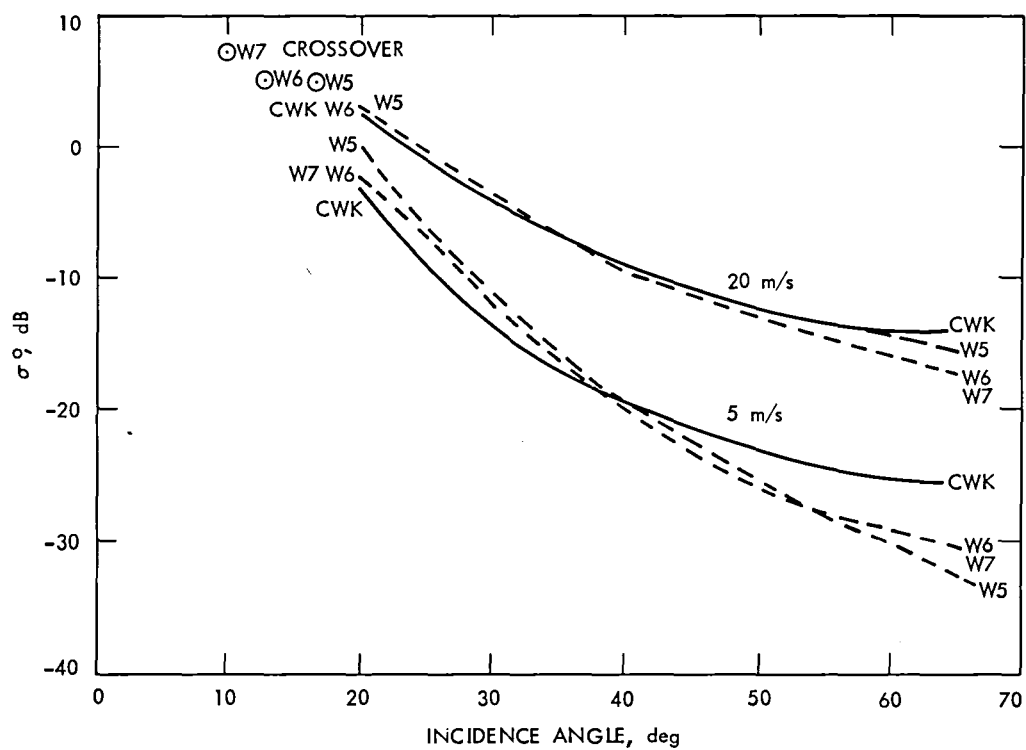


Figure 4-8. σ° Comparisons for Model Functions W-5, W-6, W-7, and CWK for V-Pol Upwind

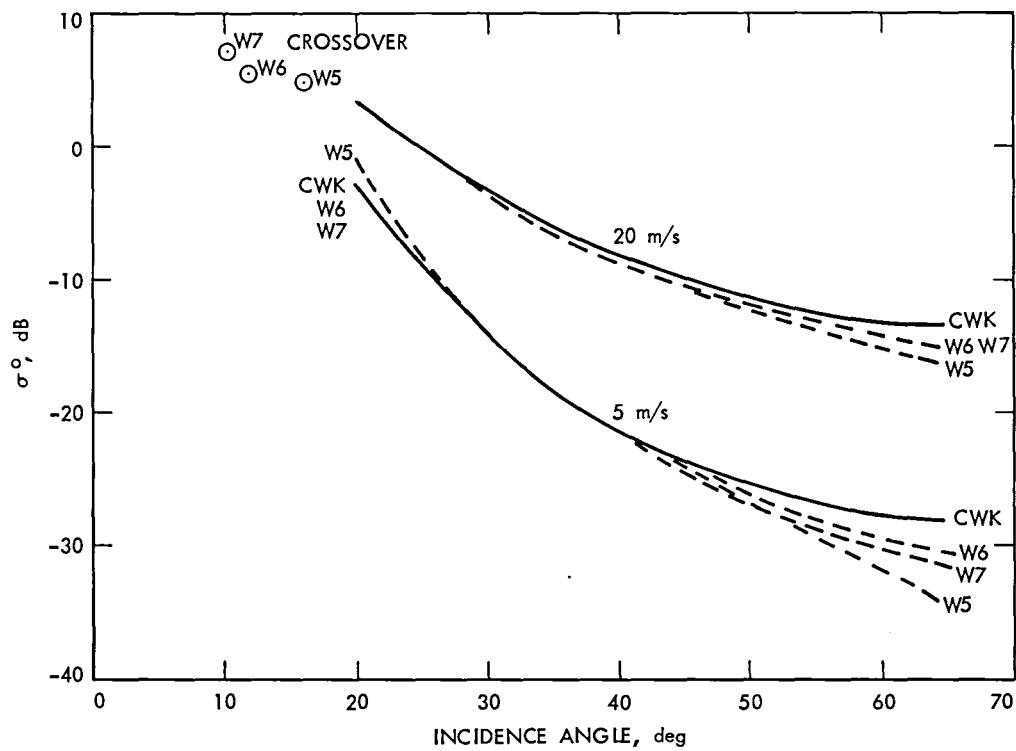


Figure 4-9. σ^0 Comparisons for Model Functions W-5, W-6, W-7, and CWK for V-Pol Downwind

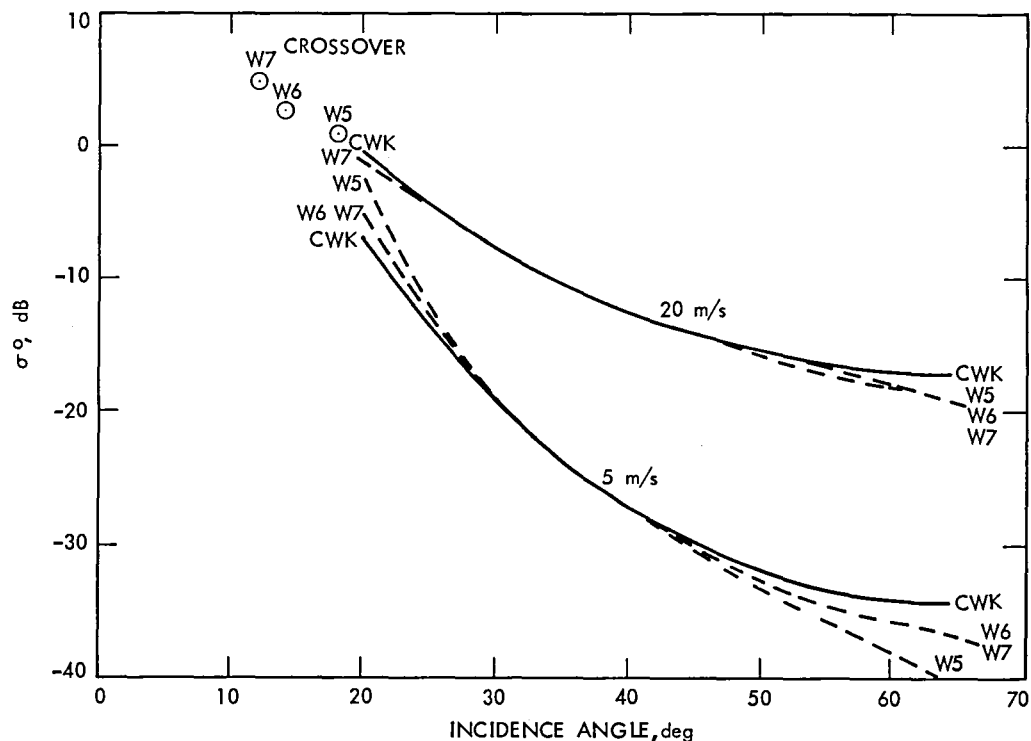


Figure 4-10. σ° Comparisons for Model Functions W-5, W-6, W-7, and CWK for V-Pol Crosswind

angles ($\theta < 25$ deg; $\theta > 50$ deg), probably because of the small σ° data set. In general, the slopes at high incidence angles appeared less steep, while at the low incidence angles the trend is difficult to estimate (see Figures 4-11 and 4-12).

Wind vector comparisons were performed for Revs 331 and 1093 (for which prior wind field analyses existed). Statistics were computed for the SASS minus surface truth scalar differences for surface truth quality code $Q = 2$ (± 1 m/s) and $Q = 1$ (± 2 m/s) and for nonattenuating atmospheric precipitation codes $P = 1-5$. The results are summarized in Table 4-4.

4. JASIN Workshop

The comparison of the W-7 and CWK model functions was continued at the JASIN workshop. The G-H tables were used to identify conditions where the winds

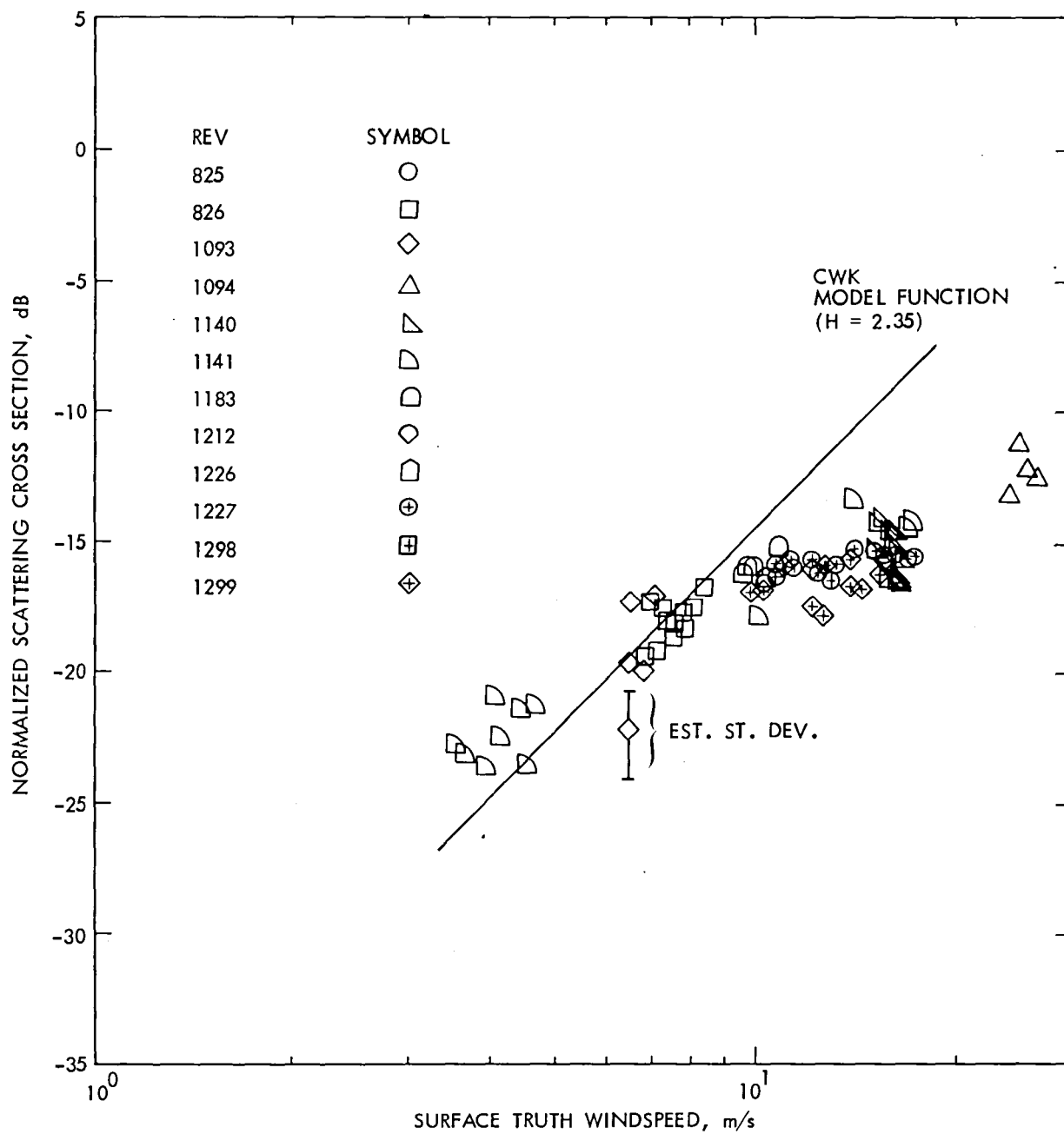


Figure 4-11. SASS σ° vs $\log_{10} U$ for $\theta = 52^\circ$, V-Pol, Downwind Aspect

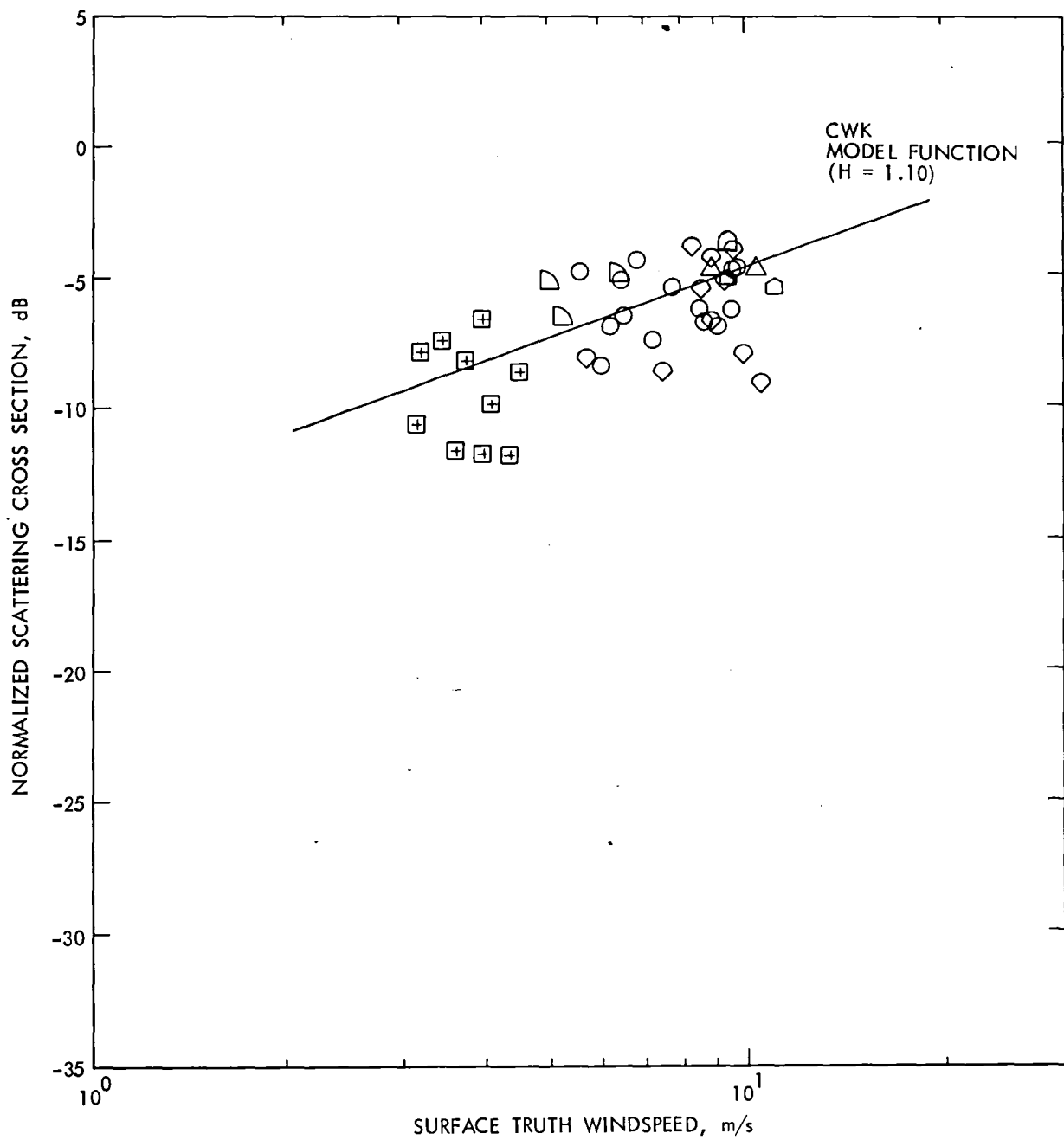


Figure 4-12. SASS σ^0 vs $\text{Log}_{10} U$ for $\theta = 22^\circ$, H-Pol, Crosswind Aspect

Table 4-4. Wind Speed and Direction Statistics for SASS Minus Surface Truth Fields Analyses (Quality 1 and 2, Precipitation 1-5, Nonattenuation Atmosphere)

	W-5				W-6				CWK			
	Number of Aliases				Number of Aliases				Number Of Aliases			
	1&2	3	4	All	1&2	3	4	All	1&2	3	4	All
Revolution 331												
Number Pts	19	26	216	261	15	24	208	247	4	32	211	247
Wind Speed												
Mean	-0.5	-0.3	0.4	0.3	0.2	-0.04	0.5	0.4	0.5	0.1	0.3	0.3
RMS	0.7	0.8	1.3	1.2	1.2	0.9	1.3	1.3	1.1	1.1	0.9	0.9
STD	0.5	0.8	1.2	1.2	1.2	0.9	1.3	1.3	1.1	1.1	0.8	0.9
Wind Direction												
Mean	-4.8	-7.7	5.6	3.5	1.9	-4.5	6.3	5.0	2.6	-1.6	8.2	6.8
RMS	5.3	9.6	15.7	14.7	11.8	12.1	15.6	15.1	14.9	9.9	15.8	15.2
STD	2.1	5.9	14.7	14.3	12.1	11.5	14.3	14.3	17.0	9.9	13.5	13.5
Revolution 1093												
Number Pts	106	39	189	334	102	41	205	348	91	54	203	348
Wind Speed												
Mean	-0.6	-1.6	-1.9	-1.5	-0.5	-1.0	-1.4	-1.1	-1.2	0.1	-1.6	-1.2
RMS	2.2	3.0	3.2	2.9	2.3	2.7	3.0	2.8	2.2	2.1	2.8	2.6
STD	2.2	2.6	2.6	2.5	2.3	2.5	2.6	2.5	1.9	2.1	2.3	2.2
Wind Direction												
Mean	-3.6	0.01	-8.7	-6.1	-4.8	-1.7	-8.3	-6.5	-3.6	-5.3	-8.2	-6.6
RMS	14.5	14.8	20.0	17.9	15.6	18.7	20.4	19.0	11.7	22.1	19.6	18.3
STD	14.1	15.0	18.1	16.9	15.0	18.8	18.7	17.8	11.2	21.7	17.8	17.1

calculated from the two models would be expected to differ. The exponent H is the critical parameter since it determines the sensitivity of the backscatter to the wind. Of principal interest is the fact that the exponents for the two models do not agree at low and high incidence angles, which will lead to differences in the computed winds at these angles. In the middle range of incidence angles, there is a closer agreement.

Examples of σ° versus $\log U$ for various incidence angles plots are shown in four figures. The first (Figure 4-13) shows the graphs for upwind H-pol. At low incidence angles, W-7 lies above CWK, and at high incidence angles it lies considerably below. Thus, the greatest differences would be expected at a low and high incidence angles. Curves for the low incidence angle range 20 to 28 deg for H-pol upwind are shown in Figure 4-14. The W-7 model function always predicts a lower wind than CWK for low winds. Figure 4-15 for H-pol upwind and incidence angles of 50, 54, and 58 deg shows CWK everywhere above W-7. The two model functions will not intersect until the winds reach 25 m/s or so. For all winds less than 20 m/s, the W-7 model function will always predict a higher wind than CWK at high incidence angles. The last of these four figures (Figure 4-16) for V-pol downwind shows agreement between the two model functions for low incidence angles. In an overall sense, the two model functions tend to agree closely for intermediate incidence angles and at 20 m/s.

The difference in wind speed predicted by the two models for a given σ° was determined using the following procedure:

- (1) For 5 m/s and 10 m/s and a given wind direction, the corresponding mean was calculated for σ° from the two models.
- (2) Wind speeds were calculated for both models using the σ° determined above.
- (3) The wind speed difference (W-7 minus CWK) was computed.

The results of this procedure are presented in Table 4-5 and Figures 4-17 and 4-18. The figures show the same general behavior for all conditions. At low incidence angles, wind calculated from the W-7 model will be lower than those calculated from the CWK model, while the reverse will be true at high angles. For the intermediate angles, the two models will agree. This generality is fairly good but is not true for all conditions, as can be seen from the figures. For example, at downwind, H-pol W-7 will predict higher winds for almost all angles, and V-pol there will be little difference between the two models for all angles for the crosswind and downwind cases. It must be emphasized that the above analysis does not assure that either model function is correct; that can only be determined by comparison with surface wind observations, which are stratified according to wind speed and incidence angle.

Further analyses of the CWK and W-7 algorithms were made using methods similar to those mentioned in the GOASEX I and II workshops [see Born et al., 1979 and 1980]. There are some significant differences, however, as shall be discussed.

Table 4-5. Difference in Model Calculated Wind, $U_7 - U_c$, for Nominal Winds at 5 and 10 m/s (U_7 and U_c Are the W-7 and CWK Calculated Winds, Respectively)

θ	Upwind		Crosswind		Downwind	
	U = 5	U = 10	U = 5	U = 10	U = 5	U = 10
V-Polarization						
20	-2.4	-2.8	-3.1	-3.3	-0.2	0
24	-2.7	-3.2	-1.4	-1.6	-0.4	-0.6
28	-2.5	-3.0	0	0.5	0	-0.2
32	-1.7	-1.5	-0.3	0	0	0
48	1.0	1.2	0.2	0	0	0.6
50	0.9	1.0	0.2	0	0	0
54	1.2	1.2	0.4	0.5	0	-0.6
58	1.6	1.7	0.5	0.8	0.3	0.3
60	2.9	4.3	0.6	1.2	0.7	1.5
H-Polarization						
20	-1.7	-2.4	-2.4	-2.7	0.6	-0.9
24	-2.3	-3.1	-1.1	-1.6	0.4	-0.7
28	-1.9	-2.9	-0.2	-0.8	1.3	0.7
32	-1.4	-1.8	0	0	1.2	1.0
48	0.9	1.0	1.2	1.0	2.0	1.6
50	1.2	1.4	1.5	1.6	1.7	2.1
54	1.6	1.6	1.8	2.3	2.6	2.8
58	2.4	3.1	2.0	2.5	2.9	3.5
60	3.0	3.9	2.6	3.5	3.4	4.0
$\Delta U = U_7 - U_c \text{ (m/s)}$						

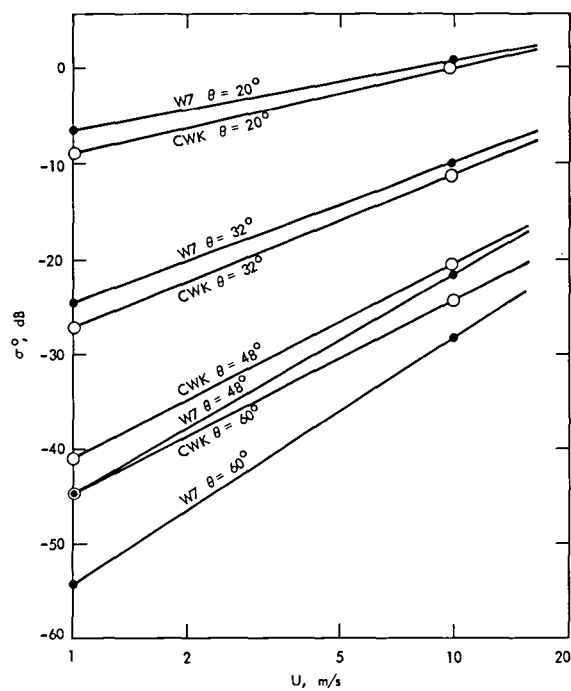


Figure 4-13. σ^0 vs Wind Speed for Constant Incidence Angle for CWK and W-7 Model Functions, Upwind and H-Pol

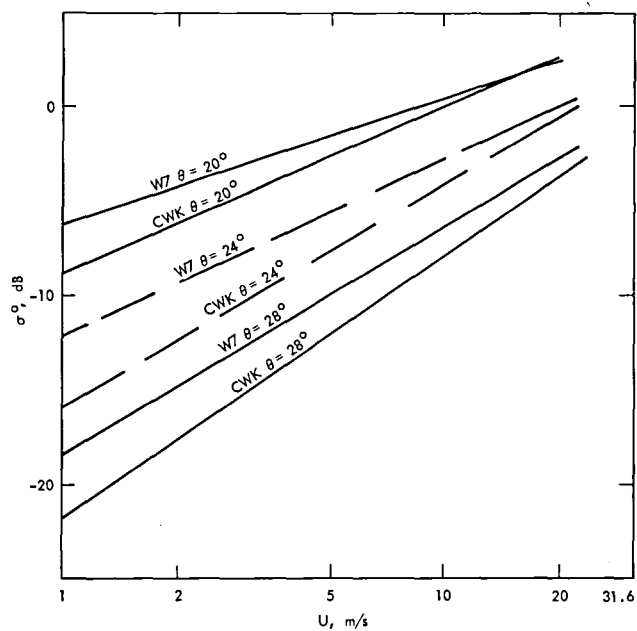


Figure 4-14. σ^0 vs Wind Speed for Incidence Angles 20 to 28 deg for CWK and W-7 Model Functions, Upwind and H-Pol

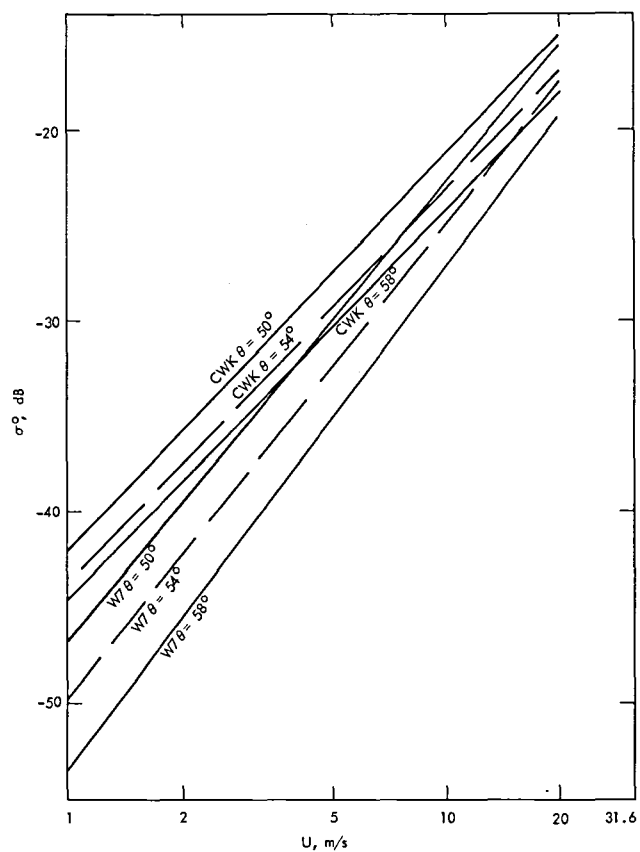


Figure 4-15. σ^0 vs Wind Speed for Incidence Angles 50 to 58 deg for CWK and W-7 Model Functions, Upwind and H-Pol

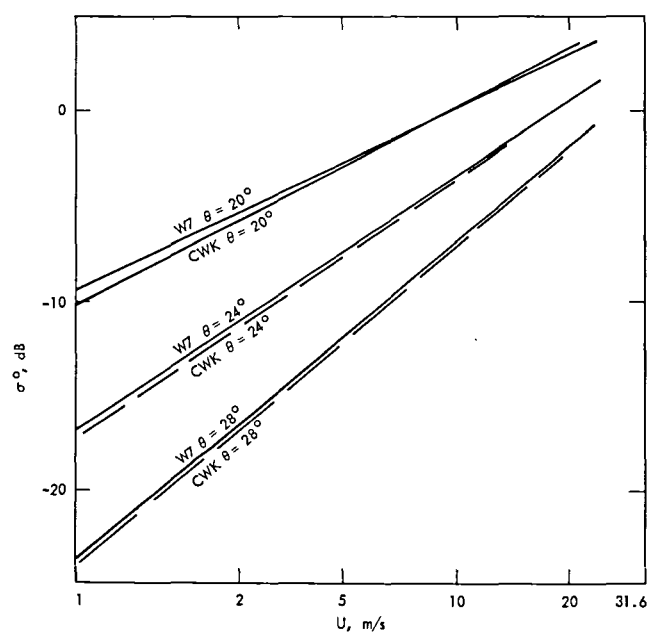


Figure 4-16. σ^0 vs Wind Speed for Incidence Angles 20 to 28 deg for CWK and W-7 Model Functions, Downwind and V-Pol

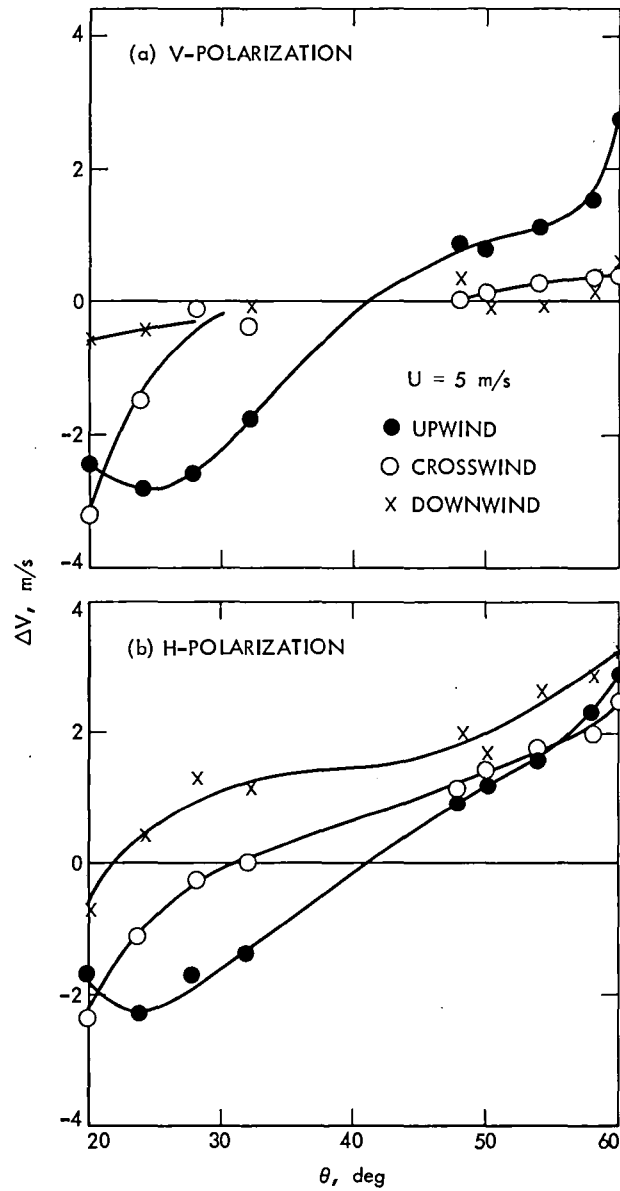


Figure 4-17. Differences Between the Wind Speeds Predicted by W-7 and CWK for Wind Speeds Near 5 m/s

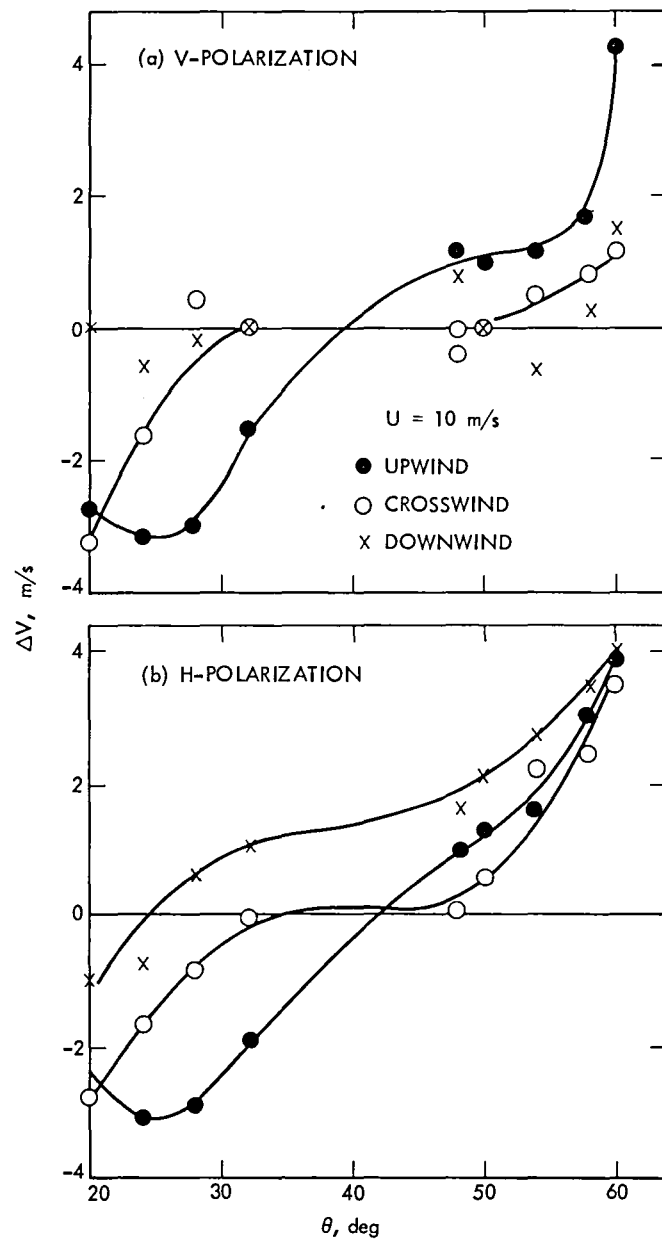


Figure 4-18. Differences Between the Wind Speeds Predicted by W-7 and CWK for Wind Speeds Near 10 m/s

The analyses centered about the primary equation (1) used in relating the backscatter σ° to the wind speed (or stress). The first study attempted to test the validity of the primary equation for the JASIN data. In this regard, an attempt was made to make the comparison as model-independent as possible. To do this, the comparisons were divided into incidence angle bins of 4 deg, ranging from 20 to 60 deg. The incidence angles referred to hereinafter will be the center points of those bins. In the previous studies, bins of 10-deg incidence angle were selected and the data normalized to downwind direction by using one of the model function tables. The reduction of the bins to only 4 deg was meant to minimize the need for a model function. The wind direction was taken into account by averaging the σ° 's from the two beams (forward and aft) in the area of spot observation. The resultant average of the two sets of σ° should be nearly independent of wind direction [see Grantham et al., 1975]. The following is a summary of the procedures of the analysis:

- (1) A scan of 50-km radius is used to search about each spot observation.
- (2) The cells which are found are separated by polarization, beam, and incidence angle bin.
- (3) All σ° values for each incidence angle bin are adjusted to coincide with the central θ value of the bin by interpolation in the model function tables.
- (4) A single value of σ° with an associated polarization and incidence angle for each spot observation is computed using the distance-weighted average of the individual σ° (from the spot observation) for each bin, polarization, and beam.

Note that the only use of the model function was in step (3) and only to interpolate through at most ± 2 deg in incidence angle. Table 4-6 shows the resulting statistics using the W-7 algorithm, while Table 4-7 is the same except that the CWK function was used. The differences are usually insignificant, as expected, but there are a few major exceptions. The most disconcerting observation is the behavior of the SASS at high incidence angles, especially for H-pol. As can be seen, the correlation between σ° and $\log U$ approaches zero for incidence angles greater than 52 deg. Correlations for other angles range between 0.8 - 0.9, except at 34 deg at H-pol, when r drops below 0.8. The small sample size at high incidence angles and the normalized standard deviation of the σ° measurement may be responsible for the poor correlation, but at this point it would seem that values at high incidence angle do not follow the power law relationship.

The second study was comparison of the two model functions by a simple statistical evaluation of observed σ° against model σ° . Here, each cell σ° was compared against a σ° value taken from the model functions, given the satellite azimuth, incidence angle, and the surface truth wind speed and direction. Tables 4-8 and 4-9 give the results for W-7 and CWK, respectively. Here, differences do occur, mainly at the high and low incidence angles. (Incidence angles here refer only to the center value of a bin that includes all angles ± 2 deg of the center value.) Correlations are a bit better for CWK at low incidence angles and a bit

Table 4-6. Statistics for σ° vs Log U (Neutral Wind at 19.5 m)
Using W-7 Algorithm to Interpolate to Desired Incidence
Angles

Pol	Inc	R	M ₁	M ₂	B ₁	B ₂	Size
H	22.0	0.960	21.03	22.55	-24.55	-25.97	11
H	26.0	0.907	24.95	29.63	-32.52	-36.75	23
H	30.0	0.813	13.25	18.04	-25.85	-29.94	21
H	34.0	0.746	15.57	25.48	-32.10	-40.37	19
H	38.0	0.909	24.38	28.84	-42.56	-46.49	25
H	42.0	0.891	27.60	34.08	-48.60	-54.48	27
H	46.0	0.838	28.76	39.97	-52.28	-62.82	40
H	50.0	0.883	26.25	32.91	-51.47	-57.59	34
H	54.0	0.441	11.22	50.82	-37.33	-72.05	24
H	58.0	0.015	0.172	15.46	-26.57	-15.53	9
V	22.0	0.9669	21.05	22.26	-24.18	-25.29	8
V	26.0	0.882	21.13	26.25	-27.95	-32.42	20
V	30.0	0.827	12.27	16.04	-23.92	-27.20	26
V	34.0	0.839	16.97	22.63	-31.67	-36.57	22
V	38.0	0.885	24.90	30.97	-40.92	-46.19	26
V	42.0	0.906	28.68	34.38	-45.63	-50.70	31
V	46.0	0.871	31.15	40.33	-50.57	-58.88	38
V	50.0	0.900	23.51	28.29	-43.54	-47.93	42
V	54.0	0.849	22.06	29.48	-41.92	-48.35	29
V	58.0	0.646	12.86	26.75	-33.83	-46.38	10

Columns indicate polarization, incidence angle, correlation coefficient, slope of σ° regressed onto log v, slope minimizing scatter in direction perpendicular to regression line, y-intercept for m₁ line, y-intercept for m₂ line, and sample size.

Table 4-7. Statistics for σ° vs Log U Using the CWK Algorithm to Interpolate to Desired Incidence Angles

Pol	Inc	r	m_1	m_2	b_1	b_2	Size
H	22.0	0.9521	20.92	22.70	-24.55	-26.22	11
H	26.0	0.8978	23.55	28.48	-31.13	-35.56	23
H	30.0	0.8208	13.60	18.30	-26.02	-30.03	21
H	34.0	0.7545	16.09	25.91	-32.55	-40.75	19
H	38.0	0.9128	24.23	28.47	-42.45	-46.18	25
H	42.0	0.9083	25.84	30.71	-46.85	-51.26	27
H	46.0	0.8553	26.42	35.17	-50.13	-58.36	40
H	50.0	0.8758	21.16	26.61	-46.45	-51.47	34
H	54.0	0.4456	9.78	41.47	-35.72	-63.50	24
H	58.0	-0.0043	-0.46	-32.25	-25.53	0.9628	9
V	22.0	0.9665	21.71	22.99	-24.95	-26.12	8
V	26.0	0.8717	21.55	27.38	-28.29	-33.38	20
V	30.0	0.8312	13.07	17.11	-24.66	-28.18	26
V	34.0	0.8292	17.61	24.08	-32.35	-37.96	22
V	38.0	0.8869	25.11	31.14	-41.16	-46.40	26
V	42.0	0.9076	28.86	34.47	-45.83	-50.81	31
V	46.0	0.8760	31.33	40.13	-50.80	-58.76	38
V	50.0	0.9000	23.71	28.55	-43.70	-48.14	42
V	54.0	0.8423	21.80	29.54	-41.60	-48.29	29
V	58.0	0.6405	12.54	26.37	-33.38	-45.87	10

Table 4-8. Statistics for Comparison of Observed σ_o° With Model - Derived σ_{TH}° , Using the W-7 Algorithm

$(\sigma_{TH}^\circ - \sigma_o^\circ)$	$ \sigma_{TH}^\circ - \sigma_o^\circ $	σ_D	σ_A	R	M	B	Size	Inc	Pol
0.415	1.17	1.56	1.11	0.666	0.565	-1.7942	20	22.0	H
0.801	1.60	2.07	1.53	0.624	0.423	-4.349	45	26.0	H
0.713	1.74	2.28	1.65	0.531	0.446	-6.837	46	30.0	H
1.47	2.18	2.42	1.81	0.786	0.814	-2.001	37	34.0	H
-0.096	1.83	2.57	1.80	0.875	0.947	-1.143	44	38.0	H
0.145	1.72	2.20	1.38	0.332	0.828	-3.797	50	42.0	H
-0.081	2.02	2.60	1.64	0.685	0.918	-2.185	83	46.0	H
-0.460	1.69	2.26	1.56	0.803	0.883	-3.483	84	50.0	H
-3.58	3.82	5.28	5.11	0.076	0.126	-25.593	53	54.0	H
-6.12	6.22	4.53	4.38	-0.001	-0.001	-30.066	18	58.0	H
0.534	1.36	1.60	0.998	0.621	0.5748	-1.507	17	22.0	V
0.928	1.70	2.05	1.47	0.688	0.424	-3.852	47	26.0	V
0.537	1.58	2.05	1.41	0.568	0.564	-4.756	49	30.0	V
1.24	1.95	2.29	1.72	0.840	0.872	-0.931	39	34.0	V
0.636	2.31	3.26	2.39	0.819	0.724	-4.938	58	38.0	V
-0.081	2.24	3.07	2.10	0.831	0.739	-5.476	64	42.0	V
0.123	1.95	2.70	1.87	0.755	0.700	-6.727	81	46.0	V
0.971	1.64	2.02	1.53	0.872	0.822	-4.810	111	50.0	V
-2.03	2.34	1.99	1.61	0.870	0.848	-5.303	73	54.0	V
-2.80	2.85	1.77	1.68	0.831	0.863	-5.608	16	58.0	V

Columns (from left) refer to: mean difference, mean absolute difference, standard deviation of differences, standard deviation of absolute differences, correlation coefficients, slope of regression line model σ_o° vs observed σ_o° , y-intercept (bias), sample size, central incidence angle, and polarization.

Table 4-9. Statistics for Comparison of Observed σ_o° With Model - Derived σ_{TH}° ,
Using the CWK Algorithm

$(\sigma_{TH}^\circ - \sigma_o^\circ)$	$ \sigma_{TH}^\circ - \sigma_o^\circ $	σ_D	σ_A	R	M	B	Size	Inc	Pol
-0.45	1.28	1.53	0.946	0.7075	0.6821	-2.06	20	22.0	H
0.188	1.45	1.94	1.30	0.6783	0.4473	-4.74	45	26.0	H
0.383	1.62	2.18	1.51	0.5578	0.4432	-7.20	46	30.0	H
1.17	2.01	2.26	1.57	0.8158	0.8550	-1.54	37	34.0	H
0.35	1.71	2.37	1.68	0.8793	0.8528	-2.80	44	38.0	H
0.92	1.91	2.19	1.40	0.8181	0.6919	-6.15	50	42.0	H
1.30	2.12	2.23	1.47	0.6953	0.7830	-4.30	33	46.0	H
1.43	2.02	2.03	1.43	0.8119	0.7669	-4.61	84	50.0	H
-0.80	2.70	4.51	3.70	0.0807	0.1077	-23.28	53	54.0	H
-2.63	3.80	3.99	2.90	-0.035	-0.040	-27.51	18	58.0	H
-0.253	1.42	1.76	1.08	0.6388	0.7374	-1.51	17	22.0	V
0.161	1.65	2.03	1.20	0.6905	0.4778	-4.17	47	26.0	V
-0.192	1.62	2.01	1.21	0.6228	0.6798	-4.08	49	30.0	V
0.70	1.87	2.30	1.51	0.8566	0.8566	-0.012	39	34.0	V
0.40	2.23	3.25	2.39	0.8242	0.7560	-4.52	58	38.0	V
0.01	2.17	3.03	2.11	0.8372	0.7647	-4.84	64	42.0	V
0.68	2.04	2.74	1.95	0.7479	0.6971	-6.23	81	46.0	V
0.15	1.44	1.97	1.36	0.8778	0.8364	-3.37	111	50.0	V
-0.47	1.66	2.11	1.39	0.8485	0.7926	-4.93	73	54.0	V
-1.25	1.53	1.77	1.59	0.8095	0.7309	-6.76	16	58.0	V

better for V-pol at high incidence angles for W-7. H-pol has hardly any correlation at high incidence angles. An analysis of the mean difference and the mean absolute difference shows that W-7 undergoes systematic errors at high incidence angles for both polarizations. For mid-incidence angle ranges, both models behave similarly.

It is not correct to infer or judge the quality of either model based on the preliminary results found in Tables 4-6 through 4-9, but indications are that the basic power law seems to break down at high incidence angles, especially for H-pol. It is no wonder, then, that the models would fail at those ranges. To evaluate which model fails the least would be counter-productive at this point. For V-pol the situation is a bit better, with correlations higher than 0.8 for high incidence angles. W-7 exhibits slightly better correlations and a better slope than CWK for these angles, but the absolute differences and mean differences show an offset not found for CWK.

To improve the confidence on the statistical analysis, the σ° data base was enlarged to include the GOASEX measurements. In addition, the procedure was slightly modified to test the models using various χ bins as well as incidence angle bins.

Again, the calculations involved comparing σ° values with each surface truth point. The σ° were located by scanning 50 km from the ship or buoy. All values within 50 km were used unless the "SDN" flag (standard deviation of the background noise) exceeded an arbitrary value of 0.5. The σ° 's were then separated by relative azimuth, χ , and incidence angle, θ . These results are given in Tables 4-10 and 4-11. For the first three columns, only values of σ° with coincident values of $|\chi_i - \chi| \leq 20$ deg were accepted, where χ_i is the angle indicated at the top of the column. For the column marked "All," the azimuth angle was disregarded. Instead, as before, σ° values for each beam were derived separately and then combined by simple averaging. Theoretically, that should have compensated for the angular dependence. The statistics, though, were somewhat inferior to the single angle cases, probably because of the increased noise in combining the forward and aft beams. An alternate conclusion is that both models have incorrect crosswind slopes.

Coincident values of $|\theta_i - \theta| \leq 4$ deg were accepted, but all others rejected. The selected σ° values were then interpolated by use of the model functions to the corresponding $\sigma^\circ(\chi_i, \theta_i)$ values. This was the only use of the model functions in this study. The individual σ° values were then interpolated by distance weighting to the geographic location of the surface truth spot where a $\log U_{19.5}$ value had been derived. Thus, at most one average σ° value was available for each spot for each incident and azimuth angle bin. Statistics for all spot observations with "hits" were then derived.

The results are presented for H-pol and V-pol in Tables 4-10 and 4-11, respectively. The columns are for $\chi = 0$ (upwind), 90 (crosswind), 180 (downwind), and "All" (average over all directions). The rows are grouped by incidence angle bins for 8-deg intervals. In each group is contained the correlation coefficient, r , the slope, m , and the y-intercept, b , of σ° regressed onto $\log U_{19.5}$. The last row of each group ("Size") indicates the sample size used for each category. The statistics for this combined data set are similar to those for the JASIN set alone with some noticeable exceptions; therefore, the same general conclusions hold.

Table 4-10. Statistics for σ° vs Log U Using the CWK and W-7 Model Functions for H-Polarization

$\chi=$	CWK				W-7			
	0°	90°	180°	All	0°	90°	180°	All
$\theta = 24$								
r	0.851	0.742	0.923	0.872	0.848	0.748	0.924	0.875
m	19.92	14.79	13.13	16.15	20.40	15.06	15.24	17.28
b	-25.90	-22.46	-18.52	-23.64	-25.91	-22.54	-20.39	-24.77
Size	8	27	18	97	8	27	18	97
$\theta = 32$								
r	0.898	0.810	0.851	0.890	0.908	0.814	0.879	0.888
m	17.32	17.27	18.71	17.34	17.35	17.88	23.54	18.33
b	-29.76	-32.79	-32.17	-31.25	-29.72	-33.48	-36.90	-32.18
Size	12	31	17	121	12	31	17	121
$\theta = 40$								
r	0.897	0.964	0.948	0.953	0.911	0.966	0.938	0.949
m	14.47	24.64	23.69	23.05	15.92	26.32	26.63	24.82
b	-32.48	-45.25	-43.22	-42.11	-33.51	-47.01	-46.54	-43.83
Size	12	21	14	101	12	21	14	101
$\theta = 48$								
r	0.850	0.858	0.951	0.807	0.874	0.890	0.942	0.806
m	21.86	18.98	26.10	19.86	24.41	21.99	32.00	22.19
b	-43.33	-46.18	-49.94	-43.71	-45.65	-49.22	-55.91	-45.93
Size	15	18	14	101	15	18	14	101
$\theta = 56$								
r	0.605	0.067	0.676	0.383	0.562	0.072	0.686	0.380
m	11.42	15.67	15.03	8.576	11.10	18.06	18.99	9.63
b	-35.58	-30.42	-40.75	-33.89	-35.62	-31.27	-44.76	-35.08
Size	12	8	5	42	12	8	5	42

Table 4-11. Statistics for σ° vs Log U Using the CWK and W-7 Model Functions for V-Polarization

χ°	CWK				W-7			
	0°	90°	180°	All	0°	90°	180°	All
$\theta = 24$								
r	0.877	0.867	0.911	0.804	0.686	0.865	0.921	0.801
m	20.41	15.24	20.22	17.30	21.38	14.71	20.26	16.39
b	-26.07	-22.21	-25.24	-23.54	-26.42	-21.62	-25.07	-22.53
Size	8	26	15	102	8	26	15	102
$\theta = 32$								
r	0.918	0.818	0.878	0.873	0.892	0.824	0.868	0.867
m	20.48	20.78	19.95	18.40	18.49	21.25	18.93	17.45
b	-31.36	-35.12	-31.01	-30.75	-29.49	-35.79	-29.96	-29.81
Size	11	36	17	122	11	36	17	122
$\theta = 40$								
r	0.846	0.958	0.949	0.941	0.822	0.958	0.950	0.937
m	14.25	25.24	26.19	24.23	14.12	25.36	25.52	23.78
b	-29.10	-43.30	-42.55	-40.24	-28.92	-43.46	-41.90	-39.79
Size	13	27	12	110	13	27	12	110
$\theta = 48$								
r	0.803	0.947	0.921	0.890	0.832	0.951	0.917	0.892
m	23.55	26.64	28.90	24.94	26.25	27.23	29.15	25.00
b	-40.48	-48.95	-47.04	-43.97	-43.02	-49.47	-47.25	-44.02
Size	12	22	16	116	12	22	16	116
$\theta = 56$								
r	0.899	0.827	0.990	0.888	0.895	0.820	0.990	0.866
m	22.52	22.83	28.27	24.25	22.74	22.16	28.34	24.24
b	-41.01	-45.20	-45.71	-43.49	-41.24	-44.47	-45.81	-43.54
Size	11	14	6	55	11	14	6	55

Alternate Opinion

Concerning the above analysis, the following comments are offered: In general, one can note that the correlations for the most part are higher for V-pol than H-pol. The problem is that the average of σ° is not a constant with wind direction. The limiting case is the level of the upwind-downwind ratio. It is common knowledge that this ratio is significant for H-pol and quite larger than for V-pol. Analytically (based on the UK model of σ° , for explanation purposes):

$$\sigma_{\text{fore}}^\circ = A_0 + A_1 \cos \phi + A_2 \cos 2\phi$$

$$\sigma_{\text{aft}}^\circ = A_0 + A_1 \cos (\phi + 90^\circ) + A_2 \cos 2(\phi + 90^\circ)$$

where

$$A_0 = (\sigma_u^\circ + \sigma_d^\circ + 2\sigma_c^\circ)/4$$

$$A_1 = (\sigma_u^\circ - \sigma_d^\circ)/2$$

$$A_2 = (\sigma_u^\circ + \sigma_d^\circ - 2\sigma_c^\circ)/4$$

Therefore,

$$\begin{aligned}\sigma_{\text{avg}}^\circ(U, \theta, \phi) &= (\sigma_{\text{fore}}^\circ + \sigma_{\text{aft}}^\circ)/2 \\ &= A_0 + (A_1/\sqrt{2}) \cos (\phi + 45^\circ)\end{aligned}$$

The variation from constant then depends on the difference between the "true" upwind and downwind returns divided by $\sqrt{2}$ times $\cos (\phi + 45^\circ)$. To illustrate the error, take a given model and pick a wind speed and incidence angle; then vary ϕ . It is hypothesized that the error is significant and affects the results.

E. SASS/SURFACE TRUTH WIND VECTOR COMPARISONS SUBPANEL

1. SASS/Surface Observation Data Quality Assessment

As an initial check data quality, the WMO and 60-min Autologger Priority Revolution statistics were examined to search for major discrepancies between SASS-measured and surface-observed wind speed/direction. Gross discrepancies in speed greater than 4 m/s and direction greater than 40 deg were flagged as questionable. The choice of 4 m/s and 40 deg was rather arbitrary. It was mainly based on the fact that a fair number of speed

differences around 3 to 3.5 m/s and direction differences around 30 to 35 deg were found to exist. The number of differences greater than 4 m/s and 40 deg was far fewer, and so these were considered gross discrepancies. The results can be summarized as follows:

a. WMO Reports

- (1) Rev 557: A few points of speed differences of 12 to 22 m/s in one small region of triangle. Initial work suggests this is related to thunder storms.
- (2) Rev 791: SASS wind speeds low compared to WMO observations. No initial explanation for the discrepancy.
NOTE: SASS also low compared to 60-min W2 Autologger.
- (3) Rev 929: Some differences between WMO observation and SASS. Probably related to a shear zone in NW corner of triangle (at edge of SASS swath). Also, front appears in right place in Rev 930.
- (4) Rev 599: SASS speeds low compared to WMO speeds.
NOTE: No such bias occurs in comparison of SASS and 60-min W2 Autologger.
- (5) There is no general bias or rms deviation between SASS and all four platform ships (Meteor, Endurer, John Murray, Hecla) over the 23 priority revolutions.

b. Conclusion From WMO Observations. Surface observations can all be considered good quality. The larger SASS discrepancies can be related to some peculiar meteorological conditions. The slight negative SASS bias in Rev 791 is unexplained at this point.

c. 60-Min Autologger Reports

- (1) Buoy J1 gives consistently low wind speeds and incorrect wind directions compared to SASS. It first appears in priority revolution listings on 21 August. Guymer says J1 direction known to have failed 19 August, speed failed 29 August.
- (2) Discovery gives mostly inconsistent wind direction through whole record. Guymer says this is due to known problems which have been corrected in later data version.
- (3) Tydeman shows mostly higher speeds and a few large direction differences. Values in a single revolution tend to be all of one sign. No explanation for discrepancies.

- (4) John Murray shows significant number of large discrepancies. No general pattern for whether it is higher or lower than 4 m/s or 40 deg.
- (5) Buoys H2 and W2 appear to be good overall. There are occasional instances of higher or lower values of either speed or direction compared to SASS.

d. Conclusion Form 60-Min Autologgers. Apparently some bad data from buoy J1 and Discovery that is explainable in terms of malfunctioning wind recorders. Corrections should be made before running any future statistics. Discrepancies between Tydeman and John Murray might be worthy of further examination.

2. SASS/60-Min Autologgers Comparisons

A question examined was whether there were any systematic differences between SASS-measured wind speed and surface-observed as a function of the separation difference between the two. For the sake of a first stage comparison, the SASS winds were compared to the "standard" buoy W2 60-min Autologged winds. The results are shown in the scatter plot of Figure 4-19. The SASS winds in this plot were produced by the Wentz-7 algorithm. There appears to be a positive bias in the SASS winds of approximately 1 m/s. (That is, SASS winds are, on the average, 1 m/s larger than W2 winds.) There is no obvious dependence of rms deviation between the two as a function of spatial separation. The scatter is quite considerable. Most speed differences are contained within $-2 \text{ m/s} < \text{speed difference} < 3 \text{ m/s}$. [NOTE: There are relatively few observations with small separation distance. Scatter for separations less than 30 km is not very well resolved.]

Another question addressed was whether there were any systematic differences between SASS wind speed and observed wind speed as a function of observed wind speed. Again, as a first cut, only the W2 buoy data was used in the intercomparison. The results are shown in Figure 4-20 and 4-21 for SASS winds produced by the Wentz-7 algorithm. Figure 4-20 shows the scatter plot for each of the 23 priority revolutions. Figure 4-21 shows only the median (not the mean) and the total range of variation for each of the 23 priority revolutions. The median was chosen rather than the mean value because of the small number of sample observations. With only a few observations, the mean value cannot be accurately estimated in the presence of outliers. These outliers may be noise or they may be typical values that have just been undersampled. The median gives more weight to the outliers and, if no outliers are present, is equal to the mean value.

Overall, the plots look like random scatter. The SASS winds, again, tended to be higher than W2 winds. (The bias appears to be about 1 m/s.) The scatter does not appear to vary as a function of speed. It is significant to point out that the wind speed differences tend to cluster for single revolutions. That is, all speed differences for any particular revolution tend to be biased either

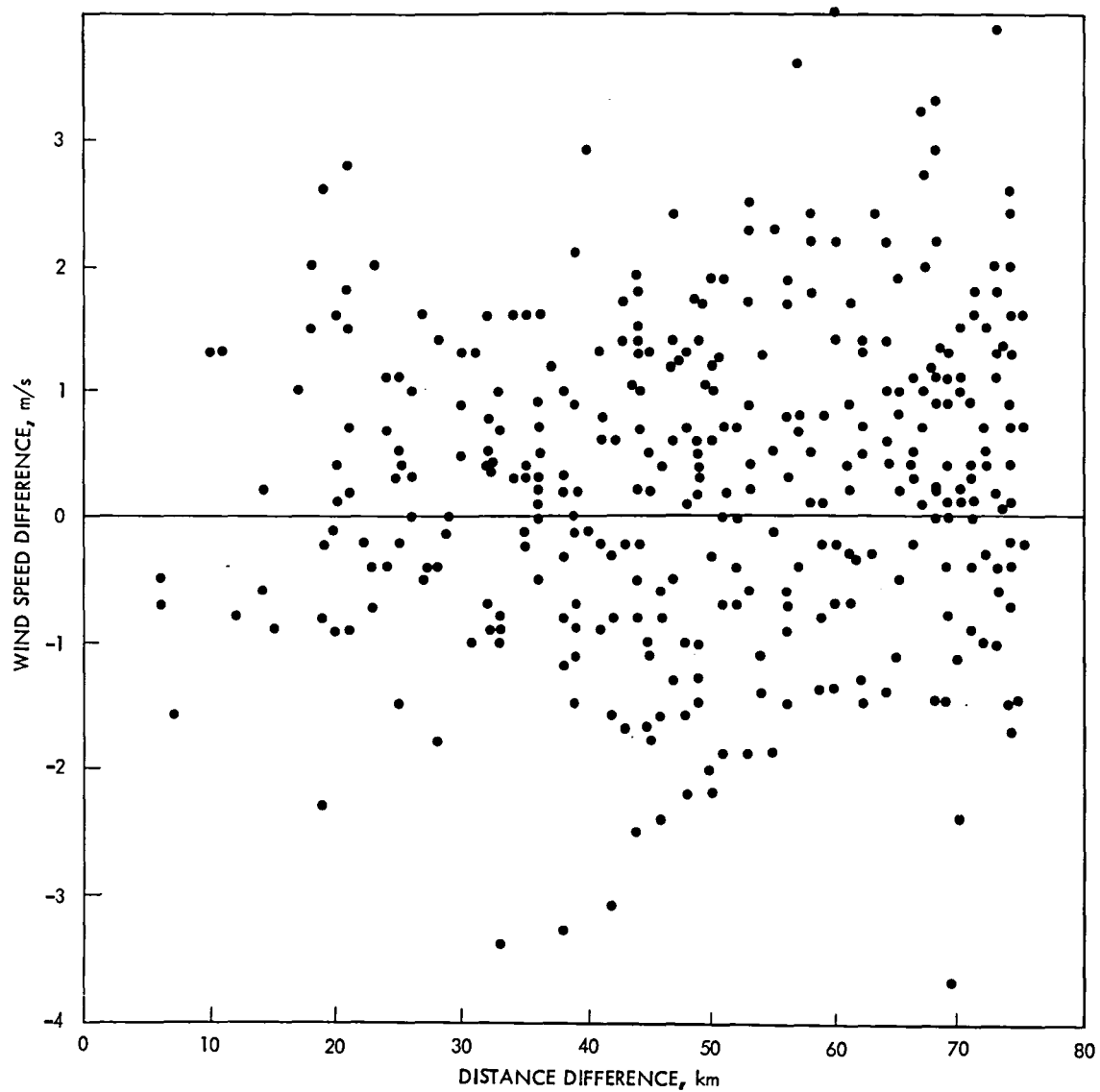


Figure 4-19. SASS Minus Autologger Buoy W2 Winds Versus Separation Distance for W-7 Model Function

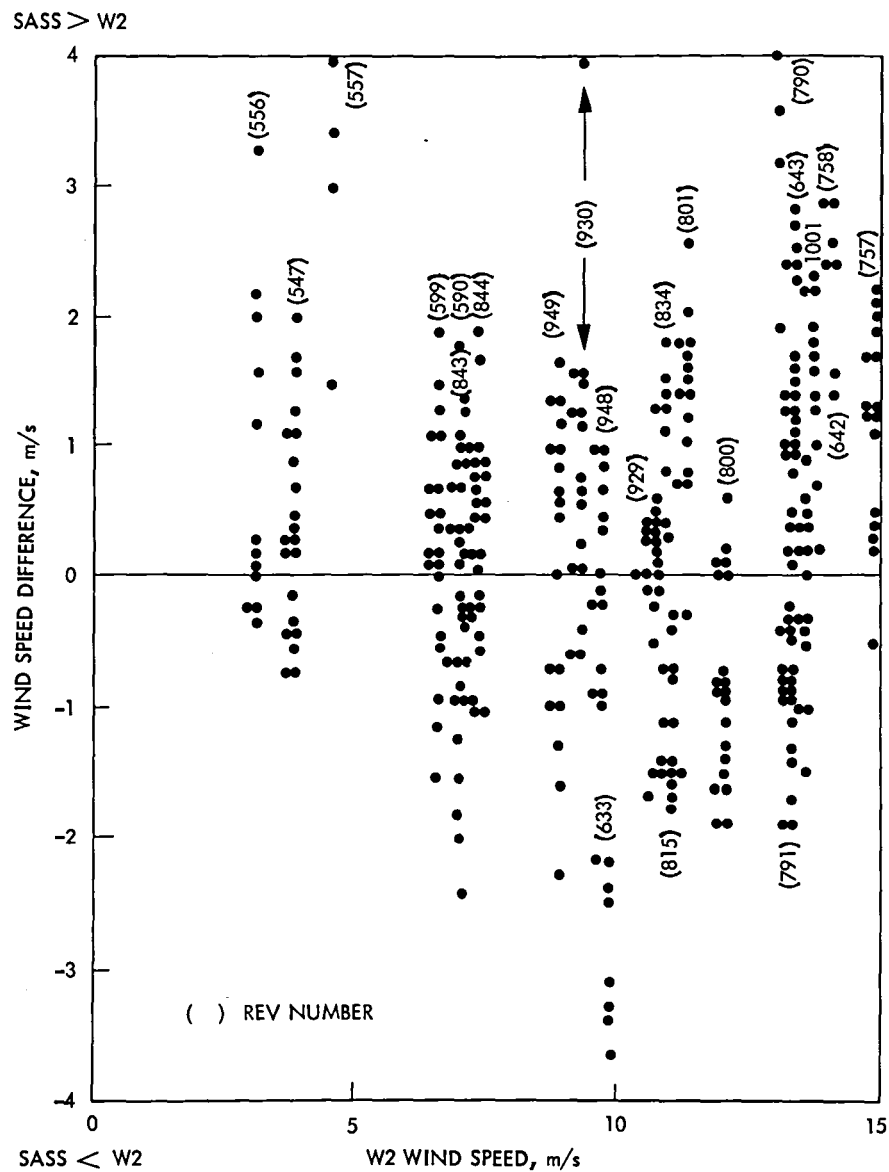


Figure 4-20. SASS Minus Autologger Buoy W2 Winds Versus W2 Wind Speed for W-7 Model Function

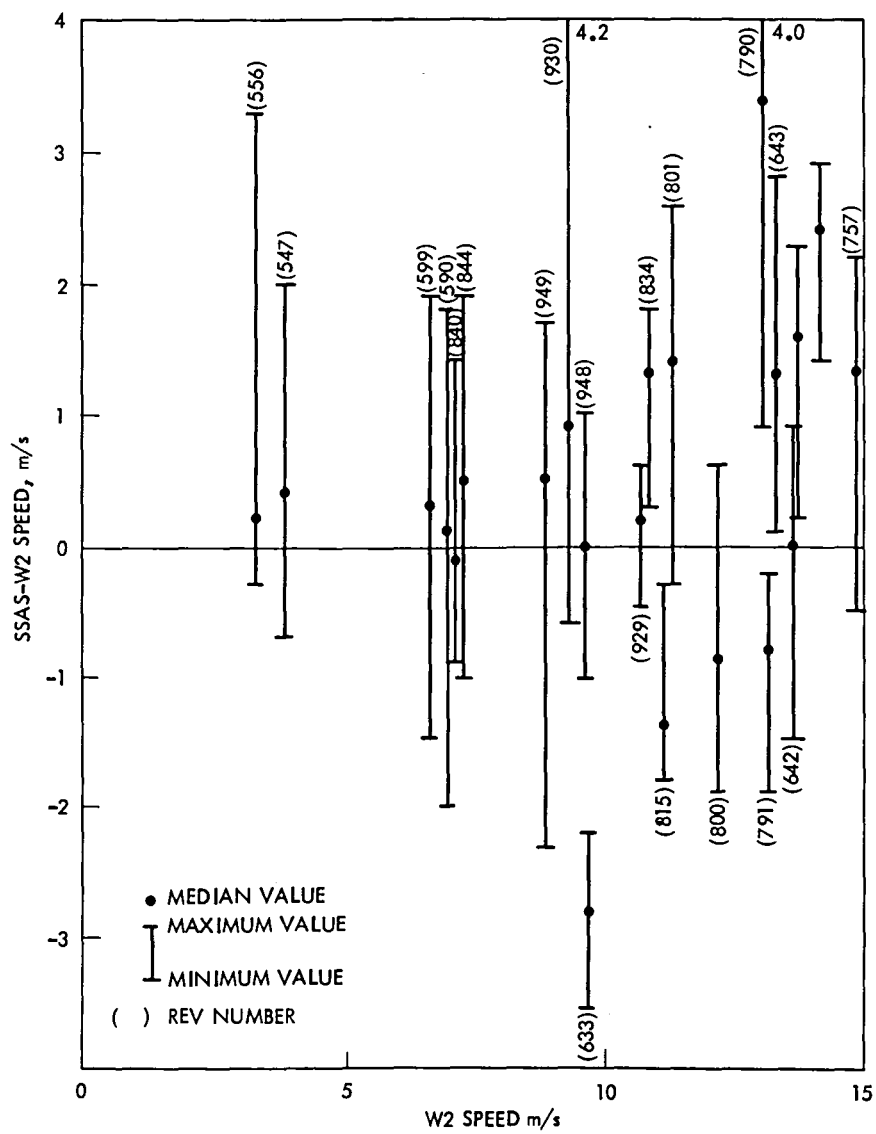


Figure 4-21. SASS Minus Autologger Buoy W2 Winds Median Value Versus W2 Wind Speed for W-7 Model Function

positive or negative. This suggests that some other important variable has not been considered (Perhaps incident angle?).

Finally, the question of systematic wind speed differences as a function of meteorological wind speed was addressed for SASS winds produced by the CWK algorithm. Again, only the W2 buoy data was used and the results are shown in Figures 4-22 and 4-23. Figure 4-22 shows the full scatter plot for each of the 23 priority revolutions, while Figure 4-23 shows only the median (not the mean) and total range of variation for each of the 23 priority revolutions.

These plots do show systematic behavior and generally find that CWK SASS winds are smaller than W2 winds at medium speeds (6-13 m/s) and larger than W2 winds at lower and higher wind speeds. Also, effects of incidence angle have not been considered in this plot.

ADDENDUM

Wind recorder intercomparisons conducted at Woods Hole Oceanographic Institution subsequent to the JASIN-Seasat Workshop determined that the wind speeds recorded by the W2 cup/vane anemometer were too high. The recorded values need to be multiplied by 0.87 to get the true wind speed. For a wind speed of 7-8 m/s, this results in a bias of about 1 m/s high for the W2 record. The effect this would have on the SASS versus W2 wind speed comparisons performed here would be to raise the SASS speed bias to about 2 m/s too high. The W2 wind direction appears to be correct.

3. Comparison of Wind Direction Errors for Different Polarization Pair Combinations

The combined polarization (V and H) and cell pairing options for deriving wind solutions produce different combinations of polarization pairs. These combinations are either like polarization (VV or HH) or different polarization (VH or HV) pairs from the fore and aft antenna beams. In reviewing the wind vector plots (sea-chicken plots) of SASS winds, it was noted that in many instances the derived wind directions for the HV or VH combinations differed from either the HH or VV combination. In general the wind speeds from any combination were in good agreement. Statistics on wind direction differences were generated by comparing the SASS measurement to the small scale wind field (see Subsection E-5) using a selected set of the priority revolutions for different polarization combinations. The mean and standard deviation of the wind direction difference were determined for each of HH + VV combinations and the VH + HV combinations. The results are summarized in Table 4-12.

For five of the eleven cases processed, the difference between the two polarization sets is not significant; however, for the remaining six, the HV + VH combination is much poorer, especially when considering the rms value. The reason for this inconsistency is probably the improper specification of the model function (see Subsection D). Therefore, it was recommended that only VV

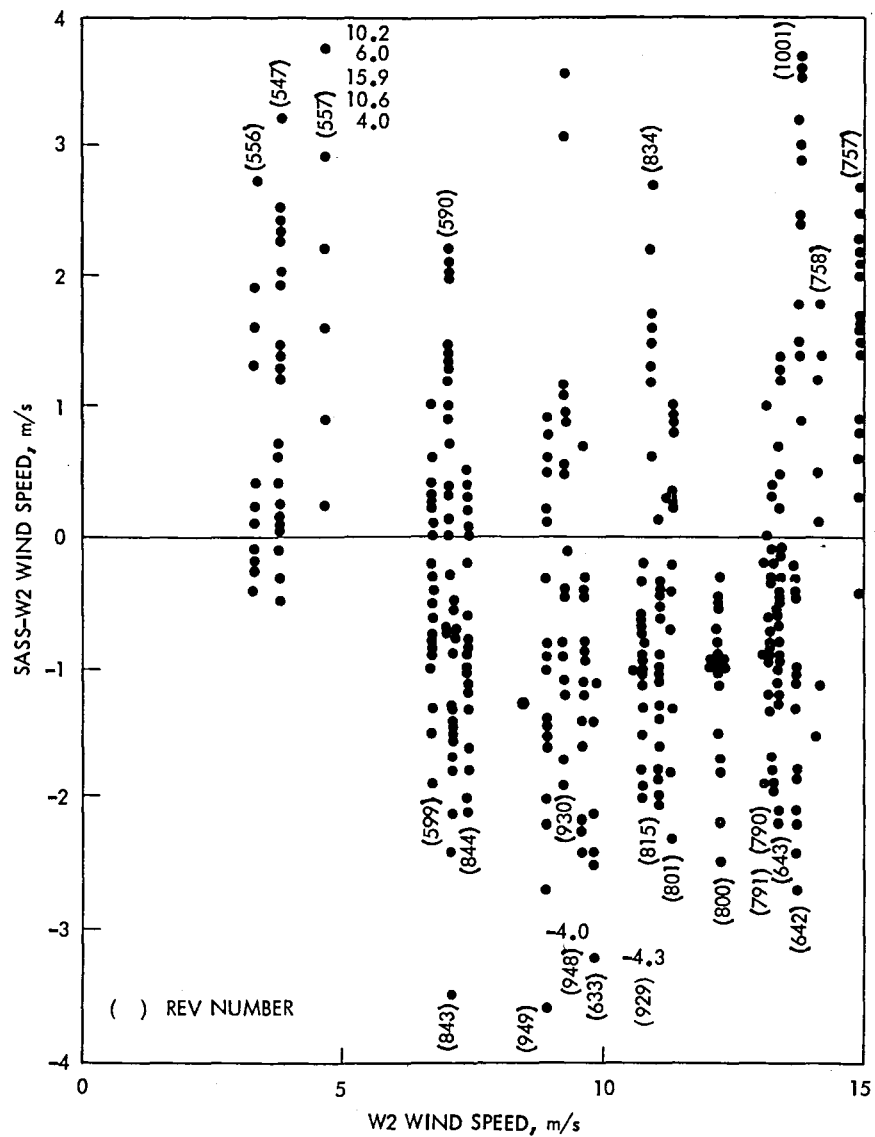


Figure 4-22. SASS Minus Autologger Buoy W2 Winds Versus W2 Wind Speed for CWK Model Function

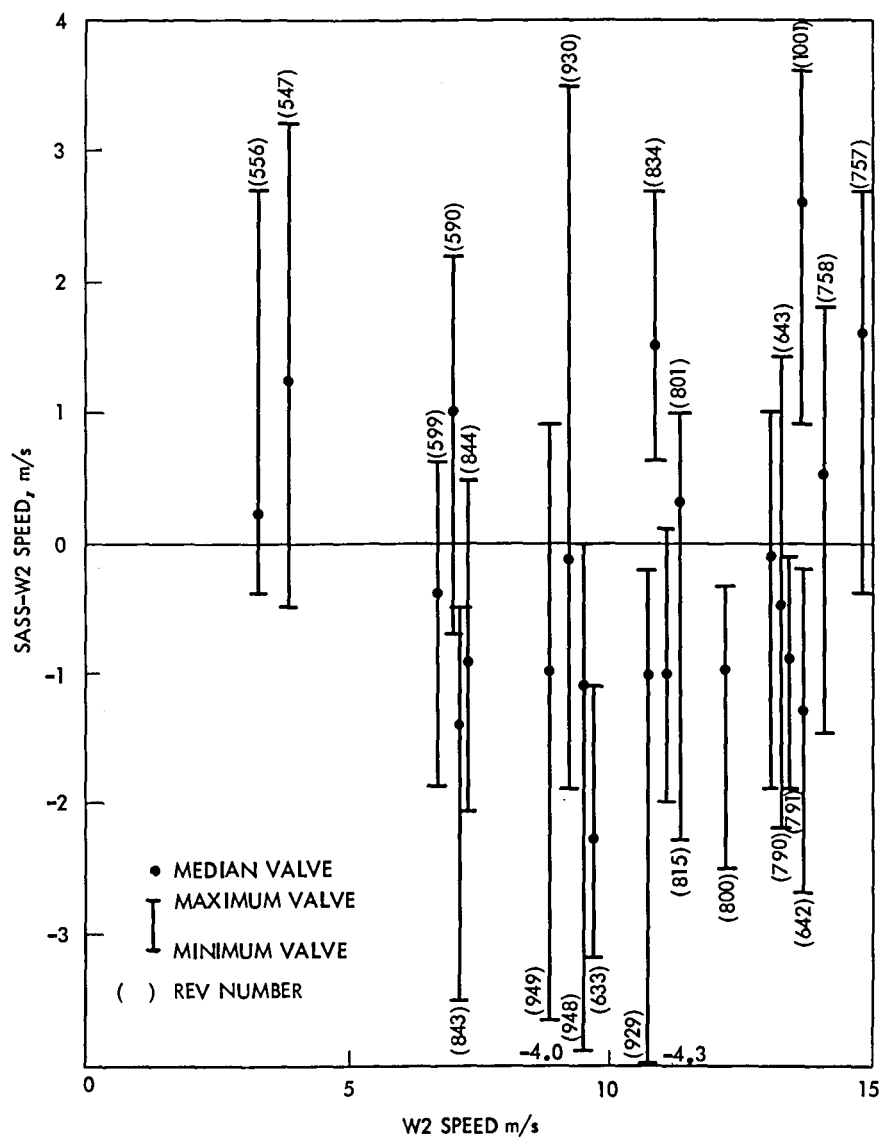


Figure 4-23. Median Value of SASS Minus Autologger Buoy W2 Winds Versus W2 Wind Speed for CWK Model Function

Table 4-12. SASS-Surface Observation Wind Direction Statistics
as a Function of Polarization Pairs

Rev	VV + HH Pol Pair Combinations			VH + HV Pol Pair Combinations		
	Mean Diff, deg	Standard Deviation	N	Mean Diff, deg	Standard Deviation	N
547	1.1	17.9	17	-2.5	28.3	9
556	9.1	14.3	10	16.6	15.8	11
590	6.6	10.4	27	-5.9	5.5	7
599	4.1	16.6	18	18.1	13.4	15
790	6.0	14.6	9	3	6.9	9
791	-8.8	8.6	9	-2.5	9.8	11
844	-8.3	11.4	28	-9.8	15.6	16
830	-0.4	19.4	21	21.3	22.2	15
948	-10.8	13.6	25	-17.1	14.7	12
949	-7.3	7.8	20	-4.2	13	20
1001	-6.1	10.2	19	-20.6	13.1	20

and HH combinations should be used to derive wind vector solutions in the GDR production processing.

Subsequent to the JASIN workshop, the W-7 and CWK model functions were combined and were tuned using the JASIN data set. The new model function known as SASS-I was tested as discussed above. The statistics for this set showed little difference between VV, HH, and HV or VH combinations. Therefore, the recommendation was not adopted and all combination polarization pairings were used.

4. Comparison of SASS Estimates and Surface Observations of the Wind Vector

Comparisons in this section are limited to the JASIN triangle and illustrate the effectiveness of the SASS to provide wind speed and direction information over the ocean. In this comparison, the direction solution nearest the surface observation is used. The potential of possible techniques to remove aliases in the wind direction is discussed in a following section. Wind estimates from the SASS, using either the W-7 or CWK model functions, on the average satisfy the requirements set by the user groups.

There were up to eight meteorological platforms providing windfield measurements within the JASIN triangle. During the 23 selected orbits of good SASS coverage of the triangle, the SASS cell winds were compared to those spot observations. To be meaningful, the spot value should be averaged over a time which makes it compatible with a 50 x 20 km SASS cell measurement. The WMO averages were 2-min averages taken on the hour. The data-loggers provided time series of 1-6 min averages, which were used to form 15- and 60-min averages centered on the hour.

Initial WMO spot comparison contained some obvious errors (vane failures, biased ship winds). The data was despiked by removing spot values that were inconsistent with other, better, nearby measurements or known to be in error due to instrument failure or systematic bias found in intercomparisons. The WMO values obtained from the JPL (Klose) program were:

Set	$\overline{\Delta V}$	$\sigma_{\Delta V}$	$\overline{\Delta \chi}$	$\sigma_{\Delta \chi}$	N
Unedited WMO	0.8	1.7	-3	18	975
60 min	0.7	2.6	4	25	1159
15 min	0.85	2.9	4.5	26	787
Despiked WMO	0.7	1.6	-4	16	847
60 min	0.1	2.2	-0.3	18	860
15 min	0.4	2.4	-0.6	18	610

The spot comparisons were separated by stratification (stable, neutral or unstable) with no evident differences. They were also available by individual platform and orbit. There were significant (± 2 m/s, 20 deg) differences, orbit or platform related.

Further comparison of SASS-derived wind estimates for 29 revs and combined V- and H-polarization measurements (radius of 75 km) with spot observations by weather ships and 60-min wind averages from data buoys is shown in Tables 4-13 through 4-16. In these tables, three revolutions are underlined that have large difference statistics (see Subsection G for further discussion). The most obvious was Rev 557 with a mean difference $\bar{x} = 4.46$ m/s and a standard deviation $\sigma = 4.72$ m/s. For this case, the high SASS wind speeds were very localized (within a 30-km radius) and up to five times the average field (22 m/s in a 4-5 m/s field). This region was subsequently identified with a local thunderstorm-associated disturbance through shiplog and passive microwave (SMMR) data. Further, for Revs 929 and 1001, there was some evidence of frontal activity not included in the field analysis, but the data were not nearly as conclusive as for Rev 557. In Tables 4-13 through 4-16, summary statistics are calculated with and without these revolutions present. These tables illustrate the effectiveness of SASS to infer the wind vector using either the W-7 or CWK model function, although, in this comparison, the CWK model function appears to produce slightly better results.

As illustrated by Tables 4-13 through 4-16, statistics are not the same for the Autologger and spot observations. The longer time averages of wind speed by

Table 4-13. SASS Minus Spot Observations, Statistics
by Revolution, W-7 Model Function, V- and H-
Polarizations Combined, Autologger 60-Min Averages

Case	Rev	Speed Diff		Direction Diff		N	$\overline{W/S}$, m/s	$\overline{\theta}_i$
		Mean	Std Dev.	Mean	Std Dev.			
Priority 23 V/H - Pol	547	-0.22	1.85	11.9	20.5	80	4.45	38.0
Wentz-7	556	0.25	1.60	16.0	28.1	59	4.21	43.0
Autologger (9)	557	4.46	4.72	15.6	25.2	66	5.33	53.0
60 min avg.	590	-1.44	1.39	0.5	30.7	96	8.49	33.0
	599	-0.03	0.89	8.9	15.3	98	6.88	47.0
	633	-2.42	1.15	-1.3	9.7	37	9.16	25.0
	642	-0.51	1.28	5.3	12.5	67	13.80	49.0
	643	1.43	0.85	-8.1	11.7	65	13.30	49.0
	757	1.17	0.80	-2.7	6.40	16	14.88	35.0
	758	2.29	0.61	0.4	12.2	7	14.12	55.0
	790	2.9	1.33	-2.4	9.5	7	12.4	54
	791	-0.76	1.69	-10.2	16.4	52	12.52	37.0
	800	-0.31	1.14	5.2	19.3	53	10.90	47.0
	801	1.32	1.05	17.5	21.7	47	10.22	49.0
	815	-0.34	1.76	18.3	31.9	56	9.61	30.0
	834	1.52	0.93	11.6	43.4	37	10.59	30.0
	843	1.36	1.66	7.9	10.8	51	7.21	52.0
	844	0.75	1.04	16.7	43.0	52	7.08	48.0
	929	2.42	4.09	-8.8	25.4	60	8.64	53.0
	930	2.37	2.25	-4.6	19.6	55	7.48	45.0
	948	2.21	2.30	-23.1	-12.3	46	6.03	47.0
	949	0.80	2.38	-11.6	12.2	31	8.38	48.0
	1001	4.53	3.62	-5.5	12.1	21	10.33	25.0
Without under- lined Revs	Total	0.28	1.91	4.1	25.2	1012		
All Revs	Total	0.71	2.63	3.9	25.4	1159		

Table 4-14. SASS Minus Spot Observations, Statistics by Revolution,
W-7 Model Function, V-and H-Polarizations Combined,
WMO Standard Observations

Case	Rev	Speed Diff		Direction Diff		N	$\overline{W/S}$, m/s	$\overline{\theta}_1$
		Mean	Std Dev.	Mean	Std Dev.			
Priority 23								
V/H Pol	547	0.03	1.01	-10.5	11.2	46	4.91	38.0
Wentz-7	556	1.14	1.78	1.6	32.7	36	3.48	43.0
Spot Obs.	<u>557</u>	<u>2.93</u>	<u>4.27</u>	<u>11.5</u>	<u>30.5</u>	34	4.41	53.0
	590	0.02	1.17	-6.5	15.4	50	6.97	33.0
	599	0.75	2.42	1.6	20.6	44	5.87	47.0
	757	0.38	0.81	-6.9	7.4	32	15.67	35.0
	758	1.49	0.71	-5.1	13.7	10	14.83	55.0
	790	0.13	2.57	15.9	13.9	24	15.58	54.0
	791	-1.46	1.43	-7.1	12.0	37	13.72	37.0
	800	0.93	1.43	-2.8	7.4	58	9.86	47.0
	801	1.59	1.39	6.2	12.4	55	10.01	49.0
	815	0.23	1.43	5.2	14.7	56	9.40	30.0
	834	0.83	1.45	17.6	22.6	43	11.57	30.0
	843	0.68	0.93	-1.0	13.3	81	7.35	52.0
	844	1.26	0.69	-14.9	10.4	103	6.68	48.0
	<u>929</u>	<u>0.86</u>	<u>1.02</u>	<u>5.7</u>	<u>15.1</u>	62	9.90	53.0
	930	1.32	1.12	-8.2	14.6	73	8.65	45.0
	948	1.11	1.27	-13.2	16.7	67	7.56	47.0
	949	0.90	1.42	-10.6	11.3	64	8.10	48.0
Without under- lined Revs	Total	0.75	1.49	-3.84	17.4	879		
All Revs	Total	0.83	1.69	-2.7	18.2	975		

Table 4-15. SASS Minus Spot Observations, Statistics by Revolution,
CWK Model Function, V- and H-Polarizations Combined,
Autologger 60-Min Averages

Case	Rev	Speed Diff		Direction Diff		N	$\overline{W/S}$, m/s	$\overline{\theta}_i$
		Mean	Std Dev.	Mean	Std Dev.			
Test Set 3								
V/H Pol	547	0.07	1.76	8.6	20.3	80	4.45	38.0
CWK-Func	556	0.01	1.57	14.0	23.8	59	4.21	43.0
Autologger (9)	557	2.73	4.51	11.3	27.9	66	5.33	53.0
60 min avg.	590	-0.69	1.54	6.6	28.1	96	8.49	33.0
	599	-0.67	0.71	10.2	17.2	98	6.88	47.0
	633	-1.55	1.28	-5.4	9.3	37	9.16	25.0
	642	-1.51	1.15	7.0	13.0	67	13.80	49.0
	643	-0.55	1.05	-7.5	11.3	65	13.30	49.0
	757	1.49	0.84	-0.1	9.2	16	14.88	35.0
	758	0.34	1.24	-4.2	15.4	7	14.12	55.0
	790	-0.11	1.60	-7.4	9.0	7	12.38	54.0
	791	-0.87	1.64	-9.8	15.3	52	12.52	37.0
	800	-0.44	1.10	5.6	18.7	53	10.90	47.0
	801	-0.23	1.48	17.1	22.0	47	10.22	49.0
	815	-0.03	1.84	10.2	30.6	56	9.61	30.0
	834	1.77	0.77	11.7	41.2	37	10.59	30.0
	843	0.17	1.78	6.4	8.8	51	7.21	52.0
	844	-0.35	1.11	16.3	38.6	52	7.08	48.0
	929	1.30	4.06	-9.4	24.6	60	8.64	53.0
	930	1.27	2.56	-3.1	17.5	55	7.48	45.0
	948	1.34	2.76	-20.6	16.0	46	6.03	47.0
	949	-0.23	2.25	-4.9	12.4	31	8.38	48.0
	1001	5.64	3.84	-2.0	13.5	21	10.33	25.0
Without under- lined Revs	Total	-0.19	1.77	4.3	23.7	1012		
All Revs	Total	-0.16	2.47	3.9	24.0	1159		

Table 4-16. SASS Minus Spot Observations, Statistics by Revolution, CWK Model Function, V- and H-Polarizations Combined, WMO Standard Observations

Case	Rev	Speed Diff		Direction Diff		N	$\overline{W/S}$, m/s	$\overline{\theta}_i$
		Mean	Std Dev.	Mean	Std Dev.			
Test Case 3								
V/H - Pol	547	0.06	1.20	-8.8	11.2	46	4.91	38.0
CWK-Func.	556	1.08	1.66	12.5	27.8	36	3.48	43.0
Spot Obs.	557	1.68	3.79	-2.9	35.4	34	4.41	53.0
	590	0.51	1.27	-2.5	11.0	50	6.97	33.0
	599	0.01	2.03	-1.2	22.4	44	5.87	47.0
	757	0.69	0.86	-4.3	9.9	32	15.67	35.0
	758	-0.35	1.44	-8.3	16.8	10	14.83	55.0
	790	-1.86	2.07	11.6	12.3	24	15.58	54.0
	791	1.62	1.61	-7.7	13.0	37	13.72	37.0
	800	0.66	1.44	-1.8	8.7	58	9.86	47.0
	801	0.02	1.76	4.0	14.7	55	10.01	49.0
	815	0.32	1.47	13.3	14.2	55	9.38	30.0
	834	1.10	1.78	9.8	23.7	43	11.57	30.0
	843	-0.95	0.81	0.9	14.0	81	7.35	52.0
	844	0.42	0.95	-8.7	12.4	103	6.68	48.0
	929	-0.37	1.10	2.1	17.6	62	9.90	53.0
	930	0.69	1.41	-6.3	16.9	73	8.65	45.0
	948	0.18	1.31	-12.0	16.8	67	7.56	47.0
	949	-0.06	1.50	-4.9	12.6	64	8.10	48.0
Without underlined Revs	Total	0.13	1.57	-1.7	17.1	878		
All Revs	Total	0.15	1.70	-1.5	18.1	974		

the Autologger are probably comparable with those from SASS because of its larger resolution.

5. Comparison of SASS Estimates and Analyses of Surface Wind Fields

a. Triangle. The 23 priority revolution fields for the JASIN triangle (small-scale fields) were furnished to Langley by the University of Washington on February 10, 1980. These were isotach fields on a latitude-longitude grid using meteorological ship and buoy data. The fields were also used by JPL in a SASS comparison program. The triangle fields were compared to spot observation values to get:

Platform	$\overline{\Delta V}$	$\sigma_{\Delta V}$	N
Buoys 33 and W2	0.01	0.27	28
Buoys S13	-0.03	0.35	16
Meteor	0.40	0.8	21

The first SASS/field comparison yielded:

$$\overline{\Delta V} = 0.6; \sigma_{\Delta V} = 1.0; \overline{\Delta X} = 2.0; \sigma_X = 12.0$$

There were several orbits that contributed large error statistics. Most obvious was Rev 557 with:

$$\overline{\Delta V} = 4.0; \sigma_{\Delta V} = 4.3; \overline{\Delta X} = 11; \sigma_X = 26; N = 28$$

The very high SASS measurements were regional (within a 30-km radius) and up to 5 times the average field (22 m/s in a 4.5-m/s field). This region was subsequently identified with a local thunderstorm-associated disturbance through ship log and SMMR data. It was removed from subsequent statistics as the field did not reflect this localized disturbance. Other fields contributed high bias or standard deviations, but there did not exist sufficient collaborating evidence of local variations missed by the fields analysis to remove them from the statistics. Some of these orbits were associated with extreme incidence angles in the SASS beam, and these regions of the SASS swath were subsequently correlated with large bias in the model function. Revs 633 and 958 had low incidence angles and $\overline{\Delta V} = -2.5$ and -2.6 , respectively, while Revs 643, 833, and 1002 had high incidence angles with $\overline{\Delta V} = 1.6, 2.8, \text{ and } 3.5$, respectively. In addition, Revs 790, 929, 930, 948, 949, and 1001 exhibited high bias and/or σ . Although there was some evidence of frontal activity in the region (particularly on Revs 929-930), the surface observations did not define an anomalous condition definitely enough to exclude these revolutions from the general statistics.

Prior to the workshop, SASS minus fields wind speed and wind direction statistics were computed by Langley using all of the 23 priority revolutions and SASS wind vectors that fell within the JASIN triangle. These statistics were recalculated by JPL (Boggs) at the workshop, excluding Rev 557 and expanding the comparison to points slightly beyond the boundary (outside) of the triangle. These added points increased the number of comparisons from about 400 to over 600 and were used in compiling the following statistics given in Tables 4-17 through 4-20. In these tables, the differences are stratified by both incidence angle (5 deg) and wind speed (2 m/s) bins. The mean of all wind speed and incidence angle bins wind speed estimates, from both models, when compared with the wind field, are within the ± 2 m/s guideline. For both the W-7 and CWK models, the standard deviation of the differences lies outside this guideline only a few times.

While only limited comparisons exist at low and high incidence angles over a wide range of wind speeds, the W-7 model appears to produce slightly better results at low incidence angles. The CWK model, however, appears to be slightly superior at large incidence angles (> 50 -deg bins). In the mid-angular region, neither model appears superior. The difference between field and SASS winds does appear to be a function of wind speed. No clear definition of this wind speed sensitivity of the difference is possible because of the limitation of the data set. This observation does, however, appear to agree with results presented in Figure 4-11.

As with the direct comparison between surface observations and SASS estimates of wind directions, neither model function produces significantly better wind direction estimated in comparison with the wind field. The mean differences, using the SASS estimate nearest the surface wind direction, lie within the direction requirement of ± 20 deg. However, the standard deviation of the direction estimates, for certain combinations of wind speed and incidence angle, does extend beyond this requirement.

Further comparisons were made considering only wind estimates, W-7, and CWK model functions, orthogonal measurements of the same polarization. The differences between these estimates and the wind field are shown in Figures 4-24 through 4-27. For the W-7 case, there appears to be a strong correlation between the mean difference and the incidence angle for both polarizations. For CWK, this effect is weakly displayed for only H-polarization.

b. Large Fields. Winds on a polar stereographic grid approximately 5-20W and 55-65N at quarter grid points were supplied to Langley. These winds were derived from WMO surface pressures, temperatures (air and sea), and dew points plus all JASIN measurements, land and sea synoptic reports. They agreed with triangle fields to 0.5 m/s with a speed bias of about $-10\% |V|$. Field days were 8/22/07, 8/23/07, 8/25/07, 8/31/07, 9/1/067, and 9/2/07. Data for creating large-scale fields on 8/21/06, 8/24/07, and 9/5/07 have been requested from Ashville. The initial six large-scale fields were furnished to Langley on August 21, 1980. Statistics for these fields will be reported at a later date.

Table 4-17. SASS Minus Small-Scale Fields Statistics for Wind Speeds and Directions, W-7 Model Function and V-Polarization

WIND BINS	INC BINS								
	20-25	25-30	30-35	35-40	40-45	45-50	50-55	55-60	
0- 6	0	0	5	6	12	13	13	0	49
	.00	.00	-.16	-.30	-.35	.90	1.82	.00	.58-mean
	.00	.00	.67	1.20	1.24	1.45	2.50	.00	1.68-rms
	.00	.00	.72	1.27	1.24	1.18	1.79	.00	1.59-σ
	.00	.00	-21.86	12.40	15.04	8.94	17.78	.00	10.06-mean
	.00	.00	23.56	25.57	19.63	15.60	26.91	.00	22.09-rms
	.00	.00	9.84	24.49	13.18	13.30	21.03	.00	19.87-σ
6- 8	6	6	10	3	16	19	20	6	86
	-1.20	-2.26	-1.47	.25	1.11	1.32	1.56	2.29	.62
	2.04	2.37	1.97	1.66	1.37	1.53	1.85	2.51	1.83
	1.81	.79	1.39	2.01	.82	.78	1.03	1.11	1.73
	.92	13.37	6.39	-7.30	-6.82	-3.23	-1.96	-7.48	-1.48
	16.74	18.49	15.29	16.37	14.51	16.62	8.08	13.91	14.45
	18.32	13.99	14.64	17.94	13.22	16.75	8.04	12.84	14.46
8- 10	8	11	5	2	7	23	15	4	75
	-1.66	-.36	-.11	3.45	1.31	1.29	1.29	2.32	.75
	2.34	1.53	1.95	3.47	1.83	1.50	1.66	2.34	1.83
	1.77	1.56	2.18	.49	1.38	.80	1.08	.36	1.68
	21.61	10.10	-8.46	-4.30	14.26	-6.63	3.16	28.22	4.54
	32.54	11.90	13.05	29.32	20.06	16.43	22.00	38.54	21.55
	26.01	6.61	11.10	41.01	15.24	15.37	22.54	30.30	21.21
10-12	3	6	3	1	8	7	16	5	49
	.51	.16	.42	.49	.61	.53	1.33	2.84	.99
	1.39	.91	.43	.49	.79	.68	1.55	2.94	1.44
	1.58	.99	.08	.00	.53	.46	.82	.85	1.06
	8.53	3.82	5.53	-9.10	-5.64	-7.46	-1.72	6.02	-.79
	15.55	12.13	14.28	9.10	6.71	8.78	8.84	7.38	9.82
	15.92	12.61	16.12	.00	3.89	5.01	8.96	4.78	9.89
12-14	2	1	10	4	5	11	9	6	48
	1.90	.44	.29	.53	-.05	1.21	2.15	3.08	1.26
	2.16	.44	1.15	1.45	2.31	1.78	2.43	3.31	2.10
	1.46	.00	1.17	1.55	2.58	1.37	1.19	1.31	1.70
	-10.05	-12.90	-1.31	4.82	-12.00	-1.85	-.30	7.72	-1.32
	12.63	12.90	5.23	9.48	15.76	11.39	8.76	10.52	10.35
	10.82	.00	5.34	9.43	11.42	11.78	9.28	7.83	10.37
14-16	3	3	4	4	1	1	7	6	29
	.19	-.59	.84	1.69	3.07	1.51	1.07	2.32	1.20
	.76	.90	.92	1.69	3.07	1.51	2.45	2.44	1.93
	.90	.84	.42	.07	.00	.00	2.38	.83	1.54
	-19.77	-10.77	-7.82	-8.90	2.50	27.30	10.94	-5.58	-2.95
	20.01	11.34	9.35	10.13	2.50	27.30	20.73	8.62	15.03
	3.78	4.36	5.91	5.58	.00	.00	19.01	7.19	15.00
	22	27	37	20	49	74	80	27	336
	-.66	-.66	-.23	.76	.62	1.15	1.53	2.58	.84
	1.98	1.58	1.45	1.75	1.52	1.49	2.01	2.75	1.81
	1.91	1.46	1.45	1.61	1.40	.96	1.32	.97	1.60
	5.66	6.26	-3.12	.92	1.40	-1.93	3.57	4.11	1.54
	23.74	13.67	13.95	19.10	15.92	15.30	16.93	17.73	16.65
	23.60	12.38	13.78	19.57	16.02	15.29	16.65	17.57	16.60

Table 4-18. SASS Minus Small-Scale Fields Statistics for Wind Speeds and Directions, CWK Model Function and V-Polarization

WIND BINS	INC BINS								
	20-25	25-30	30-35	35-40	40-45	45-50	50-55	55-60	
0- 6	0	0	5	6	12	13	13	0	49
	.00	.00	.72	.13	-.32	.32	1.00	.00	.36-mean
	.00	.00	.94	1.11	1.27	1.13	1.80	.00	1.36-rms
	.00	.00	.69	1.21	1.28	1.13	1.56	.00	1.32-σ
	.00	.00	-17.58	10.25	15.32	10.92	20.48	.00	11.54-mean
	.00	.00	20.36	22.86	19.54	16.00	26.27	.00	21.23-rms
	.00	.00	11.47	22.38	12.68	12.18	17.11	.00	18.00-σ
6- 8	6	6	10	3	16	19	20	6	86
	.65	-.72	-.53	.55	.88	.73	.39	1.11	.45
	1.48	.92	1.45	1.75	1.22	1.16	1.42	1.68	1.34
	1.45	.63	1.42	2.03	.87	.93	1.40	1.39	1.28
	2.50	16.40	9.01	-1.67	-2.47	-.43	-.28	-4.62	1.37
	15.97	18.90	14.65	19.16	14.44	16.78	8.28	11.40	14.37
	17.28	10.29	12.18	23.37	14.69	17.23	8.49	11.42	14.39
8-10	8	11	5	2	7	23	15	4	75
	-.46	.42	.46	3.44	1.30	.74	.10	.80	.54
	1.71	1.37	1.78	3.46	1.82	1.05	1.36	1.21	1.49
	1.76	1.36	1.92	.62	1.38	.75	1.40	1.05	1.39
	16.21	13.08	-8.02	-3.15	13.99	-3.29	8.30	29.95	6.58
	23.54	16.16	13.92	29.92	20.01	14.85	21.89	39.64	20.47
	18.25	9.94	12.72	42.07	15.45	14.81	20.96	29.99	19.51
10-12	3	6	3	1	8	7	16	5	49
	1.09	.61	.62	.68	.40	.09	.42	1.74	.58
	1.45	1.08	.62	.68	.66	.55	.92	1.86	1.02
	1.18	.98	.06	.00	.57	.58	.85	.72	.85
	7.93	4.47	.57	-10.40	-3.95	-3.77	-.57	4.30	-.08
	18.24	15.40	13.00	10.40	5.75	6.74	8.42	6.66	10.08
	20.11	16.15	15.91	.00	4.47	6.03	8.67	5.68	10.18
12-14	2	1	10	4	5	11	9	6	48
	2.29	1.11	.30	.40	-.33	.37	.76	.99	.53
	2.40	1.11	1.14	1.27	1.99	.89	1.16	1.52	1.34
	1.00	.00	1.16	1.39	2.19	.85	.92	1.27	1.25
	-4.25	-5.50	-.14	4.87	-11.90	-.57	.73	7.10	-.26
	8.15	5.50	4.00	9.20	15.64	12.30	10.26	11.53	10.50
	9.83	.00	4.21	9.01	11.35	12.89	10.85	9.95	10.61
14-16	3	3	4	4	1	1	7	6	29
	.87	-.04	.82	1.58	2.88	.03	-.47	.97	.60
	1.09	.62	.87	1.59	2.88	.03	2.18	1.13	1.52
	.82	.76	.32	.14	.00	.00	2.30	.67	1.42
	-13.50	-4.10	-2.37	-1.37	5.00	-19.30	4.29	-1.63	-.80
	13.76	5.06	4.17	2.71	5.00	19.30	15.43	11.02	11.04
	3.24	3.64	3.96	2.70	.00	.00	16.01	11.94	11.21
	22	27	37	20	49	74	80	27	336
	.48	.18	.24	.90	.48	.54	.41	1.12	.50
	1.62	1.14	1.26	1.70	1.41	1.03	1.45	1.51	1.35
	1.59	1.15	1.25	1.48	1.34	.88	1.40	1.04	1.26
	5.43	9.31	-1.27	2.69	3.18	.60	5.16	5.42	3.38
	18.66	15.57	12.65	18.03	15.80	14.75	16.31	18.07	15.91
	18.27	12.72	12.76	18.29	15.64	14.84	15.57	17.56	15.57

Table 4-19. SASS Minus Small-Scale Fields Statistics for Wind Speeds and Directions, W-7 Model Function and H-Polarization

WIND BINS	INC BINS								
	20-25	25-30	30-35	35-40	40-45	45-50	50-55	55-60	
0- 6	0	0	4	7	8	9	2	0	30
	.00	.00	.64	-.46	.52	.71		.00	.68-mean
	.00	.00	1.31	.89	1.12	.97		.00	1.70-rms
	.00	.00	1.32	.82	1.06	.69		.00	1.58- σ
	.00	.00	-10.25	3.59	24.67	6.52		.00	11.98-mean
	.00	.00	33.98	18.25	26.97	15.10		.00	27.16-rms
6- 8	.00	.00	37.40	19.32	11.64	14.44		.00	24.79- σ
	7	11	8	4	15	29	16	3	93
	-2.32	-1.92	-1.24	-.33	.41	.81	1.71	3.18	.19
	2.91	2.43	1.36	1.30	1.11	1.06	1.98	3.41	1.78
	1.88	1.57	.61	1.45	1.07	.69	1.03	1.51	1.78
	19.43	9.83	4.17	3.62	-6.35	-3.57	-3.45	-5.60	.23
8- 10	30.52	23.58	14.94	18.31	13.84	15.43	18.17	11.54	18.32
	25.42	22.48	15.34	20.72	12.73	15.27	18.43	12.36	18.42
	7	11	4	3	6	25	11	3	70
	-1.08	-.68	-1.45	1.00	.55	.30	.77	1.52	.08
	1.90	1.82	2.47	1.53	.76	.97	1.23	1.62	1.44
	1.68	1.77	2.30	1.42	.57	.95	1.00	.70	1.45
10-12	7.17	2.77	-2.05	-5.07	5.08	-7.11	-3.15	36.23	-.23
	15.03	8.05	17.46	17.55	12.44	14.61	24.00	38.62	17.53
	14.27	7.93	20.02	20.58	12.44	13.03	24.95	16.35	17.66
	4	7	3	0	8	13	12	6	53
	1.43	.98	.82	.00	-.78	-.18	.57	2.34	.52
	1.53	1.58	.85	.00	.81	.60	.87	2.44	1.26
12-14	.62	1.34	.27	.00	.24	.60	.69	.75	1.16
	-.82	1.59	2.70	.00	-.95	.58	-.39	-5.48	-.41
	10.22	18.69	6.65	.00	4.41	7.20	8.52	19.79	11.53
	11.77	20.11	7.45	.00	4.60	7.47	8.89	20.83	11.63
	1	2	6	4	4	9	9	5	40
	1.87	2.27	-.03	-1.10	-1.78	-.49	1.81	2.90	.53
14-16	1.87	2.28	1.06	1.27	2.34	1.14	2.53	3.13	2.04
	.00	.25	1.16	.72	1.75	1.09	1.87	1.32	2.00
	-9.00	-19.70	-2.53	-6.87	-32.82	-10.37	.32	-.66	-7.90
	9.00	20.56	14.42	19.78	34.29	16.55	19.21	13.08	19.42
	.00	8.34	15.55	21.42	11.43	13.68	20.37	14.61	17.96
	3	4	4	3	1	1	9	6	31
14-16	.12	1.01	1.15	1.95	2.36	-1.12	.83	1.60	1.07
	.72	1.25	1.18	1.96	2.36	1.12	2.19	1.77	1.74
	.87	.85	.33	.21	.00	.00	2.15	.82	1.39
	-26.50	-25.37	-6.10	-12.57	-15.80	25.80	9.36	1.33	-4.55
	26.73	25.74	8.31	13.19	15.80	25.80	18.08	15.68	18.77
	4.28	4.98	6.52	4.91	.00	.00	16.40	17.12	18.51
	22	35	29	21	42	86	59	23	317
	-.72	-.37	-.22	-.00	.06	.34	1.30	2.27	.40
	2.12	1.97	1.45	1.33	1.24	.98	2.04	2.52	1.66
	2.04	1.96	1.45	1.36	1.25	.92	1.58	1.12	1.61
	4.29	.25	-1.63	-1.94	-.52	-3.29	1.89	2.77	-.36
	22.10	19.10	17.89	17.84	18.73	14.51	21.02	20.38	18.45
	22.19	19.38	18.13	18.17	18.95	14.21	21.11	20.65	18.48

Table 4-20. SASS Minus Small-Scale Fields Statistics for Wind Speeds and Directions, CWK Model Function and H-Polarization

WIND BINS	INC BINS								
	20-25	25-30	30-35	35-40	40-45	45-50	50-55	55-60	
0- 6	0	0	4	7	8	9	2	0	30
	.00	.00	.97	-.49	-.54	-.43		.00	-.06-mean
	.00	.00	1.24	.75	.92	.60		.00	1.13-rms
	.00	.00	.89	.61	.80	.45		.00	1.15- σ
	.00	.00	-24.15	1.51	17.22	2.56		.00	6.14-mean
	.00	.00	28.06	10.99	23.64	15.79		.00	23.77-rms
	.00	.00	16.49	11.75	17.31	16.53		.00	23.36- σ
6- 8	7	11	8	4	15	29	16	3	93
	-.89	-.99	-.75	-.58	-.14	-.48	-.48	.38	-.52
	2.10	1.78	1.04	1.45	.93	.89	1.02	1.11	1.23
	2.06	1.56	.78	1.54	.95	.76	.93	1.28	1.12
	10.77	16.31	12.99	10.07	-3.12	.64	-.53	-4.70	3.75
	29.60	21.80	16.91	15.93	14.20	15.44	18.66	11.14	18.12
	29.78	15.17	11.58	14.24	14.33	15.70	19.27	12.38	17.83
8-10	7	11	4	3	6	25	11	3	70
	.24	-.07	-1.50	1.10	.14	-1.08	-1.60	-1.57	-.72
	1.68	1.41	2.30	1.52	.53	1.39	1.91	1.74	1.55
	1.80	1.47	2.01	1.29	.56	.88	1.10	.90	1.39
	5.69	5.48	-10.17	18.57	5.22	-2.18	3.83	39.27	3.60
	13.50	12.25	20.77	22.88	14.62	16.71	24.76	42.42	19.50
	13.22	11.49	20.90	16.38	14.96	16.91	25.66	19.66	19.31
10-12	4	7	3	0	8	13	12	6	53
	2.85	1.73	.84	.00	-1.09	-1.49	-1.77	-.77	-.53
	2.90	2.35	.87	.00	1.19	1.61	1.89	.91	1.78
	.59	1.72	.29	.00	.50	.64	.69	.52	1.71
	-4.68	2.27	-3.17	.00	-3.40	.38	-4.44	-9.72	-2.76
	11.28	20.47	6.84	.00	6.00	7.12	9.34	20.13	12.29
	11.85	21.98	7.42	.00	5.29	7.40	8.58	19.31	12.09
12-14	1	2	6	4	4	9	9	5	40
	3.80	3.51	.08	-1.23	-2.40	-1.68	-.29	-.86	-.63
	3.80	3.58	1.22	1.38	3.04	1.86	1.73	1.54	2.02
	.00	.96	1.33	.73	2.15	.84	1.81	1.43	1.95
	-5.40	-13.60	-2.23	-5.80	-25.25	-6.90	5.96	.96	-4.35
	5.40	15.34	9.18	11.68	26.35	14.98	20.06	16.40	16.82
	.00	10.04	9.76	11.71	8.71	14.10	20.32	18.31	16.45
14-16	3	4	4	3	1	1	9	6	31
	2.43	2.51	1.91	2.85	3.15	-2.59	-1.60	-1.19	.40
	2.52	2.59	1.92	2.86	3.15	2.59	2.61	1.41	2.37
	.80	.70	.20	.29	.00	.00	2.18	.81	2.38
	-23.83	-20.90	-.05	-7.93	-15.10	17.70	6.33	4.78	-2.93
	24.34	21.48	2.98	9.55	15.10	17.70	15.36	14.71	15.96
	6.06	5.72	3.44	6.50	.00	.00	14.84	15.24	15.94
	22	35	29	21	42	86	59	23	317
	.82	.50	.09	.06	-.49	-.95	-.98	-.86	-.44
	2.31	2.05	1.46	1.57	1.38	1.30	1.87	1.34	1.64
	2.22	2.02	1.49	1.60	1.30	.89	1.61	1.06	1.58
	.89	4.14	-1.95	2.84	-.50	-.61	3.40	3.43	1.18
	21.02	18.62	16.45	14.23	16.95	14.91	20.73	21.72	17.88
	21.50	18.41	16.62	14.28	17.15	14.99	20.63	21.92	17.87

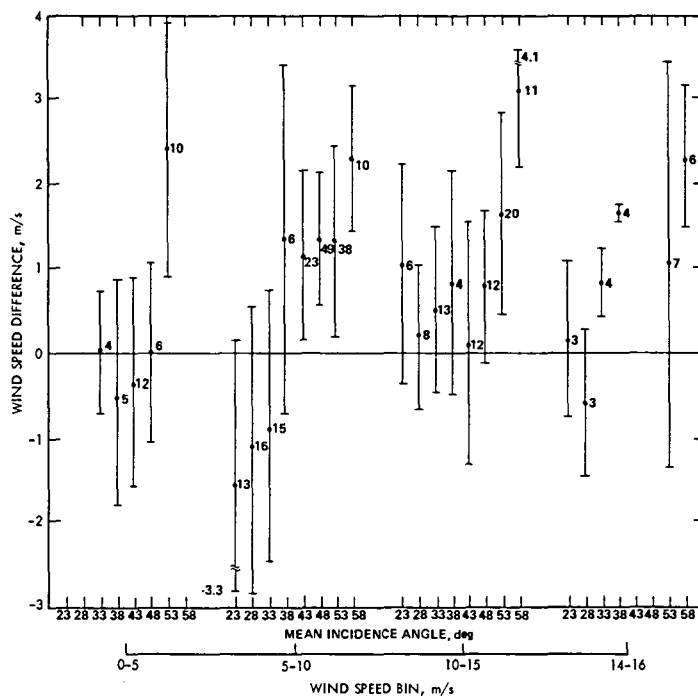


Figure 4-24. Mean Wind Speed Difference Between SASS and Small-Scale Surface Fields, V-Polarization, W-7 Model Function

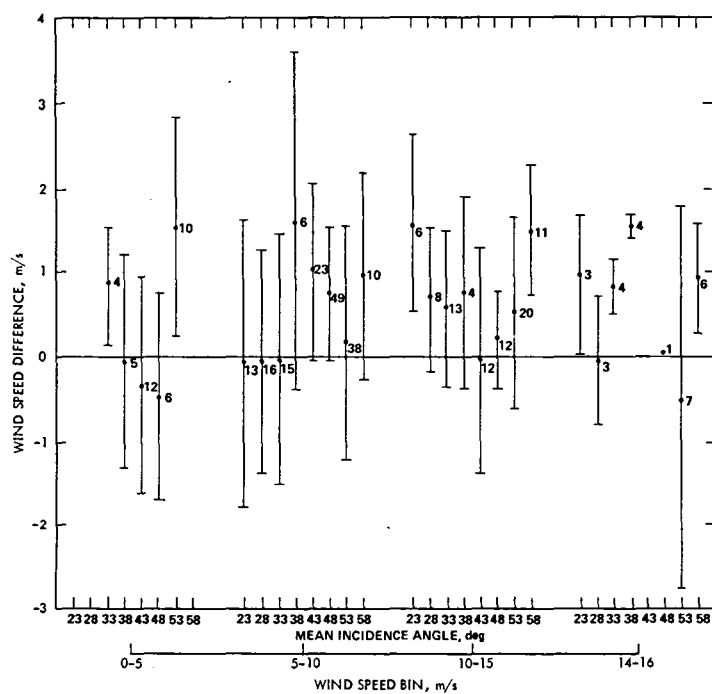


Figure 4-25. Mean Wind Speed Difference Between SASS and Small-Scale Surface Fields, V-Polarization, CWK Model Function

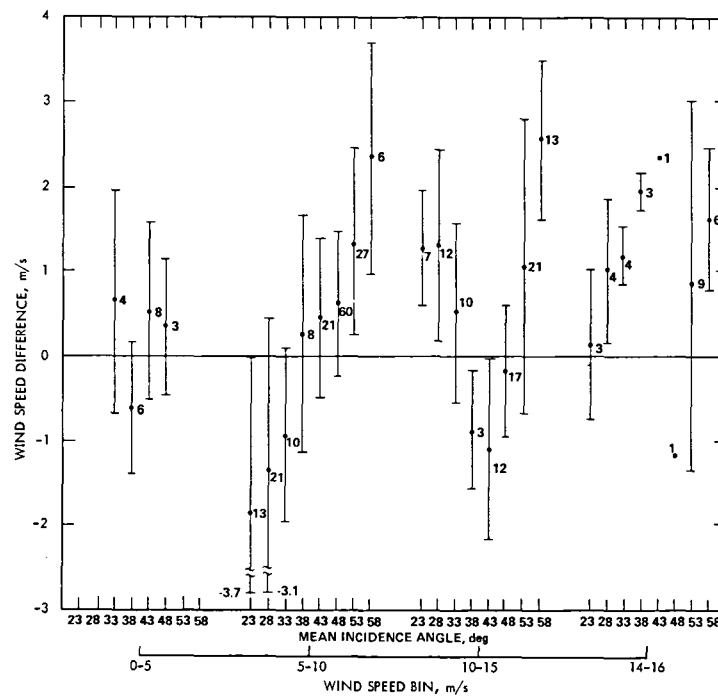


Figure 4-26. Mean Wind Speed Difference Between SASS and Small-Scale Surface Fields, H-Polarization, W-7 Model Function

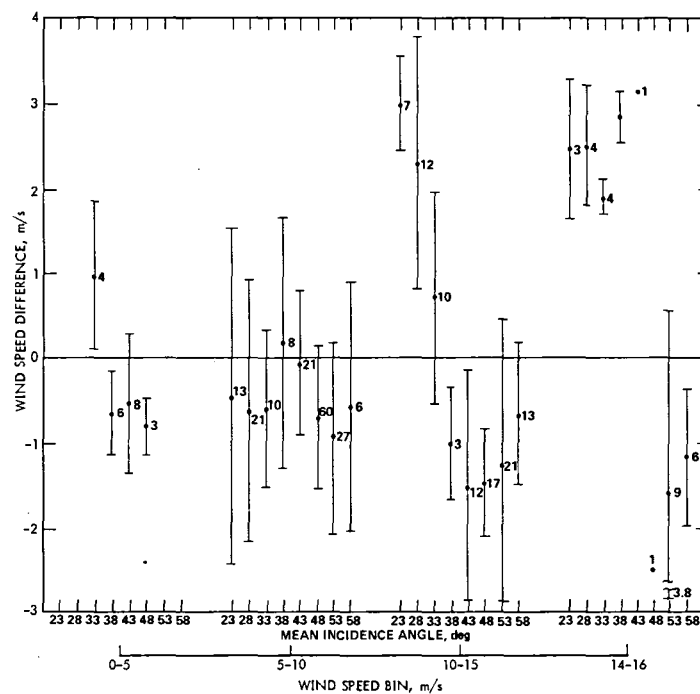


Figure 4-27. Mean Wind Speed Difference Between SASS and Small-Scale Surface Fields, H-Polarization, CWK Model Function

F. SASS WIND DIRECTION AMBIGUITY REMOVAL SUBPANEL

1. Introduction

An inherent feature of the Seasat scatterometer (SASS) is that the wind algorithm yields as many as four solutions for wind direction. In previous workshops (GOASEX I and GOASEX II) statistical comparisons between SASS and "surface truth" were mainly performed by selecting the SASS wind direction closest to the comparison data base (i.e., surface truth) direction. Using this approach, it was shown that the SASS-measured wind direction was within the specifications, i.e., ± 20 deg. Unfortunately for the users of SASS winds, the geophysical data record will be these multiple solution wind vectors. Therefore, a scheme is required whereby the correct wind direction may be selected.

As a result, the SASS Wind Ambiguity Removal (WAR) subpanel was assigned the task of assessing the ability of a trained marine meteorological analyst to select the correct wind direction from the solutions (up to four) that are generated by the SASS wind algorithm. This task was to be performed without any additional information, such as conventional surface observations, computer prognosis, satellite visible and infrared imagery. Since these data sets normally would be available to the analyst in an operational setting, this experiment represents a "worst case" situation.

2. Data Set

The 12 Seasat SASS revolutions listed in Table 4-21 were used for the SASS wind direction ambiguity removal experiment. The quality of the "SASS only" analysis was assessed by intercomparing these analyses with the following in situ comparison data sets which are also noted in Table 4-21:

- (1) VIRR infrared imagery
- (2) British Meteorological Office Charts
- (3) JASIN Surface Data Set
- (4) University of Washington Boundary Layer Model Fields (i.e., UW-Brown Fields)

The original direction ambiguity removal analysis was done using Wentz's Model 2 G-H table and the SASS data output on a 1/2-deg lat/lon grid. At the workshop, the analysis was upgraded using the Wentz Model 7 G-H table and the SASS wind vectors based on the pairing of orthogonal SASS footprints.

3. Procedure

The alias removal subpanel of the SASS panel was assigned the task of selecting a unique direction for each SASS observation, as determined by a 1/2-deg latitude binning algorithm. This task had the double purpose of assessing the capability of meteorological analysis technique for alias removal on the basis of SASS data alone, and of possibly laying a foundation for an alias removal algorithm. It is, therefore, important to document (see Section 3.2 of JPL

Table 4-21. SASS Revolutions Used for Wind Direction Ambiguity Removal

Rev	DOY	Date	Time of Pass at Jasin Met. Triangle	Preferred Wind Field from SASS		Analysis Available		British Met. 0 Anal.	UW Brown Anal.	VIRR Imagery Available
				AES/JPL	UCLA	Date	Time			
790	233	8/21/78	05:48Z	✓		8/21/78	06:00Z	✓		
791	233	8/21/78	07:25Z	✓		8/21/78	06:00Z	✓		✓
800	233	8/21/78	22:46Z		✓	8/22/78	00:00Z	✓	✓	✓
801	234	8/22/78	00:23Z		✓	8/22/78	00:00Z	✓	✓	✓
814	234	8/22/78	22:14Z	✓		8/23/78	00:00Z	✓	✓	✓
815	234	8/22/78	23:53Z	✓		8/23/78	00:00Z	✓	✓	✓
843	236	8/24/78	22:51Z	✓		8/25/78	00:00Z	✓	✓	✓
844	237	8/25/78	00:29Z	✓		8/25/78	00:00Z	✓	✓	✓
929	242	8/30/78	23:13Z		✓	8/31/78	00:00Z	✓	✓	*
930	243	8/31/78	00:51Z		✓	8/31/78	00:00Z	✓	✓	*
948	244	9/01/78	06:52Z		✓	9/01/78	06:00Z	✓	✓	*
949	244	9/01/78	08:31Z		✓	9/01/78	06:00Z	✓	✓	*

* VIRR failed shortly after Rev 844.

internal document 622-220, April 1980) the conceptual methodology of the subjective alias removal technique, without in any way suggesting that the anticipated algorithm should not be founded thereon.

An activity flowchart of the procedure used is shown in Figure 4-28. It is not uncommon for two analysts to produce different wind fields analyses given the same data. Therefore, to reduce the dependence on the analyst, separate ambiguity removal experiments were performed by two independent teams. One group was located at UCLA, Los Angeles, and a second group (AES/JPL) was located at the Atmospheric Environment Service, Toronto. Both teams performed a wind vector selection for each of the 12 revolutions listed in Table 4-21 using only SASS data.

The data input for this subjective treatment consisted of SASS wind vector ("sea chicken") plots of the appropriate orbits on a scale considerably greater than the JASIN area. This spatially extended information permitted recognition of cyclonic scale weather phenomena more readily than from data solely within the JASIN area.

An example of the "raw analysis" by the UCLA group of the 1/2-deg lat/lon grid data is shown in Figure 4-29.

4. Results of Evaluation

a. Feature Identification. The ability of SASS to successfully identify synoptic meteorological features is based on an analyst's knowledge of the behavior characteristics of all SASS vectors at a point relative to the behavior characteristics of the neighboring measurements. The methodology for recognizing these meteorological features is discussed in Section 3.2 of JPL internal document 622-220. From these results, it may be said that SASS wind fields can be interpreted to identify synoptic meteorological features without the aid of external measurements.

b. Qualitative Comparison of SASS-Only Analyses With Operational Data and Selection of a Preferred Analysis. A second stage in the alias removal process consisted of consultation of conventional, operational information, and revision of the SASS-only analyses where deemed necessary.

The data consulted was minimal. Available to the subpanel were (1) VIRR imagery for revolutions noted in Table 4-21, and (2) daily weather reports and charts, published by the British Meteorological Office (BMO), Bracknell, Berkshire. It should be noted that these weather charts are small and contain reports from only the few official weather ships. The VIRR imagery and BMO weather charts are documented in Section 6 of JPL internal document 622-220.

As it transpired, this additional information was used formally only in the selection of one from the AES or UCLA analyses as the "preferred solution." In no case was the preferred solution revised or re-edited on the basis of the data consulted. However, there were a number of incidences in which the weather chart pressure analysis could have been improved by incorporating SASS data.

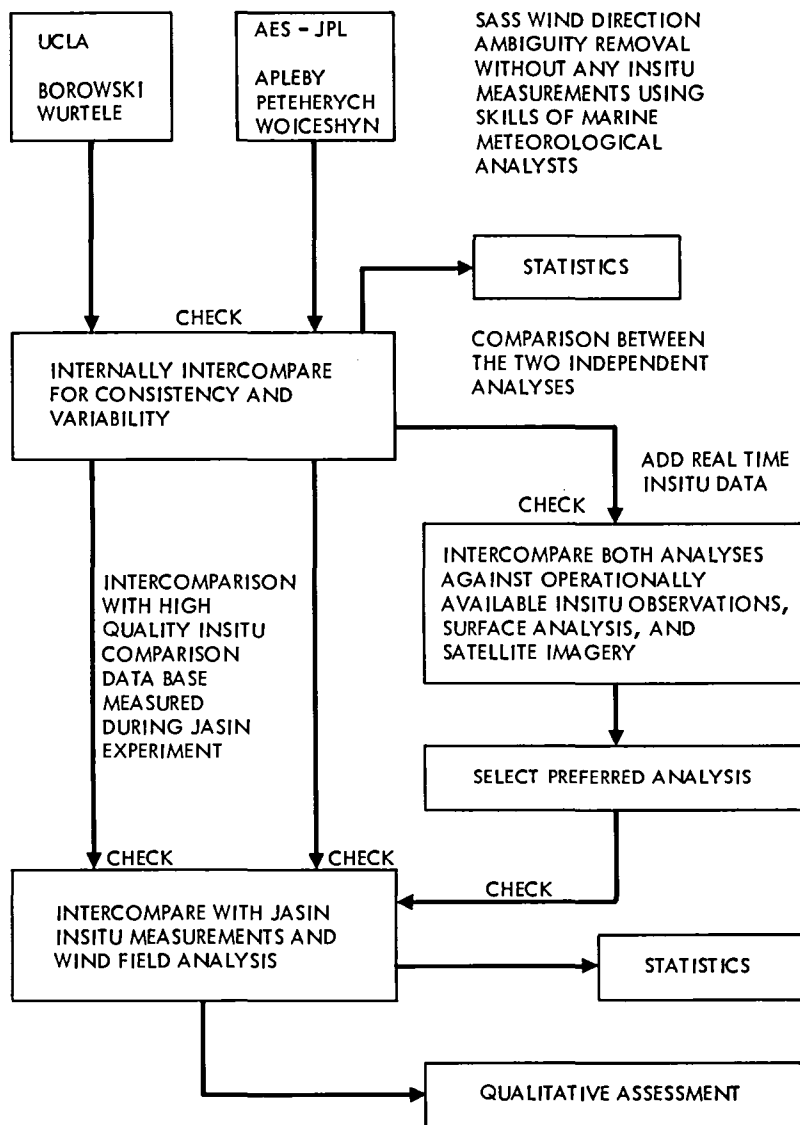


Figure 4-28. SASS Wind Direction Ambiguity Removal Subpanel Procedure

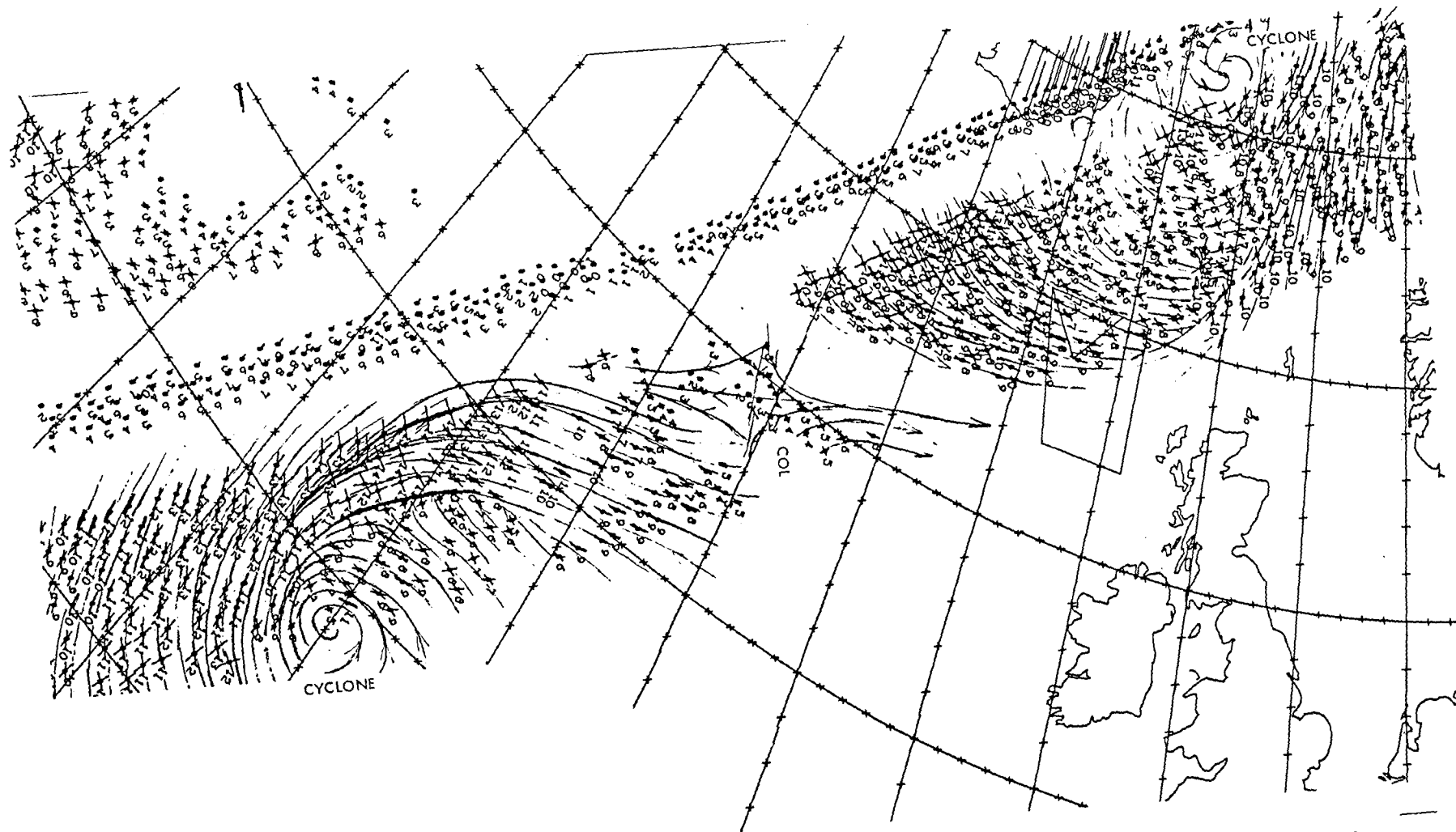


Figure 4-29. A pattern of Singular-Point Patterns From Rev 801, 00:24, 8/22/78, Cyclone-Col-Cyclone
 (Note the large area of low speeds in the neighborhood of the col)

An orbit-by-orbit description of the process of selection of the preferred solution is found in JPL internal document 622-220. As an example, Rev 949 is discussed below.

Rev 949 (Figures 4-30 and 4-31). Here the analyses differed in the JASIN area, UCLA specifying northwesterly flow and AES westerly. An anticyclonic center was located mean 52N 17W in both analyses, associated with a col just south of Iceland. The BMO chart (Figure 4-32) was consistent with these structures, confirming somewhat better the northwest rather than the west current across the JASIN area. Thus, UCLA was designated preferred solution.

c. Qualitative Comparisons of SASS-Only Analysis With the UW-Brown JASIN Area Wind Fields. Revolution 949 (Figure 4-30 and 4-31) is discussed below as an example. The reader is referred to JPL internal document 622-220 for the remaining nine revolutions.

Rev 949 (Figures 4-30 and 4-31). Overall agreement between the three fields is very good. The UCLA wind directions probably are incorrect in the southwestern part of the JASIN area but agreement elsewhere is excellent. In particular, the SASS data reveals a col south of Iceland, which is in agreement with the Brown field and the UCLA wind directions. Although the AES/JPL SASS field does not represent this area nearly as well, it does better represent the southwest corner of the JASIN area.

d. Estimated Quality of the SASS Wind Directions as Compared to the JASIN In Situ Measurements and the UW-Brown Fields. Prior to the above intercomparisons, a qualitative intercomparison between the AES/JPL and UCLA choices of SASS wind vectors indicated that approximately 80 percent identical choices were made between the two analysis teams over SASS track lengths of 2000 to 3000 km. A check on identical choices for the 172 SASS vectors involved in the intercomparisons used in Tables 4-22 and 4-23 indicates that 93 percent of the direction choices between the AES/JPL and UCLA teams were identical. Further, there were 80 percent identical choices made with the SASS "closest to in situ measurement" vectors by the AES/JPL choices, and 84 percent agreement with the UCLA choices and "preferred" choices. The "problem" revolution that resulted in higher statistics for both AES/JPL team choices was Rev 948, and for the UCLA team it was Rev 930.

For this exercise, SASS winds within a 50-km radius of either the Gardline Endurer, the Hecla, the Meteor, and the John Murray were intercompared, resulting in a total of 172 SASS directions to 27 in situ measurements from the research ships. Thus, a little more than six SASS measurements, on the average, were intercompared to each in situ measurement. The statistical results between the different classes of SASS directions to the in situ research ship measurements and to the UW-Brown wind fields were shown in Tables 4-22 and 4-23, respectively. Included for reference is the quality index of the UW-Brown fields as compared to the in situ ship observations in the meteorological triangle area. In all intercomparisons, more of an inflow angle than the ship observations is indicated for the SASS winds and a moderate outflow for the UW-Brown wind fields. The reason for this is not yet understood. The target standard error for the scatterometer was ± 20 deg. All classes of SASS data, when intercompared to the research ship observations, are within a degree or so of meeting that target.

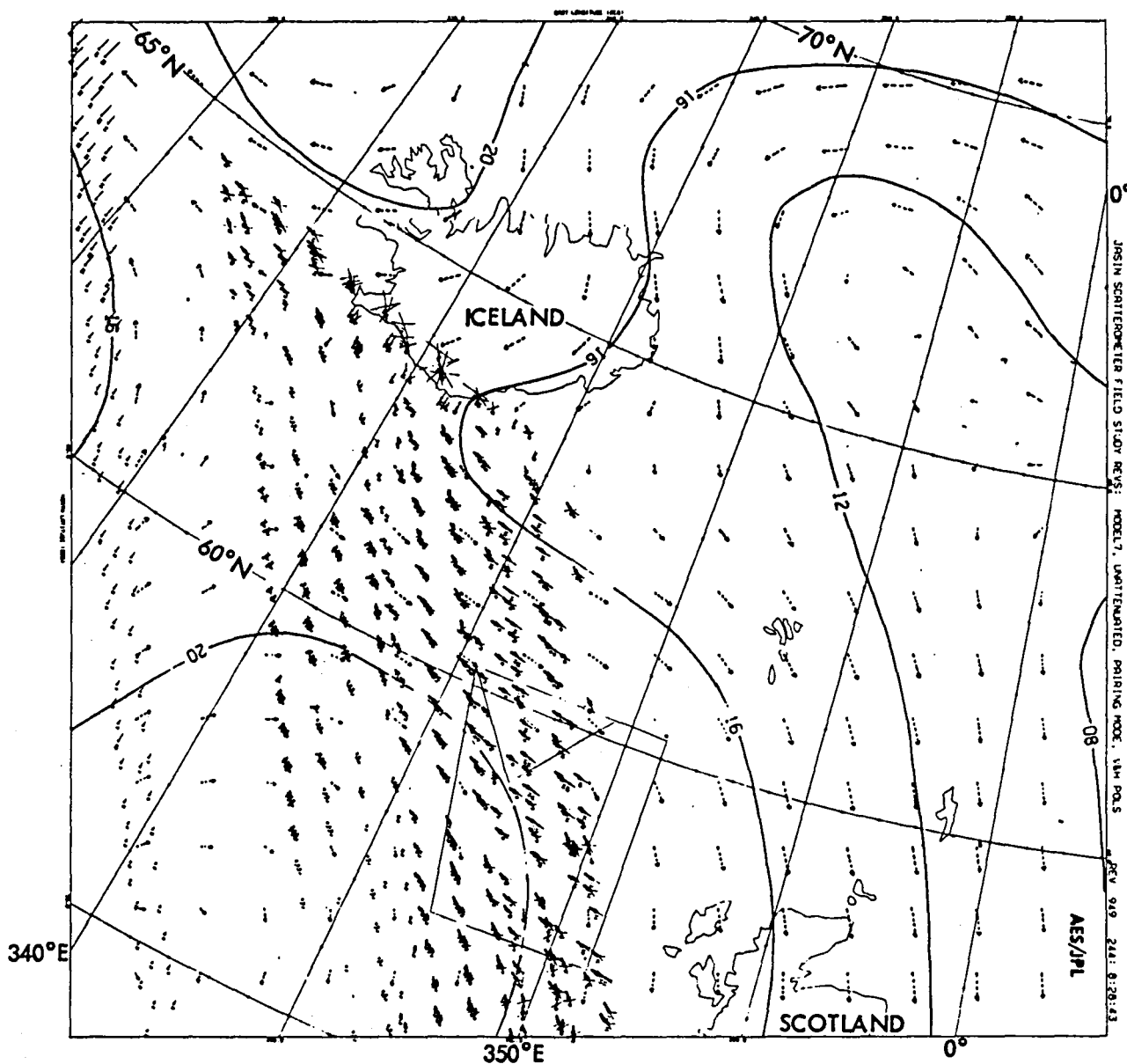


Figure 4-30. UW-Brown Sea Level Pressure Analysis and Derived Wind Vectors Superimposed Over the AES/JPL Team's SASS-Only Direction Analysis for Rev 949 (Contours are pressures in millibars (08 is read as 1008 mbars, and 98 as 998 mbars). The field vectors are dashed, and the chosen SASS vector selection is thickened. The SASS data is shown with ambiguities.)

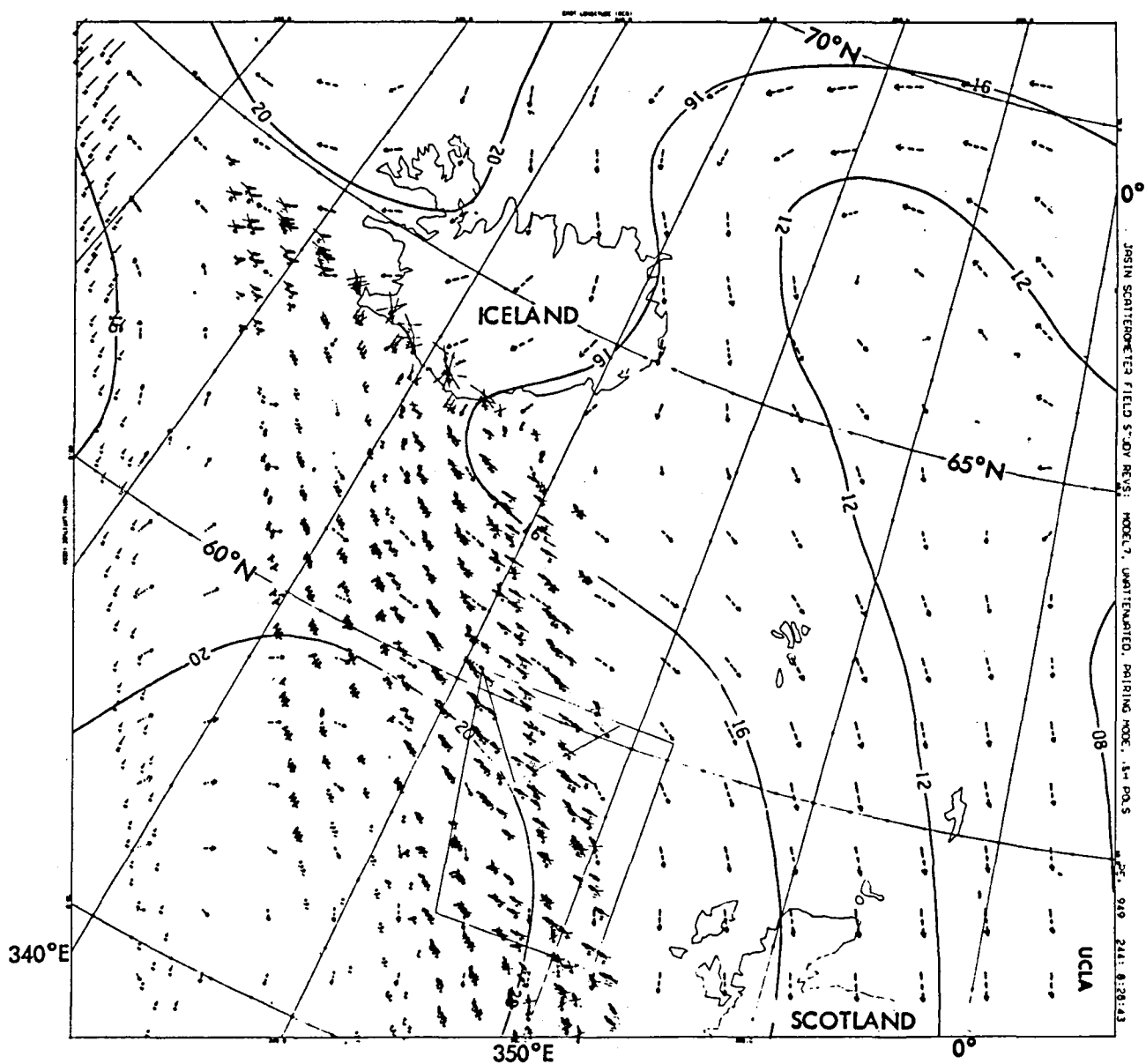


Figure 4-31. UW-Brown Sea Level Pressure Analysis and Derived Wind Vectors Superimposed Over the UCLA Team's SASS-Only Direction Analysis for Rev 949 (Contours are pressures in millibars (08 is read as 1008 mbars, and 98 as 998 mbars). The field vectors are dashed, and the chosen SASS vector selection is thickened. The SASS data is shown with ambiguities.)

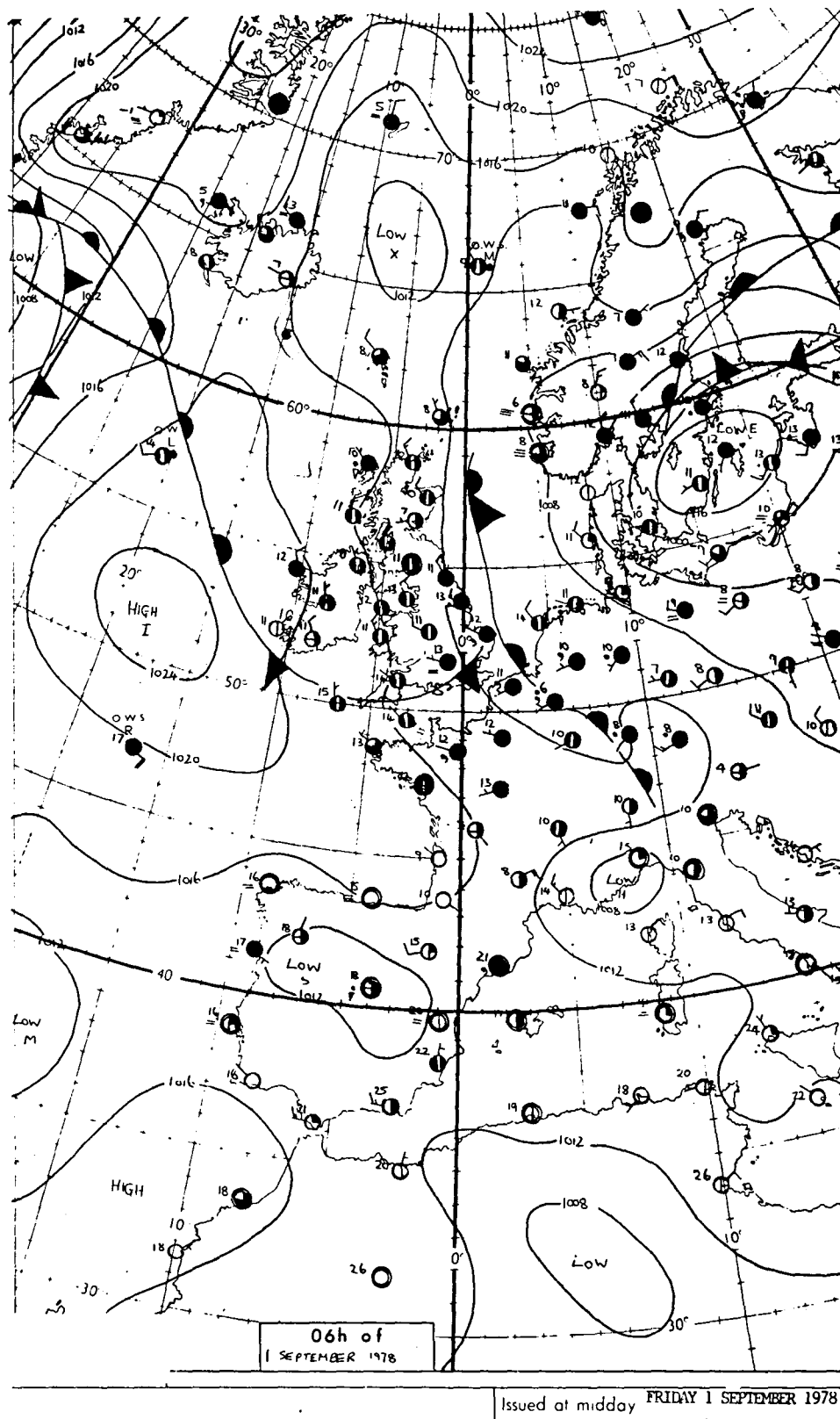


Figure 4-32. WMO Surface Analysis for 1 September 1978, 0600Z (Revs 948 and 949)

Table 4-22. Statistics for Direction Differences (Degrees) From Comparisons Made Against In Situ Ship Observations in the JASIN Meteorological Triangle Area

Direction Diff. for:	Mean ΔX	Std. Dev. N-1 Weighting	RMS	No. of Comparisons
UW-Brown Fields - JASIN Obs.	+2.6	13.9	13.8	18
Closest SASS Dir. - JASIN Obs.	-6.1	13.3	14.6	172
AES/JPL SASS Dir. - JASIN Obs.	-9.4	20.9	22.9	172
UCLA SASS Dir. - JASIN Obs.	-6.2	17.6	18.6	172
"Preferred" AES/JPL/UCLA SASS Dir. - JASIN Obs.	-6.2	17.6	18.6	172

Table 4-23. Statistics for Direction Differences (Degrees) From Comparisons Made Against UW-Brown Wind Fields Derived From Surface Pressure Measurements in the JASIN Meteorological Triangle Area

Direction Diff. for:	Mean ΔX	Std. Dev. N-1 Weighting	RMS	No. of Comparisons
JASIN Ship Obs. - UW-Brown Fields	-2.6	13.9	13.8	18
Closest SASS Dir. - UW-Brown Fields	-7.7	17.4	19.0	172
AES/JPL SASS Dir. - UW-Brown Fields	-12.1	24.6	27.4	172
UCLA SASS Dir. - UW-Brown Fields	-7.1	19.7	20.9	172
"Preferred" AES/JPL/UCLA SASS Dir. - UW-Brown Fields	-7.1	19.7	20.9	172

The challenging and positive aspect of these directional intercomparisons was that both the AES/JPL and UCLA SASS analyses presented only one directional vector for the intercomparison to the in situ measurements and wind field. Yet, the statistics were nearly the same as when four directions were preferred for intercomparisons to the same in situ measurements (see Table 4-22). In fact, it appears that the wind fields derived from the in situ measurements themselves are of no higher quality than the SASS direction comparison of the nearest SASS vector to the in situ measurements.

5. Summary, Conclusions, and Recommendations

a. Summary. The original assignment was threefold:

- (1) Assign marine meteorologists to filter out ambiguous SASS winds, leaving only the "true" wind direction, using their meteorological pattern recognition training and experience. This was done by two independent marine meteorological teams, one of which was AES/JPL and the other UCLA. These teams were not to use any in situ measurements other than SASS data alone. These SASS-only solutions were sealed and delivered to R. A. Brown of the University of Washington.
- (2) Intercompare the results from both parallel efforts above with each other and with available operational weather charts and Seasat VIRR imagery. This was to be followed by selecting a "preferred" analysis based on the available additional data and make modifications to the original SASS-alone analyses where necessary. Inasmuch as at least one of either UCLA or AES/JPL analyses agreed with the available operational weather charts, no modifications were felt necessary.
- (3) Intercompare the AES/JPL, UCLA, and "preferred" analyses with the withheld JASIN meteorological comparison data base. This latter data set became available at the workshop only after parts (1) and (2), above, were completed. An intercomparison of the closest SASS direction vector to the JASIN withheld data set was also done.

b. Conclusions

- (1) Ambiguity removal using marine meteorological analyst's skill and SASS data alone was proved. From these results, it may be said that SASS wind fields are capable of being able to being interpretable in identifying synoptic meteorological features without the aid of in situ measurements.
- (2) For any given SASS data set, the success of selecting the "correct" direction will depend on:

- (a) The skill of the analyst.
 - (b) Analyst's experience of the geographical climatology of the region.
 - (c) The extent of the SASS data coverage in space and time.
 - (d) The analyst's experience with SASS data.
- (3) Consistency between two independent analyses is generally excellent. Agreement on ambiguity removal is only low in areas where the analysts themselves have low confidence. These are usually areas of mesoscale features unfamiliar to the analysts. In no instance was a cyclone vortex mistaken for an anticyclonic vortex, or vice versa.
- (4) Comparison of AES/JPL to UCLA ambiguity analysis resulted in 92 percent identical choices in the JASIN triangle area. In general, over larger areas, i.e., 1000 to 3000 km of SASS data along the track, the general agreement was about 80 percent.
- (5) No re-editing of the preferred SASS kinematic analysis was necessary when the SASS was compared to the published British Meteorological Office Weather Charts and available VIRR imagery. However, there were a number of incidences in which the weather chart pressure analysis could have been improved by incorporating SASS data.
- (6) Kinematic analysis using SASS data alone has significant meteorological information of operational value. (Ambiguity removal would be enhanced with additional data (i.e., conventional observations and satellite imagery) and may remove most of the remaining uncertainty in the analysis if available.)
- (7) Comparisons of the preferred SASS vectors (determined from SASS data alone) to the "withheld" JASIN comparison data base in the meteorological triangle area resulted in the following preliminary direction statistics:

SASS to Ship Obs

$$\bar{D} = -6 \text{ (SASS-Obs)}$$

$$\sigma = 18 \text{ deg}$$

$$\text{RMS} = 19 \text{ deg}$$

$$\text{for } N = 172$$

SASS to UW Fields

$$\bar{D} \approx -7 \text{ deg (SASS-UW)}$$

$$\sigma \approx 20 \text{ deg}$$

$$\text{RMS} = 21 \text{ deg}$$

$$\text{for } N = 172$$

c. Recommendations

- (1) In the current state of the art of alias removal using SASS data alone, the following condition is necessary for a reasonable prospect of success:

3000 to 6000 km of track

The following conditions are highly desirable:

Both sides of swath

Two orbits in a region

Two independent analysts

- (2) Commit resources to develop a handbook of alias removal techniques containing a catalog of features for pattern recognition.
- (3) Investigate feasibility of a man-computer interactive alias removal scheme.

G. SASS ANOMALIES SUBPANEL

1. SASS Anomaly Study

As previously discussed in Subsection E-1, four revolutions were examined to explain large differences (>4 m/s, >40 deg) between the SASS-inferred wind vectors and the WMO reports. For two revolutions, faulty surface data were the cause and were subsequently removed. For Rev 929, the location of a front within the JASIN triangle was detected through an analysis of cloud imagery and the time series of wind vector from the autologger platforms. These gradient wind situations (10- to 100-km scale lengths) are difficult to resolve except in the high observation density region near the southern vertex of the triangle; thus, the "surface truth" data for frontal conditions in other regions are of a lesser quality. Further, the SASS wind vectors are also less accurate in gradient wind situations because of imperfect registration of the forward and aft antenna beam resolution cells and the effect of spatial averaging. For the last case, Rev 557, extremely large wind speed differences of order 10 to 20 m/s were obviously not a problem of the above type and, therefore, required further investigation.

A plot of the SASS multiresolution wind vectors for Rev 557 is shown in Figure 4-33. The anomalous wind vectors occurred in a region from the southern vertex to a point halfway along the eastern side of the JASIN triangle. For this pass, the SASS was in mode 4 (dual-polarized viewing to the right side only). A careful analysis of the SASS data uncovered no instrumental nor algorithmic problems;

JASIN SASS PRIORITY REVS: MODEL7, UNATTENUATED, V&H POLS

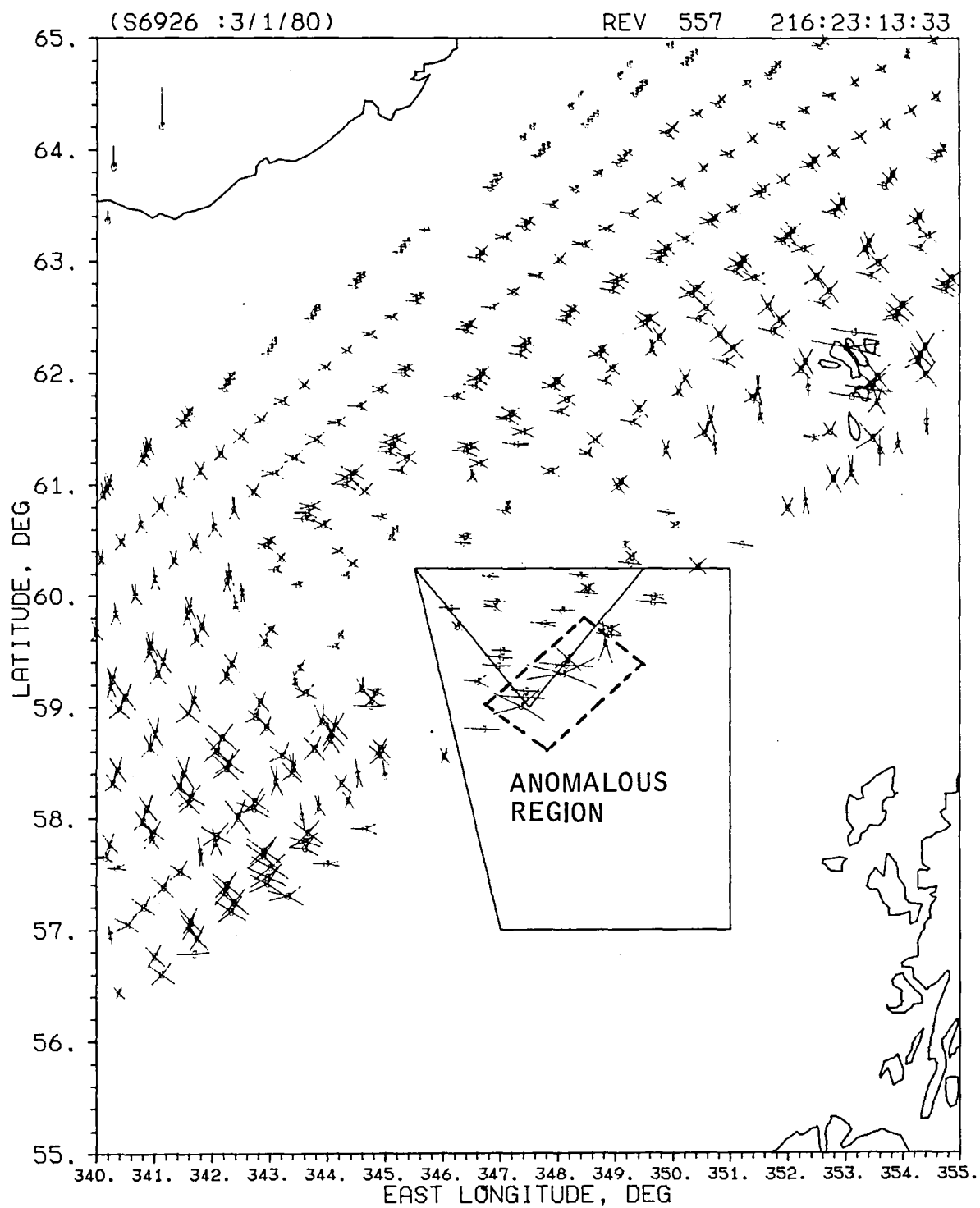


Figure 4-33. SASS Wind Vectors for Rev 557

moreover, large values of σ° were observed on all four antenna beams. Further, an examination of the SASS wind vector plot (Figure 4-34) for Rev 556 (100 min earlier) revealed no apparent irregularities; therefore, the "surface truth" was examined for possible explanation.

2. Analysis of Surface and Upper Air Data for Revs 556 and 557

Inspection of the WMO logs for the evening of 4 August 1979 revealed that thunderstorm activity had been reported at three of the ships (Meteor, Discovery, and Shackleton), all located near the southern corner of the JASIN triangle. Time series of surface variables from all available platforms showed a wind veer of 50 deg and an increase of speed of 3 to 4 m/s. At Meteor these changes were accompanied by a pressure jump. The times at which the wind changes occurred at each of the platforms suggested southwestward propagation of the shear line at 5 m/s. A synoptic chart based on the observations at or near 2130Z is shown in Figure 4-35.

Meteorological office analysis at this time showed fronts approaching the area from both the west and the northeast and a NOAA-5 IR picture at 2000Z showed a region of general cloud associated with the westward of the two fronts. At 59N, 350E, there was evidence of deep convective clouds (also seen on VIRR further west at 2300Z). Some idea of the upper air structure in between the fronts can be gained from radiosonde ascents from Gardline Endurer, which reveal a convective boundary layer capped by an inversion at 800 mbars. The air from 800 to 400 mbars is potentially unstable and has an equivalent potential temperature of 40°C, indicating that it did not originate from the sea surface in the JASIN area (θ only 30° to 35°C). Winds at midlevels were from 105 deg, which would tend to carry the storm toward the Meteor. Discovery reported lightning to the south from 2200Z until midnight, consistent with this. These features are also shown in Figure 4-35.

The inference is that most unstable air above an occlusion was lifted ahead of the more active cold front approaching from the west. The convection was able to penetrate upward some 4 or 5 km with associated thunder and eventually perturbed the surface airflow producing maximum 2-min wind speeds of 7 or 8 m/s. The storm appears to have propagated along the occluded front, which was aligned WNW/ESE. Rainfall accompanying the feature was probably short-lived.

3. SASS σ° Analysis

To confirm the hypothesis of thunderstorm activity, the σ° contours were constructed for Revs 556 and 557. For Rev 556 (Figure 4-36), the cross section signature versus θ was established in regions of reasonably uniform wind speed and direction at latitudes 61N and 55.5N. The mean curve was used to normalize the cross sections for doppler cells at incidence angles between 23 and 46 deg. Since the normalization factor in this angular region is quite steep (1.3 dB/deg), the σ° variation across-track must exceed approximately 5 dB to be considered significant. Further, the interpolation is complex because both changes in wind speed and wind direction cause σ° to vary (e.g., a 4-6 dB change in backscatter is expected as winds move from nearby upwind inside the triangle to crosswind below 59N). Thus, if wind speed were constant, the contours would decrease to the south because of the veer of the wind.

JASIN SASS PRIORITY REVS: MODEL7, UNATTENUATED, V&H POLS

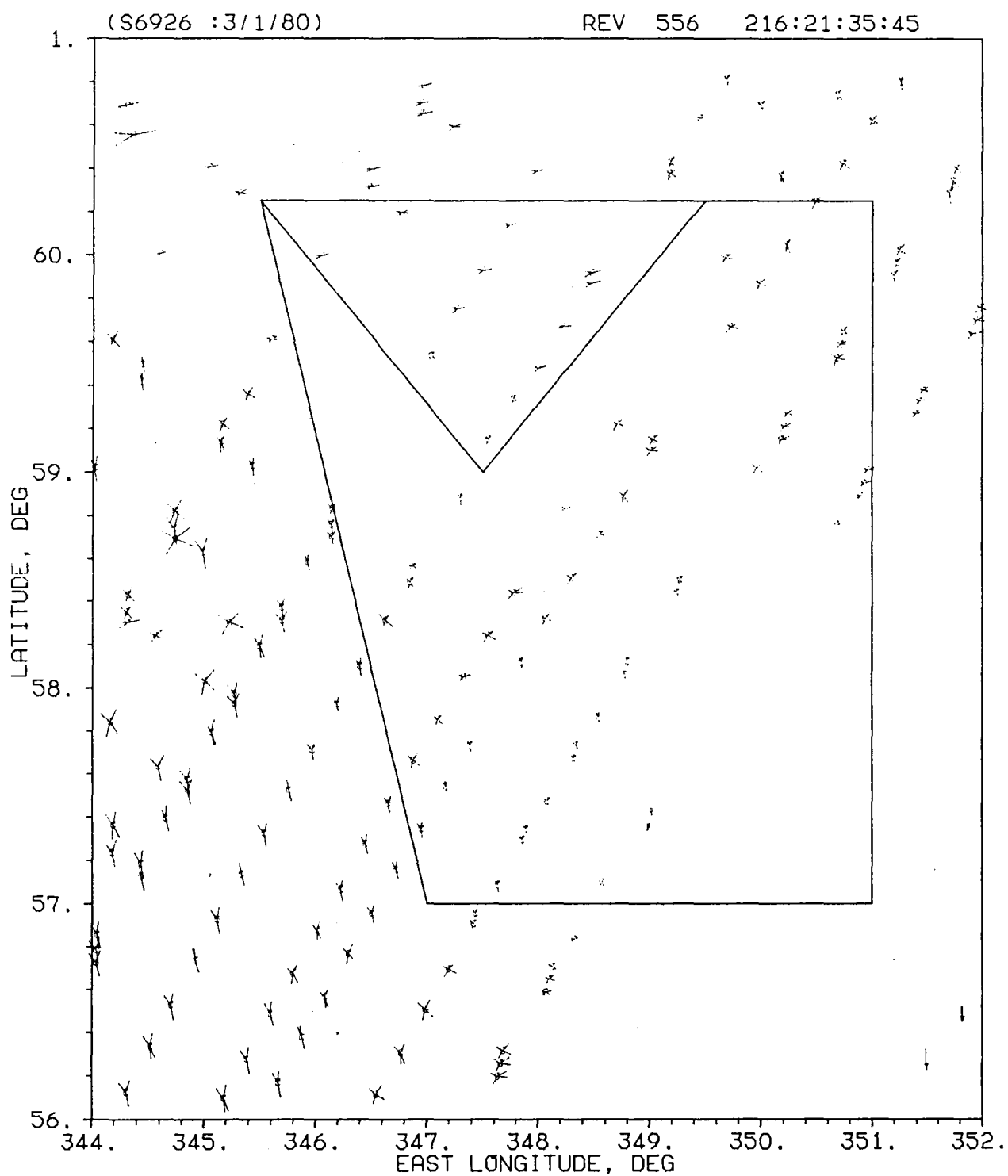


Figure 4-34. SASS Wind Vectors for Rev 556

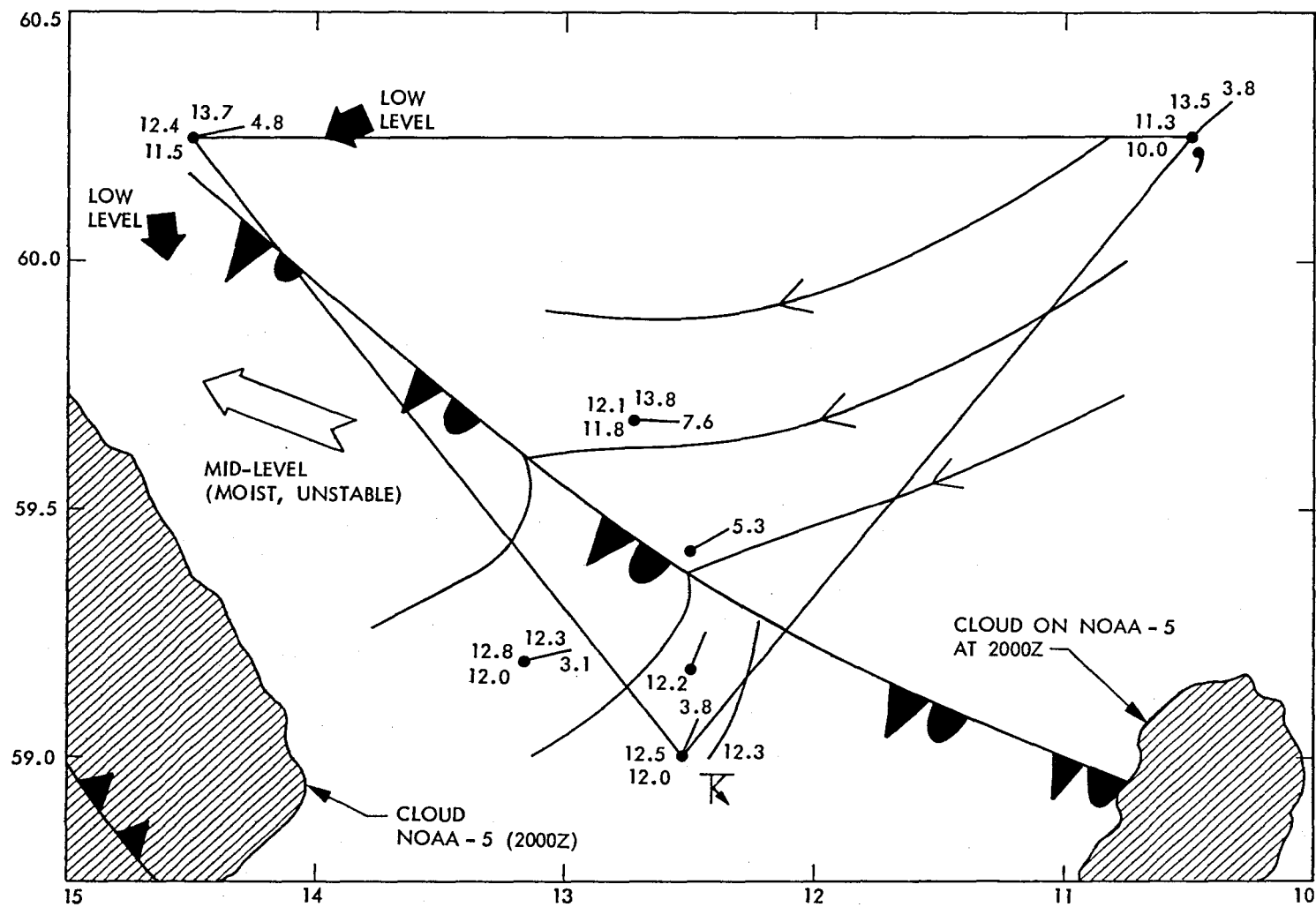


Figure 4-35. Surface Chart for Approximately 2130Z (Rev 556)

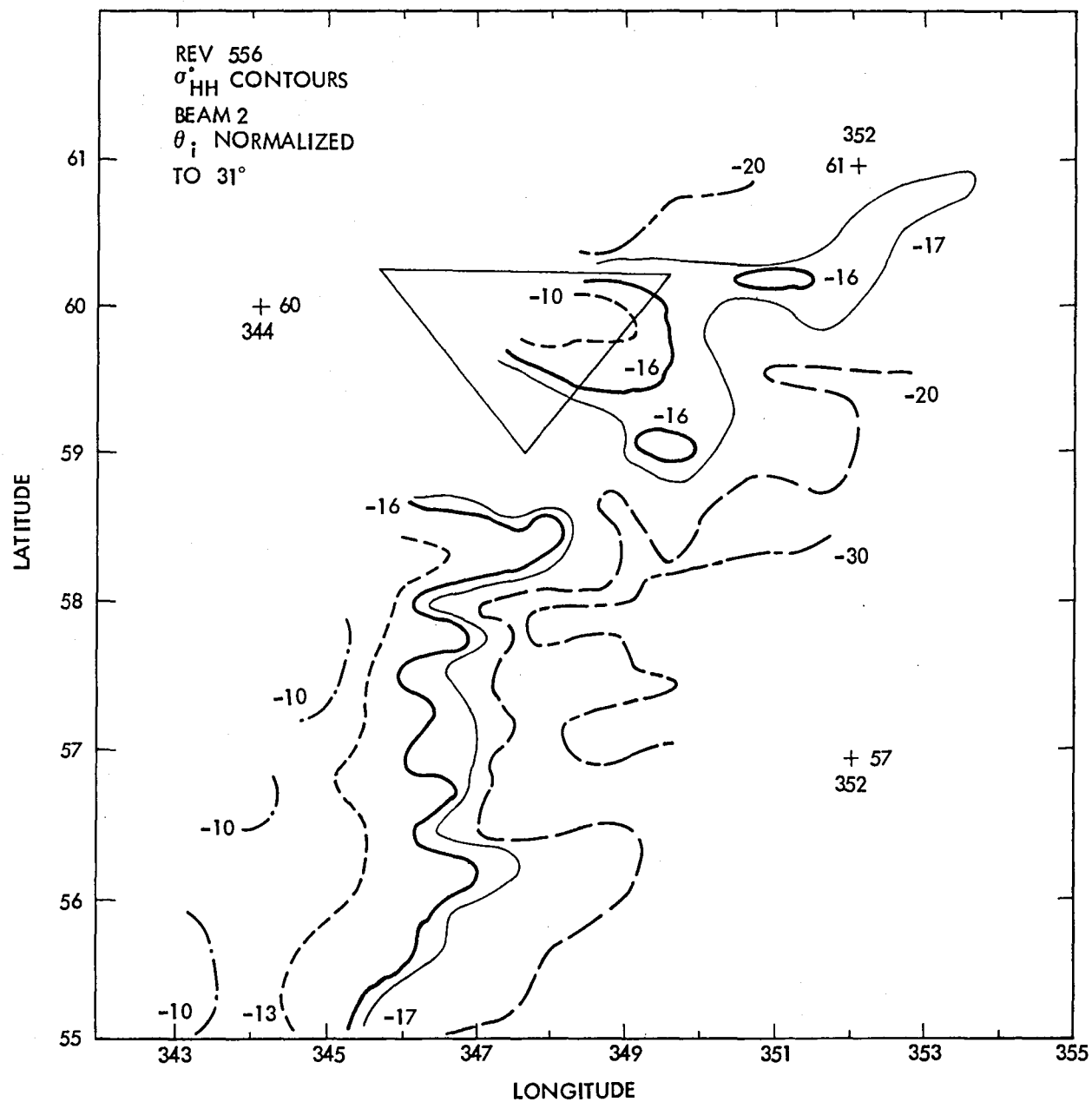


Figure 4-36. SASS σ_{HH}° Contours for Rev 556

Figure 4-36 shows a gradual increase in σ° from east to west with only one possible region of increased σ° at 59N, 349.5E. This region closely corresponds to the region of increased water vapor and liquid water measured by SMMR (see Figures 5-40 and 5-41). Also, a simultaneous pass of SAR indicated a small feature believed to be a rain cell located near 58°30'N, 349.5°E (Figure 4-37).

Approximately 100 min later (Rev 557), however, the situation had changed dramatically. During this pass, the SASS was operated in mode 3 (dual-polarization viewing to the left), and the rearward viewing beam 4 was used to construct the vertical and horizontal polarized σ° contours (Figures 4-38 and 4-39). For this case, the region of interest lies between incidence angles of 48 and 63 deg, where the slope of the σ° signature is less severe. Assume a mean wind speed of 5 m/s, slopes of 0.8 dB/deg for horizontal and 0.4 dB/deg for vertical were used to normalize to an incidence angle of 55 deg. Also, the interpretation for this case is simplified since, in the region of interest, the antenna beam is pointing approximately upwind.

Several regions of high backscatter are observed along a 300-km to 400-km line south and parallel to the eastern side of the JASIN triangle. It is suggested that these regions are associated with increased ocean roughness in the vicinity of the convective storm cells. The size of thunderstorms (typically 5 km) is small compared to the resolution cell of SASS at the outer edge of the swath (18 x 80 km orientated approximately north/south for beam 3 and east/west for beam 4). Because of this, we believe that the inferred wind vectors would be severely degraded due to spatial averaging and imperfect registration of beams 3 and 4 doppler cells. Also, the strong rain may significantly modify the ocean surface roughness, thereby invalidating the σ° /wind vector relationship, as well as produce scattering in the atmosphere.

In summary, for the first time, mesoscale atmospheric disturbances have been shown to produce serious errors in the SASS-inferred ocean wind vector. Because this is not representative of the synoptic scale for oceanic winds, this revolution was removed from the "surface truth" data set before the statistics were calculated. However, since mesoscale features do occur, it is important that the user of SASS winds be alerted to potential problems. After all, these phenomena are no doubt just one example of many anomalies that will be observed as the full Seasat oceanic geophysical data record is analyzed.

4. Post-Workshop Analysis

After the JASIN workshop, additional analysis was performed on Rev 557. The conclusion from this study is that the anomalous SASS winds occurred in a region where deep mid-level convection was taking place. Three possible explanations for the unrealistic satellite winds have been proposed: (1) that the regions of high backscatter are associated with high wind speeds in the vicinity of the convective cells which are small compared with the SASS resolution cell (18 x 70 km); (2) the large raindrops in the storm may significantly modify the ocean surface roughness, thereby invalidating the relationship between σ° and wind vector; and (3) the rain may be responsible for additional backscatter in the atmosphere.

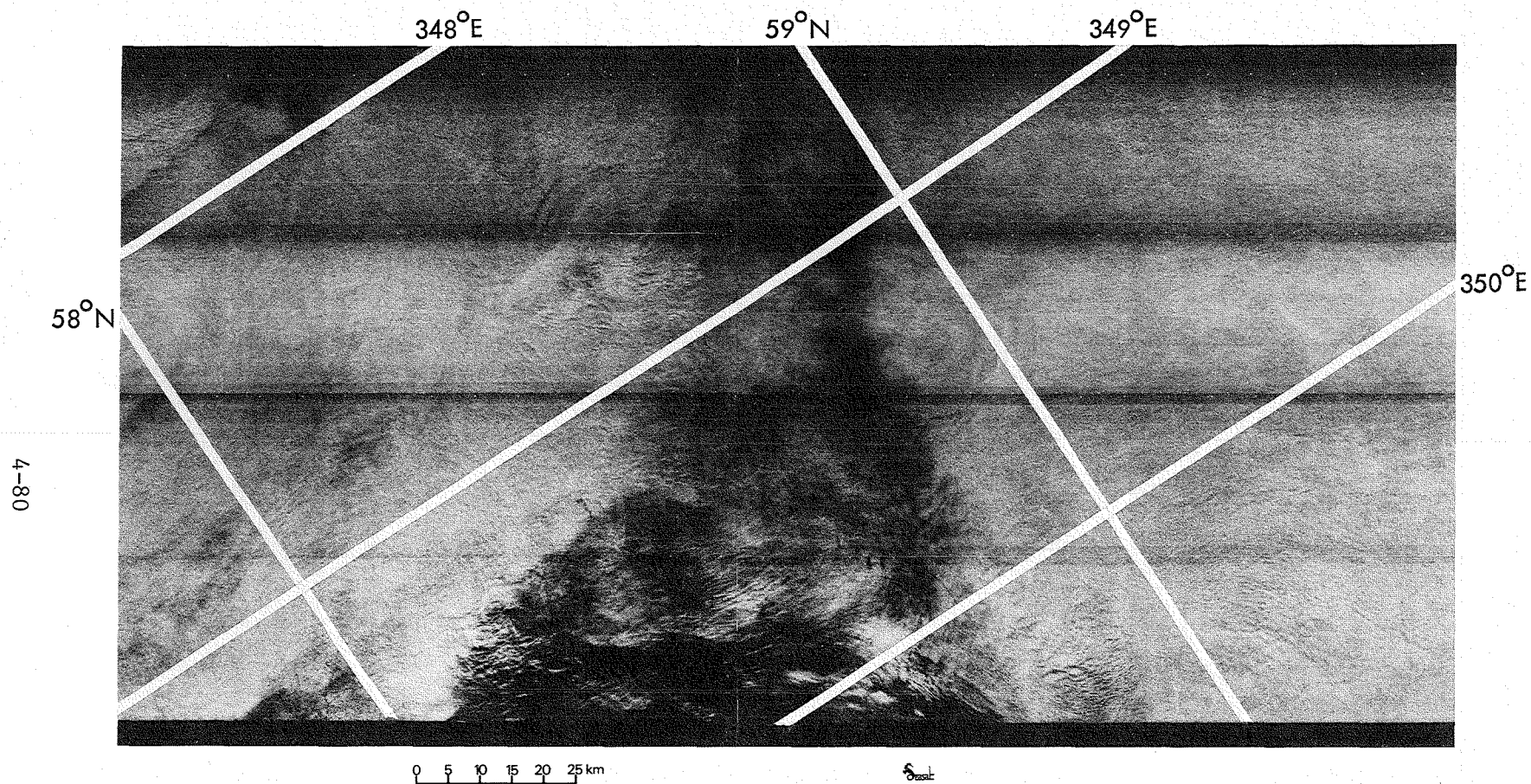


Figure 4-37. Synthetic Aperture Radar Image - Rev 556 (The dark area appears to coincide with areas of heavy rain.)

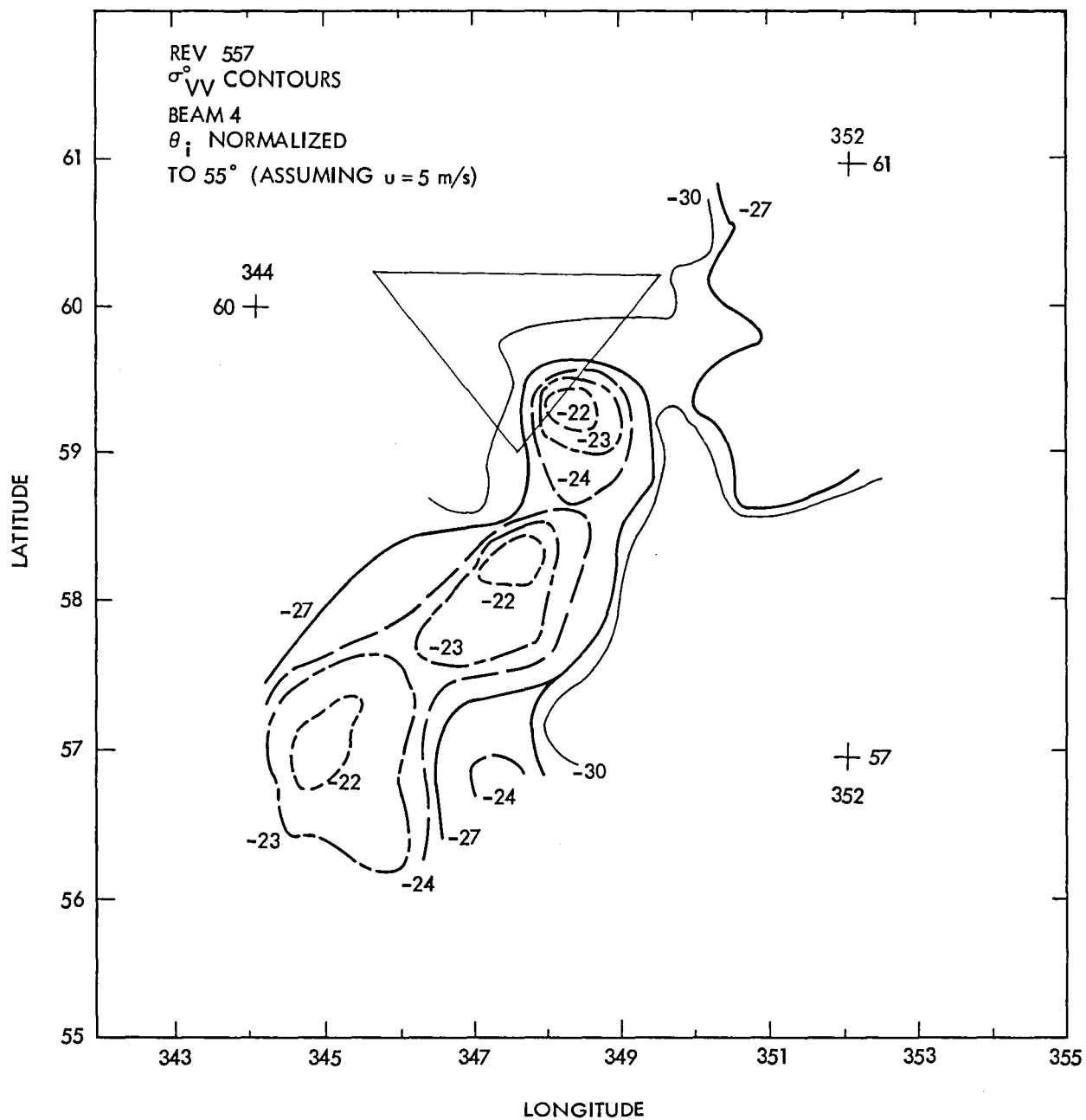


Figure 4-38. SASS σ_{VV}° Contours for Rev 557

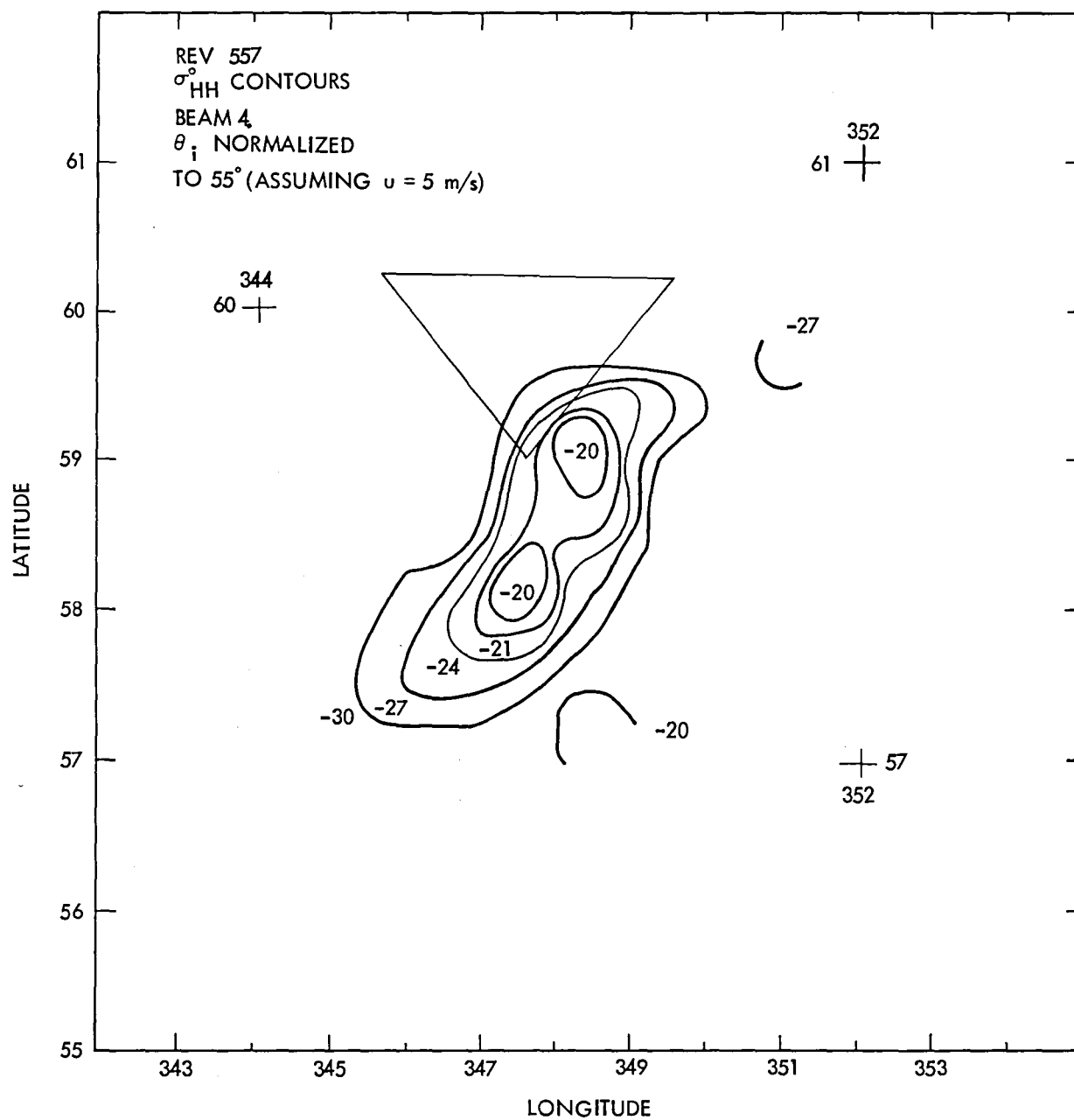


Figure 4-39. SASS σ_{HH}° Contours for Rev 557

Concerning the first explanation, it well known that thunderstorms can produce large gusts at the surface through the evaporation of precipitation into the downdraught. On this occasion, however, there was no evidence from surface data sampled at 1-min intervals that gusts exceeded 8 m/s, which is consistent with the observed thermodynamic structure.

For the second explanation, recent radar scattering experiments conducted in a wind/wave tank have shown that the backscatter from small-scale surface roughness produced by artificial rain predominates for light wind conditions (<10 m/s). However, to account for the large σ° , the affected area would have to be several tens of kilometers in extent with moderate rain rates (5-10 mm/h).

Finally, for the last explanation, from Mie scattering calculations, we conclude that the large σ° could be the result of backscatter from a single localized cell of intense rain. Assuming a thunderstorm of 1-km diameter and vertical rain column of 5 km, this would require rain rates of approximately 50-70 mm/h to account for the observed received power level of -162 dBw. However, this is unrealistic from the meteorological analysis. Considering scattering from larger rain cells, an alternate rain condition of 12 mm/h over 10-km diameter and 5-km vertical extent could also explain the observed received power level. But, even this rain rate over such a large region is doubtful. Therefore, we conclude that the anomalous SASS winds were probably caused by a combination of the above.

H. CONCLUSIONS

A major objective of the JASIN workshop was to demonstrate that winds near the sea surface could be calculated to an accuracy of ± 2 m/s for speed and ± 20 deg for direction by means of SASS data without prior knowledge of the comparison data obtained by meteorological instruments. The two candidate model functions both demonstrated that the winds from SASS agree with the JASIN meteorologically determined winds to within ± 2 m/s from 4 to 16 m/s and ± 20 deg in direction with the two exceptions indicated by Tables 4-13 and 4-15, where the rms direction scatter is larger than 20 deg. All of the other gross statistics demonstrate that the major JASIN objective was met.

For this comparison, the meteorological data were far superior to the routine data provided by the conventional meteorological network, and they were, in some ways, superior to the data used in the GOASEX workshops. It was impractical to cross calibrate the anemometer systems on the data buoys, ocean weather ships and the "Oceanographer" for these previous workshops, and, thus, there were probably some biases present in the meteorological measurements. The JASIN workshop benefitted from the extreme care used in the JASIN program to reduce this source of scatter in the data.

A review of the GOASEX I and II workshop reports demonstrates that there has been a marked improvement in the statistical comparisons for this JASIN workshop. The combined effect of bias and standard deviation for the previous workshops produced quite large root-mean-square differences. The biases have been reduced to the point where they are almost, but not quite, negligible. The standard deviations are now well under 2 m/s. This improvement would not have

occurred had there not been simultaneous activity directed toward improving both meteorological data base and the model functions.

The JASIN workshop might not have been a success. As Figures 4-28 to 4-31 show, the wind data were available over the full range of incidence angles. These tables and many of the other analyses show that the largest sources of bias and scatter are those for low and high incidence angles. Had the JASIN data, by accident, been concentrated on the inner and outer edges of the SASS swaths, the gross statistics could easily have fallen outside of the required bounds. Conversely, had the JASIN data been concentrated in the middle of the SASS swaths, the errors inherent in both model functions might not have been recognized.

The readers of this JASIN report need not concern themselves with which of the two candidate model functions is the better. Neither survived for the production of the SASS winds for the STORMS workshop of October 1980 and for the fiscal year 1980 production of a global data set for 45 days of Seasat data.

As can be understood from the analyses that have been made, the two candidate model functions differed the most at low and high incidence angles. They differed predominantly because of the lack of good meteorological data for both low and high incidence angles prior to the JASIN workshop. They and their predecessors, to a greater or lesser extent, tended to agree over the middle range of incidence angles. The JASIN data, therefore, provided an excellent opportunity to improve the model function even further by means of the data at high and low incidence angles. A final model function was derived by a final minor adjustment of a model function that reduced the overall bias to a small amount and eliminated the larger biases at the high and low incidence angles. These results will be described in subsequent reports.

An effort was made in GOASEX II to identify the various sources for the differences between the winds of the comparison data set and the SASS winds. These differences are not all errors in the SASS winds. They can be placed in three categories: (1) instrument errors and instrument biases in the meteorological data, (2) communication noise and other error sources inherent in backscatter measurements plus model function errors, and (3) actual differences between the two vector winds being compared that result from nonsynopticity and mesoscale fluctuations in the wind. The last reason for the differences is not strictly an error of measurement but results in an actual difference. The study given in the GOASEX II report is being extended, but even such preliminary results strongly suggest that the differences between the SASS and meteorological winds are to a large extent actual differences. For the synoptic scale, further averaging of the SASS winds can produce a much more accurate vector wind.

REFERENCES

- Black, P. "Comparison of SMMR and Airborne Radar Rain Rates in Hurricane Ella," paper presented at the Seasat Storms Workshop, Virginia Key, Florida, October 29-31, 1980.
- Born, G. H., et al., Seasat Gulf of Alaska Workshop Report: Executive Summary, JPL Internal Document 622-101, May 1979.
- Born, G. H., et al., Seasat Gulf of Alaska Workshop II Report, JPL Internal Document 622-107, January 1980.
- Bracalente, E. M., Boggs, D. H., Grantham, W. L., Sweet, J. L., "The SASS Scattering Coefficient σ^0 Algorithm," IEEE J. Oceanic Engineering, Vol. OE-5, No. 2, April 1980.
- Dome, G. J., Wentz, F., Moore, R. K., Birrer, I. J., Hawkins, J., and Schroeder, L. C., "Atmospheric Attenuation Effects Observed by SASS in Hurricanes," paper presented at the Seasat Storms Workshop, Virginia Key, Florida, October 29-31, 1980a.
- Dome, G. J., Moore, R. K., Birrer, I. J., and Van Sickle, K., "Use of a Satellite Multi-Frequency Radiometer to Determine Attenuation Suffered by a Satellite Radar," University of Kansas, 1980b.
- Grantham, W. L., et al., "An Operational Satellite Scatterometer for Wind Vector Measurements Over the Ocean," NASA TMX-72672, March 1975.
- Grantham, W. L., Bracalente, E. M., Jones, W. L., and Johnson, J. W., "The Seasat-A Satellite Scatterometer," IEEE J. Oceanic Engineering, Vol. OE-2, No. 2, April 1977.
- Griffith, C. G., "Comparison of Rainfall Rates Derived From Satellite IR Imagery With SMMR Rainfall Rates Derived for Hurricanes Fico and Ella," paper presented at the Seasat Storms Workshop, Virginia Key, Florida, October 29-31, 1980.
- Johnson, J. W., Williams, L. A., Bracalente, E. M., Beck, F. B., and Grantham, W. L., "Seasat-A Satellite Scatterometer Instrument Evaluation," IEEE J. Oceanic Engineering, Vol. OE-5, No. 2, April 1980.
- Jones, W. L., Schroeder, L. C., and Mitchell, J. L., "Aircraft Measurements of the Microwave Scattering Signature of the Ocean," IEEE Trans. Antennas and Propagation, Vol. AP-25, No. 1, January 1977.
- Jones, W. L., Wentz, F. J., and Schroeder, L. C., "Algorithm for Inferring Wind Stress from Seasat-A," AIAA J. Spacecraft Rockets, Vol. 15, No. 6, November-December 1978.

BIBLIOGRAPHY

"Air-Sea Interaction Project: Summary of the 1978 Field Experiment," Royal Society, Dec. 1979.

Barrick, D. E., Woiceshyn, P. M., Wilkerson, J. C., Born, G. H., and Lane, D. B., Seasat Gulf of Alaska Workshop II Report, JPL Internal Document 622-107, Jan. 1980.

Overland, J. E., Woiceshyn, P. M., and Wurtele, M. G., "High Resolution Wind Fields from the Seasat Scatterometer," submitted to Monthly Weather Review (1980).

Woiceshyn, P. M. (editor), Seasat Gulf of Alaska Workshop Report, JPL Internal Document 622-101, Volume II, 1979.

Woiceshyn, P. M., Appleby, W., Borowski, M., Peteherych, S., and Wurtele, M. G., SASS Wind Direction Ambiguity Removal Subpanel Report, JPL Internal Document 622-220, Apr. 1980.

SECTION V

SMMR PANEL REPORT

A. INTRODUCTION AND OVERVIEW

During the Scanning Multichannel Microwave Radiometer (SMMR) Mini-Workshop II of September 1979, the spacecraft data from some passes led to geophysical determinations that agreed very well with the available surface truth. For other passes, however, the geophysical determinations, especially for surface wind speed, were very different from surface truth. Activities during the workshop to understand this marked difference in passes revealed that the thermal environment of the instrument changed due to solar heating by amounts much larger than had been reported during engineering assessment studies. Subsequent investigations showed that the time scale for thermal change varied with temperature. During the time of the Gulf of Alaska Seasat Experiment (GOASEX), rapid thermal heating occurred during direct solar illumination of the SMMR followed by a slower cooling as the instrument became shadowed. Since the housekeeping temperatures used in the calibration algorithms were averaged over a time scale longer than that of the rapid thermal build-up, but shorter than that of the cooling, the accuracy of the geophysical determinations depended upon what thermal changes the SMMR was experiencing. Post Mini-Workshop II studies concluded that improper averaging of the housekeeping temperatures and other problems of the calibration algorithms had led to the discrepancies between SMMR determinations and surface truth seen on some of the passes.

The calibration problems uncovered from Mini-Workshop II evaluation efforts, the desire to provide a significant amount of Seasat SMMR data to the ocean community, and the hope that evaluation activity focus can finally be shifted from sensor file inadequacies to assessment of geophysical file accuracy all contributed to establishing the following SMMR Evaluation Task Group (ETG) objectives for the JASIN workshop effort:

- (1) Revise and Test the Calibration Algorithms. The calibration algorithms had to be revised to remedy the inadequacies mentioned above. The revisions were to be tested on the large data set that would be generated for the JASIN workshop.
- (2) Complete Verification of the Sensor File for Data Release. The sensor file is produced by both the calibration algorithms and the antenna pattern correction (APC) algorithms. Since the APC algorithms had performed as expected in Mini-Workshop II, it was optimistically hoped that they would cause no surprises during the JASIN workshop. Furthermore, if sufficient testing of the calibration algorithms could be accomplished, verification of the sensor file could be completed. The

ETG could then authorize release of sensor file data, which includes antenna temperatures and brightness temperatures.

- (3) Evaluate Additional Approaches to Geophysical Determinations. Evaluation efforts in previous workshops considered geophysical determinations only from algorithms developed by Frank Wentz and Tom Wilheit. Additional promising approaches should be evaluated to improve algorithms for geophysical data production and to assist in estimating the ultimate limitations in geophysical determination from SMMR data.
- (4) Examine a Wide Range of Geophysical Considerations. To test the geophysical retrievals from SMMR measurements as fully as possible, a wide range of geophysical conditions should be examined. While the experiments in the JASIN area provided a good range of sea-surface wind speeds, the sea-surface temperatures (SSTs) and columnar water vapors varied no more than a few kelvins and about 2 g/cm^2 , respectively. For this reason, a set of passes in the Northwest Pacific, exhibiting sea-surface temperature from 10° to 26°C , and a set of passes in the tropics, exhibiting columnar water vapor from 3 g/cm^2 to almost 7 g/cm^2 , were processed.

Selection of a data set consistent with the ETG objectives was accomplished with the following rationale: First, in the JASIN area, passes were initially screened to include only those having greater than 50 percent SMMR coverage of the extended JASIN area. The resulting passes were further filtered by applying criteria emphasizing coincident coverage by the scatterometer, intensive radiosonde data taken, a sampling of a wide range of wind speeds, and a sampling of passes covering the duration of the JASIN experiment. The surviving passes are listed in Table 5-1. Second, in the Northwest Pacific area, selection of the passes was motivated by a desire to study an area which should be free of radio frequency interference (RFI), free of land effects, and also geophysically interesting. In this area the Kuroshio current generates a region of relatively high sea-surface temperature gradients. Surface comparison data were available in the form of expendable bathythermograph (XBT) sea-surface temperature measurements. These XBTs were deployed from aircraft flights out of Adak, Alaska, and from ships on the U.S. to Japan commercial shipping routes. No other quantitative surface truth data (e.g., winds, water vapor, etc.) were available during the workshop for this area, although weather maps for the Pacific area were available, and images of the SMMR data showed the major patterns of clouds and probable rainfall locations. The Northwest Pacific passes are listed in Table 5-2. Third, in tropical regions, passes were chosen to extend the rather limited range of meteorological conditions encountered in the area of the JASIN experiment, especially concerning atmospheric water vapor, liquid water, and sea-surface temperature. There are several atolls and islands in the Pacific Ocean of very small areal extent which have World Meteorological Organization (WMO) radiosonde stations (see Table 5-3). The subset of passes investigated which were roughly coincident with measurements at these stations are listed in Table 5-4. Fourth, a set of passes studied in previous workshops was rerun after algorithm modifications to help evaluate calibration algorithm performance. Wind fields coincident with these passes had been developed by Vince Cardone and were modified for the JASIN workshop to insure consistency. The passes are listed in Table 5-5. The three GOASEX passes were used by Frank Wentz in determining brightness temperature biases, so his geophysical algorithms were "tuned" to them. The Atlantic pass had very high winds that had caused damage to the Queen Elizabeth II.

Table 5-1. SMMR Passes in the JASIN Area

Item	Date	DOY	Rev ^a	JASIN ^b GMT	Radio- sonde	A/C ^c	Winds	Comments
1	7-21	202	355D	20:30:00			24	Early high winds, poor surface truth
2	7-27	208	432A	05:23:10	X		19	SASS
3	7-30	211	475A	05:30:24	X		14	SASS
4	8-4	216	547A	06:15:09	X		10	SASS
5	8-4	216	556D	21:36:10	X		7	SASS
6	8-7	219	590A	06:22:17	X	E,C,M	11	SASS
7	8-7	219	599D	21:43:15	X	E,C,M	10	SASS
8	8-10	222	633A	06:29:24			6-12	SASS, 1 MET ship (Meteor), front
9	8-10	222	642D	21:50:17			25-30	SASS, Ph1-Ph2 break, front, 8'-15' waves
10	8-13	225	676A	06:37:01				SASS, Ph1-Ph2 break, high winds
11	8-16	228	719A	06:43:21				SASS Ph1-Ph2 break, high winds
12	8-18	230	748A	07:20:00			20-28	SASS, 1 MET ship (Meteor)
13	8-18	230	757D	22:43:00			32	SASS, 2 MET ships present
14	8-19	231	762A	06:48:42			26	SASS (poor coverage)
15	8-21	233	791A	07:25:07	X	E,C	28	SASS
16	8-21	233	800D	22:45:36	X	E,C	16	SASS
17	8-22	234	805A	06:53:42	X		18	Light rain
18	8-23	235	829D	23:21:49	X	E,C,M	26	
19	8-24	236	834A	07:30:12	X	E,C,M ²	20	SASS
20	8-24	236	843D	22:50:47	X	E,C,M ²	18	SASS
21	8-26	238	872D	23:29:30			3-4	SASS
22	8-27	239	886D	23:00:00	?	?	8-9	
23	8-39	242	929D	23:15:00	?	?	22	
24	9-1	244	944D	00:23:25	?	?	16	
25	9-1	244	949A	08:31:08	X		18	
26	9-1	244	958D	23:53:48	X		12	

Table 5-1 (contd)

Item	Date	DOY	Rev ^a	JASIN ^b GMT	Radio- sonde	A/C ^c	Winds	Comments
27	9-5	248	1001D	00:06:11			26	SASS, 1 MET ship (Meteor)
28	9-5	248	1006A	08:15:09			26	SASS, 1 MET ship (Meteor)
29	9-8	251	1049A	08:27:59				High Winds, no MET ships
30	9-14	257	1135A	08:53:19				High Winds, no MET ships

^aA = Ascending; D = Descending

^bMid-Pass time.

^cA/C Code is E = Electra, C = Convair, M = Mystere, and M² = two Mystere flights.

B. DEVELOPMENTS IN SMMR ALGORITHMS

1. Sensor File Algorithm Development

Since Mini-Workshop II, a large effort in sensor file algorithm modification has occurred. The problems alluded to in the Introduction have been addressed, which resulted in a number of changes in the calibration algorithms. A detailed discussion regarding treatment of the large thermal changes and concomitant thermal gradients in the instrument is given in Appendix B of this report. The procedures for determining the parameters in the physical model of the SMMR on which the calibration algorithms are based are explained in Appendix C. The alternative to averaging housekeeping temperatures on a time scale slower than the thermal changes was to use the housekeeping temperature directly. These measurements from platinum sensors are accurate to tenths of a kelvin. The only other potentially troublesome noise sources are fairly easily identifiable blunder points.

The only change in the antenna pattern correction algorithms was correction of a software problem which produced errors below the one kelvin level in brightness temperatures.

Table 5-2. SMMR Passes in the Northwest Pacific

Item	Date	DOY	Rev ^a	Time Span (GMT)
1	9/19	262	1208 D	11:41:00 - 12:05:00
2	9/19	262	1214 A	21:14:00 - 21:37:00
3	9/19	262	1215 A	22:53:00 - 23:16:00
4	9/20	263	1222 D	11:12:00 - 11:36:00
5	9/20	263	1223 D	12:52:00 - 13:17:00
6	9/20	263	1228 A	20:43:00 - 21:08:00
7	9/21	264	1229 A	22:24:00 - 22:48:00
8	9/21	264	1236 D	10:43:00 - 11:07:00
9	9/21	264	1237 D	12:23:00 - 12:48:00
10	9/21	264	1242 A	20:14:00 - 20:38:00
11	9/21	264	1243 A	21:54:00 - 22:18:00
12	9/21	264	1244 A	23:35:00 - 23:57:00

^aA = Ascending; D = Descending.

Table 5-3. Radiosonde Stations in the South Pacific Ocean

Station	Lat.	Lon.	Area, km ²	Percent of Grid 3 Area ^a	Comments
Tango	29N	135	-	-	Weather ship
Midway	28.22N	182.63	15	0.5	
Guam	13.55N	144.83	541	19	Sta. elevation 111 m
Wake Island	19.28	166.65	8	0.3	
Eniwetok	11.35N	162.35			
Johnston Island	16.73N	190.48	1.3	0.04	
Woleai	7.38N	143.92			
Truk	7.47N	151.85	118	4.0	
Ponape	6.87N	158.22	455	16	
Kwajalein	8.72N	167.73	16	0.5	
Majuro	7.03N	171.38	10	0.3	
Koror	7.33N	134.48	8	0.3	
Yap	9.48N	138.08	54	1.9	
Kapangamarangi	1.08N	154.77	<76	<2.6	
Tarawa	13.5 N	172.92	23	0.8	
	9.42S	159.97	6475	222	On Guadalcanal Is.
	17.75S	168.30	915	31	On Efate Is. in New Hebrides
	22.27S	166.45	19,099	655	On New Caledonia
Funafuti	8.52S	179.22	2.8	0.1	
	17.75S	177.46	10,386	356	On Vita Levu Is. in Fiji Islands
Canton Island	2.77S	188.28	9	0.3	
Pago Pago	14.33S	189.28	135	4.6	On Tutuila Is. in American Samoa
Penrhyn	9.02S	201.93	10	0.3	} On Hiva Oa Is. in the Marques Is. in French Polynesia
Atuoma	9.82S	220.98	200	6.9	
	17.55S	210.38	1042	36	
Tuamotu	18.07S	219.05			On Hao Island

^aGrid 3 is 54 x 54 km².

Table 5-4. SMMR Passes in the Tropics

Item	Date	DOY	Rev	Time Span (GMT)
1	7/23	204	382	17:10:15 - 17:25:30
2	7/23	204	383	18:50:15 - 19:04:15
3	7/23	204	384	20:36:15 - 20:47:15
4	7/26	207	427	20:43:30 - 20:54:30
5	7/28	209	447	06:56:00 - 07:01:00
6	7/28	209	454	18:05:45 - 18:18:30
7	8/3	215	542	21:35:30 - 21:46:30
8	8/6	218	584	17:56:30 - 20:10:00
9	8/9	221	626	18:22:50 - 18:39:40
10	8/9	221	627	20:03:25 - 20:17:15
11	8/9	221	628	21:49:00 - 22:01:15
12	8/23	235	628	21:04:40 - 21:18:20

Table 5-5. SMMR Passes to Test Algorithm Revisions

Item	Date	DOY	Rev ^a	Time Span (GMT)	Comments
1	9/25	268	1298A	18:25 - 18:42	} GOASEX area passes used in "tuning" Wentz geophysical algorithm. All were studied in previous workshops.
2	9/13	256	1120D	7:57 - 8:07	
3	9/14	257	1135D	9:07 - 9:29	
4	9/11	254	1094A	11:53 - 12:04	Atlantic pass of high wind speeds.

^aA = Ascending; D - Descending.

2. Geophysical File Development

Since an ETG objective was to evaluate additional geophysical algorithms, data were run through several new algorithms for the JASIN workshop. The following descriptions present changes made in the Wentz and Wilheit cases, and discuss the different approaches in the other cases.

a. Wentz Algorithm. The Seasat-JASIN version of the SMMR Non-Linear Geophysical Algorithm was adjusted to optimize environmental parameter retrievals for three North Pacific passes analyzed during the SMMR Mini-Workshop II. In an attempt to improve overall SMMR performance, biases for 10 brightness temperature channels along with 10 emissivity parameters were estimated by performing a least-squares fit to a data base of instrument and surface observations. The instrument data consists of 10 brightness temperatures on grid 1 cells derived from GOASEX passes 1135, 1120, and 1298. These cells were selected on the basis of available surface truth, of which SASS winds are a part; thus only the outermost two columns of the SMMR swath were used. The corresponding surface data set contains sea-surface temperatures derived from a National Marine Fisheries Service (NMFS) map, SASS wind speeds, water vapor fixed to Mini-Workshop II values, and preselected cloud-free cells. The cloud-free cells were identified by examining the liquid water content computed from 37-GHz H-pol T_B , along with wind, SST, and water vapor, for all candidate cells. The resulting population distribution of liquid water stratified by 0.002-g/cm^2 intervals for 133 cells is shown in Figure 5-1. It may be assumed that cloud-free conditions are by nature prevalent; thus the cells belonging to the mode of the distribution were said to be cloud-free. Since the uncertainty on the liquid water estimated (based on uncertainties of 1 K on T_B and SST, 1.5 m/s in wind, and 0.2 g/cm^2 in water vapor) is 0.004 g/cm^2 , which is very close to the standard deviation of the distribution, the number of cells most probably free of liquid was 84 cells, or 63 percent of the population, in the neighborhood of the mode. These data were weighted according to uncertainties of 1 K in T_B , 1 K in SST, 5 cm/s in SASS-determined friction velocity, and 10 percent in water vapor. All 84 cells were assumed to contain no liquid water.

Estimates of biases in T_B derived from the data described above are given in Table 5-6. These biases tend to be unreasonably large in the sense that it is not likely that they have their source in the surface truth or in the geophysical algorithm. The estimated emissivity parameters, or $\Delta\epsilon/\Delta U^*$, for each channel are essentially the responses of surface emissivity to wind. Examples of the resultant variation in emissivity for 10.7-GHz H-pol and 37-GHz H-pol with friction velocity are shown in Figures 5-2 and 5-3.

These results indicate that 37-GHz H-pol has a greater sensitivity to wind than does 10.7-GHz H-pol. This suggests that, on a relatively cloud-free cell, the 37-GHz H-pol channel is a better indicator of wind than the 10.7-GHz H-pol. In fact, estimates obtained for all channels show that wind sensitivity tends to increase with frequency for the H-pol with relatively mild and flat response for the V-pol (see Figure 5-4).

In summary, the estimated biases in the T_B 's given in Table 5-6 seem to be unreasonably large, indicating that they probably originate in either the radiometric calibration algorithm or the antenna pattern correction algorithm, or

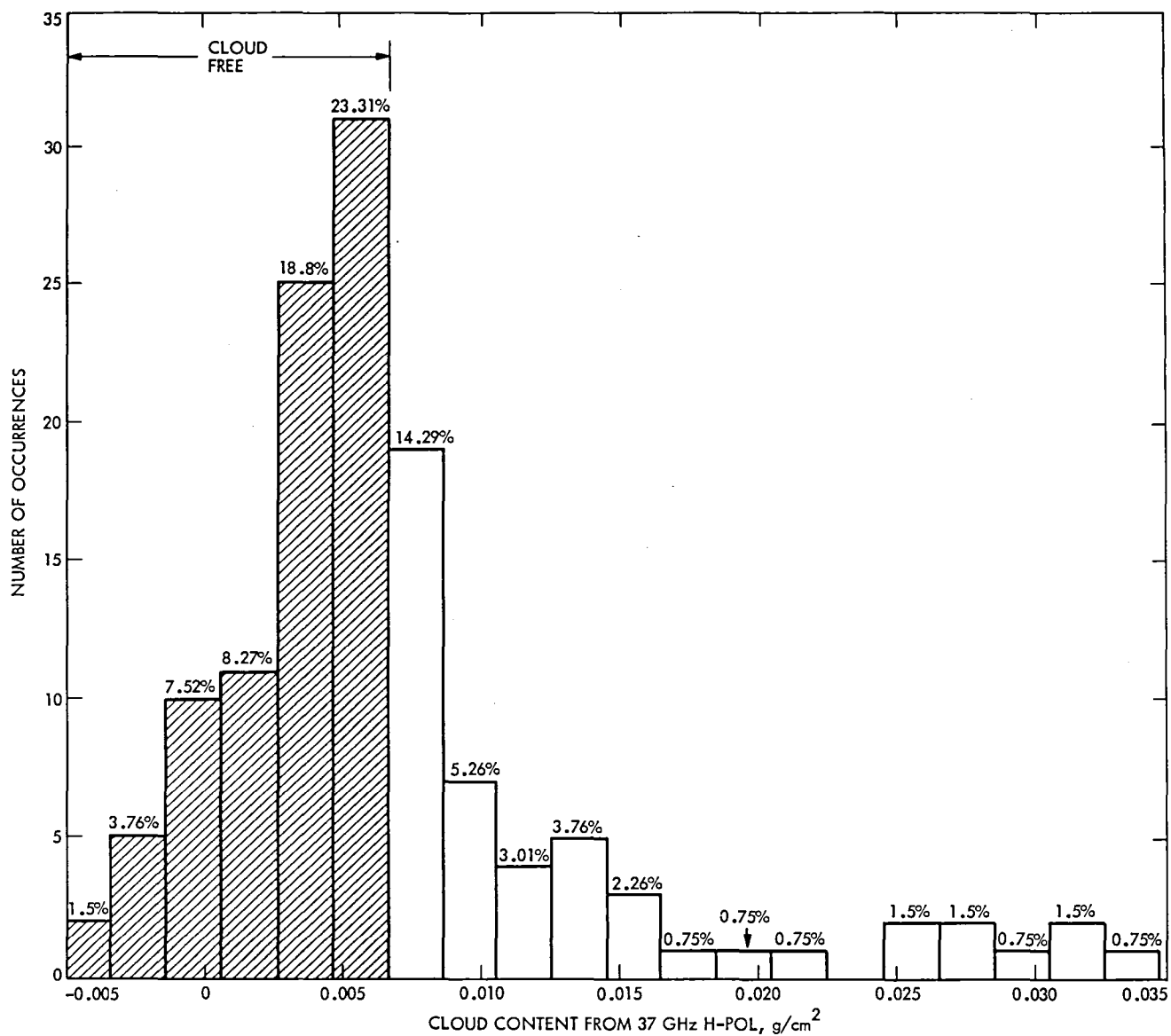


Figure 5-1. Distribution of Cloud Content for GOASEX Passes

Table 5-6. Biases (K) Added to APC T_B 's in Wentz Algorithm

Frequency, GHz	Pol V	Pol H
6.6	1.89	-3.37
10.7	7.02	5.64
18	12.21	5.06
21	3.79	-5.50
37	8.25	4.32

both. Also, this analysis predicts a greater change in emissivity with wind for the high-frequency channels than earlier expected. Thus, SMMR wind retrievals should be best for scenes that contain little or no liquid water.

b. Wilheit Algorithm. The changes in the Wilheit algorithm were minor. The geophysical parameter biases of +14 K for SST, -8 m/s for wind speed, and 0.025 g/cm² for columnar water vapor density used in the Mini-Workshop II were removed. The branch of the algorithm for wind speeds greater than 7 m/s was used for all data (as in the Mini-Workshop II). The brightness temperature inputs to the Wilheit algorithm had the Wentz biases of Table 5-6 added to provide a common input for both geophysical determinations.

c. Rosenkranz Algorithm Description. Given a set of radiometric measurements a_{jmn} , where index j denotes the radiometer channel number (1 to J), and m and n are spatial indices, the most commonly used method of estimating the corresponding geophysical parameters \hat{P}_{kmn} has historically been to apply a linear operator D :

$$\hat{P}_{kmn} = \sum_{j=1}^J D_{kj} (a_{jmn} - \bar{a}_j) + \bar{P}_k$$

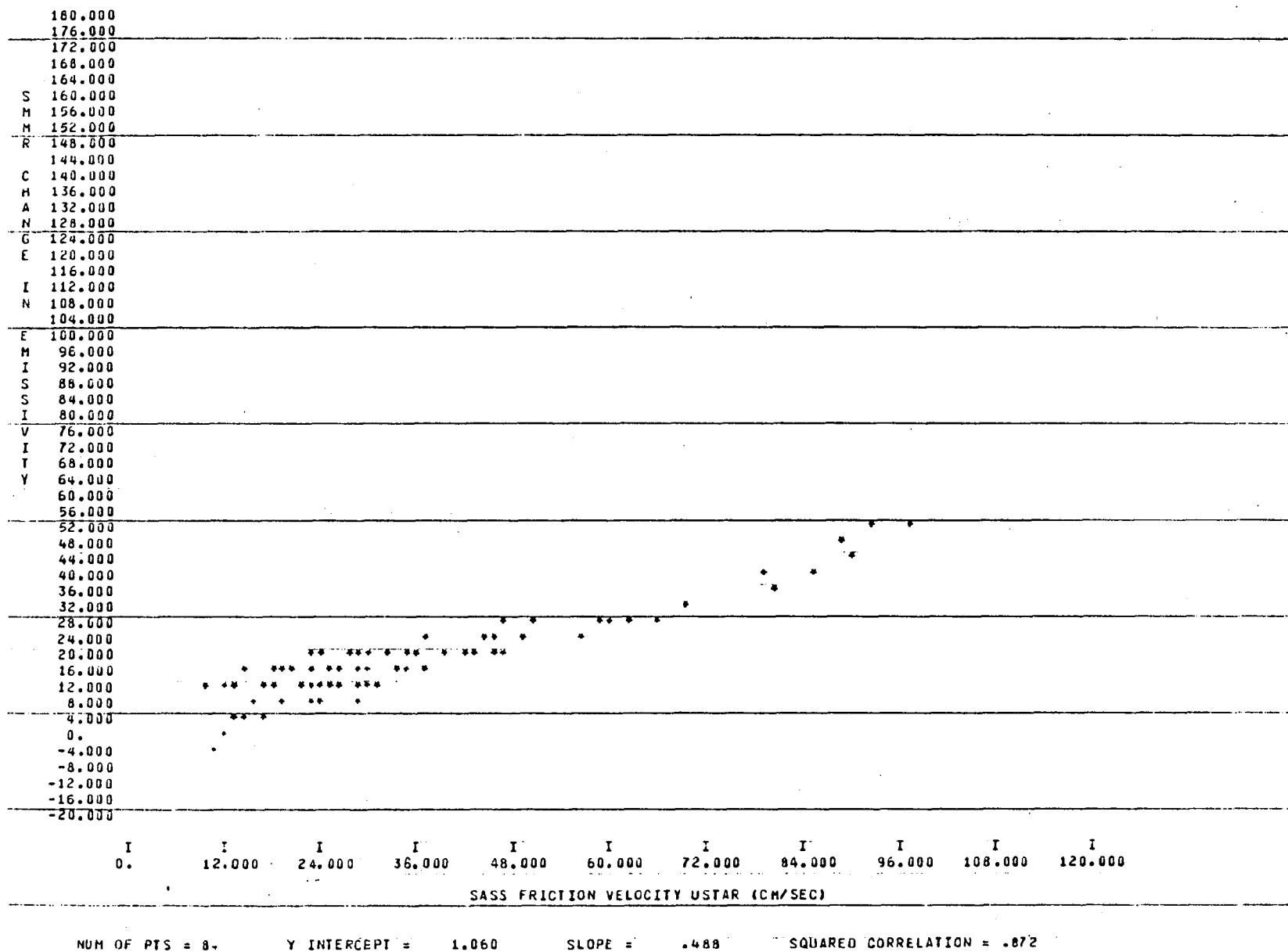


Figure 5-2. SMMR Wind Speed Emissivity vs SASS Friction Velocity for 10.7-GHz H-Pol

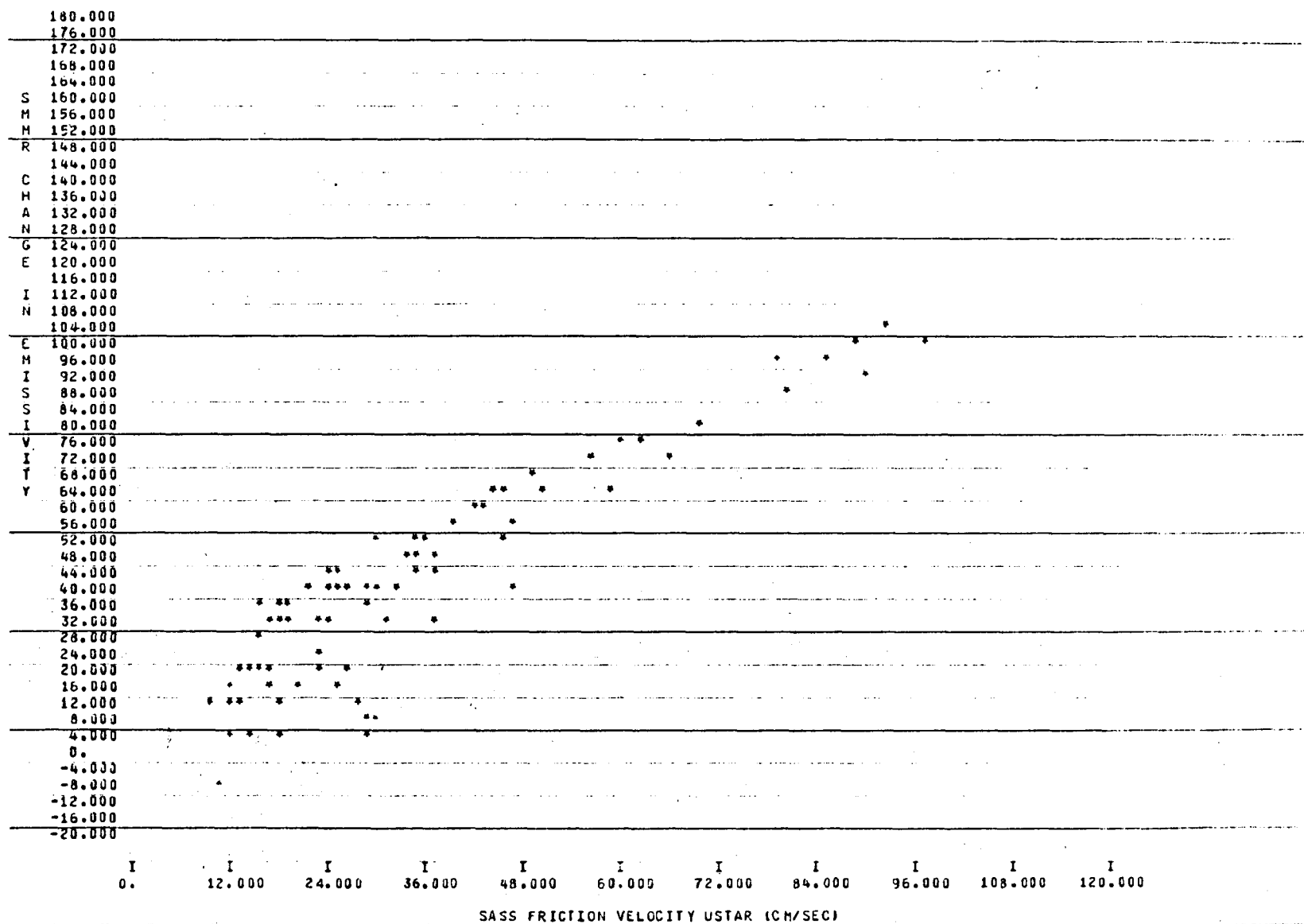


Figure 5-3. SMMR Wind Speed Emissivity vs SASS Friction Velocity for 37-GHz H-Pol

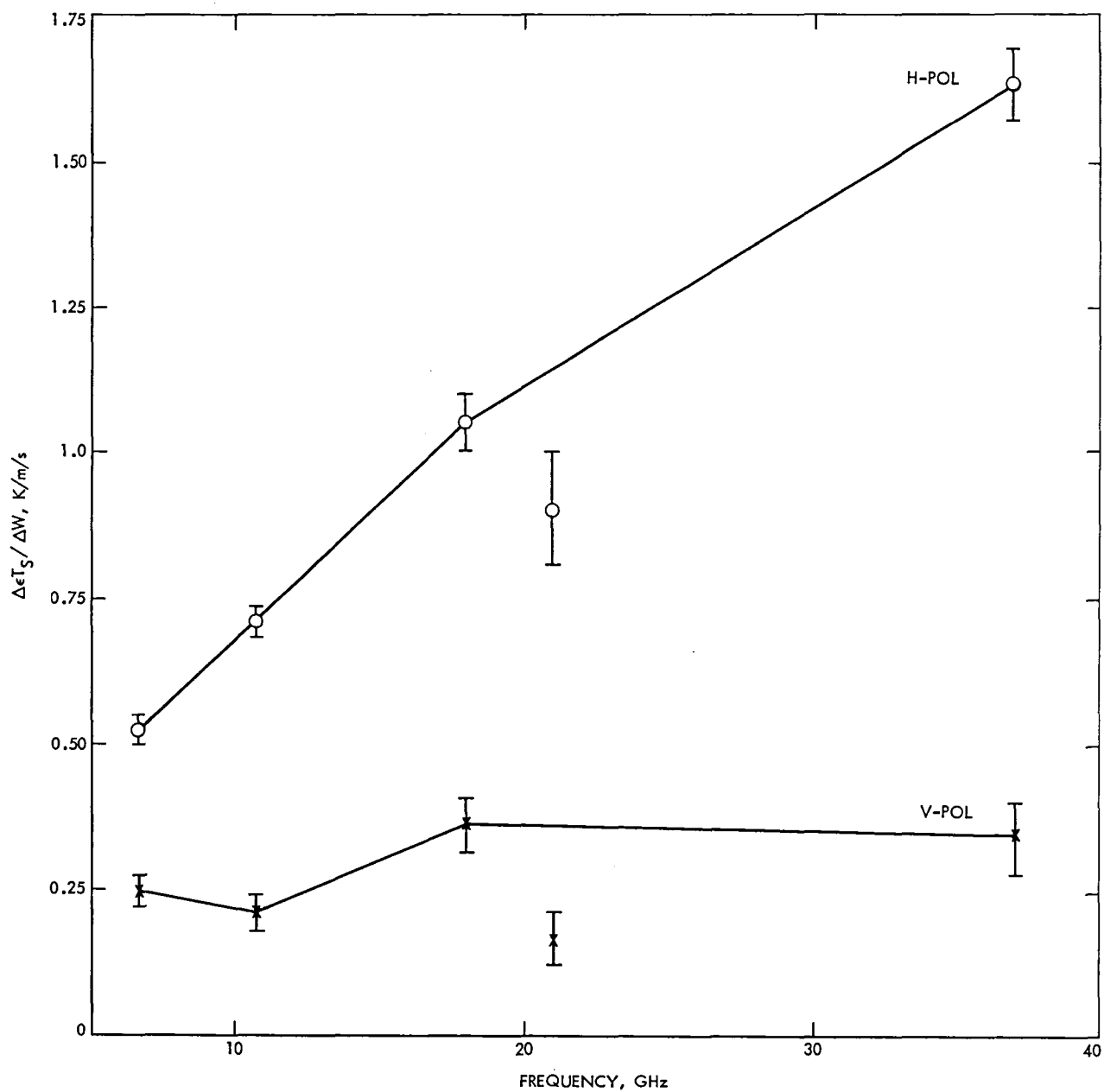


Figure 5-4. T_B Sensitivity to Wind vs Frequency

This method is not directly applicable to SMMR data because it implicitly assumes that the measurements are spatially commensurate, whereas the SMMR resolution and sampling rate vary with channel. The cell formatting of SMMR data is an attempt to circumvent this difficulty by providing spatially commensurate weighted averages of the measurements on four different grid sizes. However, the commensurability is not complete, since it is possible to lower the resolution of the short wavelength measurements but not to improve the resolution at the long wavelengths.

Commensurability of the measurements is obtained by transformation to a representation $A_{j\mu\nu}$, where μ and ν are spatial frequency indices. Then a linear estimate of the geophysical parameter coefficients is

$$\hat{P}_{k\mu\nu} = \sum_{j=1}^{J_{\mu\nu}} D_{kj\mu\nu} A_{j\mu\nu}$$

Although this equation has the same structure as the previous one, this operator D is in fact much more powerful since it is allowed to depend on the indices μ and ν . If the coefficients $D_{kj\mu\nu}$ are chosen to minimize the rms error in \hat{P}_k , then they are zero for $j > J_{\mu\nu}$, where $J_{\mu\nu}$ defines the boundary of the measurements on a graph of channel versus spatial frequency.

For the JASIN workshop, the measurements used as input to the algorithm were cell temperatures at the highest resolution available at each frequency (with the exception of 37 GHz, for which a 54-km resolution was used). A baseline value of brightness temperature, computed theoretically for the associated Earth incidence angle θ , was subtracted from each measurement before the measurements were Fourier transformed. The definition of the transform was

$$A_{j\mu\nu} = \frac{1}{2M_j^2} \sum_{n=0}^{2M_j-1} \sum_{m=0}^{M_j-1} \left(a_{jmn} - \bar{a}_j(\theta) \right) \cos \left(\pi\mu(m+1/2)/M_j \right) e^{-i\pi\nu(n+1/2)/M_j}$$

where M_j^2 is the number of cells in each block for channel j . Two blocks were transformed at a time, thus the higher limit on n . The implied symmetry of the cosine transform reduces smearing at the sides of the parameter fields (though not at the ends). The retrieved parameter coefficients were inverse transformed to 54-km size cells. This is approximately the resolution of wind speed, water vapor, and liquid water, but the resolution of temperature is limited by the 10.7-GHz cell size to ~100 km.

Due to the high occurrence of 6.6-GHz radio frequency interference on ascending passes over the JASIN area, it was necessary to process them in a special manner. Normally, all ten channels are used to retrieve parameters, but for the ascending JASIN passes an eight-channel retrieval was used, excluding the 6.6-GHz data entirely.

It has been noted elsewhere that there are discrepancies between theory and measurement for SMMR. Constant offsets were added to the parameters to compensate for these discrepancies. These offsets were determined from a comparison of Rev 1135 in the vicinity of weather ship Papa with surface truth catalogued in the first Seaset GOASEX report. Separate offsets were obtained for the 10- and 8-channel D operators.

Figure 5-5 shows a comparison of wind speed retrieval using the Rosenkranz algorithm with buoy and ship measurements in the JASIN area, where the eight-channel operator was used for ascending passes and the ten-channel operator for descending passes. Data points with rain rates >0.8 mm/h were excluded. The error statistics are: mean -1.1 m/s, standard deviation 1.8 m/s with ten channels; mean -3.9 m/s, standard deviation 2.0 m/s with eight channels. It appears that the offset for the eight-channel retrieval was inaccurately determined.

Plotted in Figure 5-6 are comparisons of retrieval versus radiosonde-measured water vapor content, for both the JASIN area and the tropical Pacific. No difference in performance was found between the ten- and eight-channel operators, but there is a clear tendency to underestimate high water vapor contents. This underestimate is ascribable to the definition of the operator D at a baseline water vapor content of 2 g/cm^2 . In the tropics, with vapor $\approx 4 \text{ g/cm}^2$, the incremental sensitivity of brightness temperature to water vapor is reduced by the high opacity of the atmosphere.

d. SMMR-SASS Algorithm. The SMMR-SASS combined geophysical algorithm processes SMMR brightness temperatures (T_B 's) and SASS backscatter coefficients (σ° 's) to improve overall environmental parameter retrievals. In particular, the SMMR water channels (18, 21, and 37 GHz) are used to correct SASS σ° 's for atmospheric attenuation and thus improve SASS wind estimates, while SASS winds assist SMMR by providing separability between SST and wind effects. The SMMR and SASS sensor files are read in a simultaneous manner so that T_B 's and σ° 's are colocated for attenuation correction purposes and forward and aft beam σ° 's are colocated for pairing and wind vector determination. Then the combined geophysical processing is done to produce wind (w), wind direction (X), SST (T), water vapor (V), and rain rate (R) in one step without looping between sensor inputs and geophysical outputs.

Comparisons of SMMR winds to SASS winds were done for the three GOASEX passes (1135, 1120, and 1298) used for T_B bias and emissivity determinations (see Subsection a. Wentz Algorithm) and for pass 331 over hurricane Fico. Figure 5-7 is representative of wind retrievals for a fair weather pass condition for which SMMR is expected to perform best, for column 1 on grid 1 for Rev 1135. SMMR-SASS winds compare well within 1.5 m/s rms over much of the pass with anomalous departures as large as 8 m/s rms for 4 cells, which contain large amounts of liquid water ($>0.02 \text{ g/cm}^2$). Note that this region is also accompanied by erratic and most likely erroneous sea-surface temperature retrievals. The water vapor compares favorably with two radiosonde reports from weather station Papa and Johnston Island, but may also be suspect over the four rain cells mentioned above. The Fico pass (Figure 5-8) shows that the SMMR-SASS winds track each other quite well but disagree by 3 m/s bias on the open ocean flanks of the hurricane. As observed for pass 1135, the greatest departures occur when the liquid water exceeds 0.02 g/cm^2 near the eye of the hurricane.

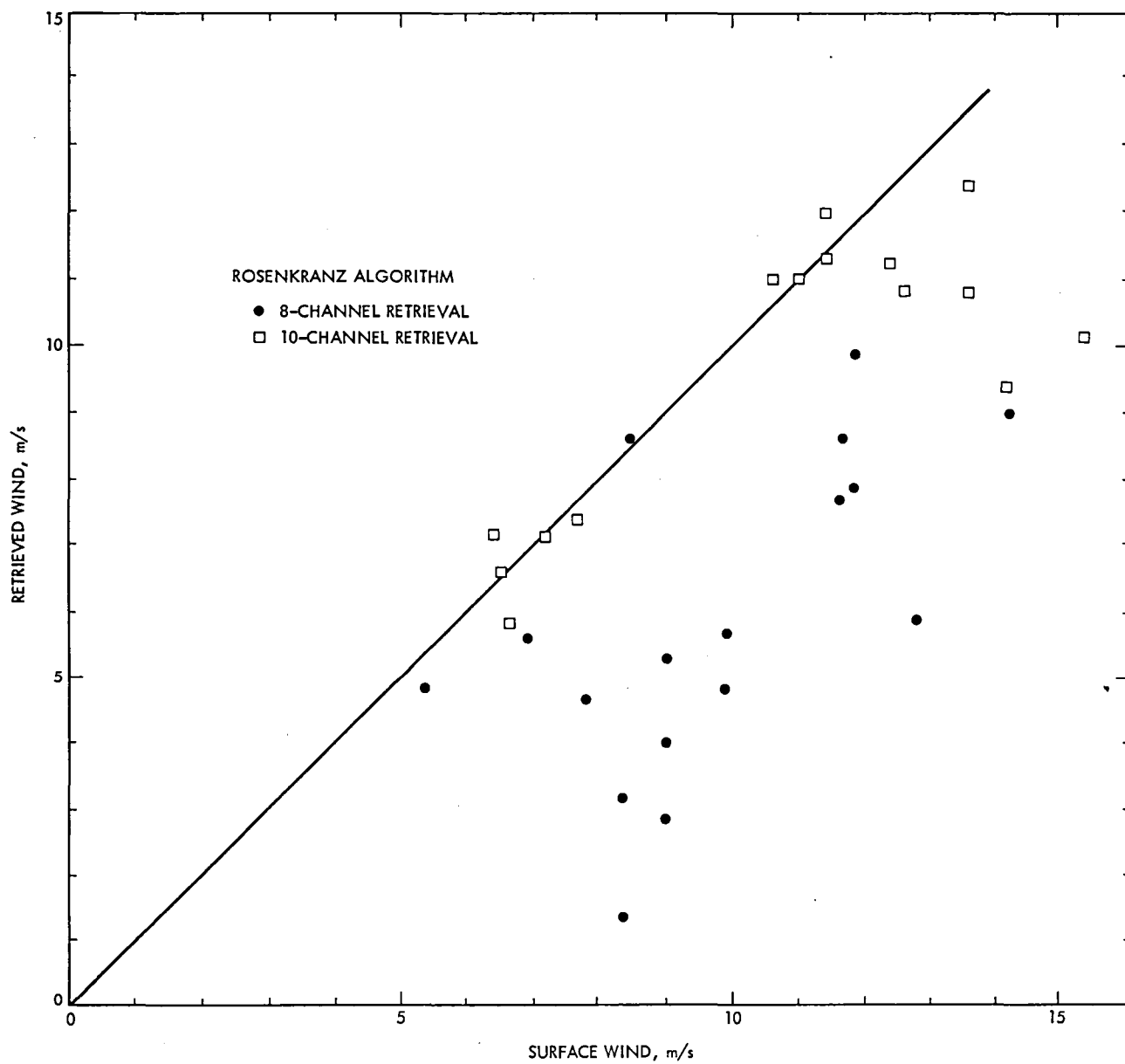


Figure 5-5. JASIN Wind Speed Comparisons - Rosenkranz Algorithm

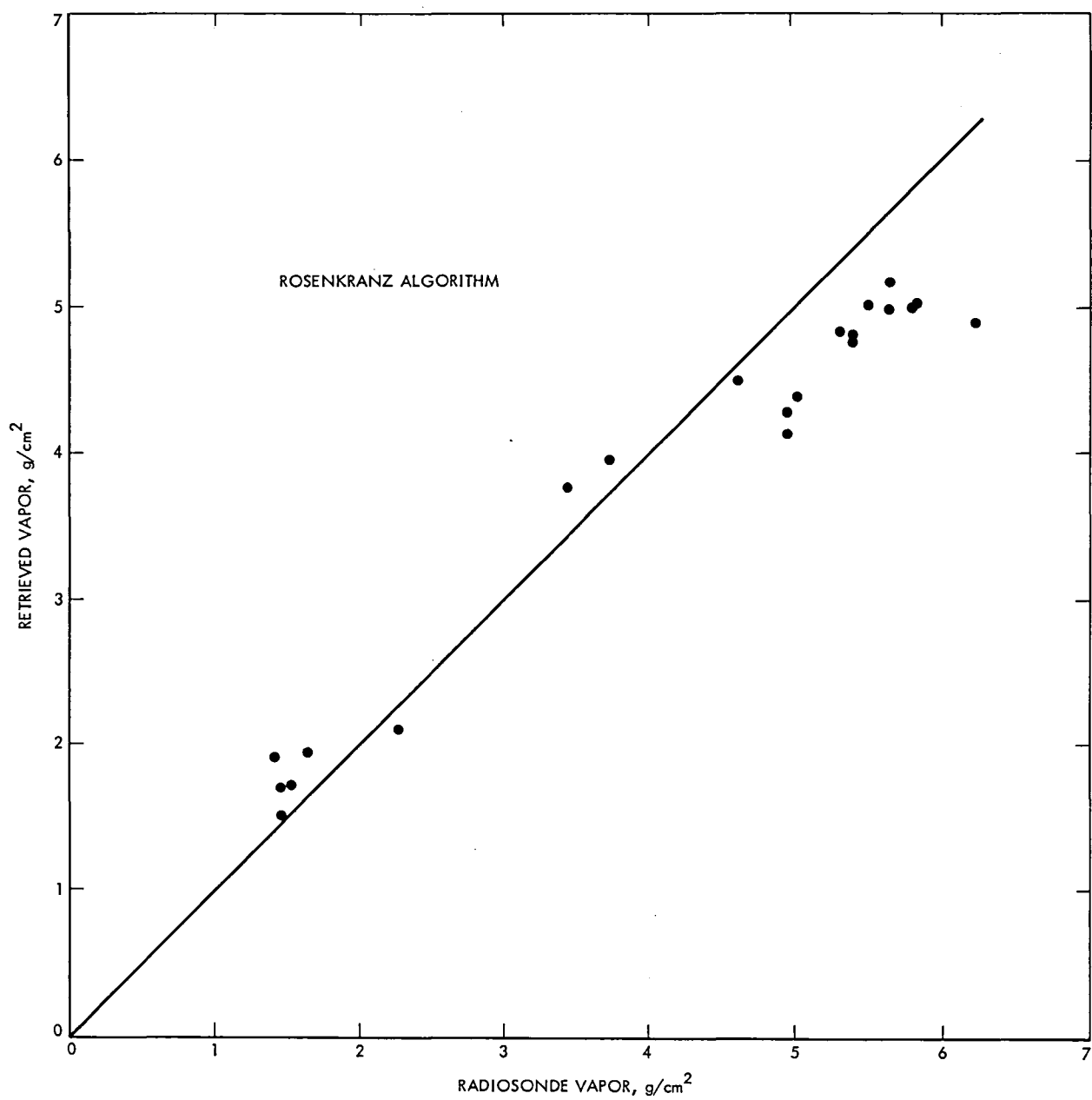


Figure 5-6. Water Vapor Comparisons - Rosenkranz Algorithm

This Page Intentionally Left Blank

This Page Intentionally Left Blank

REMOTE SENSING SYSTEMS
 SMMR-SASS REV 331 GRID 1 COL 2
 ROW 1 THRU 28 BEGIN TIME 17225741

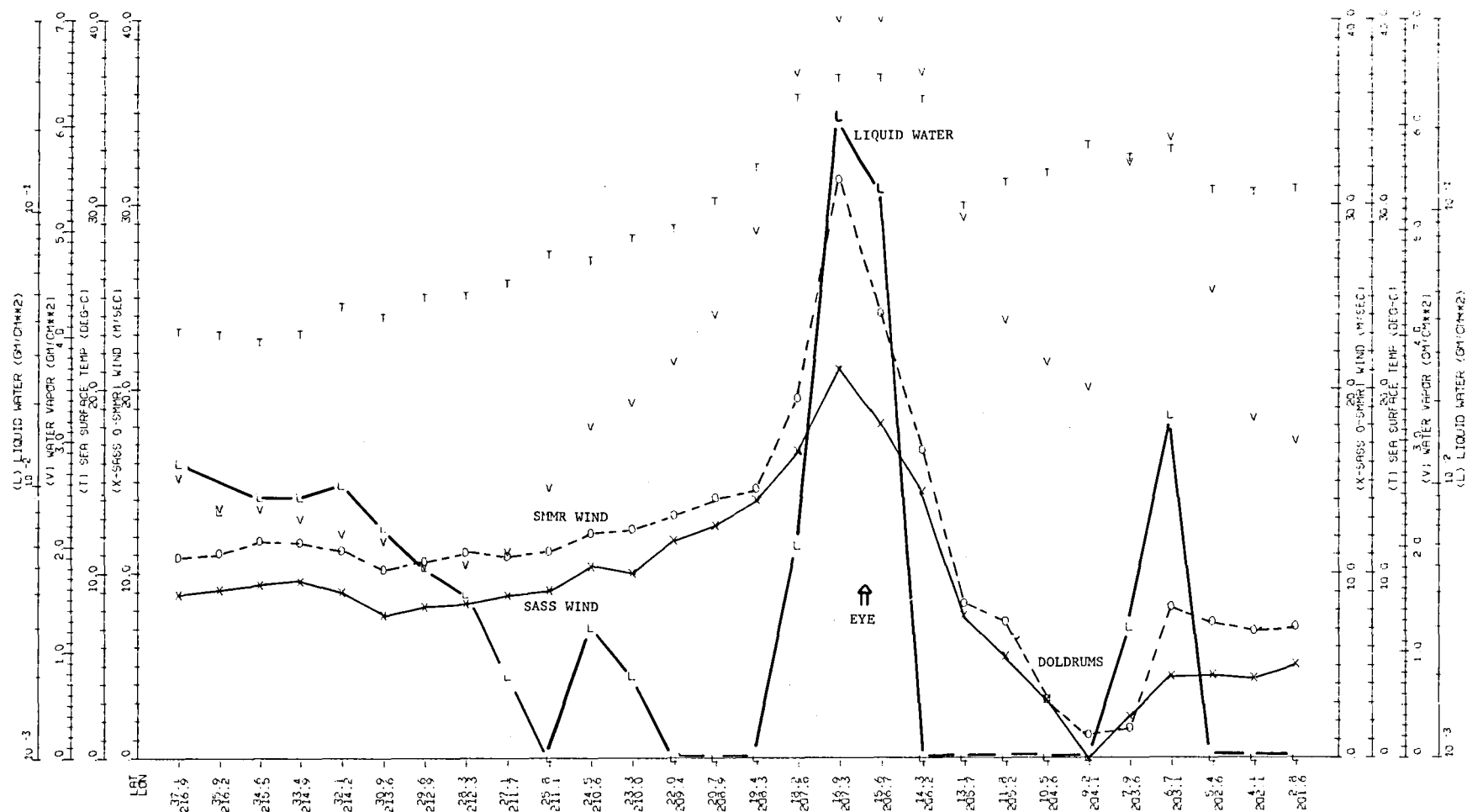


Figure 5-8. SMMR-SASS Geophysical Retrievals for Rev 331 (FICO)

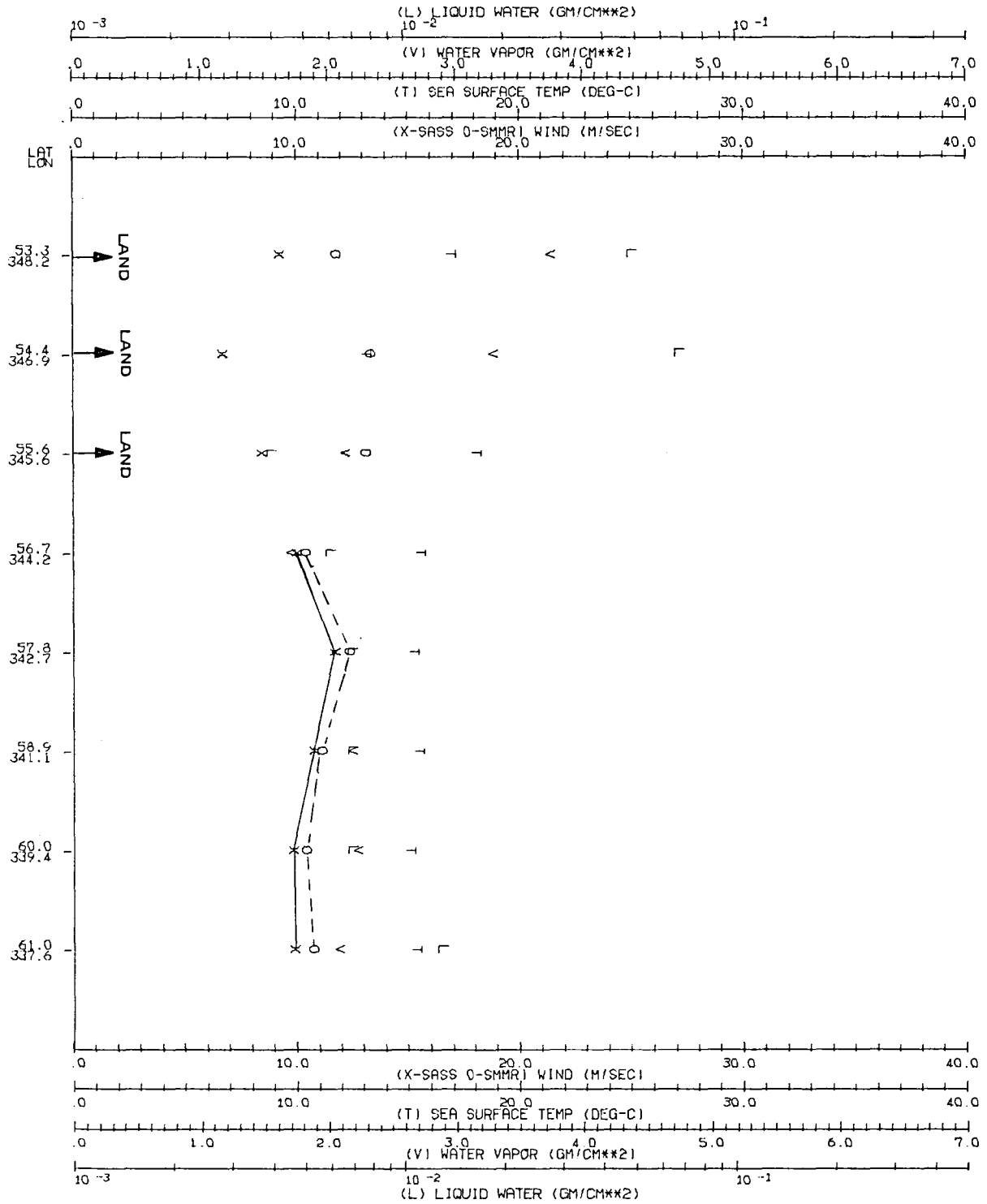
Similar behavior is exhibited on various JASIN phases (see Figures 5-9 and 5-10) in that SMMR-SASS winds track but show pass-dependent biases ranging from 0 - 3 m/s. As expected, overall retrievals are degraded when large amounts of liquid water are present. Preliminary results indicate that a threshold of 0.02 g/cm^2 marks the transition between good and poor environmental parameter estimates.

As described above, SMMR-SASS SSTs are derived from SASS rather than SMMR-inferred winds. Therefore, any differences between SMMR-SASS and SMMR SSTs may be attributed to the difference between the SMMR and SASS winds. Comparisons between the differences of SMMR-SASS and SMMR SSTs with respect to the difference of SMMR and SASS winds over the JASIN Intensive Area (JIA) show that this is, indeed, the case (see Figure 5-11). These results suggest that a 4-m/s overestimate of SMMR wind caused a 3 K underestimate of SST. This is a significant effect, particularly when one considers the magnitude of the pass-dependent SMMR wind biases over JASIN. Though the sensitivity of SST retrievals to wind requires further investigation, these preliminary findings indicate that, in the absence of other error sources, a 1.3-m/s knowledge of wind is required to estimate SST to within 1 K.

e. Bierman Algorithm. The Bierman algorithm is identical to the Wentz algorithm in its geophysical model, and differs only in the method of solution for the geophysical variables. The Wentz algorithm takes all channels on grid 1 to solve for SST, then takes all channels except 6.6 GHz on grid 2 to solve for wind speed, then takes all channels except 6.6 and 10.7 GHz on grid 3 to solve for vapor, cloud, and rain. The Bierman algorithm takes one of three regions, containing one, two or four grid 1 cells; four, six or nine grid 2 cells; and nine, fifteen or twenty-five grid 3 cells, respectively, and solves simultaneously for all geophysical variables at all grid 3 positions within each region, using all frequency channels on their intrinsic resolution grid; i.e., 6.6 GHz is on grid 1, 10.7 GHz on grid 2, and 18, 21, and 37 GHz on grid 3. In addition, the correlation in the retrieval variables is taken into account. This primarily affects SST, since the SST at any grid 3 position is highly correlated with nearby positions.

This approach takes into account the measurement structure more correctly than the Wentz algorithm. Note that in the solution for any region, the frequencies are effectively weighted by the number of measurements, resulting in 6 to 9 times more emphasis on 18, 21, and 37 GHz than on 6.6 GHz. If the geophysical model and T_B 's (as corrected by the Wentz biases) are correct, this is the proper procedure. However, if errors exist, the SST and wind speed determinations will suffer due to the deweighting of the channels most sensitive to these parameters. Thus, any systematic differences between the Wentz and Bierman algorithms may be useful diagnostic tools.

Figure 5-9. SMMR-SASS Geophysical Retrievals for Rev 791



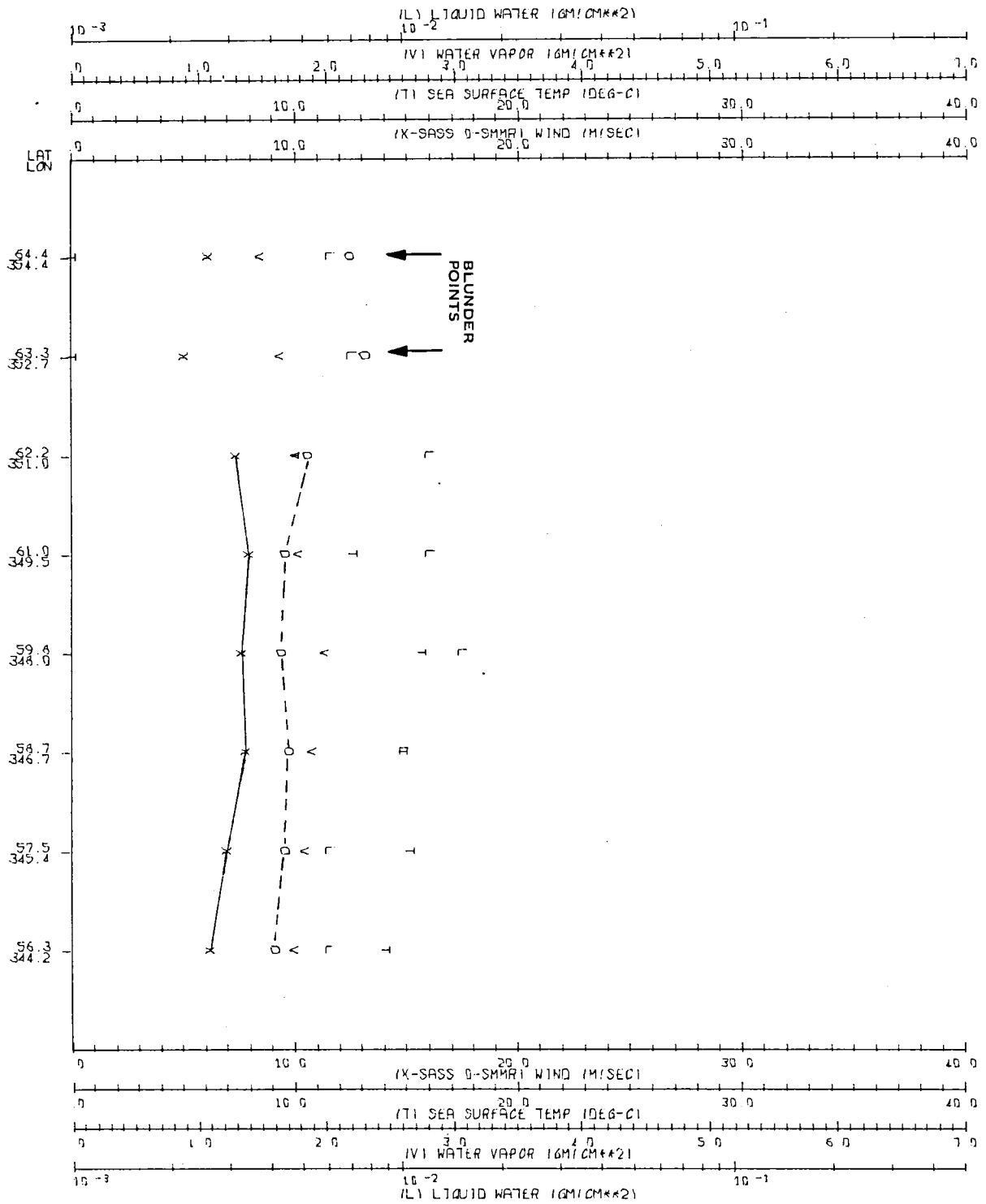


Figure 5-10. SMR-SASS Geophysical Retrievals for Rev 599

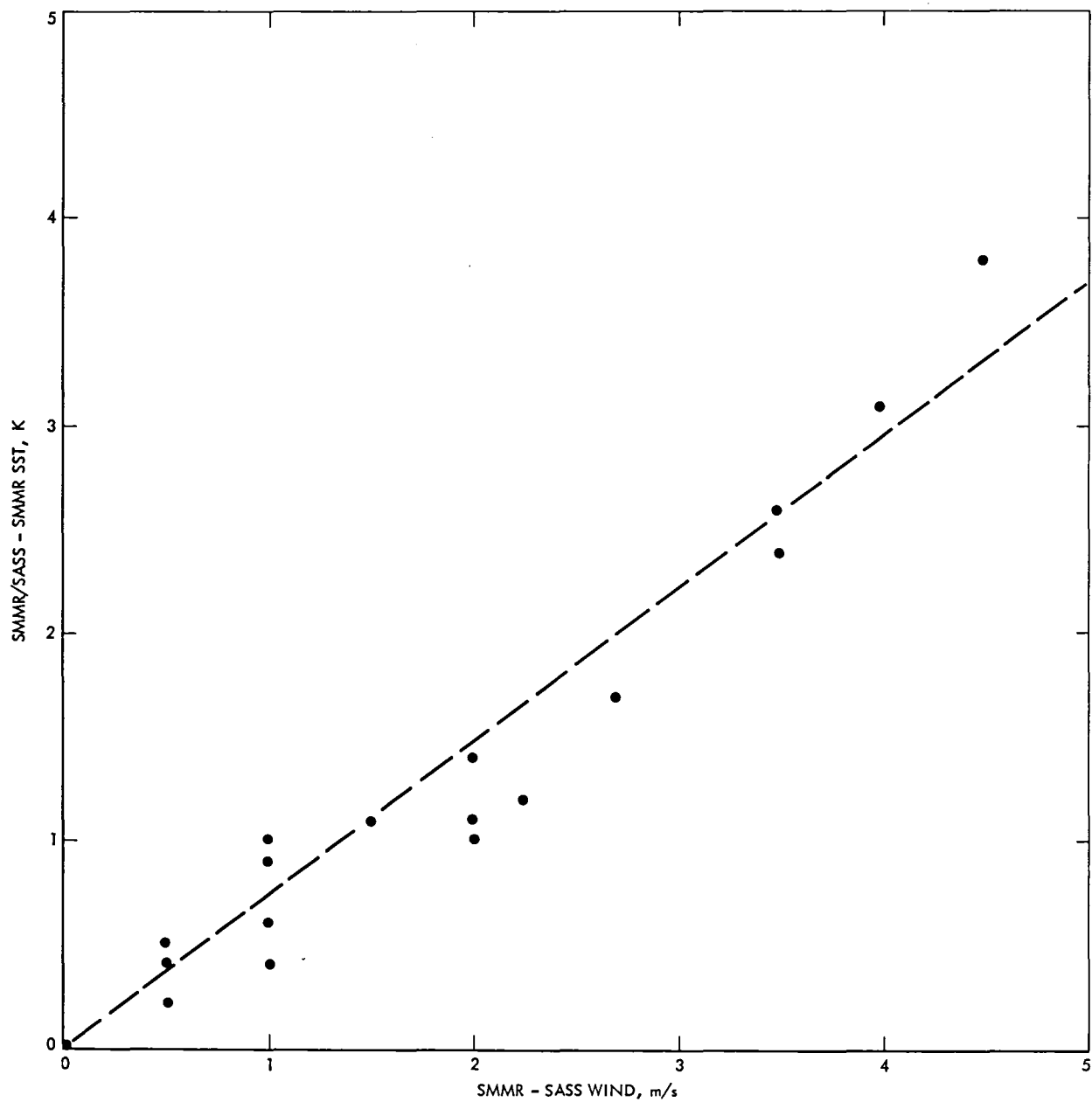


Figure 5-11. Difference Between SSMR-SASS and SSMR SST vs Difference Between SSMR-SASS and SSMR Wind

C. ATMOSPHERIC WATER EVALUATIONS

1. JASIN Area Evaluations of Integrated Water Vapor

a. Comparisons for Wentz Algorithm. The surface truth data sets available to the workshop included, in total, 320 radiosonde flights from the JASIN ships for comparison with the 30 selected Seasat revolutions. Many of the radiosonde flights were designed only to reach 500 mbars. Figure 5-12 shows the mean water vapor content of different layers of the atmosphere for each of the data sets. It suggests that the water vapor content above 500 mbars might be estimated to within $\pm 0.2 \text{ g/cm}^2$. However, initial comparisons suggested that the Seasat determinations were at least this good. It was, therefore, decided to limit comparisons to radiosonde flights which reached pressures of 250 mbars or less, and which are launched within $\pm 2 \text{ h}$ of the overpass time. These stringent requirements resulted in the set of 19 comparisons shown in Table 5-7. The mean magnitude of the difference between overpass time and radiosonde launch time was 45 min, the maximum difference being 95 min. Seasat values of the water vapor content were obtained from plots of the Wentz algorithm determinations covering the JASIN area. The actual value used was obtained by linear interpolation between the nearest data points. The difference between the Seasat and in situ values shown in Table 5-7 are plotted against the radiosonde water vapor values in Figure 5-13. There is no obvious relationship.

One point, representing a John Murray flight, has considerably greater difference. Examination of spacecraft and the radiosonde data for this comparison shows no reason for its rejection. It has, therefore, been retained in the statistics.

Table 5-8 summarizes the comparison for each of the ships and for the total set. Except for the one John Murray value, there is no significant difference between the various ships. The overall mean difference of $0.12 \pm 0.12 \text{ g/cm}^2$ compares well with the estimated accuracy of the radiosonde determinations. Indeed, it suggests that the value of within $\pm 0.2 \text{ g/cm}^2$ represents an overestimate of the error for this data set.

b. Comparisons With Other Algorithms. Only a limited number of revolutions had been processed for each of the other algorithms. This results in a subset of only six comparisons. The mean results are shown in Table 5-9. On the evidence of this small sample, the only significant difference between the algorithms is a negative bias of the Wilheit determinations compared to those of Wentz. A fuller comparison of Wentz and Wilheit algorithms will be made when further revolutions have been processed.

c. Analysis of Effect of Sidelobe Correction. An example of the horizontal distribution of total water vapor is shown in Figure 5-14. A warm front resulted in enhanced values over the JASIN triangle compared to areas to the northeast. The corresponding radiosonde determinations are shown at the corners of the triangle and show good agreement. Time series of such plots would provide very valuable data input to the JASIN experiment. The cost of

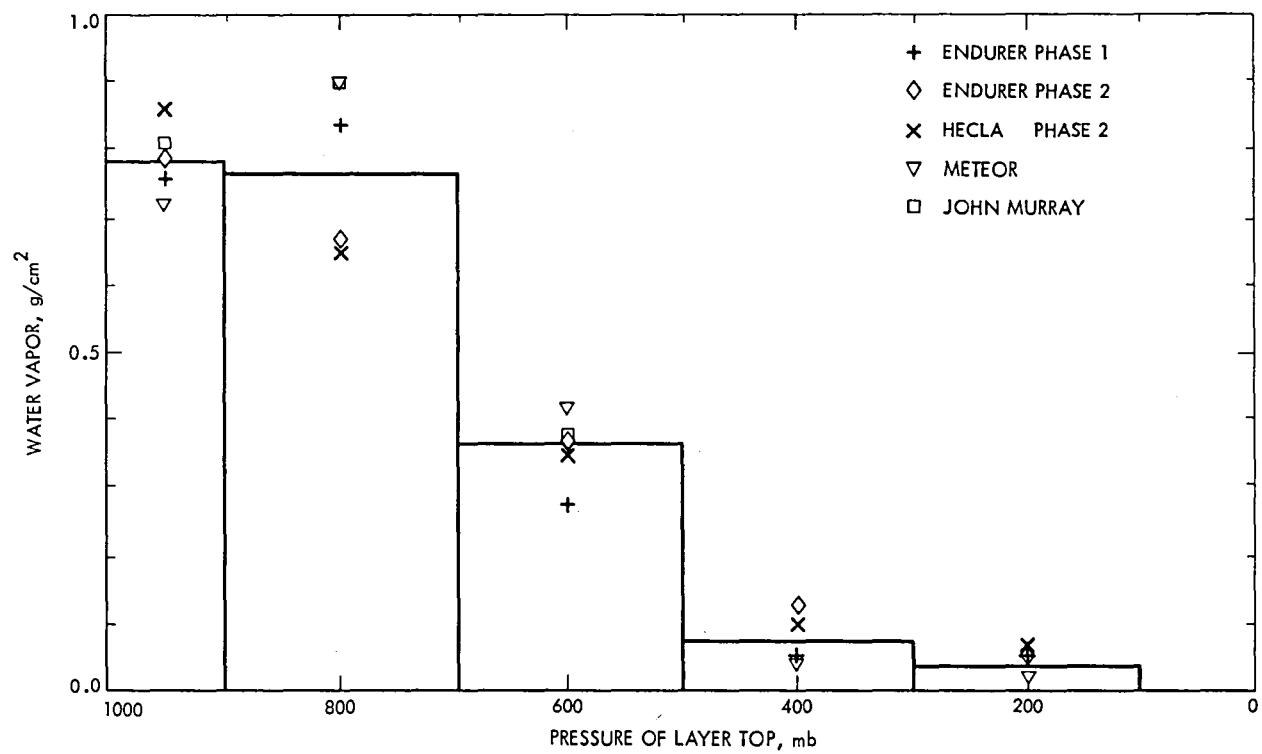


Figure 5-12. Mean Water Vapor Content for Each Atmospheric Layer Calculated From Each Data Set

Table 5-7. Surface Truth (S/T) and Spacecraft (S/C) Determinations of Total Water Vapor Content (Wentz Algorithm)

DOY	S/C Time, GMT	Rev	Flight	S/C Time, GMT	Top Pressure, mbars	S/T Q, g/cm ²	S/C Q, g/cm ²	Difference S/C Minus S/T
219	0622	590	G104	0557	200	1.40	1.50	+0.10
219	2142	599	J083	2143	207	1.40	1.89	+0.49
233	2245	800	H041	2357	235	2.19	2.12	-0.07
233	2245	800	M(*)	234/ 00	200	2.05	2.12	+0.07
234	0653	805	H042	0608	220	1.53	1.81	+0.28
235	2321	829	G140	236/ 0026	130	1.82	1.66	-0.16
235	2321	829	H061	2358	155	1.46	1.70	+0.24
235	2321	829	M(*)	236/ 00	200	1.61	1.73	+0.12
236	0730	834	G141	0557	135	1.50	1.60	+0.10
236	0730	834	H062	0555	215	1.61	1.52	-0.09
236	2250	843	H077	2347	180	2.13	2.05	-0.07
238	2328	872	M(*)	239/ 00	200	2.47	2.58	+0.11
239	2259	886	H098	2358	170	2.79	2.93	+0.14
242	2312	929	H119	2355	195	2.82	3.10	+0.28
242	2312	929	M(*)	243/ 00	200	3.68	3.69	+0.01
244	0022	944	G221	0009	120	1.87	2.10	+0.29
244	2353	958	G238	2359	180	2.01	2.20	+0.19
244	2353	958	H245	0037	190	1.96	2.19	+0.24
244	2353	958	M(*)	245/ 00	200	2.21	2.25	+0.04

KEY TO SHIPS: G = Gardline Endurer, H = Hecla, M = Meteor,
J = John Murray.

* Indicates Meteor Synoptic Report.

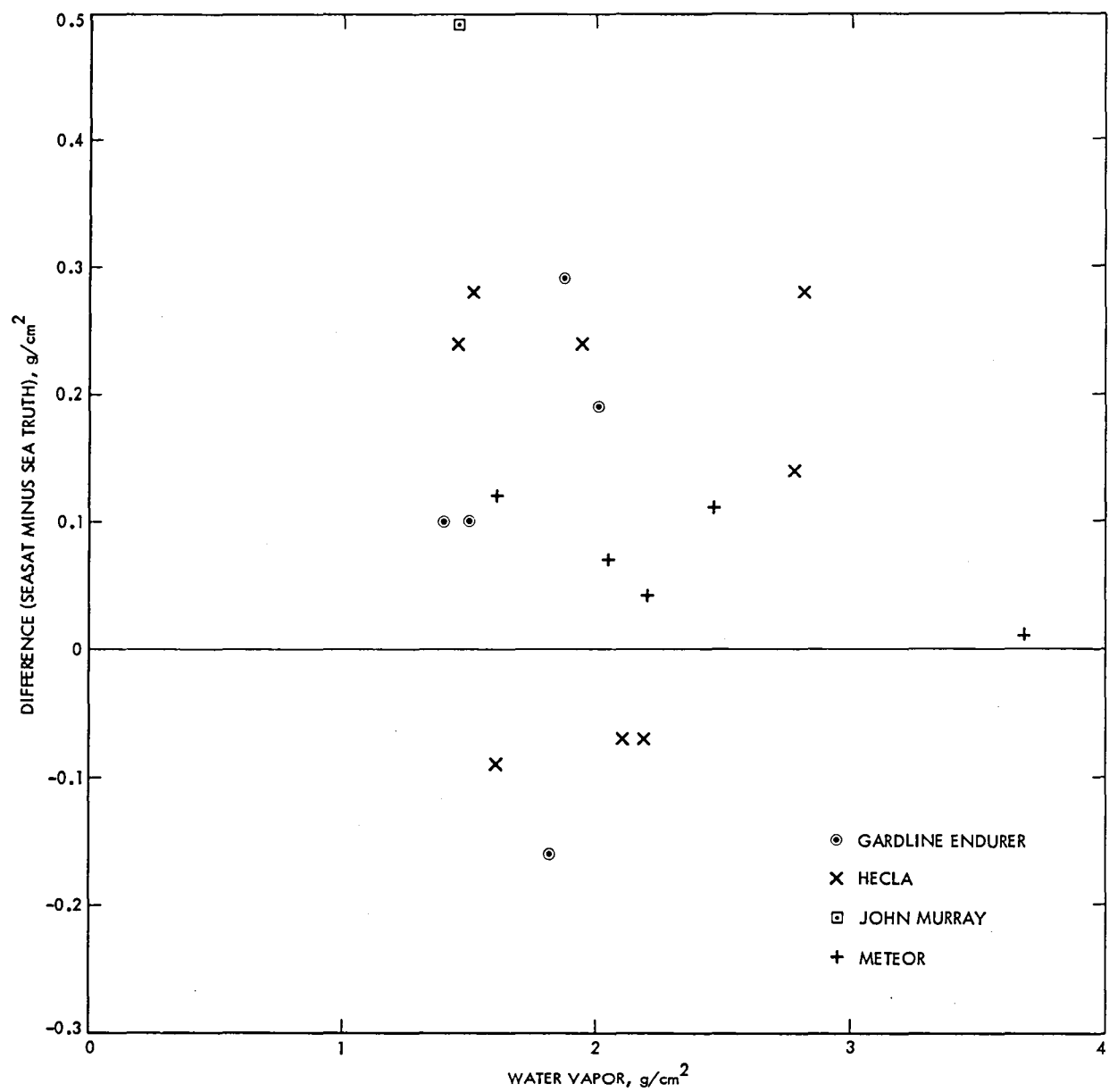


Figure 5-13. Water Vapor Comparisons - Wentz Algorithm

Table 5-8. Difference in Water Vapor Content (Seasat Minus Surface Truth)

Ship	Number of Points	Mean Difference, g/cm ²	Standard Deviation*
Endurer	5	0.10	0.09
Hecla	8	0.12	0.10
John Murray	1	0.49	--
Meteor	5	0.07	0.04
All	19	0.12	0.12

*The standard deviation shown is that of individual measurements from the mean for each set (Wentz Algorithm).

Table 5-9. Comparison of the Different Algorithms for Total Water Vapor*

Algorithm	Mean Difference Seasat - Surface Truth, g/cm ²	Standard Deviation	N
Wentz	+0.18	0.15	6
Wilheit	-0.33	0.15	6
Bierman	+0.14	0.13	6
Rosenkranz	+0.22	0.14	6

*The same six comparisons were used in each case.

5-31

processing further revolutions would be much reduced by ignoring the brightness temperature sidelobe corrections. Figure 5-15 shows the magnitude of the brightness temperature sidelobe corrections for the same revolution and the Wentz algorithm. Over most of the area, the sidelobe corrections are small, particularly so in the JASIN area. Similarly, small differences were found for liquid water. The result of this and two other comparisons shows that for determination of water vapor and liquid water in the JASIN area, there is no need to apply the sidelobe corrections.

The distribution of sidelobe corrections bears a qualitative resemblance to the departure of SMMR SSTs for this revolution from the sea truth. This is quantitatively shown in Figure 5-16, where SST error is plotted against the sidelobe correction to water vapor determinations. For each of three revolutions, the individual points on grid 3 were binned and averaged using increments of 0.1 g/cm^2 of sidelobe correction to water vapor. The error bars give the standard deviation of the mean, assuming that all grid 3 determinations are independent. If this is not true, the error bars should be increased by a factor of 3.

The plot confirms again that the ascending revolution is different. In all cases, the SST error tends to increase with increasing value of the sidelobe correction. It is suggested that this relationship be examined further in investigating the errors in the SMMR SST values which may have been caused by the proximity of land.

2. JASIN Area Evaluations of Liquid Water and Precipitation Predictions

The precipitation which occurred in JASIN was typically very light. Out of the 30 SMMR revolutions, only a few show coincidence between reported precipitation at the ships and SMMR, viz., Revs 355, 432, 929, and 1006.

Table 5-10 gives a summary. During these revolutions, the rain appears to have been of the type called "wide spread" with several ships reporting some form of precipitation. For this situation the Wentz algorithm predicts the rain occurrence very well. Only in one case was an estimate of the rain rate possible. From John Murray rain gauge measurements between 20:00Z and 21:00Z on July 21, we can estimate a rain rate of 0.2 mm/h . Wentz algorithm predicts 0.0 to 0.2 mm/h at the footprints surrounding the ship location.

There are several occasions when ships report light rain or showers close to the time of the overpass and the algorithm does not predict rain, viz., revs 547, 556, 590, 597, and the series on August 21: 790, 791 and 800. For these last three revolutions, the ships report showers, and the Wentz algorithm gives liquid water content of 0.017 , 0.008 , and 0.010 g/cm^2 , respectively, which is less than the threshold value of 0.05 g/cm^2 used to infer rain. With showery precipitation, the footprints of the SMMR would not be filled with the heavy concentrations of liquid water associated with the convective cloud elements producing the showers. This is an inherent limitation of the SMMR resolution, and is not dependent on the algorithm.

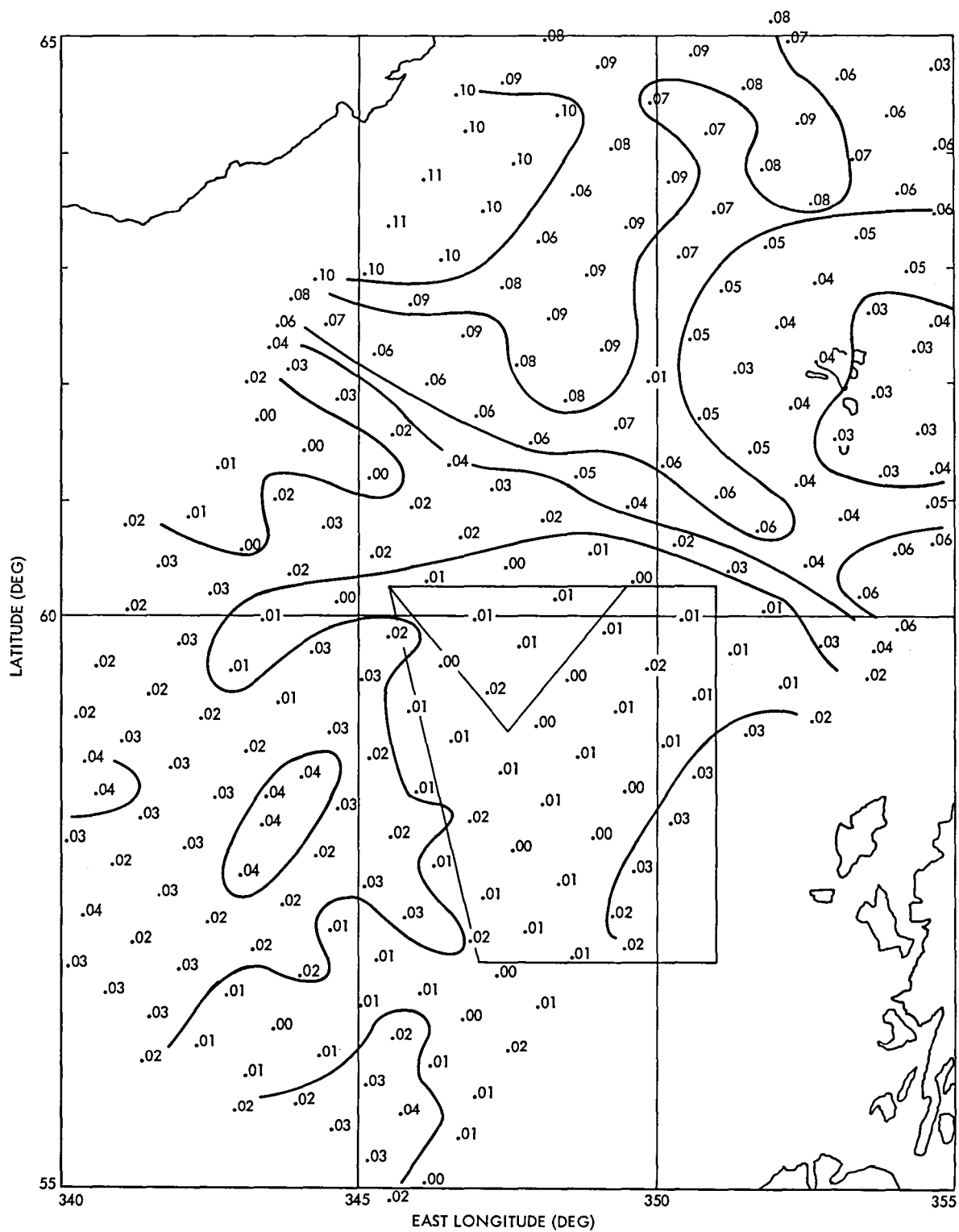


Figure 5-15. Contour Plot of Contribution of Sidelobe Corrections to Water Vapor - Wentz Algorithm

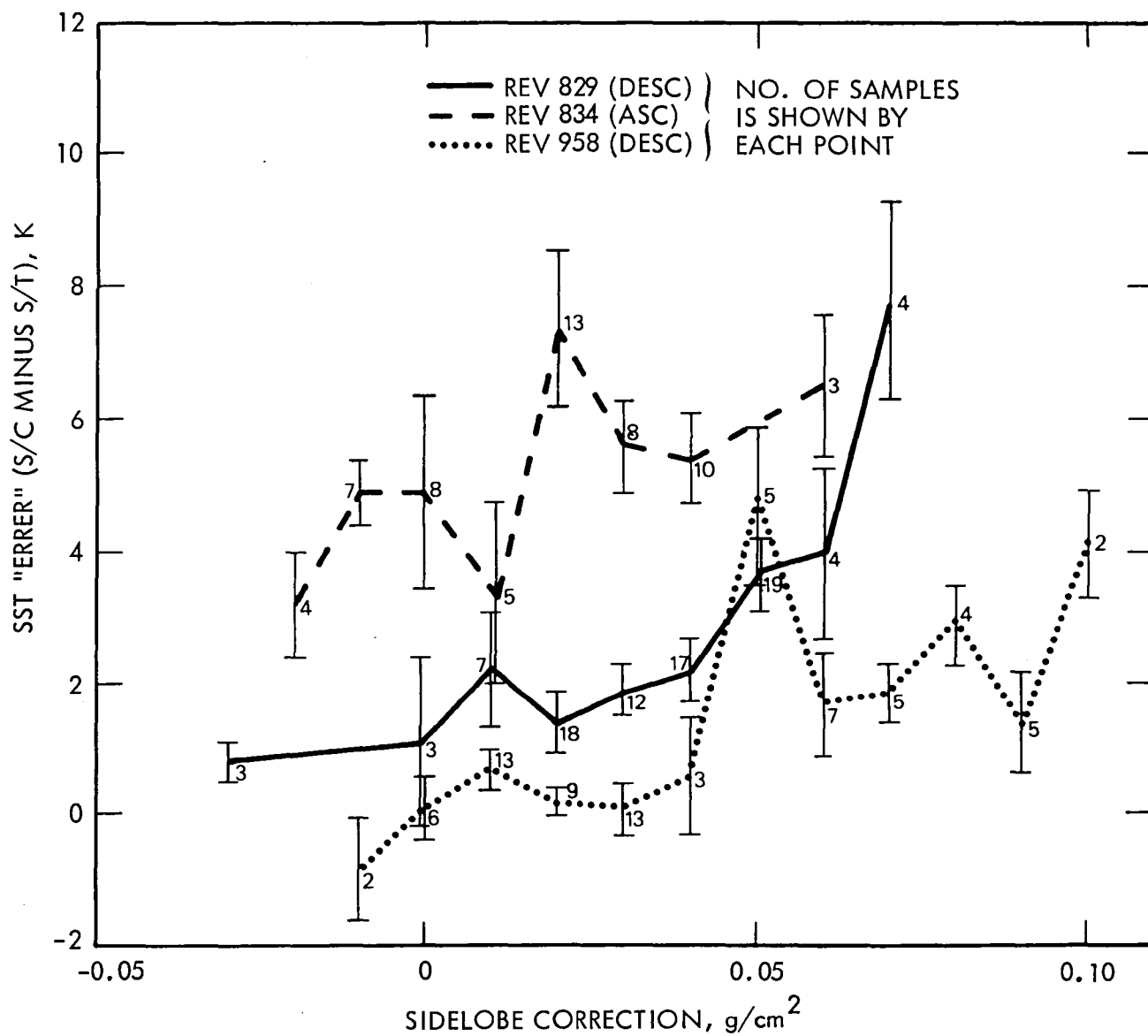


Figure 5-16. Correlation of SST "Error" With Sidelobe Correction

Table 5-10. Precipitation in the JASIN Area During Seasat Revolutions

1978 Date				SMMR on Seasat				Truth from Ship Reports				
Rev	DOY	Mo/Day	Time	X = Yes		Location	ATL a Gauges, mm	Meteor b Radar	Precip. X = Yes	Station	Comment or wwWC	Time
				Wilheit	Wentz							
355	202	7/21	20:29		X	Meteor up to Hecla			X	JMU at NE corner 0.2 mm/h 20-21Z	616 616	20 21
										DIS	656 608	18 24
										TYD	632 636	20 21
										CHA Radar shows belt of heavy rain approx 1 mi to S		
431	208	7/27										
432	208	7/27	05:23		X	Between Meteor Hecla			X	HEC	606 606	06 05
										MET	156	06
										TYD	612 596	05 06
474						Meteor Hecla			X	GEN	∇ ∇	03 04
475			05:30		--				--			
546	216	2/4							X	JMU JMU	615 205	04 05
547	216	8/4	6:15		X	South of triangle						
556	216	8/4	21:36		--		5.0	6:00 to 11:00	X	CHA	626	24
557	216	8/4							X	MET CHA ATL	615 626 609 Stewart's log reports rain	24 24 24
										DIS	Lightning to South	
589	219	8/7					Trace of rain		X	JMU & GEN	∇ East and West	
590	219	8/7	22:13		--				X	GEN	∇'s, SE	06 07
599	219	8/7	21:42	--	--				X	GEN	Drizzle ∇'s, NW	21
632	222	8/10							--	DIS		22
633	222	8/10	06:29	X	X	On West edge			--			
642	222	8/10	21:50		--				X	ATL SHA	603 626	24 24
643	222	8/10							X			
675	225	8/13							X	SHA	622	06

Table 5-10 (contd)

1978 Date				SMMR on Seasat				Truth from Ship Reports				
Rev	DOY	Mo/Day	Time	X = Yes		Location	ATL a Gauges, mm	Meteor b Radar	Precip. X = Yes	Station	Comment or wwWc	Time
676	225	8/13	6:36						X			
718	228								--			
719	228		6:43		--				--			
748	230	8/18	7:21		X	SE towards Scotland			--			
757		8/18	22:44	--	--				--			
758	231	8/19							--			
762			6:48		--							
790	233	8/21							X	PLA	V's	03:30
791	233	8/21	7:24	--	--				X	JMU	V's	07 on horizon
										PLA	V's	03:30, 08-12
800	233	8/21	22:45		--				X	TYD CHA	V's ILR	22:40 20-23
801	234	8/22					} 11.00	14:30 16:30	X	TYD CHA PLA	608 ILR R	00 00 01-08
805	234			--	--							
814	234	8/22							X	} DIS PLA HEC	V V's R	18 20:50 23
815												
829	235			--	--							
829												
833												
834	236	8/24	07:30		--		Trace		X	JMU GEN SHA	V's V IR	08 Seen 12
843	236	8/24	22:51						X	SHA	V's on horizon	24
844												
872					--							
886					--							
929	242	8/30	23:12		X	SE of triangle toward Scotland		10:30 ↓ 19:58	X	HEC TYD W=6 Several Ships	636, 3.6 mm R	23 00-01:45
930												
944					--							
948	244	9/1					--			SHA	V's	06 occasional

Table 5-10 (contd)

1978 Date				SMMR on Seasat				Truth from Ship Reports					
Rev	DOY	Mo/Day	Time	X = Yes		Location	ATL ^a	Meteor ^b	Precip. X = Yes	Station	Comment or wwW ^c	Time	
				Wilheit	Wentz		Gauges, mm	Radar					
949					--								
958	244	9/1			--				X	PLA PLA	612 R	12 10:30- 13:40	
959													
1001	248	9/5	05:41	X	X	S&W of triangle 1 mm/hr	23.0 mm		--				
1002	248												
1005													
1006	248	9/5	08:14		X	SE of Meteor and up toward GEN			X	} HEC GEN SHA PLA	606 616 608 602 612 R	06 09 09 12 09 06-24Z	
1045		9/8											
1048	251	9/8							X		SHA PLA	636 R	06 01:50- 04:45
1049			8:27		X	By Scotland	6.0						
1134									--				
1135					--				--				

^aAtlantis rain amounts are totals over some time interval. For details see Atlantis Cruise Report.

^bMeteor's radar did not always operate when it rained.

^cwwW is World Meteorological organization code: ww = present weather (60's indicate rain, 50's indicate drizzle); W = past weather during last 3 hours (5 = drizzle, 6 = rain).

JMU - John Murray
DIS - Discovery
CHA - Challenger

MET - Meteor
GEN - Guardline Endurer
HEC - Hecla

SHA - Shackelton
PLA - Planet
ATL - Atlantis

V - showers
IR - Intermittent Rain
ILR - Intermittent Light Rain
R - Rain

From the data collected in Table 5-11, an intercomparison in the JASIN area of the Wentz and Wilheit liquid water algorithms can be made. It reveals a nonlinear relationship for values less than 0.12 g/cm^2 (Figure 5-17). The relationship can be expressed as a power function of the form $L_{\text{Wentz}} = a(L_{\text{Wilheit}})^b$. The line in Figure 5-17 is produced with $a = 1.065$ and $b = 1.39$. An intercomparison of the rain algorithms suggests a linear relationship between the two with a standard deviation of less than 0.3 mm/h (Figure 5-18). JASIN meteorological observations indicated rain for Revs 355 and 1006, while showers were evident for Revs 791, 800, 834, 843, and 958. Both algorithms identified the widespread rain but were unable to predict the showers. (See Table 5-11 and Figure 5-18).

3. Tropical Area Evaluation of Integrated Water Vapor

The integrated amount of columnar precipitable water vapor calculated from radiosonde data on atmospheric pressure, temperature, and dew point was compared to Wentz algorithm predictions, choosing only cases of coincidence between radiosonde and Seasat sampling within 3 h. Radiosondes take approximately 1 h to rise through the troposphere, so the averages actually are within 2-1/2 h or less. The results are shown in Table 5-12. The Wentz predicted values are consistently a bit too high.

The island of Guam was included in order to check effects of land in the field of view. Two examples of the water vapor prediction from the Wentz algorithm are seen in Figures 5-19 and 5-20. In Figure 5-19 the values seem to be generally somewhat elevated around Guam, while in Figure 5-20, they are too high mainly to the SW of Guam. There also seems to be unrealistically high values on neighboring scan lines in this case. One possible cause for the SMMR water vapor being high is that the biases applied to the T_B 's are too large for the tropics. That is, in the tropics, where the Earth scene brightness temperatures are closer to the temperature of the SMMR warm reference load, smaller T_B biases may produce more accurate T_B 's. (See Subsection H-2).

However, the Rosenkranz algorithm water vapor is too low in the tropics (see Subsection B-2-c). This may result from the use of a linear algorithm when nonlinear effects are important. Nonetheless, this suggests that it is premature to blame the water vapor discrepancy in the tropics on problems with the brightness temperatures.

4. Tropical Area Liquid Water and Precipitation Algorithm Intercomparison

Since the surface truth for both liquid water and precipitation in the tropical areas was unavailable, an intercomparison of the determinations of these quantities by the Wentz and Wilheit algorithms was made. As seen in Figure 5-21, a relationship between the liquid water algorithms exists for values below 0.12 g/cm^2 . This is similar to the relationship in the JASIN area, except that the intercept is not zero. Above 0.12 g/cm^2 the correlation breaks down. Data affected by land have not been identified in this correlation, so the scatter may be from land effects as well as algorithm error.

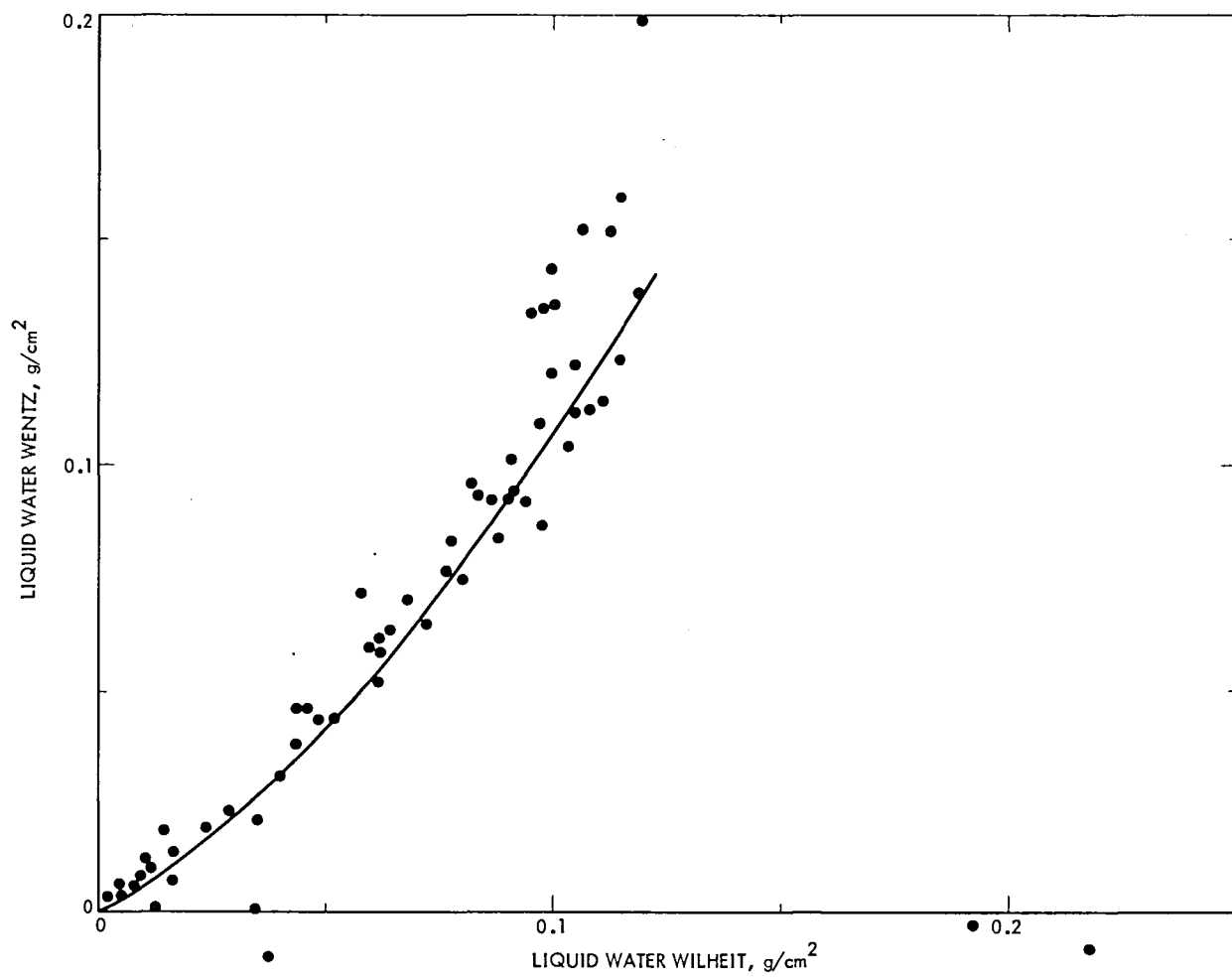


Figure 5-17. Wentz vs Wilheit Liquid Water - JASIN

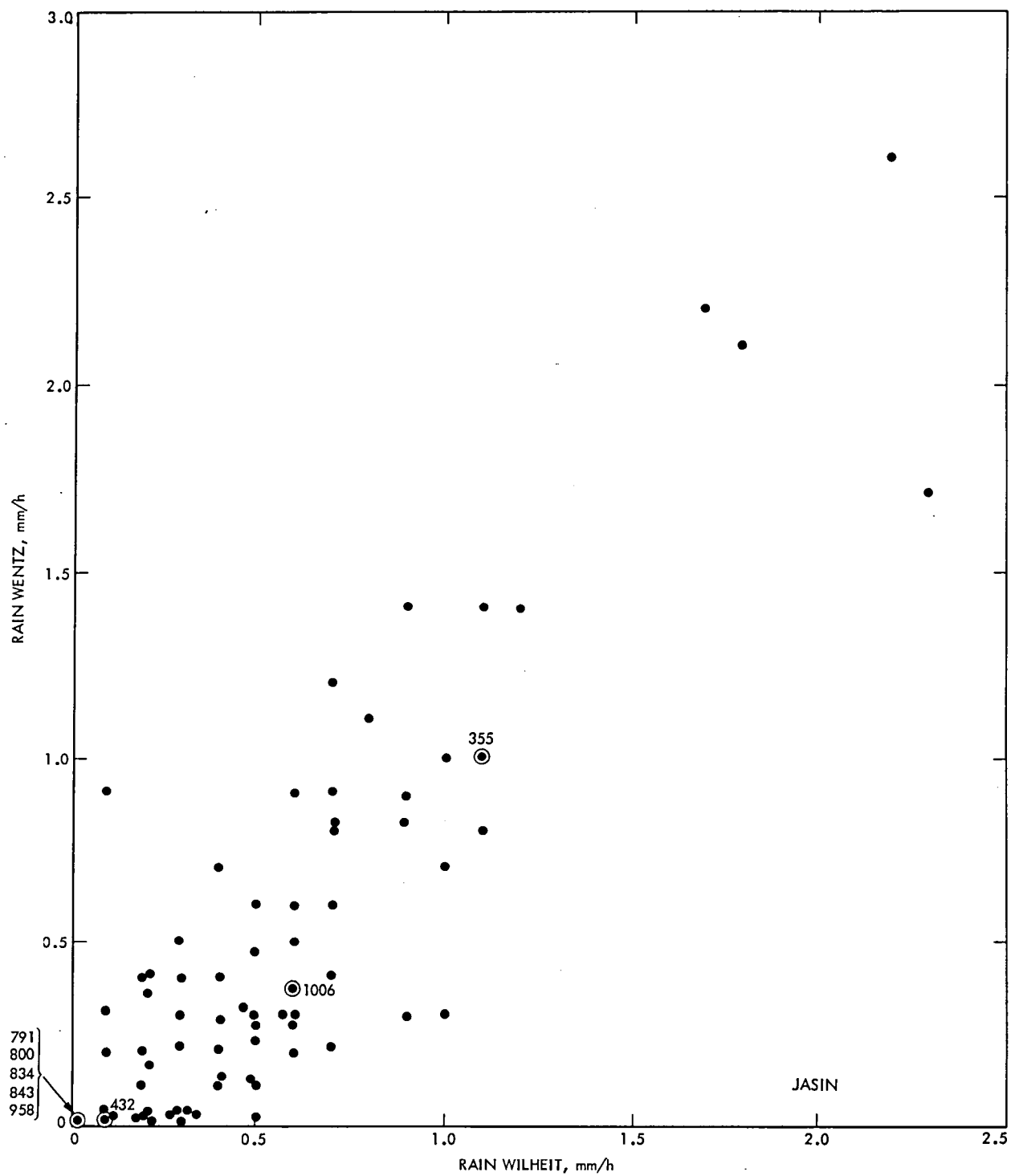
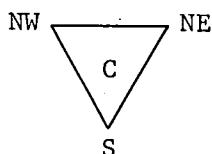


Figure 5-18. Wentz vs Wilheit Rain - JASIN

Table 5-11. Rain Rate and Liquid Water Algorithms for Wilheit and Wentz at Ship Locations Reporting Precipitation in the JASIN Experiment



Corresponding Ship and Triangle Locations

Rev	Rev time, Mo/d/h	Wilheit		Wentz		Satellite observ. and ship location	Stations below report precipitation in WMO code wwW or as comments at a time near satellite overpass*	
		Liq. water, g/cm ²	Rain, mm/h	Liq. water, g/cm ²	Rain, mm/h			
355	7/21/20	0.100	1.10	0.120	1.00	(S)	Meteor	616
432	7/27/05	0.044	0.10	0.037	0.00	(NE)	Hecla	606
		0.040	0.10	0.031	0.00	(S)	Meteor	606
		0.049	0.00	0.044	0.00	(S)	Tydeman	612,596
547	8/04/06	0.024	0.00	0.020	0.00	(NE)	John Murray	605
		0.029	0.10	0.024	0.00			
556	8/04/22	0.014	0.00	0.020	0.00	(S)	Challenger	626
590	8/07/06	0.011	-	0.009	0.00	(NW)	Gardline Endurer showers	
599	8/07/22	0.016	-	0.014	0.00	(S)	Discovery	
633	8/10/06	0.113	0.90	0.151	1.40	No surface reports of precipitation		
		0.119	0.70	0.137	1.20			
		0.093	0.40	0.101	0.70			
642	8/10/22	0.043	0.20	0.039	0.00		Atlantis	603
		West of Seasat Path					Shackelton	626
676	8/13/07	0.060	0.25	0.060	0.30	(S)	Shackelton/Hecla	622
		0.091	0.20	0.094	0.63	(S)		
719	8/16/07	0.046	0.10	0.045	0.00	(NW)		
748	8/18/07	0.035	0.20	0.220	0.00	South of JASIN area ~50°N 350°E		
		0.690	7.00	0.070	0.30			
		0.086	0.90	0.099	0.70			
		0.115	0.80	0.126	1.10			
791	8/21/07	0.004	0.00	0.004	0.00	(C)	John Murray	showers
		0.010	0.00	0.008	0.00	(S)	Planet	showers

*ww from 60-65 indicates intermittent light rain to continuous heavy rain. Numbers in the 50s indicate drizzle.

W-6 indicates rain as past weather. W-5 indicates drizzle as past weather.

Table 5-11 (contd)

Rev	Rev time, Mo/d/h	Wilheit		Wentz		Satellite observ. and ship location	Stations below report pre- cipitation in WMO code wwW or as comments at a time near satellite overpass*	
		Liq. water, g/cm ²	Rain, mm/h	Liq. water, g/cm ²	Rain, mm/h			
834	8/24/07	0.004	0.00	0.006	0.00	(C)	John Murray	showers
		0.002	0.00	0.004	0.00	(NW)	Gardline Endurer	showers
		0.008	0.00	0.008	0.00	(S)	Shackelton	interm. rain
843	8/24/23	0.000	0.00	0.001	0.00	(S)	Shackelton	
929	8/30/23	0.061	0.30	0.061	0.15	(NE)	Hecla	636
		0.070	0.50	0.070	0.30	(NE)	Hecla	
958	9/01/24	0.008	0.00	0.016	0.00		Meteor (23Z)	505
		0.004	0.00	0.005	0.00	- Position	(24Z)	025
		0.001	0.00	0.012	0.00	- above (S)		
		0.001	0.00	0.034	0.00			
1001	9/05/00	0.105	0.60	0.112	0.90			
		0.082	0.80	0.097	0.70	- SW corner of		
		0.059	0.60	0.073	0.30	- large scale area		
		0.068	0.30	0.064	0.20			
1006	9/05/08	0.004	0.00	0.003	0.00		Hecla	616
		0.077	0.60	0.076	0.37	(S)	Gardline & Planet	608,612
		0.010	0.00	0.012	0.00	Between NW & NE	Shackelton	602

*ww from 60-65 indicates intermittent light rain to continuous heavy rain. Numbers in the 50s indicate drizzle.

W-6 indicates rain as past weather. W-5 indicates drizzle as past weather.

Table 5-12. Precipitable Water Vapor at Tropical Stations

Rev	DOY	Mo/Day	Time, h:min	Wentz, g/cm ²	Radiosonde Data			SMMR, Wentz Minus Radiosonde	Comment
					STA	Amount	Time		
384	204	7 23	20:38	3.02	TANGO	2.92	24:00z	0.10	
				6.68 ^a	Guam ^a	5.50	24:00	(1.18) ^a	
427	207	7 26	20:45	7.76	TANGO	6.88	12:00	(2.09)	Rain within 200-km distance (surrounding SMMR numbers all approximately 6.65)
						5.67	24:00		
				7.07 ^a	Guam ^a	5.71	24:00	(1.36) ^a	
542	216	8 4	21:37	8.02	TANGO	7.15 ^b	24:00	0.87	
628	221	8 9	21:51	5.43	TANGO	5.39	24:00	0.04	
				6.5 ^a	Guam ^a	6.22	24:00	(0.28) ^a	Rain
828	235	8 23	21:06	6.34	Wake	5.44	24:00	0.80	SMMR has locally high values by 0.2, 0.4 g/cm ²
				6:21	Kwajelein	5.65	24:00	0.56	
				6.45	Majuro	5.80	24:00	0.65	

^aGuam is a large island, values probably show land effects.

^bNo data between 1013.6 and 599 mbars.

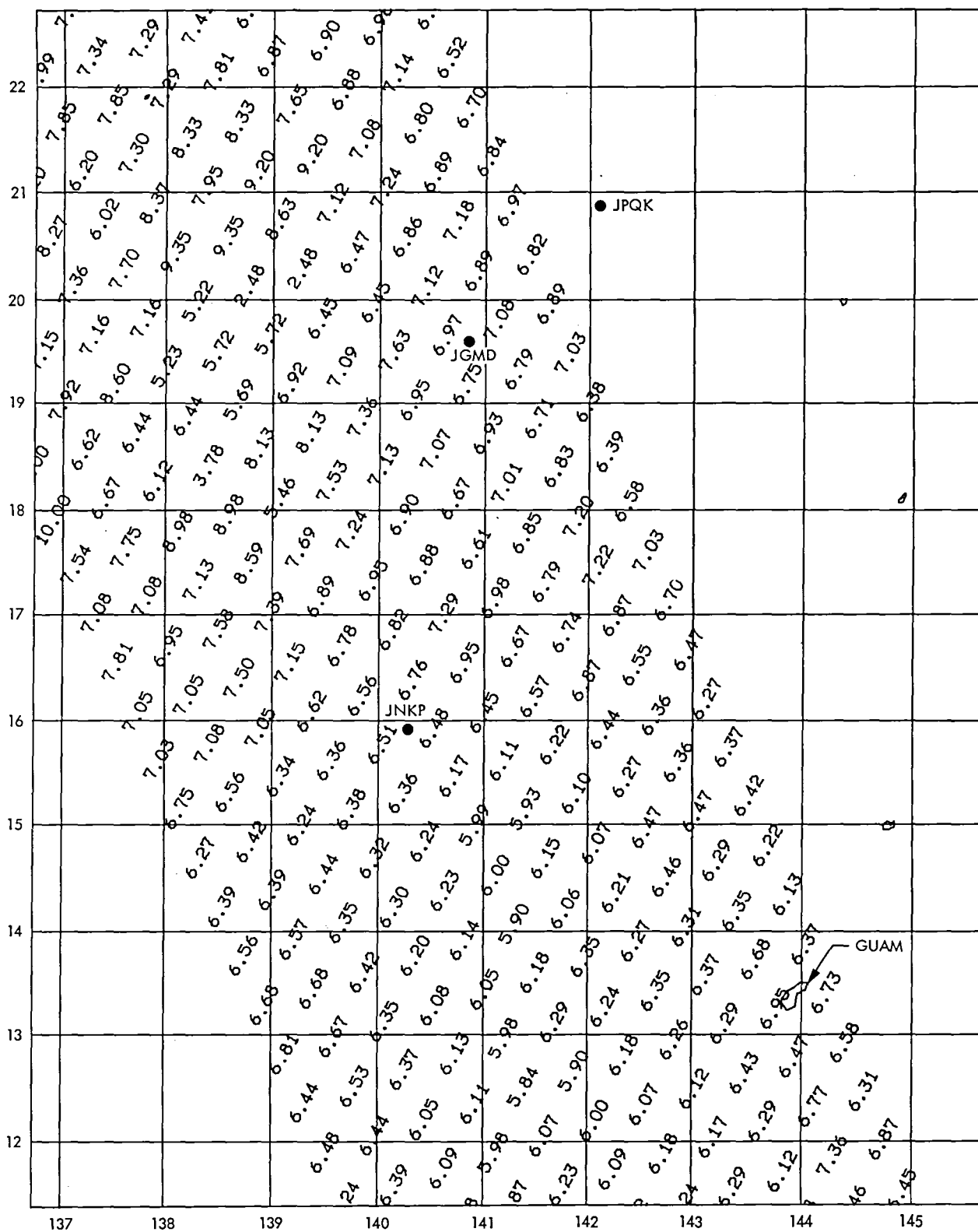


Figure 5-19. Wentz Water Vapor Near Guam - Rev 384

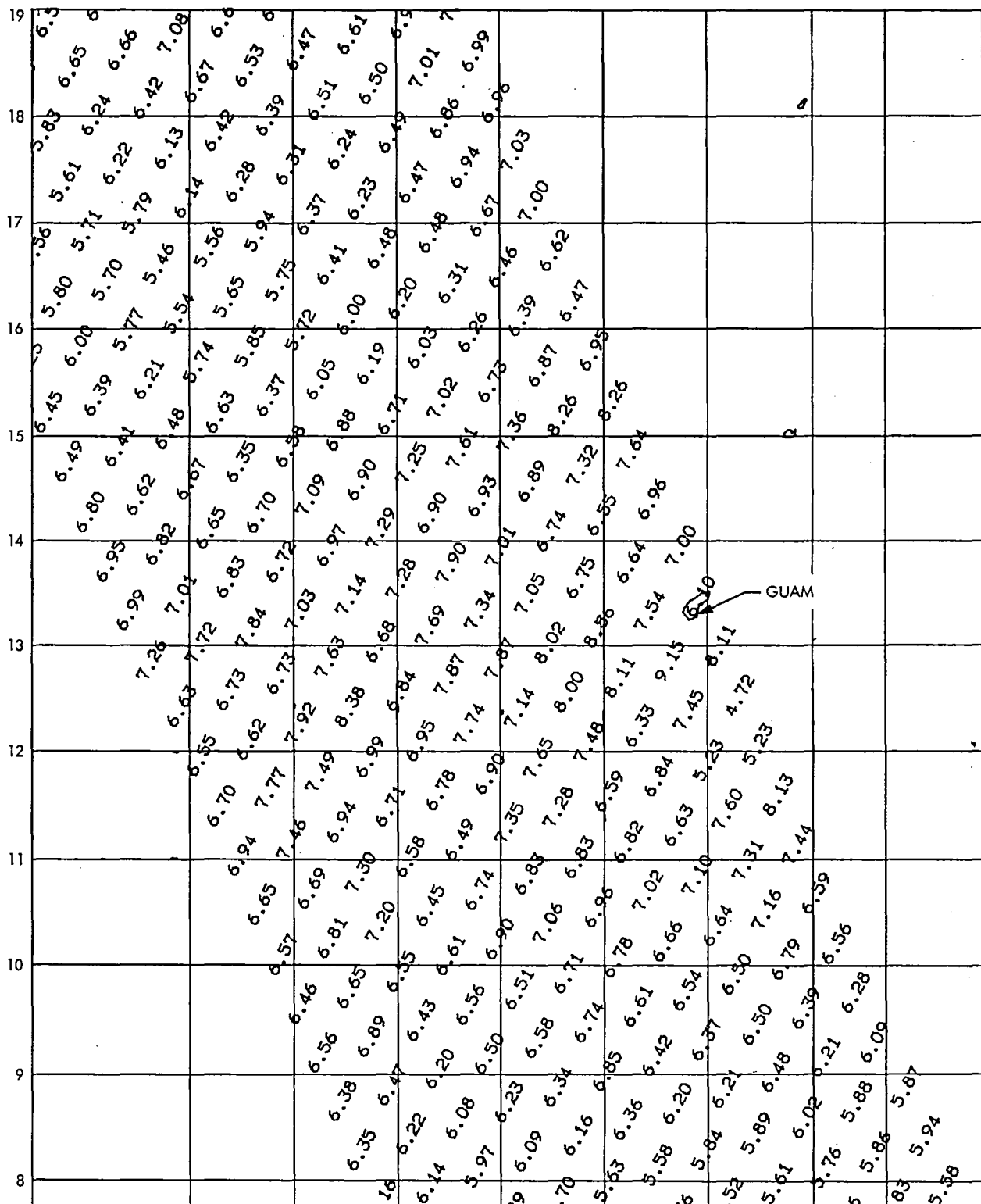


Figure 5-20. Wentz Water Vapor Near Guam - Rev 628

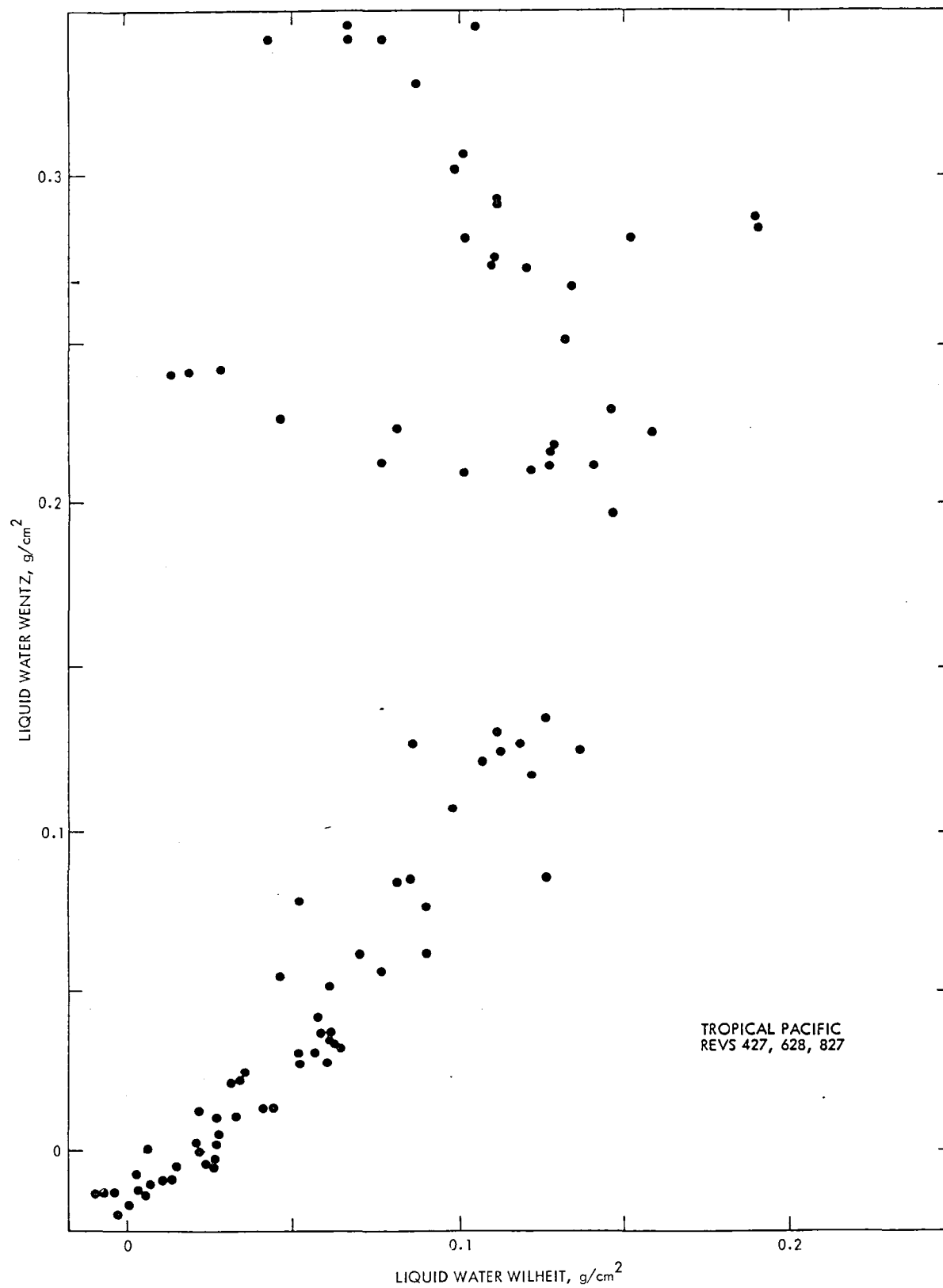


Figure 5-21. Wentz vs Wilheit Liquid Water - Tropics

The Wentz and Wilheit rain algorithms show a large amount of scatter in their correlation (Figure 5-22). Wilheit values are typically larger and give, in some cases, between 0.1 and 1.5 mm/h of rain where the Wentz algorithm predicts zero rain. This indicates that some risk may be involved in using the algorithms to flag regions where other parameter determinations might be compromised by rain in the field of view.

D. SURFACE WIND SPEED EVALUATIONS

Studies conducted during the JASIN workshop were directed primarily toward the comparison of accuracy of the Wentz SMMR winds in the GOASEX data set (here used to describe the aggregate of Revs 1120, 1135, 1298, and 1094, the latter a North Atlantic pass over an intense storm) to that exhibited for the JASIN data set.

A preliminary comparison of SMMR and JASIN surface wind data is shown in Figure 5-23. A merging program, which accounted for the intrinsic resolution of SMMR wind determinations, was used to colocate spacecraft and JASIN measurements. Over the 8 high priority SMMR revolutions, 18 comparisons were found, divided about evenly between ascending and descending revolutions. The SMMR data scatter (standard deviation approximately 2.04 m/s) about a positive bias of 2.71 m/s with some suggestion in the plot that the bias is mainly attributable to data from descending orbits. To check this behavior, the SMMR grid 3 wind plots in the JASIN data set were used to produce, by hand, 21 comparisons at the Meteor station. Surface winds at the station were averaged from several platforms in the immediate vicinity of that station. The 21 comparisons are shown in Figure 5-24. There it is seen that three of the comparisons were made at cells at or near rain cells. In Figure 5-24, for the larger data set, there is less support for a significant difference in the error structure between ascending and descending revolutions. Overall, the SMMR winds remain biased high by 2.6 m/s with a standard deviation of 1.9 m/s. The positive bias was also noted in a subjective comparison of field plots of SMMR and SASS wind data for overlapping JASIN revolutions. With a few exceptions (e.g., Revs 958, 1001), the SMMR winds are systematically higher than the SASS winds over the entire domain shown in the plots (55-65°N, 355-340°W).

It is known that for the GOASEX calibration revolutions (1120, 1298, 1135) SMMR and SASS winds are highly correlated with no significant level change between the wind estimates. Thus, little bias should be expected between SMMR wind estimates and surface truth in those revolutions. This appears to be the case. In Figure 5-25 the SMMR winds are compared to the winds derived from fields produced completely independently of satellite data for Revs 1298 and 1094. While SASS data from 1298 were used by Wentz in the T_b calibrations, no data from Rev 1094 whatsoever was used. The comparisons from the two revolutions are consistent and indicate much smaller biases for the SMMR wind estimates than for the JASIN set. The somewhat higher standard deviations are believed due to the lower accuracy of the field estimates than for the JASIN surface truth. For example, the clusters of points circled on the scatter plot are associated with probable errors in the fields in data void, large gradient regions. In those areas, the SMMR and SASS winds are in close agreement.

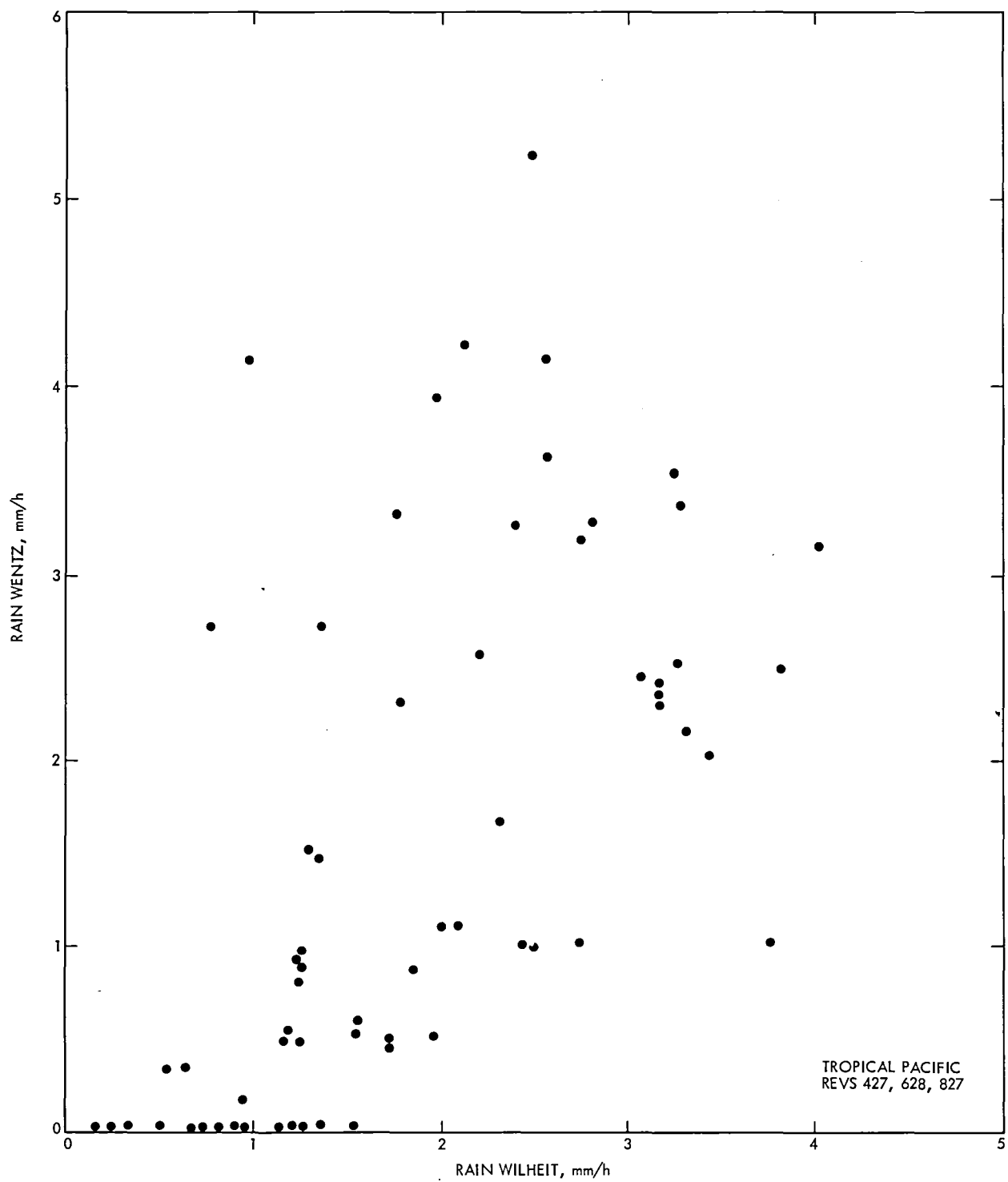


Figure 5-22. Wentz vs Wilheit Rain - Tropics

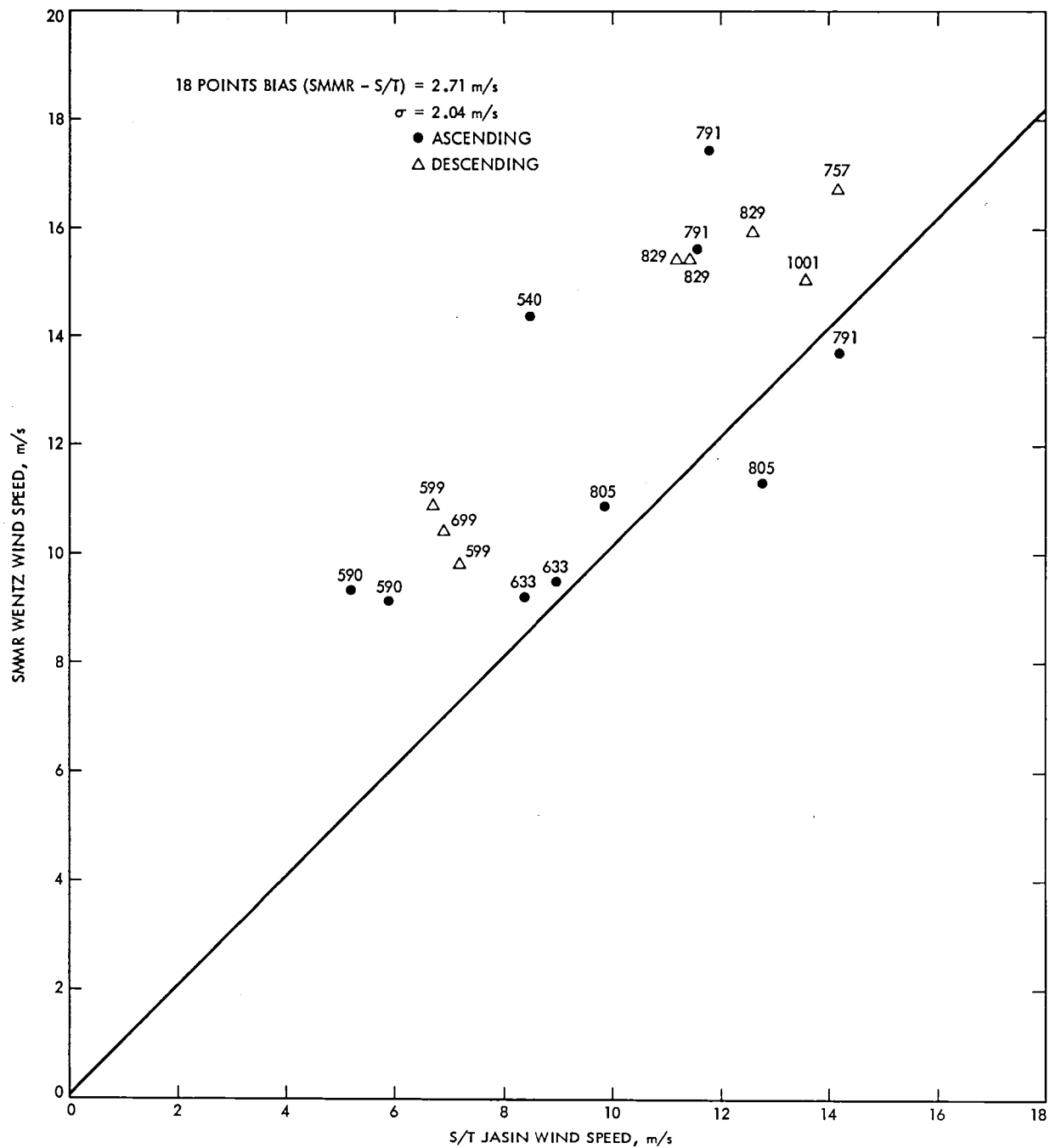


Figure 5-23. Wentz Wind Speed Comparisons - JASIN High Priority Set

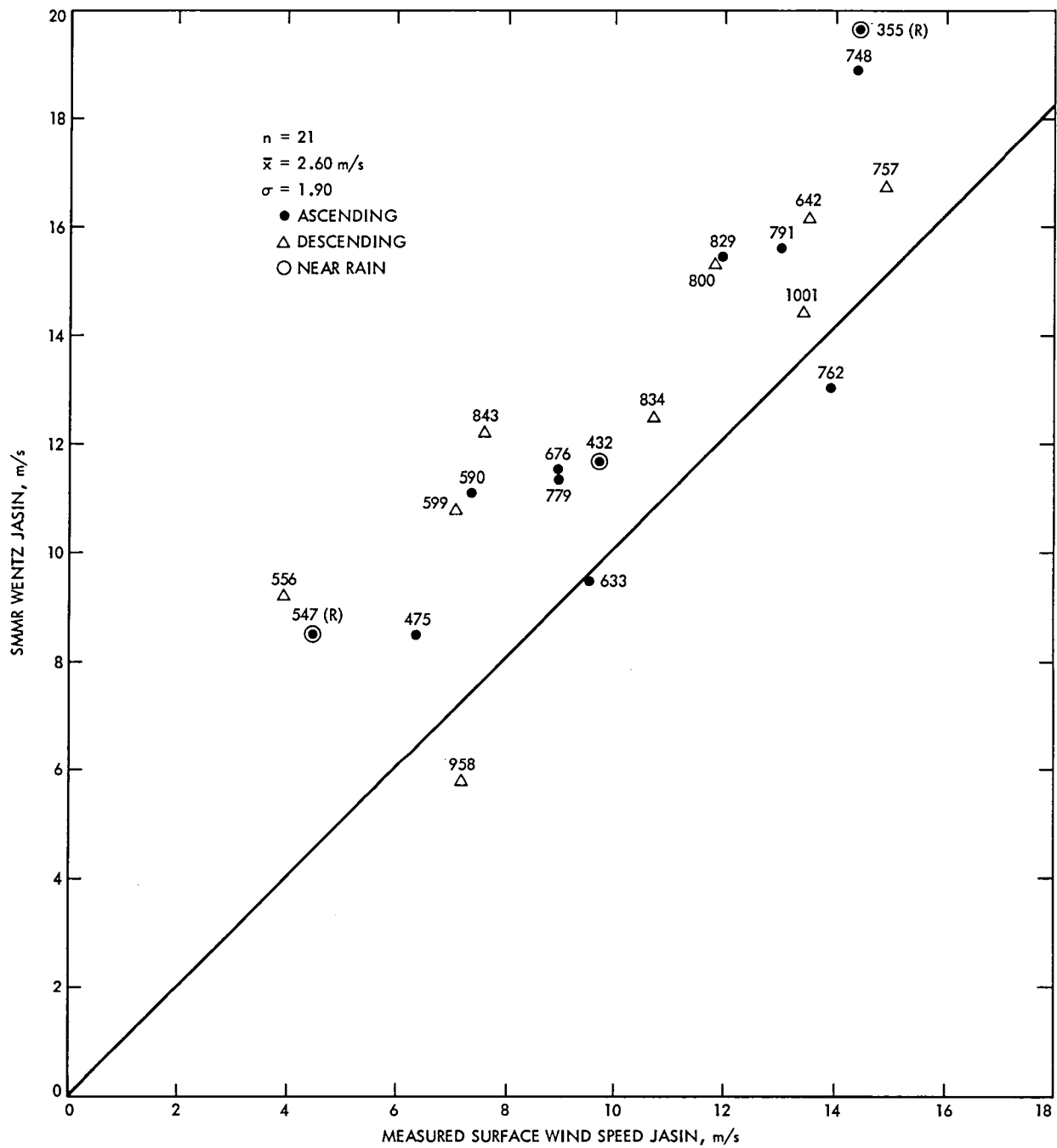


Figure 5-24. Wentz Wind Speed Comparisons - Meteor Hits

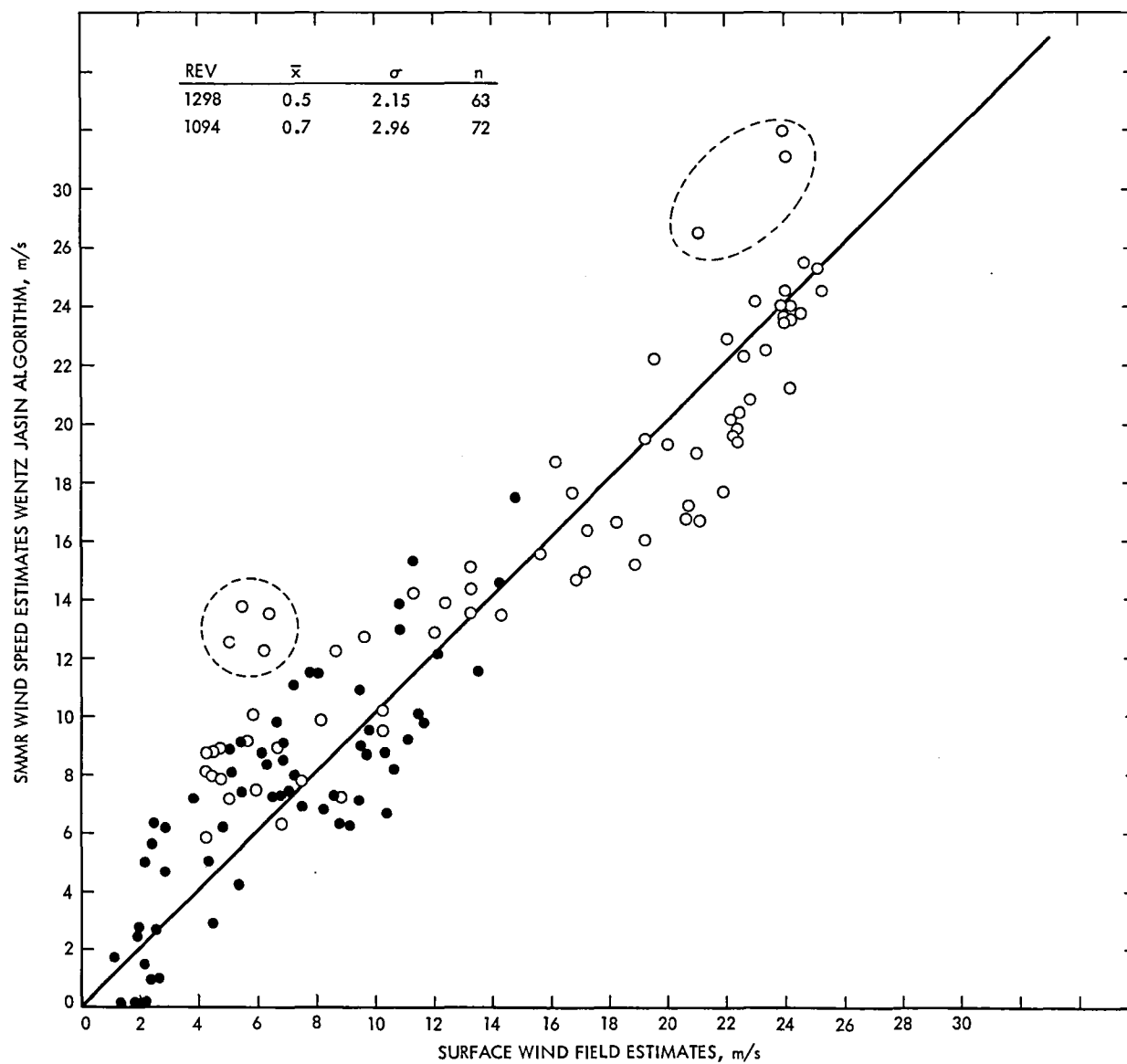


Figure 5-25. Wentz Wind Speed Comparisons - GOASEX Revs 1298 and 1094, Wind Fields

Spot comparisons were also made for the GOASEX data set, as shown in Figure 5-26. Since few buoy hits are provided in the four revolutions used, all surface data, including transient ship reports, were used. The four revolutions provide 50 such hits, with an error very much like that exhibited in the field comparisons ($\bar{x} = 0.6$ m/s, $\sigma = 2.7$ m/s for the hits, $\bar{x} = 0.6$ m/s, $\sigma = 2.6$ m/s for the fields). JASIN comparisons for the eight high priority revolutions are also shown in Figure 5-26.

We conclude tentatively that the SMMR winds away from land and rain by about two grid 3 distances exhibit skill in measuring surface wind speed comparable to that in the surface truth data against which they are being evaluated and that 2-m/s accuracy is evident. However, there is strong evidence of a level change in the SMMR winds between the GOASEX data set and the JASIN data set, with SMMR winds in JASIN biased high by about 2 m/s. Since SASS winds do not appear to have a "variable bias" over the Seasat mission, it is suggested that in addition to the other measured discussed at the workshop, an extensive program of SMMR-SASS intercomparison be started in order to identify the spatial and temporal nature of the level shifts.

E. SEA-SURFACE TEMPERATURE EVALUATIONS

1. JASIN Area Evaluations

a. Radio Frequency Interference (RFI) Considerations. Examination of the images made from raw counts from the spacecraft (SDR images) showed that the JASIN area was contaminated by RFI for all of the ascending revolutions, whereas the descending revolutions, with one exception (Rev 1001), did not show visible RFI in the images. RFI affects only the 6.6-GHz frequency channels. The interference is at times very strong (~ 400 K) just off the south coast of Iceland, but this strong interference only extends a north-south (along track) distance of ~ 100 km, even though it is present along the entire 600-km cross-track distance. The RFI in the rest of the area is low level and erratic. Typically, about one antenna temperature (T_A) measurement out of every five or ten measurements shows a jump of ~ 5 K. The jumps are independent of polarization, probably because the V and H measurements are displaced in time by ~ 4 s and in space.

The rapid variability of the RFI as seen by the moving spacecraft is consistent with multiple-path phase interference from a single source. Strong transmission is known to occur in Germany, probably directed along the Earth's horizon. If this is a main RFI source, ascending revolutions would be more affected since for them the spacecraft looks back at Germany on the horizon, whereas Germany is not on the horizon in descending revolutions. Since approximately ten T_A measurements are averaged to get one T_B measurement, the 5 K jumps in T_A due to RFI will alone raise the 6.6-GHz T_B 's by ~ 0.5 K on the average. Smaller jumps plus any steady level of RFI could probably raise the 6.6-GHz T_B 's by ~ 1 K. This will raise the spacecraft (S/C) SST by ~ 2 K in the ascending revolutions, as observed. Hence, RFI is the probable source of the SST asymmetry between ascending and descending revolutions. A strong enough steady source of RFI in both types of revolutions could explain the overall bias in SST to be discussed later.

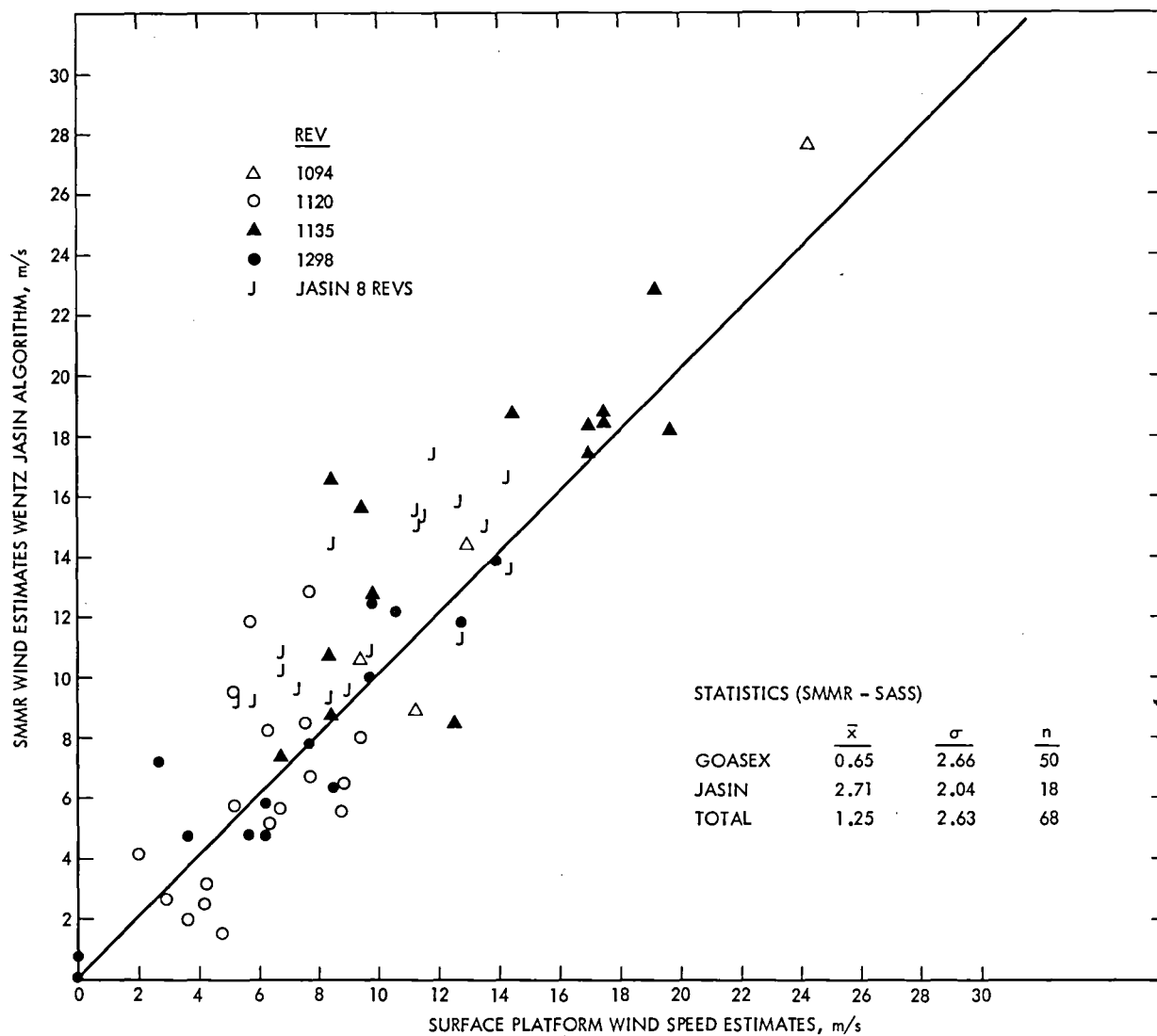


Figure 5-26. Wentz Wind Speed Comparisons - GOASEX Revolutions, Spot Reports

b. SST and Wind JASIN Intensive Area (JIA) Comparisons of All Algorithms. All independent S/C measurements of SST were compared to the high quality JASIN S/T in the following way. The files of S/C - S/T hits were sorted by distance. Starting with the closet hit, that S/C measurement was taken as an independent measurement, and all S/T measurements within a radius of 75 km were averaged to obtain the S/T comparison point. All other S/C measurements dependent on the S/C point (those within 150 km) were then eliminated. The file was then searched for the next (independent) S/C measurement closest to an S/T point, and so on. This procedure was followed for all algorithms except Rosenkranz, where a radius of 27 km was used for the S/T and all S/C measurements on grid 3 were taken to be independent. The statistics are given in Table 5-13. A similar procedure for the wind comparisons was performed, using grid 2 as the independent samples (43 km instead of 75 km), and the results are given in Table 5-14.

In this SST data set, Wentz and Rosenkranz have both a smaller bias and a smaller scatter than the Bierman and Wilheit algorithms. The Wentz-Bierman comparison is interesting because the algorithms are identical in their geophysics and differ only in the weights of the different frequency measurements and in that Bierman takes into account some of the correlation of the geophysical variables. Not only is Bierman's scatter 50 percent larger, but the SST bias is 4 K larger as well! The probable cause is Bierman's 6 to 9 times heavier weight on the higher frequencies, which are affected more by atmospheric parameters than by SST, and more by errors in the cloud opacity model.

The Rosenkranz-Wilheit comparison is also interesting. Both are linear algorithms, yet the Rosenkranz scatter is 50 percent less than the Wilheit scatter. The probable reason here is that Wilheit's algorithm is much more heavily dependent on the 6.6-GHz frequency than the Rosenkranz algorithm, and thus RFI is more important.

In this wind speed set, all algorithms have about the same scatter. Bierman and Wentz have about the same bias as well. The large bias of Wilheit is interesting. In this version of Wilheit, Wentz's biases were applied to the T_B 's before they were processed by the Wilheit algorithm, and no further correction was made. Hence, it is not necessarily valid to conclude that the large wind speed bias is due to the Wilheit algorithm. However, both algorithms produce roughly identical T_B 's from given geophysical variables, and, in addition, Tom Wilheit agrees that the biases he derives are roughly the same as those of Wentz. It may prove interesting to learn the source of this bias.

c. SST Statistics - All of JASIN, Wentz Algorithm. The extensive body of S/C data processed for JASIN allows an examination of the repeatability of S/C measurements of SST. The JASIN area was divided into six regions as shown in Figure 5-27, and histograms were plotted for all the independent grid 1 estimates of SST for each region for ascending and descending revolutions

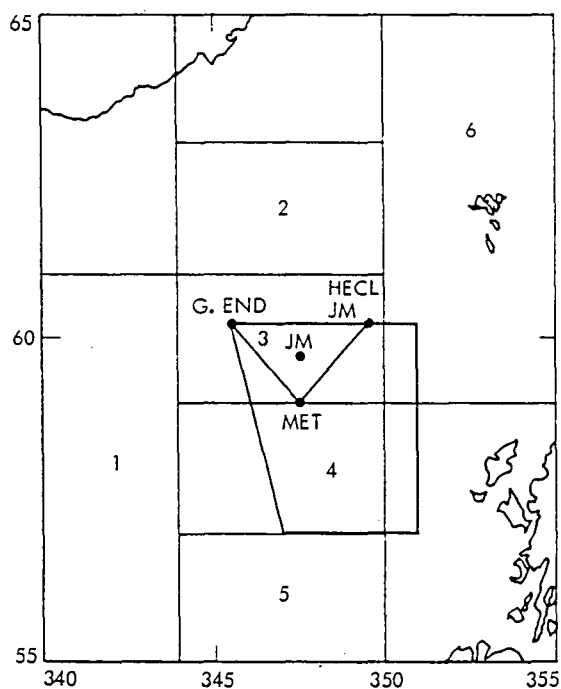
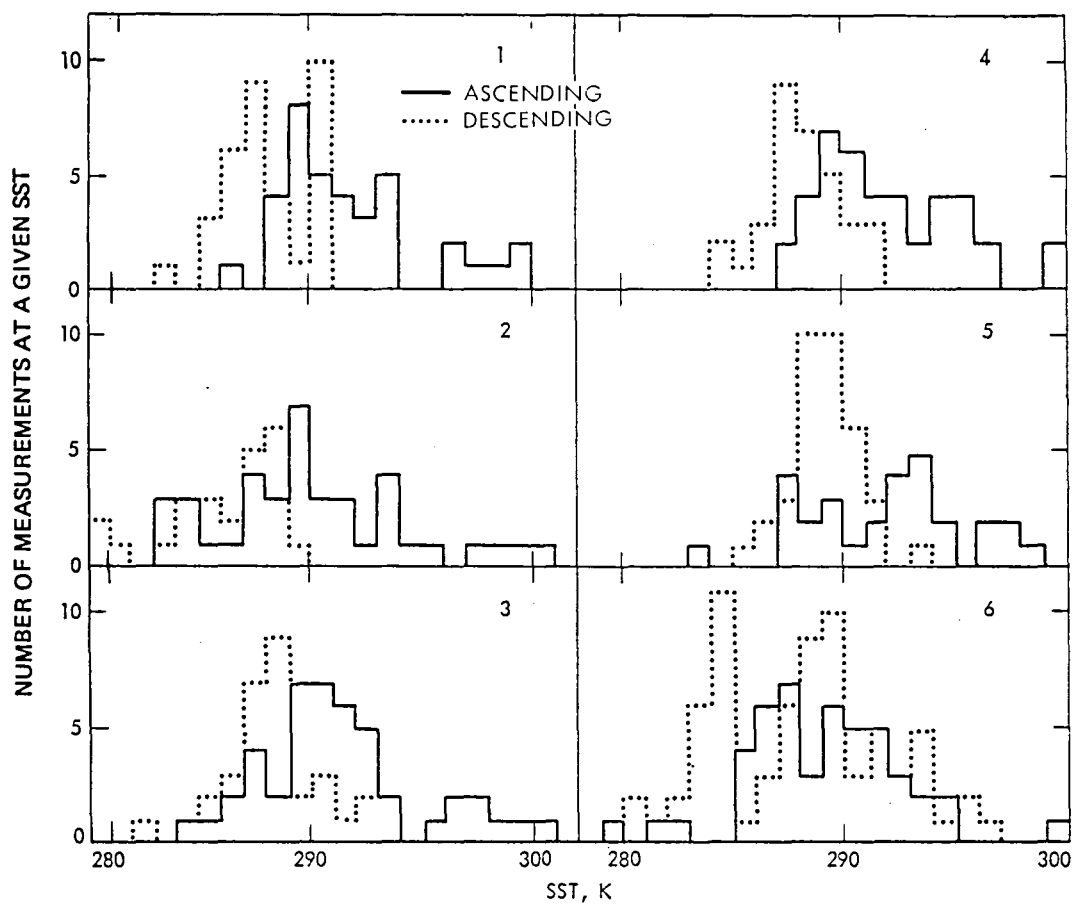


Figure 5-27. Histograms of SST for Six Different Regions of JASIN Separately for Ascending Revolutions (dotted lines) and Descending Revolutions (solid lines)

Table 5-13. SST Statistics for the Eight Priority Revolutions

Algorithm	All Revs			Ascending Revs			Descending Revs		
	N	Bias	σ'	N	Bias	σ'	N	Bias	σ'
Bierman	18	7.2	3.3	10	8.6	3.1	8	5.4	2.6
Rosenkranz	19	1.9	2.1	9	2.7	2.5	10	1.2	1.3
Wentz	18	3.1	2.2	10	3.5	2.5	8	2.6	1.7
Wilheit	18	6.7	3.1	10	7.0	3.2	8	6.2	2.9

Table 5-14. Wind Speed Statistics for the Eight Priority Revolutions

Algorithm	All Revs			Ascending Revs			Descending Revs		
	N	Bias	σ'	N	Bias	σ'	N	Bias	σ'
Bierman	18	1.8	2.2	10	1.2	2.3	8	2.5	1.8
Rosenkranz	19	- 2.3	2.0	10	- 3.3	2.0	9	- 1.2	1.4
Wentz	18	2.7	2.0	10	2.3	2.5	8	3.2	0.9
Wilheit	18	12.7	1.9	10	12.7	2.1	8	12.8	1.8

separately. As can be seen from Figure 5-27, the scatter is disappointing. Table 5-15 details the mean and standard deviation for each region, with the two points with SST > 300 K excluded.

There is unquestionably a difference between ascending and descending revolutions. The deduced SST is 2.9 ± 0.2 K higher in the ascending revolutions, and the mean scatter is 3.2 K versus 2.3 K for the descending revolutions. The most likely source of this is RFI as discussed earlier.

However, the scatter is fairly large even in the descending revolutions. Region 6 has a much larger scatter than the other regions, which may be due to the small islands within it. Without region 6, the average σ is 2.0 K - larger than the 1.5 K found in previous workshops.

Table 5-15. SST Means and Standard Deviations for Each Region of JASIN

a) Ascending Revs										
Region	All Points Without Rain				All Points				Number of Pegged Points	
	N	Mean	σ	σ_{mean}	N	Mean	σ	σ_{mean}		
1	30	290.9	2.4	0.4	37	291.9	3.3	0.5	0	
2	33	289.5	4.1	0.7	38	289.8	4.1	0.7	3	
3	38	290.8	3.5	0.6	43	290.9	3.3	0.5	0	
4	32	291.2	2.5	0.4	40	291.8	2.8	0.4	0	
5	24	291.9	3.1	0.6	29	291.8	3.6	0.7	0	
6	38	288.6	3.9	0.6	43	288.8	3.8	0.6	2	
b) Descending Revs										
Region	All Points Without Rain				All Points				Number of Pegged Points	
	N	Mean	σ	σ_{mean}	N	Mean	σ	σ_{mean}		
1	32	287.9	1.8	0.3	34	288.0	1.9	0.3	0	
2	21	287.0	2.9	0.6	22	287.1	2.8	0.6	0	
3	26	288.0	2.2	0.4	31	288.1	2.1	0.4	0	
4	27	288.0	2.0	0.4	33	288.2	1.9	0.3	0	
5	31	289.2	1.3	0.2	36	289.2	1.6	0.3	0	
6	56	287.4	3.8	0.5	71	288.0	3.9	0.5	8	
c) Comparisons										
Ascending - Descending				Difference Between Regions						
Region	Δ SST	σ	Δ Region	No Rain		All Points				
				Δ SST	σ	Δ SST	σ			
1	3.0	0.5	5-2	Asc.	2.4	0.9	2.0	1.0		
2	2.5	0.9		Des.	2.2	0.6	2.1	1.7		
3	2.8	0.7	1-6							
4	3.2	0.6		Asc.	2.3	0.7	3.1	0.8		
5	2.7	0.6		Des.	0.5	0.6	0.0	0.6		
6	1.2	0.8								
All	2.7	0.3								

It is interesting to compare the standard deviation (σ) with that given by the Wentz algorithm fit. Typically, the algorithm produced a fit with a reduced variance of unity for a standard deviation of ~ 1.5 in the T_B 's. This in turn implies that any individual deduced SST is accurate to ~ 1.3 K. Clearly, the observed scatter is larger. An independent scatter of ~ 1.5 K is needed to bring 1.3 K up to 2.0 K.

There are several possible explanations for this discrepancy. First, low-level RFI may still be present in the descending revolutions. The RFI need only increase the scatter in the 6.6-GHz T_B 's by ~ 0.7 K to do this, and interference of this small amount may be difficult to detect. Second, land contamination is certainly a possibility. A rough estimate of the possible maximal error caused by the resolution of the World Brightness Map used in the APC was ~ 0.7 K. This amount is also large enough to account for the scatter.

The larger question is why is the mean-deduced SST so high? The SST throughout the area is 284-286 K. Even the descending revolutions are biased high by 3 ± 1 K. This is more difficult to explain than the scatter. The two hypotheses above (RFI and land contamination) are still the only obvious possibilities. Yet, if RFI were at a level of 1.5 K in the mean, one would perhaps expect to see splotchiness in the SDR images of the descending revolutions, just as in the ascending revolutions. The RFI for ascending revolutions would then contribute 3.0 K in the mean, yet the ascending images qualitatively appear much worse than "twice as splotchy" as the descending images. Of course, if the RFI in descending revolutions comes from a different source, there may be no reason to expect it to be splotchy at all.

The maximal error of 0.7 K quoted above for land effects virtually rules out land contamination as the source of the bias. However, due to the peculiar geometry of the area, land contributions may be larger than that rough estimate. (Recall that region 6 looks much worse than the other regions, probably because of the small islands.) Hence, it is important to examine in detail what the APC corrections are in this area and how it generates them.

There is at least one encouraging note. In spite of the bias and the increased scatter, the SMMR is able to resolve the 2 K SST gradient over the extended JASIN area. The gradient between regions (1 and 5) and (2 and 6) is 1.7 ± 0.3 for all of the data. Although the gradient between regions 1 and 6 for descending revolutions is only 0.5 ± 0.6 , it is only 2σ away from the mean gradient and thus can plausibly be explained as statistical error.

Finally, as noted in Table 5-15, there are eight pegged points in region 6 for the descending revolutions, all of which were in the upper part away from land. These were all points in which the Wentz algorithm obtained a fit to the T_B 's within a mean σ of 6 K, and that had a fitted SST below 273 K. In addition, the ascending revolutions in region 2 and three points pegged at 310 K. Further work should examine the cause of this pegging.

d. SST Plots - All of JASIN, Wentz Algorithm. Two cross sections (along and cross track) through the JIA were picked, and the S/C SST was plotted along these cross sections for each revolution in Figures 5-28 through 5-31. In

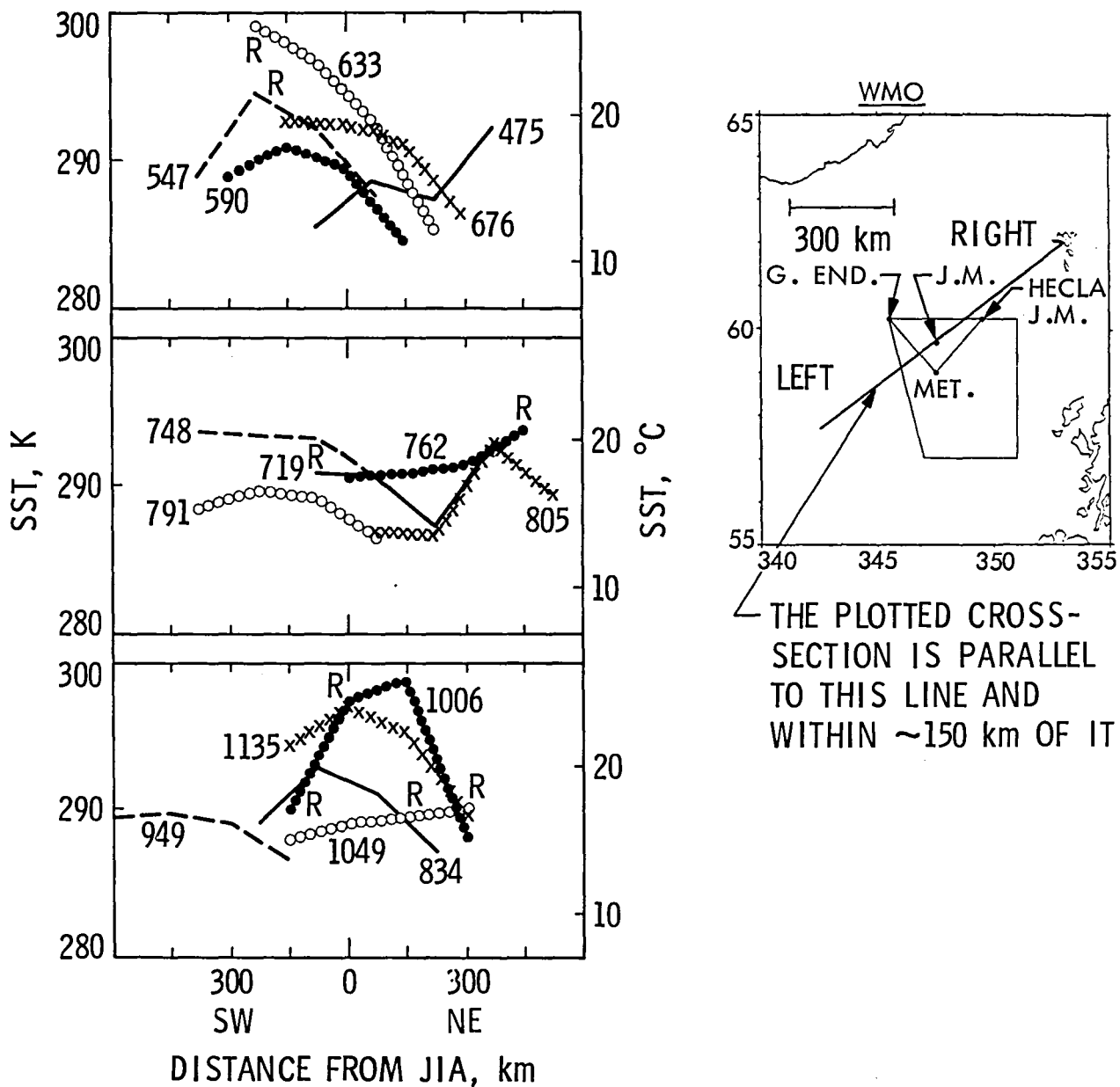


Figure 5-28. Wentz SST Plots - "Open Ocean" Cross Section, Ascending Revolutions

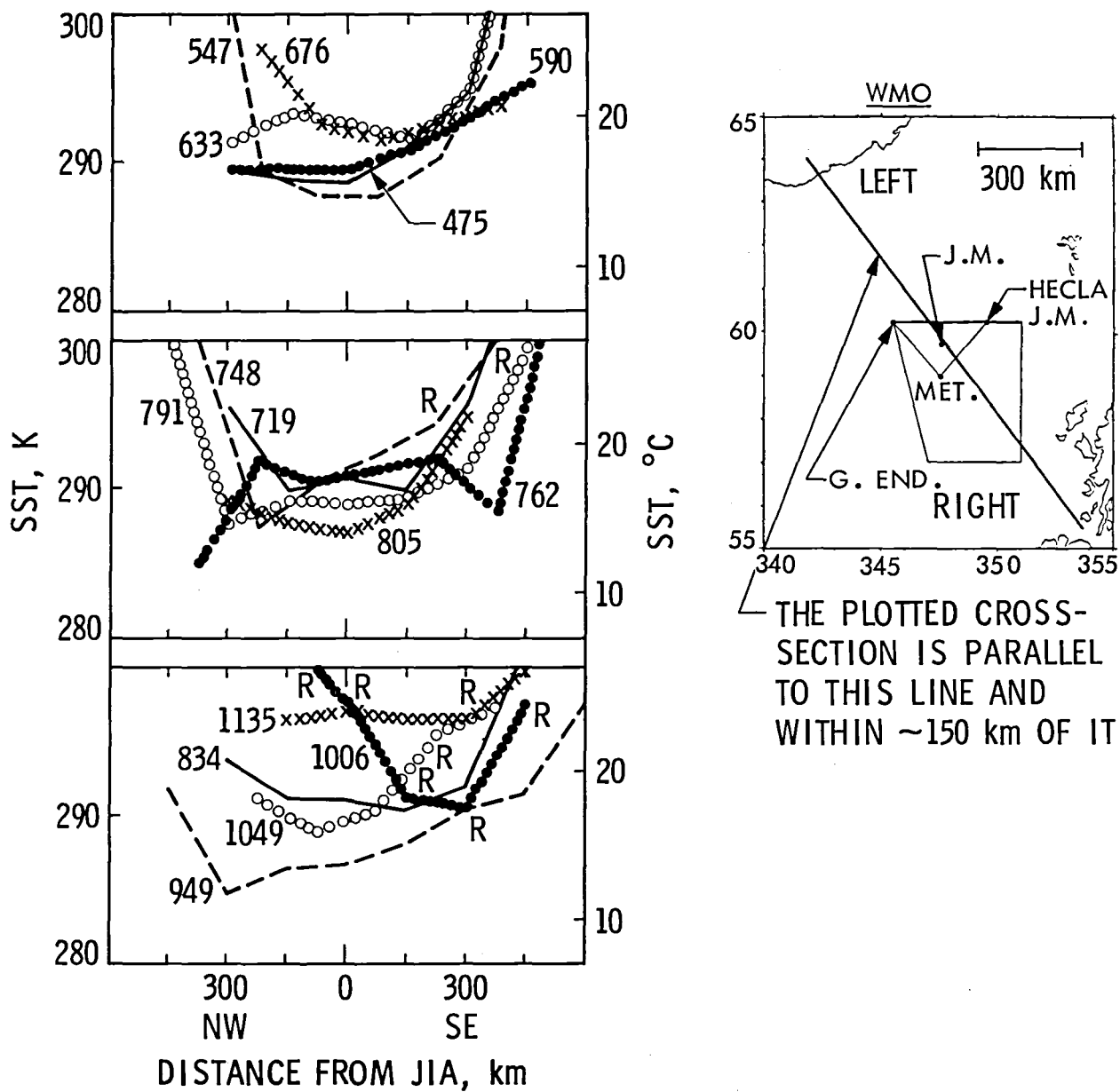


Figure 5-29. Wentz SST Plots - "Land to Land" Cross Section, Ascending Revolutions

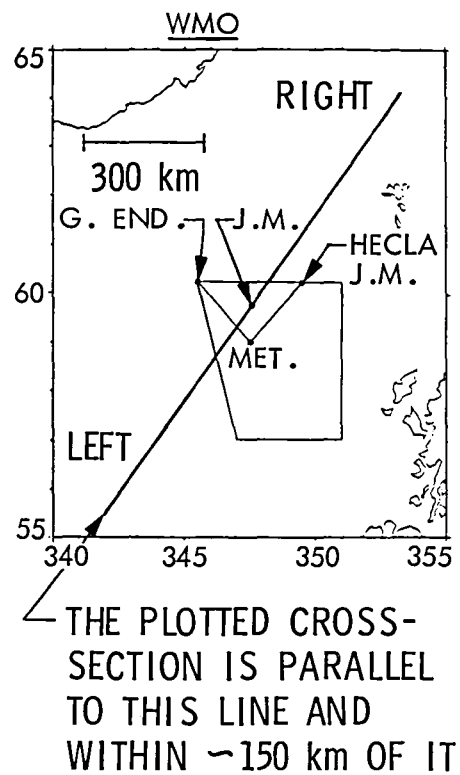
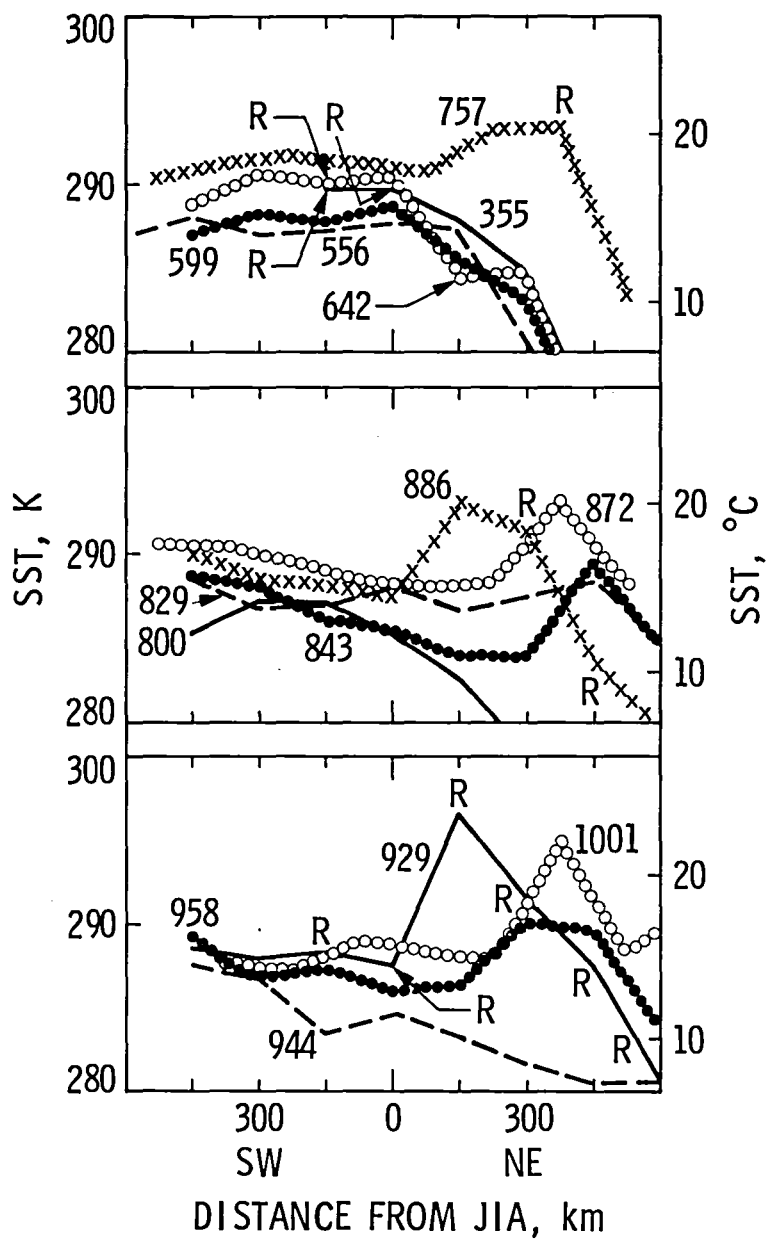


Figure 5-30. Wentz SST Plots - "Open Ocean" Cross Section, Descending Revolutions

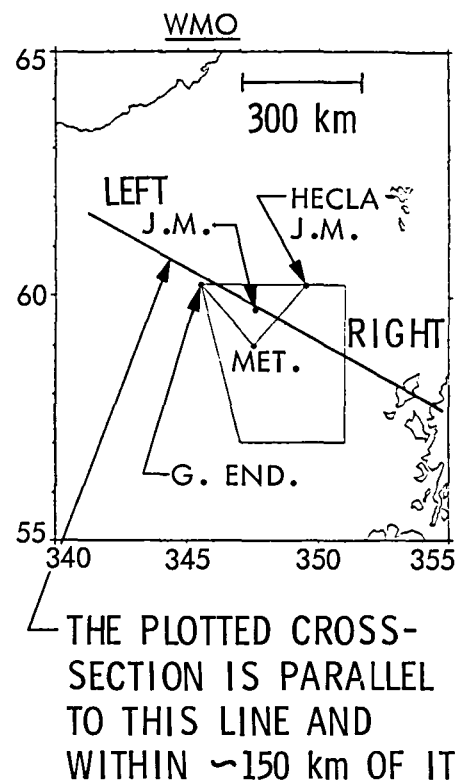
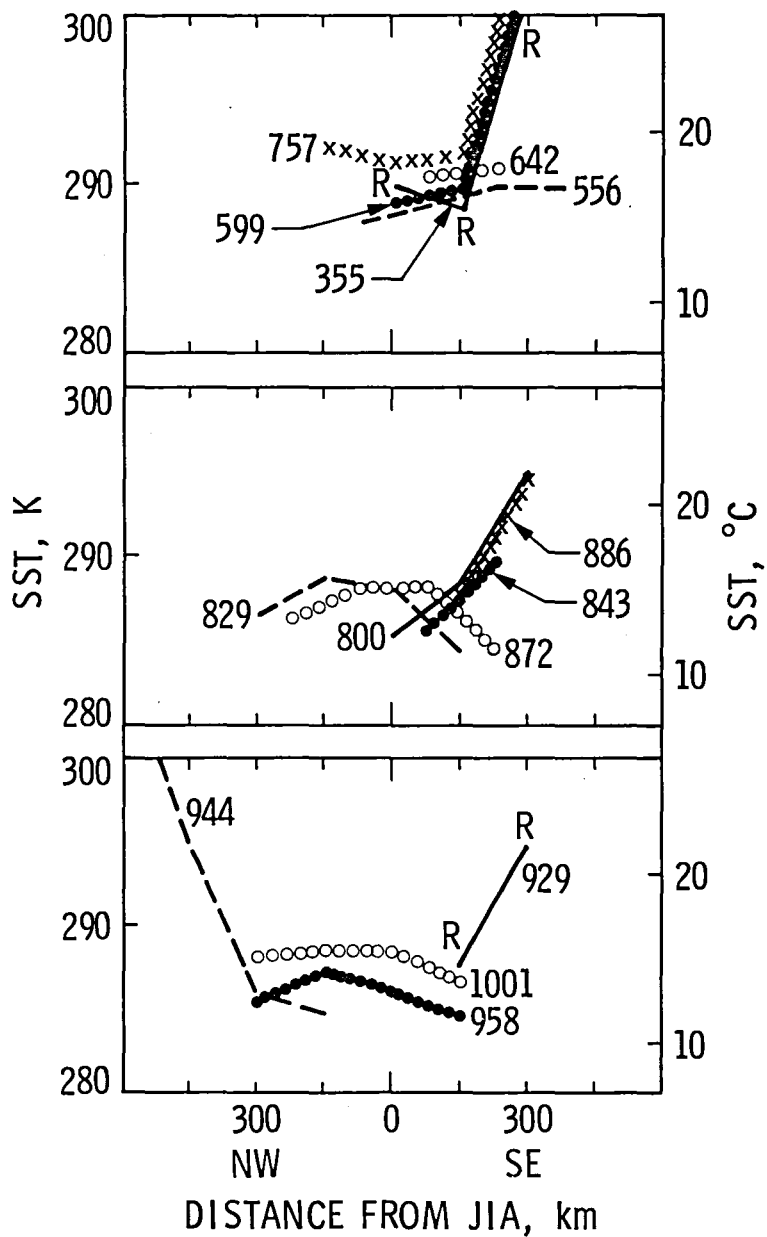


Figure 5-31. Wentz SST Plots - "Land to Land" Cross Section, Descending Revolutions

this way, the large body of data can be seen at once, as well as the systematics of each revolution and the time history of the SST determinations.

First, the good news. There is no apparent tendency for early or late revolutions to be different, even though the temperature of the spacecraft increased dramatically at about revs 500-550 and varied considerably within each orbit thereafter. Thus, the calibration algorithm seems to be doing its job, at least to first order.

Unfortunately, several revolutions stand out. Rev 663 shows an incredible 15 K drop in SST in the open ocean cross section. Even excluding the leftmost point as rain contamination leaves a 10 K drop. According to S/T, a front was passing through at that time, with high winds, clouds, and rain on the left side of the cross section and low winds and clouds on the right side. The wind S/T comparison for Rev 633 at the JIA also differs from the bias shown in other revolutions. The probable explanation is that the algorithm has substituted a variation in SST for variation in other geophysical variables. Since Rev 633 is an ascending revolution and, therefore, contaminated by RFI, it is also possible that RFI has fooled the algorithms.

Revs 1001 and 1135 show anomalous peaks in SST in the center of the open ocean cross section. Sun glint was suggested and then ruled out as the cause, both because the minimum sun angle is only 11 deg and because the minimum sun angle occurs at the right edge, not at the center. Again, RFI may be the culprit.

It was hoped that the land-to-land cross sections would reveal the presence or absence of land contamination. But, apparently due to the way in which the APC corrects for land, it would not necessarily show up as a gradient on these plots. Nevertheless, one conclusion can be drawn. Because the curves are not flat for a considerable distance in the middle of the cross section, there is no evidence for the absence of land contamination. Thus, there remains a definite possibility that land contamination is responsible for the SST bias.

e. Extended Revolutions - SST Comparison. In order to check for land and RFI contamination, two descending revolutions were extended toward the equator. The SST comparisons to the August means for the column farthest from land are plotted in Figure 5-32.

Something is unquestionably affecting the S/C SST in JASIN (and near the Azores)! The S/C SST agrees very well with the August mean SST except in the JASIN area and where strong RFI is encountered from the Azores. The fall-off from near-perfect agreements near JASIN occurs near 55°N latitude, when the S/C is ~700 km away from Ireland. The S/C SST is ~2 K high at 58°N latitude, at a distance of ~350 km from land. If the estimates of land contamination given previously by the creators of the APC hold up (which must be checked), there is little doubt that RFI is the source of the SST bias in the JASIN area.

f. Cross-Correlation Analyses. Much has been made in the past about the possible failure of the geophysical algorithms to uncouple the retrieved geophysical variables. In order to take the discussion beyond the subjective

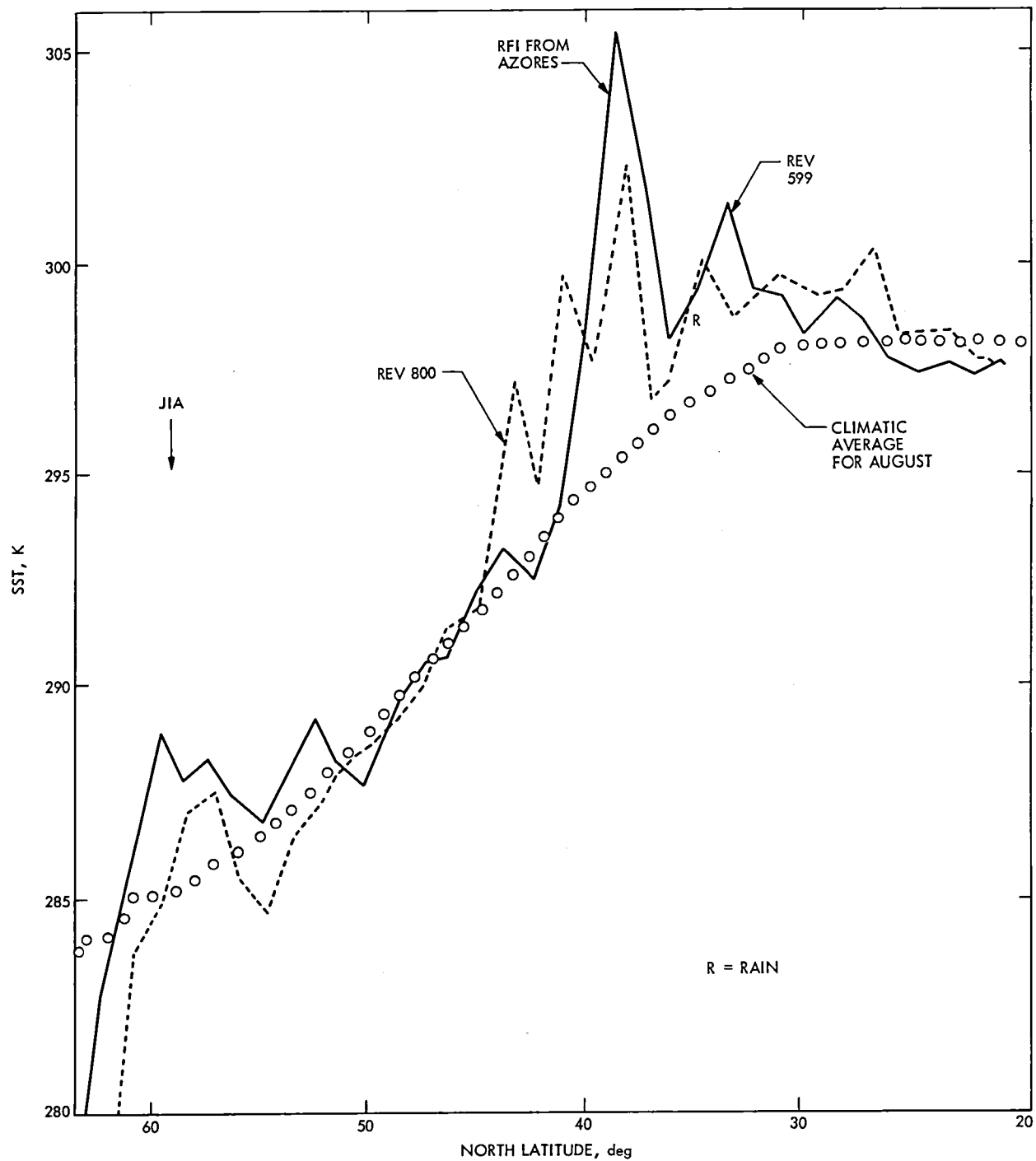


Figure 5-32. Wentz SST Comparisons, Extended JASIN Revs 599 and 800

realm, regressions of SST on wind, vapor, and cloud were performed on the eight-revolution priority set for all the algorithms. Only the points south of a line between (60, 340) and (65, 350) and north of a line between (55, 345) and (60, 355) latitude and longitude were used to avoid obvious land contamination, and only SSTs in the range 275-308 were used. The results are given in Table 5-16 along with the probability of obtaining a correlation coefficient greater than that observed, from a random data set of the same size. For the Wilheit and Wentz algorithms, this probability was calculated with the number of points equal to 16N/121, since the SST on those algorithms is calculated only on grid 1 and interpolated to grid 3 on the computer file. There is some question as to whether the number of independent points for the other two algorithms should also be reduced since the main input to SST is through the 6.6-GHz channels. Fortunately, the conclusions are largely independent of that question.

There is an apparently significant correlation of SST with all the other retrieved variables, although the non-zero natural correlation among the other variables confuses the issue as to whether the correlations are caused by only one of the other variables. Figure 5-33 shows the individual points producing the strongest observed correlation, SST versus cloud for the Rosenkranz algorithm, to give the reader an idea of what the correlation looks like.

The significance of the correlations comes primarily from the large number of points in the data set. Since the correlation coefficient is always less than 0.36, less than 20 percent of the variance in the SST distribution can be ascribed to the correlations. Thus, these correlations, even if real, are not the dominant cause of poor retrievals in general, although they may be in specific cases. Nonetheless, one can readily see that a significant slope is visible in the means of SST determined at each cloud value in Figure 5-33.

Note that this correlation analysis would not pick up errors in the algorithms that would flatten out one variable at the expense of another, such as might have happened in Rev 633. Also, this analysis may have been confused by the RFI, so it is important to analyze more data.

2. Northwest Pacific Area Evaluations

a. Coverage and Surface Truth. The main region of interest, roughly between latitudes 30° and 50°N, and longitudes 145° and 195°E, is shown in Figure 5-34. Seven revolutions are displayed there; and additional five revolutions (not shown in the figure) fill in the gaps between the seven revolutions shown, providing near-complete geographic coverage of the area. In all, there are seven ascending revolutions and five descending revolutions occurring between the dates 19 to 21 September 1979.

Figure 5-35 is the National Marine Fisheries Service (NMFS) monthly mean sea-surface temperature (SST) contour map for the month of September, showing the general features of the strong SST gradients between approximately 35 and 45°N latitudes. The more accurate XBT spot measurements (accuracy ~0.2 K) were used in the actual SMMR SST comparisons. Of these, 63 were ship XBT measurements made between 17 and 24 September and 18 were measurements from XBTs dropped by aircraft on 20 September.

Table 5-16. Correlation of S/C SST With Other S/C-Derived Variables

Algorithm	N	Wind Slope	r ^a	Prob- ability ^b	Cloud Slope	r ^a	Prob- ability ^b	Vapor Slope	r ^a	Prob- ability ^b
a) All Points Away From Land										
Bierman	1228	-0.121	-0.11	0.00	59.8	0.20	0.00	2.008	0.26	0.00
Rosenkranz	1226	-0.152	-0.18	0.00	102.4	0.35	0.00	2.198	0.29	0.00
Wentz	1196 ^c	-0.139	-0.14	0.10	72.8	0.30	0.00	2.138	0.31	0.00
Wilheit	1228 ^c	-0.206	-0.17	0.08	54.6	0.22	0.03	1.918	0.22	0.03
b) All Points Away From Land With Cloud < 0.05 g/cm ²										
Bierman	1189	-0.136	-0.12	0.00	88.6	0.20	0.00	1.927	0.23	0.00
Rosenkranz	1198	-0.156	-0.18	0.00	125.6	0.36	0.00	2.213	0.28	0.00
Wentz	1155 ^c	-0.136	-0.14	0.10	104.0	0.26	0.01	1.846	0.25	0.01
Wilheit	1179 ^c	-0.220	-0.17	0.08	77.9	0.20	0.04	1.717	0.18	0.07

^aCorrelation Coefficient.

^bProbability of obtaining a correlation coefficient greater than that observed from a random data set of the same size.

^cThe number of independent points is 16N/121.

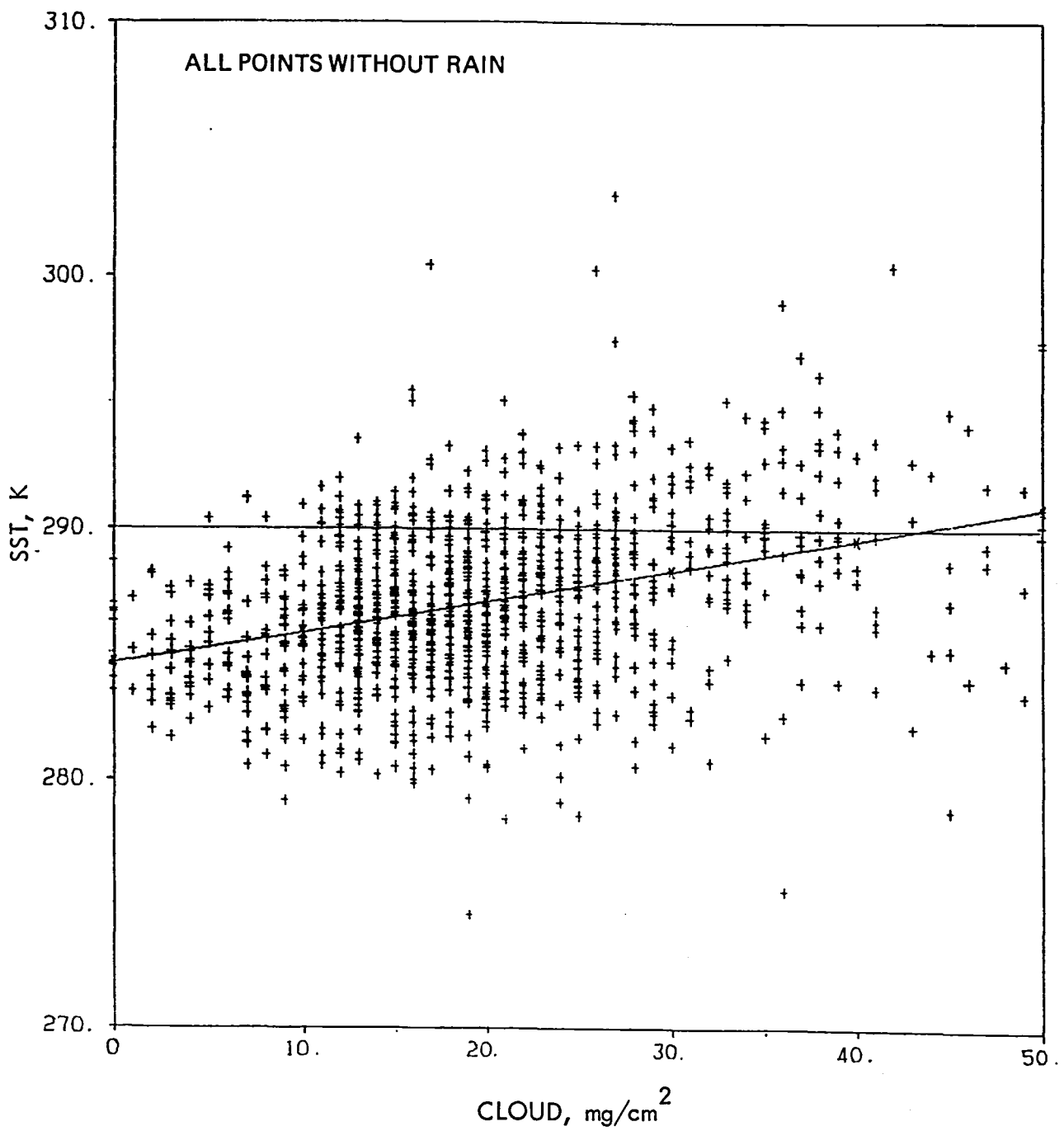


Figure 5-33. SST Correlation With Liquid Water, Rosenkranz Algorithm

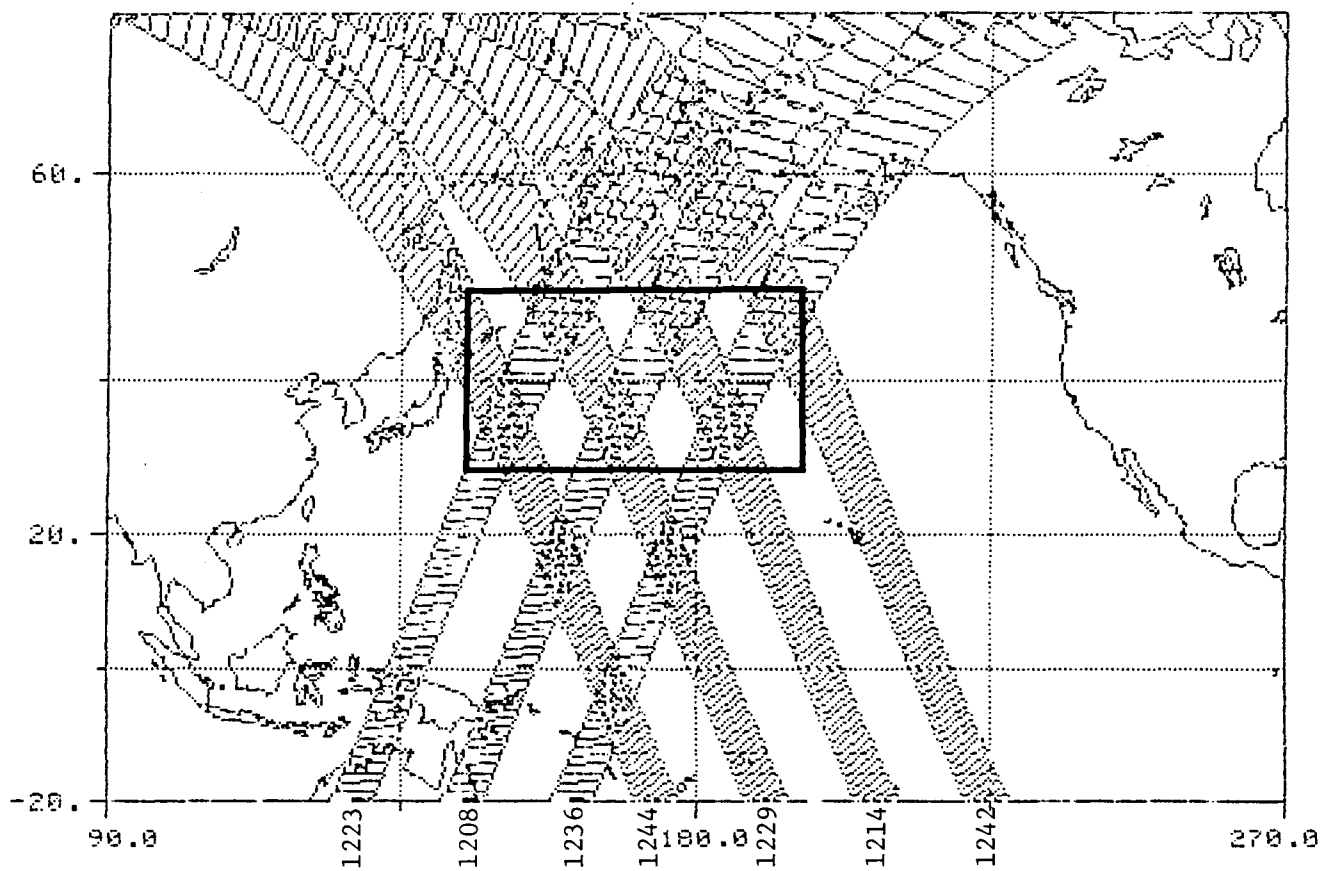


Figure 5-34. SMMR Coverage of the Northwest Pacific Area

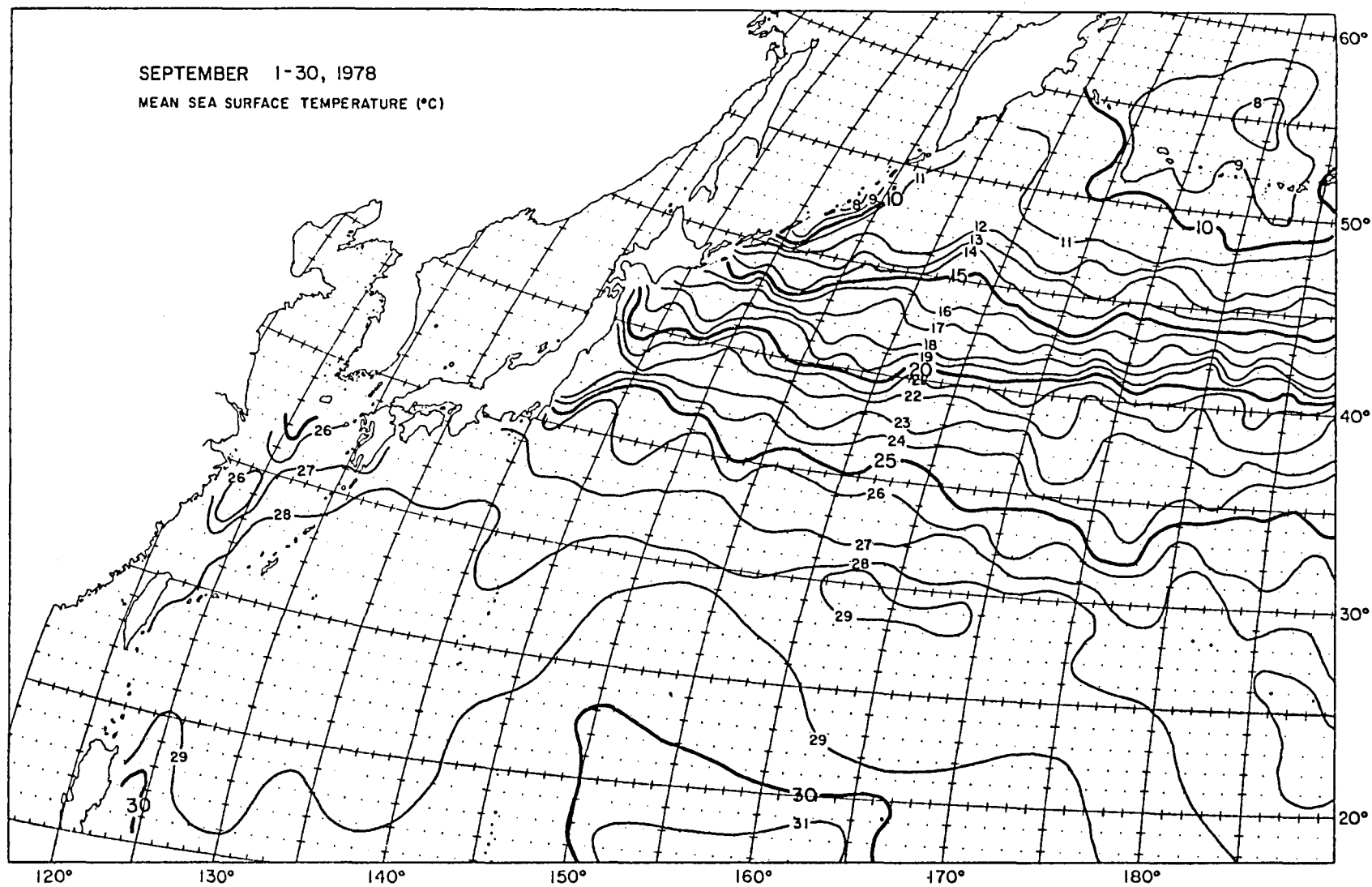


Figure 5-35. National Marine Fisheries Service September 1978 Monthly Mean SST Contour Map

b. Data Comparisons. The SMMR SSTs for the Pacific revolutions were obtained using the Wentz algorithm. Other alternative algorithms were not run due to lack of time. For purposes of comparison, the data were divided into ascending and descending revolutions, and the SMMR data was colocated manually with the XBT locations. Figure 5-36 is a scatter plot of the SMMR vs XBT SSTs for the descending revolutions; Figure 5-37 is a similar plot for the ascending revolutions. The statistics of the comparisons for the two sets independently and combined are given in Table 5-17. No attempt at filtering the SMMR data was routinely made in the SMMR processing algorithms. Thus, problems such as bit errors, rain cells, sunglint, small islands, etc., all show up as anomalous SSTs in the retrievals. This is evident particularly in Figure 5-37. Sunglint was found to be a problem in columns 2, 3, and 4 of the SMMR swath for all the ascending revolutions between latitudes of approximately 30° and 50°N. Since the range of influence and intensity of the sunglint effect depends on the variable surface roughness (i.e., wind speed), it is difficult to correct, and causes a high bias and rms scatter in the retrievals.

In the absence of automatic filtering, the SMMR data for both ascending and descending revolutions were filtered manually, for all occurrences of sunglint (sunglint angle less than 10 deg), rain, land (small islands), and bad data

Table 5-17. Comparison Statistics for Unfiltered SMMR and XBT SSTs

Type Revolutions	Number of Points	Bias, K (SMMR - XBT)	Standard Deviation About Bias, K
Descending	56	0.73	1.66
Ascending	59	4.86	3.82
All	115	2.85	3.62

Table 5-18. Comparison Statistics for Filtered SMMR and XBT SSTs

Type Revolutions	Number of Points	Bias, K (SMMR - XBT)	Standard Deviation About Bias, K
Descending	52	0.53	1.49
Ascending	14	0.70	1.19
All	66	0.57	1.43

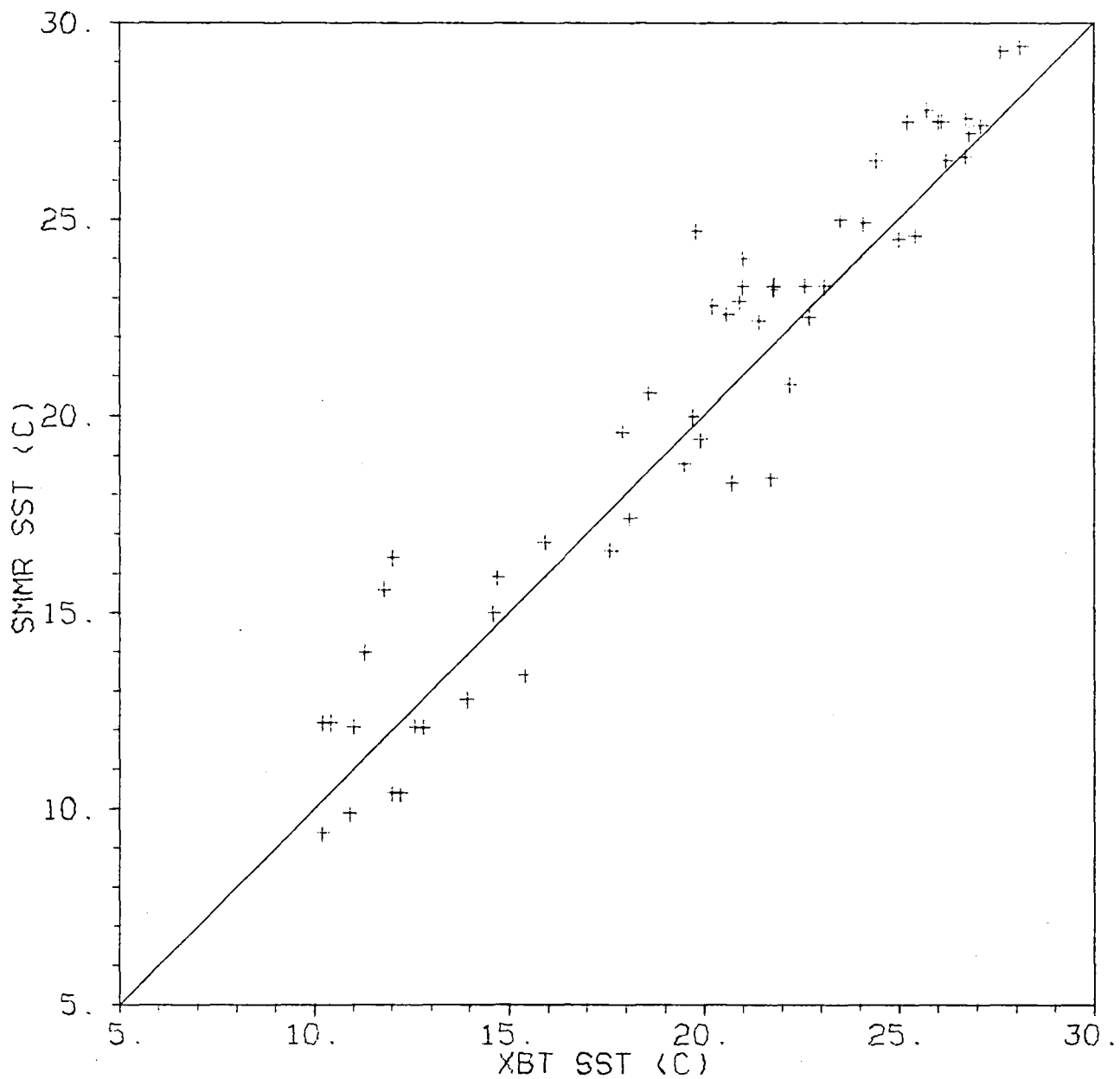


Figure 5-36. Wentz SST Comparisons - NW Pacific, Descending
Revolutions, Unfiltered

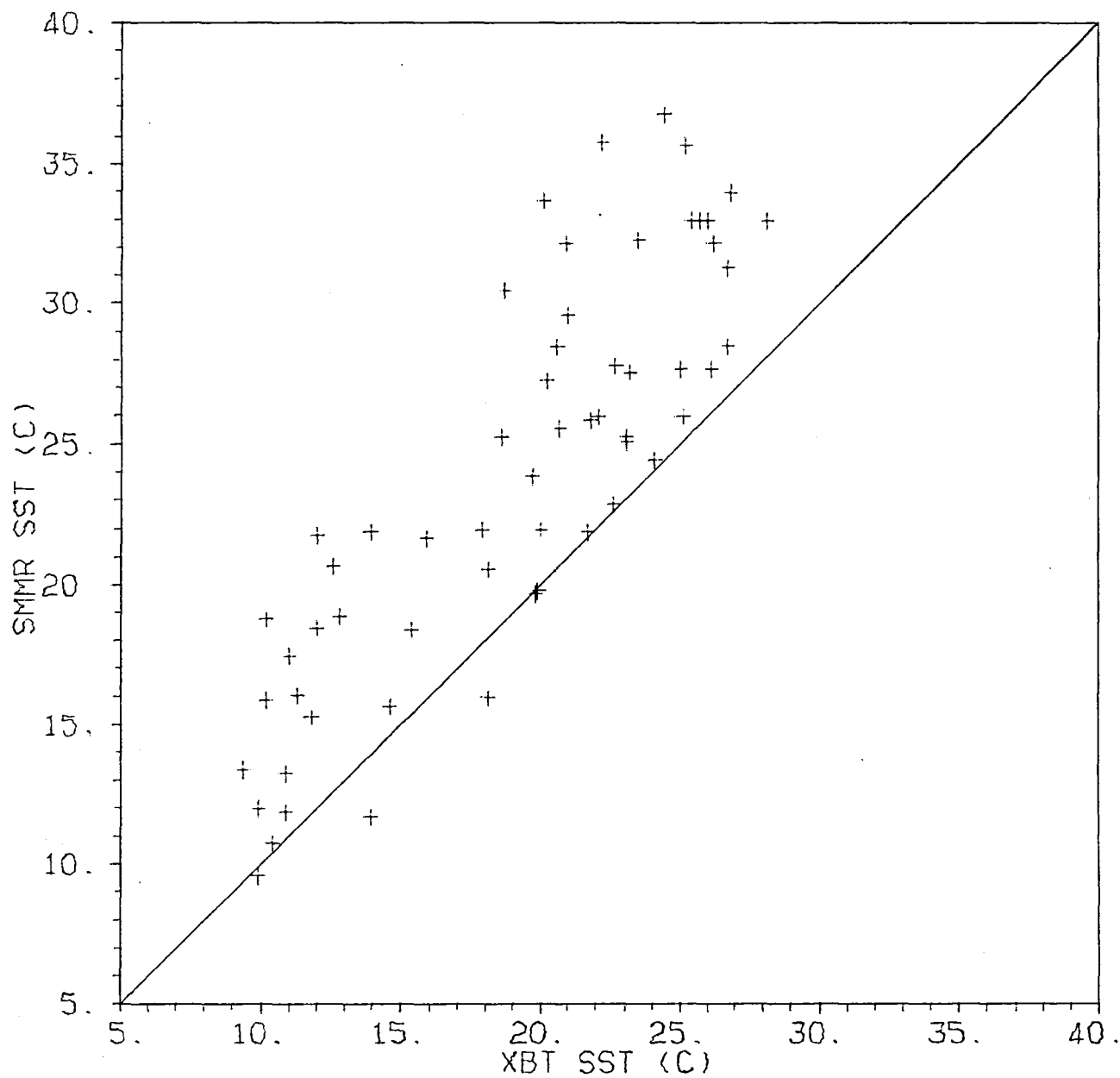


Figure 5-37. Wentz SST Comparisons - NW Pacific, Ascending
Revolutions, Unfiltered

(bit errors propagating through to T_B 's). The results are plotted in Figures 5-38 and 5-39, and the statistics are given in Table 5-18. It is clear that once the data are filtered, both ascending and descending revs give similar results for SST retrievals. No clear bias difference exists between ascending and descending revs, and furthermore the standard deviations about the bias are within the SMMR SST accuracy goals. However, of the original 59 points for the ascending revs only 14 remain after filtering (about 70 percent of the data were discarded due to sunglint). For the descending revs only 4 points had to be discarded, all due to rain.

This study leads to the conclusion that under certain favorable conditions the SMMR appears capable of retrieving sea-surface temperatures within the desired accuracy of 1.5 K. From the SMMR data processed so far, it appears that unfavorable conditions include (1) close proximity to land, (2) radio frequency interference (RFI), (3) sunglint, (4) rain cells, and (5) bit errors and data drop-outs in the satellite-to-Earth data transmission. It should also be noted that instrument calibration anomalies are not evident in the Northwest Pacific data set. However, it is known that on occasions when the sun enters directly into the beam of the sky calibration horns, questionable calibrations result, and these occasions should be considered in the list of unfavorable conditions given above.

3. Tropical Area Evaluations

In the tropical region of the Pacific, where we had Seasat data, we also obtained surface observations from "ships of opportunity." They are listed in Table 5-19. These temperature measurements are not of the same high quality as the JASIN data, but demonstrate unequivocally that the Wentz SMMR algorithm overestimates SSTs in the tropics. A few extreme overestimates of SST can be attributed to rain in the field of view or in the vicinity (see comments in the table).

F. SMMR AND SASS INTERCOMPARISON

1. Case Study of Thunderstorms in JASIN

SASS measurements for Rev 557 indicate anomalies near the southern corner of the JASIN triangle that have been related to thunderstorm activity (see SASS anomaly section). Figure 5-40 shows the integrated water vapor distribution for the previous pass since SMMR data was not available for Rev 557. Also marked are the approximate positions of the fronts in the JASIN area derived from the surface analysis (Figure 4-35 (in SASS)). Time series of water vapor derived from the JASIN radiosondes show maxima at the time of frontal passages. The SMMR also indicates maximum values of water vapor in the neighborhood of the fronts. Drier air occurs to the northeast and southwest well behind the fronts. Within the moist region, higher water vapor values occur in two regions: A and B. The distribution of liquid water shown in Figure 5-41 shows values equal to or greater than 0.05 g/cm^2 , the threshold for precipitation, near both A and B.

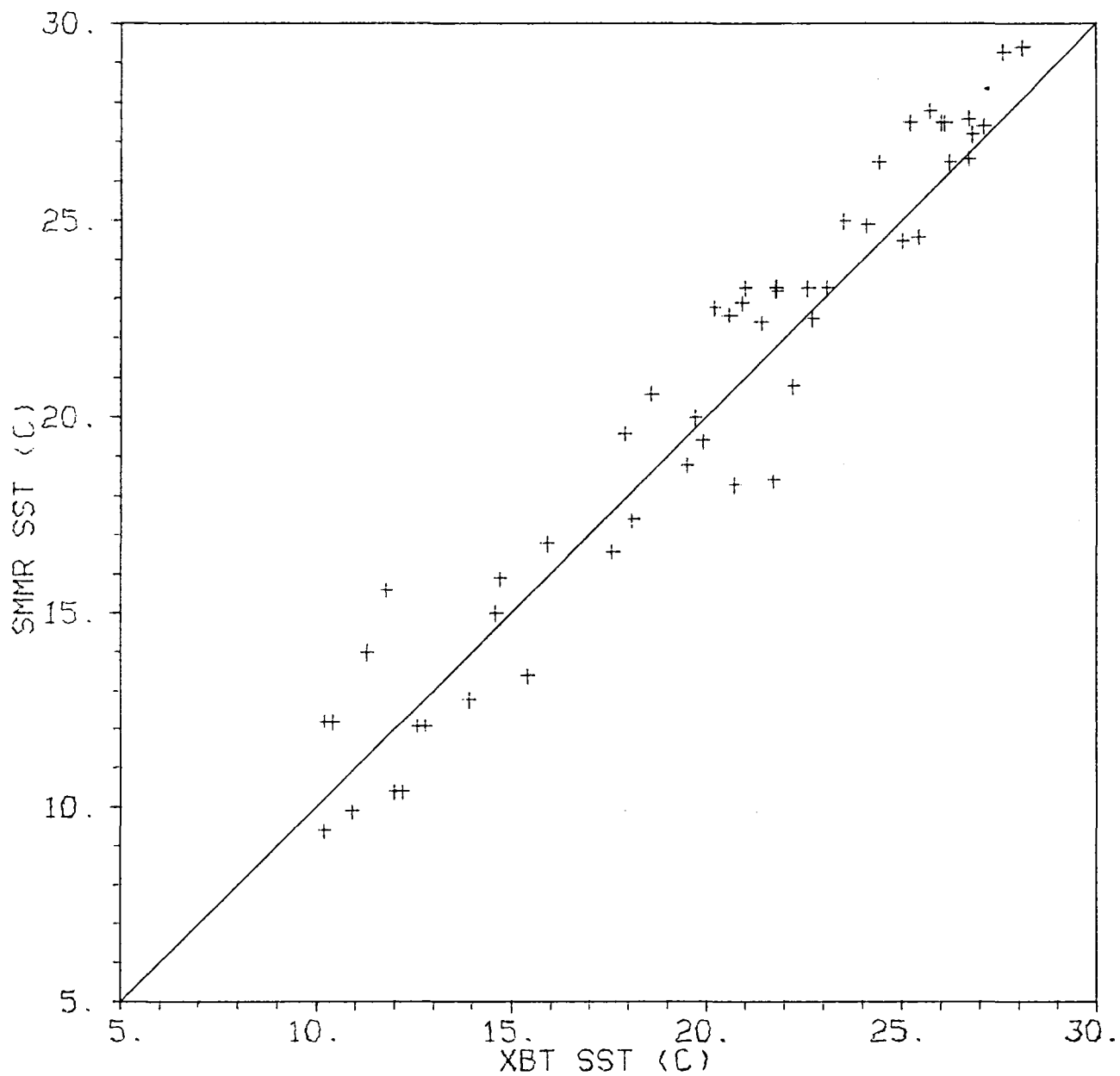


Figure 5-38. Wentz SST Comparisons - NW Pacific,
Descending Revolutions, Filtered

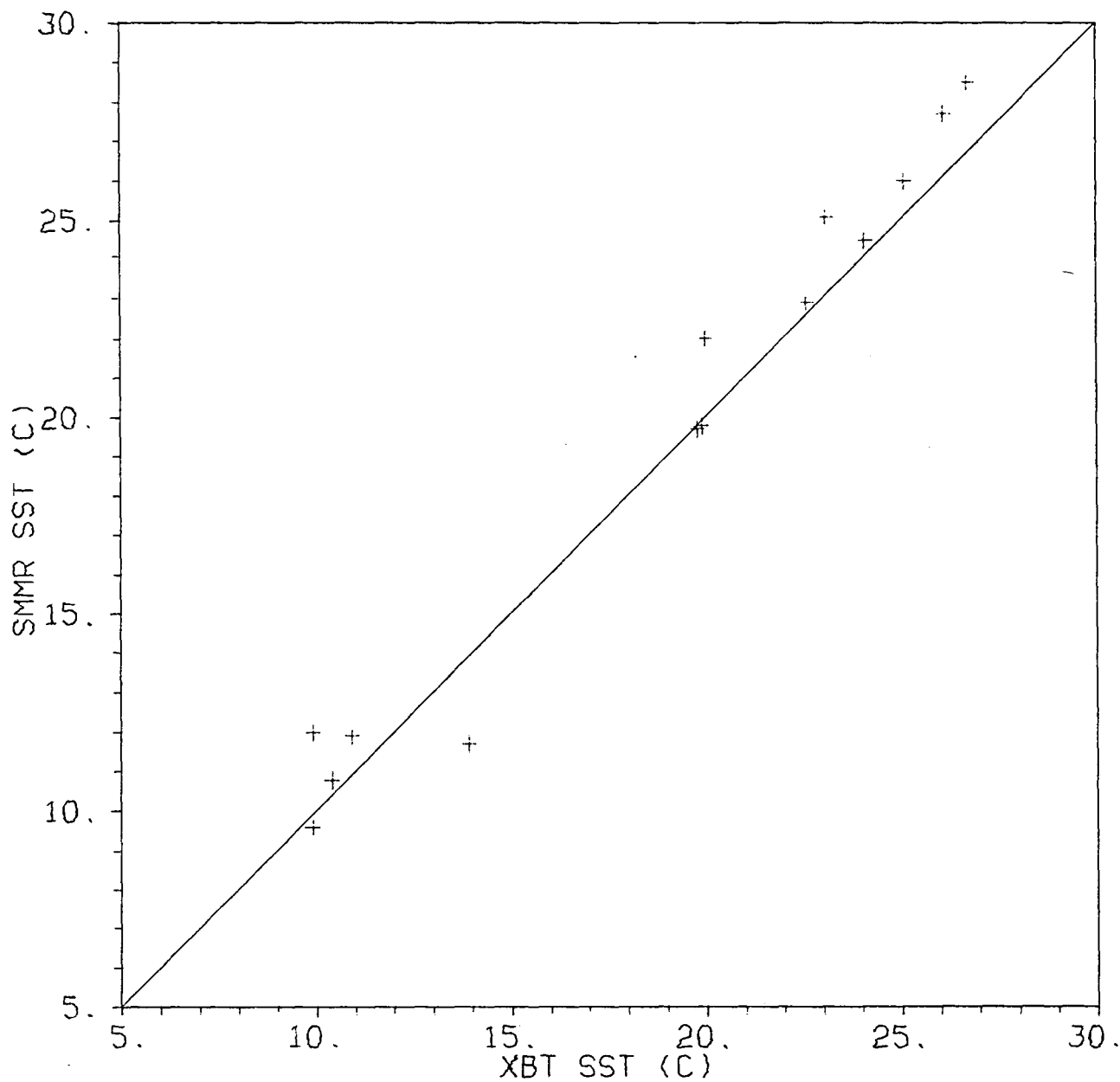


Figure 5-39. Wentz SST Comparisons - NW Pacific,
Ascending Revolutions, Filtered

Table 5-19. SMMR Sea-Surface Temperature (Wentz Algorithm) in the Tropical Pacific Compared to "Ships of Opportunity" Measurements

Rev*	DOY:mo:day:h:min	SMMR SST, °C	Ship Data at 12:00 GMT				SMMR MINUS Ship SST, °C	Comment
			Name	°N Lat	°E Lon	SST, °C		
384	204:07:23:20:35	29.8	TANGO	29	139.3	26.6	3.2	
		33.0	JGZK	26.5	136.9	27.5	5.5	
		36.0	JGMD	19.6	141.7	28.0	8.0	Rain
		30.5	JKEV	28.5	135.1	27.8	2.7	
		31.7	JRYS	27.6	136.7	28.0	3.7	
		33.5	JHJF	10.6	144.8	27.5	6.0	
		33.5	JNKP	15.8	141.1	28.5	5.0	Rain with- in 200 km
		32.1	SMEC	7.6	146.8	30.0	2.1	
427	207:07:26:20:12	30.7	JBUM	20.6	144.7	28.0	2.7	SMMR misses ship by 100 km
		35.9	JCFH	18.3	140.9	26.0	9.9	Rain
		33.8	JFTI	17.0	140.9	29.0	4.8	Rain with- in 200 km
542	215:08:03:21:35	29.0	JGXV	20.7	134.0	26.5	2.5	
		30.9	7JBU	28.5	133.9	28.0	2.9	
628	221:08:09:21:49	29.2	8JCL	30.3	135.8	28.0	1.2	
		30.5	JCRK	25.6	136.7	27.0	3.5	
		28.3	JFMF	29.7	136.8	31.0	-2.7	
		35.3	JKLC	15.3	143.5	30.5	4.8	
		30.0	JCHU	25.8	133.3	26.8	3.2	

*These revolutions are all ascending.

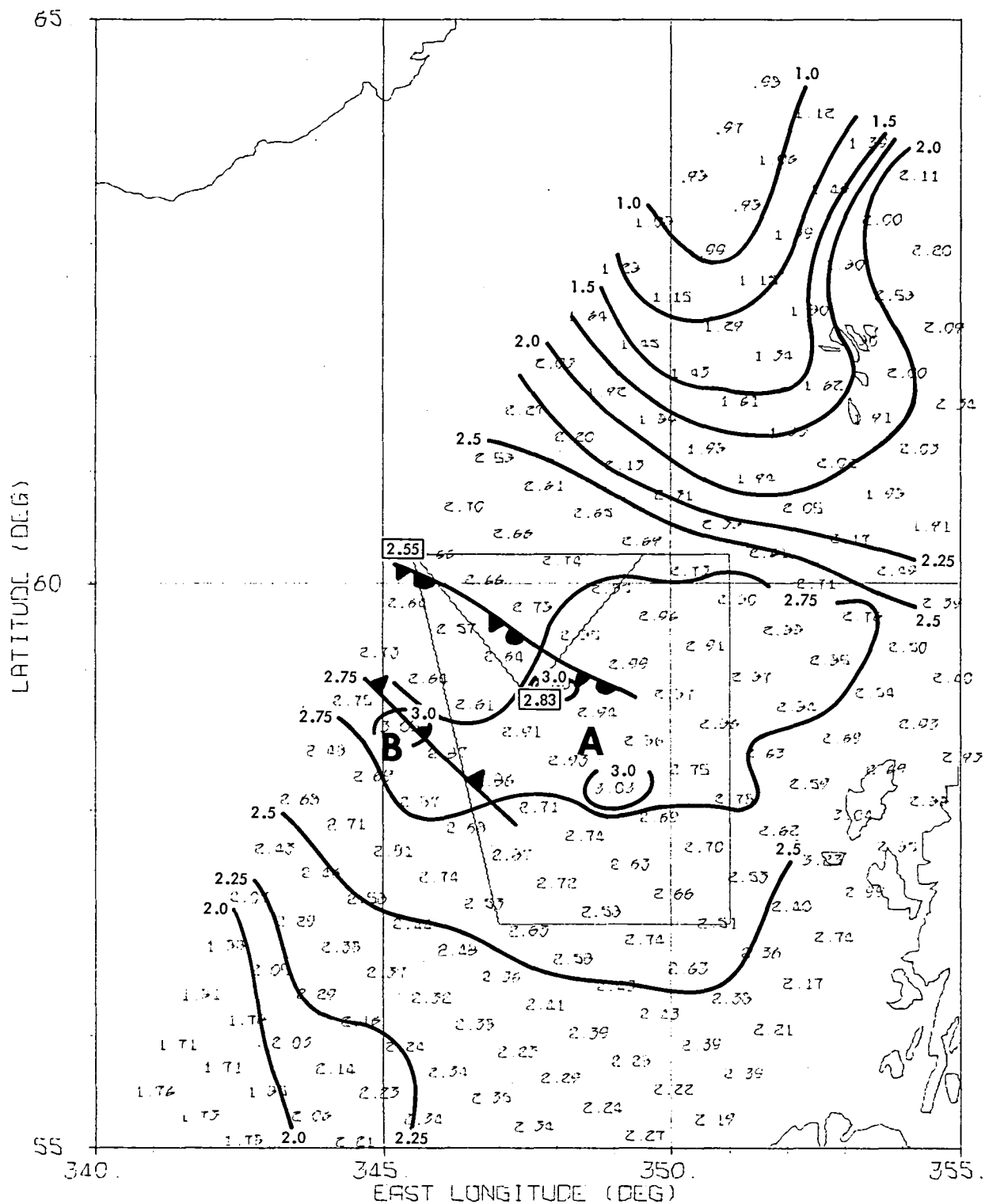


Figure 5-40. Wentz Water Vapor Distribution, Rev 556;
Radiosonde Values are shown in Boxes

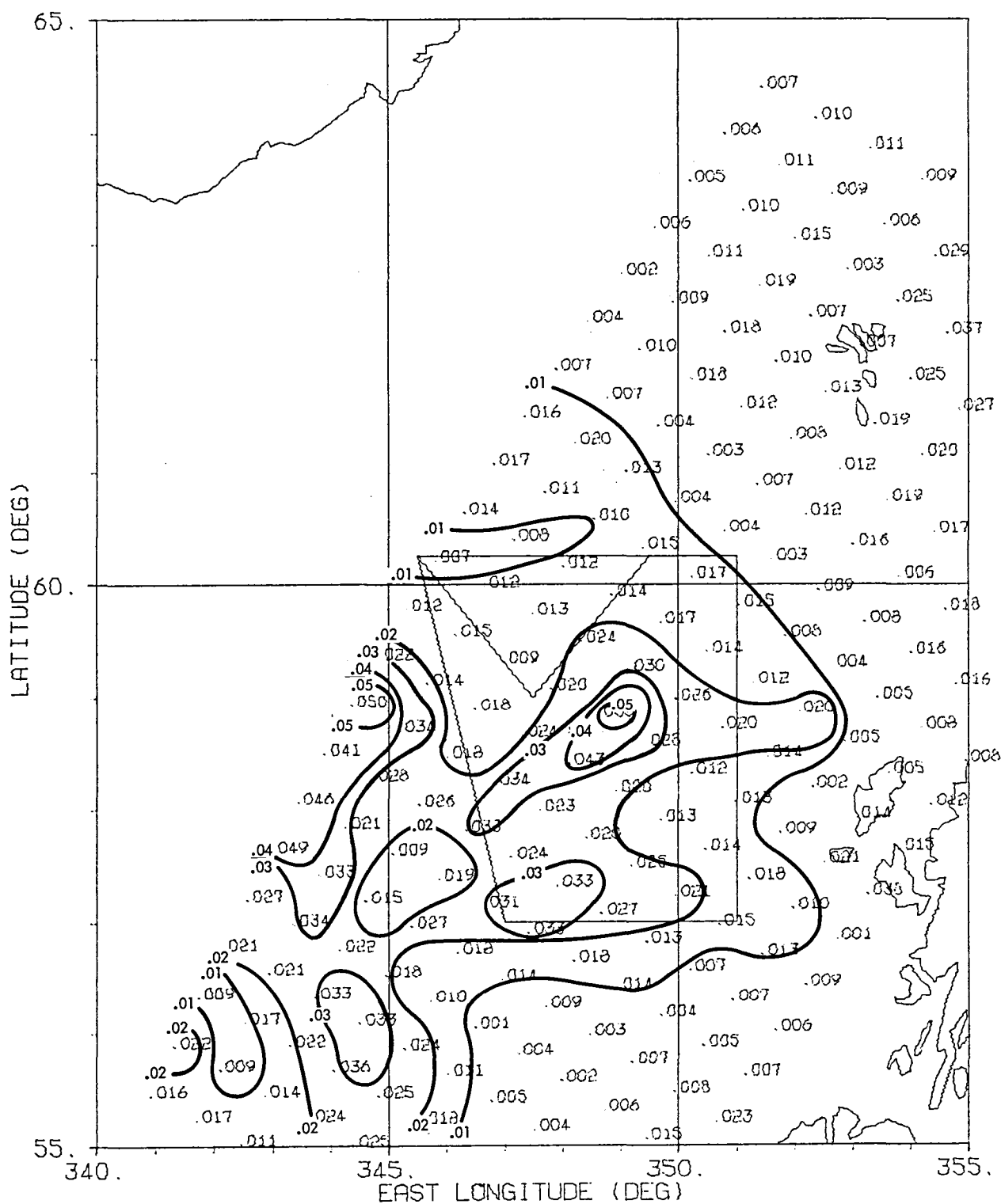


Figure 5-41. Wentz Liquid Water Distribution, Rev 556

Region A corresponds to the region of the developing thunderstorm detected by SASS on the following orbit. That a SASS anomaly was not noted for Rev 556 may have been due to data loss because of a calibration frame.

One can examine the 18-, 21-, and 37-GHz brightness temperatures which provide the predominant input to the water vapor and liquid water predictions. They all show a maximum in the area of interest. As an example, the 18-GHz V brightness temperature is shown in Figure 5-42.

2. Relative Bias Between SMMR and SASS Wind Determinations

For eight revolutions (547, 556, 590, 633, 757, 791, 800, 834) both SASS and SMMR coverages of the triangle fields were very good. Each instrument wind prediction was compared to the University of Washington-produced wind fields at the three corners and the center on these revolutions. The mean difference $\bar{\Delta}$, standard deviation σ , and number of cases N were:

	<u>SASS-Fields</u>	<u>SMMR-Fields</u>	<u>SMMR-SASS</u>
$\bar{\Delta}$	0.0	3.7	3.8
σ	1.57	1.6	1.7
N	22	22	32

Several revolutions did not have well-defined fields of every corner. In addition, the one corner comparison from Rev 633 was dropped since both field and SASS (a high incidence angle) values were questionable.

Since land interference sources were considered a possible reason for the high SMMR bias, comparisons were made for Rev 800 down to latitude 21°. These comparisons yielded:

	Latitude <u>40-47°</u>	<u>30-47°</u>	<u>20-47°</u>	<u>20-30°</u> (open ocean)
$\bar{\Delta}$	3.3	3.1	3.0	2.8
σ	1.8	1.7	1.8	1.9
N	30	70	116	42

This comparison shows that, even though the bias $\bar{\Delta}$ does decrease when more points away from land are included, when only those points in open ocean are compared, the SMMR remains biased high relative to the SASS. Further SMMR-SASS intercomparisons are needed to understand why this relative bias appears in the JASIN passes and not in the GOASEX passes (see Subsection D).

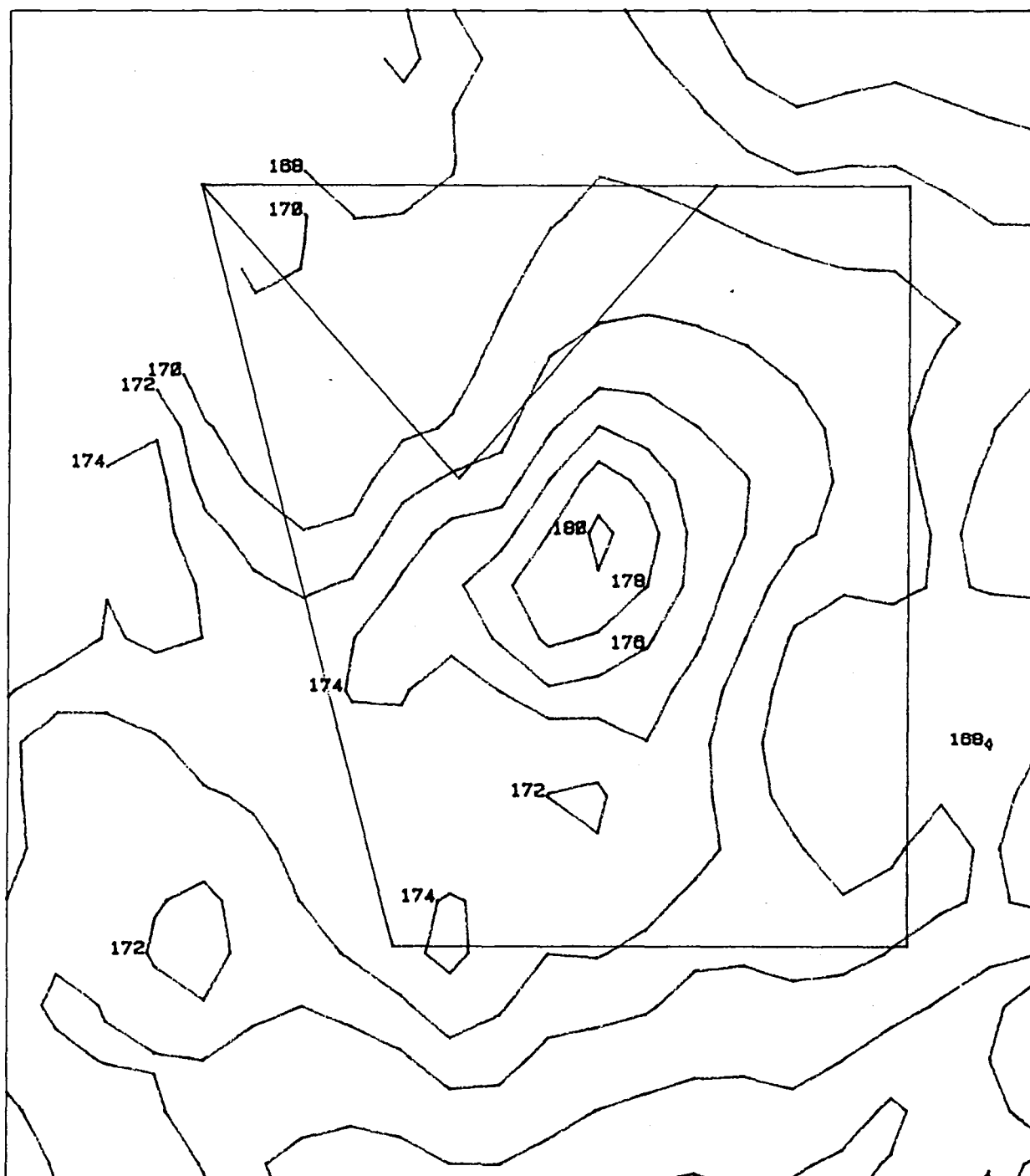


Figure 5-42. SMMR 18-GHz T_B Contours, Rev 556

G. CONCLUSIONS AND SUMMARY

1. Atmospheric Water Determinations

JASIN water vapor retrievals from passes within ± 2 h of radiosonde flights that reached pressures of 250 mbars or less exhibit a standard deviation of 0.12 g/cm^2 about a bias of 0.12 g/cm^2 , which compare favorably with the estimated accuracy of the radiosonde determinations. Results from the three JASIN passes for which sidelobe corrections were not made in the APC revealed no reduced accuracy in the water vapor retrievals. In the tropics, nine comparisons with radiosondes within ± 3 h of spacecraft overpasses show the SMMR water vapor retrievals to be 15 percent high, but land contamination from Guam is probably present in three cases.

In JASIN, the SMMR predicts very well the "widespread" rain reported by several ships. The only quantitative comparison gives estimates from 0.0 to 0.2 mm/h in cells around the John Murray where 0.2 mm/h was measured. Light rain or shower activity of areal extent less than a SMMR footprint causes increases in liquid water estimates, but is not classified as rain.

2. Wind Determinations

Wind retrievals away from land and rain by more than 150 km exhibit a skill comparable to that of the surface truth against which they are being compared. Data from both GOASEX and JASIN areas have standard deviations of 2 m/s, which is within design specification for wind speed accuracy. There is no significant difference in comparisons between ascending and descending passes in either area. However, the wind retrievals showed a high bias of 2.7 m/s in the JASIN area, which is about 2 m/s higher than that shown in the GOASEX area. Intercomparisons with SASS winds on an extended pass out of the JASIN area show that land contamination cannot explain this bias shift.

3. SST Determinations

In the open ocean in the Northwest Pacific when rain and sunglint are absent, the SST estimates exhibit a standard deviation of 1.5 K about a warm bias of 0.6 K. The surface truth in these comparisons has an accuracy of about 0.2 K. Under these favorable conditions, the SMMR meets the design specification for SST accuracy. Under less favorable conditions, the performance is not as good. In the JASIN intensive area, comparisons show a scatter of 2.2 K about a warm bias of 3.1 K, with retrievals from descending passes better than those from ascending. This degradation is probably due to RFI and land contamination, but this must be established quantitatively. Comparisons in the extended JASIN area have qualitatively the same features with a 3 K warm bias and slightly more scatter. The north-south 2 K SST gradient in surface truth over the extended JASIN area can be resolved by suitable data averaging. Correlation of JASIN SST

retrievals with those of wind, vapor, and cloud are non-negligible statistically and may lead to poor SST retrievals in particular cases, but are not a dominant cause of variance in the SST distribution.

4. Sensor File Algorithm Development

The JASIN Workshop has not uncovered any problems that can directly be attributed to inadequacies in the APC. Land contamination quite likely contributes in some way to the high SST and wind bias levels in the JASIN area. However, examination of passes extending out of the JASIN area shows that the high wind biases persist in the open ocean, which probably rules out the APC as a major cause.

The radiometric calibration algorithms also seem to perform as expected. Significant differences of results between ascending and descending passes have been ascribed to sunglint in the Northwest Pacific and to RFI in the JASIN area. Improper calibration in a changing spacecraft thermal environment does not seem to be the cause.

5. Assessment of SMMR Algorithm Status

For certain subsets of the data examined, SMMR performance is very good. The SST determinations in the Northwest Pacific show a scatter of 1.5 K, and the wind determinations in the GOASEX and JASIN areas have a standard deviation of 2 m/s. These results are within the Seasat mission design specifications. Integrated water vapors in JASIN are determined at least as accurately by SMMR as by the radiosondes to which they are compared. Much progress has been made since the Mini-Workshop II five months ago. The sensor file algorithms apparently are producing reliable brightness temperatures, with the "good" and "bad" revolution distinctions now eliminated.

Continued improvements in the SMMR algorithms are not likely to result in determinations significantly more accurate than those cited above. More likely, gains will occur by considerably enlarging the amount of data for which determinations of that accuracy can be made. To accomplish this, the high levels of the JASIN SST and wind retrievals relative to those of GOASEX must be understood. The effect of RFI and land contamination on these levels must be clarified. The physical origin of the large brightness temperature biases required by the geophysical algorithms must be determined. Thresholds for land, cloud, rain, and sunglint contamination must be quantitatively established, and subsequently raised as algorithms for correcting for these effects are developed and improved. SMMR ETG considerations and algorithm development activities must concentrate on achieving the required understanding in these areas.

H. RECOMMENDED DIRECTIONS FOR SMMR EVALUATION ACTIVITIES

1. General Remarks

In the JASIN workshop, the most prominent SMMR problem is the variability of the relative "mean" between spacecraft data and surface truth. Selected comparisons between SMMR determinations and surface truth exhibit standard deviations about the mean difference that are within design specifications. The means, however, vary with the data set in ways, at best, only qualitatively understood. Their variation with land proximity, with general brightness temperature (T_B) level, with possible radio frequency interference, and with whether the pass is ascending or descending has been noted. In past workshops, problems in the geophysical determinations pointed to specific data processing changes that should be made. For example, in the GOASEX I workshop of January 1979, the cross-track gradients in sea-surface temperature called for additional compensations to be made in the antenna pattern correction algorithms. Unfortunately, JASIN workshop geophysical problems do not seem to provide us with such clear suggestions as to where their causes lie.

2. The Problem of Large T_B Biases

The consensus of the SMMR workshop participants was that pursuing an understanding of the rather large brightness temperature biases required by the Wentz algorithm could suggest approaches to solving the variable relative mean problem. This recommendation is based upon the qualitative consistency of somewhat independent determinations of the brightness temperature biases. Wilheit examined GOASEX data and Gautier examined JASIN data, each using models and methods different from Wentz and each other, to estimate T_B biases. Qualitatively, the variation of the biases with frequency agrees relatively well in the three cases. However, the spread between these three independent estimates, as shown in Figures 5-43a and 5-43b, is rather large, reaching 9 K for 21-GHz H. The largest spread between GOASEX biases and JASIN biases occurs at 6.6-GHz H, suggesting possible RFI contamination.

The T_B biases should be checked for the same kinds of variation as seen in the mean differences between geophysical determinations and surface truth. This would allow their characteristic dependencies to be established and give insight into the cause for their magnitude. Specific dependencies that should be investigated are the following:

- (1) The Bias Dependence on Brightness Temperature Level. A large amount of atmospheric water produces high brightness temperatures that should have a no polarization difference. During the JASIN workshop, investigations of storms having high attenuations showed that before biases are added, the 18-, 21-, and 37-GHz channels appear to saturate at values between 250 and 260 K, independent of polarization and consistent with theoretical models. However, when the biases determined from

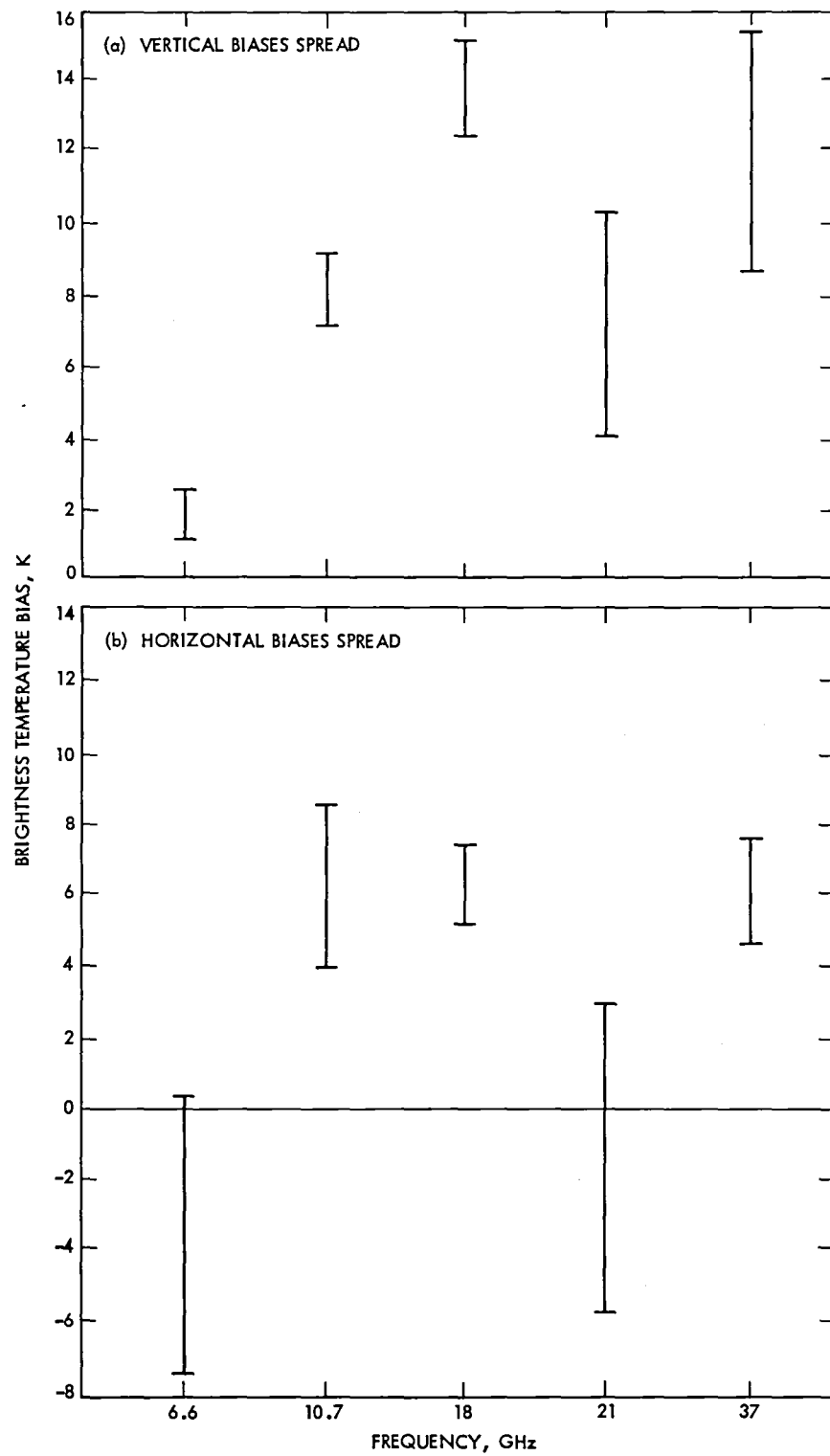


Figure 5-43. Brightness Temperature Biases vs Frequency for (a) Vertical and (b) Horizontal Polarizations

geophysical conditions of predominantly low T_B level (see Subsection B-2-a) are added, the vertical and horizontal polarizations separate. This suggestion of bias dependence on brightness temperature level should be further investigated by producing data over areas such as the Amazon rain forest, where polarization differences are known to disappear. The rain forest acts like a quasi-black body having a T_B that is unpolarized and near 280 K. Any consistent and significant polarization in the T_B measurements could indicate where problems in the calibration or the antenna pattern correction algorithms lie. Also plots of 21-GHz T_B 's as computed from the model function using actual radiosonde data versus the measured T_B values may possibly show how the T_B correction varies with T_B level.

- (2) Temporal Variation of T_B Bias. The thermal environment of the spacecraft changes on basically two time scales. A long-term change occurs because of the precession of the orbit with respect to the sun of approximately 1 deg/day. Early in the mission, the orbit orientation was such that the SMMR was shielded from the sun throughout a revolution. Hence, the thermal environment was stable. From about Rev 500 until about Rev 600, the sun illuminated the SMMR during ascending passes for increasingly longer periods of time. After about Rev 600, the duration of illumination became roughly constant. This alternating occlusion on descending passes and illumination on ascending passes results in the short-term thermal environment change. Level bias of T_B should be investigated for both long-term and short-term changes.
- (3) Change of T_B Level at Ocean/Land Interfaces. Simulations performed before the SMMR Mini-Workshop II indicated that the data more than two resolution cells from the interface should be reliable. This assertion should be checked in more detail, using spacecraft data whenever possible. It is certainly possible that the JASIN sea-surface temperature determinations with the intrinsically coarse resolution of 150 km could be suffering from land contamination effects.

3. Possible Approaches to Eliminating Large T_B Biases

As explained above, independent checks show that large biases are required to make the SMMR brightness temperature consistent with inputs expected by the geophysical algorithms. If we assume this to be the case, the question arises as to which algorithms give rise to or fail to compensate for these large T_B biases. The calibration algorithm activities discussed in Appendix C showed biases of no more than 1 to 2 K were present in the thermal-vacuum data taken before launch. Furthermore, these biases were removed before subsequent data processing. The antenna pattern correction algorithms have been shown in simulations to be

self-consistent to within 1 to 2 K. Consequently, it appears only conceptual errors in sensor file algorithms could account for such large T_B biases. Approaches suggested by the SMMR panel to uncover these possible errors vary in scope and focus. Two fairly specific suggestions were pursued in the JASIN workshop. The first was to see whether the large T_B biases called for a cold calibration reference point different from the cosmic background level of 3 K. A simple analysis showed each channel required a different cold calibration reference, which brings into question the correctness of this explanation, since several channels share each cold reference. This suggestion will be pursued in more depth in post-JASIN activities. The second was to see whether ferrite switch leakage, currently assumed to be zero, would introduce large biases in the calibration. A quick study showed the neglect of the leakage could not account for biases of the size Wentz determined.

Three other approaches were put forth that called for quite substantial efforts and could not be carried out within the workshop. These were:

- (1) Recalibrate Using the Engineering Model of the SMMR. This effort would require a new thermal-vacuum data base to be generated, measurements of all attenuation parameters used in the calibration algorithms to be redone, and simulations of the space thermal environment to account for temporal variations from solar heating to be carried out. Note that this approach assumes whatever is wrong with the SMMR in space is also identically wrong with the Engineering Model.
- (2) Perform Detailed Simulations to Produce Antenna Temperatures. This approach would start with ocean scenes of varying geophysical conditions and land contamination. From the best understood models of air-sea interactions and atmospheric effects, the expected brightness temperatures could be generated. Using antenna range measurements, these brightness temperatures could be converted to simulated antenna temperatures. Comparisons of the simulated T_B 's and T_A 's, produced under well-controlled conditions, with those derived from SMMR measurements should check whether the spacecraft T_A 's also have large biases. Thus, this approach tests whether the large T_B biases are produced in the APC.
- (3) Correlate the Antenna Temperatures with the Housekeeping Temperatures. If the current calibration algorithms adequately handle the problems uncovered in the Mini-Workshop II, correlations between the antenna temperature and housekeeping temperatures should not exist. A careful study should be carried out to verify this. A more elaborate play on this theme would be to correlate the differences in T_A 's or T_B 's calculated in approach (2), above, with housekeeping temperatures.

PARTICIPATING MICROWAVE RADIOMETER PANEL MEMBERS

V. J. Cardone	OW
T. J. Chester	JPL
K. B. Katsaros	Univ. Wash.
C. Gautier	Univ. Wisc.
R. G. Lipes	JPL
E. G. Njoku	JPL
P. Rosenkranz	MIT
F. J. Wentz	RSS
T. T. Wilheit	GSFC
B. B. Wind	JPL

OTHER PARTICIPANTS IN JASIN WORKSHOP EVALUATIONS

R. A. Brown	Univ. Wash.
E. J. Christensen	RSS
T. Guymer	IOS
T. Liu	JPL
A. Milman	SASC
A. L. Riley	JPL
P. Taylor	IOS

SECTION VI

ALTIMETER WIND EVALUATION

As part of the JASIN experiment program, buoys and ships were deployed in a designated region (see Figure 6-1) of the North Sea to take weather and oceanographic data. Seasat overflights of the JASIN experiment area provided the opportunity to evaluate the Seasat data by comparison with the JASIN surface observations. This portion of the report is concerned with the Seasat altimeter wind measurement evaluations. Wave height evaluation for JASIN is covered in Appendix D (A Comparison of Satellite and Sea Surface Measurements of Significant Wave Height, D. J. Webb, 1979) and Appendix E (A Comparison of Seasat-1 Measurements of Wave Height With Measurements Made by a Pitch-Roll Buoy: Preliminary Report, D. J. Webb, 1980).

As shown in the summary (Table 6-1), the altimeter winds are in moderate agreement with winds measured on the surface, and with the SMMR winds after the 3-m/s SMMR bias discussed in Subsections V-D and V-F-2 has been removed. Before drawing conclusions from these data, it is necessary to note the following factors which affect the quality of the comparison:

- (1) Except for Rev 762, the surface measurements were all at least 60 km from the ground track.
- (2) For one of the passes (Rev 432), there was a sharp change in wind speed over a short distance.
- (3) The altimeter value of wind speed obtained from the backscatter coefficient, σ^0 , is very sensitive to small changes in σ^0 . We can write, approximately,

$$\Delta\sigma^0 \approx -3\Delta\omega/\omega$$

where σ^0 is in dB and ω in m/s. Thus, at 9 m/s, the measurement accuracy of 1 dB in σ^0 corresponds to about 3 m/s in ω .

- (4) SMMR measurements are displaced in time from the altimeter measurements by about 100 s.

Table 6-1 contains a comparison between wind speeds as determined by (a) the altimeter, (b) the SMMR, and (c) the surface instruments on either buoy or ship. This is the extent of available data appropriate for wind comparisons. SASS data for the JASIN workshop was not processed for these passes.

The statistics in Table 6-2 are based on the numbers in Table 6-1. Considering that the altimeter specifications imply a 3-m/s accuracy, the Table 6-2 values are well within reasonable expectations. The correlation of the altimeter with SMMR is good, and with surface is very good. The standard deviations of the two altimeter comparisons are each well below the specification value for altimeter alone, not accounting for the contribution to the difference from the errors

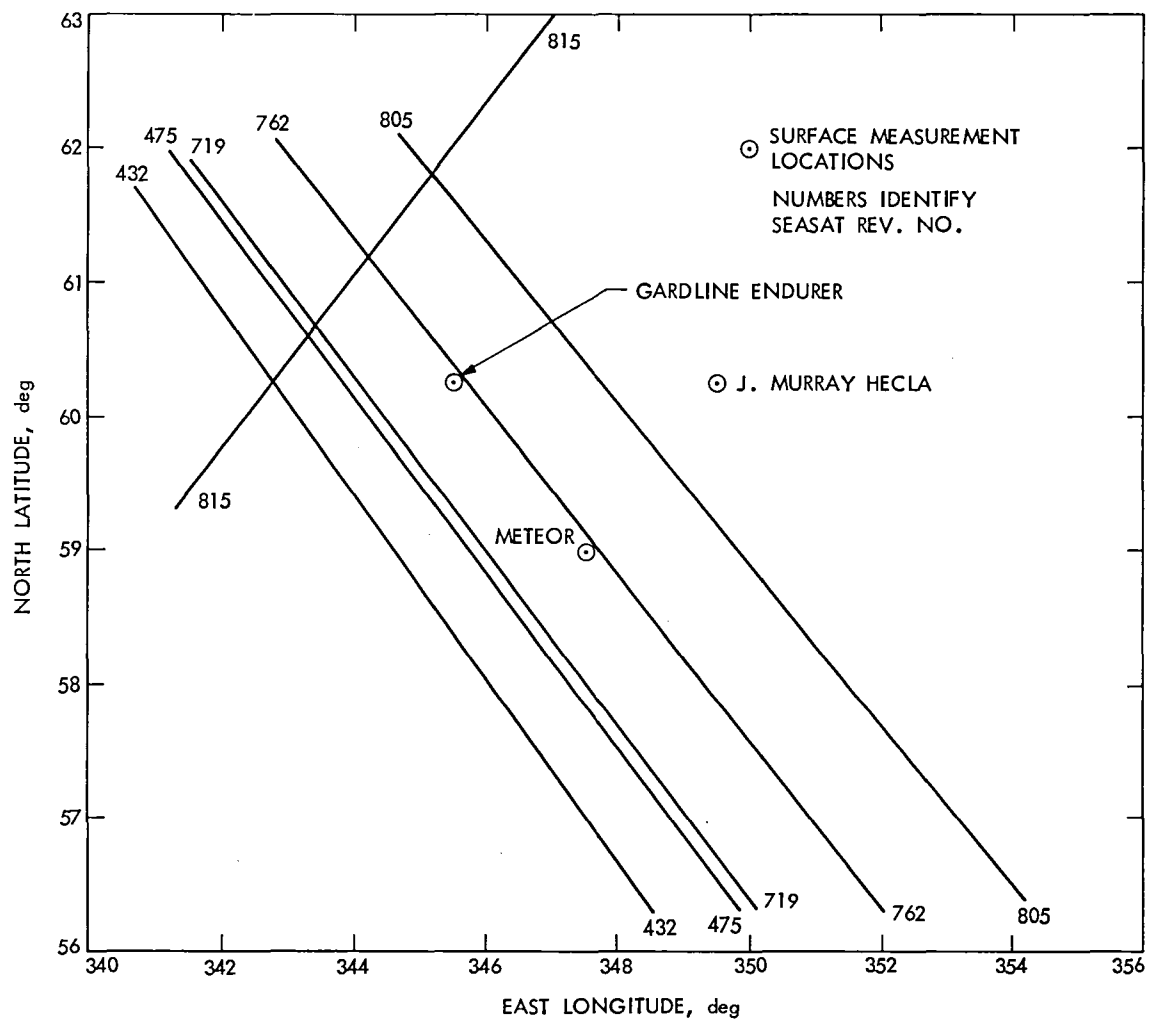


Figure 6-1. Orbit Passes Used for JASIN Area Study

Table 6-1. Wind Data Comparison: Windspeed (m/s)

Rev	Altimeter	SMMR ^a	Surface ^b	Distance From Ground Track ^c , km
432 ^d South	9.0	13	10	100
432 ^e North	5.0	7.0	4.4	100
475	4.6	5.5	6	70
719	8.6	10	9	60
762	10.8	11	14	10
805	8.5	8.5	10	60
815	9.6	-	10.3	60

^a3-m bias has been removed.

^bAdjusted to 19.5 m.

^cDistance to closest surface measurement.

^dSouthern portion of pass.

^eNorthern portion of pass.

in the other measurements. Thus, on the basis of these comparisons, the altimeter measurement looks good. However, the small number of samples and the narrow range of wind speeds (5 to 14 m/s) make it difficult to draw any general conclusions about the accuracy of Seasat altimeter winds.

Table 6-2. Wind Data Comparison Statistics

	ALT-SMMR	ALT-Surface	SMMR-Surface
Mean difference (m/s)	-1.42	-1.15	0.27
Standard deviation of difference (m/s)	1.47	1.12	2.36
Correlation	0.845	0.950	0.721

SECTION VII

SAR PANEL REPORT

A. INTRODUCTION

In general, a synthetic aperture radar (SAR) maps the radio reflectivity of a surface. The particular SAR on Seasat mapped, with a resolution of 25 m, the reflectivity of 1.275-GHz radio waves from areas 100 km wide by 300-3000 km long. The maps, called images, showed a variety of features including what appear to be ocean surface waves, internal waves, oceanic fronts, slicks, and wind gusts. The goal of the various Seasat workshops has been to characterize in some detail the ability of SAR to measure ocean surface waves as well as to understand the mechanisms that produce other features in the SAR images.

The members of the Synthetic Aperture Radar Experiment Team who participated in the first Seasat workshop, GOASEX, considered primarily the ability of the Seasat SAR to observe ocean surface waves. They noted that:

- (1) Waves with amplitudes of 1.0 to 3.5 m could be seen, but not waves with amplitudes less than 1 m.
- (2) No azimuthally traveling waves were seen (these are waves with crests perpendicular to the satellite velocity vector).
- (3) Waves seen by SAR tended to have wavelengths 11 percent longer than waves observed on the surface.
- (4) Contrary to their expectations, they could not see an oceanographic ship that should have been in the images.
- (5) The SAR could be used as a scatterometer to measure ocean-surface winds.

The second workshop, the subject of this report, sought to:

- (1) Assess the ability of SAR to observe ocean waves during a wider variety of conditions than were encountered in GOASEX.
- (2) Determine what phenomena might cause other features seen in SAR images.
- (3) Investigate the ability of SAR to produce detailed maps of the surface wind field.

As our work progressed, we noted that we were hampered by a lack of detailed information about the performance of the radar; i.e., the accuracy to which the position of points in the image were known, the precise geometric and density scales of the optical images, the stability of these scales, and the resolution of scenes in the image. We were able to obtain only a portion of the information we needed, and strongly recommended that the SAR system be thoroughly documented,

including detailed information on the radar, its performance, and the various ways that data were processed to produce the archived images.

B. ABILITY OF SAR TO OBSERVE OCEAN WAVES

During the times the JASIN area was observed from space, the ocean surface waves varied in height from 1.1 to 5.7 m, the wind speed varied from 3 to 13 m/s, and the angle between the direction of wave propagation and the perpendicular to the satellite velocity varied from 3 to 73 deg. On ten occasions the surface wave heights and dominant wave directions were measured by pitch-roll buoys; on four other occasions, wave height was measured by Waverider buoys, and wave directions were estimated by trained observers; and on one occasion wave height was measured by a shipboard wave recorder. The accuracy of these surface observations was estimated by intercomparing the various calibrated measurements. The results, described earlier in Subsection II-E, indicate that the surface observations can be used to assess the performance of SAR.

Of the ten SAR images of the surface that have been analyzed up to the time of this report, only three show surface waves clearly, and one other shows waves faintly.

An assessment of the ability of SAR to observe waves at JASIN was reported in a paper on the "Remote Sensing of the Ocean Waveheight Spectrum Using Synthetic-Aperture-Radar Images," presented at the Conference on Oceanography From Space by John F. Vesecky, Hanny M. Assal, and Robert H. Stewart, and reprinted in Appendix F. Quoting from their abstract:

"Problems in the detection and measurement of ocean waves from their SAR images [are discussed], in particular the measurement of the wavenumber spectrum of ocean-wave-height fluctuations $F(k, \theta)$. Comparisons on a limited set of pitch-roll buoy and Seasat SAR measurements during the 1978 JASIN experiment reveal that degradation of SAR resolution caused by wave orbital motion is a crucial factor in the detection of waves by SAR images. Thus, waves with small slopes travelling perpendicular to the SAR flight path are more easily detected than waves with large slopes travelling along the flight path. Although the SAR estimates in this comparison were found to contain significant biases, they were in rough agreement with buoy measurements, provided the ocean wavelength was between about 120 and 400 m and the ocean wave direction was not approximately along the SAR flight path."

In general, the SAR observations of wavelength were (12 ± 7) percent longer than waves observed at the surface for the four images that showed waves, the waves became more visible as the height of the waves increases, no waves less than 1.4 m high were detected, and SAR observations of wave direction agreed well with surface observations, differing by only (7 ± 6) deg.

In the above analysis, the wave height spectrum was obtained by first Fourier transforming the SAR image to produce a vector wavenumber spectrum that gives the distribution of wave energy as a function of wavelength and direction of propagation. This was then integrated over all angles to obtain wave energy as a function of wavelength. While performing these calculations, we noted that the wave signal

in the Fourier transform of the SAR image was not much greater than the background noise in the transform. Therefore, we restricted the integration over angle to include only that relatively narrow band of angles that included the wave signal. This produced better defined wave spectra than those reported in the GOASEX report. We also noted that the short wavelength asymptote of the spectrum is dominated by noise, and is most likely the spectrum of the speckle in the image rather than the spectrum of small waves.

C. LARGE FEATURES IN THE IMAGES

Synthetic aperture radar images of the ocean often show features which are 1.0 to 5.0 km in extent and which appear to be internal waves, oceanic fronts, slicks, and the gustiness of the wind. In order to determine what phenomena might produce these features, we first assembled images of JASIN areas which were 100 km wide by 300 km long reproduced at a scale of 1:1,000,000. These images not only showed entire features, but they could also be superposed on bathymetric maps to determine if the features seen in the images were associated with bottom topography.

Secondly, we superposed images taken either 8 or 15 hours apart to determine if any features persisted over these intervals on the assumption that atmospheric phenomena are ephemeral while oceanic phenomena such as fronts are persistent.

From these comparisons, we conclude:

- (1) Features which look like internal waves are almost always found over seamounts and at the edge of the continental shelf. These patterns are ephemeral, probably depend on the stage of the tide, and clearly resemble internal-wave patterns seen in pictures of the ocean made from space by Landsat.
- (2) We could identify no large feature that persisted as long as 8 or 15 hours. However, the superposition of the two images was inexact (see Subsection E), and small, weak, persistent features could have been overlooked. Four pairs of images were collected 8 hours apart, and three pairs were collected 15 hours apart. One pair included St. Kilda Island, and the pair was accurately superposed. Half (three) of the other pairs showed land at one end or the other of each image, and these could be superposed with an accuracy of a few kilometers. But three pairs had no land in one or the other image, and the superposition was less precise. Nevertheless, we can state that no large bold features persisted. This implies that either the features were not oceanic or the conditions for seeing the phenomena were not persistent.
- (3) Windrows of streaks were clearly seen in images collected on pass 1006 when wind speed at the surface was 12 m/s. The windrows were aligned in the direction of the wind, and were spaced either 1.3 or 2.6 km apart. If we can assume that changes in reflectivity over large areas are due to changes in wind velocity, then this is the first clear observation of roll vortices in the surface boundary layer of the atmosphere over the ocean.

- (4) Scatterometer observations of wind on pass 557 were anomalous relative to surface observations of wind. After analyzing all available information, the SASS team concluded that thundershowers influenced their radio signals leading to false determinations of wind velocity. Their evidence included entries in ship weather logs that stated thunderstorms were observed in the JASIN area, infrared images from weather satellites that showed cumulus clouds, and weather synopses that indicated thunderstorms were likely. The SAR image recorded 90 minutes earlier on pass 556 showed an area roughly 50 km in size with very low reflectivity upwind of the region with thunderstorms seen by the scatterometer. We conclude that rain probably smoothed the sea surface, producing the feature seen in the image.

D. SHIPS

Thirteen ships participated in JASIN, most for extended periods of time, but none was clearly seen in any of the images. The ships ranged in size from 50 to 100 m, and winds ranged from 3 to 12 m/s, but on no occasion was the sea calm. Calm seas have very low reflectivity, and ships tend to be seen under these conditions, probably as a result of both the increased contrast with the sea and the reduced rolling and pitching that tends to smear the image of ships. This failure to see ships may be due in part to the absence of strong ship wakes which have high radar reflectivity. The ships tended either to move slowly or to be still. But the more likely explanation is that SAR cannot image ships in a rough sea.

Based on our evidence and that of the GOASEX workshop, we conclude:

- (1) No strong reflections are seen from 50- to 100-m long ships in moderate seas for wind velocities greater than three meters per second.
- (2) Conversely, SAR cannot be used to determine the position of oceanographic ships as an aid to performing research at sea.

E. MEASUREMENTS OF WIND SPEED USING SAR

Previous studies of aircraft and spacecraft data suggest that the reflectivity of radio signals from the ocean is a function of surface wind speed and direction. The JASIN data provide a base for further studies of these effects. During the workshop the variations in radar reflectivity (backscatter) with wind speed were investigated using SAR images collected during passes 757 and 791, together with simultaneous measurements of wind velocity made by SASS.

The backscatter of 1.3-GHz radio signals received by the SAR was calculated from measurements of the emulsion density of the 70-mm photographic negatives produced by the JPL optical correlator, and calibrated using the gray-scale

steps (calibration wedges) on the same piece of film. Wind speed and direction were taken from the listings of SASS observations produced for the workshop, choosing those values that coincided most with the position of the SAR observations.

A comparison of backscatter to wind speed for pass 791 shows that increasing wind speed produces increasing backscatter. This was expected, and strengthens the conclusions of both the GOASEX and other studies that SAR can be used to measure wind speed.

The comparisons between similar observations collected on pass 757 are anomalous. The backscatter decreased by 0.6 dB instead of increasing by 0.4 dB as expected from the SASS observations of the wind. T. W. Thompson, who compared the sets of data, concludes that the anomaly cannot be due to shifts in wind direction relative to the spacecraft velocity vector (SAR observes scatter only in one direction and cannot measure wind velocity, SASS measures wind velocity), but that it may result from the inexactness of the coincidence of SAR and SASS observations (the two instruments did not view exactly the same area on the surface).

F. DOCUMENTATION OF THE SAR SYSTEM

The application of synthetic aperture radar images to the study of the ocean surface was hindered by the lack of information about the location of the images, the methods used to process the radar data in order to obtain the images, and assessments of the performance of the radar. These problems can be illustrated by considering the studies (discussed above) that we attempted using SAR images of the JASIN area:

- (1) Are oceanic features visible in the images? To answer this question we assumed that oceanic features persist for hours to days, then looked for features in images obtained either 8 or 15 hours apart. This in turn required images to be superimposed one on top of the other. Without knowing the exact location of the images, we could not be certain that small features did not persist.
- (2) Can the SAR observe the ocean-wave directional spectrum? We Fourier-transformed the SAR images and compared the transforms with wave spectra obtained from buoys on the sea surface. The comparison showed significant differences between the two sets of observations, but we do not know whether these are real or the result of the processing. In one instance (pass 791) waves seen in the JPL digitally processed image are aligned at an angle that differs by 10-20 deg from waves in the JPL optically processed image. In other instances (passes 547 and 791) the wavelengths of the dominant waves seen in the JPL optically processed images differed by 12-14 percent from dominant wavelengths measured by the buoy. Either difference could be real or a consequence of the processing, and resolution of the discrepancy requires more information about the processing and the geometric scales of the images.

- (3) On some days the SAR clearly saw ocean waves; on other days it did not. What are the criteria that enable the radar to see waves? Again, the information about image processing and SAR performance is required. If the point-target response (or the ability of the SAR to resolve features on the surface) is 40 m as indicated by some studies, then we expect that wavelengths shorter than 80 to 120 m will be blurred and invisible. But if the response was 60 m instead of 40 m, even longer wavelengths would be obscured.

Because considerable work would have been required to answer all these questions, we did not attempt much at the workshop. However, the problem of determining the positions of features in the SAR images was studied by T. W. Thompson and B. Holt, and their work is summarized here.

In theory, and ultimately in practice, the position of objects in an image should be known within a few hundred meters. The calculation requires a precise knowledge of the orbit, the time data were collected, and the steps used to process the data. All can be known to sufficient accuracy, but for some passes the exact times were not recorded with the SAR data, and for other passes the details of the processing were not recorded. Both produce practical uncertainties of many kilometers in calculated positions of features in the images.

To estimate the accuracy of the positions in the images processed by the JPL optical correlator, the apparent positions of known landmarks were compared with their exact locations determined from maps. For the purposes of this comparisons, the JASIN data were placed into six classes (Table 7-1).

Table 7-1. Classes of JASIN Data

Class	Time Recorded	Landmarks
Class I	Yes	At both ends of image
Class II	Yes	At one end of image
Class III	Yes	None in image
Class IV	No	At both ends of image
Class V	No	At one end of image
Class VI	No	None

The differences between apparent and true positions were calculated for various coastal landmarks imaged on passes 791, 834, and 1049. The standard deviation of the distance was 10 km; and, in some cases, the distance was nearly constant from one end of the image to the other, suggesting that the recorded times were in error.

Thompson and Holt also investigated the stability of the mapping scales as a function of position in the image. The 70-mm negatives mapped terrain with a scale of 1:500,000, and contain timing marks every 10 seconds. The satellite's velocity relative to Earth's surface (as recorded in the Sensor Data Record) varied from 6.641 to 6.695 km/s during pass 791, and the interval

between 10-s marks should vary only from 132.8 to 133.9 mm. The average measured distance was 133.7 mm, in good agreement with the calculated value. However, all time marks were not correctly spaced: two marks were 20 and 5 mm in error, respectively.

The ability to determine ocean positions on SAR images that have no time recorded was tested using the image collected on pass 547. This shows England and Iceland at opposite ends of the image. The great circle distance between landmarks was 1827 km, and the distance calculated from the image, assuming a scale of 1:500,000, was 1809 km, an error of 1 percent.

Thus, we have two methods of locating the positions of oceanic features. The first is an absolute method that uses only the time code, the spacecraft ephemeris, and the known scale factor of 1:500,000 to find the positions of points with an accuracy of 10 km. This is poor accuracy, and further information about the method of processing SAR data should reduce the error in positions to a few hundred meters. The second method finds the relative distance between landmarks and ocean features using either the known scale factor or the time marks plus the spacecraft velocity. This gives locations accurate to 1 km.

Points in the sixth class of image cannot be accurately located. Because time was not recorded in the SAR data, we must refer back to the logs of the receiving that originally recorded the SAR data -- this was Oak Hanger, England for the JASIN data -- to obtain the time at the station when data were recorded. If this time is accurate to one second, a reasonable but untested assumption, then locations are unknown by 6.6 km, the distance the spacecraft travels in one second. To this distance must be added the additional uncertainties of 10 km noted above, to yield an estimate of 12 km uncertainty for the position of features in this class of image.

Thus, for the purpose of our work, we estimate that oceanic features can be located with the accuracy given in Table 7-2.

Table 7-2. Accuracy of the Location of Features in SAR Images

Class	Accuracy	Comments
I, II, IV, V	1 km	Position relative to landmarks in image
III	10 km	Position calculated from time code
VI	12 km or greater	No landmarks, no time recorded in SAR data

Note that this is the best accuracy with which features can be located using the original 70-mm images. The 1:1,000,000 scale images superposed on maps had somewhat larger errors because the map projection of the SAR image is

not the same as that of the bathymetric maps, and the photographic reproduction did not yield scales of exactly 1:1,000,000. More accurate superposition requires that both map and image be reproduced at the same scale using the same projection, work that is best done on digital computers rather than in the photographic laboratory.

Because of the remaining difficulties in understanding SAR images, we strongly recommended that the SAR system, methods of processing the data, and tests of the system be well documented. If the system is not well understood, and in some aspects it is not, we recommend that studies be performed to characterize the system and its accuracy. We further recommend that this work be summarized in a form for publication in the scientific literature, with complete details included in a technical report.

APPENDIX A
DETAILS OF WMO COMPARISONS

This Page Intentionally Left Blank

APPENDIX A

DETAILS OF WMO COMPARISONS

1. PROCEDURE

Intercomparison data from each platform were initially surveyed for coding errors and inconsistencies resulting from ship maneuvers. Intra-platform means and standard deviations of each variable were calculated for each participating vessel during intercomparison periods. These statistics were employed when estimating atmospheric stability or when relating inter-platform disagreement to the absolute meteorological state. Intercomparison time series of inter-platform sensor disagreements were produced by taking the mathematical difference between observed variables for each platform taking part in the intercomparison. Inter-platform means and standard deviations of these disagreements were calculated, and, assuming the disagreements to be normally distributed, the 90 percent confidence intervals of the estimates of the mean inter-platform sensor disagreements were calculated [Miller and Kahn, 1962].

Resulting from this initial procedure, then, was a time record of inter-platform sensor disagreements. Consistent disagreement throughout JASIN implied that the sensors in question behaved in a constant manner, and it remained only to explain these errors in terms of known physical disparities, e.g., non-uniform sensor heights, or to attribute the errors to instrument bias. Inconsistent disagreement required further analysis of inter-platform error in terms of atmospheric stability or in terms of trends or drifts to be estimated by regression techniques. Inconsistencies unexplained by these considerations or by change in bias remained as error in the four-ship system.

For this report Meteor was selected as the meteorological standard to which the variables from the other vessels were corrected. Meteor was chosen because of her presence at more intercomparisons, because of her preferred method of station keeping, and because of her station's proximity to many of the other JASIN ships and buoys which eventually must be tied into this analysis. Meteor's WMO values thus remain uncorrected unless systematically indicated by data from the other three ships.

2. RESULTS

a. Winds. Hecla, although her anemometer at 20 m was 3 m lower than Meteor's, generally recorded greater wind speeds, the disparity increasing with absolute wind speed. By linearly regressing Hecla's winds on Meteor's, this error can be explained ($r = 0.97$) by assuming that Hecla's anemometer oversped and had a higher starting velocity. It is known that the anemometer which was used for Hecla's WMO winds was large and heavy, so this assumption is not without basis. The wind speeds reported from John Murray and Gardline Endurer were generally lower than those from Meteor, reflecting the lower anemometer heights aboard these ships, 11 m and 15 m, respectively. A large portion of this disagreement was explained by the expected wind speed difference that would have been

registered by anemometers at these respective heights in a non-neutrally stratified constant flux layer (Businger et al., 1971). On some occasions this difference amounted to as much as 10 percent of the absolute wind speed, and since most of the disagreement between Meteor and John Murray and Gardline Endurer was explained by this procedure, no corrections were applied to wind speeds from the latter ships. For the JASIN period the overall accuracy to which wind speed can be determined from WMO observations taken by the four ship network is, to date, about 1.5 m/s.

As determined by intercomparisons during the period 22 July to 9 August, Meteor underestimated wind direction by about 15 deg. Curiously, this is about the error that would have arisen had wind direction been referenced to magnetic, rather than true, north. At the beginning of phase 2 on 20 August, this error is no longer present, but definitely reappears by 5 September. Indications are that it may have reappeared as early as 29 August. Exact determination of its duration must await intra-platform comparison of WMO and autologged wind directions. Wind directions from Hecla and Gardline Endurer appear reasonable as recorded and no corrections are necessary. John Murray suffered a measured displacement of about -15 deg in the alignment of her WMO wind vane. It is thought that this shift occurred in heavy seas between phase 0 and phase 1 and remained constant throughout the remainder of JASIN. Inter-platform means confirm this assumption and also suggest that the initial vane alignment was in error by about -5 deg. These corrections have been adopted.

b. Pressure. Meteor's WMO air pressures were obtained from her autologging pressure sensor; WMO pressures from each of the other ships were obtained from several precision aneroid barometers (PABs) and from an autologging pressure sensor. In this report only PAB is considered. All PAB pressures except John Murray's were corrected according to manufacturer's specifications provided with the instruments. However, Gardline Endurer pressures were not corrected after 1600 on 19 August and if 1000 mbars or greater should be increased by 0.1 mbar. Additionally, all pressures were corrected to sea level except Gardline Endurer's, which should be increased by about 0.2 mbar accordingly. After these considerations, Gardline Endurer's pressures were still on the average about 0.1 mbar lower than Meteor's, and this value has been adopted as a bias. Hecla's PAB disagreement with Meteor increased by about 0.3 mbar on 28 July. Apparently, the PAB was replaced just after this intercomparison. The disagreement remained constant throughout the remainder of JASIN, which suggests that either the replacement PAB suffered from the same offset or that the replacement was actually made prior to 28 July. Current intra-platform analysis on Hecla's pressure signals should shed more light on this. After adopting this 0.3-mbar correction to Hecla's pressures from 28 July, consistent disagreement with Meteor's pressures was found to be on the average 0.1 mbar, and this value has been accepted as an additional bias to be added to all of Hecla's pressures. During all intercomparisons between Meteor and John Murray, Meteor generally reported higher pressure, and the disagreement increased with increasing absolute pressure. Linear regression on these variables ($r = 0.99$) allows John Murray's PAB to be corrected as a function of absolute pressure. This is perhaps a manifestation of PAB error at room temperature for which no correction was applied aboard John Murray during JASIN.

c. Temperatures. Meteor always recorded lower air temperatures than the other three ships. This has been taken as an indication that she exhibited less "heat island" effect and that her temperatures are most representative. Spot comparisons between Meteor and buoys K2 and K3 tend to confirm this belief. On the average Hecla, John Murray, and Gardline Endurer dry-bulb temperatures are biased 0.3°C, 0.5°C, and 0.5°C too high, respectively. Expected temperature differences arising from observation of temperature at different levels in a non-neutrally stratified atmosphere (accounting for no more than 0.2°C) have been considered, but not included, in these corrections. Computer wet-bulb temperature corrections are not as great, being about -0.3°C, -0.3°C, and -0.1°C.

An entry in Meteor's log on 27 July states that prior to 1300 her bucket sea-surface temperatures had been up to 0.5°C too low and that logged values had been corrected after that time. However, no indication is given of exactly how these temperatures were corrected. Intra-platform comparison of bucket temperature with sea intake temperature comparisons indicate: 0.3°C is to be added to Meteor's sea bucket temperature prior to 1300 on 27 July, no correction from then until 0100 on 3 August, 0.4°C is to be subtracted from 0100 on 3 August to 1200 on 9 August, and no correction thereafter. Because of significant gradients in sea-surface temperature over the area occupied by the ships during intercomparisons, it has been impossible, as of yet, to apply sea bucket corrections to the other ships. Due to this fact the overall uncertainty is 0.8°C.

3. SUMMARY OF CORRECTIONS

The corrections mentioned in the previous section enable one to correct the WMO observations as logged from the four JASIN meteorological ships. All corrected values are standardized to Meteor and are referenced to the original sensor heights at which the observations were made, except for pressure which is referenced to sea level.

a. Wind speed (m/s).

METEOR = METEOR
HECLA = 0.89 (HECLA) + 0.30
MURRAY = MURRAY
ENDURER = ENDURER

b. Wind direction (°T).

METEOR = METEOR + 16 to 1300, 9 Aug.
 = METEOR + 3 1300, 9 Aug. to
 1400, 29 Aug.
 = METEOR + 16 1400, 29 Aug. on
HECLA = HECLA
MURRAY = MURRAY + 5 to 1200 28 Jul.

= MURRAY + 19 1300, 28 Jul. on
ENDURER = ENDURER

c. Pressure (mbars).

METEOR = METEOR
HECLA = HECLA + 0.08 to 0600, 28 Jul.
= HECLA + 0.40 0600, 28 Jul. on
MURRAY = 1.00640 (MURRAY)
-6.23
ENDURER = ENDURER + 0.38 to 1700, 19 Aug.
= ENDURER + 0.38 1700, 19 Aug. on
if $P < 1000$
= ENDURER + 0.48 1700, 19 Aug. on
if $P \geq 1000$

d. Dry-bulb temperature (°C).

METEOR = METEOR
HECLA = HECLA -0.3
MURRAY = MURRAY -0.5
ENDURER = ENDURER -0.5

e. Wet-bulb temperature (°C).

METEOR = METEOR
HECLA = HECLA -0.3
MURRAY = MURRAY -0.3
ENDURER = ENDURER -0.1

f. Sea bucket temperature (°C).

METEOR = METEOR + 0.3 to 1300, 27 Jul.
= METEOR 1300, 27 Jul. to
0100, 3 Aug.
= METEOR - 0.4 0100, 3 Aug. to
1200, 9 Aug.
= METEOR 1200, 9 Aug. on
HECLA = HECLA
MURRAY = MURRAY
ENDURER = ENDURER

REFERENCES

Businger, J.A., Wyngaard, J.C., Izumi, Y., and Bradley, E.F., 1971:
"Flux-Profile Relationships in the Atmospheric Surface Layer,"
J. Atmos. Sci., Vol. 28, pp. 181-189.

Miller, R.L., and Kahn, J.S., 1962: Statistical Analysis in the
Geological Sciences, John Wiley and Sons, New York, 483 pp.

APPENDIX B

THERMAL EFFECTS IN THE SMMR

This Page Intentionally Left Blank

APPENDIX B

THERMAL EFFECTS IN THE SMMR

After the Mini-Workshop II, it was discovered that the SMMR instrument experienced large unanticipated temperature changes through the mission. Subsequent to about Rev 600, the peak instrument temperature during each orbit increased by more than 10 K, while the minimum instrument temperature was roughly unchanged. The cold calibration counts also increased and varied throughout each orbit. In addition, the peak cold counts during each orbit in the low-frequency channels (6.6 and 10.7 GHz) occurred simultaneously with the minimum cold counts in the high-frequency channels (18, 21, and 37 GHz). This unexpected 180-deg phase change called into question the ability of the SMMR T_A calibration algorithm to account for these variations.

Subsequent investigation revealed that the observed cold count variations probably result from system gain changes due to dynamic thermal gradients within the instrument. As such, they are, indeed, taken into account in the calibration algorithm. The remainder of this appendix explains how these gain changes arise.

The system gain is determined by a cascade of components which includes a temperature compensation network to maintain gain stability. The SMMR is designed such that the temperature sensing device in this network is physically located (in the video amplifier) at some distance from some of the more temperature-sensitive components (the mixer/preamp). Thus, a difference in temperature between the locations of the video amplifier (bay 18) and the mixer/preamp (bay 1) will result in a gain variation. The gain sensitivity to such a thermal gradient is large enough to explain the observed calibration variation.

The flight temperature data indicate the presence of damped thermal waves propagating through the instrument bays from the surface illuminated by solar flux. The mixer/preamp components are positioned in the instrument such that those of the lowest frequency are near the outer surface of instrument and those of highest frequency are located innermost from the surface. Furthermore, the IF/video components are located in the opposite fashion with the highest frequency channel components located near the outer surface. This arrangement maximizes the thermal gradient and reverses the sign of the gradient of the low-frequency channel components with respect to those of the high-frequency channels. The net effect is a reversal in the phase of the gain variations between these two types of channels.

Calculations of the cold count variations were carried out for each channel using RF component temperature variations determined from spacecraft telemetry data. Video amplifier temperatures are not telemetered to the Earth, and it was necessary to hypothesize values for these temperatures. The temperature fluctuations with time were modeled as "saw-tooth" waves and were characterized by the time of minimum temperature and maximum temperature, and by the amplitude of the temperature fluctuations. The values used for these parameters, for orbit 1206, are shown in Figure B-1 as a function of component position from the louvers. The solid lines represent characteristics of the mixer/preamp temperature variation as implied from telemetry data, and the dashed lines represent the characteristics of the video amplifier inferred from a fit of the model to the measured cold

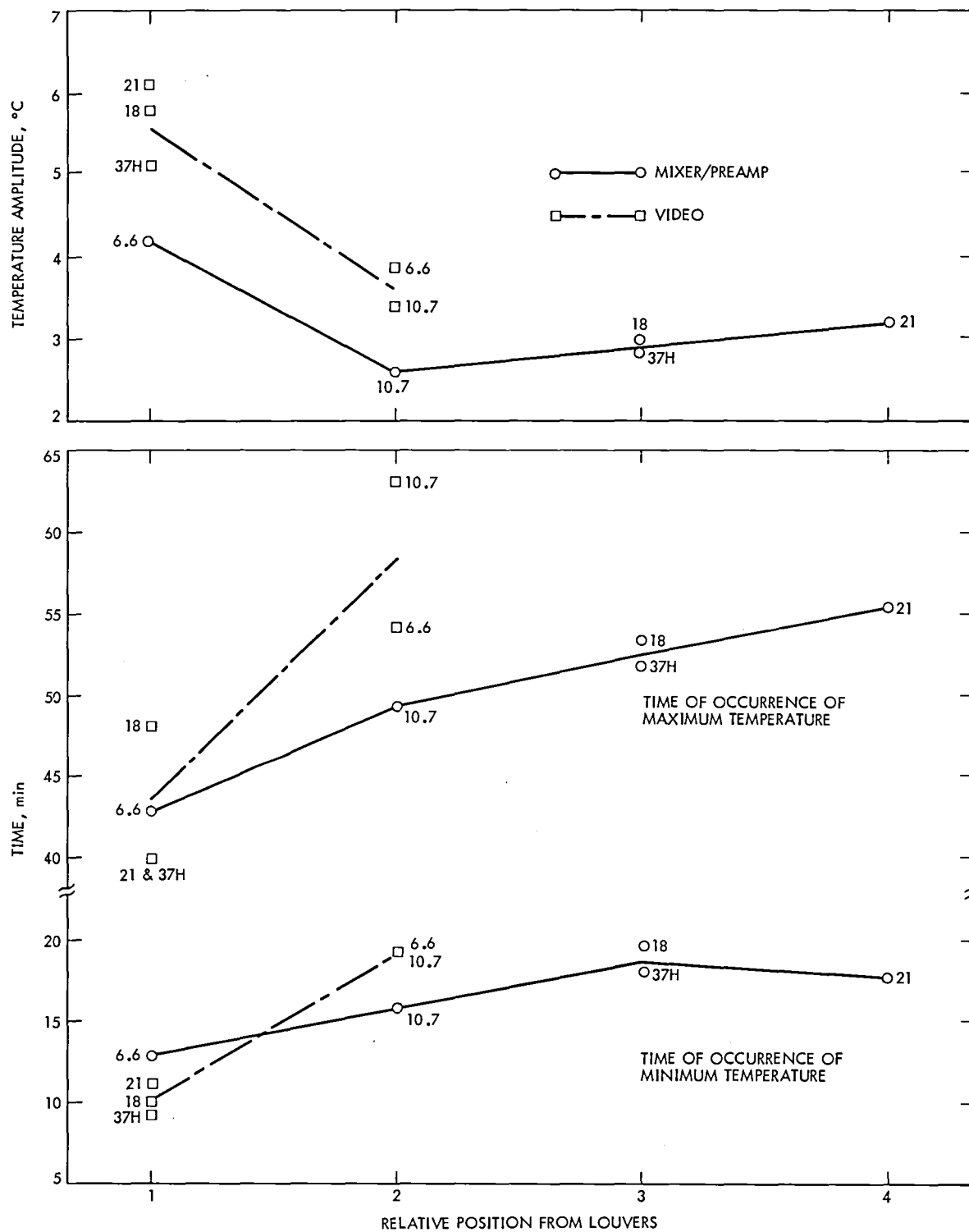


Figure B-1. Characteristics of SMMR Component Temperature Variations

calibration data. Note that the mixer/preamp components closest to the louvers (position 1) experienced about a 4 K temperature variation and that the model implies about a 5.5 K temperature variation of the video components in position 1. The times of maximum and minimum are referenced to the time at which solar illumination of bay 1 begins.

Two examples of the measured and predicted values of the cold calibration data are shown in Figure B-2 for the 6.6-GHz channel and the 21-GHz channel. The phase difference of these channels is predicted. Similar calculations for other SMMR channels also showed good fits.

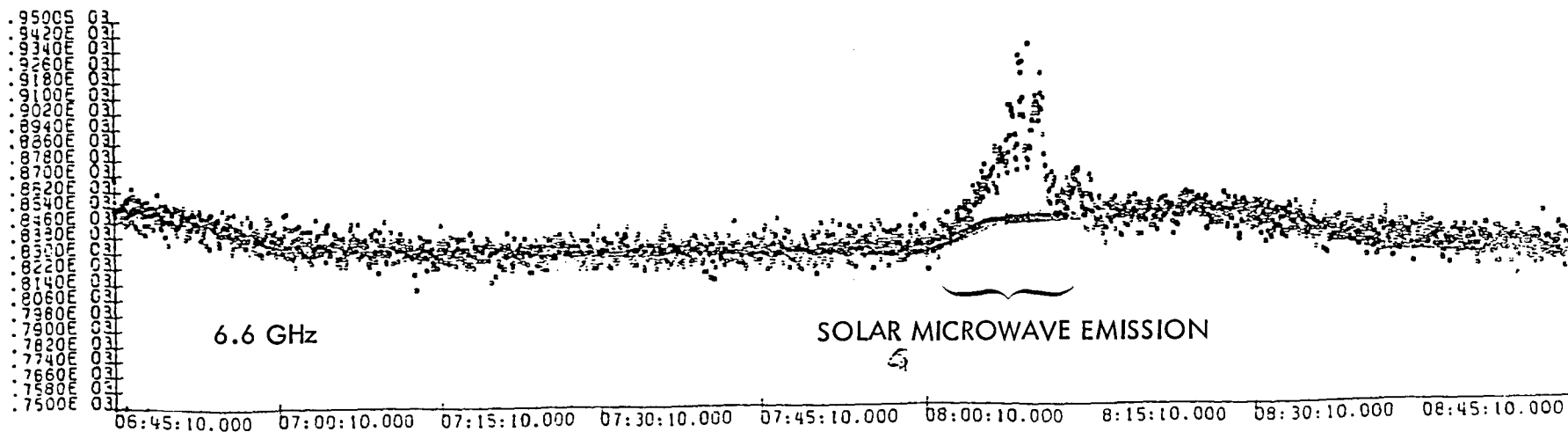


Fig. B-2. Cold Calibration Counts for Rev 1206 at 21 and 6GHz

APPENDIX C

DESCRIPTION OF WORK ON CALIBRATION ALGORITHMS

This Page Intentionally Left Blank

APPENDIX C

DESCRIPTION OF WORK ON CALIBRATION ALGORITHMS

1. BACKGROUND

After the Mini-Workshop II, further work revealed that the T_A algorithm used to convert raw counts into antenna temperatures was incorrect. The fundamental observation was that the range in separation between 10.7 GHz H and 6.6 GHz H was greater than could be accounted for by geophysical variation (noted originally in SMMR Mini-Workshop II Report). The major cause of this was found to be an ad hoc " α_9 " or "gradient" term added to the T_A calibration equation in order to improve the residuals in the thermal vacuum (T/V) data set, combined with the large observed gradients in the instrument temperatures during each satellite orbit. The clinching observation that this term should not be present is the correlation of T_A with instrument temperature that is obvious in some orbits.

In addition, the present calibration coefficients were derived piecemeal rather than simultaneously determined. Thus, it was important to rederive the coefficients from T/V.

2. DERIVATION OF SMMR TEMPERATURE TRANSFER ALGORITHM

The following temperatures to the input of the mixer (T_N') are functions of the effective antenna temperature of the sky, T_S , or of the target simulating the Earth, T_A , the various transmission coefficients, α_N , and the physical temperature of various parts of the instrument, T_N . From the schematic diagram for the instrument in Figure C-1 and a resulting simplified model seen in Figure C-2, the following expressions for the radiative transfer through the relevant paths can be obtained:

Signal from Target:

$$T_A' = T_A \alpha_6 \alpha_7 \alpha_8 + T_6 (1-\alpha_6) \alpha_7 \alpha_8 + T_7 (1-\alpha_7) \alpha_8 + T_8 (1-\alpha_8)$$

Dicke Switch Ref.:

$$T_D' = T_3 \alpha_9 + T_3 (1-\alpha_9) = T_3$$

Ambient (Hot) Cal load:

$$T_{AMB}' = T_3 \alpha_5 + T_3 (1-\alpha_5) = T_3$$

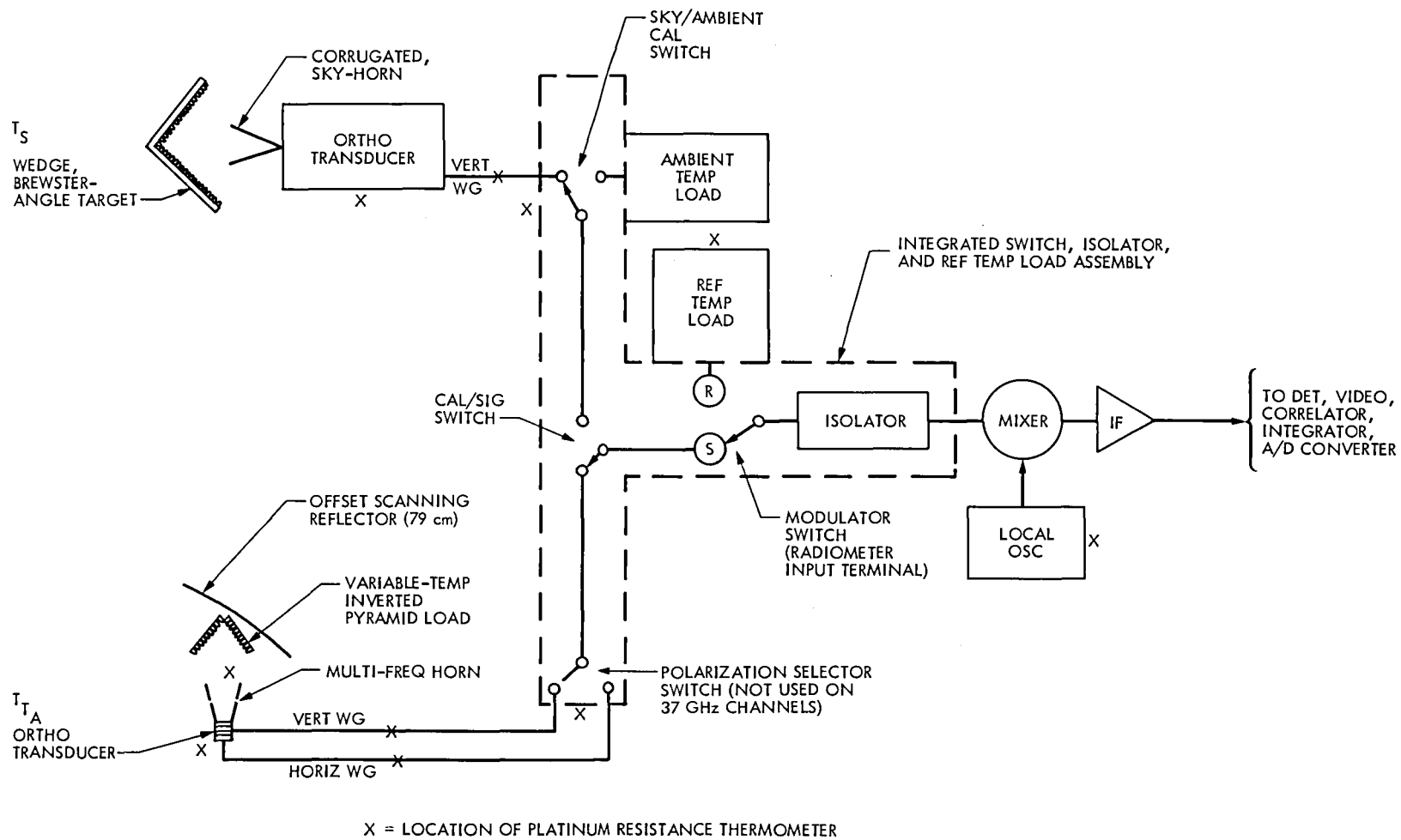
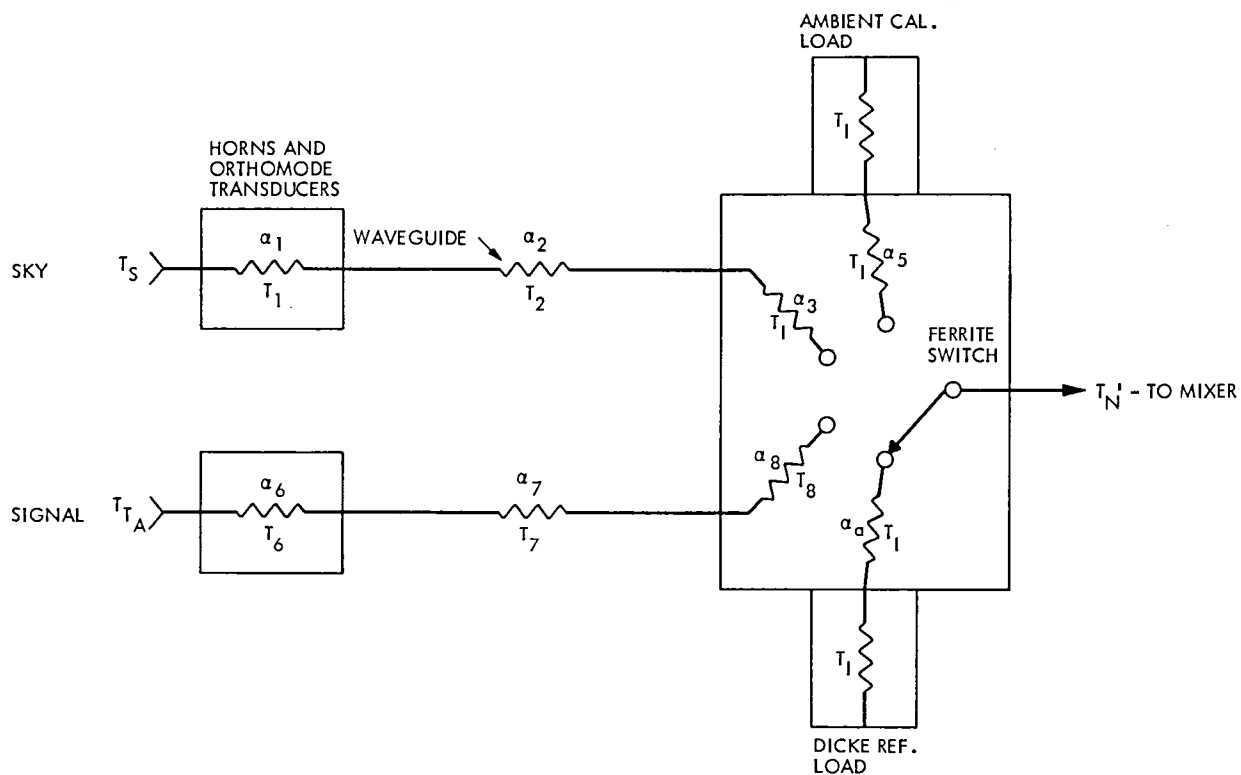


Figure C-1. Schematic Diagram of SMMR Instrument



NOTES:

- α_1 AND α_6 = TRANSMISSION COEFFICIENTS OF BORN AND ORTHOMODE COMBINED
- THE FERRITE SWITCH ALWAYS SWITCHES BETWEEN THE DICKE REF. LOAD AND ONE OF THE OTHER 3 PORTS
- CALIBRATION IS AMBIENT CAL LOAD AND SKY (≈ 300 K, 3 K)
- T_n 's ARE MEASURED BY PLATINUM RESISTANCE THERMOMETERS (K)

Figure C-2. Model of SMMR for Calibration Algorithm

Sky Cal:

$$T'_S = T_S \alpha_1 \alpha_2 \alpha_3 + T_1 (1-\alpha_1) \alpha_2 \alpha_3 + T_2 (1-\alpha_2) \alpha_3 + T_3 (1-\alpha_3)$$

For a Dicke switched radiometer with a digital output, the output is related to the temperature at the input by:

$$(C_N - C_D) = G (T'_N - T'_D)$$

where

C_N = counts when the input to the mixer is T'_N (N can be T,D,A,S)

C_D = counts when the input is the Dicke load

G = gain of the system (counts/K)

By using the expressions for the temperatures seen through the four paths, the common gain G can be eliminated and the target temperature can be expressed in terms of the other measured counts and temperatures as:

$$T_A = \frac{(C_T - C_A)}{(C_A - C_S)} \cdot \left[\frac{T_3 \alpha_3 - T_S \alpha_1 \alpha_2 \alpha_3 - T_1 (1-\alpha_1) \alpha_2 \alpha_3 - T_2 (1-\alpha_2) \alpha_3}{\alpha_6 \alpha_7 \alpha_8} \right] + \frac{T_3 - T_8 (1-\alpha_8) - T_6 (1-\alpha_6) \alpha_7 \alpha_8 - T_7 (1-\alpha_7) \alpha_8}{\alpha_6 \alpha_7 \alpha_8}$$

It should be noted that:

- (1) C_A and C_S are measured during the calibration; T'_N 's are read out during each calibration; some of the α_n are measured during construction and testing, others must be fitted from T/V data.
- (2) C_T is digital output of each measurement of the Earth (or simulation target).
- (3) T_A is the corresponding antenna temperature of the Earth (or simulation target).

- (4) Until problems were uncovered in Mini-Workshop II, the T_A equation also had a small "ad hoc" correction term $\alpha_9 (T_3 - T_6)$ added to compensate for large temperature gradients between the signal horn and the ferrite switch. (α_9 was determined empirically.) Also a nonlinear term of the form $\alpha_{10} (T_3 - T_S)^2 (C_T - C_A)^2 / (C_A - C_S)^3$, as well as biases T_0 for each channel, were added to improve the fit to the T/V data.

3. PROCEDURE FOR DETERMINING ATTENUATION COEFFICIENTS

Without the ad hoc "gradient" term, the T_A equation can be written as

$$T_A - T_6 = T_0 + \left(\frac{\alpha_1}{\alpha_6} \right) A_3 + \left(\frac{1}{\alpha_6} \right) A_5 + \alpha_{10} A_6 \quad (C1)$$

where

$$A_3 = \left(\frac{C_A - C_T}{C_A - C_S} \right) \frac{\alpha_2 \alpha_3}{\alpha_7 \alpha_8} (T_S - T_1)$$

$$A_5 = \left(\frac{C_T - C_A}{C_A - C_S} \right) \frac{\alpha_3 (T_3 - T_2) - \alpha_2 \alpha_3 (T_1 - T_2)}{\alpha_7 \alpha_8}$$

$$+ \frac{(T_3 - T_8) + \alpha_8 (T_8 - T_7) + \alpha_7 \alpha_8 (T_7 - T_6)}{\alpha_7 \alpha_8}$$

and

$$A_6 = \frac{(T_3 - T_S)^2 (C_T - C_A)^2}{(C_A - C_S)^2}$$

The coefficients to be determined are α_1 , α_6 , and α_{10} . They are different for each frequency, but α_1 and α_{10} are common to both polarizations whereas α_6 is different for each polarization. Hence, for each frequency, the system to be solved is

$$\begin{pmatrix} T_A^V - T_6^V \\ T_A^H - T_6^H \end{pmatrix} = \begin{pmatrix} 1 & 0 & A_3^V & 0 & A_5^V & A_6^V \\ 0 & 1 & 0 & A_3^H & \beta A_5^H & A_6^H \end{pmatrix} \begin{pmatrix} X_1 = T_0^V \\ X_2 = T_0^H \\ X_3 = \frac{\alpha_1}{\alpha_6} \\ X_4 = \frac{\alpha_1}{\alpha_6} \\ X_5 = \frac{1}{\alpha_6} \\ X_6 = \alpha_{10} \end{pmatrix} \quad (C2)$$

where $\beta = X_4/X_3$. The system would be linear without β . In fact, the derived values of X_3 and X_4 depend very weakly on the value assumed for β ; only one iteration is required for convergence.

4. RESULTS

The T/V data set of 290 points was obtained from Paul Swanson and Lyman Lyon. Gaps existed in the sequence numbers of the points, indicating that some sections of bad data had previously been discarded. Due to errors in their tape drive, 23 points were unreadable, leaving 267 points. When the coefficients were originally derived, the data set was edited to 158 to 179 points, depending on frequency and polarization, by iteratively eliminating points with discrepant residuals. Unfortunately, no clear record of which points made up the final data set survived. Using existing records, it was eventually determined that just one criterion - demanding that the standard deviation of the temperature across both the target and sky wedges be less than 1.4 K - reproduces the residuals of Swanson and Lyon for their data set. One additional point consistently had a residual of 25 K, and was excluded. This left 173 points as the basis for the following analyses.

As mentioned above, the computer program was checked by computing the residuals for the Swanson and Lyon coefficients, with α_9 nonzero and with $\alpha_{10} = 10^{-4}$. For every channel, the bias of the residuals was within 0.1 K of zero and the rms residual agreed with their values to within 0.1 K. (Note that T_0 and α_{10} were subsequently modified by Lance Riley using a very restricted subset of 30 points. For almost every channel, those coefficients degraded the fit to the T/V set, simply due to the small size of the restricted data set on which they were based.)

The effect of removing α_9 is shown in Table C-1 (σ^1 is the standard deviation about the mean). In all cases, α_9 is formally significant at the 99 percent confidence level due to the large number of data points in the sample, reminding us that statistical arguments should be applied sparingly to ad hoc terms! The largest change is for 10.7 and 6.6 GHz, as predicted from the magnitude of α_9 .

Regression without α_9 gave poor results, independent of whether α_{10} was included in the fit. Figure C-3 shows the values of the deduced parameters and the residuals without α_{10} . Note that 10.7 and 6.6 GHz are not much improved over just $\alpha_9 = 0$ in the former coefficients; worse, the α 's are 1.5 for 10.7 GHz! The large α 's are due to the X_5 term, which corrects the observed counts for the contribution of temperature gradients through the instrument. In particular, note that X_3 and X_4 , the ratios of α 's, are well determined, but X_5 is an order of magnitude more uncertain. Since the value of X_5 is needed to scale the individual α 's from X_3 and X_4 , all the α 's for 10.7 GHz are driven to ~ 1.5 even though the ratios of α 's in X_3 and X_4 make sense.

Only the housekeeping temperatures (T_{1-3}, T_{6-8}) and the counts distinguish 10.7 GHz from the other frequencies. Examination of the temperatures revealed that, although 10.7 GHz always stood out, there was no systematic difference. For example, T_2 may be highest (or lowest) for 10.7 GHz for some points, T_3 may be highest (or lowest) on other points, or both may be normal. Substitution of one temperature for another does not improve the fit or lower the α 's.

The residuals for 10.7 GHz fall into two classes for each set of coefficients mentioned above with $\alpha_9 = 0$. Points with positive residuals were virtually all taken when the instrument temperature was low ($T_3 < 290$) and when the target temperature was stepped upward, while points with negative residuals were taken with $T_3 > 290$ and when the target temperature was stepped downward. The effect was exaggerated for low target temperatures and tended to vanish at high temperatures. Unfortunately, most of the 173 points in the usable data set were taken in the first four days of testing when the target temperature was always stepped upward for $T_3 < 290$ and vice versa. Hence it is difficult to assign one or both of these conditions as the cause of this correlation with the residuals.

The data set was then partitioned at $T_3 = 290$ K with the results shown in Figures C-4 and C-5. The high temperature set (90 points) yields much better results than the low temperature set (83 points) - the residuals are smaller, the bias T_0 is nearly zero, and the α 's are closer to unity. Note that X_3 and X_4 have nearly the same values in both of these sets and in the combined sets - the difference is primarily X_5 , the gradient correction. An understanding of this discrepancy is needed because large gradients actually exist in space.

Thus, from the T/V data set, the "best" set of α 's should be those from the high-temperature set. They are given in Table C-2, both with and without the α_{10} term. Because the α_{10} term is ad hoc and does not improve the residuals tremendously, the set without α_{10} was used for JASIN. For convenience, the entire current set of α 's is given in Table C-3.

Table C-1. The Effect of Removing α_9 in the Thermal Vacuum Data

Freq, GHz	Swanson & Lyon with α_9				Swanson & Lyon without α_9				Riley without α_9			
	$\langle \text{res} \rangle_V$	σ_V	$\langle \text{res} \rangle_H$	σ_H	$\langle \text{res} \rangle_V$	σ_V^1	$\langle \text{res} \rangle_H$	σ_V^1	$\langle \text{res} \rangle_V$	σ_V^1	$\langle \text{res} \rangle_H$	σ_H^1
6.6	-	1.0	-	0.8	0.7	1.4	0.6	1.1	-1.4	1.4	-0.6	1.1
10.7	-	0.8	-	1.1	-1.4	1.9	-1.4	2.4	1.6	1.9	2.2	2.4
18.0	-	0.8	-	0.9	0.0	1.1	0.0	1.2	0.0	1.1	0.3	1.1
21.0	-	0.6	-	0.6	0.0	0.6	0.0	0.6	0.0	0.7	0.1	0.7
37.0	-	1.0	-	0.7	0.5	1.2	0.2	0.9	-0.4	1.3	-0.2	0.9

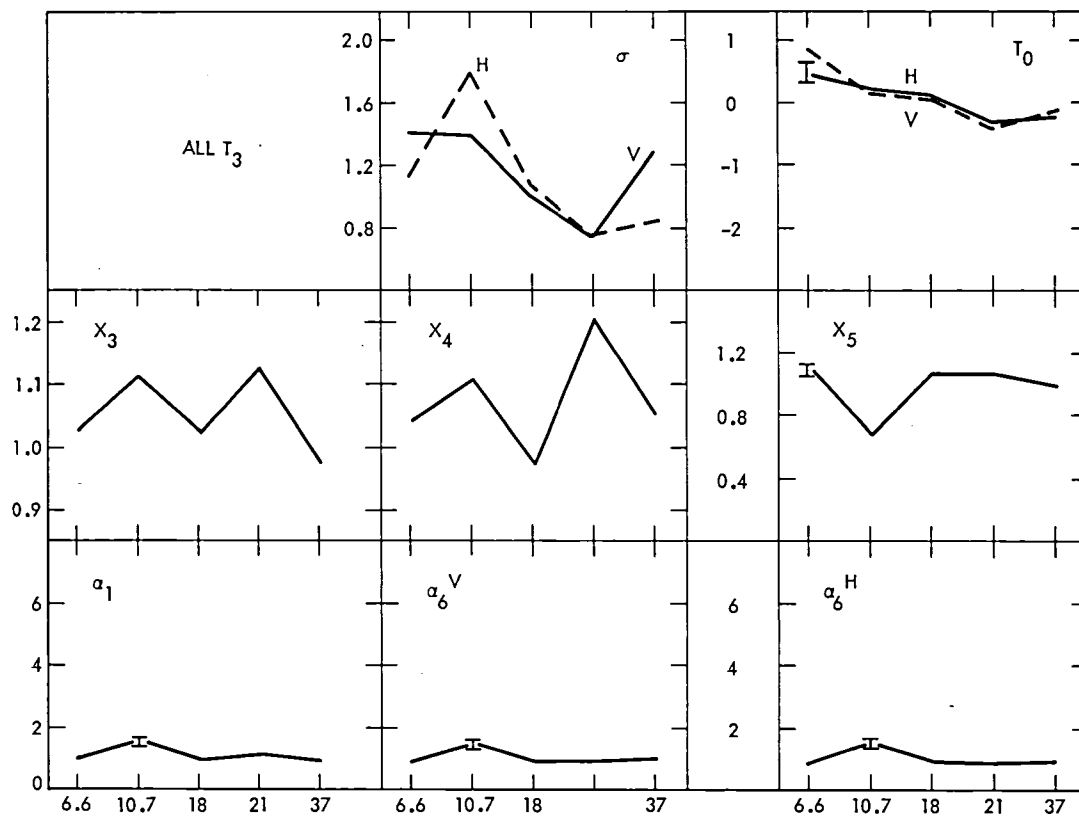


Figure C-3. Values of Deduced Parameters and Residuals in Thermal Vacuum Without α_{10}

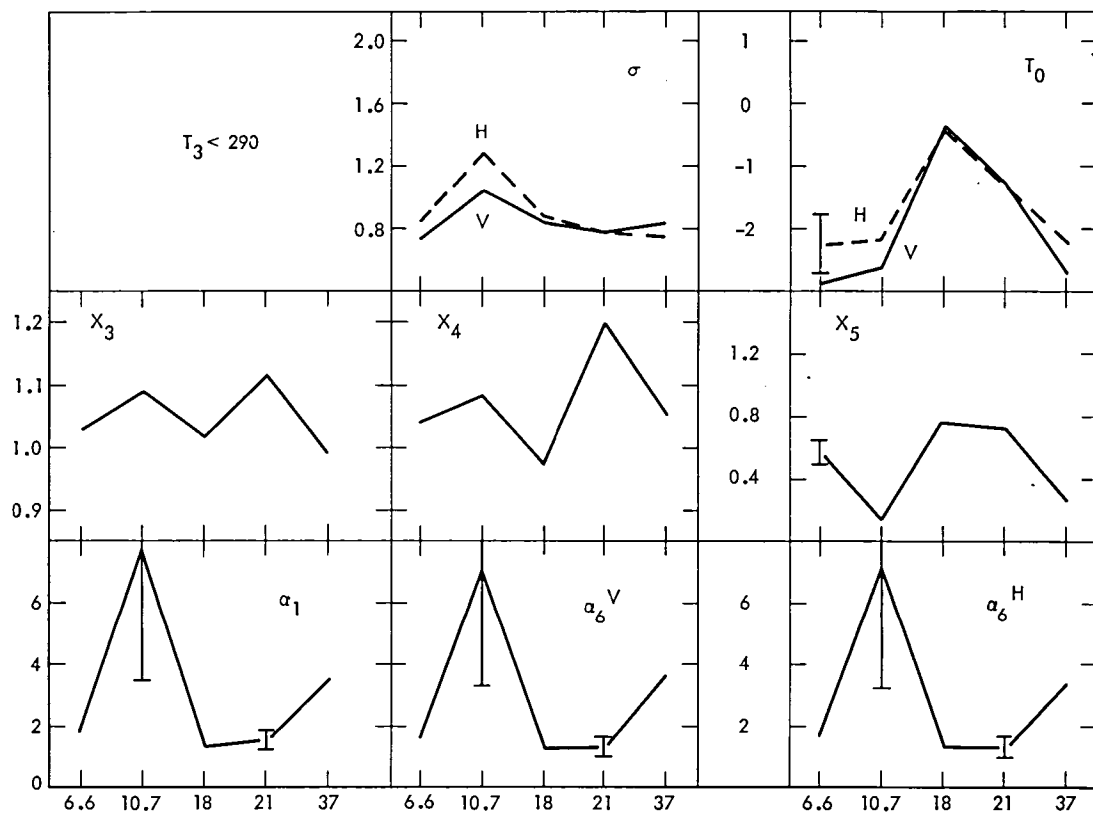


Figure C-4. Values of Deduced Parameters and Residuals in Thermal Vacuum Without α_{10} , for $T_3 < 290$

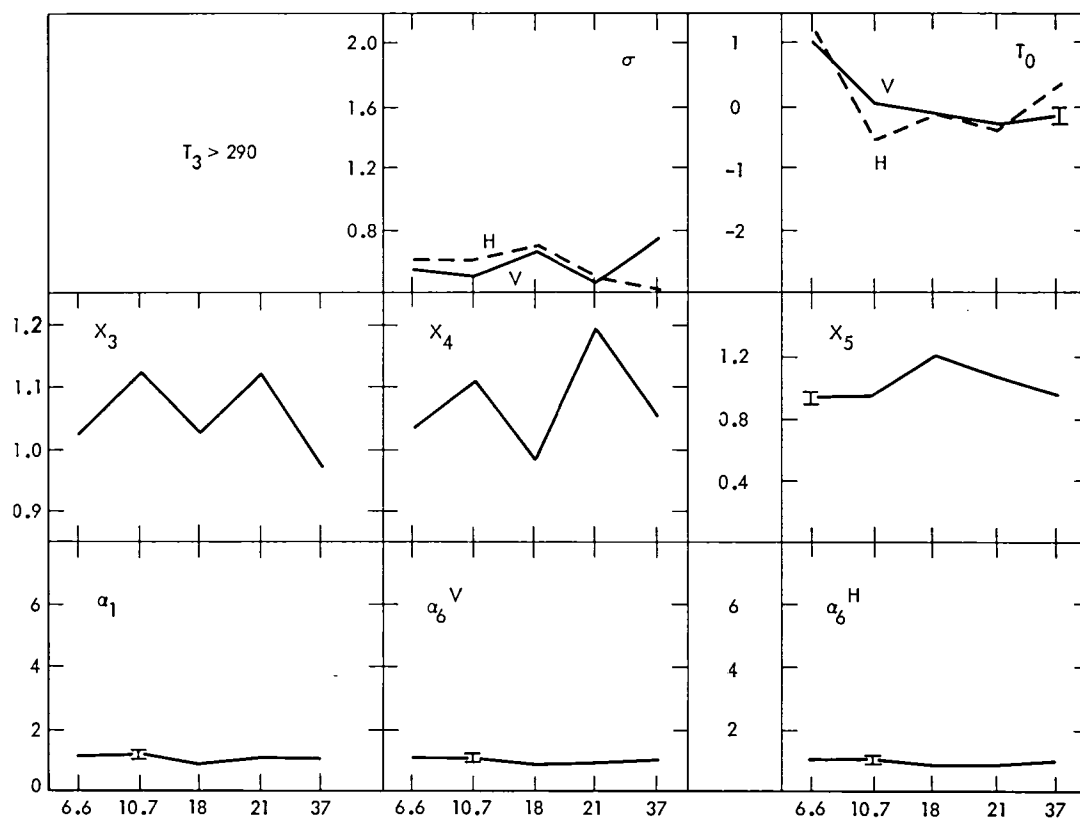


Figure C-5. Values of Deduced Parameters and Residuals in Thermal Vacuum Without α_{10} , for $T_3 > 290$

Table C-2. The Best-fit Coefficients for the High-Temperature Set

Freq	T_0^V	T_0^H	X_3	X_4	X_5	α_1	α_6^V	α_6^H	σ_V	σ_H	
(a) Without α_{10}											
6.6	1.016 (0.077)	1.320 (0.078)	1.027 (0.001)	1.043 (0.001)	0.951 (0.018)	1.080 (0.021)	1.052 (0.020)	1.035 (0.020)	0.57	0.61	
10.7	0.007 (0.074)	-0.523 (0.073)	1.121 (0.001)	1.113 (0.001)	0.965 (0.016)	1.161 (0.020)	1.036 (0.018)	1.043 (0.018)	0.52	0.62	
18.0	-0.115 (0.104)	-0.094 (0.104)	1.032 (0.001)	0.985 (0.001)	1.203 (0.033)	0.858 (0.023)	0.832 (0.022)	0.871 (0.024)	0.68	0.71	
21.0	-0.289 (0.070)	-0.334 (0.071)	1.124 (0.001)	1.197 (0.001)	1.076 (0.024)	1.045 (0.023)	0.929 (0.121)	0.873 (0.020)	0.47	0.52	
37.0	-0.078 (0.079)	0.438 (0.089)	0.971 (0.001)	1.054 (0.001)	0.946 (0.031)	1.026 (0.033)	1.057 (0.034)	0.974 (0.032)	0.77	0.45	
(b) With α_{10}											
Freq	T_0^V	T_0^H	X_3	X_4	X_5	α_1	α_6^H	α_6^H	α_{10}	σ_V	σ_H
6.6	0.989 (0.073)	1.304 (0.074)	1.032 (0.002)	1.048 (0.002)	0.931 (0.018)	1.109 (0.022)	1.074 (0.021)	1.058 (0.021)	0.341-4 (0.081-4)	0.52	0.60
10.7	-0.016 (0.073)	-0.547 (0.073)	1.125 (0.002)	1.117 (0.002)	0.954 (0.017)	1.179 (0.020)	1.048 (0.018)	1.055 (0.018)	0.252-4 (0.086-4)	0.50	0.62
18.0	-0.107 (0.086)	-0.088 (0.086)	1.043 (0.002)	0.997 (0.002)	1.152 (0.028)	0.906 (0.022)	0.868 (0.021)	0.909 (0.022)	0.710-4 (0.078-4)	0.57	0.58
21.0	-0.300 (0.065)	-0.338 (0.065)	1.130 (0.001)	1.203 (0.001)	1.050 (0.023)	1.076 (0.023)	0.952 (0.021)	0.895 (0.019)	0.368-4 (0.066-4)	0.43	0.48
37.0	-0.098 (0.081)	0.445 (0.091)	0.974 (0.002)	1.058 (0.002)	0.926 (0.033)	1.053 (0.037)	1.080 (0.038)	0.955 (0.035)	0.158-4 (0.072-4)	0.77	0.43

Table C-3. Current Calibration Coefficients for the T_A Algorithm

Channel	α_1	α_2	α_3	α_6	α_7	α_8	T_0
6.6 V	1.080	0.949	0.794	1.052	0.920	0.832	1.016
6.6 H	1.080	0.949	0.794	1.035	0.920	0.813	1.320
10.7 V	1.161	0.912	0.891	1.036	0.920	0.933	0.007
10.7 H	1.161	0.912	0.891	1.043	0.920	0.912	-0.523
18 V	0.858	0.912	0.891	0.832	0.955	0.871	-0.115
18 H	0.858	0.912	0.891	0.871	0.937	0.849	-0.094
21 V	1.045	0.870	0.832	0.929	0.944	0.841	-0.289
21 H	1.045	0.870	0.832	0.873	0.955	0.851	-0.334
37 V	1.026	0.912	0.803	1.057	0.916	0.837	-0.078
37 H	1.026	0.912	0.741	0.974	0.933	0.832	0.438

5. DISCUSSION

The critical problem that must be solved is the difference between the two data sets. Even though the high-temperature set apparently gives almost reasonably results (note that the α 's are still >1 in some cases), it may be contaminated by the same problem that affects the low-temperature set, albeit less so. Unfortunately, at this time, it is not even clear if this is an instrument temperature effect or a target temperature effect, since the two cannot be clearly separated. Worse, if the problem is related to temperature gradients, the data from space may be even more contaminated. The clues we do have are given below.

- (1) The separation of high and low residuals in the entire data set is most evident for 10.7 GHz, but is also noticeable in all frequencies except 21 GHz. The separation is largest at low target temperatures. Even in the low-temperature set alone, 10.7 GHz stands out as by far the worst channel.
- (2) If just the coefficients from the high-temperature set are used, the residuals for the low-temperature set are ~ -3 K for 6.6 GHz, $\sim +5$ K for 10.7 GHz, $\sim +2$ K for 18 GHz, and ~ -1 K for 21 and 37 GHz.

- (3) The instrument temperature T_3 is 2-3 K lower for 6.6 and 10.7 GHz than for the other channels for the two coldest instrument temperature settings (~272 and ~281 K for 6.6 GHz). At the higher instrument temperatures (~300 and ~310 K), no such discrepancy exists. Since T_6 is always approximately the same for all frequencies, the gradient $T_3 - T_6$ is significantly more negative for 6.6 and 10.7 GHz, ~-8 to 2 K vs ~-4 to 2 K. It is not surprising that T_3 is lower for 6.6 and 10.7 GHz for $T_3 < 290$ because the cooler for the instrument in T/V was directly underneath the 6.6-GHz instrument box, with 10.7 on top of 6.6 GHz, and the other channels on top of 10.7 GHz.
- (4) In the low-temperature set, the best fit X_5 is small. This implies that a better fit is obtained by not correcting as much for instrument gradients as the calibration equation would demand if $\alpha_6 \sim 1$.
- (5) The bias T_0 is significant nonzero in the low-temperature set, again indicating that the calibration equation is not correct.
- (6) Both 6.6 and 10.7 GHz have waveguide-coax-waveguide instead of a single waveguide between the feed horn and mixer. Perhaps there is some attenuation at the conversion points that is not properly taken care of in the equation.
- (7) T_7 , the temperature of the "waveguide," is not measured for 6.6 and 10.7 GHz, but is instead the average of T_6 and T_8 . For 6.6 and 10.7 GHz, T_2 , the temperature of the waveguide between the cold horn and mixer, is often several degrees different from the average of T_1 and T_3 in the low-temperature set. However, if the equation is correct, and the α 's are ~0.9, an error of 2 K in T_7 gives an error of only ~0.2 K in T_A .
- (8) Unfortunately, although the housekeeping temperatures were indeed measured simultaneously with the observations in T/V, they were written onto a different tape with no time tag! Hence, Swanson and Lyon had to empirically correlate the temperatures with the observations. The one point with a 25 K residual mentioned above would have essentially zero residual if the housekeeping temperatures from the next data point were used. Thus, it is possible that an error in correlation produces the high-low temperature separation observed.

APPENDIX D

A COMPARISON OF SATELLITE AND SEA SURFACE
MEASUREMENTS OF SIGNIFICANT WAVE HEIGHT

This Page Intentionally Left Blank

A COMPARISON OF SATELLITE AND SEA SURFACE
MEASUREMENTS OF SIGNIFICANT WAVE HEIGHT

by

D. J. Webb

Report No. 85.
(1979)

Institute of Oceanographic Sciences,
Brook Road, Wormley, Godalming, Surrey.

ABSTRACT

During the JASIN experiment in the summer of 1978, a series of sea surface wave measurements were made for comparison with wave heights deduced from the SEASAT-1 altimeter.

Comparisons were made on eight separate occasions during which the significant wave height ranged from 0.7 to 2.0 metres.

For waves above one metre, a good correlation was found between the satellite and sea surface measurements. On the two occasions when the waves were below 90 centimetres, a poorer correlation was observed.

From the point of view of oceanographers interested in measuring wave fields regularly over remote areas of ocean, altimeters of the type used in SEASAT-1 appear to be accurate and extremely useful.

INTRODUCTION

In the summer of 1978, the United States of America launched a satellite, SEASAT-1*, which carried a number of instruments for monitoring the ocean surface. The main aim of the mission was to check the performance of the instruments and to check the quality and usefulness of the data they returned.

One of the instruments included was an altimeter. Physically this measures the time taken for a radar pulse to reach the sea surface and be reflected back to the satellite. If the satellite's orbit is known accurately, this information may be used to determine the earth's geoid and to observe the tides and other large scale features on the sea surface.

The radar altimeter looks at a circular region of ocean directly below the satellite, which is about 10 kms across. Within this region, that part of the radar pulse being reflected from the tops of the sea waves returns to the satellite before that reflected from the troughs of the waves. As a result the radar pulse returning to the satellite will be distorted compared to the pulse returned from an ocean with no waves. The higher the sea waves are, the greater the distortion, and so in principle the distortion can be used to measure the height of the waves.

The design of the SEASAT-1 altimeter was developed from instruments used earlier on SKYLAB and GEOS-3. The earlier instruments had provisions for measuring wave heights but their accuracy was relatively poor. In the most recent of them, GEOS-3, the r.m.s. error in estimating the significant wave height was approximately 75 cms (Rufenach and Alpers 1978, Fedor et al 1979). More importantly the data from GEOS-3 could only be obtained when it was within range of a dedicated ground station. In SEASAT-1 improvements in design meant that an r.m.s. error of 10 cms or less was to be expected and also a copy of all the altimeter data was stored on board the satellite for retrieval when it passed over a suitable ground station.

Thus, from an oceanographic point of view, the SEASAT-1 altimeter

* Before launch SEASAT-1 had the name SEASAT-A

was very important. It promised accurate measurements of wave height over large and remote regions of ocean, where even crude wave height data is at present rarely available. In addition, it was expected to operate for two years or more and so it would go some way towards providing the long term statistical information on wave climate which is often required.

In the summer of 1978, the Institute of Oceanographic Sciences was involved in JASIN, the Joint Air-Sea Interaction Project. This was an international oceanographic and meteorological experiment, sponsored by the Royal Society, which took place in the North Atlantic, near 59°W, 12°30'W, between July and September. Being early in SEASAT's life and as wave measuring equipment would be present, it seemed to be a good occasion for checking on the altimeter's ability to measure wave heights.

Other wave measuring instruments were also operating during JASIN but in this report we concentrate on comparing the wave height measurements made by the SEASAT-1 altimeter with those made by the Institute of Oceanographic Sciences' pitch-roll buoy.

THE PITCH-ROLL BUOY MEASUREMENTS

The pitch-roll buoy used was a development of the design described by Cartwright and Smith (1964) and Clayson and Smith (1970). The buoy is free floating, has a low moment of inertia and a large righting moment so that it closely follows the sea surface. It contains a gyro to give a vertical reference.

The buoy measures the vertical acceleration, the slope of the sea surface and the compass heading of the buoy; and records the data internally every 1/2.048 of a second. The buoy is powered by batteries which will last for four hours continuous running.

The pitch-roll buoy was carried on RRS Discovery. In operation it was necessary to fit in with the other experiments being carried out, but when possible the buoy was launched two hours before and recovered two hours after the satellite pass. This was done partly to give a long record, giving good statistics on the wave field. But also it was appreciated before the experiment, that it would rarely be practical to place the buoy directly below the satellite

track and a long recording time meant that any important horizontal changes in the wave field had a chance to show up as a change with time at the measurement point as the wave field progressed past that point.

PROCESSING THE PITCH-ROLL BUOY DATA

While at sea, sections of the data were listed to ensure that the sensors were working properly. Later plots and other tests of the data were used to check for errors. For estimating wave heights, only the vertical acceleration signal was used, but the output from the other sensors was used to monitor the overall performance of the buoy. Thus the pitch and roll sensors showed when the gyro started precessing because the power supply had gone low.

The accelerometer signal was analysed by fourier transforming sections of data 125 seconds long (256 data cycles). The very lowest frequency components which contain a contribution from the long term drift of the gyro were then dropped and the other fourier components combined to give the r.m.s. water elevation during that data period. Up to forty-eight such periods were processed and combined to give a mean value for the estimated r.m.s. water elevation and an estimate of the error of the mean.

Comparisons between the SEASAT-1 altimeter and the pitch-roll buoy were made on eight occasions. The positions of the buoy on these occasions and the results obtained are given in Table 1.*

THE SEASAT ALTIMETER

The design and operation of the SEASAT-1 altimeter has been described by MacArthur (1976) and a more detailed report is due to be published in 1979. The design built upon experience gained with instruments installed in SKYLAB and GEOS-3. All of these instruments attempt to use a very short radar pulse, so that the leading edge of the returned signal from the sea surface is not

** The significant wave height given in the tables is defined as being four times the r.m.s. water elevation.*

affected by the finite antenna beamwidth.

SKYLAB had a 13.9 GHz pulsed radar, which tracked the leading edge of the returned signal giving the satellite altitude. There were also eight sample-hold gates arranged around the tracking point which allowed samples of the leading edge to be obtained. A pulse width of 100 ns was used, and this gave an altitude precision of under one metre.

GEOS-3 was designed to operate at a higher altitude and so, in order to get more power into the radar pulse using the amplifiers available, a longer pulse was needed. The solution adopted was to use pulse expansion and compression filters. These allowed a 1 μ s pulse to be used which became 12.5 ns when compressed.

SEASAT-1 orbited at a height of approximately 800 kms and covered the ground at a speed of 6.6 km sec⁻¹. The altitude used is similar to GEOS-3, but in SEASAT-1 the altimeter was designed to give a much improved resolution by using a swept frequency radar pulse. The returned signal is correlated with a replica of the transmitted signal, with the result that any time delay in the returned signal becomes mapped into a frequency offset. Thus, the range gating used in the earlier instruments is now replaced by frequency filtering.

The technique allows in SEASAT-1, a 3.2 μ s chirped pulse to give the same effective resolution as a 3.125 ns pulse of fixed frequency. The returned signal from this narrower pulse can also be sampled with the same resolution of 3.125 ns allowing the distance to the sea surface to be measured, in principal, to an accuracy of better than 10 cms. The distortion of the leading edge of the returned signal should also enable the wave height to be measured to an accuracy of better than 10 cms.

The radar altimeter transmits at a rate of 1000 pulses per second. After each pulse, an on board computer fourier transforms the correlated returned signal to give 63 samples describing the effective compressed returned pulse. The tracking system used to measure the distance to the ocean surface keeps the leading edge of the returned signal in the centre of the window of 63 samples.

Interference from different scatters on the sea surface means that the returned signal is very noisy. It is therefore smoothed by averaging each of the 63 samples over 50 pulses. An example of this 'smoothed' pulse is shown in Figure 1, but as can be seen a lot of random noise is still present.

Wave heights are estimated from the leading edge of the smoothed pulse. On board the satellite a very simple method of doing this was used. From the 63 samples describing the smoothed pulse, groups of samples, called gate triplets and arranged around the tracking point, were used to compute running averages giving estimates of the slope of the leading edge of the pulse. Depending on the wave height, different gate triplets gave the most sensitive result. The estimate of pulse slope was then used in a look-up table to give the significant wave height.

Ten times each second, a copy of the altimeter data, including the latest estimate of wave height and the 63 samples describing the smoothed pulse, was transmitted to the ground. For regions around the UK this data was received by RAE Oakhanger. A second copy of the data was stored on board and transmitted once each orbit to a NASA ground station.

PROCESSING THE SATELLITE ALTIMETER DATA

The satellite data received at RAE Oakhanger was combined with attitude and orbit data from NASA to produce ISDRs, the Individual Sensor Data Records. The data for the eight passes monitored by the pitch-roll buoy were made available to I.O.S.

The uncorrected wave heights estimated by the satellite as it passed between 57°N and 61°W, near the JASIN region, are plotted in figures 2 to 9. The satellite moves at 6.6 km sec⁻¹, so each pass represents over 500 km of ocean. The noise seen in the plots is believed to come predominantly from statistical fluctuations in the smoothed pulse mentioned previously, but it is possible that some comes from fluctuations in the actual surface wave field. The signal may also be affected by ships.

The data shown is raw data and two known corrections have to be

made. The first, the so called $\sin^2 x/x^2$ correction, is to correct for end effects in the fourier transforms carried out on board the satellite. This correction is different for each of the gate triplets and is greatest for low amplitude waves. The second correction, the attitude correction, is to allow for the satellite not looking exactly vertically at the earth's surface.*

In order to make a comparison with the pitch-roll buoy, the time of closest approach to the buoy was determined and then the average wave height taken by eye from the plots. Listings of the altimeter derived wave height, and the gate triplet used were also available. In this manner, the average wave height could be estimated to better than 10 cm accuracy. The $\sin^2 x/x^2$ and attitude corrections were then made and the results obtained are shown in Table II. As can be seen in this table, the corrections required were large, a typical value being 60 cm. Of this about 16 cm was due to the attitude correction and the rest was due to the $\sin^2 x/x^2$ correction.

During six of the eight passes, the gate triplet used for calculating most of the wave heights was number 2. But during passes 3 and 8, when the significant wave height was below 90 cms, both triplets 1 and 2 were used. The effect of the different gate triplets can be seen in figures 4 and 9, where the raw wave height is seen to jump as the satellite altimeter changes from using one gate triplet to the other.

The switching from one gate to the other is probably a result of random fluctuations in the returned signal. The resulting jumps in the raw wave height data then probably arise from the different $\sin^2 x/x^2$ corrections that have to be made.

COMPARISON

In order to compare the altimeter and pitch-roll buoy measurements of significant wave height, they are shown plotted against

* The corrections were made with the use of tables supplied by W. Townsend of the NASA Wallops Flight Centre.

each other in Figure 10. The dots correspond to the corrected and the crosses to the uncorrected satellite data. The estimated standard deviation of the pitch-roll buoy measurements are shown. No similar quantity was calculated for the satellite data, but as mentioned earlier, the uncorrected values were estimated, from figures 1 to 8, to better than 10 cm accuracy.

For significant wave heights of above one metre, the agreement between the satellite and pitch roll buoy measurements is very good. The largest discrepancy occurs during run 7 when the pitch roll buoy gives 1.16m and the satellite 11 cm less. For this run the point of closest approach of the satellite to the buoy was 125 km and so the discrepancy may be due to a spatial change in the wave field.

Below one metre the agreement between the two instruments is not so good. For the gate 2 satellite measurements this is probably due to the large $\sin^2 x/x^2$ corrections needed and in fact this appears to be overcorrecting the waveheights in this region.

Gate triplet 1 was only used extensively during runs 3 and 8. In both cases the satellite measurement is within 10 cms of the pitch-roll buoy measurement. However, one disturbing feature is that in run 8, gate triplet 1 gives lower waves than in run 3, whereas gate triplet 2 and the pitch-roll buoy indicate higher waves.

CONCLUDING REMARKS

The comparisons reported here were carried out in periods of low seas and so represent a severe test of the altimeter's ability to resolve waves. However, despite this, the agreement between the satellite altimeter and pitch-roll buoy measurements is very good, the discrepancy often being less than 5 cms.

If the pitch-roll buoy measurements are assumed to be correct the results indicate that the SEASAT-A altimeter is a very accurate instrument for measuring wave heights. Its performance represents a significant advance over the performance of the GEOS-C altimeter. Also the results do not preclude the possibility that for wave heights above one metre, the satellite altimeter, with its ability

to sample a large region of ocean, may be a more accurate instrument for measuring the mean sea state than the pitch-roll buoy.

Below one metre, the performance of the satellite altimeter is not so good. This poor behaviour appears to be mainly due to the fourier transform algorithms used on the satellite. If Gate triplet 2 had not been used in its insensitive region below one metre or if the fourier transform algorithm had been carried out so that a large $\sin^2 x/x^2$ correction was not necessary, better performance may have been obtained.

Unfortunately, this study did not include wave heights above two metres, and so we cannot be certain that the satellite actually continued to operate successfully when measuring higher wave fields. But it is known that the $\sin^2 x/x^2$ correction actually becomes less for higher waves and no additional corrections are expected to become necessary until one reaches waves of 20 m or so when the effects of the finite beamwidth of the radar pulse start having an effect. (This finite beamwidth gives the decay of the signal near gate +30 seen in figure 1). Thus it seems very unlikely that the performance of the altimeter would be any worse for waves of up to say 15m.

In conclusion, and from the point of view of an oceanographer interested in the statistics of wave fields over large and often remote areas of ocean, I think that the SEASAT-1 altimeter was extremely successful and that its early failure in October 1978 is to be regretted.

REFERENCES

- Cartwright, D.E. and N.D. Smith (1964). Buoy techniques for obtaining directional wave spectra. Buoy Technology pp 112-124, Marine Technology Society, Washington.
- Clayson, C.H. and N.D. Smith (1970). Recent advances in wave-buoy technology at the National Institute of Oceanography. Conference on Electrical Engineering in Ocean Technology pp 289-306. IERE Conference Proceedings No. 19, London.
- Fedor, L.S., T.W. Godbey, J.F.R. Gower, R. Guptill, G.S. Hayne, C.L. Rufenach, E.J. Walsh, (1979). Satellite altimeter measurements of sea state - an algorithm comparison. Journal of Geophysical Research (In press).
- McArthur, J.L. (1976) Design of the SEASAT-A radar altimeter. OCEANS 76 Conference record. pp 10B-1 to 10B-8.
- Rufenach, C.L. and W.R. Alpers (1978). Measurements of ocean wave-heights using the GEOS-3 altimeter. Journal of Geophysical Research 83 (C10) 5011-5018.

ACKNOWLEDGEMENTS

I would personally like to acknowledge the work of Dr. C. Clayson and K. Birch in building and operating the pitch-roll buoy and to acknowledge the help of the officers and crew of RRS Discovery during the JASIN experiment.

Thanks also to the Space Group at RAE Farnborough for supplying the altimeter raw data and W. Townsend of the NASA Wallops Flight Centre for supplying the tables for correcting the raw data.

This study was a component part of SURGE (the SEASAT Users Research Group of Europe) and was funded by a United Kingdom Department of Industry Contract. I am also indebted to NASA and its agencies for making SEASAT possible and making the data available.

TABLE 1. The Pitch-Roll Buoy Results

Pass Number	Buoy Position		Day & Time of Satellite Pass	Wave analysis period		Number of 125 sec records	Significant wave height	S.D. of estimate
	Latitude	Longitude		Start time	End Time			
1	59°03'N	12°30'W	197/0424	0205	0238	16	2.26m	0.10m
2	59°24'N	12°26'W	211/0530	0505	0628	40	1.43m	0.03m
3	59°39'N	12°21'W	212/2200	2117	2236	40	0.76m	0.02m
4	58°59'N	12°51'W	214/0537	0444	0624	48	1.15m	0.02m
5	59°12'N	12°53'W	215/2206	2114	2157	21	1.70m	0.05m
6	59°09'N	13°12'W	217/0544	0450	0630	48	1.10m	0.03m
7	59°09'N	13°29'W	218/2214	2126	2249	40	1.16m	0.02m
8	59°12'N	12°35'W	221/2221	2140	2303	40	.84m	0.02m

TABLE II The Seasat-1 Altimeter results

Pass Number	Nearest approach to buoy Day and Time Latitude Longitude			Distance to buoy	Satellite attitude	Significant Wave Heights			
						Uncorrected Gate 1	Uncorrected Gate 2	Corrected Gate 1	Corrected Gate 2
1	197/04:24:08	59°02'N	12°33'W	10 km	0.29°	-	2.6m	-	2.21m
2	211/05:30:25	58°52'N	13°54'W	100 km	0.28°	-	2.0m	-	1.47m
3	212/21:59:37	59°44'N	12°51'W	35 km	0.27°	1.2m	1.5m	0.85m	0.47m
4	214/05:37:30	59°02'N	12°43'W	10 km	0.26°	-	1.8m	-	1.19m
5	215/22:06:53	59°01'N	12°33'W	25 km	0.26°	-	2.15m	-	1.66m
6	217/05:44:27	58°50'N	10°57'W	100 km	0.27°	-	1.75m	-	1.11m
7	218/22:14:06	58°27'N	11°58'W	120 km	0.21°	-	1.70m	-	1.05m
8	221/22:21:06	58°29'N	10°28'W	140 km	0.09°	1.1m	1.55m	0.76m	0.69m

SEASAT WAVEFORM. FILE 1.

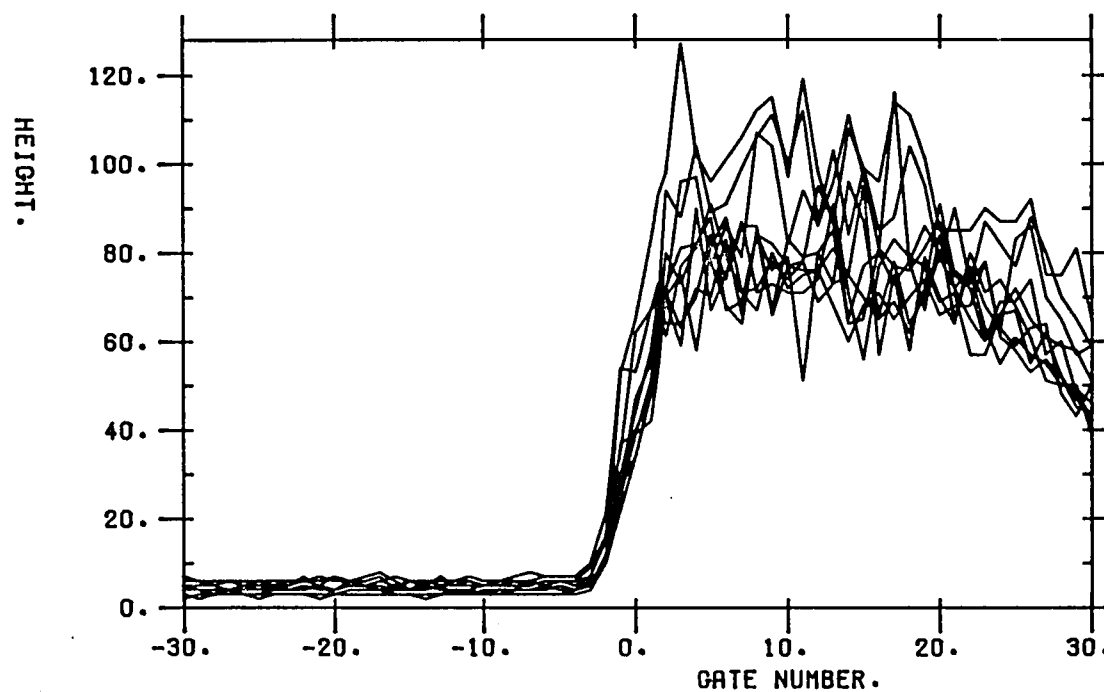


Figure 1. Ten of the 'smoothed' pulses used to estimate wave heights. These each represent an average of fifty raw pulses. Each sample gate has a width of 3.125 ns.

SEASAT WAVE HEIGHTS. 1978/197 4:23:25.8

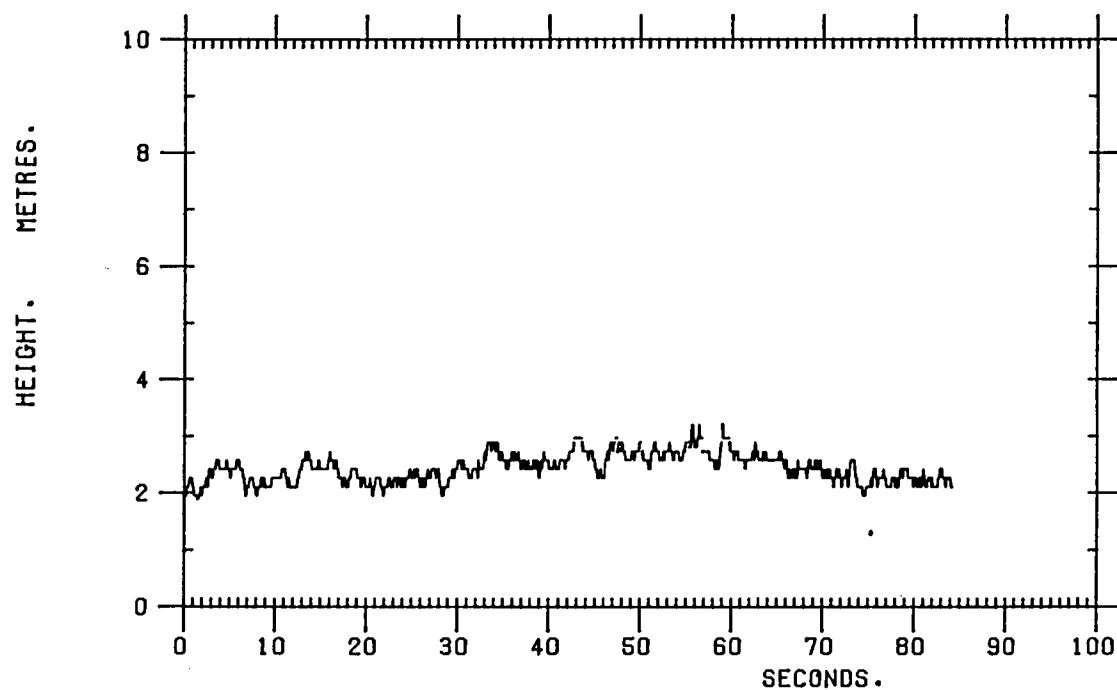


Figure 2. Values of significant wave height calculated by the altimeter on the morning of day 197 (16th July) as it passed northwestward between 57°W and 61°W. During this period the satellite travelled approximately 550 kms. Closest approach to the pitch-roll buoy occurred at 42 seconds when the sub-satellite point was within 10 kms of the buoy. Gate triplet 2 was used for most of the pass, with gate triplet 3 being used for a few higher waves. Breaks in the plot indicate a change from one gate to another.

SEASAT WAVE HEIGHTS. 1978/211 5:29:46.6

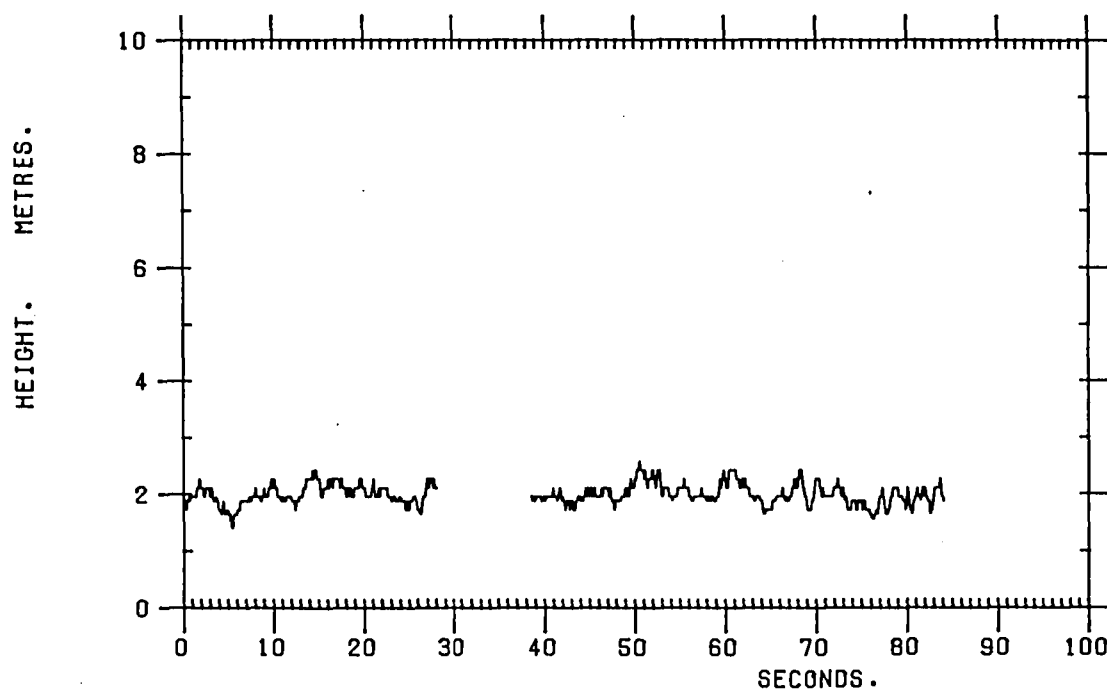


Figure 3. Uncorrected wave heights during pass 2. Closest approach occurs at 39 seconds, just after the gap in the data, when the separation was 100 kms. Gate triplet 2 was used during all of the pass. The gap in the data seen here between 28 and 38 seconds, and similar gaps in Figures 5 and 7, are due to loss of signal at the RAE Oakhanger groundstation.

SEASAT WAVE HEIGHTS. 1978/212 21:59:10.0

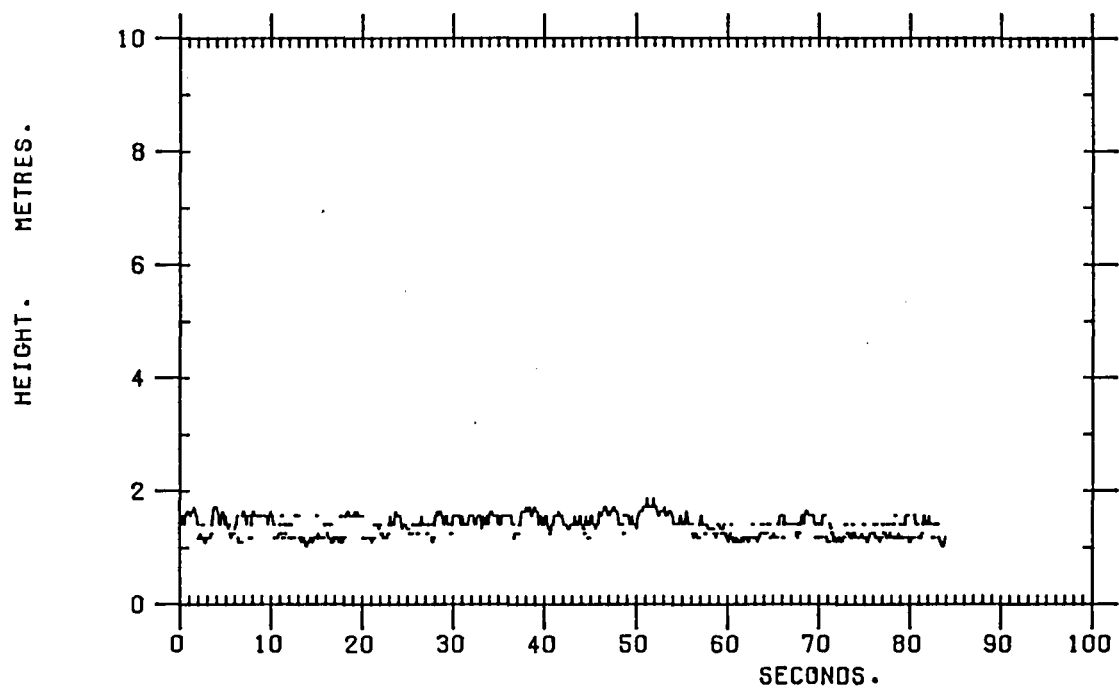


Figure 4. Uncorrected wave heights during pass 3. Closest approach occurs at 28 seconds when the separation was 35 kms. Both gate triplets 1 and 2 were used, triplet 1 giving the lower wave heights.

SEASAT WAVE HEIGHTS. 1978/214 5:36:47.9

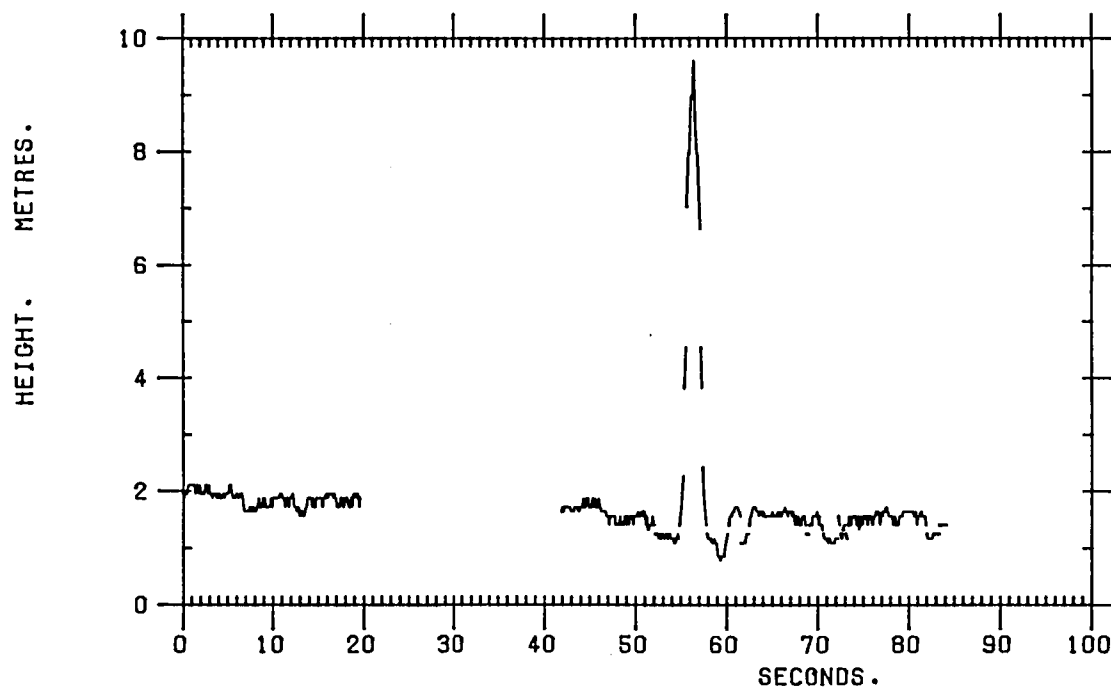


Figure 5: Uncorrected wave heights during pass 4. Closest approach was at 42 seconds when the buoy was within 10 kms of the sub-satellite point.

SEASAT WAVE HEIGHTS. 1978/215 22: 6:11.0

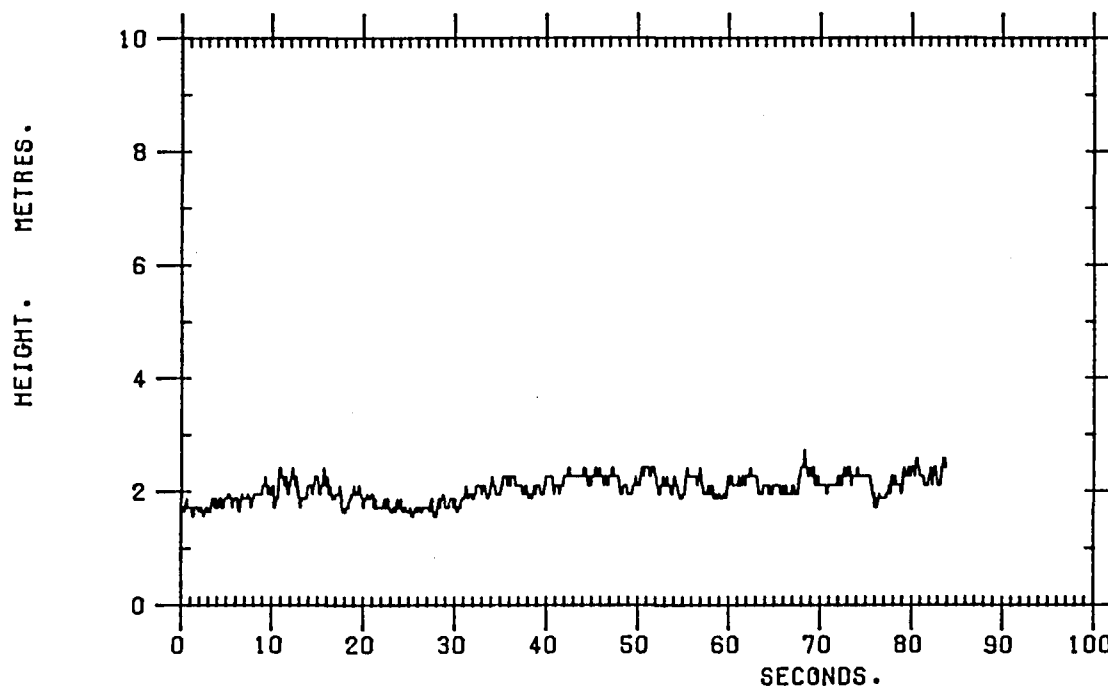


Figure 6: Uncorrected wave heights during pass 5. Closest approach was at 42 seconds when the separation was 25 kms. During these evening runs the satellite passed across the area from N.E. to S.W.

SEASAT WAVE HEIGHTS. 1978/217 5:43:49.1

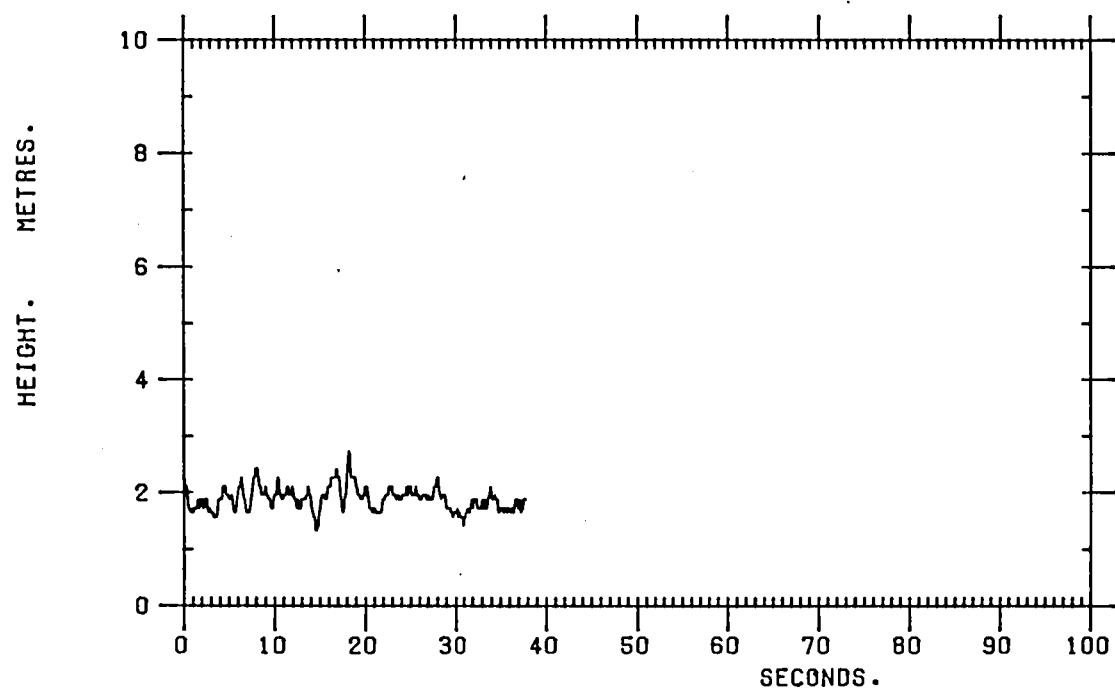


Figure 7: Uncorrected wave heights during pass 6. Closest approach would have been at 53 seconds. The nearest data received, at 37 seconds, was approximately 100 kms from the buoy.

SEASAT WAVE HEIGHTS. 1978/218 22:13:11.9

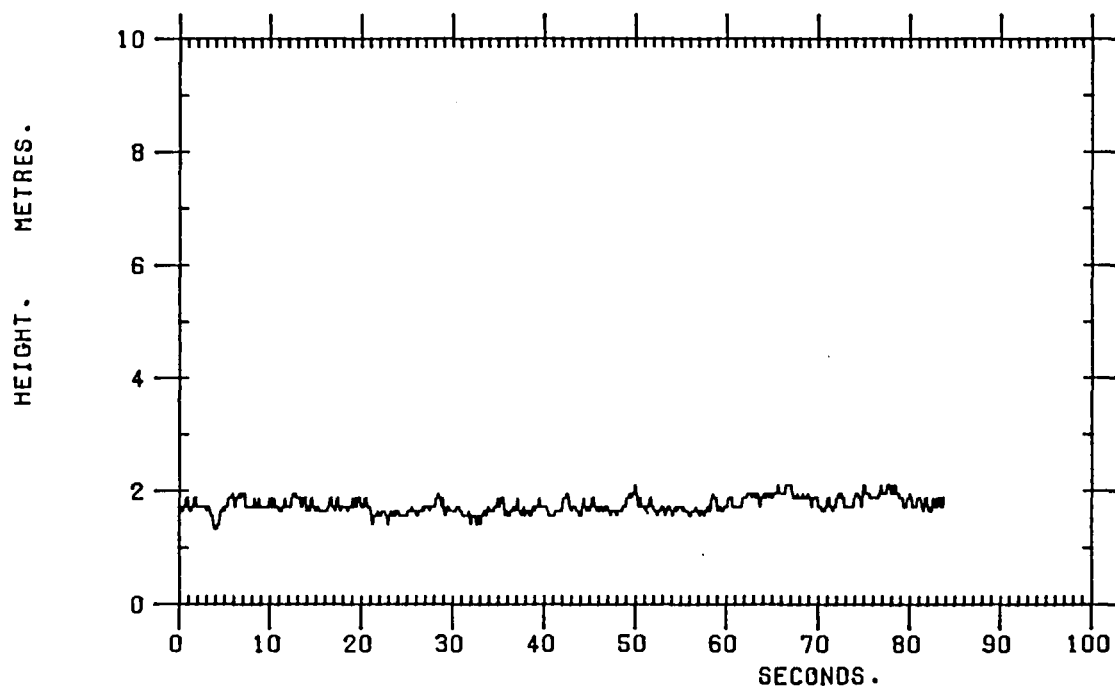


Figure 8: Uncorrected wave heights during pass 7. Closest approach is at 55 seconds when the separation is 125 kms.

SEASAT WAVE HEIGHTS. 1978/221 22:20:12.7

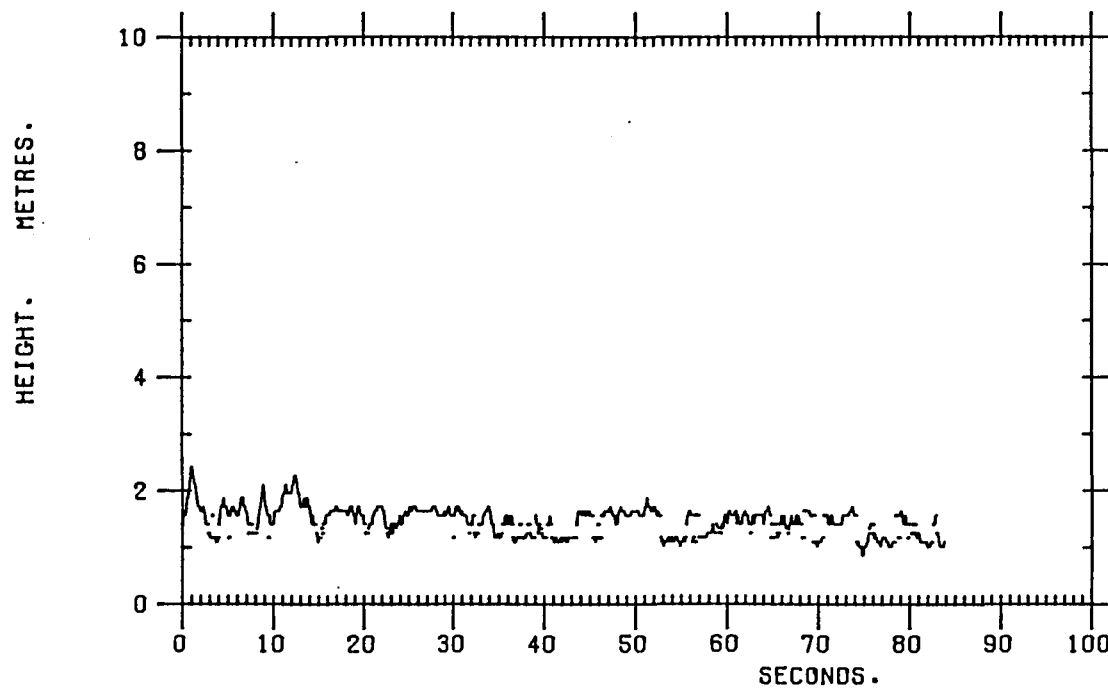


Figure 9: Uncorrected wave heights during pass 8. Closest approach is at 54 seconds when the separation is 140 kms.

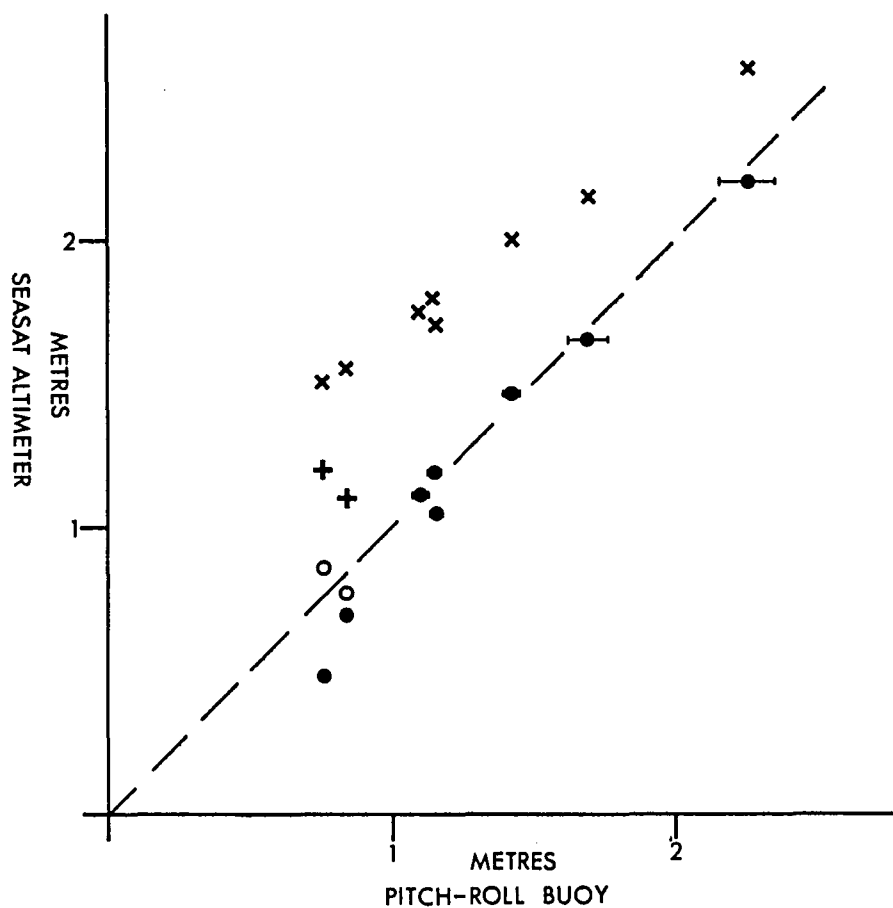


Figure 10: The altimeter and pitch-roll buoy estimates of wave height plotted against each other. ● Corrected and x uncorrected altimeter wave heights using gate 2. ○ Corrected and + uncorrected altimeter estimates using gate 1. The error bars refer to the pitch-roll buoy estimates only. The r.m.s. error on the uncorrected altimeter values is believed to be or order ± 10 cms.

APPENDIX E

A COMPARISON OF SEASAT-1 MEASUREMENTS OF WAVE HEIGHT
(PROCESSED BY JPL SEASAT ALGORITHMS)
WITH MEASUREMENTS MADE BY A PITCH-ROLL BUOY
PRELIMINARY REPORT

This Page Intentionally Left Blank

A COMPARISON OF SEASAT-1 MEASUREMENTS OF WAVE HEIGHT
(PROCESSED BY JPL SEASAT ALGORITHMS)
WITH MEASUREMENTS MADE BY A PITCH-ROLL BUOY.
PRELIMINARY REPORT

D.J. Webb

February 1980

CSIRO Division of Fisheries and Oceanography
P.O. Box 21, Cronulla, NSW 2230, Australia

Abstract

Measurements of significant wave height made by a pitch-roll buoy during the Jasin experiment are compared with measurements made at the same time by the Seasat-1 radar altimeter as processed by the Jet Propulsion Laboratory (J.P.L) Seasat algorithms. Comparisons were made on eight occasions and during the comparisons the wave height was below 2.5 m. The difference between the pitch-roll buoy and Seasat-A measurements had a mean value of $0.04\text{ m} \pm 0.05\text{ m}$ and the standard deviation of individual values about the mean was 0.12 m.

INTRODUCTION

During the Jasin experiment, which took place in the Rockall Trough near 59°N , $12^{\circ}30'\text{W}$ between July and September 1978, an intercomparison was carried out between wave heights measured by an Institute of Oceanographic Sciences pitch-roll buoy and those measured by the Seasat-1 radar altimeter. The pitch-roll buoy, its deployment and the method of data analysis used have been described in an I.O.S. Internal Report (Webb 1979).

This earlier report compared the pitch-roll buoy results with raw Seasat-1 data obtained in real time by the R.A.E. Farnborough facility at Oakhanger in Hampshire U.K. This data had appended to it the estimates of satellite position and orientation needed for processing the raw data to give corrected wave heights. The processing was then carried out using tables supplied by W. Townsend of the NASA Wallops Island Flight Centre, U.S.A.

More recently the same data has become available in a form in which it has already been processed by the standard J.P.L. algorithms. In this report the pitch-roll buoy results are compared with this processed form of the Seasat-1 wave heights.

THE ALTIMETER IGDR SENSOR FILE

The processed Seasat-1 wave heights are available in the form of Seasat IGDR sensor files. Similar but not so complete information is available in the IGDR geophysical files (Ronai 1979).

In constructing the Sensor Files, the raw wave height data passes through three main algorithms (Lorell 1979). The first AL.IG.S-34/0/E corrects for a filter error on board the satellite affecting the three gates used to measure the lowest wave heights (MacArthur 1976). The

correction tables used are the same as those used by Webb (1979), and as mentioned in that earlier report, at the lower end of each gate's range, the correction appears to be much too large and this leads to a significant underestimate of the wave height.

The first algorithm is applied to the 10 records-a-second data stream received from the satellite. The next algorithm AL.IG.S-04/0/E averages the data over one second intervals. An estimate of both the wave height and the error of the estimate, at the mean time of the interval, is obtained assuming that the wave height has a linear trend.

This averaging algorithm does not distinguish between wave heights obtained from the different gates, which is a pity in view of the apparent overcorrection mentioned previously. The result is expected to be an underestimate of wave height in the region where gates 1 and 2, and where gates 2 and 3 overlap.

The third algorithm AL.IG.S-16/0/E corrects the wave height for the tilt of the satellite. Again the same table is used as was used by Webb (1979). This table has one serious flaw in that it is a coarse table and contains jumps which are comparable with the differences found between the satellite and the pitch-roll buoy.

The sensor data record also contains information on the position of the sub-satellite point and the tilt of the satellite. This data differed slightly from the data supplied for the earlier study. The nearest sub-satellite point to the pitch-roll buoy was found to have changed typically by 10 kms and the tilt of the satellite by 0.10 degrees. These changes may reflect either a revision of the satellites orbit or a difference in the geoid used.

ANALYSIS AND RESULTS

The positions of the sub-satellite point were used to determine the point of nearest approach to the pitch-roll buoy. The mean wave-height was then obtained by making a further average over 21 of the one second averages, centred on the time of closest approach. An estimate of the error of the mean was also obtained.

This further averaging was carried out because there was still apparently a lot of noise in the one second averages. The noise may be due, in part, to the interference pattern which affects the individual radar pulses and it may also be due to local variations in the ocean wave field.

Comparisons were made on eight separate occasions. The results of the pitch-roll buoy observations are given in Table 1 and the results from the J.P.L. processed Seasat-1 observations are given in Table 2. The results are plotted against each other in Figure 1.

In terms of the difference between the pitch-roll buoy and the satellite measurements, the mean difference is $0.04 \text{ m} \pm 0.05 \text{ m}$. The standard deviation of individual values about the mean is 0.12 m . Similar results are obtained for the ratio of the pitch-roll buoy measurements to the satellite measurements. The mean value is then 1.06 ± 0.04 and the standard deviation of the individual values is 0.12 .

DISCUSSION

During the comparisons, the wave heights were below two metres, which means that the signal to noise ratio for the waveheight measurements was small. Thus the set of intercomparisons reported here represent a severe test of the altimeter's ability to measure waves. However, the mean difference between the two instruments of 6% is comparable with the difference between other instruments when measuring waves. The standard deviation of individual comparisons about the mean value is somewhat larger (12%).

For many ocean wave studies such differences are unimportant and for these the Seasat-1 radar altimeter can be considered a successful wave height measuring instrument. For studies, such as in the design of oil rigs, where a 12% error can be critical a better understanding of the differences observed is required.

It is unfortunate that higher waves could not also be included in this intercomparison. However, with higher waves the ratio of signal to noise in the radar pulse becomes larger, the filter corrections become less and no additional corrections are required until one reaches 20 m waves when the finite beam-width of the radar pulse starts to have an effect. Thus it seems unlikely for the performance of the altimeter to be any worse for waves of up to 15 m.

REFERENCES

- Lorell, J. (1979). Seasat algorithm development facility — altimeter sensor algorithm specifications. J.P.L. Document 622-202.
- McArthur, J.L. (1976). Design of the Seasat-A radar altimeter. Oceans 76 Conference record pp. 10B-1 to 10B-8.
- Ronai, P. (1979). Seasat Interim Geophysical Data Record (IGDR) User's Handbook. Initial Version-Altimeter. J.P.L. Document 622-697.
- Webb, D.J. (1979). Institute of Oceanographic Sciences Internal Report No. 85.

Table 1. The pitch-roll buoy results (from Webb 1979)

Pass Number	Buoy Position		Wave Analysis Period		Significant Wave Height	S.D. of Estimate
	Latitude	Longitude	Start Time	End Time		
1	59°03'N	12°30'W	0205	0238	2.26 m	0.10 m
2	59°24'N	12°26'W	0505	0628	1.43 m	0.03 m
3	59°39'N	12°21'W	2117	2236	0.76 m	0.02 m
4	58°59'N	12°51'W	0444	0624	1.15 m	0.02 m
5	59°12'N	12°53'W	2114	2157	1.70 m	0.05 m
6	59°09'N	13°12'W	0450	0630	1.10 m	0.03 m
7	59°09'N	13°29'W	2126	2249	1.16 m	0.02 m
8	59°12'N	12°35'W	2140	2303	0.84 m	0.02 m

Table 2. The Seasat-1 altimeter results

Pass Number	Nearest Approach to Buoy			Distance to Buoy	Significant Wave Height	S.D. of Estimate
	Latitude	Longitude	Day and Time			
1	59°07'N	12°26'W	197/04:24:07	10 kms	2.26 m	0.05 m
2	58°33'N	13°12'W	211/05:30:15	119 kms	1.59 m	0.04 m
3	60°01'N	12°38'W	212/21:59:34	49 kms	0.66 m	0.03 m
4	59°09'N	12°39'W	214/05:37:29	26 kms	0.91 m	0.05 m
5	59°04'N	12°43'W	215/22:06:55	22 kms	1.71 m	0.03 m
6	59°59'N	12°32'W	217/05:44:48	112 kms	1.01 m	0.04 m
7	58°11'N	12°35'W	218/22:14:15	137 kms	1.21 m	0.04 m
8	57°59'N	11°25'W	221/22:21:19	174 kms	0.76 m	0.03 m

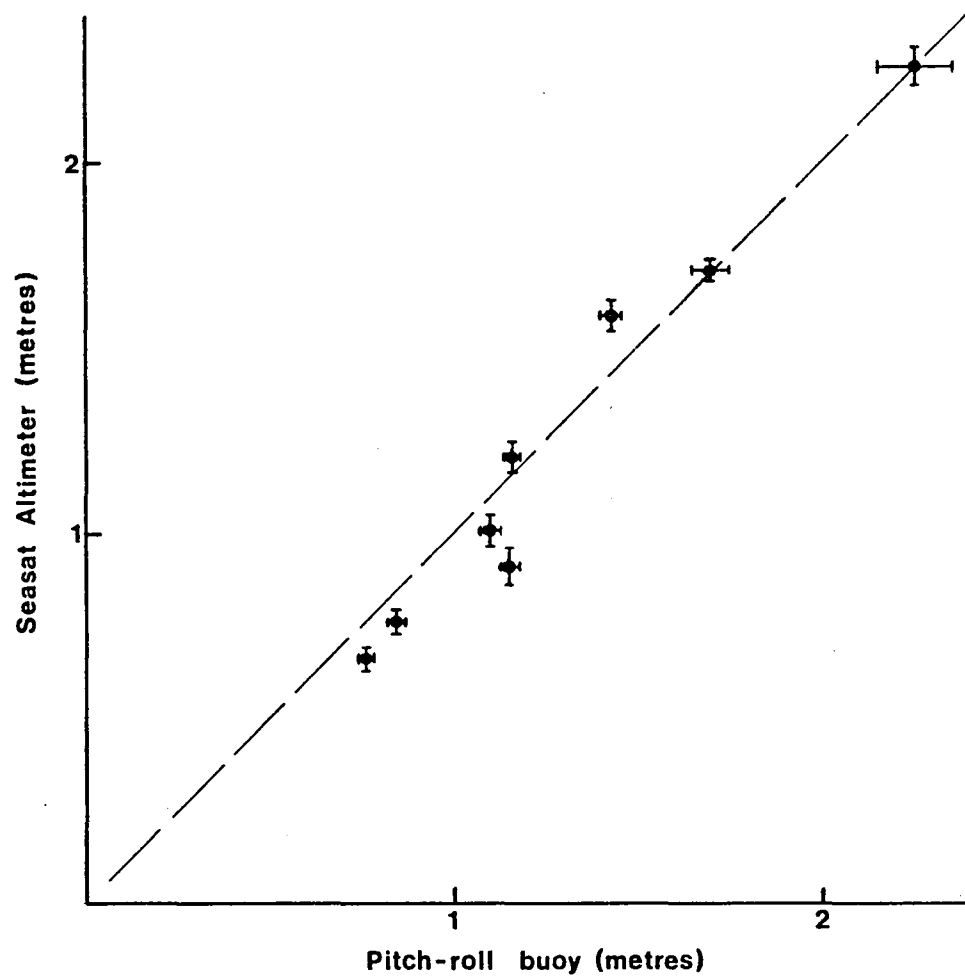


Figure 1. Comparison of Seasat Altimeter and Pitch-Roll Buoy Significant Wave Heights

APPENDIX F

REMOTE SENSING OF THE OCEAN WAVEHEIGHT SPECTRUM
USING SYNTHETIC-APERTURE-RADAR IMAGES

This Page Intentionally Left Blank

REMOTE SENSING OF THE OCEAN WAVEHEIGHT SPECTRUM
USING SYNTHETIC-APERTURE-RADAR IMAGES

John F. Vesecky and Hany M. Assal
Center for Radar Astronomy, Stanford, CA 94305

Robert H. Stewart
Scripps Institution of Oceanography, La Jolla, CA 92038
Jet Propulsion Laboratories, Pasadena, CA 91103

Abstract

Because synthetic aperture radars (SAR) can form images of large oceanic areas, they are well suited to studying wave generation, propagation and interaction with coasts and islands. Here we discuss problems in the detection and measurement of ocean waves from their SAR images, in particular the measurement of the wavenumber spectrum of ocean-wave-height fluctuations $F(k, \theta)$. Comparisons on a limited set of pitch-roll buoy and SEASAT SAR measurements during the 1978 JASIN experiment reveal that degradation of SAR resolution caused by wave orbital motion is a crucial factor in the detection of waves by SAR images. Thus waves with small slopes traveling perpendicular to the SAR flight path are more easily detected than waves with large slopes traveling along the flight path. Although the SAR estimates in this comparison were found to contain significant biases, they were in rough agreement with buoy measurements, provided the ocean wavelength was between about 120 and 400 m and the ocean wave direction was not approximately along the SAR flight path.

Because radars are capable of observing surface roughness over large ocean areas at frequent time intervals, they are well suited to studying problems in wave generation, propagation and interaction with coasts and islands (Stewart, 1978; Vesecky, et al., 1980). In this paper, we focus on high resolution (~ 10 's m) synthetic aperture radar (SAR) images of the ocean surface (obtained from aircraft or satellites) and their potential for studying gravity waves. At present, the quantitative interpretation of SAR images in terms of the directional wave-number spectrum of ocean-wave-height fluctuations $F(k, \theta)$ is still rather limited. Our long term objective is to assess the limitations on wave spectrum measurements using SAR images and, within these limitations, to put algorithms for such measurements on a firm quantitative footing both theoretically and experimentally.

Successful interpretation of SAR images is critically dependent on understanding the relationship between intensity fluctuations in SAR images and ocean surface roughness. This relationship depends on the interplay of several physical mechanisms involving modulation of the radar reflecting properties of the small-scale (~ 0.25 m) ocean surface by large-scale (~ 100 m) ocean waves (tilting and straining) as well as distortion of the SAR imaging process by ocean wave orbital velocity. Our approach to the interpretation problem is first, to obtain estimates of $F(k, \theta)$ from SAR images using a very simple algorithm based on the assumption that SAR image intensity fluctuations are proportional to ocean wave-height fluctuations. We then compare these estimates with similar estimates obtained from a wave buoy, noting the factors which influence wave visibility in SAR images and the differences between buoy and SAR estimates of $F(k, \theta)$. This experimental evidence can then be used to

better understand the radar-wave ocean-wave interaction and hence develop better algorithms for estimating F from SAR images.

COMPARISON OF SAR AND BUOY MEASUREMENTS OF WAVES DURING JASIN 1978

During the summer of 1978, extensive meteorological and oceanographic measurements were made off the west coast of Scotland (Fig. 1) as part of the 1978 Joint Air-Sea Interaction (JASIN) experiment. To take advantage of JASIN surface measurements, SEASAT SAR images (25 cm radar wavelength) were collected frequently over the JASIN area during July-September, 1978. Here we report initial comparisons between wave spectra measurements by pitch-roll buoy (Stewart, 1977) and from SEASAT SAR images supplied by the SEASAT Project at Jet Propulsion Laboratory. In Fig. 1 we show the areas imaged by SAR during four SEASAT passes and the locations of the areas in the images which were used to estimate $F(k, \theta)$. The buoy was located within the FIA area (Fig. 1). Table 1 summarizes other observed variables. We define $F(k, \theta)$ in terms of the ocean-wave-height variance

$\langle \zeta^2 \rangle$ by

$$\langle \zeta^2 \rangle = \int_0^{\infty} \int_0^{2\pi} F(k, \theta) k dk d\theta. \quad (1)$$

Our comparisons will be directly between the spatial SAR measurement of F and the temporal buoy measurement. In processing SAR images about 20 km square were digitized (256 levels) at about 20 m intervals and the results Fourier transformed. Making the simple assumption that SAR image intensity fluctuations are proportional to ocean wave height fluctuations we immediately have an estimate for F (within a multiplicative constant).

This estimate for F , F_{SAR} , is displayed as a wavenumber spectrum $F_{SAR}(k)$ averaged over a range of angles θ , $F_{SAR}(k) = \int_{\bar{\theta}-\Delta\theta}^{\bar{\theta}+\Delta\theta} F_{SAR}(k, \theta) d\theta$ or a

directional distribution $F_{\text{SAR}}(\theta)$ averaged over a range of wavenumbers,

$$F_{\text{SAR}}(\theta) = \int_{k_1}^{k_2} F_{\text{SAR}}(k, \theta) k dk \text{ --see Figs. 2 and 3 respectively.}$$

The pitch-roll buoy (Stewart, 1977) was deployed from the Woods Hole Research Vessel Atlantis II for periods of about one hour coinciding with SEASAT passes. The ocean wave frequency spectra $F(\omega, \theta)$ obtained from the buoy were converted to wavenumber spectra using the Jacobian $(g^2/2\omega^3)$ appropriate to deep-water waves; g is gravitational acceleration.

In Fig.2 we compare SAR and buoy measurements of $F(k)$ for August 4, 1978. For the buoy we display the omnidirection spectrum $F(k)$ while for the SAR we display $F(k, \theta)$ averaged over a 30° angular sector $(\bar{\theta} \pm 15^\circ)$ for two cases. The solid line corresponds to $F_{\text{SAR}, A}$ with $\bar{\theta}$ taken along the dominant wave direction. This yields our best estimate for $F(k)$ since increasing the size of $\Delta \theta$ simply adds noise. The dashed line $F_{\text{SAR}, 0}$ is for $\bar{\theta}$ taken away from the dominant wave direction and corresponds to image fluctuations unrelated to waves, i.e. noise for our purposes. However, we note that this noise is what might be expected from a SAR viewing a uniform scene, i.e., a flat spectrum at long wavelengths, going to zero for wavelengths shorter than the resolution of the radar. The signal to noise ratio (S/N) is the difference between the two curves. Finally, the SAR spectrum is normalized along the ordinate to the peak of the buoy spectrum.

It may be argued that we should subtract an estimate of the noise from the SAR spectrum in Figure 2 before comparing the spectrum with the buoy observations. We have not done so for two reasons: 1) the estimate of noise is not well known. It varies with position in the Fourier-transform plane, and tends to form bands

at large angles to the wave directions; and 2) subtracting an estimate of noise does not substantially alter our conclusions stated below.

In Fig. 2 the SAR spectrum corresponds reasonably well with the buoy wave-height spectrum, and less well with the wave-slope spectrum. The latter (not displayed) peaks at still higher wavenumber, and is slightly broader than either the SAR or the waveheight spectrum. Nevertheless, the differences are minor, and we are unable to distinguish clearly between height or slope spectra using the present set of data. As in the GOASEX and DUCK-X experiments, the SAR tends to overestimate the dominant wavelength (Barrick, 1980). Useful SAR measurements ($S/N > 1$) occur over a limited wavelength range (≈ 120 to 400m). At high wavenumbers $F_{\text{SAR}, A}$ lies above $F_{\text{SAR}, 0}$ possibly due to non-linear effects in the radar-wave ocean-wave interaction transferring spectral energy to larger wavenumbers. The SAR directional distribution averaged over $K = 0.022$ to 0.045 (Fig. 3) is reasonably close to the buoy measurement of both dominant wave direction and beamwidth (see also Table 1). Note that the peak rises only about a factor 3.5 above the background of non-gravity-wave related fluctuations.

In Table 1 we list comparisons between SAR and buoy measurements for other SEASAT passes. Note that SAR images 834-4 and 1006-5 did not show waves. In the latter half of Table 1 we list a number of variables which might influence the visibility of ocean waves in SAR images. We note that relatively high values of wind speed, $H_{1/3}$ or wave slope ($H_{1/3}/\Lambda$), where Λ is ocean wavelength) are not associated with waves visible in SAR images for this set of observations. The more crucial factors appear to be the number (n_{az}) of SAR resolution cells per ocean wavelength along the azimuth (flight path) direction and the angle between the perpendicular to the flight path and the dominant wave direction θ . The number n_{az} is calculated from

$n_{az} = (\Lambda/\sin\theta \langle d_a \rangle \rho_a)$ where Λ is the dominant ocean wavelength, $(\Lambda/\sin \theta)$ the wavelength along the azimuth direction, ρ_a the SAR azimuth resolution (40 m for SEASAT) and $\langle d_a \rangle$ the average resolution degradation given by Alpers and Rufenach (1979) for wave orbital motion effects. In Table 1 we find that images where $n_{az} < 2$ generally do not show waves and vice-versa. Note that image 834-6 is 185 km from the buoy-measured waves from which n_{az} was calculated, while 834-4 was only 55 km away. Since n_{az} decreases with increasing ocean waveheight and frequency, we would expect to find waves with large slopes less visible, as demonstrated in Table 1. Long SAR integration times also decrease n_{az} .

Table 1 also shows that range-traveling waves ($\theta \neq 90^\circ$) are more visible in SAR images. Further experimental evidence demonstrating this tendency was reported by Vesecky, Assal and Stewart (1979) for an aircraft SAR experiment off Pt. Arguello, CA. In this experiment a single ocean area was viewed from eight aspects by a 25 cm wavelength airborne SAR. Analysis of the images along the lines discussed above showed that S/N (see Fig. 2) decreased slowly with increasing θ dropping about 5 dB from the maximum at 5° to the noise level ($S/N = 0$) at 80° . We suggest that the reason that waves traveling perpendicular to the flight path are more easily detected in SAR images is simply that n_{az} is generally larger for waves with $\theta \neq 90^\circ$ (see Table 1) largely due to the $(\sin \theta)^{-1}$ factor in the expression for n_{az} .

CONCLUSIONS

We summarize preliminary conclusions based on this limited data set as follows:

1. For waves clearly visible in SAR images, the simple assumption that SAR image-intensity fluctuations are proportional to ocean-surface-height

fluctuations is not far wrong and slightly better than proportionality to ocean-wave-slope fluctuations.

2. Although biases occur, SAR wave spectra $F_{\text{SAR}}(k, \theta)$ are in approximate agreement with buoy spectra, provided $120 \leq \lambda \leq 400$ m and $\theta \neq 90^\circ$. Corrections for the radar-wave ocean-wave interactions should improve the agreement.

3. Visibility of ocean waves in SAR images is largely limited by inadequate resolution along the azimuth (flight path) direction caused by wave orbital motion.

4. Visibility of ocean waves in SAR images can change radically over a distance of ~ 150 km (see Table 1, images 834-4 and 834-6).

ACKNOWLEDGEMENTS

The authors wish to thank the SEASAT Project at Jet Propulsion Laboratory, the SEASAT SAR team, the JASIN Experiment and the crew of the Atlantis II for help with data collection and reduction. We are grateful to Dennis Douglas, Kurt Graf, Dennis Tremain and Chris Wilson at SRI International for help in image digitization. Thanks also to Michal Plume at Stanford for calculating the resolution degradation, to Kim Fisher at Stanford for manuscript preparation and to Ben Holt at JPL for help with a variety of data. We are grateful to the Office of Naval Research (Physical Oceanography Branch contract N00014-80-C-0440) and the National Oceanic Atmospheric Administration (contract MO-A01-78-00-4318) for financial support.

REFERENCES

- Alpers, W.R. and C.L. Rufenach: 1979, The effects of orbital motions on synthetic aperture radar imagery of ocean waves, IEEE Trans. Antennas and Propagat., AP-27, 685-690.
- Barrick, D.E. (chairman) et al.: 1980, "SEASAT Gulf of Alaska Workshop II Report, "JPL Report 622-107, Jet Propulsion Laboratory, Pasadena, CA.
- Stewart, R.H.: 1977, A discuss-hulled wave measuring buoy, Ocean Engng., 4, 101-107.
- Stewart, R.H. (ed.): 1978, Special Issue on IUCRM Colloquium on Radio Oceanography, Boundary-Layer Meteorology, 13, Nos. 1, 2, 3, and 4.
- Vesecky, J.F., H.M. Assal and R.H. Stewart: 1979, Synthetic Aperture Radar Observations at Various Aspects of Ocean Waves (abstract only), Programs and Abstracts, URSI 1979 Spring Meeting, International Union of Radio Science, National Academy of Science, Washington, D.C., p. 246.
- Vesecky, J.F., S.V. Hsaio, C.C. Teague, O.H. Shendin and S.S. Pawka: 1980, Radar observations of wave transformations in the vicinity of islands, J. Geophys. Res. (in press).

TABLE 1
WAVE MEASUREMENTS DURING JASIN 1978

SEASAT IMAGE	DATE	SAR obs.	Buoy obs.	DOMINANT WAVELENGTH		PRIMARY DIRECTION		ANGULAR WIDTH		DISTANCE Buoy to SAR
		Time UT	Time UT	Buoy	SAR	Buoy	SAR	Buoy	SAR	
547-5	4 AUG 78	0615	0600	170 m	194 m	263°	268°	30°	40°	0
556-1	4 AUG 78	2135	2100	151 m	141 m	280°	273°	53°	> 40°	65 km
834-4	24 AUG 78	0730	0700	147 m	none	≈295°	none	35°	none	55 km
834-6	24 AUG 78	0731	0700	147 m	185 m	≈295°	263°	35°	32°	185 km
1006-5	5 SEPT 78	0815	0700	105 m	none	109°	none	60°	none	120 km

SEASAT IMAGE	WIND SPEED	DIRECTION OF WIND ARRIVAL	$H_{1/3}$	$H_{1/3}/\lambda$	SAR SAMPLES Per Δ_{az}, n_{az}	ϕ^*	θ^{**}	RAIN	SAR S/N
547-5	3.6 ms^{-1}	15°	1.6 m	0.0094	2.6	113°	23°		5.0 dB
556-1	3.0 ms^{-1}	30°	1.5 m	0.0099	7.3	263°	7°	YES	2.0 dB
834-4	7.8 ms^{-1}	280°	2.8 m	0.019	0.58	150°	60°		0 dB
834-6	7.8 ms^{-1}	280°	2.8 m	0.019	0.58	150°	60°		6.3 dB
1006-5	11.9 ms^{-1}	120°	3.6 m	0.034	0.233	324°	54°		0 dB

* ϕ = angle between SAR flight vector and \mathbf{k} , where \mathbf{k} is ocean wavenumber

** θ = angle between \mathbf{k} and perpendicular to flight path (range direction), 0 to 90°

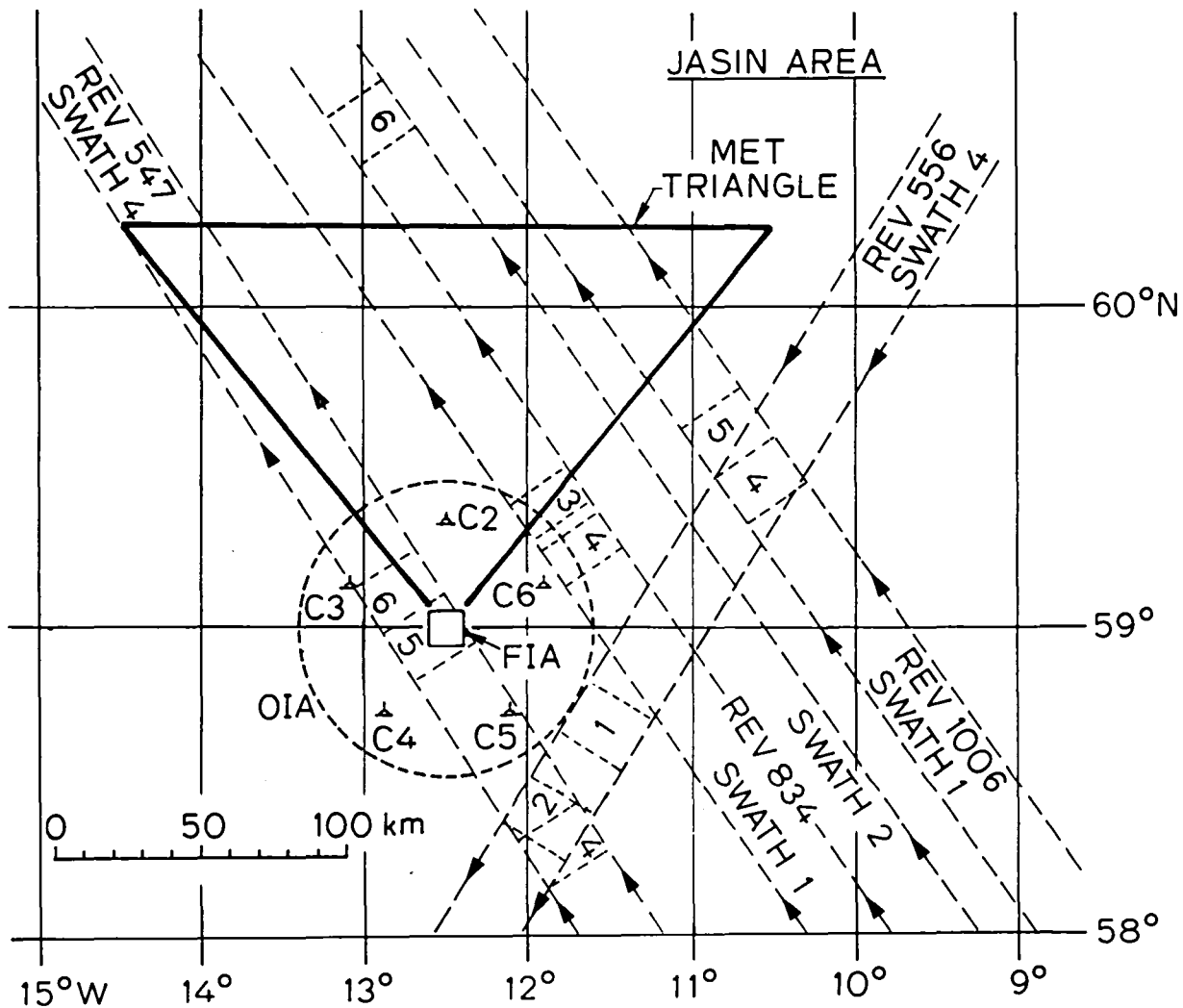


Fig. 1 JASIN experiment area off the west coast of Scotland showing the oceanic areas observed by the SEASAT SAR. Each SAR observation is 100 km in width, and is divided into four swaths each 25 km wide. The images used to make SAR estimates of waves are identified by revolution (REV) and image number, e.g., 547-5 overlays the FIA area. FIA and OIA are the Fixed Intensive Array and Oceanographic Intensive Area respectively. Depths beneath SAR images are everywhere greater than about 300 m. Buoy measurements used here were within the FIA area.

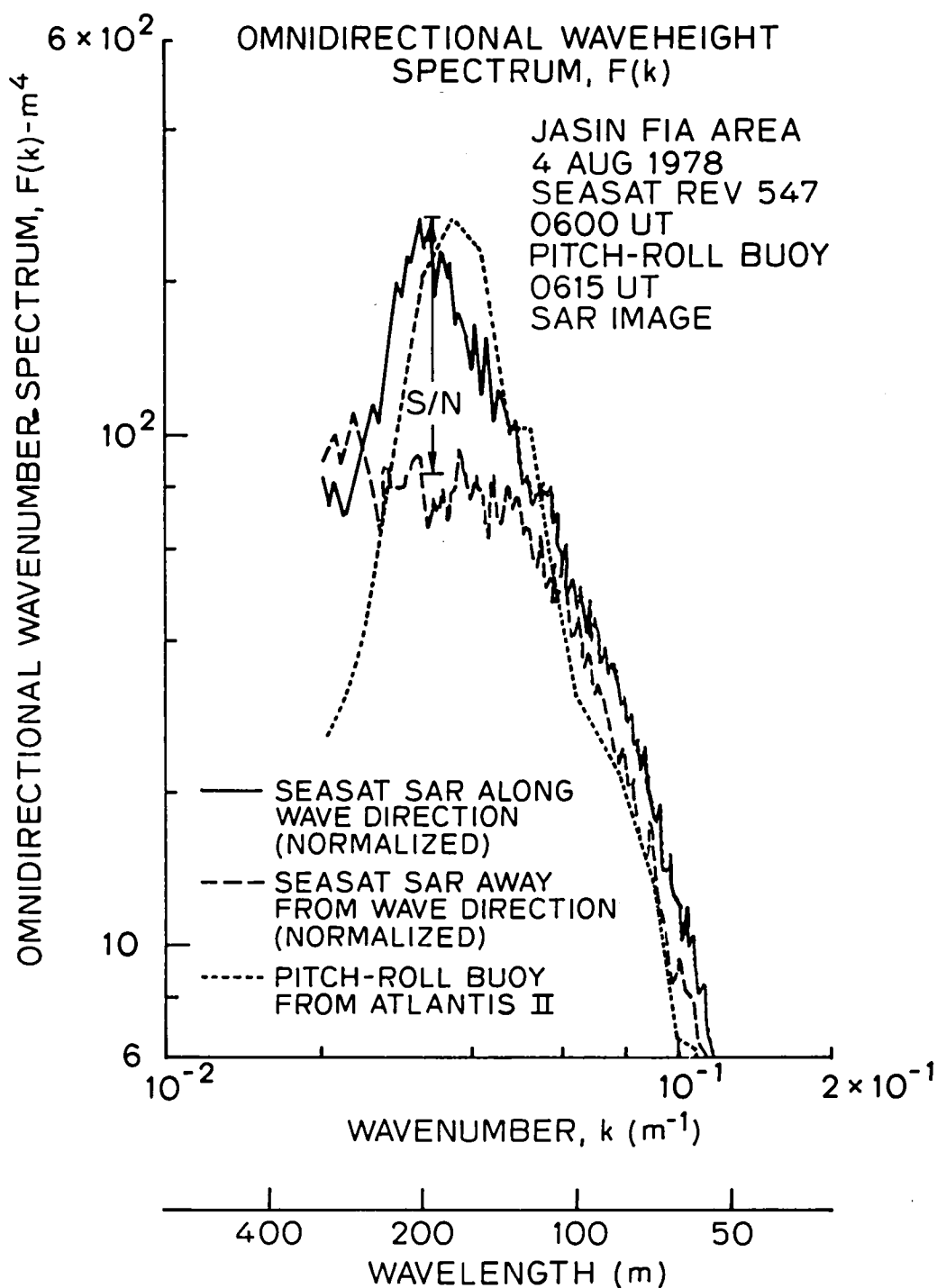


Fig. 2 Comparison between wavenumber spectra derived from pitch-roll buoy measurements and from a 20 x 20 km SEASAT SAR image. The SAR spectra are not truly omnidirectional, but rather $F_{SAR}(k, \theta)$ is averaged over an angular interval, $\bar{\theta} \pm 15^\circ$. SAR Spectra are shown for $\bar{\theta}$ along the dominant wave direction and away from this direction.

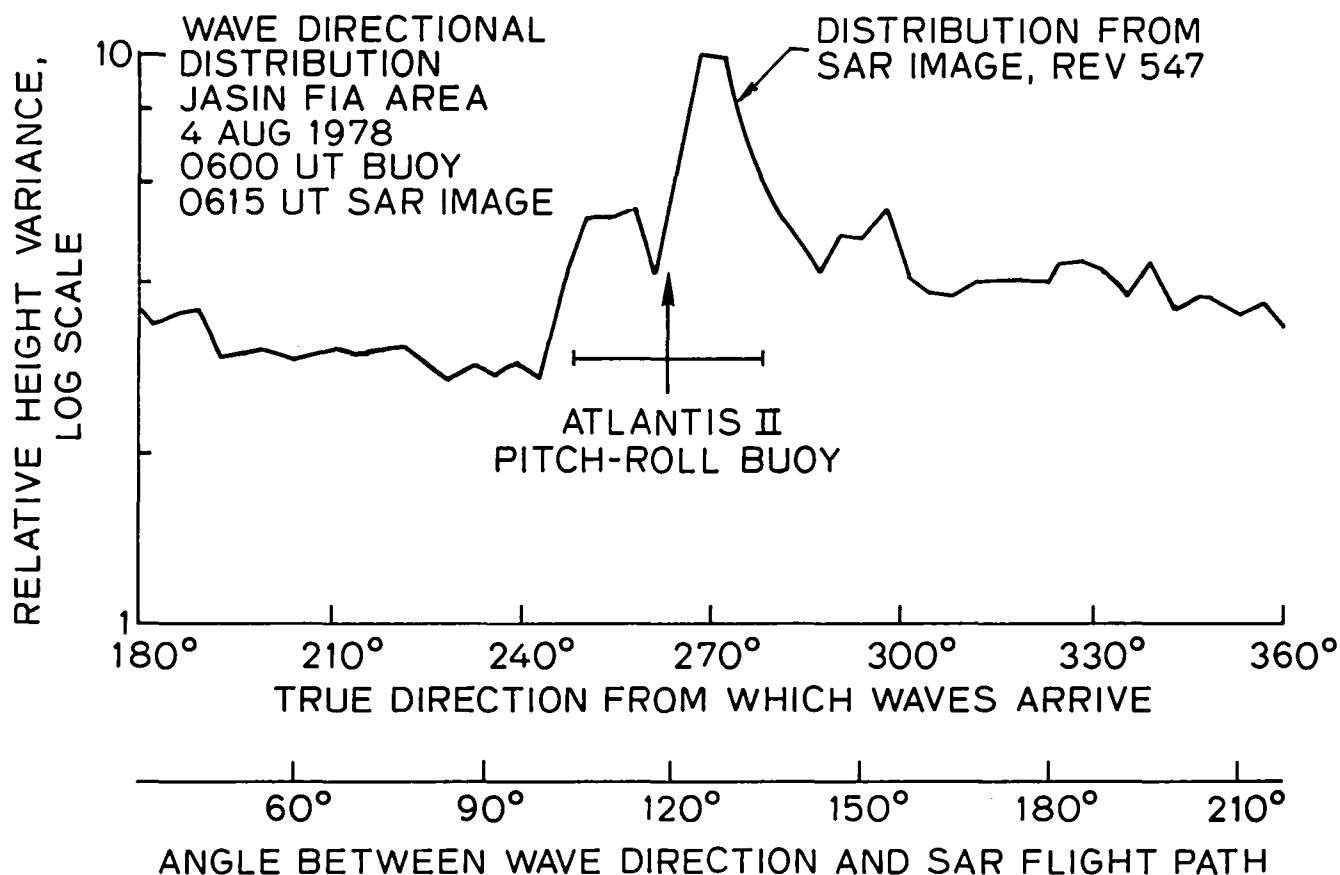


Fig. 3 Comparison of ocean wave directional distribution derived from pitch-roll buoy measurements and from a 20 x 20 km SEASAT SAR image. The distributions refer to ocean wavelengths near the dominant wavelength of about 170 m.

APPENDIX G

SEASAT-JASIN WORKSHOP

SURFACE TRUTH USER'S GUIDE


This Page Intentionally Left Blank

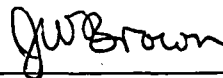
Seasat-JASIN Workshop

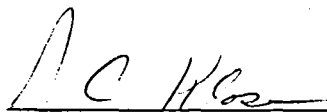
Surface Truth User's Guide

Prepared by:

Approved by:


G.V. Cowdery


J.W. Brown


J.C. Klose

December 1980

National Aeronautics and
Space Administration

Jet Propulsion Laboratory
California Institute of Technology
Pasadena, California

CONTENTS

<u>Section</u>	<u>Page</u>
1 INTRODUCTION -----	1-1
1.1 OVERVIEW -----	1-1
2 JPL PROCESSING OF JASIN OBSERVATIONS -----	2-1
2.1 SURFACE -----	2-1
2.2 RADIOSONDE -----	2-4
3 STDR PROCESSING -----	3-1
3.1 WMO SHIP DATA -----	3-1
3.2 OSU B3/B4 DATA -----	3-3
3.3 RADIOSONDE DATA -----	3-6
3.4 AUTOLOG DATA -----	3-9
4 AVERAGE WIND PROCESSOR -----	4-1
4.1 GENERAL DESCRIPTION -----	4-1
4.2 JOB CONTROL LANGUAGE - FROM TERMINAL -----	4-1
5 SURFACE TRUTH EDITOR -----	5-1
6 MERGE PROCESSING -----	6-1
6.1 GENERAL DESCRIPTION -----	6-1
6.2 BUILDING THE SURFACE DATA FILE -----	6-2
6.3 LISTING FILE CONTENTS -----	6-2
6.4 MERGING SPACECRAFT WITH SURFACE DATA -----	6-3
7 MSGDR REPORT -----	7-1
7.1 SAMPLE RUNSTREAM -----	7-1
7.2 BIN REPORT -----	7-3
APPENDIX A	
SAMPLE REPORT REQUEST FORM -----	A-1
APPENDIX B	
SURFACE TRUTH RECORD FORMATS -----	B-1

SECTION 1

INTRODUCTION

1.1 OVERVIEW

This document describes the computer programs developed to support the Seasat-JASIN Workshop. These programs performed the following functions:

- (1) Prepare JASIN surface truth data.
- (2) Merge prepared JASIN surface data with Seasat observations,
- (3) Statistically compare coincident surface and satellite observation sets.

The products produced by these programs were used to determine the validity of the Seasat geophysical products.

SECTION 2

JPL PROCESSING OF JASIN OBSERVATIONS

2.1 SURFACE

All surface observations used during the Seasat/JASIN Workshop were prepared at the Institution of Oceanographic Science (IOS), Wormley, England under the direction of T. H. Guymer. Meteorological observation types included wind speed and direction, sea surface temperature, wet bulb temperature, dry bulb temperature, and sea level atmospheric pressure. All observation records were time tagged and located.

IOS-prepared observations were recorded on magnetic tape and shipped to the Jet Propulsion Laboratory (JPL) in Pasadena, California. At JPL, the observations were operated on by a sequence of processors whose final product was a merged surface and satellite observation data record. From the merged file a statistics processor selected desired subsets of merged records, and generated reports that displayed the difference between the individual surface and satellite observations and a statistical summary of all comparisons.

Initial data processing of Joint Air-Sea Interaction (JASIN) surface observations at JPL adjusted wind speeds from their recorded height to a standard height of 19.5 meters above the sea surface. A surface layer model developed by W. T. Liu, at the University of Washington, was used to make this adjustment. In addition to anemometer height, the model requires dry bulb, wet bulb, and sea surface temperature to accurately model the surface layer. In most cases, these three temperatures were available with the surface wind observation, but in those instances where one or more were missing, the following assumptions were made: 1) If either wet bulb or dry bulb was missing, a relative humidity of 0.70 was assumed, and 2) if either dry bulb or sea surface temperature was missing, a neutral atmospheric stability was assumed (accomplished by setting both dry bulb and sea surface temperature to 12.0 degree C).

The surface layer model also produced a surface layer stability code corresponding to the range of Z/L values listed in Table 2-1. This stability code was carried along with the surface wind observation for later use in stratifying surface and satellite observation comparison statistics.

Table 2-1. Z/L State Table

Z/L	Stability Code		
-1 to -0.10	1	}	unstable
-0.10 to -0.01	2		
-0.01 to -0.001	3		
-0.001 to 0	4	}	neutral
0 to 0.001	5		
0.001 to 0.01	6	}	stable
0.01 to 0.03	7		
0.03 to 0.05	8		
0.05 to 0.10	9		
0.10 to 1.0	0		

The surface data record received from IOS represented a complete time history of surface observations by platform. For the workshop only those observations that had a high likelihood of being matched with satellite observations were needed. Two editing schemes were used to select those observations. Selected observations were then entered into the workshop surface observation data base.

Wind observations from the Meteorological (MET) ships and the mooring S13, and sea surface temperature observations from MET ships and auto-log platforms were treated as spot observations. Spot observations were edited by selecting only those observations that bracketed a satellite overpass time. Then linear interpolation was used to compute surface observations at the time of the overpass. Only the interpolated spot observations were entered into the workshop surface observation data base.

High density wind observations (from platforms having auto-log recorders) were used to produce average wind observations. Averaging intervals of 15 and 60 minutes centered about the satellite overpass time were chosen. Only the average wind records were entered into the workshop surface observation data base; the spot observations used in computing the average wind records were not compared with satellite observations.

Observations from the workshop surface observation data base were merged with satellite observations from each pass being studied in the workshop. Previous editing steps guaranteed that all surface observations were sufficiently close in time to the satellite observations and that only a distance tolerance needed to be checked to determine coincidence. Seventy-five km was chosen as the maximum distance separating coincident surface and satellite observations. All parts of the surface and satellite observations that met this coincidence criterion were combined to form a merged data record.

A Seasat Scatterometer (SASS) wind observation can have up to four solutions or aliases, each with a different wind speed and direction. When merging SASS winds with surface observations, the SASS wind solution that was closest in wind direction to the direction of the surface observation was selected for inclusion into the merged data record. The remaining solutions were not kept and, therefore, not compared with surface observations.

A merged record contains two comparable sets of observations, one set containing surface observations and the other satellite observations. The content of the two sets is satellite instrument dependent. For SASS merged records the observation sets contain wind speed and direction; for SMMR merged records the two sets contain sea surface temperature and wind speed. All merged records contain the time and distance separating surface and satellite observation sets.

Merged files were stratified based on a value or a range of values of one or more parameters in the merged record. Once stratified, merged files were passed through a statistics package. Here, differences between surface and satellite observations for all merged records were computed and displayed. Additionally, for each satellite pass, a statistical summary was displayed. This

summary included the minimum value, the maximum value, and the mean value for each surface observation type; the minimum value, the maximum value, and the mean value for each satellite observation type, the mean difference between coincident surface and satellite observations of like type, and the standard deviation about the mean differences.

2.2 RADIOSONDE

JASIN radiosonde observations were prepared at IOS under the direction of P. Taylor. Processing procedures of IOS used the raw radiosonde data to compute the total water vapor in a column of air bounded by the sea surface at the bottom and the maximum height of the balloon flight at the top. All radiosonde water vapor observations were time tagged and earth located.

IOS-processed radiosonde observations were recorded on punched cards and sent to JPL. Because the number of radiosonde flights was small (~250) when compared to the number of surface meteorological observations (~100,000), there was no need to edit the radiosonde observations prior to entry onto the workshop surface truth data base. All radiosonde observations received from IOS were entered into the workshop surface truth data base.

When merging radiosonde observations with satellite observations, both time and distance tolerances had to be checked to determine coincidence. One hour was chosen as the maximum time separation and 75 km was chosen as the maximum distance separation. All pairs of radiosonde and satellite observations that met both coincidence criteria were combined to form merged records. The resultant merged file was passed through the statistics package and the results were used to validate the Scanning Multichannel Microwave Radiometer (SMMR) water vapor observations.

SECTION 3

STD R PROCESSING

3.1 WMO SHIP DATA

The MET ships reported their hourly observations in the World Meteorological Organization (WMO) format. WMO observations were received from England on magnetic tape in the following format:

9-Track, 1600 BPI, ASCII, UNLABELLED, RECORD LENGTH = 112 characters
Block Length = 24 records (2688 characters).

The first four blocks are header records, which contain 24 28A4 records each. Remaining blocks are structured as specified by record format shown in Table 3-1.

Table 3-1. WMO Ship Format

Format	Missing Value Code	Variable
1X		Fill
I2		Day
I2		Month
I2		Year
I4		Hour (GMT)
21X		Fill
I3	999	Wind direction (degrees from true North)
1X		Fill
F4.1	99.9	Wind speed (meter/sec)
33X		Fill
F6.1	9999.9	Temperature dry (degrees C)
F6.1	9999.9	Temperature wet (degrees C)
1X		Fill
F5.1	999.9	Sea surface bucket temperature (degrees C)
10X		Fill

Table 3-1. WMO Ship Format (continued)

Format	Missing Value Code	Variable
I5	99999	Latitude (degrees/min)
I5	99999	Longitude (West) (degrees/min)
A1		Corrected record flag (if * present ignore this record)

- 1) To convert WMO ship data from ASCII to UNIVAC SDF format for STDR processing, follow this sample runstream:

```
@ASG,TJ TAPE., U9V,REEL #
@Rewind TAPE.
@CAT,P FILE.
@ASG,A FILE.
@UOM*UOM.UNBLOCK,AN TAPE.,FILE.,112,2688
@FREE TAPE.
```

Successive files on the tape reel may be processed by omitting the last step and repeating steps 3 - 5, using different files. FILE must be cataloged sufficiently large. Default value is 128 tracks.

- 2) To generate a WMO STDR, follow the sample runstream:

```
@USE 70.,WMO-DATA. (WMO-DATA. is FILE. from previous step)
@ASG,A 70.
@CAT,P FILE-1.
@CAT,P FILE-2.
@USE 71.,FILE-1.
@USE 72.,FILE-2.
@ASG,A 71.
@ASG,A 72.
@CAT,P PRINT-FILE.
@USE 101.,PRINT-FILE
@ASG,A 101.
@XQT SEASAT-ADF*SURFACE.STDR
TAPE REEL NUMBER (CR) 1-6 characters
output files will be copied to this tape
using EZIO.
```

WRITE INITIALS (CR) 1-3 characters
this is required only when TAPE REEL NUMBER
is not blank
PROJECT ID (CR) 1-6 characters

In demand mode only, input is now echoed back and you are asked if it is correct. Respond with either YES (CR) or NO (CR). If you respond with NO(CR), the program will start back at TAPE REEL NUMBER question.

Then enter:

2 (CR) Platform type (WMO ship data).

In demand mode only platform type is echoed back and you are asked if it is correct. Respond with either YES (CR) or NO (CR). If you respond with NO the program will return to PLATFORM TYPE question.

The program now processes the data. After processing is completed you are asked if you desire a listing of FILE 71 (observation type 1). Respond with YES (CR) or NO (CR).

Next you are asked if you desire a listing of FILE 72 (observation type 2). Respond with YES (CR) or NO (CR).

@FREE 101.
@BLK,S PRINT-FILE., BLD/BOX, SITE } Demand Mode Only

FILES USED

FILE 70 - (WMO-DATA) Contains the input WMO-DATA that needs to be made into a STDR
FILE 71 - Output observation Type 1 STDR
FILE 72 - Output observation Type 2 STDR

3.2

OSU B3/B4 DATA

OSU B3/B4 data is in the format:

9-TRK, 800 BPI, ASCII, UNLABELLED
RECORD LENGTH = 80 characters
BLOCK LENGTH = 4000 characters (50 RECORDS)

The first record is a 80 character header record which is followed by one or more 4000 character data records.

Format of header record is

31X	FILL
A2	'B3 ' or 'B4'
3X	FILL
A6	'15-MIN' or 'HOURLY'
38X	FILL

The header record will tell you whether the data is from platform B3 or B4 and whether it is 15-MIN or HOURLY averages. Table 3-2 shows the format of both the 15-minute and hourly records.

- 1) To convert OSU B3/B4 data from ASCII to SDF format for STDR processing, follow this sample runstream:

```
@ASG,TJ TAPE., U9V, REEL #
@REWIND TAPE.
@CAT,P FILE.
@ASG,A FILE
@UOM*UOM.UNBLOCK,AN TAPE.,FILE.,,80,4000
@FREE TAPE.
```

Successive files on the tape reel may be processed by omitting the last line and repeating lines 3-5, using a different file. FILE must be cataloged sufficiently large. Default value on cataloging is 128 tracks.

- 2) To generate an OSU B3/B4 STDR, follow this sample runstream:

```
@USE 70.,OSU-DATA. (OSU-DATA. is FILE. from previous step)
@ASG,A 70.
@CAT,P FILE-1.
@CAT,P FILE-2.
@USE 71.,FILE-1.
@USE 72.,FILE-2.
@ASG,A 71.
@ASG,A 72.
@CAT,P PRINT-FILE.
@USE 101.,PRINT-FILE.
@ASG,A 101.
@XQT SEASAT-ADF*SURFACE.STDR
```

} Demand Mode Only

Table 3-2. OSU B3/B4 Format

15 Minute Average Record		
Format	Missing Value Code	Variable
I2		Hour (GMT)
I2		Minute
F2.1		Fraction of minute
1X		Fill
I2		Day
1X		Fill
A3		Month ('JAN', 'FEB', 'MAR',...)
1X		Fill
I2		Year
1X		Fill
F5.2	0.	Wind speed (meter/sec)
I5	0.	Wind direction (degrees from true north)
2X		Fill
F5.2	0.	Temperature dry (degrees C)
9X		Fill
F5.2	0.	Seasurface temperature (degrees C)
Hourly Average Records		
I2		Hour
I2		Minute
1X		Fill
I2		Day
1X		Fill
A3		Month ('JAN', 'FEB', 'MAR',...)
1X		Fill
I2		Year
1X		Fill
F5.2	0.	Wind speed (meter/sec)
I5	0.	Wind direction (degrees from true North)
2X		Fill
F5.2	0.	Temperature dry (degrees C)
9X		Fill
F5.2	0.	Sea surface temperature (degrees C)

(runstream continued from page 3-4)

TAPE REEL NUMBER (CR) 1-6 characters. Output files will be copied to this tape using EZ10.

WRITE INITIALS (CR) 1-3 characters. This is required only when TAPE REEL NUMBER is not blank.

PROJECT ID (CR) -6 characters

In demand mode only, input is now echoed back and you are asked if it is correct. Respond with either YES (CR) or NO (CR). If you respond with NO (CR), the program will start back at TAPE REEL NUMBER question.

Then enter:

3 (CR) Platform type (B3/B4 data).

In demand mode only, platform type is echoed back and you are asked if it is correct. Respond with either YES (CR) or NO (CR). If you respond with NO (CR) the program will return to PLATFORM TYPE question.

The program now processes the data. After processing is completed you are asked if you desire a listing of FILE 71. Respond with YES (CR) or NO (CR).

Next you are asked if you desire a listing of FILE 72. Respond with YES (CR) or NO (CR).

@FREE 101.	} Demand Mode Only
@BLK,S PRINT-FILE., BLD/BOX, SITE	

FILES USED

FILE 70 - (OSU-DATA) Containing the input OSU B3 or B4, 15 or 60 minute averaged data that needs to be made into a STDR.

FILE 71 - Output observation Type 1 STDR.

FILE 72 - Output observation Type 2 STDR.

3.3 RADIOSONDE DATA

Radiosonde data received from England is on cards. The data format is specified in Table 3-3.

Table 3-3. Radiosonde Format

Format	Missing Value Code	Variable
A1		Platform ID Code C - Gardline H - Hecla J - John Murray M - Meteor
3X		Fill
I3		Day Number
I2		Hour (GMT)
I2		Minute
I2		Latitude degrees
I2		Latitude minutes
I2		Longitude degrees (West)
I2		Longitude minutes (West)
31X		Fill
I3	999	Atmospheric water vapor to 500 mb (0.001 gram/cm ²)
15X		Fill
I3	999	Top of flight pressure (1.0 mb)
I3	999	Total atmospheric water to top pressure (0.001 gram/cm ²)

- 1) To convert the radiosonde data from cards to a SDF format file for STDR processing, follow this sample batch runstream:

```
@RUN USERID,ACCT#,SEASAT-ADF
@CAT,P FILE.
@ASG,A FILE.
@DATA,IL FILE.
      (RADIOSONDE CARD DECK)
@END
```

To generate a RADIOSONDE STDR, follow this sample runstream:

```
@USE 70., RADIO.
@ASG,A 70.
```

```
@CAT,P FILE1.
@USE 71.,FILE1.
@ASG,A 71.
```

@CAT,P FILE2.
@USE 72.,FILE2.
@ASG,A 72.

@CAT,P FILE3.
@USE 73.,FILE3.
@ASG,A 73.

@CAT,P FILE4.
@USE 74.,FILE4.
@ASG,A 74.

@CAT,P PRINT-FILE.	}	In Demand Mode Only
@USE 101.,PRINT-FILE.		
@ASG,A 101.		

@XQT SEASAT-ADF*SURFACE.STDR
TAPE REEL NUMBER (CR) 1-6 characters. Output files will be copied
to this tape using EZIO.
WRITE INITIALS (CR) 1-3 characters. This is required only when
TAPE REEL NUMBER is not blank

PROJECT ID (CR) 1-6 characters

In demand mode only, input is now echoed back and you are asked
if it is correct. Respond with either YES (CR) or NO (CR). If
you respond NO, the program will start back at TAPE REEL NUMBER
question.

Then enter:

4 (CR) Platform Type (RADIOSONDE)

In demand mode only, platform type is echoed back and you are
asked if it is correct. Respond with either YES (CR) or
NO (CR). If you respond NO, the program will return to PLAT-
FORM TYPE question.

The program now processes the data.

After processing is completed you are asked if you desire a listing of the output files. You will only be asked about the files that have data. The order in which you will be asked is FILE 71, 72, 73, and 74.

```
@FREE 101.
@BLK,S PRINT-FILE.,BLD/BOX,SITE } Demand Mode Only
```

Files used:

FILE 70 - RADIO input file. Contains the radiosonde data that needs to be made into a STDR.
 FILE 71 - Contains the output STDR for Gardline.
 FILE 72 - Contains the output STDR for Hecla.
 FILE 73 - Contains the output STDR for John Murray.
 FILE 74 - Contains the output STDR for Meteor.

3.4 AUTOLOG DATA

Autolog data received from England on tape is in the format:

9 Track, 1600 BPI, ASCII, UNLABELLED
 RECORD LENGTH = 100 characters
 BLOCK LENGTH = 80 records (8000 characters)

The first 2 blocks are header records each block containing 80 records in the format 25A4. Remaining blocks are structured as specified by record format as shown in Table 3-4.

Table 3-4. Autolog Format

Format	Missing Value Code	Variable
I1		Month (Numbers 1-9, for months Jan - Sept)
I2		Day of Month
I2		Hour (GMT)
I2		Minute
11X		Fill
I5	99999	LAT. (degrees/min)
I5	99999	LON. (West) (degrees/min)
27X		Fill
F6.2		Wind direction (degrees from true North)

Table 3-4. Autolog Format (continued)

Format	Missing Value Code	Variable
1X		Fill
F5.2	99.99	Wind speed (meter/sec)
8X		Fill
F6.2	99.99	Temperature dry (degrees C)
F6.2	99.99	Temperature wet (degrees C)
1X		Fill
F5.2	99.99	Sea surface temperature bucket (degrees C)

- 1) To convert Autolog data from ASCII to SDF format for STDR processing, follow this sample runstream:

```
@ASG,TJ TAPE., U9V, reel #
@REWIND TAPE.
@CAT,P FILE.
@ASG,A FILE.
@UOM*UOM.UNBLOCK,AN TAPE.,FILE.,,100,8000
@FREE TAPE.
```

Successive files on the tape reel may be processed by omitting the last line and repeating lines 3-5 using a different file. FILE must be cataloged sufficiently large. Default value when cataloging is 128 tracks.

- 2) To generate an AUTOLOG STDR, follow this sample runstream:

```
@USE 70.,AUTOLOG-DATA.
@ASG,A 70.
@CAT,P FILE-1.
@CAT,P FILE-2.
@USE 71.,FILE-1.
@USE 72.,FILE-2.
@ASG,A 71.
@ASG,A 72.
@USE 69.,TIME-SLICES.    } Required only if you wish to process
@ASG,A 69.               } time slices.
@CAT,P PRINT-FILE.      }
@USE 101.,PRINT-FILE.   } Demand Mode Only.
@ASG,A 101.
@XQT SEASAT-ADF*SURFACE.STDR
TAPE REEL NUMBER (CR) 1-6 characters. Output files will be
                                copied to this tape using EZIO.
```

WRITE INITIALS (CR) 1-3 characters. This is required only when
 TAPE REEL NUMBER is not blank
PROJECT ID (CR) 1-6 characters

In demand mode only, input is now echoed back and you are asked if it is correct. Respond with either YES (CR) or NO (CR). If you respond with NO(CR), the program will start back at TAPE REEL NUMBER question.

Then enter:

5 (CR) Platform Type (AUTOLOG)

In demand mode only, platform type is echoed back and you are asked if it is correct. Respond with either YES (CR) or NO (CR). If you respond with NO the program will return to PLATFORM TYPE question.

The program now processes the data. After processing is completed; you are asked if you desire a listing of FILE 71. Respond with YES (CR) or NO (CR).

Next you are asked if you desire a listing of FILE 72. Respond with YES (CR) or NO (CR).

@FREE 101.
@BLK,S PRINT-FILE.,BLD/BOX,SITE } Demand Mode Only

FILES USED

FILE 70 - (AUTOLOG-DATA) contains the input AUTOLOG-DATA that needs to be made into a STDR.
FILE 71 - Output observation Type 1 STDR.
FILE 72 - Output observation Type 2 STDR.

File TIME-SLICES is a SDF file used to select specific segments of time from the input Autolog file to be processed. It must be in the following format:

IIIIII Delta Time (sec.) (Free Format Integer)
YYMMDD HHMMSS }
YYMMDD HHMMSS } MAX OF 100 INPUT TIMES.

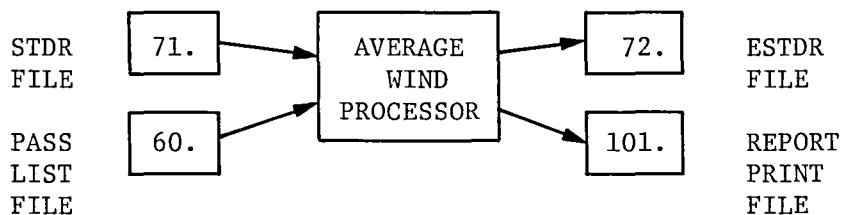
Delta time is added to and subtracted from input times to
create a time slice for processing.

SECTION 4

AVERAGE WIND PROCESSOR

4.1 GENERAL DESCRIPTION

The program operates on STDR Type one records only.



The average wind processor reads an STDR file, computes average wind records for the passes listed in FILE 60 and outputs an ESTDR file. In addition, a print report is generated in FILE 101. Messages indicating the progress of the run are output to terminal.

4.2 JOB CONTROL LANGUAGE - FROM TERMINAL

1) STDR Input File

```
@ASG,A (STDR input file).-type one records
@USE 71.,(STDR input file).
```

2) Pass List File

The file will be delivered with the program absolute and must be saved for reuse.

```
@ASG,T 60.
@INSERT SEASAT-ADF*SURFACE.FILE60,60.
@ASG,A 60.
```

3) ESTDR Output File

@ASG,A (ESTDR output file).
@USE 72.,(ESTDR output file).

4) Report Print File

@CAT,P PRINT.
@ASG,A PRINT.
@USE 101.,PRINT

5) Execute Program

@XQT SEASAT-ADF*SURFACE.AVGWIND

6) BLK Print File to Get Report

@BLK,S PRINT.,BLD/BOX, SITE

SECTION 5

SURFACE TRUTH EDITOR

The purpose of the surface truth editor is to include only those surface truth points which are within a given time and distance range of a Seasat pass. The editor can also include or exclude records by time or observation type. Interpolated spot reports are generated if one of the two adjacent observations passes the editing test (within given time and distance of a S/C pass) and they are within an interval of 6 hours. The resultant ESTDR (edited surface truth data record), is written on disk, with an option of copying to tape.

The format to include or exclude a record is listed below:

EXCLUDE platform-ID Time-1 Time-2 OBSTYP

Platform-ID is 16 characters long and should be padded with blanks if necessary. Time-1 and Time-2 are 12 characters long and are of the form YRMODYHRMNSC. This is an optional field.

OBSTYP can be of the form N_1 , N_2 , N_3 or $N_1 - N_2$ (N_1 through N_2)

The input tape for the editor is 14, the output file is 15.

A sample runstream:

```
@ASG,T FILE1.
@USE 14.,FILE1.
@ASG,T FILE2.
@USE 15.,FILE2
@XQT SEASAT-ADF*SURFACE.ESTD
EXCLUDE METEOR          780723090100 780723090400
EXCLUDE METEOR          4-5
TAPE ID Q1234 ABC
LIST HERE WILL LIST OUT THE ESTDR IN THE 132 CHAR FORMAT
END
```

If the tape ID card is omitted, FILE 15 will not be copied to tape.

SECTION 6

MERGE PROCESSING

6.1 GENERAL DESCRIPTION

The BUILD-ESTDR is a pointer structured file.

Latitude Pointer: Points to next largest latitude

Longitude Pointer: Within each latitude of the same value, this points to the next largest longitude

Time Pointer: Within each latitude and longitude of the same value, this points to the next largest time

Next Record: This points to the next logical record

Example:

REC	LAT	LON	TIME	LAT PNTR	LON PNTR	TIME PNTR	NEXT PNTR
1	10	10	10	8	5	2	2
2	10	10	20	0	0	3	3
3	10	10	30	0	0	4	4
4	10	10	40	0	0	0	5
5	10	20	10	0	6	0	6
6	10	30	10	0	7	0	7
7	10	40	10	0	0	0	8
8	20	10	10	9	0	0	9
9	30	10	10	10	0	0	10
10	40	10	10	0	0	0	0

Record zero in this file contains the address of the first data record in the file (zero if there is no data in the file), and the address of the next available location for a data record to be written at. Program BUILD-INIT sets record zero to the value of '01'. Program BUILD uses and updates these numbers during the process of adding data to the file.

The merging process uses the latitude, longitude, and time pointers as the address of the next record to be checked for a match, allowing the program to skip unnecessary records. The next record pointer allows the program to logically process records in the file, with the same latitude, longitude, and time values, no matter in what sequential order they are.

6.2 BUILDING THE SURFACE DATA FILE

- 1) To create a BUILD-ESTDR, follow this sample runstream:

```
@CAT,P BUILD-ESTDR.
@USE 71.,BUILD-ESTDR.
@ASG,A 71.
@XQT SEASAT-ADF*SURFACE.BUILD-INIT
```

- 2) To add data to a BUILD-ESTDR, follow this sample runstream:

```
@USE 70.,ESTDR.
@ASG,A 70.
@USE 71.,BUILD-ESTDR.
@ASG,A 71.
@XQT SEASAT-ADF*SURFACE.BUILD
```

6.3 LISTING FILE CONTENTS

- 1) To sequentially list a BUILD-ESTDR, follow this sample runstream:

@USE 71.,BUILD-ESTDR.	
@ASG,A 71.	
@CAT,P PRINT-FILE.	
@USE 101.,PRINT-FILE.	
@ASG,A 101.	
@XQT SEASAT-ADF*SURFACE.BUILD-DUMP.	
@FREE 101.	
@BLK,S PRINT-FILE.,BLD/BOX,SITE	

} Needed in Demand Mode Only

} Demand Mode Only

- 2) To logically list a BUILD-ESTDR, follow this sample runstream:

```
@USE 71.,BUILD-ESTDR.
@ASG,A 71.
@CAT,P PRINT-FILE.      }
@USE 101.,PRINT-FILE.    } Demand Mode Only
@ASG,A 101.
@XQT SEASAT-ADF*SURFACE.BUILD-LIST
@FREE 101.               }
@BLK,S PRINT-FILE.,BLD/BOX,SITE }
```

To list GDR FILE follow the sample runstream:

```
@USE GDRIN., <GDR FILE>
@ASG,A GDRIN.
@CAT,P PRINT-FILE.      }
@USE 101., PRINT-FILE.   } Demand Mode Only
@ASG,A 101.
@XQT SEASAT-ADF*SURFACE.GDRLIST
Enter 1 - ALT (FREE FORMAT)
   or 2 - SASS (FREE FORMAT)
   or 3 - SMMR (FREE FORMAT)
@FREE 101.
@BLK,S PRINT-FILE., <BLD>/<BOX>, <SITE> }
```

6.4 MERGING SPACECRAFT WITH SURFACE DATA

- 1) To merge a GDR file with a BUILD-ESTDR, follow this sample runstream:

```
@USE GDRIN., <GDRFILE>
@ASG,A <GDRFILE>
or
@ASG,TJ GDRIN., U9V, <REEL #>
@USE 70.,BUILD-ESTDR.
@ASG,A 70.
@CAT,P MSGDR.
@USE 71,MSGDR.
@ASG,A 71.
@CAT,P PRINT-FILE.      }
@USE 101.,PRINT-FILE.    } Demand Mode Only
@ASG,A 101.
@XQT SEASAT-ADF*SURFACE.MERGE
AL (CR)      - to process altimeter GDR file.
or
```

SA (CR) - to process SASS GDR file.
or
SM (CR) - to process SMMR GDR file.
YES (CR) - to use standard distance and time tolerances
 (distance = 150 Km, time = 60 min.)
or
NO (CR) - to enter distance and time tolerances

If previous answer was NO,
Enter distance tolerance (Km, free format)
Enter time tolerance (minutes, free format)

The program prints out the tolerances input and asks if they are correct. Respond with a YES (CR) or NO (CR). A NO response will allow you to re-enter the tolerances.

@FREE 101.	}	Demand Mode Only
@BLK,S PRINT-FILE.,BLD/BOX,SITE	}	

SECTION 7

MSGDR REPORT

7.1 SAMPLE RUNSTREAM

To generate a MSGDR Report follow this sample runstream:

```
@USE 70., MSGDR.
@ASG,A 70.
@CAT,P PRINT-FILE.
@USE 101.,PRINT-FILE.
@ASG,A 101.
@XQT SEASAT-ADF*SURFACE.REPORT
$RPTIN
RPTTYP      = _____ ,
OBTYP      = _____ ,
SC1MIN      = _____ ,
SC1MAX      = _____ ,
MAXDIS      = _____ ,
ZLMIN       = _____ ,
ZLMAX       = _____ ,
REVBK       = _____ ,
INCEXC      = _____ ,
PLTID(1)    = _____ ,
PLTID(4)    = _____ ,
PLTID(7)    = _____ ,
PLTID(10)   = _____ ,
REVL        = _____ ,
TITLE       = _____ ,
$END

@FREE 101.
@BLK,S PRINT-FILE., <BLD>/<BOX>, <SITE> }
```

For Demand Mode Only

Demand Mode Only

RPTTYP - Report type

- 1 - one S/T observation compared to one S/C observation
(default value).
- 2 - one S/T observation compared to one or more S/C observations
- 3 - one S/C observation compared to one or more S/T observations

OBTYP - Observation type

- 0 - all (default value)
- 1-9 - observation types one to nine

SC1MIN/SC1MAX

- incidence angle range in hundredths of a degree
(default values SC1MIN = 0, SC1MAX = 9999)

MAXDIS

- maximum distance between S/T and S/C observations in KM. Default value is 150 KM

ZLMIN/ZLMAX

- range for ZL values
- 1,2,3 - UNSTABLE
- 4, 5 - NEUTRAL
- 6,7,8,9,0 - STABLE
- Default values ZLMIN = 1 , ZLMAX = 10

REVBK

- for report type 1 only. Used to generate summaries after each rev
- 0 - NO (default value)
- 1 - YES

INCEXC

- include or exclude 1 to 4 platforms
- 0 - include (default value)
- 1 - exclude

PLTID(1)/PLTID(4)/PLTID(7)/PLTID(10)

- 18 characters max each. Platform ID's to be included or excluded depending on the value of INCEXC.

REVL

- list of 1 to 10 rev numbers to be used in the report, or input 0 to use all revs. (default value = 0)

7.2

BIN REPORT

To do a Bin Report, follow this sample runstream:

@USE 70., MSGDR	
@ASG,A 70	
@CAT,P PRINT-FILE.	
@USE 101, PRINT-FILE.	In Demand Mode Only
@ASG,A 101.	
@XQT SEASAT-ADF*SURFACE.BINRPT-INC	Report stratified by incidence angles
or	
@XQT SEASAT-ADF*SURFACE.BINRPT-ZL	Report stratified by ZL
@FREE 101.	
@BLK,S PRINT-FILE.,BLD/BOX,SITE	Demand Mode Only

Appendix A. Sample Report Request Form

SASS STATISTICS REPORT

REQUEST

1. Report Type (1, 2 or 3) _____
2. Observation Type (1, 7 or 9) _____
1 - Spot OBS
7 - 15 Min. Average
9 - 60 Min. Average
3. Incidence Angle Range in Hundredths of a Degree
Minimum Incidence Angle _____ SCIMIN
Maximum Incidence Angle _____ SCIMAX
4. Maximum Distance Between S/T and S/C Observations in km
Maximum Distance _____
5. ZL Range. The Z/L Code is
(1, 2, 3) - Unstable
(4 and 5) - Neutral
(6, 7, 8, 9, 0) - Stable
MINZLCODE _____
MAXZLCODE _____
6. List of From 1 to 10 Rev. # or All Rev.
Rev. List _____

7. Platform List To Be Included or Excluded,
1 to 4 Names
Include or Exclude _____
Platform _____, _____, _____, _____
8. Break Statistics Report on Change of Rev. #
Rev. Break _____ (Yes/No)
Note - Only Used for Report Type One
9. Report Title (1 to 60 Characters)

10. Spacecraft Algorithm _____

APPENDIX B

SURFACE TRUTH RECORD FORMATS

B.1 HEADER RECORD FORMAT

FORMAT VARIABLE

312	SYSTEM SOFTWARE VERSION DATE (YYMMDD -PST)
312	SYSTEM SOFTWARE VERSION TIME (HHMMSS -PST)
A6	TAPE ID
A6	PROJECT ID
5X	FILL
I5	DATA RECORD PRODUCTION YEAR (PST)
I5	DATA RECORD PRODUCTION MONTH (PST)
1X	FILL
I1	RECORD TYPE
	0 - HEADER RECORD
1X	FILL
I4	DATA RECORD PRODUCTION DAY (PST)
I4	DATA RECORD PRODUCTION HOUR (PST)
I5	DATA RECORD PRODUCTION MINUTE (PST)
I4	DATA RECORD PRODUCTION SECOND (PST)
72X	FILL

B.2 SURFACE TRUTH DATA RECORD (STDR) FORMAT

FORMAT VARIABLE

```

312    SURFACE TRUTH OBSERVATION DATE (YYMMDD - GMT)
312    SURFACE TRUTH OBSERVATION TIME (HHMMSS - GMT)
A16    PLATFORM ID
11     PLATFORM TYPE
        1 - BUOY DATA
        2 - SHIP DATA
        3 - OSU 83/B4
        4 - RADIOSONDE
        5 - AUTOLOG
15     LATITUDE (.01 DEG)
15     LONGITUDE (EAST) (.01 DEG)
11     OBSERVATION TYPE
        1 - WIND SPEED AND DIRECTION
        2 - SEA SURFACE TEMPERATURE AND WIND SPEED
        3 - ATMOSPHERIC WATER VAPOR
        4 - ATMOSPHERIC LIQUID WATER
        5 - RAIN RATE
        6 - WAVE HEIGHT AND WIND SPEED
        7 - 15 MINUTE AVERAGE WIND SPEED AND DIRECTION
        8 - 30 MINUTE AVERAGE WIND SPEED AND DIRECTION
        9 - 60 MINUTE AVERAGE WIND SPEED AND DIRECTION
11     RECORD TYPE
        1 - SPOT OBSERVATION (STDR)
1X     FILL
        OBSERVATION TYPE 1
14     WIND SPEED MEASURED (.01 METER/SEC)
14     WIND SPEED AT 19.5 METERS (.01 METER/SEC)
15     WIND DIRECTION (.1 DEGREES FROM TRUE NORTH)
21X    FILL
12     Z/L (SEE STATE TABLE)
10X    FILL
15     L (1. METERS)
15     U* (.01 METER/SEC)
34X    FILL
        OBSERVATION TYPE 2
4X     FILL
14     WIND SPEED AT 19.5 METERS (.01 METER/SEC)
15     SEA SURFACE TEMPERATURE (.01 DEG C)
77X    FILL
        OBSERVATION TYPE 3
4X     FILL
4X     FILL
15     ATMOSPHERIC WATER VAPOR (.001 GRAM/CM2)
13X    FILL
14     TOP OF FLIGHT LEVEL (MILLIBAR)
16X    FILL
15     TOTAL ATMOSPHERIC WATER VAPOR AT 500 MB (.001 GRAM/CM2)
39X    FILL

```

OBSERVATION TYPE 4
 4X FILL
 4X FILL
 15 ATMOSPHERIC LIQUID WATER (.001 GRAM/CM2)
 77X FILL
 OBSERVATION TYPE 5
 4X FILL
 4X FILL
 15 RAIN RATE (.1 MM/HR)
 77X FILL
 OBSERVATION TYPE 6
 4X FILL
 14 WIND SPEED AT 19.5 METERS (.01 METER/SEC)
 15 WAVE HEIGHT (.01 METER)
 77X FILL
 OBSERVATION TYPE 7, 8, 9
 14 WIND SPEED MEASURED (.01 METER/SEC)
 14 WIND SPEED AT 19.5 METER (.01 METER/SEC)
 15 WIND DIRECTION (.1 DEGREES FROM TRUE NORTH)
 21X FILL
 12 Z/L (SEE STATE TABLE)
 10X FILL
 15 L (1. METER)
 15 U* (.01 METER/SEC)
 14 STANDARD DEVIATION OF WIND SPEED (.01 METER/SEC)
 14 STANDARD DEVIATION OF WIND DIRECTION (.1 DEGREES FROM TRUE NORTH)
 26X FILL

B.3 EDITED SURFACE TRUTH DATA RECORD (ESTDR) SPOT FORMAT

FORMAT VARIABLE

```

312    SURFACE TRUTH OBSERVATION DATE (YYMMDD - GMT)
312    SURFACE TRUTH OBSERVATION TIME (HHMMSS - GMT)
A16    PLATFORM ID
11     PLATFORM TYPE
        1 - BUOY DATA
        2 - SHIP DATA
        3 - OSU B3/B4
        4 - RADIOSONDE
        5 - AUTOLOG
15     LATITUDE (.01 DEG)
15     LONGITUDE (EAST) (.01 DEG)
11     OBSERVATION TYPE
        1 - WIND SPEED AND DIRECTION
        2 - SEA SURFACE TEMPERATURE AND WIND SPEED
        3 - ATMOSPHERIC WATER VAPOR
        4 - ATMOSPHERIC LIQUID WATER
        5 - RAIN RATE
        6 - WAVE HEIGHT AND WIND SPEED
11     RECORD TYPE
        2 - EDITED SPOT OBSERVATION (ESTDR)
1X     FILL
OBSERVATION TYPE 1
14     WIND SPEED MEASURED (.01 METER/SEC)
14     WIND SPEED AT 19.5 METERS (.01 METER/SEC)
15     WIND DIRECTION (.1 DEGREES FROM TRUE NORTH)
14     S/C PASS NUMBER
14     DISTANCE FROM GROUND TRACK (KM)
15     TIME DELTA FROM OBSERVATION TIME (.1 MINUTES) (WITH SIGN)
8X     FILL
12     Z/L (SEE STATE TABLE)
10X    FILL
15     L (1. METERS)
15     U* (.01 METER/SEC)
34X    FILL
OBSERVATION TYPE 2
4X     FILL
14     WIND SPEED AT 19.5 METERS (.01 METER/SEC)
15     SEA SURFACE TEMPERATURE (.01 DEG C)
14     S/C PASS NUMBER
14     DISTANCE FROM GROUND TRACK (KM)
15     TIME DELTA FROM OBSERVATION TIME (.1 MINUTES) (WITH SIGN)
OBSERVATION TYPE 3
4X     FILL
4X     FILL
15     ATMOSPHERIC WATER VAPOR (.001 GRAM/CM2)
14     S/C PASS NUMBER

```

14 DISTANCE FROM GROUND TRACK (KM)
 15 TIME DELTA FROM OBSERVATION TIME (.1 MINUTES) (WITH SIGN)
 14 TOP OF FLIGHT LEVEL (MILLIBAR)
 16X FILL
 15 TOTAL ATMOSPHERIC WATER VAPOR AT 500 MB (.001 GRAM/CM2)
 39X FILL
 OBSERVATION TYPE 4
 4X FILL
 4X FILL
 15 ATMOSPHERIC LIQUID WATER (.001 GRAM/CM2)
 14 S/C PASS NUMBER

 14 DISTANCE FROM GROUND TRACK (KM)
 15 TIME DELTA FROM OBSERVATION TIME (.1 MINUTES) (WITH SIGN)
 64X FILL
 OBSERVATION TYPE 5
 4X FILL
 4X FILL
 15 RAIN RATE (.1 MM/HR)
 14 S/C PASS NUMBER
 14 DISTANCE FROM GROUND TRACK (KM)
 15 TIME DELTA FROM OBSERVATION TIME (.1 MINUTES) (WITH SIGN)
 64X FILL
 OBSERVATION TYPE 6
 4X FILL
 14 WIND SPEED AT 19.5 METERS (.01 METER/SEC)
 15 WAVE HEIGHT (.01 METER)
 14 S/C PASS NUMBER
 14 DISTANCE FROM GROUND TRACK (KM)
 15 TIME DELTA FROM OBSERVATION TIME (.1 MINUTES) (WITH SIGN)
 64X FILL

B.4 EDITED SURFACE TRUTH DATA RECORD (ESTDR) INTERPOLATED SPOT FORMAT

FORMAT VARIABLE

```

312 SURFACE TRUTH OBSERVATION DATE (YYMMDD - GMT)
312 SURFACE TRUTH OBSERVATION TIME (HHMMSS - GMT)
A16 PLATFORM ID
11 PLATFORM TYPE
    1 - BUOY DATA
    2 - SHIP DATA
    3 - OSU B3/B4
    4 - RADIOSONDE
    5 - AUTOLOG
15 LATITUDE (.01 DEG)
15 LONGITUDE (EAST) (.01 DEG)
11 OBSERVATION TYPE
    1 - WIND SPEED AND DIRECTION
    2 - SEA SURFACE TEMPERATURE AND WIND SPEED
    3 - ATMOSPHERIC WATER VAPOR
    4 - ATMOSPHERIC LIQUID WATER
    5 - RAIN RATE
    6 - WAVE HEIGHT AND WIND SPEED
11 RECORD TYPE
    3 - INTERPOLATED SPOT OBSERVATION (ESTDR)
1X  FILL
OBSERVATION TYPE 1
14 INTERPOLATED WIND SPEED MEASURED (.01 METER/SEC)
14 INTERPOLATED WIND SPEED AT 19.5 METERS (.01 METER/SEC)
15 INTERPOLATED WIND DIRECTION (.1 DEGREES FROM TRUE NORTH)
14 S/C PASS NUMBER
14 DISTANCE FROM GROUND TRACK (KM)
    DIFFERENCE BETWEEN OBSERVED VALUES
    AT ENDS OF INTERPOLATED INTERVAL:
15 WIND SPEED MEASURED (.01 METER/SEC)
15 WIND SPEED AT 19.5 METER (.01 METER/SEC)
15 WIND DIRECTION (.1 DEGREES FROM TRUE NORTH)
12 INTERPOLATED Z/L (SEE STATE TABLE)
10X FILL
15 INTERPOLATED L (1. METERS)
15 INTERPOLATED U* (.01 METER/SEC)
    DIFFERENCE BETWEEN OBSERVED VALUES
    AT ENDS OF INTERPOLATED INTERVAL:
15 L (METER)
15 U* (.01 METER/SEC)
15 Z/L (ROUNDED TO NEAREST INTEGER)
21X FILL

```

OBSERVATION TYPE 2

4X FILL

14 INTERPOLATED WIND SPEED AT 19.5 METERS (.01 METER/SEC)

15 INTERPOLATED SEA SURFACE TEMPERATURE (.01 DEG C)

14 S/C PASS NUMBER

14 DISTANCE FROM GROUND TRACK (KM)

DIFFERENCE BETWEEN OBSERVED VALUES

AT ENDS OF INTERPOLATED INTERVAL:

5X FILL

14 WIND SPEED AT 19.5 METER (.01 METER/SEC)

14 SEA SURFACE TEMPERATURE (.01 DEG C)

56X FILL

OBSERVATION TYPE 3

4X FILL

4X FILL

15 INTERPOLATED ATMOSPHERIC WATER VAPOR (.001 GRAM/CM2)

14 S/C PASS NUMBER

14 DISTANCE FROM GROUND TRACK (KM)

5X FILL

14 INTERPOLATED TOP OF FLIGHT LEVEL (MILLIBAR)

DIFFERENCE BETWEEN OBSERVED VALUES

AT ENDS OF INTERPOLATED INTERVAL:

16X FILL

15 TOTAL ATMOSPHERIC WATER VAPOR AT 500 MB

DIFFERENCE BETWEEN OBSERVED VALUES

AT ENDS OF INTERPOLATED INTERVAL:

10X FILL

15 TOP OF FLIGHT LEVEL

15 WATER VAPOR AT 500 MB

19X FILL

OBSERVATION TYPE 4

4X FILL

4X FILL

15 INTERPOLATED ATMOSPHERIC LIQUID WATER (.001 GRAM/CM2)

14 S/C PASS NUMBER

14 DISTANCE FROM GROUND TRACK (KM)

9X FILL

DIFFERENCE BETWEEN OBSERVED VALUES

AT ENDS OF INTERPOLATED INTERVAL:

14 ATMOSPHERIC LIQUID WATER

56X FILL

OBSERVATION TYPE 5

4X FILL

4X FILL

15 INTERPOLATED RAIN RATE (.1 MM/HR)

14 S/C PASS NUMBER

14 DISTANCE FROM GROUND TRACK (KM)

9X FILL

DIFFERENCE BETWEEN OBSERVED VALUES

AT ENDS OF INTERPOLATED INTERVAL:

14 RAIN RATE (.1 MM/HR)

56X FILL

OBSERVATION TYPE 6

4X FILL
14 INTERPOLATED WIND SPEED AT 19.5 METERS (.01 METER/SEC)
15 INTERPOLATED WAVE HEIGHT (.01 METER)
14 S/C PASS NUMBER
14 DISTANCE FROM GROUND TRACK (KM)
 DIFFERENCE BETWEEN OBSERVED VALUES
 AT ENDS OF INTERPOLATED INTERVAL:
5X FILL
14 WIND SPEED AT 19.5 METER (.01 METER/SEC)
14 WAVE HEIGHT (.01 METER)
56X FILL

B.5 EDITED SURFACE TRUTH DATA RECORD (ESTDR) AVERAGE WIND FORMAT

FORMAT VARIABLE

312 SURFACE TRUTH OBSERVATION DATE (YYMMDD - GMT)
 312 SURFACE TRUTH OBSERVATION TIME (HHMMSS - GMT)
 A16 PLATFORM ID
 11 PLATFORM TYPE
 1 - BUOY DATA
 2 - SHIP DATA
 3 - OSU 83/84
 4 - RADIOSONDE
 5 - AUTOLOG
 15 LATITUDE (.01 DEG)
 15 LONGITUDE (EAST) (.01 DEG)
 11 OBSERVATION TYPE
 7 - 15 MINUTE AVERAGE WIND SPEED AND DIRECTION
 8 - 30 MINUTE AVERAGE WIND SPEED AND DIRECTION
 9 - 60 MINUTE AVERAGE WIND SPEED AND DIRECTION
 11 RECORD TYPE
 4 - AVERAGE WIND OBSERVATION (ESTDR)
 1X FILL
 OBSERVATION TYPES 7, 8, and 9
 14 WIND SPEED MEASURED (.01 METER/SEC)
 14 WIND SPEED AT 19.5 METERS (.01 METER/SEC)
 15 WIND DIRECTION (.1 DEGREES FROM TRUE NORTH)
 14 S/C PASS NUMBER
 14 DISTANCE FROM GROUND TRACK (KM)
 15 TIME DELTA FROM OBSERVATION TIME (.1 MINUTES) (WITH SIGN)
 8X FILL
 12 Z/L (SEE STATE TABLE)
 10X FILL
 15 L (1. METERS)
 15 U* (.01 METER/SEC)
 14 STANDARD DEVIATION FOR WIND SPEED (.01 METER/SEC)
 14 STANDARD DEVIATION FOR WIND DIRECTION (.1 DEGREES)
 26X FILL

B.6 EDITED SURFACE TRUTH DATA RECORD (ESTDR) BUILD FORMAT

FORMAT VARIABLE

```

15    LATITUDE (.01 DEG)
15    LONGITUDE (EAST) (.01 DEG)
312   SURFACE TRUTH OBSERVATION DATE (YYMMDD = GMT)
312   SURFACE TRUTH OBSERVATION TIME (HHMMSS = GMT)
11    OBSERVATION TYPE
      1 = WIND SPEED AND DIRECTION
      2 = SEA SURFACE TEMPERATURE AND WIND SPEED
      3 = ATMOSPHERIC WATER VAPOR
      4 = ATMOSPHERIC LIQUID WATER
      5 = RAIN RATE
      6 = WAVE HEIGHT AND WIND SPEED
      7 = 15 MINUTE AVERAGE WIND SPEED AND DIRECTION
      8 = 30 MINUTE AVERAGE WIND SPEED AND DIRECTION
      9 = 60 MINUTE AVERAGE WIND SPEED AND DIRECTION
A16   PLATFORM ID
11    PLATFORM TYPE
      1 = BUOY DATA
      2 = SHIP DATA
      3 = OSU B3/B4
      4 = RADIOSONDE
      5 = AUTOLOG
11    RECORD TYPE
      2 = EDITED SPOT OBSERVATION (ESTDR)
      3 = INTERPOLATED SPOT OBSERVATION (ESTDR)
      4 = AVERAGE WIND OBSERVATION (ESTDR)
1X    FILL
      OBSERVATION TYPES 1, 7, 8, and 9
14    WIND SPEED MEASURED (.01 METER/SEC)
14    WIND SPEED AT 19.5 METERS (.01 METER/SEC)
15    WIND DIRECTION (.1 DEGREES FROM TRUE NORTH)
14    S/C PASS NUMBER
14    DISTANCE FROM GROUND TRACK (KM)
15    TIME DELTA FROM OBSERVATION TIME (.1 MINUTES) (WITH SIGN)
8X    FILL
12    Z/L (SEE STATE TABLE)
10X   FILL
15    L (1. METERS)
15    U* (.01 METER/SEC)
34X   FILL
      OBSERVATION TYPE 2
4X    FILL
14    WIND SPEED AT 19.5 METERS (.01 METER/SEC)
15    SEA SURFACE TEMPERATURE (.01 DEG C)
14    S/C PASS NUMBER
14    DISTANCE FROM GROUND TRACK (KM)
15    TIME DELTA FROM OBSERVATION TIME (.1 MINUTES) (WITH SIGN)
      OBSERVATION TYPE 3
4X    FILL

```

4X FILL
 I5 ATMOSPHERIC WATER VAPOR (.001 GRAM/CM2)
 I4 S/C PASS NUMBER
 I4 DISTANCE FROM GROUND TRACK (KM)
 I5 TIME DELTA FROM OBSERVATION TIME (.1 MINUTES) (WITH SIGN)
 I4 TOP OF FLIGHT LEVEL (MILLIBAR)
 16X FILL
 I5 TOTAL ATMOSPHERIC WATER VAPOR AT 500 MB (.001 GRAM/CM2)
 39X FILL
 OBSERVATION TYPE 4
 4X FILL
 4X FILL
 I5 ATMOSPHERIC LIQUID WATER (.001 GRAM/CM2)
 I4 S/C PASS NUMBER
 I4 DISTANCE FROM GROUND TRACK (KM)
 I5 TIME DELTA FROM OBSERVATION TIME (.1 MINUTES) (WITH SIGN)
 64X FILL
 OBSERVATION TYPE 5
 4X FILL
 4X FILL
 I5 RAIN RATE (.1 MM/HR)
 I4 S/C PASS NUMBER
 I4 DISTANCE FROM GROUND TRACK (KM)
 I5 TIME DELTA FROM OBSERVATION TIME (.1 MINUTES) (WITH SIGN)
 64X FILL
 OBSERVATION TYPE 6
 4X FILL
 I4 WIND SPEED AT 19.5 METERS (.01 METER/SEC)
 I5 WAVE HEIGHT (.01 METER)
 I4 S/C PASS NUMBER
 I4 DISTANCE FROM GROUND TRACK (KM)
 I5 TIME DELTA FROM OBSERVATION TIME (.1 MINUTES) (WITH SIGN)
 64X FILL

B.7 MERGED SURFACE TRUTH DATA RECORD (MSGDR) FORMAT

FORMAT VARIABLE

```

312    SURFACE TRUTH OBSERVATION DATE (YYMMDD - GMT)
312    SURFACE TRUTH OBSERVATION TIME (HHMMSS - GMT)
A16    PLATFORM ID
11     PLATFORM TYPE
        1 - BUOY DATA
        2 - SHIP DATA
        3 - OSU B3/B4
        4 - RADIOSONDE
        5 - AUTOLOG
15     LATITUDE (.01 DEG)
15     LONGITUDE (EAST) (.01 DEG)
11     OBSERVATION TYPE
        1 - WIND SPEED AND DIRECTION
        2 - SEA SURFACE TEMPERATURE AND WIND SPEED
        3 - ATMOSPHERIC WATER VAPOR
        4 - ATMOSPHERIC LIQUID WATER
        5 - RAIN RATE
        6 - WAVE HEIGHT AND WIND SPEED
        7 - 15 MINUTE AVERAGE WIND SPEED AND DIRECTION
        8 - 30 MINUTE AVERAGE WIND SPEED AND DIRECTION
        9 - 60 MINUTE AVERAGE WIND SPEED AND DIRECTION
11     RECORD TYPE
        5 - MERGED ALT OBSERVATION (MSGDR)
        6 - MERGED SASS OBSERVATION (MSGDR)
        7 - MERGED SMMR G1 OBSERVATION (MSGDR)
        8 - MERGED SMMR G2 OBSERVATION (MSGDR)
        9 - MERGED SMMR G3 OBSERVATION (MSGDR)
1X     FILL
OBSERVATION TYPE 1, 7, 8, 9
14     WIND SPEED MEASURED (.01 METER/SEC)
14     WIND SPEED AT 19.5 METERS (.01 METER/SEC)
15     WIND DIRECTION (.1 DEGREES FROM TRUE NORTH)
OBSERVATION TYPE 2
4X     FILL
14     WIND SPEED AT 19.5 METERS (.01 METER/SEC)
15     SEA SURFACE TEMPERATURE (.01 DEG C)
OBSERVATION TYPE 3
4X     FILL
4X     FILL
15     ATMOSPHERIC WATER VAPOR (.001 GRAM/CM2)
OBSERVATION TYPE 4
4X     FILL
4X     FILL
15     ATMOSPHERIC LIQUID WATER (.001 GRAM/CM2)
OBSERVATION TYPE 5
4X     FILL
4X     FILL
15     RAIN RATE (.1 MM/HR)
OBSERVATION TYPE 6

```

4X FILL
 14 WIND SPEED AT 19.5 METERS (.01 METER/SEC)
 15 WAVE HEIGHT (.01 METER)
 FOR ALL OBSERVATION TYPES
 14 S/C PASS NUMBER
 9X FILL
 14 Z/L (SEE STATE TABLE)
 14 SOURCE (FROM PREVIOUS RECORD TYPE)
 312 SPACECRAFT OBSERVATION DATE (YYMMDD - GMT)
 312 SPACECRAFT OBSERVATION TIME (HHMMSS - GMT)
 15 LATITUDE (.01 DEG)
 15 LONGITUDE (EAST) (.01 DEG)
 OBSERVATION TYPE 1, 7, 8, 9
 14 INCIDENCE ANGLE (.01 DEG)
 14 WIND SPEED AT 19.5 METERS (.01 METER/SEC)
 15 WIND DIRECTION (.1 DEGREES FROM TRUE NORTH)
 OBSERVATION TYPE 2
 4X FILL
 14 WIND SPEED AT 19.5 METERS (.01 METER/SEC)
 15 SEA SURFACE TEMPERATURE (.01 DEG C)
 OBSERVATION TYPE 3
 4X FILL
 4X FILL
 15 ATMOSPHERIC WATER VAPOR (.001 GRAM/CM2)
 OBSERVATION TYPE 4
 4X FILL
 4X FILL
 15 ATMOSPHERIC LIQUID WATER (.001 GRAM/CM2)
 OBSERVATION TYPE 5
 4X FILL
 4X FILL
 15 RAIN RATE (.1 MM/HR)
 OBSERVATION TYPE 6
 4X FILL
 14 WIND SPEED AT 19.5 METERS (.01 METER/SEC)
 15 WAVE HEIGHT (.01 METER)
 FOR ALL OBSERVATION TYPES
 14 TIME DIFFERENCE (.1 MIN)
 14 DISTANCE DIFFERENCE (1. KM)
 13X FILL

End of Document